



Libraries and Learning Services

# University of Auckland Research Repository, ResearchSpace

## Copyright Statement

The digital copy of this thesis is protected by the Copyright Act 1994 (New Zealand).

This thesis may be consulted by you, provided you comply with the provisions of the Act and the following conditions of use:

- Any use you make of these documents or images must be for research or private study purposes only, and you may not make them available to any other person.
- Authors control the copyright of their thesis. You will recognize the author's right to be identified as the author of this thesis, and due acknowledgement will be made to the author where appropriate.
- You will obtain the author's permission before publishing any material from their thesis.

## General copyright and disclaimer

In addition to the above conditions, authors give their consent for the digital copy of their work to be used subject to the conditions specified on the [Library Thesis Consent Form](#) and [Deposit Licence](#).

ROBERT C. PICKLE

NATURE AND POTENTIAL ORIGINS OF THE LOW-RATE  
TECTONICS OF THE HAURAKI RIFT AND NORTH-WESTERN NEW  
ZEALAND: A GEOPHYSICAL INVESTIGATION

NATURE AND POTENTIAL ORIGINS OF THE LOW-RATE  
TECTONICS OF THE HAURAKI RIFT AND NORTH-WESTERN NEW  
ZEALAND: A GEOPHYSICAL INVESTIGATION

ROBERT C. PICKLE

A thesis submitted in fulfilment of the requirements for the degree of Doctorate of  
Philosophy in Geology, the University of Auckland.

March 2019

Robert C. Pickle: *Nature and Potential Origins of the Low-Rate Tectonics of The Hauraki Rift and North-Western New Zealand: A Geophysical Investigation*, A thesis submitted in fulfilment of the requirements for the degree of Doctorate of Philosophy in Geology, the University of Auckland., © March 2019

**SUPERVISORS:**

Jennifer D. Eccles

Sigrun Hreinsdottir

Julie Rowland

AUCKLAND, NEW ZEALAND

MARCH 2019

To RGP, JLP, and KJIVHKB for their unwavering support

## ABSTRACT

---

Little is known about the nature or origin of tectonic activity throughout north-western New Zealand, beyond that it is a stable environment (velocities  $\sim 1 \text{ mm/yr}$  relative to Australia) and home to the Hauraki Rift, N-S trending, 250+  $\text{km}$  long and 25  $\text{km}$  wide on-shore/off-shore continental rift 40  $\text{km}$  east of Auckland City and oblique to the Hikurangi subduction margin. A three-year 40+ station campaign GNSS geodetic survey was done incorporating previously unused historic data to constrain the crustal motion throughout the north-western North Island and the Hauraki Rift. A screw dislocation rift model incorporating this data derived estimates for the far-field widening rate and mechanical thickness of the Hauraki Rift to be  $1.15 +/- 0.3 \text{ mm/yr}$  and  $17.5 +/- 7.7 \text{ km}$  respectively. Relative to a fixed Australian Plate reference frame, the results generally showed S-SE velocities east of the Hauraki Rift and W-SW velocities west of the rift with increasing magnitudes to the south towards the plate boundary. North of Auckland ( $\sim 37^\circ\text{S}$ ) sites maintained consistent W-SW velocity magnitudes throughout, over 700  $\text{km}$  from the plate boundary. This indicates that northernmost New Zealand may not be stable relative to the Australian Plate. Analysis of ground and satellite-based gravity anomalies in conjunction with the observation of geodetic velocity discrepancies were used to infer the location and motion of several faults not currently considered active, including N-S trending faults parallel to the west coast of New Zealand near Auckland. The observation of similar cGNSS geodetic velocities on both Norfolk Island and New Caledonia similar to those observed throughout Northland NZ may be evidence that the eastern portion of the Australian tectonic plate (east of Lord Howe Island) is mechanically separated. A Oligocene-Miocene tectonic model detailing the westward collision of the Loyalty-Three Kings arc and subsequent opening of the Norfolk Basin is presented. This model proposes that the relative motion between the Australian and "East Australian" sub-plate may be accommodated by a continuous  $\sim 2000 \text{ km}$  lineament of weakened crust, low Bouguer Anomalies, and concentrated volcanism. This feature may extend from New Caledonia along the western Norfolk Ridge through the Reinga Basin and along the western coast of the North Island of New Zealand.



## ACKNOWLEDGEMENTS

---

Aside from those this work is dedicated to I must thank my advisers Sigrun, JR, and most of all Jen. I would also like to thank Neville Palmer and GNS Science for surveying advice, assistance, and the use of their equipment, Jerome Salichon at GNS for help with SeisComP3 and GeoNet's seismic systems, and the gracious people throughout New Zealand who allowed me access to geodetic markers on their land or let me install a seismometer in their garden.

Nearly all software used in this project is freely available and open source, and this work could not have been done without it. Primarily I acknowledge the team at MIT behind GAMIT/GLOBK, and also those responsible for Generic Mapping Tools and SeisComP3. The scientific python packages SciPy and NumPy were also instrumental throughout, as well as the seismological package ObsPy and figure plotting package Matplotlib. All work was done on a modest but perpetually-running 8x 3Ghz Linux workstation and this thesis was compiled and written using LyX and LibreOffice.



## CONTENTS

---

<b>1 INTRODUCTION</b>	<b>1</b>
1.1 Aims . . . . .	2
1.2 Thesis Structure . . . . .	4
<b>2 STRUCTURE, EVOLUTION, AND KNOWN ACTIVITY OF NORTH-EASTERN ZEALANDIA</b>	<b>5</b>
2.1 The Geologic Fabric of Zealandia . . . . .	5
2.2 Tectonic History of NE Zealandia <50 Ma . . . . .	11
2.2.1 South-West or North-East Dipping Subduction? . . . . .	14
2.2.2 Arc Collision, Obduction, and Volcanism (45-23 Ma) . . . . .	15
2.2.3 Widening of Norfolk Basin (23-15 Ma) . . . . .	18
2.2.4 The Modern Hikurangi Margin Regime (15-0 Ma) . . . . .	19
2.3 Current Activity . . . . .	20
2.3.1 The Active Hauraki Rift and Wairoa North Fault . . . . .	20
2.3.2 The (Inactive?) Waikato Fault . . . . .	22
2.3.3 GNSS Geodesy 1995-2013 . . . . .	23
2.3.4 GeoNet's Seismic Catalogue of Shallow Events . . . . .	25
<b>3 POTENTIAL FIELD DATASETS &amp; INTERPRETATION STRATEGIES</b>	<b>29</b>
3.1 Magnetic Anomalies . . . . .	29
3.2 Gravity Anomalies . . . . .	30
3.2.1 The Free Air Anomaly . . . . .	30
3.2.2 The Bouguer Anomaly . . . . .	30
3.2.3 Approximations and Interpretation Strategy . . . . .	31
3.3 Datasets . . . . .	38
3.4 North-East Zealandia . . . . .	39
3.5 North-West New Zealand . . . . .	44
3.5.1 Satellite Data . . . . .	44
3.5.2 Ground-based Data . . . . .	47
<b>4 GEODETIC ANALYSIS OF NORTH-WESTERN NEW ZEALAND</b>	<b>57</b>
4.1 Introduction to Geodetic GNSS Surveying and Processing . . . . .	58

4.2	Continuous Station Geodesy . . . . .	59
4.2.1	New Zealand's Continuously Operating Reference Stations . . . . .	61
4.3	Campaign Geodesy . . . . .	63
4.3.1	Station Selection . . . . .	63
4.3.2	Field Deployment Considerations for a Low-Rate Environment . . . . .	64
4.3.3	Data Acquisition . . . . .	69
4.4	GNSS Processing with GAMIT/GLOBK . . . . .	72
4.4.1	Reference Station Selection . . . . .	72
4.4.2	Solving for Position (GAMIT) . . . . .	74
4.4.3	TimeSeries . . . . .	77
4.4.4	Solving for Velocity (GLOBK) . . . . .	78
4.4.5	Creating a Noise Model . . . . .	82
4.4.6	Processing Flow . . . . .	90
4.5	Crustal Response to Earthquakes and Slow Slip Events . . . . .	91
4.5.1	Coseismic Estimation Method . . . . .	92
4.5.2	23 December 2004 M8.1 Macquarie Island Earthquake . . . . .	93
4.5.3	13 November 2016 M7.8 Kaikōura Earthquake . . . . .	95
4.6	A New Australian Reference Frame . . . . .	98
4.7	Velocity Estimates . . . . .	103
4.8	Strain Rate Estimates . . . . .	107
5	<b>SEISMICITY OF NORTH-WESTERN NEW ZEALAND</b>	113
5.1	New Zealand Earthquake Monitoring and Archiving: GeoNet . . . . .	113
5.2	Earthquake Location Method . . . . .	114
5.2.1	New Zealand Velocity Models . . . . .	115
5.2.2	Event Detection and Wave Picking . . . . .	115
5.3	Review and Relocation of Historic Data . . . . .	120
5.3.1	1D to 3D Relocation of Historical Events from the GeoNet Catalogue 2006-2011 . . . . .	121
5.3.2	1D to 3D Relocation and Manual Review of Historical Events from the GeoNet Catalogue 2006-2017 . . . . .	123
5.4	Locating New Events During 2017 . . . . .	127
5.4.1	Original GeoNet Data . . . . .	127

5.4.2	Location of New Events 2017 . . . . .	131
5.5	Manual Review of 2017 events . . . . .	147
5.6	Addition and Utility of Station HR1 . . . . .	151
6	<b>DISCUSSION</b>	155
6.1	Interpretation of North-Western New Zealand Structure . . . . .	155
6.1.1	Fault Location via Ground Station Gravity . . . . .	159
6.2	Overview of North-Western New Zealand's Activity . . . . .	162
6.2.1	Is Plate Boundary Strain Driving the Hauraki Rift? . . . . .	168
6.2.2	Vertical Deformation Estimates . . . . .	169
6.3	Evidence for New Active Faults . . . . .	173
6.3.1	Greater Auckland Region . . . . .	173
6.3.2	Greater Taranaki Region . . . . .	176
6.4	Hauraki Rift Modelling . . . . .	179
6.4.1	Relationship to the Auckland Volcanic Field . . . . .	183
6.5	Why is Northland NZ Fast Relative to Australia? . . . . .	184
6.5.1	Anomalous Fast Velocities In the Eastern Australian Plate . . . . .	186
6.5.2	Tectonic Interpretation of NE Zealandia . . . . .	188
6.5.3	A Unifying Norfolk Ridge and Northland Model 30-15 Ma . . . . .	204
6.6	Evidence for Nonlinear Crustal Motion in NWNZ . . . . .	207
6.7	Reflections and Future Work . . . . .	211
6.7.1	In New Zealand . . . . .	211
6.7.2	In Zealandia . . . . .	214
7	<b>CONCLUSIONS</b>	217
A	<b>APPENDIX</b>	221
A.1	Shoreline Discontinuity of Satellite Gravity Data? . . . . .	221
A.2	NZ cGNSS Site TRNG / Tauranga . . . . .	222
A.3	Link Between Time-Dependent Noise and Plate Locking? . . . . .	224
A.4	Timeseries . . . . .	226
A.5	Equipment and Survey Technique . . . . .	232
A.6	Campaign Occupation Data . . . . .	233
A.7	GAMIT/GLOBK Parameters . . . . .	237
A.7.1	A Priori (APR) File . . . . .	237

A.7.2 EQ Files . . . . .	238
A.7.3 Command Files . . . . .	246
A.8 NonLinLoc Parameters . . . . .	251
A.9 SeisComP3 Parameters . . . . .	251
BIBLIOGRAPHY	259

## LIST OF FIGURES

---

Figure 2.1	Extent of Zealandia . . . . .	6
Figure 2.2	Bathymetry and features of north-east Zealandia and the east Australian Plate (part 1/2) . . . . .	7
Figure 2.3	Bathymetry and features of north-east Zealandia and the east Australian Plate (part 2/2) . . . . .	8
Figure 2.4	A stylised cross section of Zealandia . . . . .	9
Figure 2.5	Basement terranes of New Zealand (GNS Science) . . . . .	10
Figure 2.6	W-SW dipping South Fiji Basin tectonic model from Mortimer et al. (2007) . . . . .	13
Figure 2.7	NE-dipping South Fiji Basin tectonic model from Schellart (2007) . . . . .	14
Figure 2.8	Dredged rock samples and dates collected from Mortimer et al. (1998, 2007, 2018) . . . . .	17
Figure 2.9	Known faults within the greater Auckland / Hauraki Rift region . . . . .	21
Figure 2.10	Hauraki Rift velocity model 1995-2013 . . . . .	25
Figure 2.11	Seismicity from Jan 1 2006 to Dec 31 2017 up to 50 km depth, catalogued by GeoNet . . . . .	27
Figure 3.1	Flexural support chart for $T_e$ vs. load width . . . . .	34
Figure 3.2	Satellite Free Air anomaly (NE Zealandia) . . . . .	41
Figure 3.3	Satellite Bouguer anomaly (NE Zealandia) . . . . .	42
Figure 3.4	EMAG2 satellite magnetic data (NE Zealandia) . . . . .	43
Figure 3.5	Satellite Free Air Gravity anomaly (North Island, NZ) . . . . .	45
Figure 3.6	Satellite Bouguer anomaly (North Island, NZ) . . . . .	46
Figure 3.7	Ground station derived Free Air anomaly of the North Island, NZ . . . . .	48
Figure 3.8	Ground station Bouguer anomaly of NWNZ from the NZ Primary Gravity Network . . . . .	50
Figure 3.9	Ground station Bouguer anomaly of NWNZ, derived by this project . . . . .	51
Figure 3.10	At-sea Hauraki Gulf Bouguer Gravity anomaly . . . . .	52
Figure 3.11	Airborne Free Air anomaly collected by McCubbine et al. 2017 . . . . .	54
Figure 4.1	Age range of New Zealand cGNSS station network . . . . .	60

Figure 4.2	New Zealand Continuously Operating Reference Stations . . . . .	62
Figure 4.3	Map of all campaign stations surveyed 2015-2017 . . . . .	64
Figure 4.4	Seasonal effects at cGNSS station AUKT vs. KTIA . . . . .	66
Figure 4.5	Campaign data for station A934 (courtesy of GNS Science / Beavan et al. 2016). Without the 4th survey in 2015 it is difficult to isolate 2005 as an outlier occupation. . . . .	67
Figure 4.6	Day to day scatter due to weather phenomena at station A2L2 . . . . .	68
Figure 4.7	Gantt chart of all geodetic campaign data used in this project 1995-2017 .	70
Figure 4.8	Gantt chart of newly acquired geodetic data 2015-2017 . . . . .	71
Figure 4.9	Global map of reference stations used in GAMIT/GLOBK . . . . .	74
Figure 4.10	Residual timeseries for NZ cGNSS site CHTI, Chatham Island . . . . .	81
Figure 4.11	2D spatial distribution of Random Walk noise estimates in the North Island	87
Figure 4.12	Mean Power Spectrum Density of aggregate vertical timeseries data . .	89
Figure 4.13	2004 Macquarie Island and 2016 Kaikōura Coseismic offsets . . . . .	94
Figure 4.14	Modelled Kaikōura coseismic offsets . . . . .	97
Figure 4.15	Comparison of various velocity estimates defining a fixed Australian Plate	100
Figure 4.16	Statistics of GNSS data used to define many of the cGNSS sites within the anomalous eastern Australian Plate periphery . . . . .	102
Figure 4.17	North-western New Zealand geodetic velocity estimates 1995-2018 . .	104
Figure 4.18	Auckland Area GNSS velocity vectors . . . . .	105
Figure 4.19	Western North Island GNSS velocity vectors . . . . .	106
Figure 4.20	Nationwide GNSS velocities of various cGNSS sites . . . . .	107
Figure 4.21	Interpolated velocities for a subset of GNSS velocity data . . . . .	109
Figure 4.22	Rotational $\dot{\omega}$ and dilational $\dot{\sigma}$ strain rates . . . . .	109
Figure 4.23	Maximum shear strain rate $\dot{\Gamma}$ . . . . .	110
Figure 4.24	Maximum shear strain rate $\dot{\Gamma}$ at the Taranaki Peninsula . . . . .	111
Figure 5.1	Example waveform with a corresponding STA/LTA ratio . . . . .	116
Figure 5.2	GeoNet Catalogue events Jan 1 2006 - Dec 31 2011 using the 1D NZ1DR velocity model . . . . .	118
Figure 5.3	GeoNet Catalogue events Jan 1 2012 - Dec 31 2017 using the 3D NZ3DX velocity model . . . . .	119
Figure 5.4	Number of events detected by GeoNet 1996-2017 . . . . .	120

Figure 5.5	GeoNet catalogue events 2006-2012 shallower than 50 km relocated 1D to 3D NZ3DRX velocity model . . . . .	122
Figure 5.6	Catalogue GeoNet 2000-2017 relocated from 1D to 3D (2000-2011) and 3D to 3D (2012-2017) . . . . .	124
Figure 5.7	North Island seismic station coverage showing the number of stations within a distance of 0.75 Degrees . . . . .	126
Figure 5.8	2017 GeoNet catalogue events < 50 km using all stations . . . . .	128
Figure 5.9	2017 found events <50 km depth with RBAZ and HR1, and without stations SE of TVZ . . . . .	130
Figure 5.10	Move out times of various P and S phases at a hypothetical event originating at 15 km depth . . . . .	132
Figure 5.11	Power Spectrum Density of background, events, and P-wave arrivals for $M < 2.5$ events in NWNZ . . . . .	133
Figure 5.12	STA/LTA results over a range of values and bandpass filters . . . . .	135
Figure 5.13	Example STA/LTA calculation on a waveform for a range of parameters and bandpass filters . . . . .	137
Figure 5.14	Hypocentre uncertainty vs. phase plots for this study and default GeoNet parameters . . . . .	141
Figure 5.15	2017 Events found using this study's parameters vs. GeoNet's default parameters . . . . .	142
Figure 5.16	Event statistics for NWNZ seismic stations . . . . .	144
Figure 5.17	Manually reviewed and supplemented events found in 2017 . . . . .	148
Figure 5.18	Hypocentre uncertainty vs. phase plots for the reviewed 2017 events in Figure 5.17 . . . . .	149
Figure 5.19	A M4.2 at 12 km depth detected east of Whangarei by GeoNet . . . . .	151
Figure 5.20	Photo of short period seismic station HR1 . . . . .	152
Figure 6.1	Numerical estimate of plate flexure in NWNZ . . . . .	156
Figure 6.2	Satellite Bouguer anomaly (NWNZ) . . . . .	157
Figure 6.3	Interpreted seismic reflection data across the Taranaki Basin . . . . .	159
Figure 6.4	Ground station Bouguer anomaly of NWNZ . . . . .	160
Figure 6.5	Geodetic velocities of the North Island 1995-2013 [Beavan et al., 2016]. . . . .	163
Figure 6.6	Nationwide geodetic velocities of various cGNSS sites . . . . .	164
Figure 6.7	Geodetic velocities throughout NWNZ . . . . .	165

Figure 6.8	Velocity estimates relative to KTIA . . . . .	167
Figure 6.9	Second invariant of the strain rate tensor, NWNZ . . . . .	169
Figure 6.10	Vertical velocity estimates at sites throughout north-western New Zealand	171
Figure 6.11	Geodetic vectors and faults circa the greater Hauraki Rift . . . . .	174
Figure 6.12	Seismicity around the Wairoa North Fault . . . . .	176
Figure 6.13	Velocities relative to station MAHO and NPLY . . . . .	178
Figure 6.14	Auckland area geodetic vectors and Hauraki Rift model fit . . . . .	181
Figure 6.15	Histogram of 78954 randomised screw model solutions . . . . .	182
Figure 6.16	Geodetic velocity estimates of cGNSS sites in NE Zealandia . . . . .	185
Figure 6.17	Geodetic velocity estimates throughout the Australian Plate . . . . .	187
Figure 6.18	Satellite Free Air Anomaly (NE Zealandia) . . . . .	189
Figure 6.19	Interpreted Satellite Bouguer anomaly (NE Zealandia) with lineaments marked . . . . .	190
Figure 6.20	Interpreted satellite magnetic data (NE Zealandia) . . . . .	191
Figure 6.21	3D bathymetry of NE Zealandia . . . . .	192
Figure 6.22	Shipboard magnetic data of New Caledonia and Loyalty Ridge region . .	195
Figure 6.23	Structure and volcanism within the Southern Norfolk Ridge System via Stagpoole et al. (2009) . . . . .	198
Figure 6.24	Multibeam bathymetry of the northern Norfolk Basin (FAUST-2) . . . .	202
Figure 6.25	Tectonic model of NE Zealandia 30-15 Ma . . . . .	205
Figure 6.26	Timeseries for Northland cGNSS station KTIA . . . . .	208
Figure 6.27	Geodetic distance between NZ cGNSS stations . . . . .	209
Figure 6.27	Geodetic distance between NZ cGNSS stations (part 2/2) . . . . .	210
Figure A.1	Satellite Topography (North Island, NZ) . . . . .	222
Figure A.2	Timeseries of NZ cGNSS site TRNG / Tauranga . . . . .	223
Figure A.3	Photo of NZ cGNSS site TRNG . . . . .	223
Figure A.4	Relationship between plate coupling and random walk values . . . . .	225
Figure A.5	Residual timeseries for some NZ cGNSS NZ sites (part 1/5) . . . . .	227
Figure A.5	(part 2/5) . . . . .	228
Figure A.5	(part 3/5) . . . . .	229
Figure A.5	(part 4/5) . . . . .	230
Figure A.5	(part 5/5) . . . . .	231
Figure A.6	2015 Campaign occupation data . . . . .	233

Figure A.7	2016 Campaign occupation data . . . . .	234
Figure A.8	2017 Campaign occupation data (part 1/2) . . . . .	235
Figure A.9	2017 Campaign occupation data (part 2/2) . . . . .	236

---

## LIST OF TABLES

Table 4.1	GAMIT parameters . . . . .	75
Table 4.2	GLOBK parameters . . . . .	79
Table 4.3	Time-dependent noise values for various models and cGNSS stations in the North Island, NZ . . . . .	85
Table 4.4	Australian Reference Frame Definitions . . . . .	99
Table 5.1	Detection and picking parameters for this study and the GeoNet default	140
Table 6.1	Vertical subsidence estimates for most cGNSS sites in NWNZ . . . . .	172

---

## ACRONYMS

---

3KR	Three Kings Ridge
AIC	Akaike Information Criterion
AVZ	Auckland Volcanic Zone
BA	Bouguer (Gravity) Anomaly
cGNSS	Continuously Operating GNSS (Station or Site)
DSDP	Deep Sea Drilling Project
EQC	(NZ) Earthquake Commission
FAA	Free Air (Gravity) Anomaly
GNSS	Global Navigation Satellite System

GPS Global Positioning System (U.S.)  
IGS International GNSS Service  
IODP International Oceanic Discovery Program  
INSAR Interferometric Synthetic-Aperture Radar  
JMA Junction Magnetic Anomaly  
LINZ Land Information New Zealand  
Ma Mega-Annum e.g. "Million Years Ago"  
NIFS North Island Fault System  
NRMS Normalised Root Mean Square  
NWNZ North-West New Zealand (NW of TVZ)  
PSD Power Spectral Density  
RINEX Receiver Independent Exchange (data format)  
RMS Root Mean Square (error)  
SLR Satellite Laser Ranging  
SNR Signal to Noise Ratio  
SNRS Southern Norfolk Ridge System  
STA/LTA Short Term Average/Long Term Average  
TVZ Taupō Volcanic Zone  
VMFZ Veining Meinesz Fracture Zone  
WRMS Weighted Root Mean Square

## INTRODUCTION

---

The northern North Island of New Zealand is the furthest from the active Australian-Pacific plate boundary and is subsequently one of the most tectonically stable regions in a country astride an active plate boundary. However, as the 2011 Christchurch earthquake has illustrated [Cooper et al., 2011], it is unwise to assume that a "stable" area in New Zealand is without seismic hazard. As this region is home to Auckland, the country's largest city, a significant degree of risk is also present. The low activity of this region requires an extended program of high-precision geophysical measurements to determine its crustal structure and rate of deformation. Perhaps because of this, the region remains poorly understood. This project sought to address the lack of knowledge of the region's behaviour via a multifaceted geophysical investigation which primarily targeted the Hauraki Rift, a 250 km long, N-S trending structure 40 km east of Auckland.

Studies of the Hauraki Rift largely peaked in the 1980s and have since abated within the last decade [e.g. Hochstein & Nixon, 1979; Ferguson et al., 1980; Tearney, 1980; Davidge, 1982; Rawson, 1983; Hodder, 1984; Hochstein et al., 1986; Thrasher, 1986; De Lange and Lowe, 1990; Chick, 1999; Chick et al., 2001; Hochstein & Ballance, 1993; Wise et al.; 2003; Kirkby, 2008] with the exception of recent work by Persaud et al. (2016) targeting the active Kerepehi Fault within the rift zone. Collectively these researchers showed that the rift was actively widening, albeit slowly, and capable of significant earthquakes, albeit rarely. The rate and nature of widening were invariably constrained indirectly, leaving quantitative uncertainties large. Speculative explanations for the rift's ongoing driving mechanism ranged from high-angle back-arc rifting associated with the Taupō Volcanic Zone [Hochstein, 1980], to the presence of offshore stresses associated with the evolution of the Tonga-Kermadec margin [Hochstein et al., 1986; Hochstein and Ballance, 1993], to the northern continuation of the clockwise strain recorded throughout the southern North Island [e.g. Wallace et al., 2004]. Without direct measurements of the rift's motion interpretations will remain vague, qualitative, and difficult to model.

Following the installation of a continuous Global Navigation Satellite System (GNSS) reference station on the Coromandel Peninsula in 2003, the rift's rate and character were finally measured with the necessary precision by observing its satellite-derived motion east of the Hauraki Rift relative to Auckland's reference station west of it, which had been in place since

1995. This single station-to-station baseline remained the only robust quantitative evidence of the rift's ongoing widening until additional campaign geodetic surveying throughout the northern North Island in 2013, a decade later. This campaign added a second vector east of the rift, and although it was never interpreted in terms of the Hauraki Rift or published at a usable scale, it demonstrated the utility of campaign GNSS surveying as a way to resolve the regions slow deformation. However these few additional velocity solutions [e.g. Wallace et al., 2016] at discrete locations only captured a small portion of the rift, leaving a large portion of its activity unknown.

The implication of ongoing widening at the Hauraki Rift implies the existence of ongoing seismicity throughout the region, however these earthquakes remain undetected or otherwise poorly resolved due to their small magnitudes and a lack of seismic stations in the northern North Island outside of the immediate Auckland area. Knowledge of the location and frequency of earthquakes highlights the manner in which stress and strain are released and accommodated as well as areas which may have higher seismic hazard. Unfortunately the event detection framework currently employed nationwide throughout New Zealand may be insensitive to detect many of these events.

### 1.1 AIMS

The principal aim of this work is to characterise the crustal tectonics and activity of the Hauraki Rift and greater north-western New Zealand region. This is done in several ways, foremost via an annual three-year 40+ station campaign geodetic survey done 2015-2017, analysis of the region's microseismicity, and analysis of the region's potential field data. The geodetic campaign provides a distributed dataset of well-resolved horizontal velocity estimates of crustal motion. These velocity estimates are also used to derive the Hauraki Rift's mechanical thickness and far-field rate of widening, potentially locate active faulting, and to derive strain rate estimates to understand how stress and strain are distributed and partitioned away from the oblique subduction of the Pacific Plate at the Hikurangi Margin. Further still, the velocity data calculated at long-running continuous reference stations in the region are used to estimate the degree of crustal uplift or subsidence, which is increasingly relevant for coastal regions facing global sea level rise.

Analysing the microseismicity throughout the northern North Island also highlights the existence of active faulting and further shows where activity is focused. To locate and detect small earthquakes which have mostly gone unreported, a careful review and recalibration of event detection parameters is done specifically customised for the low-deformation environment of the northern North Island. Further, archived historic data from GeoNet is manually inspected to both increase the number of events found and decrease the uncertainty of their position, and the data for two additional seismic stations are incorporated to increase the ability to resolve earthquake discovery. One of these stations is installed explicitly for this project and is now a new permanent station.

This work also analyses pre-existing gravity and magnetic potential field data collected on the ground as well as derived from satellite measurements. This helps to resolve the crustal and tectonic structure of north-western New Zealand which then allows for the interpretation of the presence of faults and the extent of the Hauraki Rift. Satellite-derived data further allows for the interpretation of the continuity of the tectonic basement structure off-shore which is necessary to understand the tectonic history of north-west New Zealand within the context of north-east Zealandia.

A secondary aim for this work is to confirm that northernmost New Zealand is moving at anomalously fast velocities relative to a fixed Australian Plate reference frame, previously supposed by Tregoning et al. (2013) and Beavan et al. (2016), and additionally quantify this motion. This would imply that Australian Plate reference frames (e.g. the latest International Terrestrial Reference Frame 2014 plate model [Altamimi et al., 2017]) incorporating geodetic reference sites anywhere on New Zealand are slightly inaccurate and may impact the ability to resolve the slow deformation within the northern New Zealand region as required to meet the primary aim of this thesis. Confirmation of anomalously high velocities in northern New Zealand is done by adding ~10 new geodetic velocity estimates throughout Northland beyond what was previously available at the two continuously operating reference stations in the area, as well as deriving velocity estimates for reference sites on nearby islands throughout the eastern Australian Plate.

Having confirmed and quantified northern New Zealand's motion relative to a fixed Australian Plate reference frame, a third aim of this work is to explain this elevated velocity as well as the elevated velocities observed throughout the eastern Australian Plate on Norfolk Island, Lord Howe Island, and New Caledonia. This is done by developing a new tectonic model for north-east Zealandia describing its evolution since the Oligocene ~30 Ma. The model

builds off previous models [e.g. Schellart et al., 2006] using constraints provided by published seafloor dredging of volcanic rocks and the new constraints provided by the interpretation of this project's derived Bouguer gravity anomaly, as well as the velocity estimates of reference geodetic stations throughout the eastern Australian Plate.

## 1.2 THESIS STRUCTURE

This thesis begins with a review of both the geologic history of north-east Zealandia as well as the current state of geophysical work done in north-west New Zealand. From there, an introduction to the gravity and magnetic data is made, including the derivation of this work's Bouguer gravity anomaly and a guide as to how it will be interpreted. The methods by which the new geodetic and seismic data acquired by this work were processed, as well as some intermediate findings, are then discussed in independent chapters. The discussion includes a geophysical interpretation of north-west New Zealand and the Hauraki Rift utilising this new data, in addition to a model of the Hauraki Rift and North Island of New Zealand incorporating the newly derived geodetic velocity estimates. To explain the anomalously high velocities observed in Northland relative to a fixed Australian reference frame, a new Oligocene-Miocene tectonic interpretation and model is also presented. Finally, some observations on the challenges of geodetic surveying in the low-rate and potentially nonlinear deformation environment of northern New Zealand are discussed, including some reflections on the work accomplished and ideas for future research.

# 2

## STRUCTURE, EVOLUTION, AND KNOWN ACTIVITY OF NORTH-EASTERN ZEALANDIA

---

### 2.1 THE GEOLOGIC FABRIC OF ZEALANDIA

Present-day Zealandia [Mortimer et al., 2017; Figure 2.1] separated from the Australian/Antarctic sector of the Gondwana supercontinent ~90 Ma and continued rifting eastward until ~50 Ma, opening the Tasman Sea behind it [Gaina et al., 1998; Sutherland, 1999; Laird and Bradshaw, 2004; Mortimer, 2004]. This rifted block was comprised of (>100 Ma) fragments of marine terranes which had accreted onto the eastern margin of Gondwana and now form a continuous geologic fabric linking New Caledonia to New Zealand throughout NE Zealandia [Sutherland, 1999; Mortimer, 2004; Spandler et al., 2005; Collot et al., 2009; Mortimer et al., 2014]. The continuity of this fabric, now comprising the geologic basement of New Zealand, can be speculated from bathymetry (Figure 2.2) but is perhaps more reliably traced by magnetic anomalies. Off-shore, a system of pronounced magnetic anomalies presumably associated with the Median Batholith as well as various adjacent terranes has been observed throughout Zealandia (e.g. Figure 2.1) linking New Zealand's basement terranes west and northwards to New Caledonia [Mortimer et al., 1999; Sutherland, 1999; Mortimer et al., 2017]. On shore New Zealand, the well-defined Junction Magnetic Anomaly (JMA) [e.g. Eccles et al., 2005] within the narrow Dun Mountain Terrane [Coombs et al., 1976; Hunt, 1979] expands on this by providing detailed, local-scale evidence for the continuity of basement structure throughout both the North and South Islands.



**Figure 2.1:** Extent of Zealandia, from Mortimer et al. (2017). "North-east Zealandia" as interpreted by this project is further demarcated by the dotted black line.

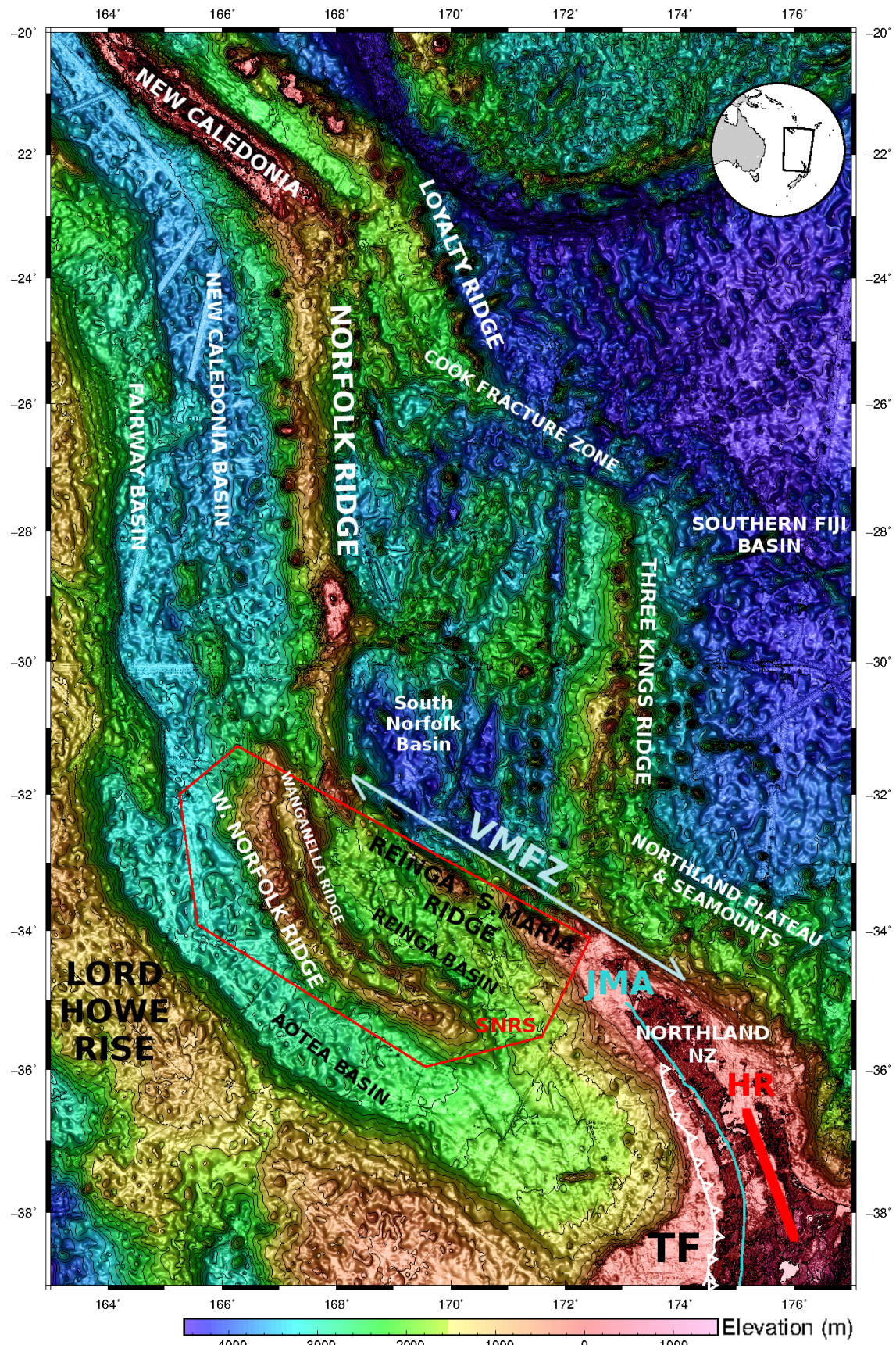


**Figure 2.2:** Bathymetry (part 1/2) [Smith and Sandwell, 1997; Becker et al., 2009] (250 m contour) and features of north-east Zealandia and the east Australian Plate. HR = Hauraki Rift, JMA = Junction Magnetic Anomaly (traced in blue), NIFS = North Island Fault System, SNRS = Southern Norfolk Ridge System (outlined in red), TF = Taranaki Fault (toothed), TVZ = Taupō Volcanic Zone, VMFZ = Veining Meinesz Fracture Zone.

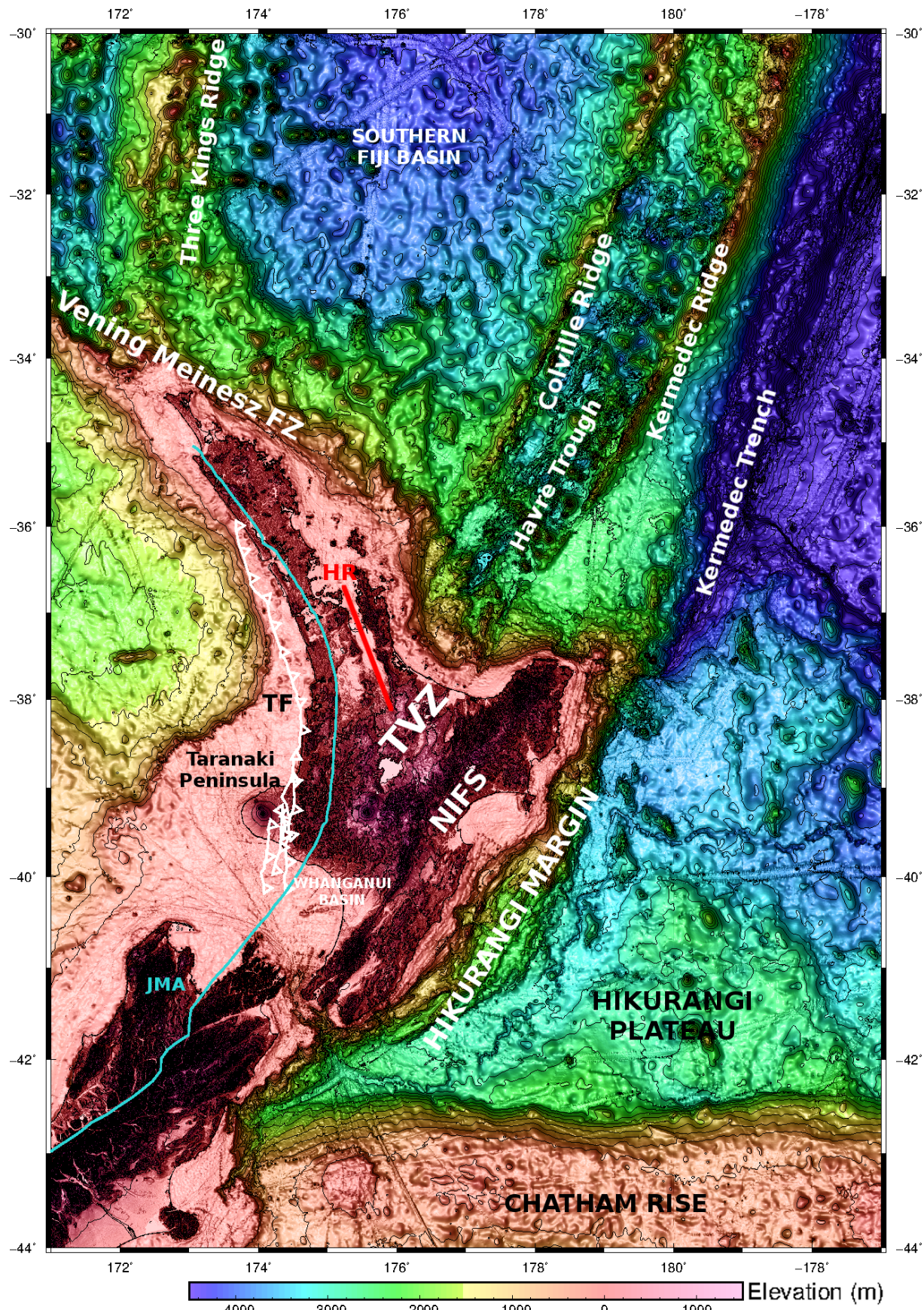


**Figure 2.3:** Bathymetry (part 2/2) [Smith and Sandwell, 1997; Becker et al., 2009] (250 m contour) and features of north-east Zealandia and the east Australian Plate. HR = Hauraki Rift, JMA = Junction Magnetic Anomaly (traced in blue), NIFS = North Island Fault System, TF = Taranaki Fault (toothed), TVZ = Taupō Volcanic Zone.

A stylised interpretation of the crustal structure of NE Zealandia is shown in Figure 2.4 [Mortimer et al., 2014]. Beyond direct sampling, the location of these terranes within NE Zealandia may be loosely inferred by the relative positioning of the pronounced magnetic anomalies associated with the Dun Mountain Terrane (e.g. JMA) and the Median Batholith. The reason these terranes are strongly magnetic is likely due to their predominant igneous composition relative to the other terranes which are generally imbricated oceanic sediments [Coombs et al., 1976; Mortimer et al., 2002; Mortimer, 2004; Mortimer et al., 2014]. Between the JMA and Median Batholith is the implied location of the Murihiku Terrane, a thick (9-13 km) mixture of volcanioclastic sandstones and mudstones atop thinned crust which probably belies its history as a back-arc and/or fore-arc basin [Ballance and Campbell, 1993; Black et al., 1993; Kamp and Liddell, 2000; Roser et al., 2002; Briggs et al., 2004; Mortimer, 2004; Mortimer et al., 2014]. The Murihiku Terrane features systemic Cretaceous east-dipping faults which were probably reactivated in the Eocene in association with the onset of the Taranaki Fault system (Figures 2.2, 2.4) [King and Thrasher, 1996; Nicol et al., 2005; Stagpoole and Nicol, 2008; Giba et al., 2010; Giba et al., 2013]. East of the JMA and north of the TVZ is the Caples-Waipapa Terrane which has a similar composition to the Murihiku Terrane but instead has a history as an accretionary complex [Black et al., 1993; Mortimer, 2004]. The Hauraki Rift resides within this material.

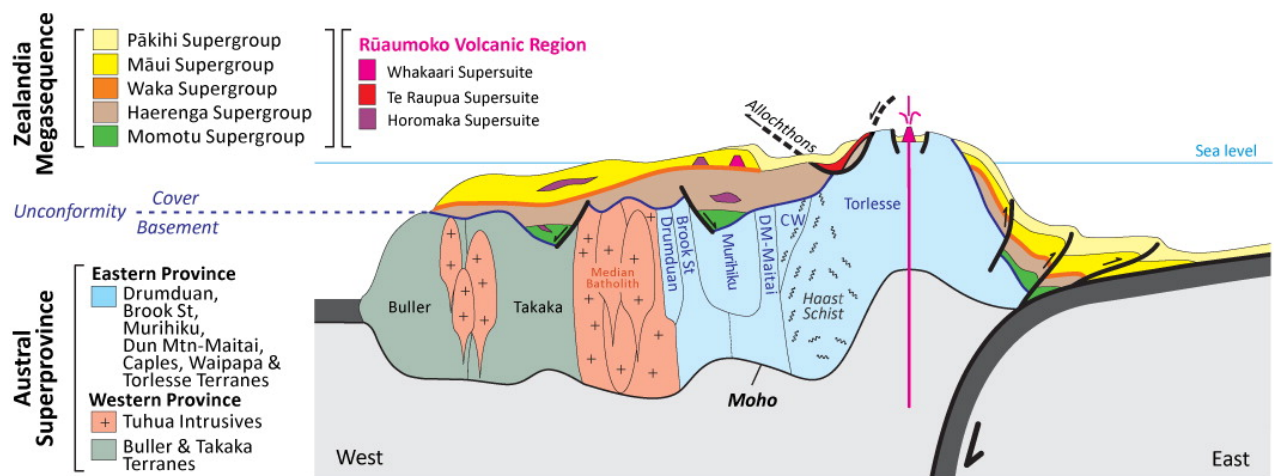
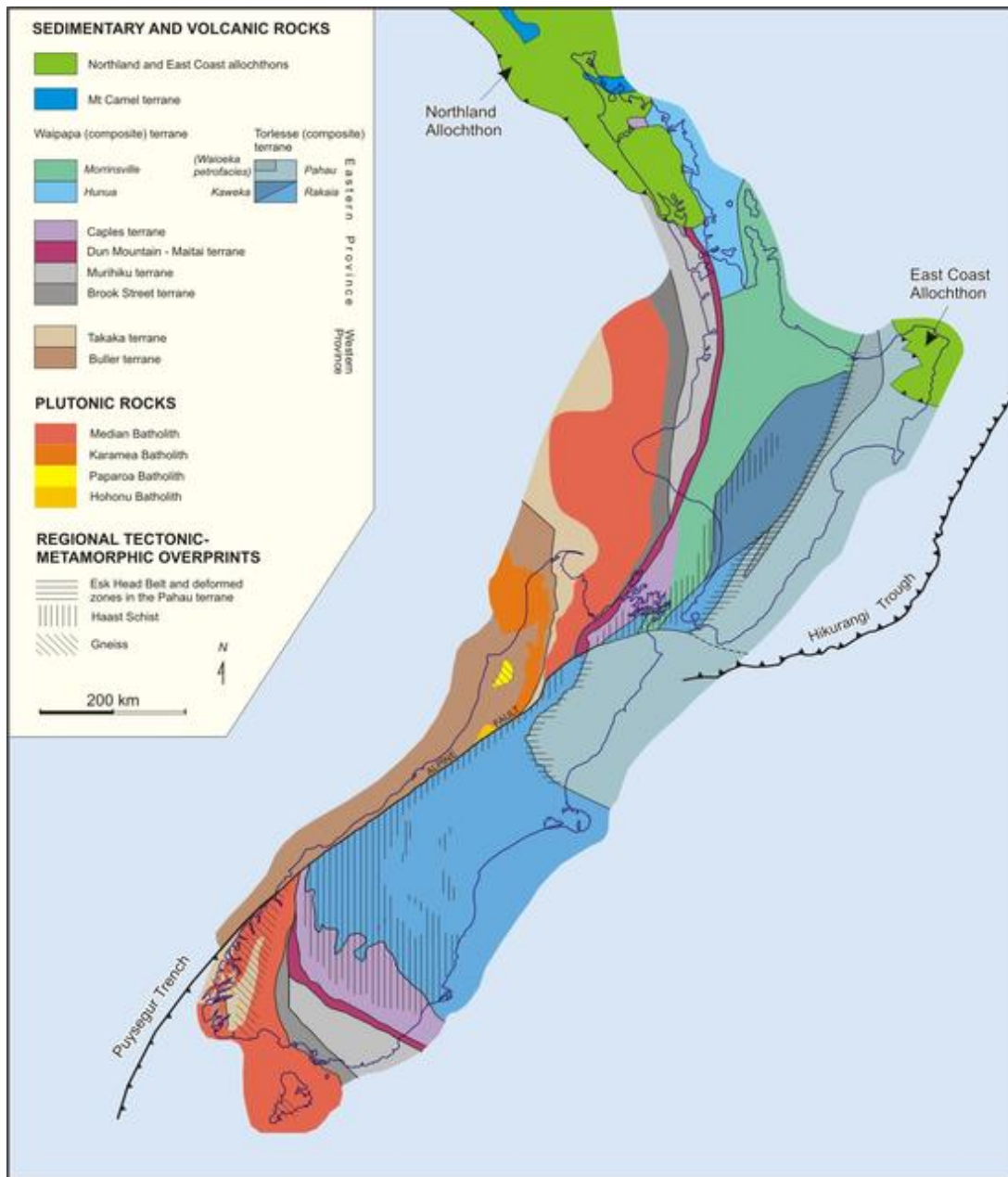


Figure 2.4: A stylised cross section of Zealandia, taken from Mortimer et al. (2014). CW = Caples and Waipapa terranes.

Though the basement terranes of Zealandia are generally continuous many have highly variable widths (e.g. Figure 2.5). The terranes also show a large sigmoidal curve between the north and south islands of New Zealand, in addition to the presence of a 440-470 km offset

along the South Island which continues to be accommodated by the Alpine Fault [Sutherland, 1999b; Lamb, 2011; Mortimer et al., 2014]. This bending is thought to be the result of the westward impact of the thickened crust of the Hikurangi Plateau on the Pacific Plate at the Hikurangi Margin (Figure 2.2) which refocused stress parallel along the Australian-Pacific plate margin [Reyners, 2013]. The result of this impact served to bend the continent and dislocate the crust along the Alpine Fault to equivalent degrees [Sutherland, 1999b], producing a NE-striking basement structure in the southern North Island transitioning to NW striking in the north.



**Figure 2.5:** Basement terranes of New Zealand (via GNS Science). The sigmoidal straining of the crust is clearly evident, as well as the ~440-470 km offset generated by the Alpine Fault.

That both the Taranaki Fault system and Hauraki Rift as well as the majority of faults between them [e.g. Edbrooke et al., 2005; Nicol et al., 2005; Williams et al., 2006; Edbrooke and Brook, 2009; Kenny et al., 2012; Lichfield et al., 2014; Langridge et al., 2016] are parallel to the basement fabric of NWNZ is unlikely to be a coincidence. This is because faults or rifts are most likely to manifest or reactivate within mechanically weaker sutured boundaries between contrasting basement structures [e.g. Jackson, 1980; Gibbs, 1984; Holdsworth and Butler, 1997]. This suggests that the orientation of Zealandia's basement is likely to have influenced how NWNZ has been shaped and restructured over time.

## 2.2 TECTONIC HISTORY OF NE ZEALANDIA <50 MA

To best interpret NWNZ's activity a thorough understanding of the tectonic history of NE Zealandia and the SW Pacific is ideal. Unfortunately this region is particularly complex and widely debated. A plethora of models have been concocted to describe the period between two major global tectonic events. The first at ~100 Ma [e.g. Matthews et al., 2012] coincided with the cessation of subduction at Gondwana's eastern margin (e.g. the Norfolk Ridge) [Laird and Bradshaw, 2004] and subsequent initiation of a proto-Tonga-Kermadec subduction ~85 Ma margin further east in the Pacific Ocean [Schellart et al., 2006; Matthews et al., 2015]. The second was at ~50 Ma which oversaw a series of global events including the 'kink' in the Hawaiian Seamount Chain [Sharp and Clague, 2006], initiation of the Izu-Bonin-Mariana subduction [Ishizuka et al., 2011], initiation of subduction east of New Caledonia [Crawford et al., 2003; Cluzel et al., 2012], the end of Tasman Sea widening [Gaina et al., 1998], and the propagation of a new plate boundary through New Zealand which would go on to form the Alpine Fault [Sutherland, 1995; Sutherland, 1999b; Lamb, 2011; Reyners, 2013; Mortimer, 2014]. However while these models vary in many ways, they invariably tend towards the conclusion that by ~45 Ma Zealandia's NE margin was being approached from the east by either a SW-dipping Colville or proto-Pacific Arc [e.g. Mortimer et al., 2007; Figure 2.6], or an NE-dipping Loyalty Arc [e.g. Crawford et al., 2003; Schellart et al., 2006; Whattam et al., 2008; Figure 2.7], either of which are presumed to be responsible for the obduction events in New Caledonia and Northland. Compressional tectonic features associated with this arc collision have been observed at the margin of NE Zealandia via seismic stratigraphy studies within the Southern Norfolk Ridge System [Stagpoole et al., 2009; Bache et al., 2012; Bache et

al., 2014] and New Caledonia Basin [Lafoy et al., 2005; Klingelhoefer et al., 2007; Collot et al., 2008; Sutherland et al., 2010]. Furthermore preliminary estimates of material removed from IODP drilling within the northern New Caledonia Trough also see evidence for Mid-Eocene modification [Sutherland et al., 2018]. This is also corroborated by seismic observations of compression at the Taranaki Fault as early as ~40 Ma [Stagpoole and Nicol, 2008; Giba et al., 2010].

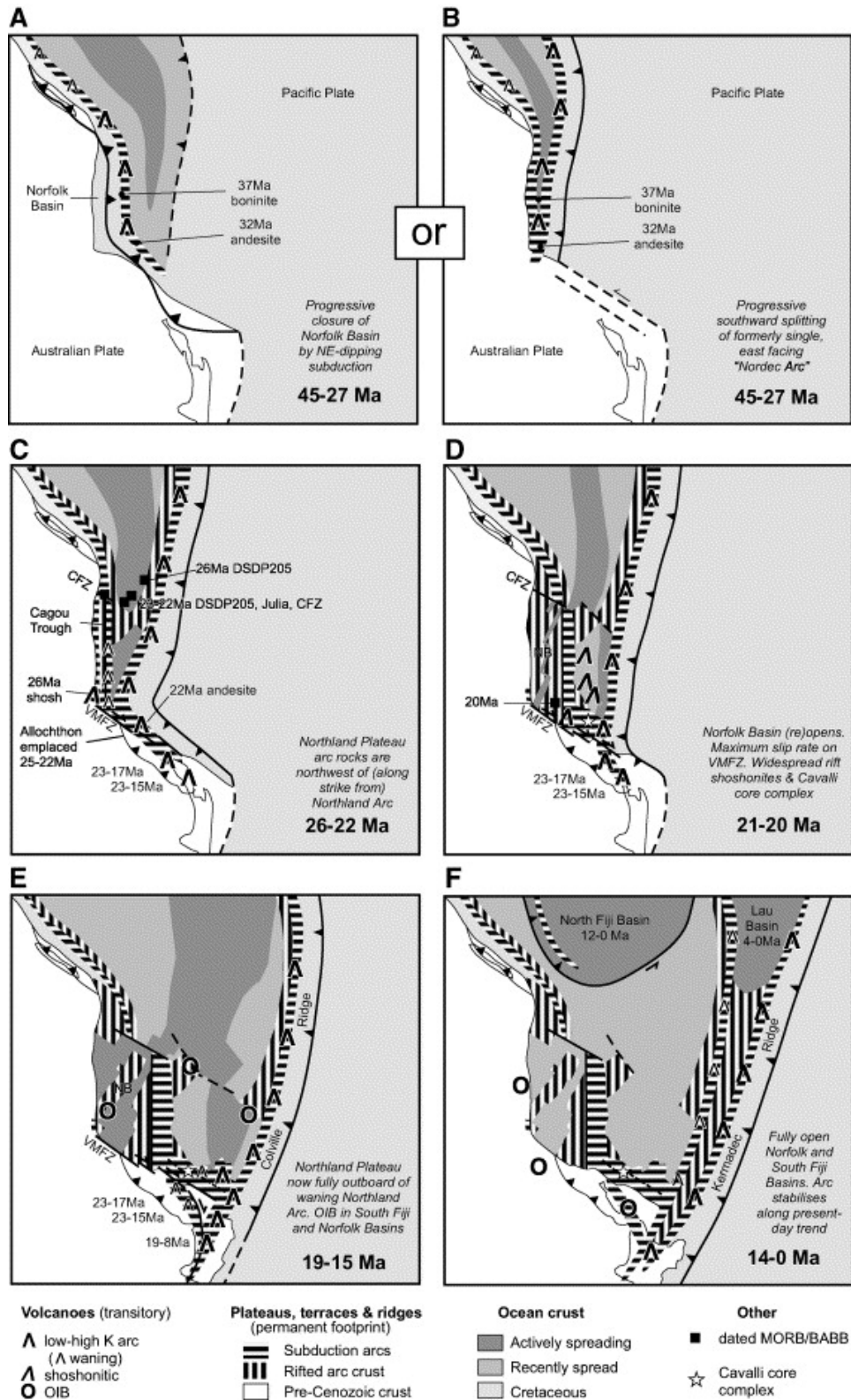


**Figure 2.6:** South Fiji Basin tectonic model from Mortimer et al. (2007) depicting the western migration of a W-SW dipping proto-Kermadec subduction arc prior to SE retreat along the VMFZ.

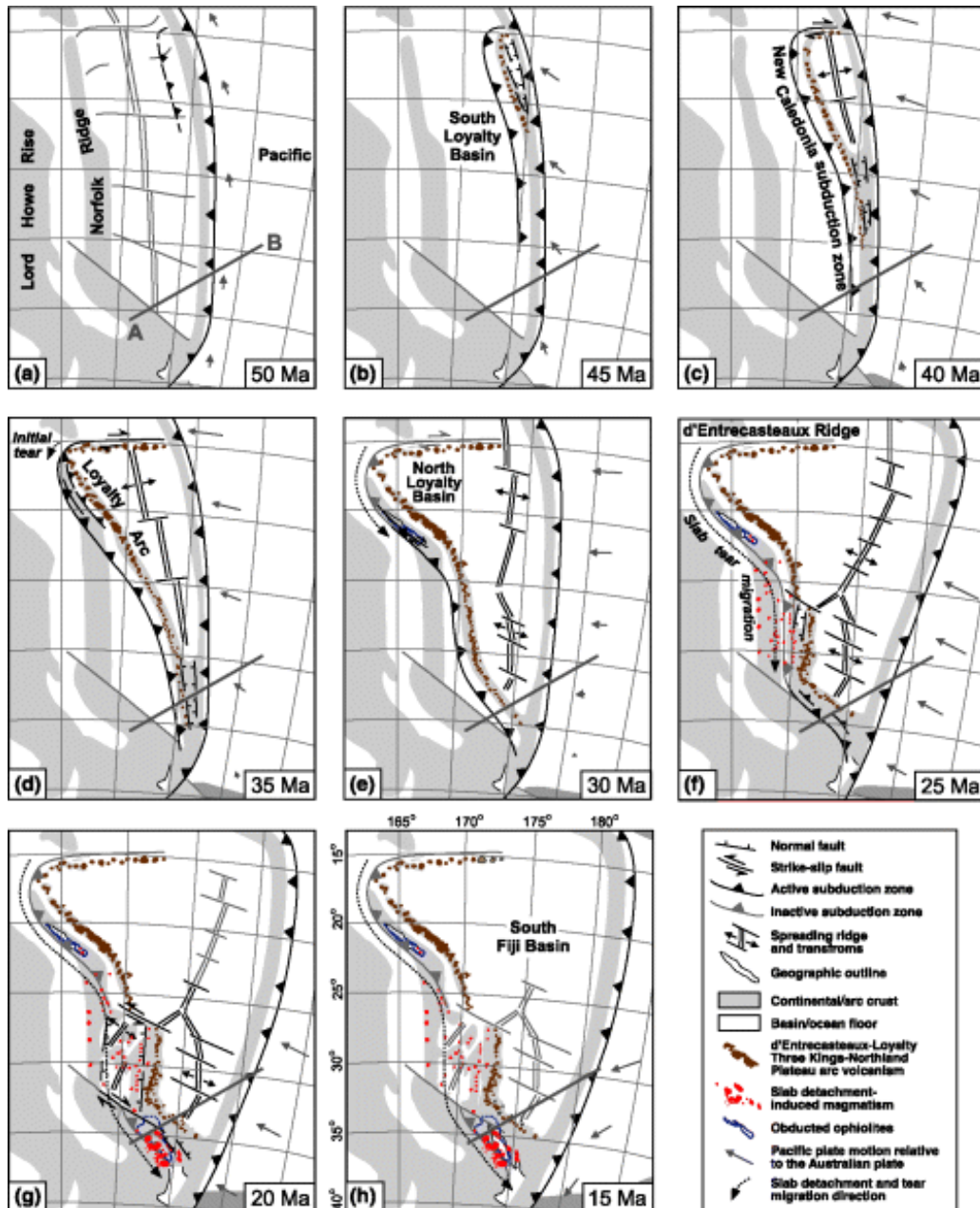


**Figure 2.7: South Fiji Basin tectonic model from Schellart (2007) depicting the SW migration of a NE dipping Loyalty-Three Kings subduction arc which consumed the Loyalty Basin between the Norfolk and Three Kings ridges.**

### 2.2.1 South-West or North-East Dipping Subduction?

The idea that a subduction arc was approaching the Norfolk Ridge from the east in the late Eocene (e.g. panels D and E, Figure 2.7; or panels A or B, Figure 2.6) appears mostly agreed, but the polarity of arc subduction is not. A W or SW-dipping model [e.g. Ballance, 1976; Mortimer

et al., 2007] is the most straightforward as it presumes a single Pacific subduction system which generated both the Northland Volcanic Arc as well as the subsequent Coromandel Volcanic Arc and TVZ volcanism [e.g. Seebeck et al., 2014]. It also offers a clear explanation for the consistent arc-type volcanism seen throughout Northland [e.g. Hayward et al., 2001; Booden et al., 2011] as well as off-shore near the Northland Plateau and Three Kings Ridge [Mortimer et al., 1998; Mortimer et al., 2007].

An E or NE-dipping model [e.g. Crawford et al., 2003; Schellart et al., 2006; Whattam et al., 2008] assumes that the Loyalty-Three Kings subduction arc migrated SW towards the margin of NE Zealandia, devouring a hypothetical Loyalty Basin between it. Here the arc-type volcanism throughout the margin of NE Zealandia is assumed to be the result of the subsequent detachment of the Loyalty Basin (now slab) from New Caledonia towards Northland [Schellart, 2007; Whattam et al., 2008]. This N-S detachment trend explains the N-S age progression of arc-type volcanism from older to younger in Northland [e.g. Hayward et al., 2001; Mortimer et al., 2007]. It also explains the timing and similarity of the New Caledonia and Northland obduction events [Rait, 2000; Spörli and Harrison, 2004; Collot et al., 2008; Herzer et al., 2009; Cluzel et al., 2012; Patriat et al., 2018] and the apparent subduction trench on the west side of the Three Kings Ridge observed by seismic studies [Kroenke and Eade, 1982; Kroenke and Dupont, 1982] as well as multibeam bathymetry [e.g. FAUST-2, Benkhelil et al., 2001]. Furthermore global seismic tomography studies have interpreted a sunken slab west of the Norfolk Ridge which is presumably the detached Loyalty Slab [Amaru, 2007; Schellart et al., 2009; van de Lagemaat et al., 2018].

### 2.2.2 *Arc Collision, Obduction, and Volcanism (45-23 Ma)*

The timing of the collision between the Loyalty-Three Kings subduction arc with the New Caledonia-Norfolk Ridge-Northland NZ border of NE Zealandia (e.g. Figure 2.7) is loosely constrained by the dating of the New Caledonia obduction event ~38-34 Ma [Fitzherbert et al., 2004; Spandler et al., 2005; Collot et al., 2008; Cluzel et al., 2012] to the north and the Northland obduction event ~25-22 Ma [Rait, 2000; Spörli and Harrison, 2004; Herzer et al., 2009] to the south. Assuming that these obduction events are related via a similar mechanism [e.g. Patriat et al., 2018], this would imply that collision first began in the north at New Caledonia, then progressively made its way south to Northland. The mid-late Eocene period leading up to

the arc collision has also been interpreted as a compressive phase for NE Zealandia which is possibly responsible for the uplift of the Reinga and Wanganella ridges [Herzer et al., 1997; Stagpoole et al., 2009; Bache et al., 2012].

The age of arc-type (or shoshonitic [Morrison, 1980]) rocks found along the margin of NE Zealandia may further improve qualitative estimates of the timing of arc collision. These rocks feature a similar N-S age progression with the oldest (~52-24 Ma) near New Caledonia, to 37-26 Ma along the Norfolk Ridge and Three Kings Ridge, to 23-15 Ma in Northland, to 15-0 Ma south of Auckland [e.g. Mortimer et al., 1998, 2007, 2018; Figure 2.8]. Despite a few outliers these ages are consistent with either a N-S progression of slab tear-off, or a N-S progression of SW subduction. The shoshonite (yellow circles, Figure 2.8) rocks found amidst the arc-type (grey lines and circles) may be explained by the partial melting of the lithospheric mantle resulting from the slab's tearaway from Zealandia's crust [von Blackenburg and Davies, 1995] or arc rifting of the Norfolk and/or Three Kings ridges [Mortimer et al., 2007].

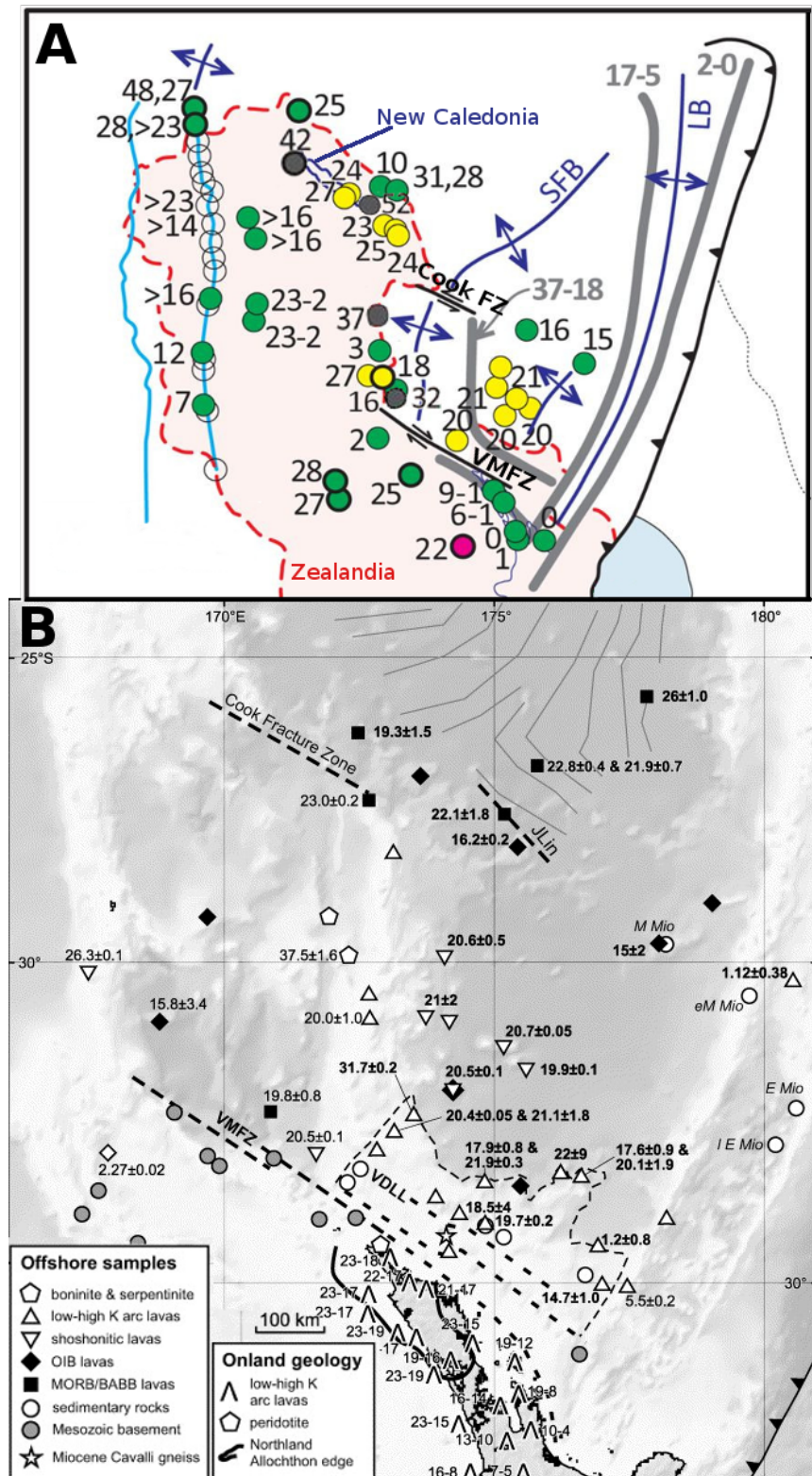


**Figure 2.8:** Dredged rock samples and dates collected from Mortimer et al. 2007 (B) and Mortimer et al. 2018 (A), which has been accentuated with additional labels and datapoints along the margin of NE Zealandia. Yellow circles = subalkaline/shoshonitic, green = alkaline (Na) basalts, pink = ultra-alkaline (Na), and grey = arc-type geochemistry. Grey lines indicate traditional arc-type rocks. The data shown here has been collected by a variety of researchers and is available the PETLAB database [Strong et al., 2016].

A key difference between SW and NE dipping subduction models is the resulting interaction between the continental margin of NE Zealandia and the Loyalty-Three Kings Arc during their collision. SW dipping models [e.g. Mortimer et al., 2007] would result in ridge-ridge compression and reverse faulting between the Norfolk and Loyalty-Three Kings ridges with little to no mechanical bonding between the ridges. NE dipping models [e.g. Crawford et al., 2003; Schellart et al., 2006] imply that the trench was between the ridges, and further that the continental margin of Zealandia was partially subducted east or north-eastward as the attached Loyalty Basin was pulled into the mantle. This would have resulted in short-lived margin perpendicular extension which could have generated normal faulting [e.g. Chemenda et al., 1995] and speculatively could have thinned or rifted the crust overall, in addition to producing isostatic uplift following the slab's detachment [e.g. Molnar and Gray, 1979]. Furthermore the partial subduction would have theoretically served to mechanically bond the features together, although the hypothetical strength of this bond cannot be easily inferred.

### 2.2.3 *Widening of Norfolk Basin (23-15 Ma)*

Following the western collision of the Loyalty-Three Kings arc into the margin of NE Zealandia, a dramatic change in tectonic stress throughout the SW Pacific began to rift the Loyalty-Three Kings arc SE away from the Norfolk Ridge [Herzer et al., 2009]. Initially the joint Loyalty-Three Kings Ridge moved in unison before the Three Kings Ridge separated, leaving the Loyalty Ridge still adjacent to the Norfolk Ridge [e.g. Ballance, 1976; Kamp, 1986; Bernardel, 2002]. The Three Kings Ridge continued moving SE from both the Norfolk and Loyalty ridges another ~270 km accommodated by the Veining Meinesz Fracture Zone (VMFZ) to the south and Cook Fracture Zone to the north, opening the Norfolk Basin behind it [Herzer and Mascle, 1996; Mortimer et al., 1998; Herzer et al., 2009] (Figure 2.2).

The timing of initial activity of the Cook Fracture Zone and VMFZ at ~23 Ma accommodating the separation of the Three Kings Ridge is constrained by the age of mid-ocean ridge basalts within the Cook Fracture Zone [Bernardel, 2002; Reyners et al., 2009]. This follows the New Caledonia obduction ~38-34 Ma [Spandler et al., 2005; Fitzherbert et al., 2004; Collot et al., 2008; Cluzel et al., 2012] by over 10 million years, but is concurrent to the timing of the Northland obduction ~25-22 Ma [Spörli, 1999; Rait, 2000; Spörli and Harrison, 2004]. This would mean that

the Three Kings Ridge began separating SE away from the Norfolk Ridge almost immediately after, or possibly during the obduction of the Northland Allochthon. The younger ~23-17 Ma age of arc volcanism offshore of Northland [Herzer, 1995; Mortimer et al., 1998; Hayward et al., 2001; Mortimer et al., 2007; Booden et al., 2011; Figure 2.8] implies that the Loyalty Slab had not yet detached prior to the completion of Northland Obduction nor cessation of the Norfolk Basin's opening. Alternatively, for SW dipping models [e.g. Mortimer et al., 2007], this would mean that the active subduction trench for the Pacific Plate beneath Northland was immediately NW (or overlapping) the actively moving VMFZ at this time.

The tectonic driver for the SE migration of the Three Kings Ridge and opening of the Norfolk Basin is unclear but may have been due to the buoyant Hikurangi Plateau on the subducting Pacific Plate becoming increasingly parallel to the Australia-Pacific subduction margin at ~23 Ma which began SW-NE strike slip faulting and likely generated SE-directed tectonic stress at the Three Kings Ridge [Reyners, 2013]. It may also have been the result of back-arc extension, presuming the eastward retreat of W or SW-dipping Pacific Plate models [e.g. Mortimer et al., 2007] or even the result of drag from mantle plumes [Sdrolias et al., 2004].

The opening of the Norfolk Basin may have also affected regions outside the basin and beyond the ridges and fracture zones encapsulating it. South of the VMFZ, seismic stratigraphy within the Reinga Basin indicate the region was in a net contraction phase from the mid-Eocene to Oligocene leading up to the initiation of the VMFZ's activity, then entered a net subsidence phase until the mid-Miocene, then resumed contraction until the Pleistocene [Stagpoole et al., 2009; Bache et al., 2012]. This sequence of events conspicuously coincides with the VMFZ activating ~23 Ma and then deactivating ~15 Ma [Bernardel, 2002; Mortimer et al., 2007; Herzer et al., 2009] which could mean that the stress associated with the Norfolk Basin's widening may have temporarily negated the compression occurring within the Reinga Basin or even resulted in extension within it.

#### 2.2.4 *The Modern Hikurangi Margin Regime (15-0 Ma)*

The cessation of activity on the VMFZ has been inferred to occur at ~15 Ma via the superposition of hotspot volcanism atop seamounts within the Norfolk Basin [Sdrolias et al., 2004; Mortimer et al., 2007]. It is unclear what the cause of this cessation was, but stress may have simply migrated SE following the SE migration of the Pacific Plate boundary [Lamb, 2011; Seebeck et al., 2014].

It is also hypothesised that at this time the Hikurangi Plateau had become increasingly parallel to the Australian-Pacific plate boundary which would serve to redirect most of the stress in the basins north of New Zealand and concentrate it towards the south along the Hikurangi Margin and the Alpine Fault [Reyners, 2013].

Following the termination of activity at the VFMZ, the greater Reinga Basin region (Figure 2.2) appears to have resumed a state of relative contraction ~15-5 Ma [Bache et al., 2012]. It is unclear what the driver of this compression would be. The Taranaki Fault had also resumed activity after a period of relative acquiescence during the VMFZ's activity but now with the majority of activity much further south (36°S), presumably in direct response to westward Hikurangi Margin compression [Stagpoole and Nicol, 2008]. The Taranaki Fault would go on to migrate southwards as the plate boundary evolved to its current position within and immediately north of the Taranaki Peninsula [King and Thrasher, 1996; Nicol et al., 2005; Giba et al., 2010] as well as south of the peninsula towards the Alpine Fault [e.g. Nicol et al., 2005].

The Hauraki Rift is also believed to have began rifting at some uncertain time following the end of the VMFZ's activity as stress at the Australian-Pacific plate boundary continued to migrate SE [Hochstein et al., 1986; Hochstein and Ballance, 1993]. By ~2 Ma most of this stress was now focussed within the Taupō Volcanic Zone (TVZ), essentially the on-shore southern extension of the Havre Trough back-arc rift [Wilson et al., 1995]. By this point the majority of NE Zealandia's known active tectonic features had ceased activity north of the TVZ and south of New Caledonia, aside from the Hauraki Rift and adjacent Wairoa North Fault.

## 2.3 CURRENT ACTIVITY

### 2.3.1 *The Active Hauraki Rift and Wairoa North Fault*

Following the cessation of tectonic activity north of NZ coeval with the SE rollback of Pacific subduction to its present arrangement as the Hikurangi Margin, NWNZ became tectonically quiet with only two known active features recognised today. These are the Wairoa North Fault and the Kerepehi Fault within the Hauraki Rift (Figure 2.9). While numerous other faults have been noted [Edbrooke et al., 2005; Edbrooke and Brook, 2009; Kenny et al., 2012], only these two have been proven to exhibit signs of current activity [e.g. Wise et al., 2003; Persaud et al., 2016] and are thus entries in the Active Faults Database [Langridge et al., 2016].

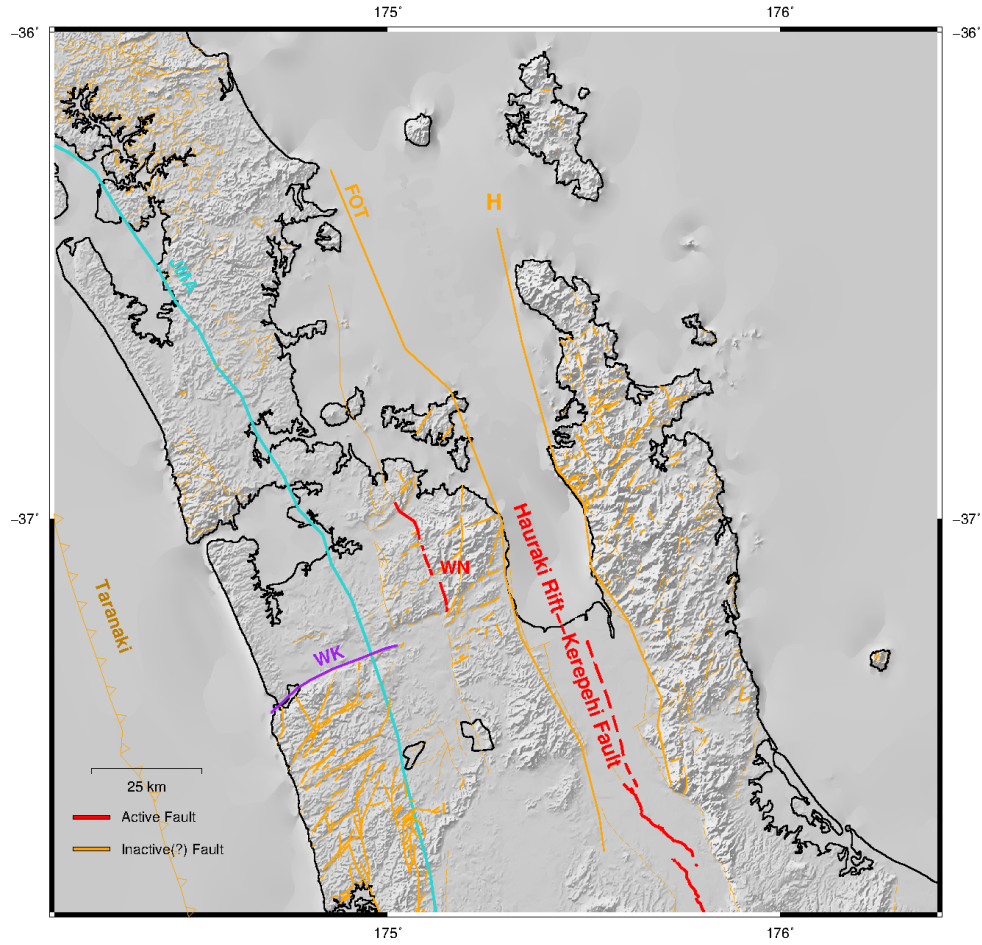


**Figure 2.9:** Known faults within the greater Auckland / Hauraki Rift region. The Junction Magnetic Anomaly, a general proxy for the trend of the basement structure [Coombs et al., 1976; Hunt, 1979; Eccles et al., 2005], is plotted in light blue. Active faults are drawn in red [Langridge et al., 2016] else drawn in gold or purple [Edbrooke et al., 2005; Kenny et al., 2012]. Topography is 100 m [LINZ; data.linz.govt.nz]. H = Hauraki Fault, FOT = Firth of Thames Fault, WN = Wairoa North Fault, WK = Waikato Fault, Taranaki = Taranaki Fault.

The Hauraki Rift's age is poorly constrained. The lower (younger) bound of the rift's age is loosely estimated to be ~7-5 Ma based on sediment accumulation [Hochstein et al., 1986; Hochstein and Ballance, 1993]. Volcanism within the rift may have been as recent as ~1.2-3.1 Ma as evident by Little Barrier Island, conspicuously located near the presumed northern extension of the Hauraki Rift in the Hauraki Gulf and featuring a distinct geochemical signature relative to the Coromandel Volcanic group [Lindsay et al., 1999]. This supports the idea that the rift may have been capable of producing volcanism after the backarc tectonic stresses had migrated into the TVZ <2 Ma [Wilson et al., 1995].

The geologic structure of the rift has been previously described by both land and marine gravity and magnetic surveys [Hochstein and Nixon, 1979; Tearney, 1980; Rawson, 1983;

Hochstein et al., 1998; Hochstein and Ballance, 1993], off-shore seismic refraction studies [Ferguson et al., 1980; Thrasher, 1986] as well as on-shore seismic refraction surveys [Hochstein et al., 1986]. From these collective measurements the Hauraki Rift was known to be 25 km wide and over 250 km long, extending from Whangarei to the TVZ at a ~340° strike [Hochstein and Ballance, 1993]. The rift zone has low gravity anomalies [Hochstein and Nixon, 1979] and a 0.7-2.5 km sediment layer [Hochstein et al., 1986]. The rift exhibits elevated heat flow [Hochstein and Nixon, 1979] and features several hot springs suggesting a thin crust and/or active mantle upwelling. The Kerepehi Fault, which exhibits both normal and right-lateral motion [Lensen, 1981; Hochstein et al., 1986; Persaud et al., 2016], bisects the rift length-wise between 10+ discrete segments and is capable of generating M5.5-7.0 earthquakes [Persaud et al., 2016] and tsunamis [Chick et al., 2001]. Parallel to the Kerepehi Fault are the Firth of Thames Fault (Figure 2.9, "FoT") to the west, and the Hauraki Fault ("H") to the east. These faults, deemed to be inactive, bind the rift boundary [Hochstein and Ballance, 1993; Edbrooke et al., 2005; Persaud et al., 2016; Langridge et al., 2016].

Twenty kilometres west and parallel to the Hauraki Rift is the Wairoa North Fault (Figure 2.9, "WN"), the only other fault north of the TVZ known to be active [Wise et al., 2003; Langridge et al., 2016]. It is situated within the Hunua Ranges amongst a small network of localised block faulting. On its southern end, perpendicular faults to the east appear to link it to the Hauraki Rift, and perpendicular faults to the west may run closely parallel to the Waikato Fault leading to the Tasman Sea. The northern vicinity of the Wairoa North Fault has various extensions that may continue north and bisect both Waiheke and Rangitoto-Motutapu Island {174.9°E, 36.8°S} in the Hauraki Gulf [Kenny et al., 2012]. Its age, basement rock, and driving mechanism is thought to be similar to that of the Hauraki Rift/Kerepehi Fault [de Lange and Lowe, 1990; Persaud et al., 2016] but it may have a higher potential for earthquakes [Wise et al., 2003].

### 2.3.2 *The (Inactive?) Waikato Fault*

Another northern North Island fault with potential but unconfirmed activity is the Waikato Fault (Figure 2.9), one of the relatively few distinct features trending ~E-W instead of basement parallel (NW-SE). Though published traces of this feature typically do not extend further east than is drawn in Figure 2.9, proximal parallel faults (e.g. the Pokeno Fault) possibly extend its reach to the Wairoa North Fault and even further east into the Hauraki Rift [Edbrooke et al.,

2005; Kenny et al., 2012]. It dips sharply ( $\sim 75^\circ$ ) to the north and has 2.7 km vertical displacement which decreases east towards the Tasman Sea shore, producing strong N-S gravity anomalies [Hochstein and Nunns, 1975]. The 1891  $\sim M6$  Waikato Heads earthquake offshore to its west [Downes, 1995] hint that it may be active.

### 2.3.3 GNSS Geodesy 1995-2013

New Zealand has a long history of geodetic surveying, with thousands of established and well-maintained trigonometric beacons located at topographic highs distributed across the country [Land Information New Zealand (LINZ); [www.linz.govt.nz](http://www.linz.govt.nz)]. These distinctly painted black and white beacons allowed for ground-based geodetic sighting between them, and repeat measurements from 1925-1983 have proven capable of accurately describing the active deformation of much of New Zealand [e.g. Walcott, 1984]. In more recent times these beacons have been retrofitted with stainless steel pins embedded in concrete at their base, providing durable marks for high-precision Global Navigation Satellite System (GNSS, historically referred to as simply "GPS") antenna positioning necessary to resolve the slower-moving parts of New Zealand. However despite the capability and ubiquity of these beacons and marks throughout the country, to date the volume of GNSS surveying done in NWNZ has been relatively sparse. This may have been due to the inherent difficulty in resolving this low deformation environment, particularly in the northern North Island which only had a single reference site prior to the strengthening of New Zealand's GNSS reference network in  $\sim 2003$  [Beavan and Haines, 2001; Beavan, 2005].

Nevertheless a scattered amount of transient campaign surveying was done throughout NWNZ, with archival data beginning as early as 1993. In 1995 a large (110+ sites) campaign survey spanning nearly all of the North Island was conducted by LINZ (then the Dept. of Survey and Land Information) as part of the GPS2000 project to establish foothold GNSS data at many of the country's notable and long-lived "1st order" geodetic markers [Beavan and Haines, 2001]. Though this campaign was done with relatively short 8-hour occupation times and often prior to the existence of any nearby continuous reference stations (the first North Island site AUCK/Auckland did not exist until June 1995), the data was still of good quality and has grown increasingly valuable with age due to the larger cumulative motion over long time periods.

Though there was some additional campaign surveying done 1996-1998, it was generally too sparse and too soon after the 1995 campaign to reliably constrain much of the northern North Island [e.g. Beavan and Haines, 2001]. Continuously operating reference site AUCK was the only robust velocity solution in the area until the construction of TAKL in 2001 (an Auckland City tidal gauge not necessarily constructed for high precision geodetic measurements), then continuous reference sites WHNG/Whangarei and CORM/Coromandel in 2003. CORM, on the east and opposite side of the Hauraki Rift as AUCK, proved especially useful as it provided the first direct measurement of the rate and right-lateral character of crustal extension across the rift. However this data has to date not been the subject of a regional study.

Unlike elsewhere throughout New Zealand and which was routinely campaign surveyed at ~3 year intervals, the northern North Island was not surveyed again until 2006 (~3 sites), and not fully surveyed (15+ sites) again until 2013 by Neville Palmer at GNS Science, contracted by LINZ as part of their new and ongoing nationwide surveying project. This survey re-measured many sites which had been occupied in 1995, nearly doubling the volume of viable velocity estimates in the northern North Island (Figure 2.10). The new campaign data confirmed that the velocity of continuous site CORM on the east side of the rift was representative of the rift's behaviour, or at least the northern portion. Regions to the south as well as nearer the rift axis remained ambiguous. The data collected in 2013 was used in the compendium of New Zealand geodetic velocity estimates published by Beavan et al. (2016) but was not presented with enough detail or at a fine enough scale to characterise the northern North Island relative to the rest of the country.

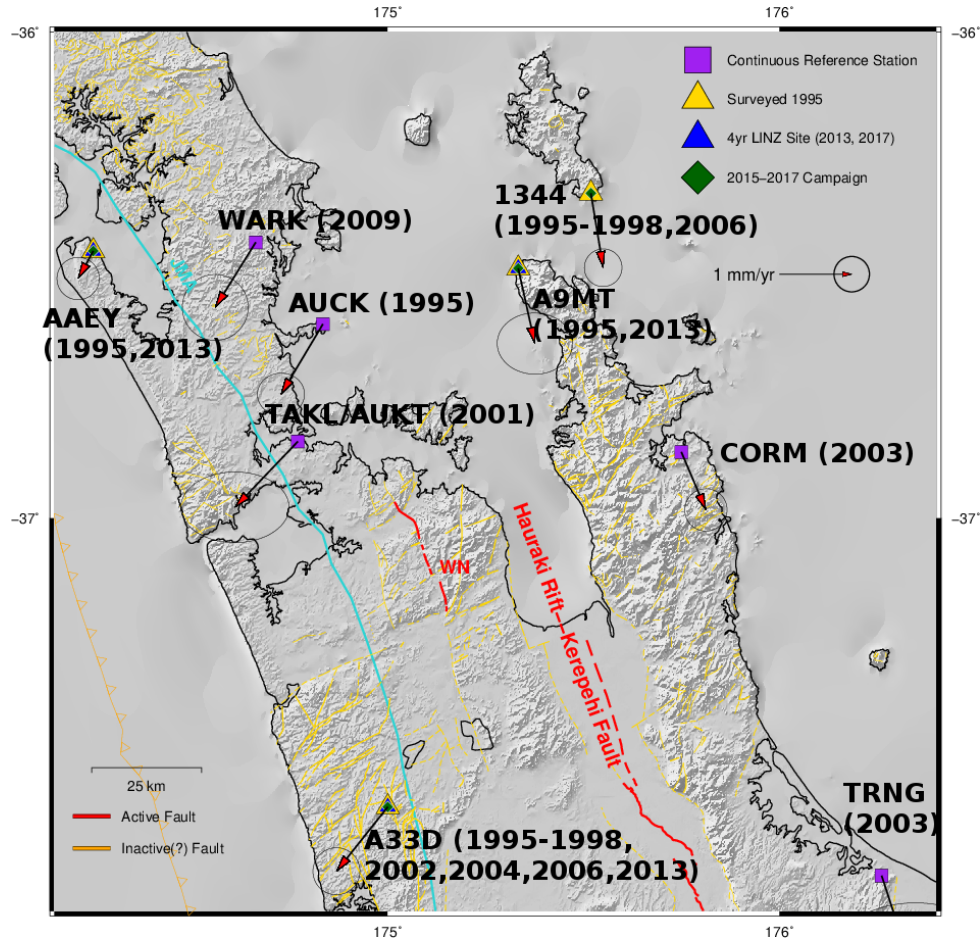


**Figure 2.10:** Velocity estimates of Auckland / Hauraki Rift region using data 1995–2013. Parenthetical dates indicate when the site was constructed or surveyed. Active faults plotted in red [Langridge et al., 2016], “inactive” in gold [Edbrooke et al., 2005; Kenny et al., 2012]. JMA = Junction Magnetic Anomaly, WN = Wairoa North Fault.

#### 2.3.4 GeoNet’s Seismic Catalogue of Shallow Events

The overall pattern of shallow seismicity seen in the North Island is dominated by stresses emanating from the Australian-Pacific plate interface as the Pacific Plate subducts SW beneath the Australian Plate at the eastern margin of continental Zealandia. Within the crust (<50 km depth; Figure 2.11) this oblique subduction produces right-lateral strain and places the majority of the North Island’s earthquakes throughout the fore-arc and along the right-lateral North Island Fault System [Anderson and Webb, 1994]. Further NE the quasi back-arc TVZ (yellow line) also produces a large quantity of earthquakes from its arc-normal extension [Bryan et al., 1999; Hurst et al., 2002; Sherburn et al., 2003] and resulting volcanism [Sibson and Rowland, 2003; Reyners et al., 2007; Clarke et al., 2009; Rawlinson, 2011]. The NE extension of the TVZ

north of 37°S (Figure 2.11, thinner yellow line) appears to show a discontinuous NW jump of strain from the TVZ axis to the Havre Trough axis [e.g. Lamarche, 2000]. West of the TVZ towards the Taranaki Peninsula {174°E, 39.3°S} activity appears distributed between the active Cape Egmont Fault System (western blue line) [Sherburn and White, 2005] and somewhat deeper near the presumed-inactive Taranaki Fault (eastern blue lines) [Stagpoole and Nicol, 2008; Giba et al., 2010; Giba et al., 2013; Uruski, 2015]

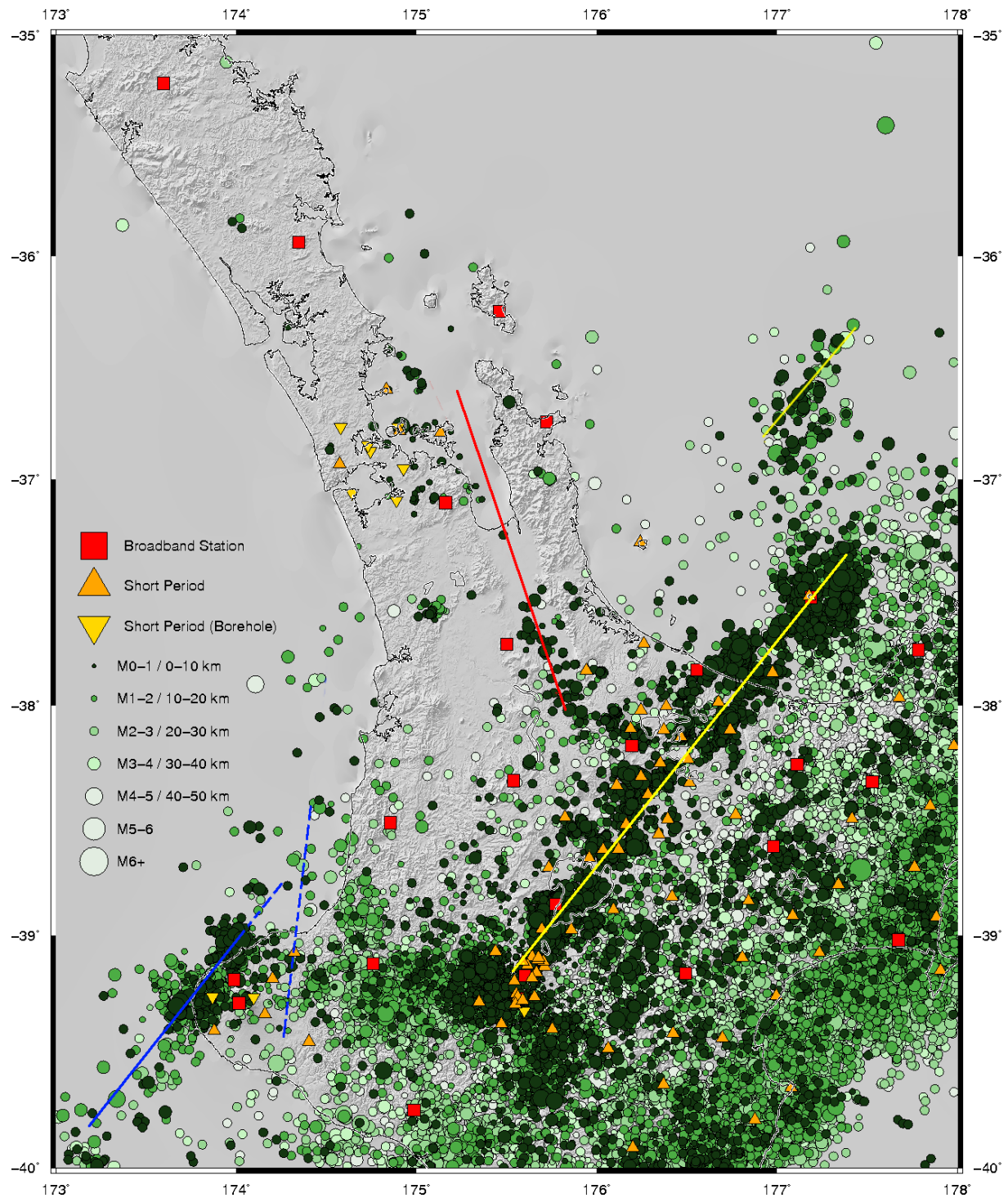


**Figure 2.11:** GeoNet catalogue seismicity from Jan 1 2006 to Dec 31 2017 up to 50 km depth. Magnitudes are plotted proportional to increasing icon size, and depths with increasingly lighter shades of green. All available seismic stations used by GeoNet are plotted, though some stations used to derive these hypocentres may be located throughout the northern half of the South Island, particularly for larger events. Red line = Hauraki Rift axis, Blue lines = Taranaki and Cape Egmont Fault systems, Yellow line = TVZ axis.

North and west of the TVZ is the known trace of the Hauraki Rift (Figure 2.11, red line). The seismic visibility of the Hauraki Rift seems to terminate north of 37.5°S, and in general seismicity seems to mostly disappear north of here with the slight exception of the Auckland area {175°E, 37°S}. However geodetic evidence 1995-2013 (Figure 2.10) suggests that much of the North Island north of 37.5°S, and particularly the Hauraki Rift region is actively straining and thus should have some degree of accompanying seismicity [Hochstein and Nixon, 1979; Hochstein et al.; 1986; Hochstein and Ballance, 1993; Chick et al., 2001]. That these events are not widely detected by GeoNet's nationwide system could be due to both a lack of seismometers in the area to adequately locate them and/or that their current detection routine is not sensitive enough to detect the incoming P-wave arrivals generated by these events. This is partially supported by the relatively high amount of events located near Auckland, the location of which are almost certainly due to the dense seismometer array surrounding it.

# 3

## POTENTIAL FIELD DATASETS & INTERPRETATION STRATEGIES

---

Knowledge of the structure and orientation of the geologic basement rock beneath north-west New Zealand (NWNZ) is critical to interpret both the region's activity as well as how strain may be accommodated. Furthermore in order to understand how NWNZ has evolved it is also necessary to understand the tectonic history and environment it resides in within north-east Zealandia and the eastern Australian Plate.

Though true knowledge of subsurface structure requires direct sampling, it can often be reasonably inferred remotely by a logical interpretation of the gravitational and magnetic potential fields above it. Indeed, geophysical studies involving analysis of gravity anomalies have been used since the eighteen century [e.g. Bouguer], and magnetic data has long been used to trace the continuity of magnetised material [e.g. Molnar et al., 1975, Reford, 1980] as well as explicitly interpret the tectonic history of the south-west Pacific [e.g. Scotese et al., 1988; Sutherland, 1999]. In this project this data is primarily used to identify the location of past or active rifting, thinning, faulting, or compression by identifying areas of contrasting density within the crust. It is also used to trace the continuity and dislocations of Zealandia's basement structure as well as interpret its tectonic history based on age constraints supplied by volcanic rocks, seismic stratigraphy, and the dating of the obduction events at New Caledonia and New Zealand.

### 3.1 MAGNETIC ANOMALIES

Magnetic anomalies are the result of ferrous material within molten rock aligning parallel to the earth's magnetic field, creating a definitive positive or negative signature at the surface, then permanently freezing in position once the rock congeals [Schubert and Turcotte, 2002]. Accordingly, igneous materials and terranes typically have the most uniform and thereby strongest magnetic anomalies (e.g. the Median Batholith, Dun Mountain-Maitai Terrane, Norfolk, Loyalty, and Three Kings Ridges, volcanoes, oceanic seafloor, etc.) [Mortimer, 2004]. As the polarity of the magnetic field flips sporadically [e.g. Berggren et al., 1985; Cande and Kent, 1995] these anomalies record a history of melting and fracturing of the (mostly oceanic) crust, providing a clear mechanism for tectonic reconstructions.

Magnetic analysis is particularly suited for NE Zealandia because it is largely comprised of accreted oceanic and otherwise igneous terranes [Sutherland, 1999; Mortimer, 2004; Spandler et al., 2005; Collot et al., 2009; Mortimer et al., 2014]. Further, the abnormally long-lasting Chron 34 period 118-83 Ma in which there were no magnetic reversals [Cande and Kent, 1995] manages to encompass ~18 Ma on either side of the termination of activity at the Norfolk Ridge ~100 Ma [Laird and Bradshaw, 2004]. This stable period allowed for the build up of strong and consistent magnetic anomalies currently comprising NE Zealandia's eastern margin.

### 3.2 GRAVITY ANOMALIES

Gravity anomalies vary depending on what can be assumed, modelled, and removed from raw gravity measurements, with each additional refinement producing a unique anomaly. Some of the required mathematics can be done mentally as a rough estimate, and others may require computational processing. The primary anomalies used in this work are the Free Air anomaly (FAA) and the Bouguer anomaly (BA). These tend to be complementary in gravity analysis with the FAA largely controlled by near-surface topographic effects and the BA dominated by subsurface density variations.

#### 3.2.1 *The Free Air Anomaly*

The Free Air Anomaly (FAA) is the deviation between a gravity measurement and an a priori reference model, typically a simple function of latitude, radial height, and degree of the Earth's oblateness [Turcotte and Schubert, 2002]. This reference model is commonly (and in this work) the 1984 Ellipsoidal Reference Gravity Formula [Decker, 1986]. The FAA is then proportional to the mass above or below the amount predicted by the reference model which is largely the result of a surface crustal feature not in isostatic equilibrium with its surroundings.

#### 3.2.2 *The Bouguer Anomaly*

The Bouguer anomaly (BA) is the FAA less the gravitational contribution of the crust's topography assuming a uniform density, making it primarily proportional to subsurface density variations. The process of calculating the gravity contribution of the topography can be done

computationally with very high precision in two ways. An advanced method is to discretise a topographic dataset into many small 3D cubes and calculate and sum the individual gravity component of each cube at each point on a map [e.g. Cordell and Henderson, 1968; Fullea et al., 2008]. This method involves a high degree of crustal modelling and may be computationally expensive, but it allows for both earth curvature and taking (or inverting) for gravity at variable heights as might happen during an aerial gravity survey [e.g. McCubbine et al., 2017] or composite dataset.

Alternatively the gravity contribution of a 3D surface may be calculated via a 2D Fourier transform [e.g. Parker's method; Parker, 1973]. This technique can quickly compute the gravity of the topographic data in the frequency domain via Fourier analysis. The largest limitation of this method is that the original gravity data must be measured to a level surface, largely limiting its application to data collected via satellite, at sea, or a "perfect" aerial survey taken at a uniform height. Additionally each horizontal layer must be modelled as a homogeneous density, and a flat-earth approximation must be assumed. Fourier analysis also requires a continuous surface of data, which theoretically limits its application to satellite-based data or data which can be reasonably interpolated. Land-based data with a large off-shore component (e.g. New Zealand) can be used by first masking offshore areas with satellite data (interpreted at sea level) and subsequently removing it, with negligible detrimental effect.

As this project exclusively utilised ground-based and satellite data, and did not assume laterally heterogeneous crustal densities, Parker's (1973) method was used. The crust was modelled to consist of two layers: the area above sealevel (density contrast  $\rho_{air-crust} = 2670 \text{ kg/m}^3$  [Turcotte and Schubert, 2002]), and the crust between some uniform arbitrary depth (here the deepest part of the ocean in our study area) and sealevel (density contrast  $\rho_{water-crust} = 1632 \text{ kg/m}^3$ , assuming a seawater density of  $1038 \text{ kg/m}^3$  [Gladkikh and Tenzer, 2012]). The 2D gravitational attraction for each of these density contrasts was calculated individually and then removed from the FAA to produce all of the BAs shown in this work using the "gravfft" code in Generic Mapping Tools [GMT 5, Parker, 1973; Luis and Neves, 2006; Wessel et al., 2013].

### 3.2.3 Approximations and Interpretation Strategy

The non-rigid, viscous behaviour of the Earth's mantle enables the crust/lithosphere to "float" atop it [Turcotte and Schubert, 2002]. This effectively means that continental and oceanic plates

generally tend towards a state of isostatic equilibrium via Pascal's Law which states that hydrostatic pressure should be equal throughout all points at the same elevation. The variable topography seen throughout the crust is then explained by Airy's hypothesis which states that the weight of the topography is counter-balanced by the presence of an equal and opposite mass directly beneath it. Thus regions of positive topography should tend to have thicker, lower-density "roots" beneath them, and regions of deep or negative topography should have thinner crust which are in-filled from below with denser mantle.

Gravity anomalies can accordingly be used to interpret whether or not a crustal or tectonic feature is likely to be in isostatic equilibrium, and additionally provide insight as to composition, thickness, and tectonic stress of the crust and/or lithosphere. Assuming perfect equilibrium, no density heterogeneity, and no active stressors, the FAA will be nearly zero as the positive topographic gravity above will be cancelled by the negative gravity below, producing a reading close to the reference gravity value at the point of measurement [e.g. Sclater et al., 1975]. The BA by contrast, having removed the gravitational effect of the topography (Section 3.2.2) will reflect only the subsurface crustal structure. Of course in reality the earth's tectonic plates have a mechanical strength which disallows the concept of "perfect" equilibrium and they have also invariably undergone a large degree of chemical and physical alteration, making them unable to be so simply interpreted. Furthermore the fundamental non-uniqueness of potential field analysis makes definitive structural interpretations impossible. Regardless, by understanding the tectonic environment and assuming an a priori structure of the plate gravity anomalies are still valuable in interpreting structure.

### 3.2.3.1 *Flexural Support*

In addition to buoyancy forces, crustal features are also supported by the tensile strength or flexural rigidity of the crust itself [Walcott, 1970; Forsyth, 1985; Fowler, 1990; Turcotte and Schubert, 2002]. The exact relationship between a (infinite or semi-infinite) plate's flexural rigidity  $D$  ( $\text{Pa} \cdot \text{m}^3$ ) is proportional to the plate's effective elastic thickness  $T_e$  ( $\text{m}$ ), a hypothetical layer not explicitly representing actual structure, as well as Young's modulus  $E$  ( $\text{N}/\text{m}^2$ ) and Possion's unitless ratio  $\nu$ . The relationship between these parameters is

$$D = \frac{E \cdot T_e^3}{12(1 - \nu^2)}$$

which can then be used in the differential equation relating the degree of plate deflection  $w(x)$ , mantle and crustal densities  $\rho_m$  and  $\rho_c$  in response to a load  $p(x)$ ,

$$D \frac{\delta^4 w}{\delta x^4} + g(\rho_m - \rho_c)w = p(x)$$

The solution for  $w(x)$  ultimately gives a periodic function solution with a flexural wavelength  $2\pi\alpha$ , where  $\alpha$  is a flexural parameter defined as

$$\alpha = \frac{4D}{g(\rho_m - \rho_c)} = \sqrt[4]{\frac{E \cdot T_e^3}{3(1 - \nu^2)g(\rho_m - \rho_c)}}.$$

This flexural parameter essentially dictates the maximum wavelength (e.g. width) of a load that a plate will be able to flexurally support. In the western North Island, Holt and Stern (1991) determined that load widths greater than  $4\alpha$  were likely to be isostatically supported. This ratio is likely to apply for much of the similarly aged and thickened [e.g. Stern et al., 1987] NWNZ, but a similar ratio is also observed for starkly contrasting environments as well (e.g. sediment loads in ocean crust [Walcott, 1972]) which may mean it is applicable to most crustal features globally. Assuming this ratio is then valid, a relationship can be derived between a theoretical maximum supporting load width and  $T_e$  (Figure 3.1). This relationship is also dependent on Young's modulus which can vary drastically between materials, so two end-member values are shown with 10 GPa, approximating softer crustal materials (e.g. clay) and 70 GPa closer to Basalt or Granite [Fowler, 1990]. Figure 3.1 hints that many if not all crustal features in NWNZ with a width  $< 200$  km are likely to be flexurally supported, assuming a  $T_e$  greater than 20+ km [Holt and Stern, 1991].

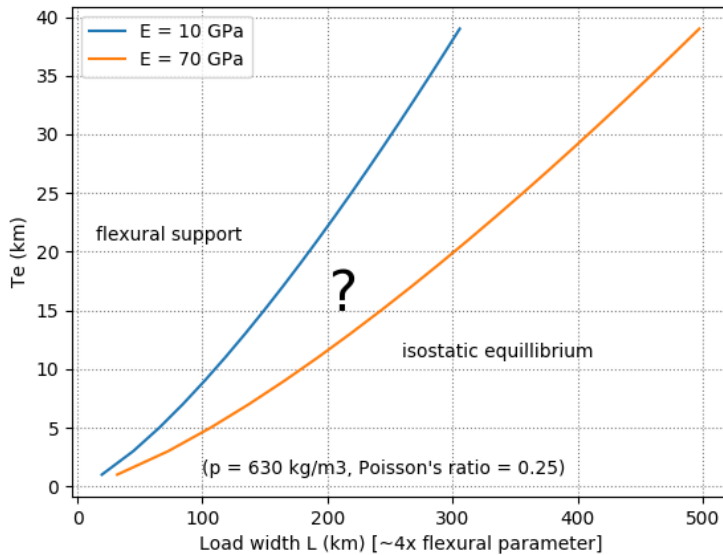


**Figure 3.1:** Flexural support chart for  $T_e$  vs. load width assuming it is equal to four times the flexural parameter  $\alpha$  [e.g. Holt and Stern, 1991]. Combinations above the blue line are very likely to be flexurally supported, and below the orange line the system is likely to be in isostatic equilibrium. Between these lines the system is uncertain, and may depend on Young's modulus  $E$  as well as other factors.

In addition to the strength of the plate, topography may also be supported or depressed by stress within the plate from nearby tectonic interactions such as faults and subduction zones, or with the addition and removal of mass at the surface or below it [McNutt, 1980]. It may also be supported *dynamically* [e.g. Molnar et al., 2015] by the flow of the mantle beneath it. In these instances the lateral transmission of stress through the plate serves to bend it upwards or downwards, effectively holding the plate against its tendency towards isostatic equilibrium. These scenarios produce strong gravity anomalies with low topographic coherences, however determining the degree of influence this added strain has on the gravitational signal is not trivial. Generally, compressional bowing of the plate upwards will produce positive FAAs as the plate is being lifted against gravity, and positive BAs as this motion is not being accommodated by thicker crust from beneath. In the opposite sense, the addition of weight at the surface of the crust (e.g. a glacier, or via obducted material) will deflect the place downwards into the mantle, generating negative FAAs and negative BAs.

### 3.2.3.2 Subduction Zones and Ridges

Active subduction trenches where denser oceanic crust sinks into the mantle are strongly dynamic features which generate strongly negative FAAs and BAs at the trench. The negative

FAAs are the result of the negative density contrast due to the water within the trench, and the negative BAs are due to sinking plate actively pulling material into the earth against its natural upward buoyancy [Turcotte and Schubert, 2002]. The oceanic plate immediately before the trench can also often bow upwards via flexural isostasy within the plate, generating relatively milder gravity highs [e.g. Levitt and Sandwell, 1995]. The ridge behind the trench invariably has both FAA and BA highs, the FAA due to the placement of denser volcanic material and the BA due to the presence of the colder and denser subducting slab beneath [e.g. Fowler, 1990].

Though there are no active subduction zones likely to affect dynamics at the margin of NE Zealandia, there are several proximal fossil subduction zones at the Norfolk, Loyalty, and Three Kings arcs (Figure 2.2). When these features ceased activity they ceased being dynamically affected by the downward pull of the subducted plate (assumed to have detached) and their trenches were gradually filled with lower-density sediment, hypothetically preserving low BAs and to a lesser extent low FAAs as the crust attempts to regain isostatic equilibrium.

The volcanic ridges resulting in the subduction process also have distinct positive gravity signatures owing to the higher density of their volcanic material and likelihood that these small features are being dynamically supported by the strength of the thicker crust [e.g. Watts and Cochran, 1974]. As the bathymetric highs of these ridges are built from volcanic eruptions and not the result of being in isostatic equilibrium with a thick sub-crustal root, they generally have stronger FAA signatures but are still usually visible in the BA due to their higher density relative to an average crustal value. In this sense volcanism is also particularly evident when buried [e.g. Ramillien and Wright, 2002].

### 3.2.3.3 *Faulting*

Normal or reverse faulting within the crust can produce regions of relative subsidence or uplift which may or may not be strongly dynamically accommodated by the tensile strength of the crust, depending on the size of the fault offset relative to the thickness of the crust [e.g. Walcott, 1970]. Smaller, dynamically compensated faults are then capable of generating significant FAAs [Okubo, 1992] with relative positive magnitudes on the uplifted side. Strike-slip faults can also produce regions where rocks of differing densities can exist on either side of the fault, producing contrasting gravity anomalies [e.g. Griscom and Jachens, 1989].

Trenches and uplifted features produced by tectonic compression can also produce similar gravity signatures as subduction trenches and ridges, depending on their scale and subsequent degree to which they are dynamically supported. This is evident throughout the Southern

Norfolk Ridge System whose "ridges" are not necessarily volcanic [e.g. Stagpoole et al., 2009; Bache et al., 2012; Bache et al., 2014; Figure 2.2].

### 3.2.3.4 *Plate Stretching and Shortening*

Often tectonic stress applied to a plate will permanently thin or thicken the crust, potentially resulting in subsidence or uplift (respectively) as it attempts to regain isostatic equilibrium [Turcotte and Schubert, 2002]. Assuming a new state of isostatic equilibrium is eventually reached, the FAA should remain neutral whereas the BA will continue to reflect the new crustal structure. Accordingly a thinned crust will be replaced from below with denser material producing higher BAs (e.g. the 300 km wide Afar Rift [Ebinger and Hayward, 1996]), and conversely thickened crust should result in lower BAs. However if the width of rifting is sufficiently small relative to the thickness of the crust, the rifted void will be mostly compensated dynamically by the rigidity of the plate rather than subside isostatically. This will generate FAAs in addition to low BAs, likely regardless of subsequent sediment in-fill e.g. the 25 km wide Hauraki Rift [Hochstein et al., 1986].

Plate shortening or compression typically results in a thickening of the plate from above and below. In scenarios of continuous compression (e.g. the continent-continent collision uplifting the Himalayas), the resulting FAA may be strongly positive in areas as the region will be dynamically supported by the horizontal stress driving the compression. Long-ago accreted terranes such as those forming Zealandia [Mortimer et al., 2004] will now likely be in isostatic equilibrium, muting their FAAs, but any regions of buckled, thrusted, or otherwise thickened crust will still generate negative FAAs and BAs [e.g. Molnar, 1975].

### 3.2.3.5 *1D Infinite Slab Approximation*

A quick way to estimate the gravity anomaly associated with a layer of constant thickness and density is described by Gauss' Law. This easily determines if a gravity anomaly at a basin or mountain range corresponds to a system in isostatic equilibrium or perhaps one under stress by some nearby active tectonics [e.g. McNutt, 1980].

The infinite slab (or plate) approximation presumes that the gravitational attraction at any point above the slab is uniform, provided that the height above the slab is dwarfed by the width of the slab (i.e. the slab appears to be "infinite"). Though this would hardly seem applicable anywhere, in practice if the width of the slab is an order of magnitude or greater this constraint

holds up remarkably well [Turcotte and Schubert, 2002]. This is typically true for continental roots and sedimentary basins when examining areas over a few hundred *km* wide.

The actual equation, relating the resulting infinite slab gravity  $\Delta g$  anomaly with the thickness of the slab is:

$$\Delta g = 2\pi G h \rho$$

where  $h$  is the thickness of the layer ( $m$ ),  $\rho$  is the density or density contrast of the layer ( $kg/m^3$ ), and  $G$  is the Universal Gravitational Constant,  $6.67408 \times 10^{11} m^3 kg^{-1} s^{-2}$ .

However because SI acceleration is rarely used in gravimetry, simplifying and converting to *mGal* ( $10^5 m/s^2$ ) gives

$$\Delta g = 4.2 \cdot 10^{-5} * h(m) * \rho(kg/m^3)$$

Often the "infinite layers" considered are either a continental root, or a basin filled with sediment, either of which composed of material with variable densities. For simplicity this project simply assumed a universal crustal density of  $2670 kg/m^3$  for both continental and ocean crust [Turcotte and Schubert, 2002] which would still produce fair relative anomalies between oceanic and continental areas. Thus for example, the gravitational attraction of a crustal root 500 *m* thick with a negative density contrast of  $600 kg/m^3$  relative to the lithosphere should give -12.6 *mGal*. Some caution must be used against over-prescribing this technique, especially in small or decidedly unique geometries such as a rift or subduction trench.

### 3.2.3.6 Boussinesq Approximation

It is also possible to calculate the gravitational change due to heating or cooling, which may be needed to interpret gravity anomalies associated with rift environments such as the Taupō Volcanic Zone (TVZ). This may be accomplished by assuming a generalised crustal thermal expansion coefficient of  $3.2 \cdot 10^{-5} ^\circ C^{-1}$  [Parsons and Sclater, 1977] which correlates a decrease of density with increasing temperature via the equation

$$\Delta \rho = (1 - \alpha \Delta T) \rho_0$$

where  $\rho_0$  is the original density,  $\alpha$  is the expansion coefficient  $3.2 \cdot 10^{-5} ^\circ C^{-1}$ , and  $\Delta T$  is the change in temperature ( $^\circ C$ ).

For instance, if a continental rift were being fluxed with a high +200  $^\circ C$  heat from below throughout its 10 *km* thick crust, the resulting gravity anomalies should only be on the order

of  $-7.1 \text{ mGal}$ . Thus thermal affects on density and hence gravity are typically much smaller than density variation associated with lithological heterogeneity and are not likely to play a large role in NWNZ outside of the TVZ.

### 3.3 DATASETS

This project utilised previously available data measured at both the global and regional scale via both satellite and ground-based field station measurements. The satellite-based gravity datum is derived from a combination of satellite measurements and shiptrack data, and on land also includes the global EGM2008 earth gravity model [Pavlis et al., 2008], and is provided for free by the Scripps Institute of Oceanography [ver. 24.1, Sandwell and Smith, 2009; Sandwell et al., 2013; Sandwell et al., 2014; Garcia et al., 2014]. It is published pre-corrected as a FAA at spatial resolutions of 1 *arcminute* ( $\sim 1.85 \text{ km}$  at  $45^\circ\text{S}$ ). This datum features heavily in this work and provides seamless transitions of onshore and offshore data. The topographic/bathymetric dataset used in tandem to this datum is also satellite-based and provided by Scripps [SRTM15, Smith and Sandwell, 1997; Becker et al., 2009] at resolution of 0.25 *arcminute*. Bathymetry is estimated from gravity by a transfer function assuming various isostatic compensation models [e.g. Dixon et al., 1983; Smith and Sandwell, 1994] and is further calibrated by shiptrack sonar data. It is also the dataset this project used to derive a satellite-based BA (Section 3.2.2).

Additional ground station gravity data was made available courtesy of V. Stagpoole and the GNS Science gravity database. This included access to 40,000+ surface gravity measurements collected in the field over the last  $\sim 70$  years as part of the New Zealand Primary Gravity Network [Robertson and Reilly, 1960]. This data is capable of variable resolutions depending on the distribution of measurements, with difficult access regions typically being relatively sparse. To accommodate for irregularly surveyed regions the data was block averaged at a resolution of 2 *arcminutes* before gridding to 1 *arcminute*. By preconditioning the data with a larger grid size than one is intending to plot at, aliasing and other spurious artefacts are negated. Problematically sparse regions were summarily over-smoothed for robustness with the GMT "surface" code, a 2D continuous curvature algorithm nearly equivalent to a minimum curvature solution but damped enough to suppress false local maxima or minima [Smith and Wessel, 1990; Wessel et al., 2013].

The ground station data came pre-corrected to the IGS1980 FAA in *mGal*. A BA of this data was also provided which was calculated by estimating and removing the gravitation effect local topography in the field at the time of measurement [e.g. Hammer, 1939]. A separate BA was derived independently using Parker's (1973) Fourier continuation method, as done with the satellite FAA data. The topography data used to numerically calculate the ground station BA was the same satellite-based SRTM15 model used to derive the satellite-based BA [Smith and Sandwell, 1997; Becker et al., 2009]. The problem of upward continuing ground-based data in the frequency domain without offshore data was resolved by overlying offshore areas with satellite data during the calculation, then subsequently removing this data afterwards.

Magnetic data is provided by the EMAG2 dataset compiled by the National Oceanic and Atmosphere Administration (NOAA) from satellite, ship, and airborne measurements in 2 *arcminute* resolution at 4 *km* above the geoid [Maus et al., 2009]. It is fully continuous both on and offshore. The datum is plotted in its original form throughout this project at resolutions sufficient to track the continuation of Zealandia's basement terranes. However is too coarse for finer analysis within onshore New Zealand.

### 3.4 NORTH-EAST ZEALANDIA

It is appropriate to first examine the broader NE periphery of Zealandia prior to a more detailed view of NWNZ. While many workers have already done potential field examinations throughout Zealandia [e.g. Molnar, 1975; Sutherland, 1999a], recent versions of the satellite gravity [e.g. Sandwell et al., 2014] and particularly magnetic data [e.g. Meyer et al., 2017] provide much-needed enhancements to both the resolution, coverage, and quality of data. The FAA (Figure 3.2), BA (Figure 3.3) and magnetic anomaly (Figure 3.4) of NE Zealandia and SW Pacific are presented independently and without annotation for clarity (see Figure 2.2 for labels). The FAA does a fair job at highlighting the N-S continuity of the basement structure from New Zealand to New Caledonia though the continuity of some lineaments is uncertain, and resolution is lost near continental New Zealand which is dominated by dynamically supported surface volcanism. The BA highlights subsurface density variations which resolves a lot of the FAA's ambiguity, and in particular supports the idea that New Zealand and the Lord Howe Rise are thick and buoyant features likely to be in isostatic equilibrium [e.g. Segev et al., 2012] and that the northern New Caledonia Trough may have areas of oceanic or significantly

thinned continental crust [e.g. Lafoy et al., 2005; Klingelhoefer et al., 2007; Collot et al., 2008]. The magnetic data also shows that the basement from New Caledonia to New Zealand is continuous between the Lord Howe Rise and Norfolk Ridge [e.g. Sutherland, 1999a] and highlights several regions of probable crustal reorganisation.

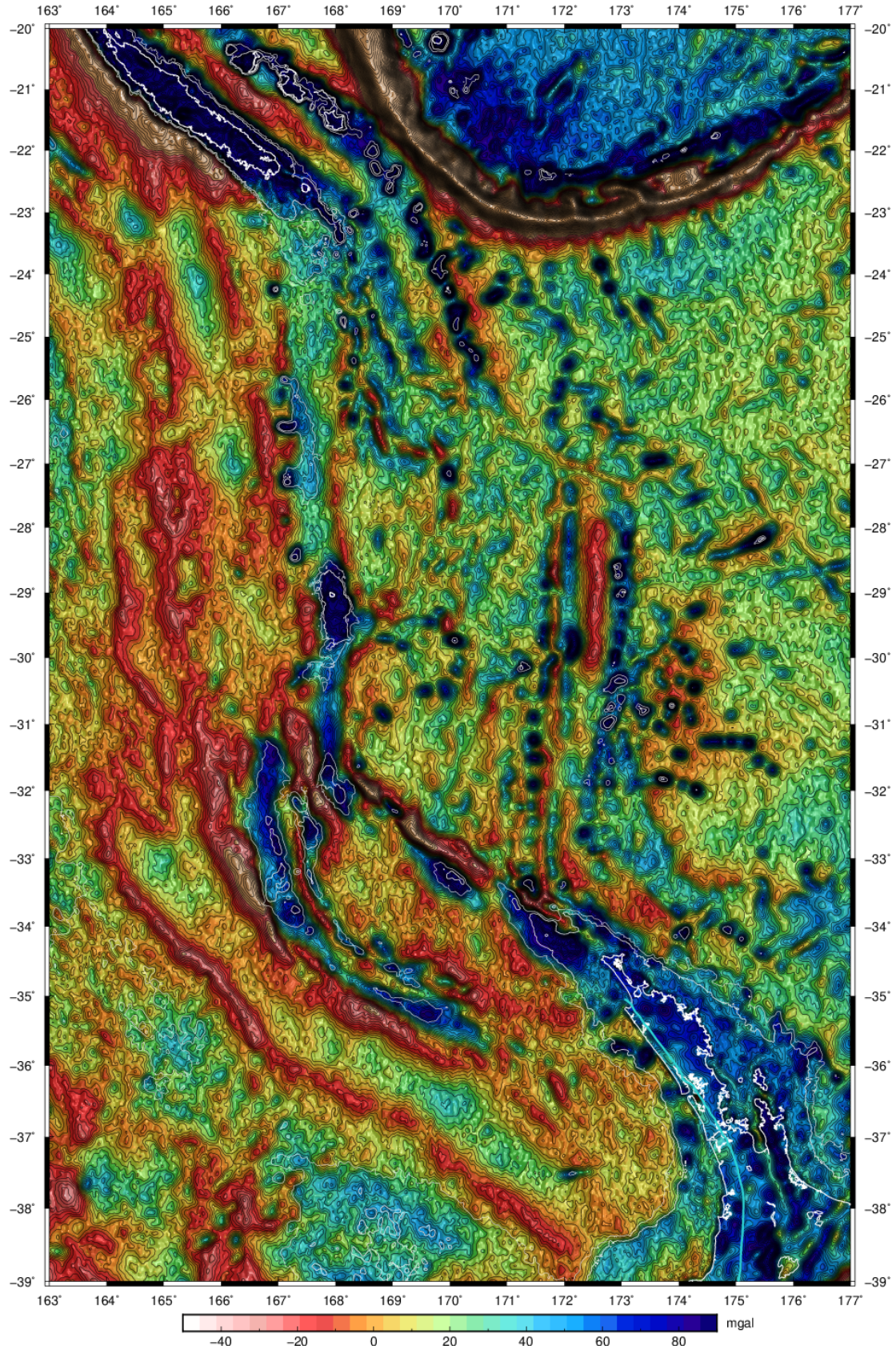


**Figure 3.2:** Satellite Free Air anomaly [Sandwell and Smith, 2009; Sandwell et al., 2013; Sandwell et al., 2014; Garcia et al., 2014] of the SW Pacific. Resolution is 0.25 arcminute and 10 mGal contours are plotted. Bathymetry [Smith and Sandwell, 1997] contours at 0, -500, and -1000 m are overlaid in white. The JMA is plotted in light blue.

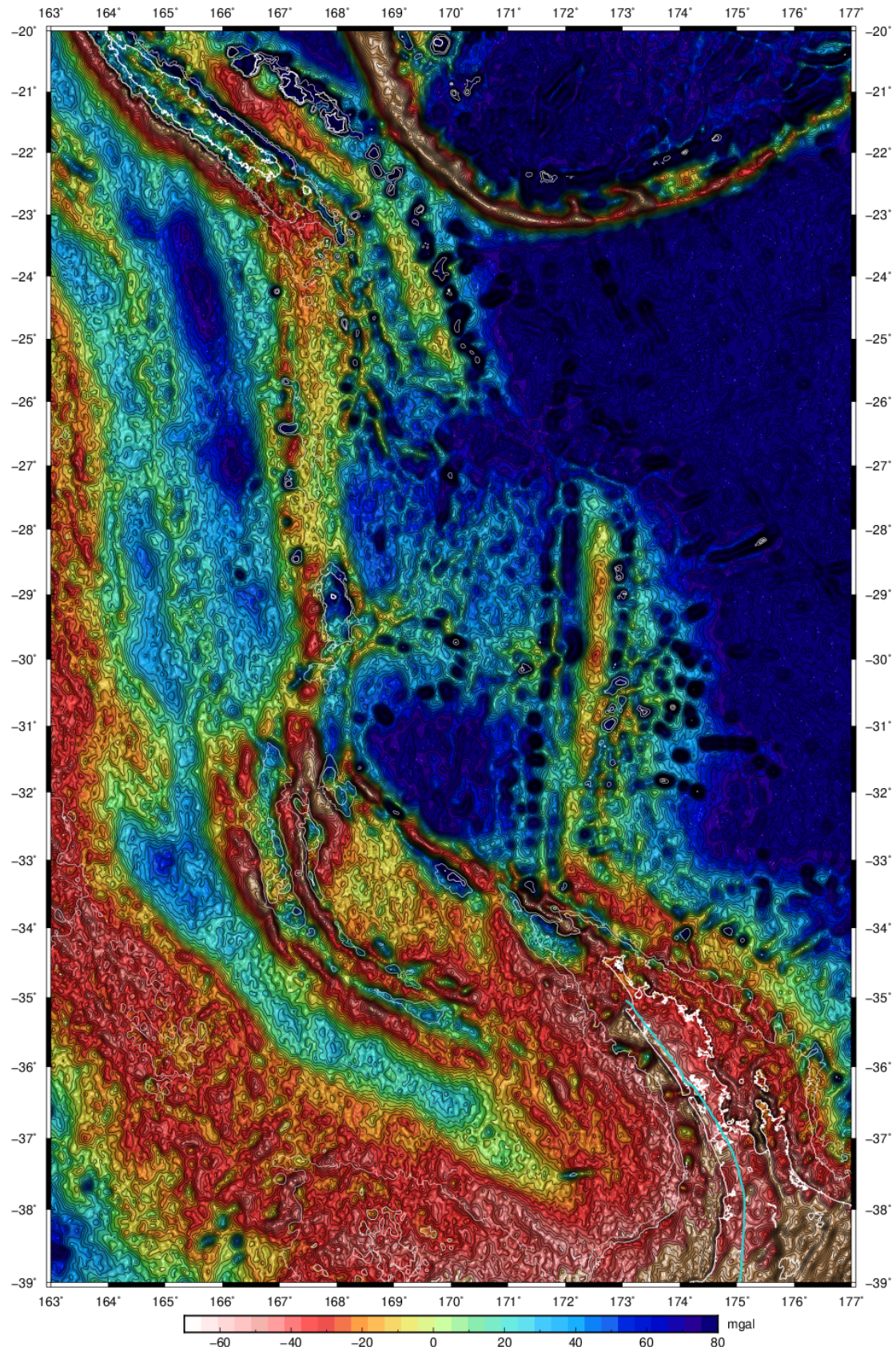


**Figure 3.3:** Satellite Bouguer Gravity anomaly of the SW Pacific derived from satellite FAA (Figure 3.2) and satellite topography (Figure 2.2) data assuming ocean water ( $1027 \text{ kg/m}^3$ ) and crustal density  $2670 \text{ kg/m}^3$ . Resolution is  $0.25 \text{ arcminute}$  and  $10 \text{ mGal}$  contours are plotted. Bathymetry [Smith and Sandwell, 1997] contours at  $0$ ,  $-500$ , and  $-1000 \text{ m}$  are overlain in white. The JMA is plotted in light blue.

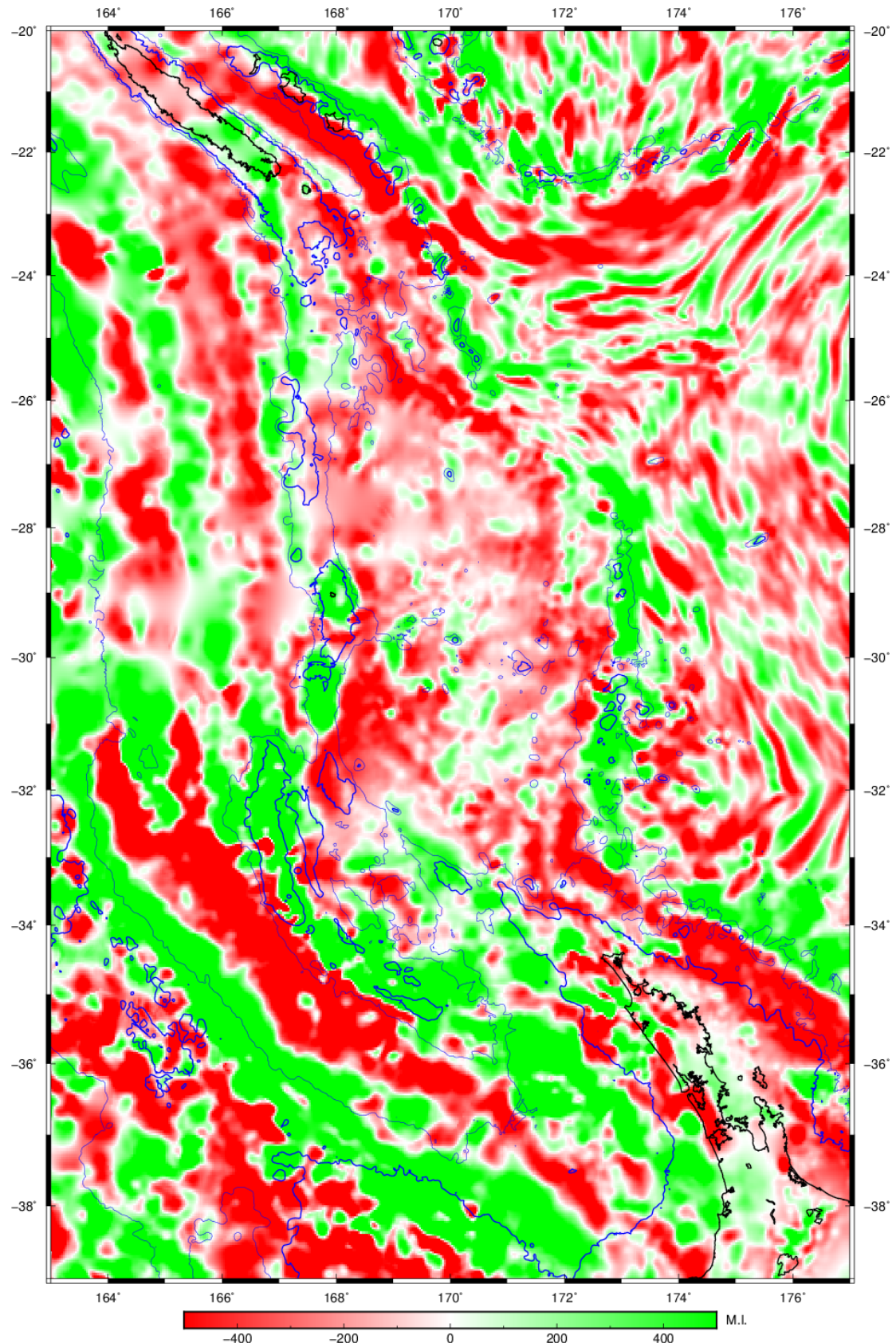


**Figure 3.4:** EMAG2 (v3) magnetic data compiled from satellite, ship, and airborne measurements in 2 arcminute resolution [Maus et al., 2009; Meyer et al., 2017]. Magnitudes have been clipped at +/- 500 nT for clarity. Positive anomalies are in green, negative red. Bathymetry [Smith and Sandwell, 1997] contours at 0, -500, and -1000 m are overlain in dark blue or black.

### 3.5 NORTH-WEST NEW ZEALAND

A closer inspection of NWNZ's FAA and BA anomalies are presented in this section, derived from satellite measurements as well as data recorded nearer the surface by individual measurements or air/sea surveys. These datasets are presented independently to highlight their advantages and disadvantages.

#### 3.5.1 *Satellite Data*

Satellite magnetic data at this scale (Figure 3.4) has a resolution of 2 *arcminutes* and is too coarse for finer structural interpretations. The FAA (Figure 3.5) highlights the degree to which NWNZ is dominated by volcanism, interpreted as large positive anomalies in blue dynamically supported by the thick continental crust of New Zealand.

The BA (Figure 3.6) has had the gravitational effect of topography removed and thus allows for better analysis of NWNZ's sub-crustal density structure, particularly at the western shoreline as well as within Northland. Note that at first glance there appears to be artefacts in the satellite gravity data at shoreline boundaries, particularly on the NW coast (addressed in Appendix A.1). These are assumed to represent real anomalies.

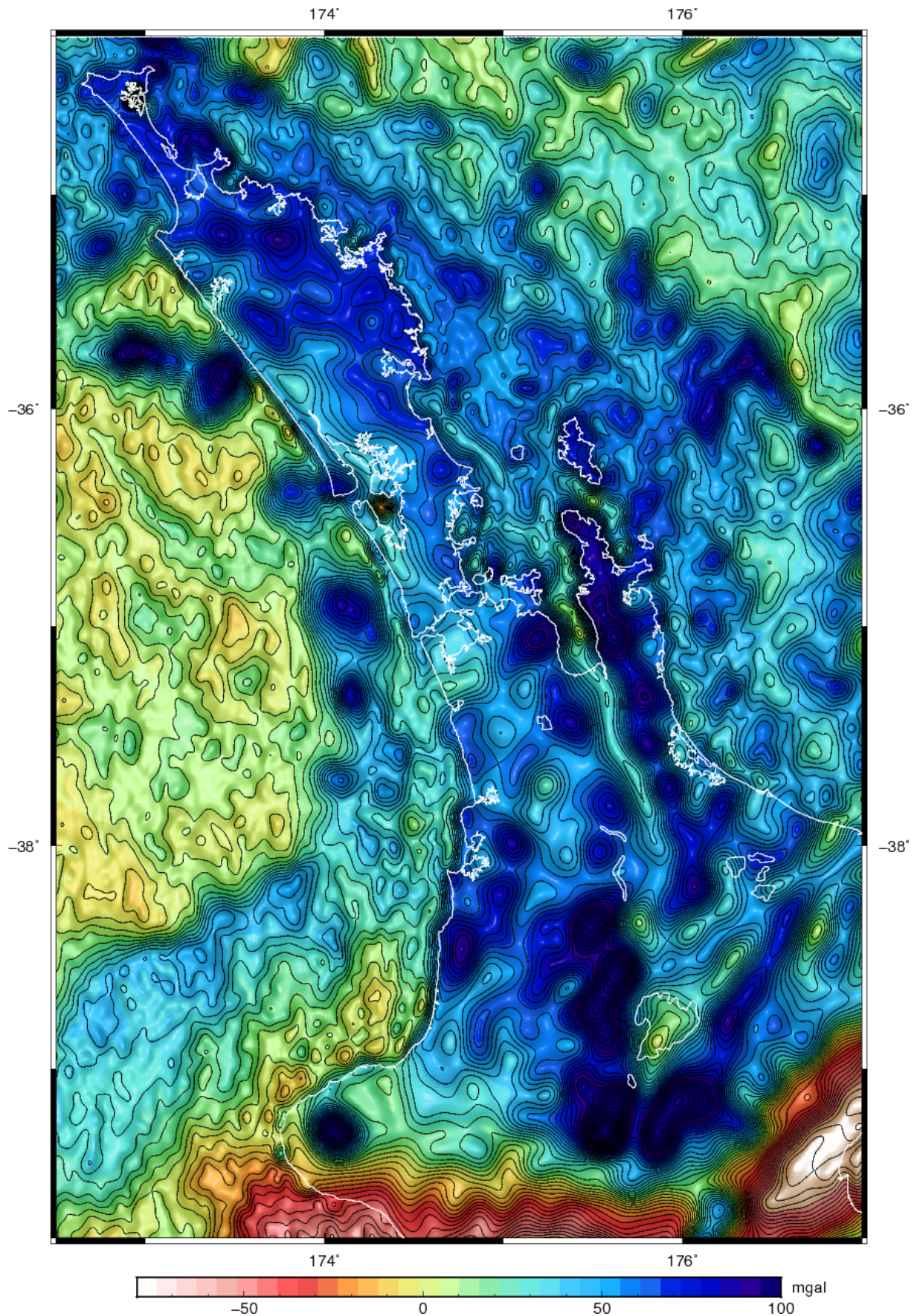


**Figure 3.5:** Satellite FAA plotted at 1 *arcminute* resolution with 5 *mGal* contours.

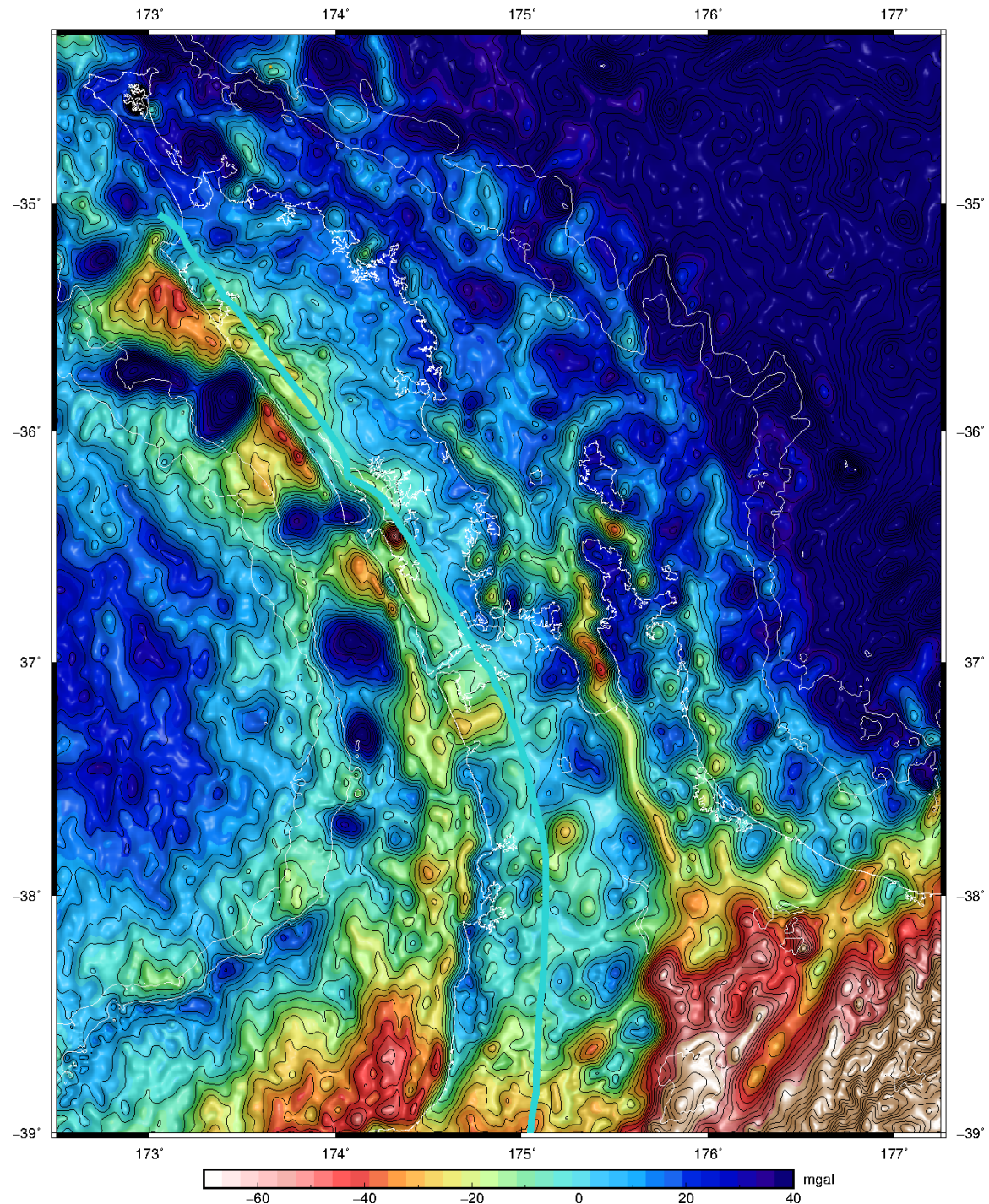


**Figure 3.6:** Satellite Bouguer anomaly created from satellite FAA (Figure 3.2) and satellite topography (Figure 2.2) data assuming ocean water and crustal densities of 1027 and  $2670 \text{ kg/m}^3$ . Resolution is 1 arcminute and 5 mGal contours are plotted. The JMA is drawn in light blue. Bathymetry at 0, -500, and -1000 m are contoured in white.

### 3.5.2 *Ground-based Data*

The ground station FAA in Figure 3.7 [Robertson and Reilly, 1960] enhances the detail of many of the faults which could only be speculatively inferred in the satellite data. This is particularly evident on the Kerepehi Fault near the Firth of Thames shore {175.5°E, 37.3°S} where a median ridge axis comprised of a down-dipping fault scarp is now apparent, previously described and shown via gravity field surveys [Hochstein et al., 1986; Hochstein and Ballance, 1993].

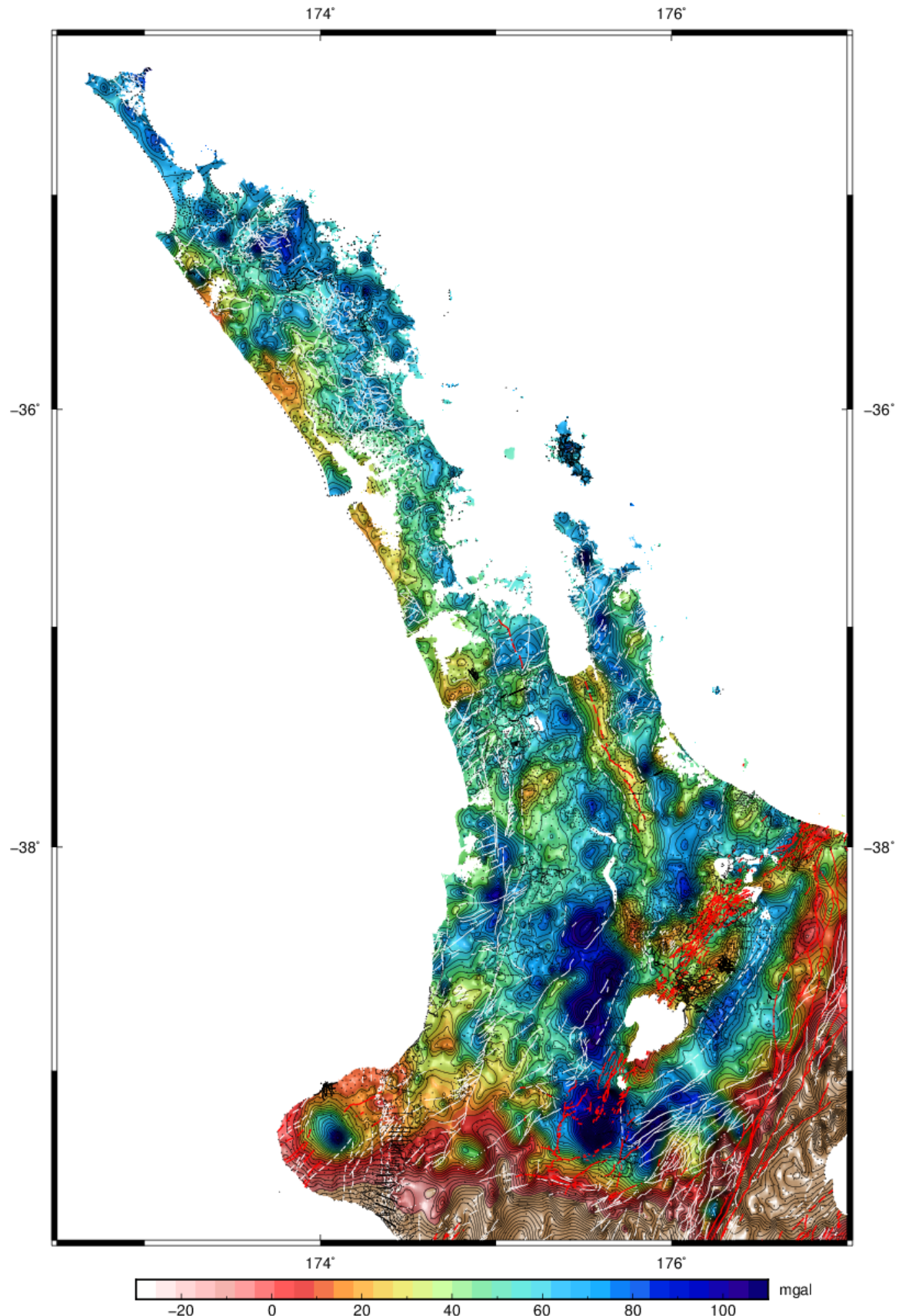


**Figure 3.7:** Free Air gravity anomaly based on ground measurements, averaged and gridded at 1 arcminute resolution. Contours are 5 mGal. Data is courtesy of the New Zealand Primary Gravity Network database [Robertson and Reilly, 1960] with individual measurement locations shown as small black dots. Active faults [Langridge et al., 2016] are plotted in red and inactive faults [Edbrooke et al., 2005; Edbrooke and Brook, 2009; Kenny et al., 2012; Lee et al., 2008; Leonard et al., 2010] in white.

Two versions of the BA are shown, the version that accompanied the FAA data from the NZ Primary Gravity Network database [Robertson and Reilly, 1960] provided by V. Stagpoole (Figure 3.8) and a version that was derived independently by this project using the ground station FAA and satellite topography (Figure 3.9). Both assumed a crustal density of  $2670 \text{ kg/m}^3$  and were interpolated identically (Section 3.3). The difference between these datasets is that the BA in the NZ gravity database was calculated by estimating and removing the gravitation effect of local topography at the time of measurement [e.g. Hammer, 1939], and the custom BA of this project (Figure 3.9) was calculated computationally by applying Parker's method (1973) to the FAA using satellite topography data. The non-continuity of the ground station FAA (i.e. lack of off-shore data) required for Fourier analysis was addressed by first substituting satellite FAA data (Figure 3.5) for the offshore regions prior to processing, and subsequently removing it following processing. The two versions are similar but the localised method which only estimates the gravitational effect of immediate topography is naturally missing some detail relative to the custom version which calculates the whole gravitational effect of topography precisely. However, much of signal apparent only in the numerically derived BA (Figure 3.9) is spurious or otherwise inconsequential for the purpose of identifying larger faults or structures.

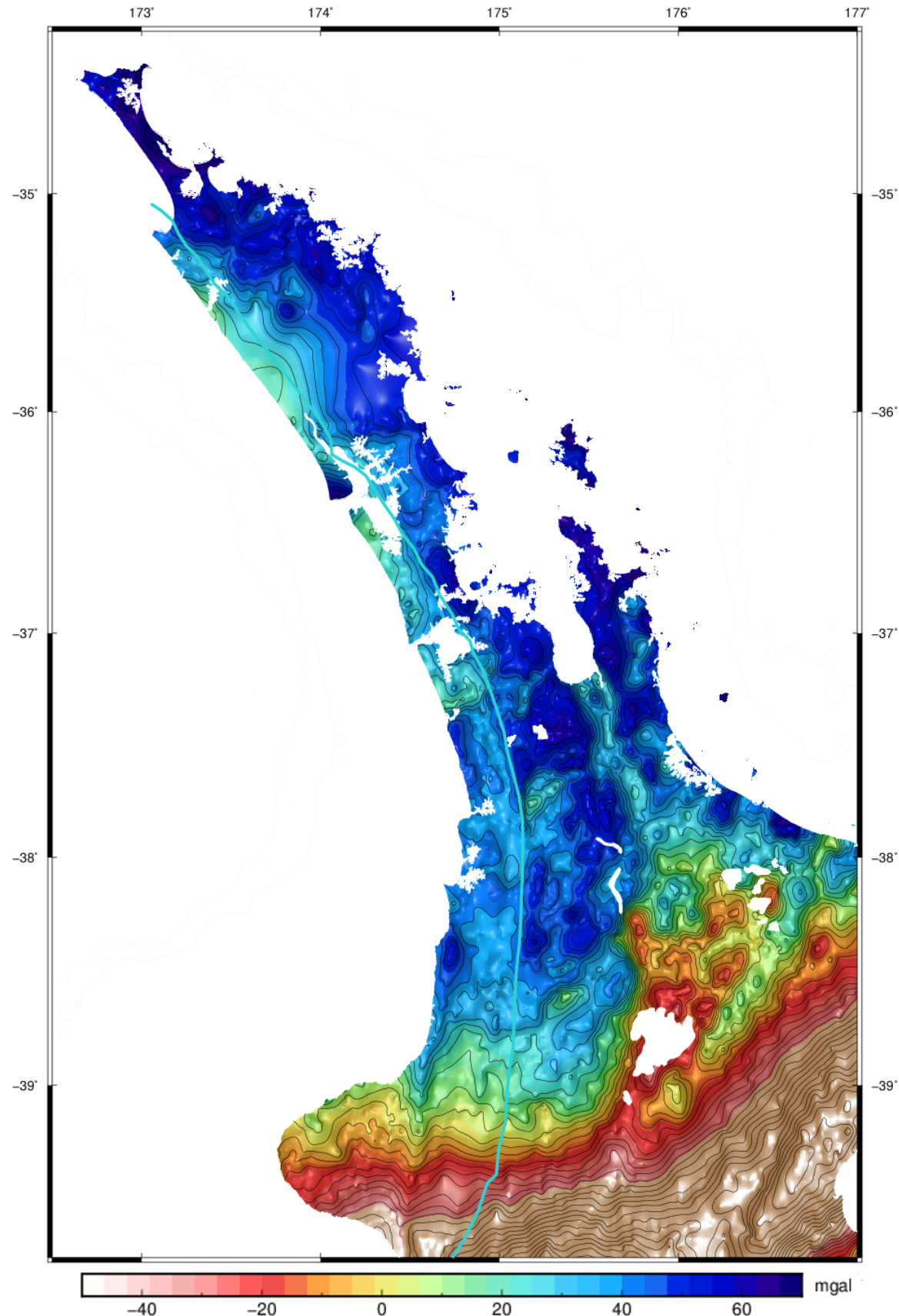


**Figure 3.8:** Bouguer gravity anomaly based on ground measurements, averaged and gridded at 1 arcminute resolution with 5 mGal contours. The JMA is shown in light blue. This datum was included in the New Zealand Primary Gravity Network [Robertson and Reilly, 1960].

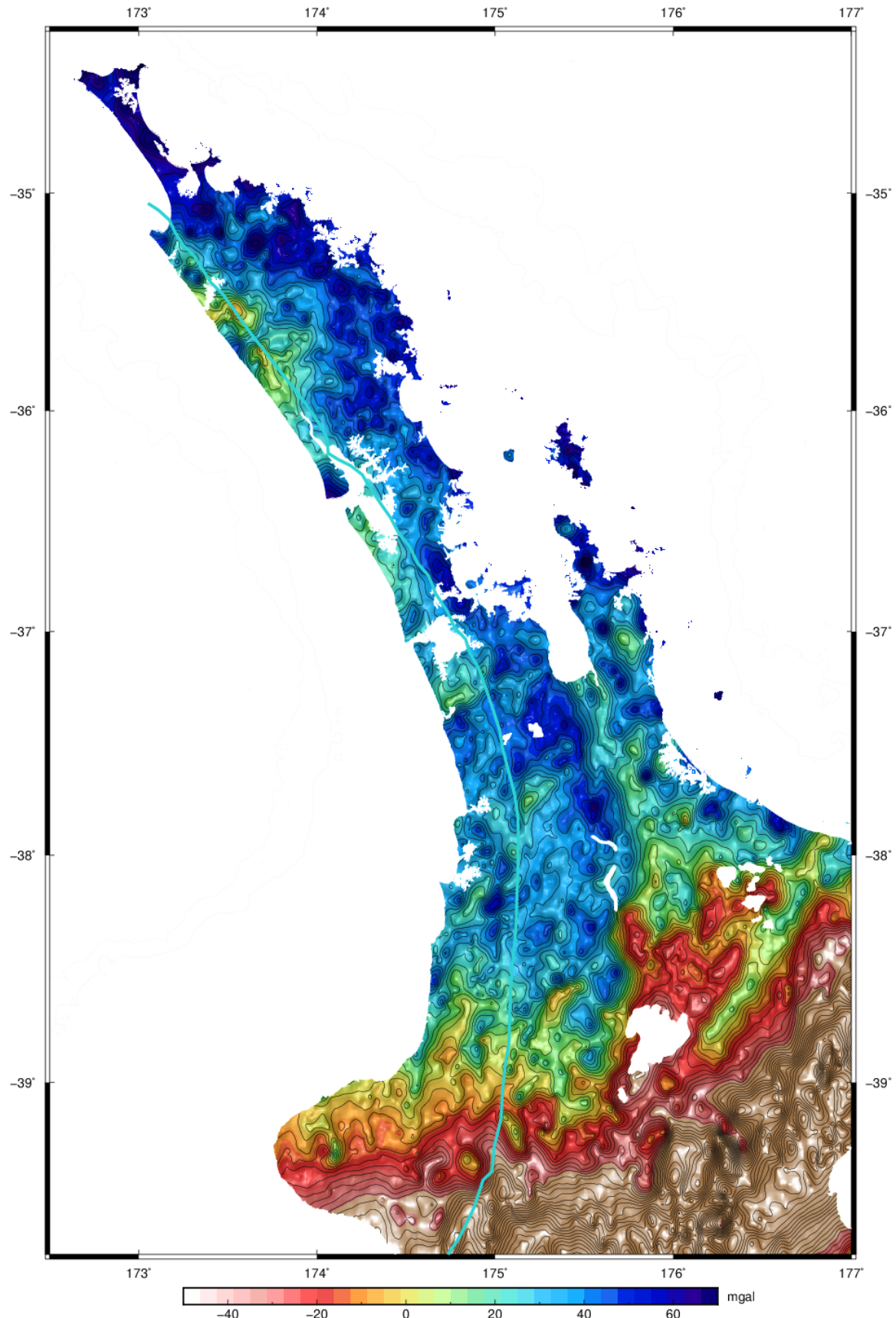


**Figure 3.9:** Bouguer gravity anomaly based on ground measurements, averaged and gridded at 1 arcminute resolution. Contours are 5 mGal. This datum was derived from the field FAA gravity datum shown in Figure 3.7 with satellite FAA (Figure 3.5) and topography used to compute the gravitational effect of the crust via Parker's method [Parker, 1973].

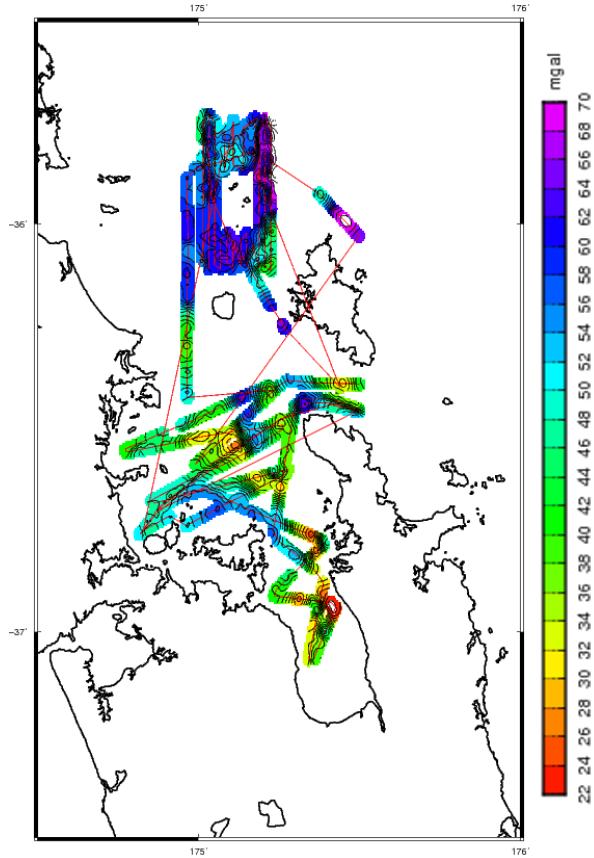


**Figure 3.10:** Bouguer Gravity anomaly taken at sea, previously published by Hochstein et al. (1986), Thrasher (1986), and Hochstein and Ballance (1993). Shiptrack lines are drawn in red.

### 3.5.2.1 At-Sea Free Air Anomaly

Previous surveys have been done in the Hauraki Gulf but they are typically sparse with only a few tracklines. Data recorded 1978-1979 and previous published by Hochstein et al. (1986), Thrasher (1986), and Hochstein and Ballance (1993) have been generously made available to this project are are re-interpolated in Figure 3.10. The data is of high quality but its sparsity makes interpretation difficult, with the only additional information compared to that available from satellite data being a detailed glimpse of the median Hauraki Rift ridge axis as a FAA low near {175.2°E, 36.5°S}.

### 3.5.2.2 Airborne Free Air Anomaly

Airborne gravity surveys conducted via plane allow for seamless coverage of both land and sea, but require specialised aircraft and are extremely sensitive to changes in speed and elevation,

making a typical air survey fraught with potential issues. Furthermore the high altitudes at which the data is being collected requires a proportionally narrow track spacing to surpass the (2.5-7 km) downward-continued resolution already available by satellite [Sandwell et al., 2014]. Nevertheless an ambitious nationwide aerogravity survey was conducted by McCubbine et al. (2017). Their survey (Figure 3.11) covered the entirety of on-shore New Zealand and 10 km off-shore with over 50,000 km of linear flight observations and a track spacing of 10 km between 2013-2014.

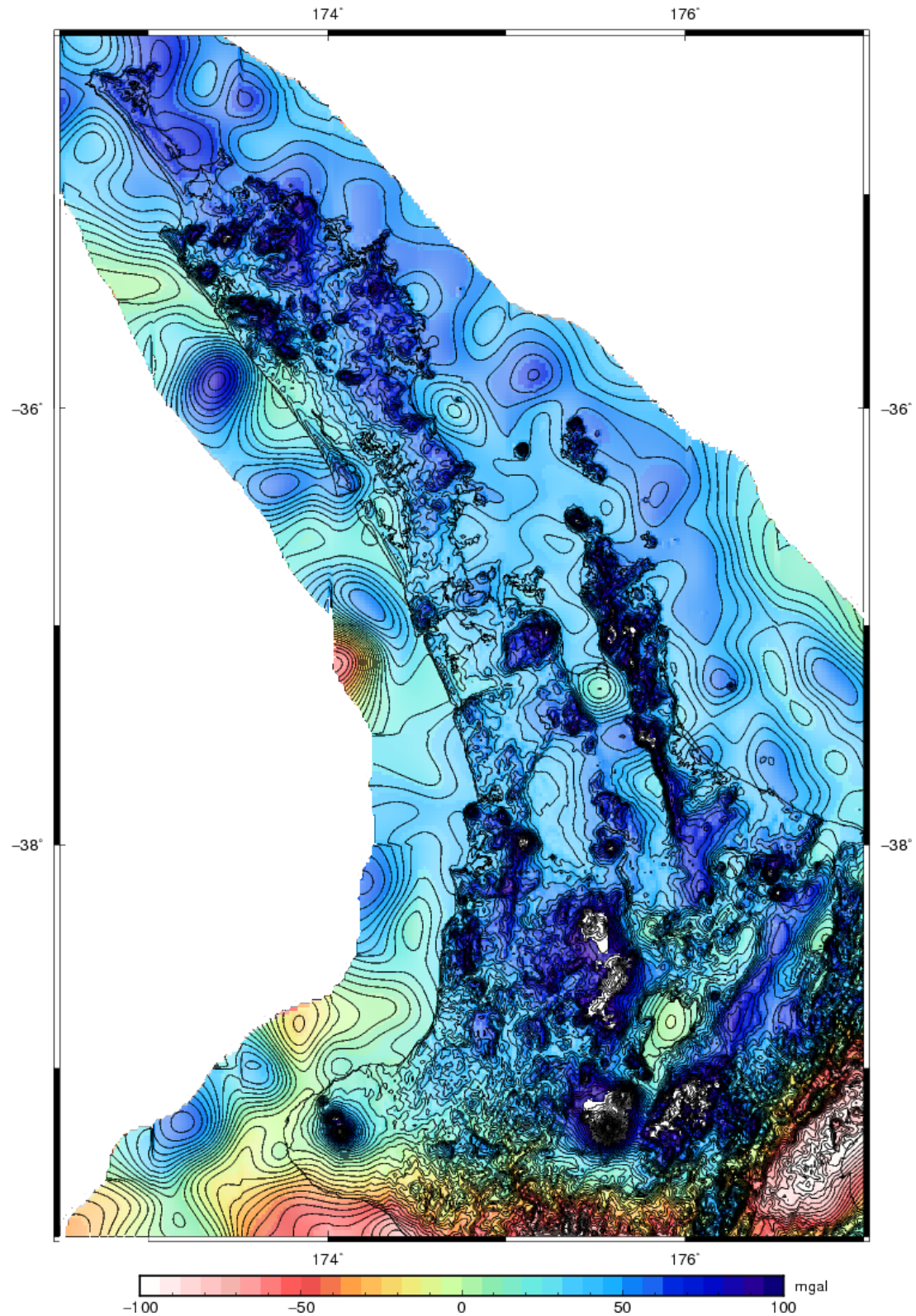


**Figure 3.11:** Free Air gravity anomaly collected via plane at variable altitudes and combined with ground station data shown in Figure 3.7 [McCubbine et al., 2017]. There appear to be artefacts near very small elevations.

The FAA in Figure 3.11 is plotted from the McCubbin et al. (2017) raw dataset which includes their airborne survey combined with the same ground station data used in Figure 3.7 as well as off-shore satellite and at-sea data. However there seems to be a anomalously strong correlation to topography with flat areas such as the Hauraki Plains (within the Hauraki Rift { $175.8^{\circ}\text{E}$ ,  $36.3^{\circ}\text{S}$ }) exhibiting the same low resolution as areas off-shore despite having high volumes of detailed field station data. In particular, the fault scarp on the Hauraki Rift axis so clearly evident in Figures 3.7 and 3.9 is now completely missing despite the fact that this data was included in their model. Further, the resolution of the combination satellite and airborne gravity is far worse than simply than the satellite gravity (e.g. Figure 3.5) alone. The data collected is nevertheless valuable for use in piecewise or point-to-point [e.g. Fullea et al., 2008] gravity analysis however the wide track spacing ( $10\text{ km}$ ) and variable altitude ( $1\text{-}3\text{ km}$ ) may make its use in Fourier-based [e.g. Parker, 1973] flat surface continuations difficult or unviable.



# 4

## GEODETIC ANALYSIS OF NORTH-WESTERN NEW ZEALAND

---

The utilisation of the Global Navigation Satellite System (GNSS) for geodetic applications has been a boon for earth scientists [e.g. Bossier, 1983], allowing for the accurate positioning of benchmarks anywhere an antenna may be placed. With repeated measurements a velocity estimate within a reference frame can be determined, which can then produce a crustal strain rate between multiple sites. These measurements are now capable of generating velocities with uncertainties at the sub-mm scale [Zumberge et al., 1997] which makes GNSS geodesy a viable option to constrain the low deformation environment of north-west New Zealand (NWNZ). Indeed, this technique has already been implemented successfully throughout NWNZ and all of New Zealand since the 1990s [e.g. Beavan et al., 2016]. This history of GNSS surveying provides a catalogue of geodetic sites with data for this project to build upon, many of which had only been recorded once and have thus never been used for tectonic studies.

GNSS geodesy is uniquely suited for constraining crustal motion in NWNZ not only due to its high precision, but also due to its relative economy and mobility potential. GNSS sites can typically be constructed by hand and GNSS equipment can be carried by foot, requiring only a relatively unobstructed sky view. Furthermore GNSS utilises freely and readily available global satellite, orbit, and reference station data, and in New Zealand there is an extensive nationwide network of geodetic markers already in place [e.g. LINZ; [www.linz.govt.nz](http://www.linz.govt.nz)]. These features set GNSS geodesy apart from many other branches of satellite geodesy which require expensive, large, or immobile stations e.g. Very Long Baseline Interferometry or Satellite Laser Ranging [Seeber, 2003; Prati et al., 2011; Jin et al., 2013] which would then limit the potential distribution and volume of measurements through NWNZ. Remote sensing via broad, swath-based deformation measurement techniques (e.g. Interferometric Synthetic-Aperture Radar or InSAR) is often complimentary alongside GNSS with each providing constraints to one another [Lohman and Simons, 2005]. InSAR has been used extensively in geoscience and works well in the nearby fast-deforming TVZ [e.g. Hamling et al., 2015]. However in the low-rate NWNZ where a high precision of horizontal measurement is critical, the relatively poor horizontal resolution achievable via InSAR renders it unviable. This is because InSAR samples a location via a single satellite over ~hours whereas GNSS records a site over the course of days to weeks amongst a dozen or more satellites.

#### 4.1 INTRODUCTION TO GEODETIC GNSS SURVEYING AND PROCESSING

GNSS measurements are taken by mounting, levelling, and aligning a stationary antenna to true north directly above a mark, then recording incoming satellite signal over time via attached receiver. These signals carry repeating codes unique to each satellite with wavelengths on the centimetre to decimetre scale, broadcast across two or more frequency bands. Inexpensive GNSS receivers (e.g. hand-held devices) simply use a single frequency of code information from four or more satellites to triangulate a position at the metre scale. Precise GNSS receivers used for surveying use two frequencies and measure differences in the *phase* of these codes which is a more complex and expensive procedure. The largest source of error in this process is typically due to inconsistencies in the clocks at either of the satellite and receiver, however these are mitigated by double-differencing between multiple satellites and reference stations [Herring et al., 2010]. This achieves accuracy on the *cm* to *mm* scale, depending on the amount of simultaneous signals across varying frequency bands these phase differences are measured [Seeber, 2003].

It is also usually necessary to know the position of the satellites with some certainty. These are derived in an inverted fashion by assuming the a priori position of ground stations and solving for their orbit paths. These are published by various agencies with various degrees of accuracy and delay for various applications. For precision applications, the International GPS Service (IGS) [Dow et al., 2009] freely provide predicted satellite orbits at several spatial and temporal resolutions, notably “RAPID” orbits (Daily release, 2.5 *cm* accuracy,  $75\pm25$  picosecond RMS @ 5 minute clock sample intervals) and “FINAL” orbits (2-3 week release, 2.5 *cm* accuracy,  $75\pm20$  picosecond RMS @ 30 second (vs. 5 minute) intervals). FINAL orbits are the best orbits available, if one can wait for them.

The finer details and mathematics involved in the conversion and triangulation from raw satellite observables to a geospatial position are well documented elsewhere [e.g. Bock et al., 1997; Zumberge et al., 1997; Seeber, 2003; King and Bock, 2004; Herring et al., 2010] and are beyond the scope of this research. For a majority of GNSS practitioners this process is implemented via a small range of existing software e.g. GAMIT/GLOBK (MIT), GIPSY-OASIS (JPL), Bernese (University of Berne), PANDA (Geodetic Technologies GmbH, Germany).

MIT’s GAMIT/GLOBK (ver. 10.61) [King and Bock, 2004; Herring et al., 2010] is widely used in the GNSS community and is also freely available under an academic or non-profit license,

and accordingly this is the software used for the majority of this work. This Fortran-based software suite solves for position from raw satellite observables data (GAMIT) and additionally computes a velocity from a timeseries of these positions in a generalised global reference frame (GLOBK) via a "Kalman filter", a linear quadratic estimator [Brown and Hwang, 1992]. This software is fast, open source, and easily customisable but without the direct support of a commercial product nor an online community, though free tutorial courses occur yearly around the globe.

## 4.2 CONTINUOUS STATION GEODESY

A continuously operating GNSS station (cGNSS) is the most effective geodetic technique to measure the movement of the crust as by definition it documents the entirety of the ongoing 3D motion of the site. Continuous measurements allow for the calculation and removal of seasonal effects and provide a means to derive statistical noise to apply to site estimates of position and velocity.

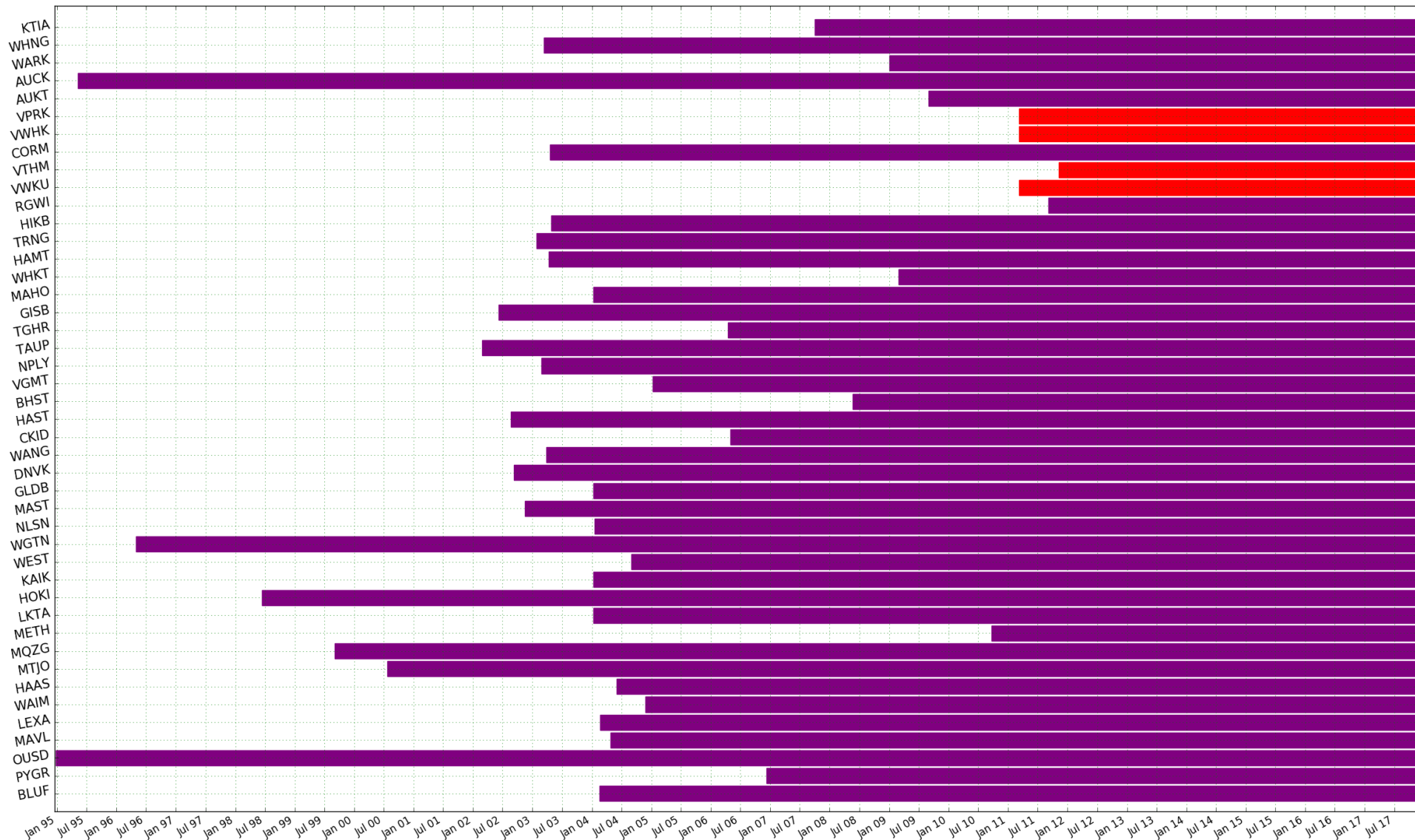


**Figure 4.1:** Age range of the primary New Zealand Continuously Operating Reference Stations network arranged by latitude. The sites in red are commercial reference stations provided by the Allterra Company.

#### 4.2.1 New Zealand's Continuously Operating Reference Stations

New Zealand's cGNSS network (Figure 4.2) is currently maintained and operated by GeoNet, which was established by the EQC in partnership with GNS Science and Land Information New Zealand (LINZ). The first sites were constructed in 1995 starting with only three stations in Auckland/AUCK, Dunedin/OUSD (Otago University School of Surveying), and Chatham Island/CHAT). The network grew slowly until around 2003 when its size ballooned following GNS Science's new partnership with LINZ in 2001 (Figure 4.1). By 2010 the density of stations in the northern North Island had reached its current state with the addition of stations in Warkworth/WARK and Kaitaia/KTIA. Since then additional stations have predominantly been placed within the TVZ, on active volcanoes, or proximal to the active plate boundary along the North Island's east coast. The network has also been strengthened in response to both the 2011 Christchurch and 2016 Kaikōura earthquakes. These newer sites are typically constructed with higher quality mounts (e.g. deep drilled braces vs. concrete pillars) resulting in less seasonal noise [Williams et al., 2004; Herring et al., 2016]. A select sampling of the northernmost commercial cGNSS stations operated by the Allterra company as base stations for professional surveyors were also graciously provided in the middle of 2017 dating back as far as 2011. Until then, the existence and availability of this data for scientific research was unknown.

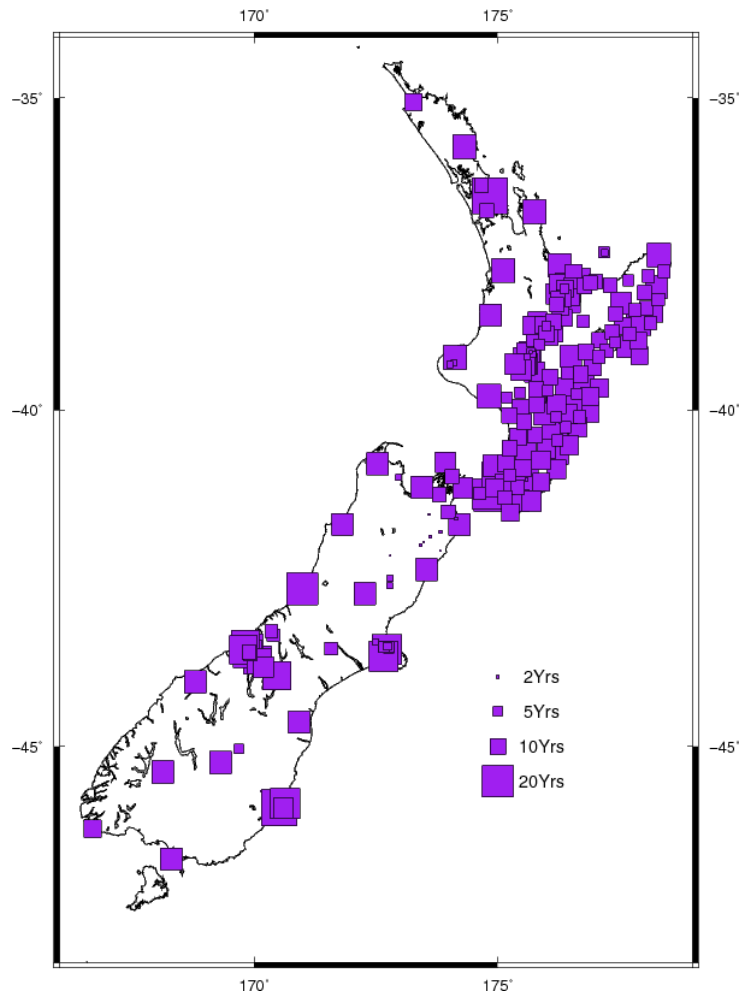


**Figure 4.2:** New Zealand Continuously Operating Reference Stations.

The current combined NZ network now offers excellent coverage of both the TVZ and the Hikurangi plate boundary region, in addition to dense networks targeting Christchurch, Kaikōura, and a perpendicular track across the Alpine Fault (Figure 4.2). These sites provide robust velocity estimates, well defined reference locations, and a means to constrain coseismic offsets in the event of an earthquake. Coverage is understandably lacking further from the plate boundary as activity diminishes, particularly in NWNZ which is a relatively low risk but high hazard (e.g. Auckland) environment. This lack of continuous stations further compounds the natural difficulty in constraining low deformation rates via GNSS.

### 4.3 CAMPAIGN GEODESY

An alternative to the commitment and cost of additional cGNSS stations is “campaign” surveying. Here sites are occupied for only a short period (hours to days) repeatedly over several years to derive a spatial displacement over that time, i.e. a velocity. The benefit is that a small amount of equipment can cover a large area with the serious drawback that the displacement that occurs between each survey is averaged out, including any coseismic offsets or potentially anomalous behaviour. Nonetheless this type of surveying has been proven effective in producing velocity estimates in the North Island of New Zealand [Beavan and Haines, 2001; Holden et al., 2014; Beavan et al., 2016] as well as in other regions of slow, millimetre scale deformation worldwide [e.g. Alchalbi et al., 2010; Bennett et al., 2012; Metzger et al., 2012]. As few cGNSS stations exist throughout the northern North Island (e.g. Figure 4.2; Beavan et al. 2016), this project opted to conduct three yearly campaign surveys to not only target the greater Hauraki Rift but also maximise the volume and distribution of measurements at sites throughout NWNZ for background.

#### 4.3.1 *Station Selection*

The primary goal of this project was to characterise the crustal tectonics and activity occurring in and around the broader Hauraki Rift as well as its surrounding region. Thus two E-W tracks sub-perpendicular to both the Wairoa North ("WN") and Kerepehi Fault were planned utilising pre-existing geodetic marks in the region (green diamonds, Figure 4.3) with the Kerepehi Fault in particular hypothesised to be acting as the Hauraki Rift's median axis (Hochstein and Nixon, 1979; Hochstein et al., 1986; De Lange and Lowe, 1990; Hochstein and Nixon, 1991; Persaud et al., 2016). The use of pre-existing marks saved a great deal of construction time as well as eased negotiation with landowners, many of whom were already familiar with their purpose and location. Moreover, their spatial distribution throughout NZ is dense enough that it did not affect planning. Equally important, and given the region's low activity and short amount of time (three years) available, it was vital to select as many sites with pre-existing data collected by GNS Science from 1995 (yellow triangles) and/or 2013 occupations (blue triangles) as reoccupying these were likely to produce more robust velocity estimates.

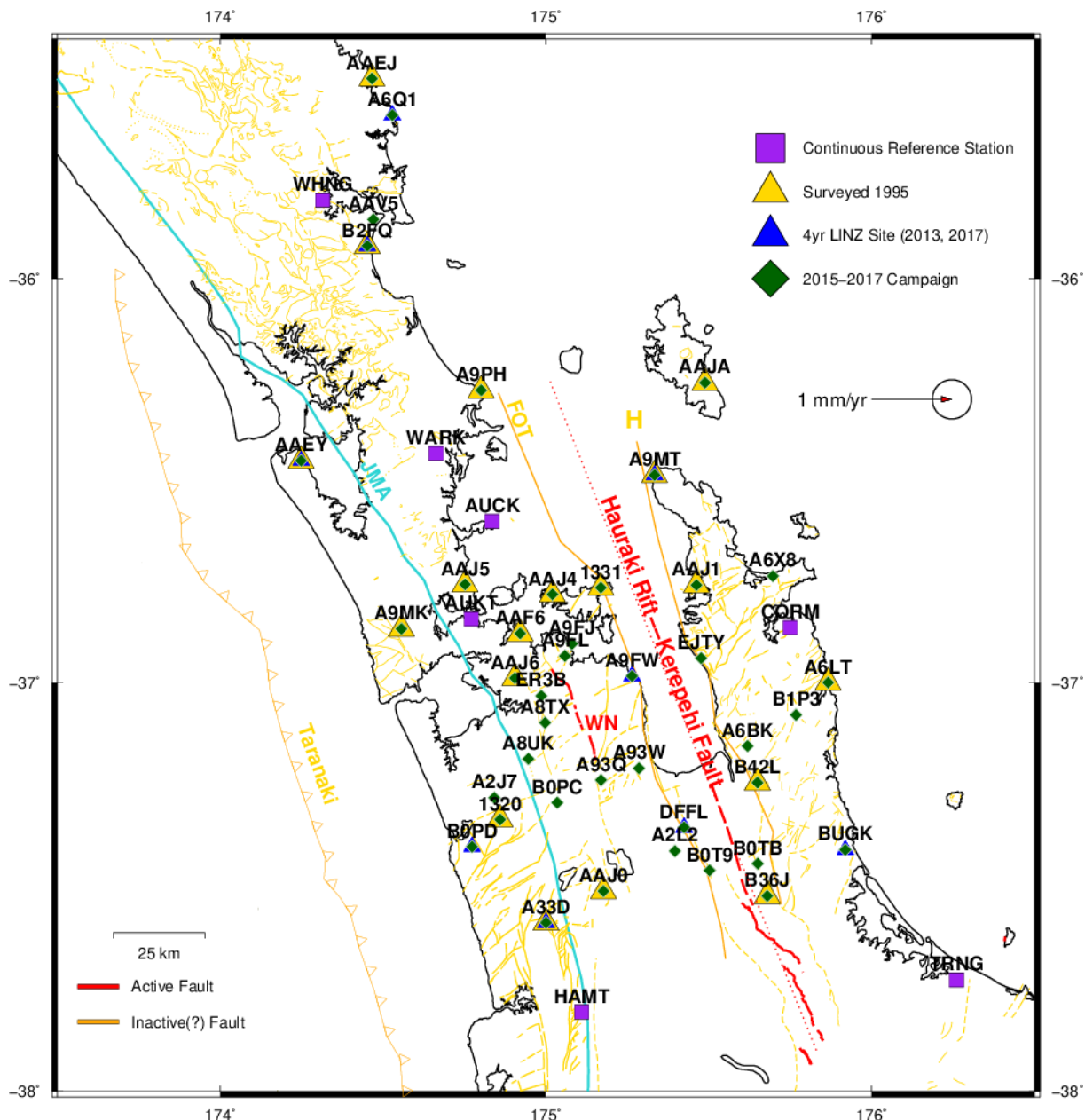


**Figure 4.3:** All campaign stations surveyed 2015–2017. Sites which had been previously occupied in 2013 (blue triangles) or 1995 (yellow triangles) were prioritised. JMA = Junction Magnetic Anomaly, WN = Wairoa North Fault, FOT = Firth of Thames Fault, H = Hauraki Fault, Taranki = Taranki Fault. Only the Wairoa North and Kerepehi Faults plotted in red are assumed to be active [Langridge et al., 2016].

#### 4.3.2 Field Deployment Considerations for a Low-Rate Environment

Deriving a velocity for previously unsurveyed NWNZ campaign sites over the course of just three years was ambitious given the near parity of the region's annual rate of relative motion

and noise in the GNSS system. To reduce uncertainty as much as possible the following measures were taken:

#### 4.3.2.1 *Consistency In Survey Season*

The earth is subjected to both annual-scale atmospheric and orbital forces which may dramatically affect GNSS solutions [e.g. Blewitt and Lavallée, 2002; Drouin et al., 2016]. While short period effects such as tidal loading or local storms are either irrelevant or unavoidable to multi-day occupations, longer-period multi-month effects (e.g. seasonal weather, non-tidal loading [Williams and Penna, 2011], orbital nutations [Zhu and Groten, 1989]) can be mitigated by conducting geodetic campaigns at a similar time of year.

An annual periodicity can clearly be seen in the chart of Auckland City tidal gauge station AUKT (Figure 4.4). This station is a somewhat dramatic example as it is unfavourably situated on a pier in the harbour but similar error profiles could hypothetically occur within the Hauraki Rift's peat bogs. By contrast, a high quality cGNSS station constructed with deep roots within the soil or otherwise situated atop bedrock can vastly reduce these anomalies [Beavan, 2005]. As temporary campaign stations will generally not utilise deep or especially stable monuments one should conservatively assume a worst-case error profile similar to AUKT and therefore attempt to conduct a campaign survey as close to the same time of year as possible to avoid this seasonal bias.

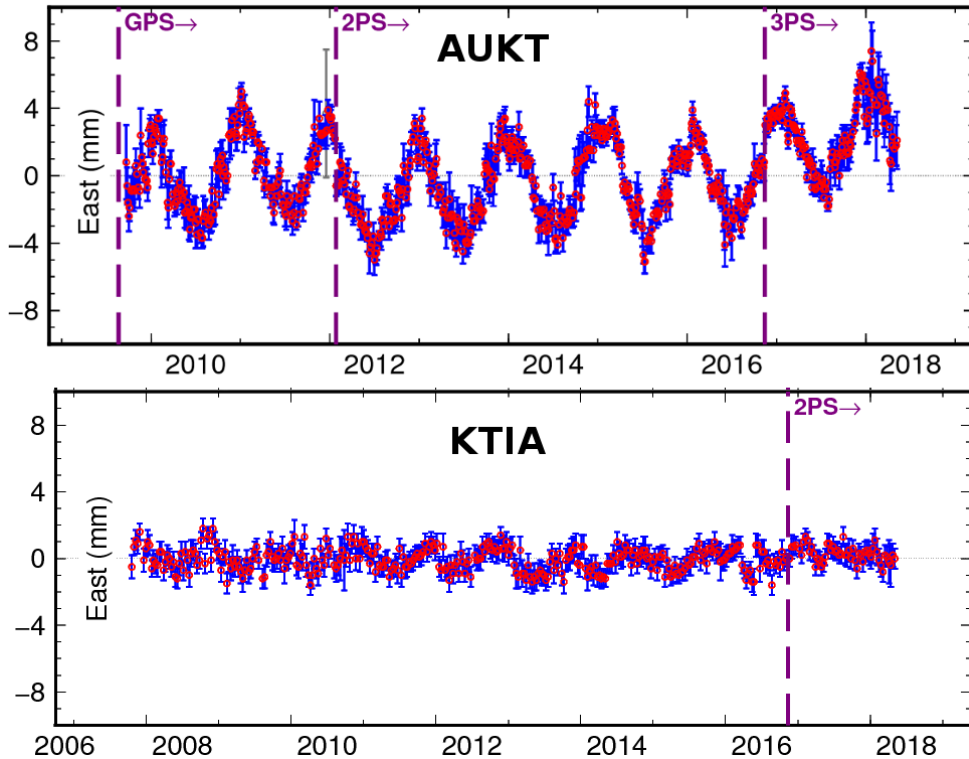


**Figure 4.4:** Season effect on ground deformation at cGNSS station AUKT unfavourably situated near Auckland harbour vs. site KTIA in Northland utilising a modern deep-drilled mount. Vertical labels in purple denote events (antenna changes, earthquakes) potentially creating a dislocation.

#### 4.3.2.2 *Three or More New Occupations Attempted for Sites Without Historic Data*

Theoretically only two surveys are needed to produce a velocity but a third survey is helpful in generating a statistically robust velocity solution. Occasionally even three surveys are inadequate. For example in the timeseries for station A934 (Figure 4.5), after the third survey in 2011 it is obvious that one or more of the campaign occupations is anomalous (assuming linear motion) but impossible to discern which using the timeseries alone. The fourth survey in 2015 makes it clear that 2005 is the probable outlier.

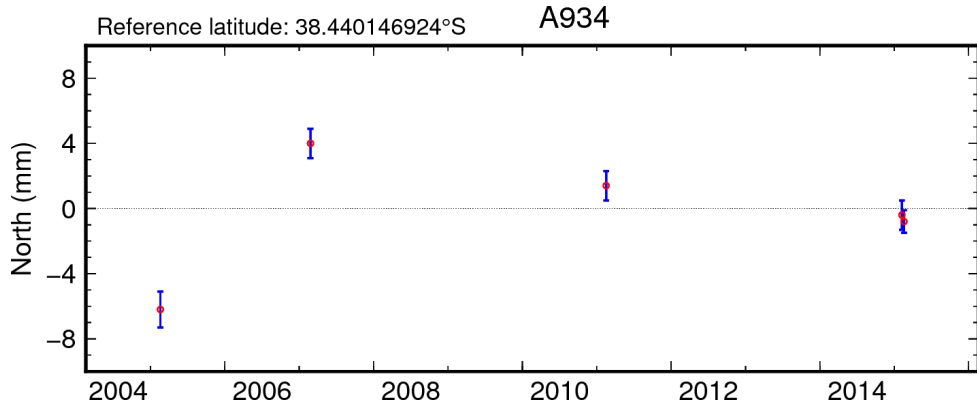


**Figure 4.5:** Campaign data for station A934 (courtesy of GNS Science / Beavan et al. 2016). Without the 4th survey in 2015 it is difficult to isolate 2005 as an outlier occupation.

#### 4.3.2.3 Occupation Times of a Week or More

Occasionally a daily solution will be over-constrained, giving it tight error bars despite the fact that its uncertainty as evident by the timeseries is in fact much higher, typically evident by a strong deviation from the linear trend. This can be the result of short-term systemic errors in the stabilisation network which can occur when large swaths of local or global reference stations are universally affected by an anomaly e.g. a solar or rainstorm, or simply an abundance of clouds [Seeber, 2003]. Averaging the calculated position over as many days as possible greatly reduces this scatter, assuming it is short-lived relative to the station occupation time.

Demonstrating this is the daily north component timeseries for station A2L2 (Figure 4.6). Its latitude is largely consistent until day-of-year 095 when a local storm arrived and persisted for over a week. The additional water vapour in the atmosphere strongly affected the magnitude of the error in addition to shifting the predicted north position entirely. A 1-2 day occupation during this period might incorrectly predict the site's latitudinal position as much as 2-4 mm from reality.

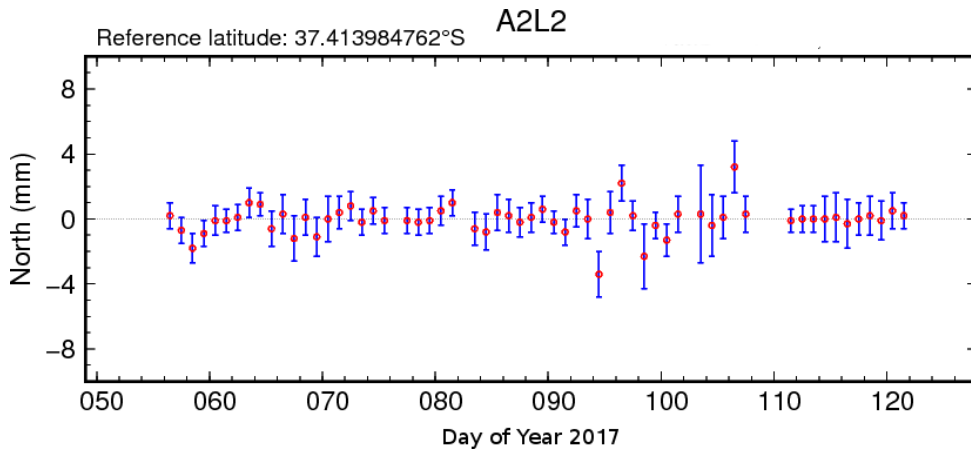


**Figure 4.6:** Day to day scatter due to weather phenomena (DOY 93-105) at station A2L2.

The downside to long occupations are typically equipment availability and power solutions. A single 12 volt, 24 Ah lead-acid battery could power an older (e.g. Trimble 5700) receiver for approximately 4-6 days, and thus two of these batteries were routinely used. Alternatively it was found that a small 10-20 watt solar panel extended the life of a single battery to 7-9 days and provided a cost-effective and logically practical alternative.

Often a site simply cannot be left alone and must be watched for security reasons. Rather than neglect these, several very short (1-7 hour) occupations were measured in 2016 and 2017 at insecure/public sites with historic 1995 data to test their achievable resolutions. It was hypothesised that despite the relatively poor resolution gained from these occupations that they would be sufficient to produce a good velocity estimate given that the surveys were over 20 years apart. In 2016, site AAF6 (Figure 4.3) was deployed for 7 hours and produced a spatial solution with horizontal errors  $< 2.0 \text{ mm}$ . In 2017, site AAJ5 was deployed for 5 hours and produced horizontal resolutions of  $\sim 1.9 \text{ mm}$ . Both sites had clear weather and unobstructed sky views. Site AAJ6, partially obstructed by a nearby tree, had two separate occupations in 2017 for 3 hours and one for 4 hours producing horizontal errors of 3.3 and 2.2 mm, respectively. The lower occupation time almost certainly resulted in the noisier solution but the adjacent tree may also have played a factor depending on the position of the satellites, the degree to which cannot be easily determined. Most interestingly is that despite the relatively similar error bars, the predicted positions between these two occupations differed by over 5 mm horizontally and vertically. The reason for this is not clear. While a direct relationship between occupation time and resolution cannot be gleaned from these occupations, they generally demonstrate that even

very poor quality short occupations can still effectively derive a reasonable velocity for many geodetic sites featuring 1995 data, even in extremely low-strain environments (e.g. Figure 2.10).

#### 4.3.3 Data Acquisition

GNSS antenna/receiver units suitable for campaign surveying were obtained from GNS Science as they became available around other commitments during the summer months between 2015-2017. The first year of the Hauraki Rift campaign spanned February-June 2015, ultimately collecting 234 survey-days of data between 36 survey sites. This year proved most time consuming due to the initial site selection and finding and establishing a relationship with landowners.

The second year from February-June 2016 saw 290 survey-days across 39 sites. Despite purposely choosing to neglect several well-constrained sites (e.g. A33D, which had been surveyed eight times 1995-2015) the size of the campaign grew in response to the preliminary velocities derived from the processing of 1995-2013-2015 data. This predominately included an expansion of additional sites with historic data (e.g. AAV5, A9MK, AAF6, B36J) but also previously unsurveyed site CAJP on Waiheke Island. The inclusion of CAJP was in response to the emergence of an anomalous rifting dynamic that was showing between the western (AAJ4) and eastern (1331) stations on the island, both featuring historic 1995 data and thus presumably reliable. At this point in time the existence of the Allterra cGNSS sites (red diamonds, Figure 4.1) was not known, particularly VWHK towards the south and centre of the island.

After the conclusion of the second year of the campaign, the November 13 2016 (UTC) M7.8 Kaikōura Earthquake struck the NE of the South Island. Though the effects of this event on our study area were not fully known at the beginning of the 2017 survey (itself delayed several months due to the available equipment routed to the earthquake response) it was presumed that many of the survey sites had been co-seismically shifted from their expected positions. As such, some of the newer campaign sites and/or sites near the Hauraki Rift were prioritised over sites with ample historic data, and these were typically surveyed twice or more in 2017 in order to strengthen their velocity estimate. In all, 356 survey-days were collected across 35 sites, from March to November. GNS Science conducted an additional survey in October of 2017 of the sites denoted by blue diamonds in Figure 4.1.

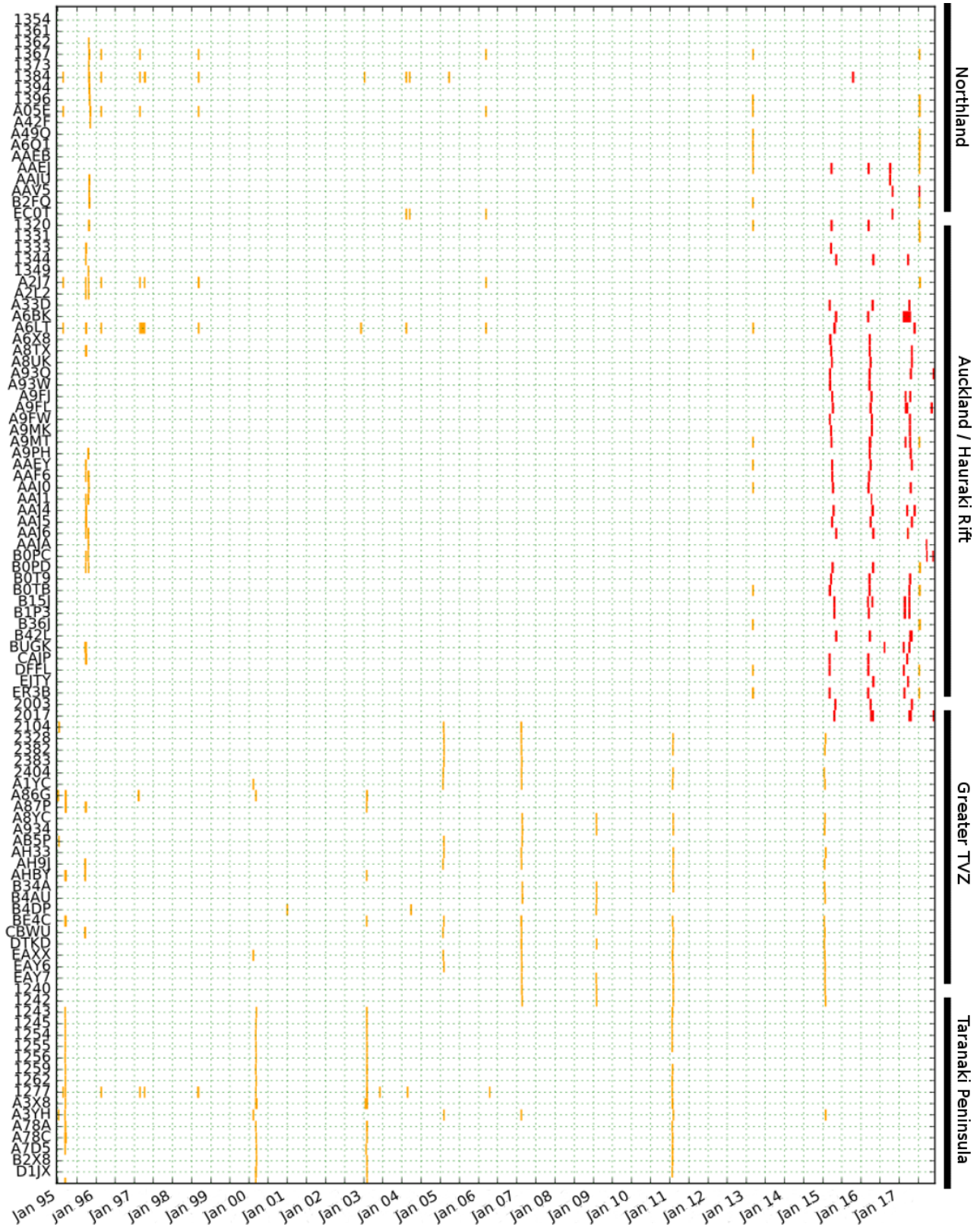


Figure 4.7: 1995-2017 total campaign data used in this project. Stations are grouped by region N-S but ordered alphabetically within each.

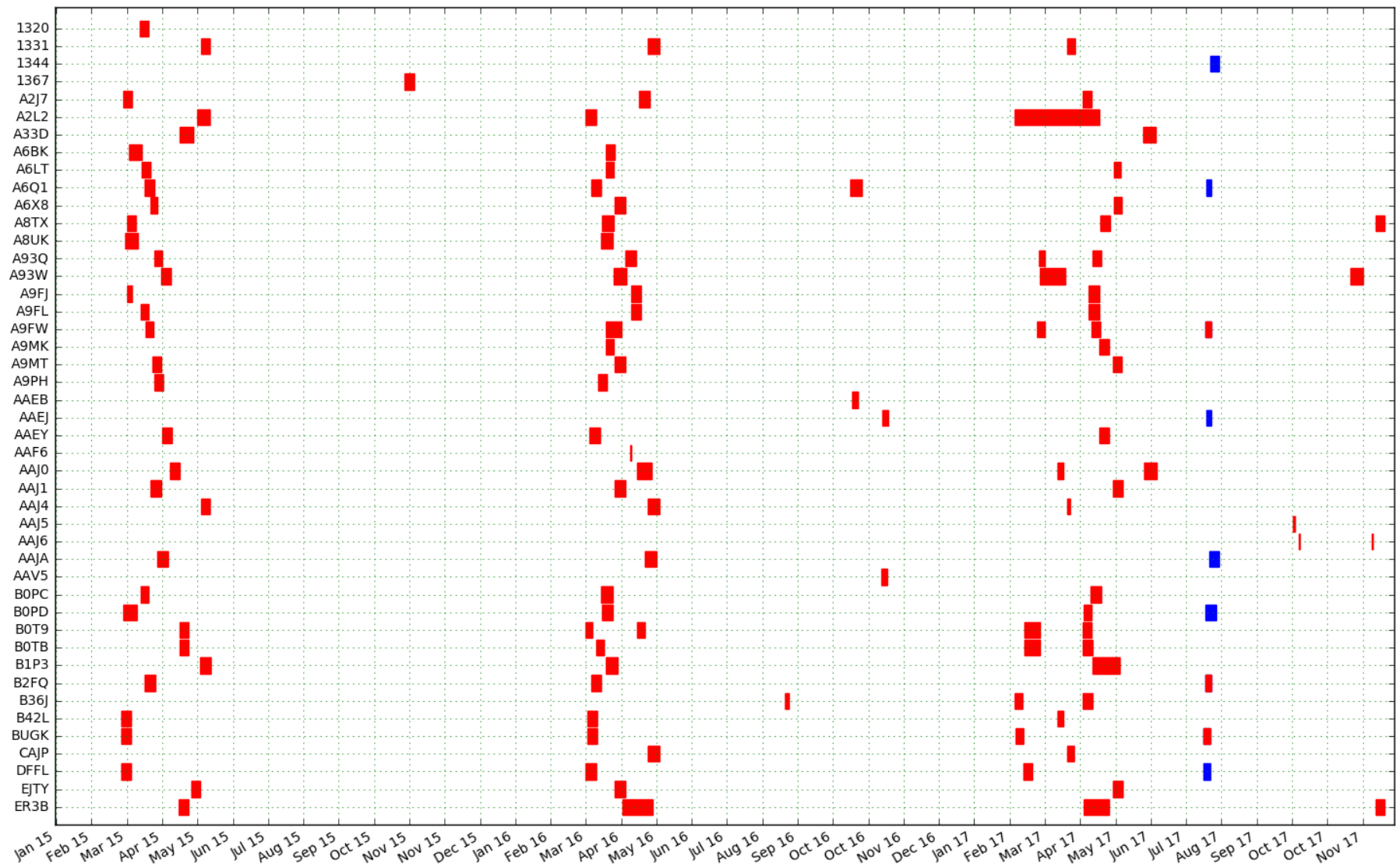


Figure 4.8: Newly acquired data 2015-2017. Sites in red were recorded by Pickle 2015-2017 and sites in blue by Neville Palmer at GNS.

#### 4.3.3.1 *Converting Raw Data to Receiver Independent Exchange (RINEX) Format*

The proprietary Trimble data recorded during the campaign was converted to the open Receiver Independent Exchange (RINEX) format using the Trimble’s “runpr00” software and the “teqc” software [Estey and Meertens, 1999] published and maintained by UNAVCO ([unavco.org/software](http://unavco.org/software)). This conversion allows the campaign data to be shared among a spectrum of users and software. RINEX header information was carefully entered by hand to document the site name, equipment hardware/serial numbers, and antenna heights and offsets. It is however noted that this information is usually superseded by the regularly updated databases used by the software.

### 4.4 GNSS PROCESSING WITH GAMIT/GLOBK

As hinted by its name, GAMIT/GLOBK [King and Bock, 2004; Herring et al., 2010] is actually two separate programs. GAMIT solves the fundamental satellites-antenna triangulation process per each 24-hour period of data, and GLOBK combines these daily solutions to produce a complete position and velocity estimate over an experiment period. The process can be iterative with GLOBK solutions fed back into GAMIT as a priori information, which in turn may encourage edits to the cGNSS sites and noise model, which require yet another GAMIT iteration, and so on. As such the arrangement of items in this section are not necessarily chronological.

#### 4.4.1 *Reference Station Selection*

In order to achieve the full resolution capable in GNSS geodesy it is necessary to incorporate data from a selection of cGNSS stations with well-constrained a priori locations and velocities (e.g. in ITRF14) which have recorded simultaneously alongside the campaign survey [Herring et al., 2010]. These selected reference sites are incorporated into GAMIT’s weighted least-squares algorithm which solves for the position of all sites (and optionally, satellites) simultaneously, making a solution increasingly robust with additional reference stations. These reference stations also provide a distributed global-scale network to constrain the earth’s rotation, a continental-scale network to constrain velocity estimates relative to a tectonic plate, and regional stations near the campaign to help mitigate the effect of local atmospheric or weather

phenomena by double-differencing between satellites and stations [Seeber, 2003; Herring et al., 2010]. The reference stations must also be reliable, well-documented, professionally maintained, and constructed with a strong cement or deep-drilled mount to reduce annual or otherwise weather-related seasonal movement.

Fundamentally the difference between a “good” and “bad” reference station is its longevity, consistency, and repeatability [Dow et al., 2009]. A station that has existed for a long period of time will probably have a very well-constrained velocity, which in turn provides a well-defined predicted position. A good station will also have as few permanent mechanical or seismic antenna offsets as possible as each discontinuity forces the user to break its timeseries into separate discrete solutions to derive its uninterrupted or interseismic velocity. This degrades the robustness of the station’s velocity estimate and increases the model complexity overall as each segment must be then solved separately. Predictable and linear behaviour is desired and sites affected by nonlinear post-seismic crustal motion should be avoided.

Finally a good reference station will also have consistent day to day “repeatability”, i.e. low scatter around its predicted position, as large deviations naturally degrade the ability of the model to solve for a least-squares solution. There are two methods to quantitatively define repeatability, the weighted root-mean-square (WRMS) and the normalised root-mean-square (NRMS) [Herring et al., 2010]. The WRMS is the  $1\sigma$  (67%) position uncertainty normalised by the number of measurements taken, with units in length. The WRMS reflects the actual noise in the data, and accordingly this tends to be the de facto parameter to describe station noise as it is independent of the model. Conversely the NRMS is dependent on the model itself and has a somewhat variable definition in GAMIT/GLOBK. Essentially it is a unitless ratio of the RMS difference of each observation to their average, effectively a measure of the true uncertainty in the data to the modelled uncertainty applied to it. Thus if the actual variability of a site’s position is greater than its modelled uncertainty (e.g. the amount of intrinsic noise assigned to it), it will have have an  $\text{NRMS} > 1.0$  and its modelled uncertainty is too small or over-constrained. Likewise, an  $\text{NRMS} < 1.0$  means that the modelled uncertainty is too great and an NRMS of 1.0 means that its modelled uncertainty perfectly reflects the actual uncertainty seen. The NRMS is primarily useful to the analyst to quickly assess how well their noise model fits the data.

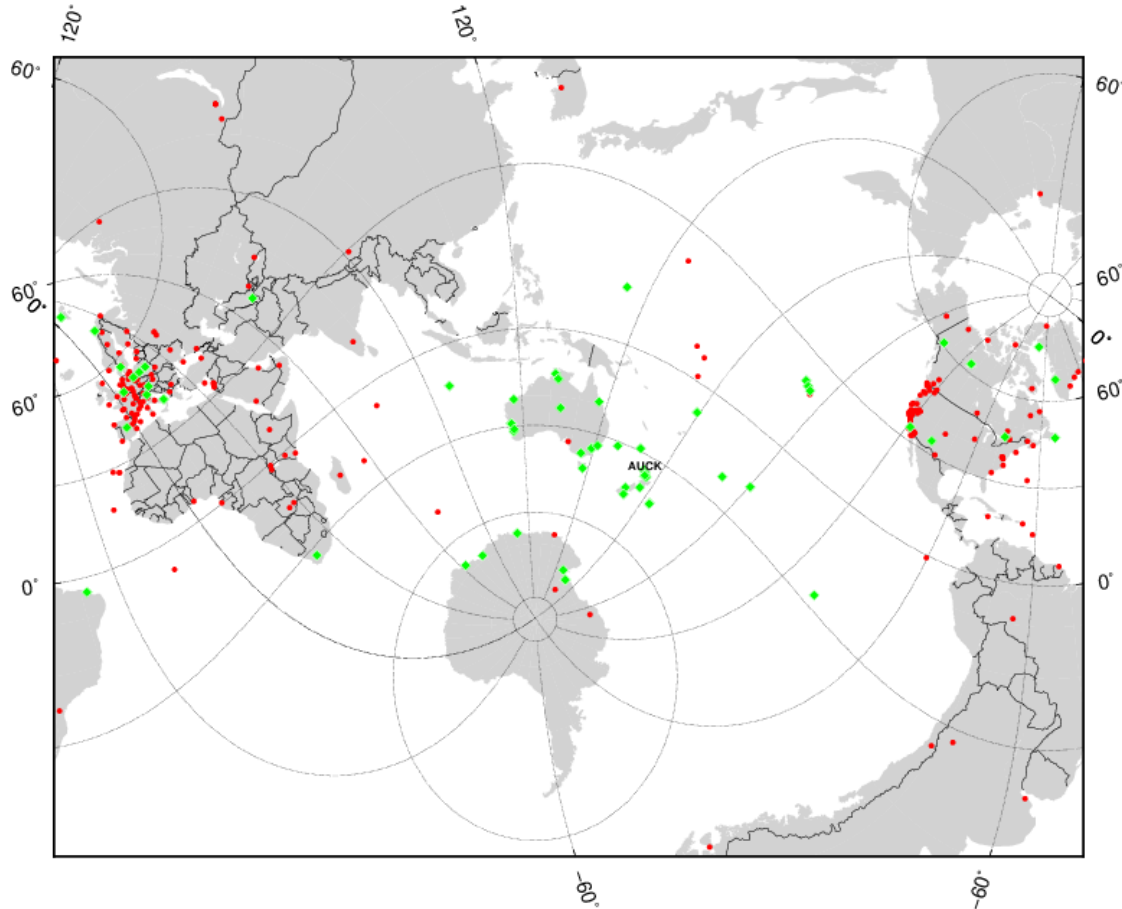


**Figure 4.9:** Global reference stations used to stabilise velocity model in GLOBK. Green stations were processed independently for this work (e.g. GAMIT and GLOBK), red stations were provided by SOPAC [Bock et al., 1997] for use in GLOBK only.

The reference stations used to stabilise the velocity model are shown in Figure 4.9. Many of these sites were established as far back as 1995 and all have good repeatability (horizontal WRMS  $< 2 \text{ mm}$ , vertical  $< 5 \text{ mm}$ ). This study also included a range of independent GAMIT solutions (e.g. collections IGS1, IGS2, EU00, and NA00) plotted in red which are provided by the Scripps Orbit and Permanent Array Center (SOPAC) [Bock et al., 1997] to combine with and strengthen the stability of the model.

#### 4.4.2 Solving for Position (GAMIT)

GAMIT uses a weighted least squares algorithm to derive a consistent, double-differenced “solution” for antenna positions over a 24 hour period, with the solution in reality being a covariance matrix combining all of the “quasi observations” needed to solve for position

[Herring et al., 2010]. These observations include satellite observables data recorded on the ground (e.g. RINEX data), the estimated orbit paths of the satellites themselves (derived from station positions or independently provided by IGS), clock uncertainties, earth orientation parameters, zenith signal path delays, antennas model specifications, and various other model parameters given in Table 4.1. A priori estimates for all of these observations are required and station locations in particular must be known within about 10 m [Herring et al., 2010]. Modern GNSS receivers are typically capable of using their own data to solve for an initial position within these specifications, else a velocity model such as the International Reference Frame 2014 (ITRF14) [Altamimi et al., 2016] may be used. GAMIT is then able to iteratively reduce the position's uncertainty initially to about 10-50 cm, then again to the millimetre level.

**Table 4.1:** GAMIT parameters

Orbit Model	FIXED (BASELINE Mode)
Orbits	IGS FINAL
Antenna Elevation Cutoff	10° (15° in 1995)
Antenna Model	IGS Absolute (AZEL)
Atmospheric Gradients	YES; constraint 0.01 m
Zenith Delay Estimation	YES
Ocean Loading Model	FES2004 [Lyard et al., 2006]

Orbits are calculated and produced to different specifications depending on their intended use. IGS [Dow et al., 2009] provide several products which are released with various delays depending on their complexity and precision. Assuming a fixed or zero-uncertainty (e.g. BASELINE mode) orbit model in GAMIT with IGS FINAL orbits (~2.5 cm accuracy, 20 picosecond clock  $\sigma$ , 30 second sampling interval) produces the most accurate results [Herring et al., 2010] with the only downside being the 12-18 day publishing delay. As this was of little concern this project used the highest quality FINAL orbits exclusively. Many agencies instead run GAMIT assuming the position of satellite orbits have non-zero uncertainty (e.g. RELAX mode), and then utilise the looser IGS RAPID orbits (~2.5 cm accuracy, 25 picosecond clock  $\sigma$ , 5 minute sampling interval). As the publishing time for RAPID orbits is 17-41 hours, this allows for quicker analysis of recent data. Other agencies estimate orbits themselves (e.g. SOPAC), which can be done with a high degree of confidence with enough terrestrial reference stations. Fortunately the nature of GAMIT's double difference method makes inconsistencies in orbits

relatively superficial assuming the site coordinates are consistent across combined solutions [Herring et al., 2010], thus making the incorporation of SOPAC's loose orbit data with this project's fixed orbit data unlikely to cause any compatibility issues.

Individual station antenna heights and hardware specifications are specified to provide the necessary vertical mark offset and model the variable response of each make/model of antenna and receiver. Often this data is catalogued and freely published by IGS and various agencies (e.g. MIT, SOPAC) but campaign data information must invariably be manually added. Inconsistencies or errors in this data are common but short-lived as they are typically detected immediately via error message or by visibly poor timeseries or velocity estimates.

Incoming satellite signals recorded at elevations less than  $10^\circ$  above horizon were disregarded as low angle data are particularly noisy due to the increased signal path sampling of the atmosphere and the likely inclusion of a larger percentage of multipath scatter off the ground [Elosequi et al., 1995]. Additional time-independent horizontal spatial uncertainty was added assuming a dry atmosphere delay of  $0.01\text{ m}$  for signals arriving at  $10^\circ$  diminishing to  $0.0\text{ m}$  at  $90^\circ$  vertical. Time-dependent "zenith delays" of the signal through the troposphere were estimated in the software. The effect of ocean tides on the crust which can cause daily  $mm$ -scale deviations were also removed based on the FES2004 model [Lyard et al., 2006] which has been the de facto GAMIT standard despite the subsequent release of newer versions of the same model [Mike Floyd, personal comm. 2017]. Finally, data outliers and cycle slips were automatically cleaned or repaired using the "autcln" code included in the GAMIT/GLOBK package.

GAMIT solutions were run at least once every five days between 1995-2018 as well as every day there existed campaign data. This was chosen to ensure that every 10-day aggregate combined solution had at least two estimates within it, and to otherwise reduce the numerical load associated in a 22+ year analysis. These solutions were supplemented with independent SOPAC solutions at a frequency of every five days between 1995-2018 as well as every day that campaign data existed. They were then loosely combined to 10-day aggregate solutions to expedite processing and strengthen each position estimate (Section 4.4.4.1).

#### 4.4.2.1 Processing 1995 Data

A considerable amount of extra care was made in processing the campaign 1995 data as it was crucial to this project. Data during this year was noisier than average, probably due to some combination of poor quality equipment, a lack of reference stations, fewer satellites, and poor

satellite coverage in the southern hemisphere but also potentially due to gradual addition of satellite yaw bias between June 1994 and November 1995 by the US Department of Defence [Bar-Sever, 1996]. Incoming satellite data below  $15^\circ$  above the horizon at many global cGNSS reference sites seemed to be particularly noisy during this period, so the cut-off was increased from  $10^\circ$  to  $15^\circ$ , and each day was otherwise meticulously examined for noisy or inconsistent reference site data which was summarily removed. Further, nearly all available global reference sites were used to stabilise the solution rather than a subset of the best performers, which helped to accurately position many sites in the poorly-covered southern hemisphere at the expense of marginally greater uncertainty. Campaign data during this period was still able to be resolved to at least  $4\text{ mm}$  horizontal and  $10\text{ mm}$  vertical uncertainty with a typical resolution closer to  $2\text{ mm}$  and  $5\text{ mm}$ .

Another critical issue was that much of the short-occupation 1995 NZ campaign data collected during the day in the NZ time zone spanned the UTC date boundary in which GNSS data and navigation regimes systems adhere to, effectively splitting an 8-hour occupation into two separate 4-hour occupations. As position uncertainty generally reduces by  $\sim 1/\sqrt{N_{obs}}$  this had the effect of increasing error  $\sim 120\text{-}150\%$ . This was addressed by changing GAMIT's daily processing "start time" from the default 00:00 (midnight) UTC to 12:00 UTC while maintaining a 24-hour observation period, thus shifting the ending time to 12:00 the following day. Accordingly navigation files for the following day had to be concatenated to the current and cGNSS site RINEX data were available for the both the current and following day.

#### 4.4.3 *TimeSeries*

Timeseries data is created by solving for the position of each individual data point and arranging them over time. This data is often normalised into a "residual timeseries" by removing a linear trend; this has been done for all timeseries shown in this project unless otherwise specified. Timeseries data is essential to visually inspect sites for outliers and offsets as well as numerically derive noise estimates.

#### 4.4.4 *Solving for Velocity (GLOBK)*

GLOBK collects all of the daily solution files created with GAMIT and runs them through a Kalman filter, a sequential least-squares estimator that allows for the implementation of stochastic processes, particularly both white and time-dependent coloured noise [Herring et al., 2010]. GLOBK can then combine and weight these individual solutions with “loose” constraints (Table 4.2) into a single matrix solution, at which point the solution is stabilised/constrained in a generalised global reference frame using a selection of a reliable cGNSS sites. This solution is then rotated via Euler pole relative to a reference frame (e.g. a tectonic plate) producing the final position and linear velocity estimates which is then plotted. Like GAMIT, it requires a priori positions and velocities.

**Table 4.2:** GLOBK parameters/tolerances for velocity solution and combination stage. Values are arranged as N E U (top)  $V_N$   $V_E$   $V_U$  (bottom) or if two values the first corresponds to position as a whole and the second velocity. These values generally were kept “loose” because the robustness of the model afforded it, and to safely incorporate daily SOPAC solutions which were ran with slightly different model parameters. The a priori satellite positions (10 m) are assumed to be far more trustworthy than the sites themselves (100 m). mas = milli-arcsecond, †=radiation pressure variance turned off to accommodate the integration of SOPAC data created with different model parameters.

Parameter	Description	Position Unit Velocity Unit	Values (Velocity Solution)	Values (Combina- tion)
apr_tran	1 $\sigma$ Model Translation	$m$ $m/year$	1 1 1 1 1 1	1 1 1 0 0 0
mar_tran	1 $\sigma$ Model Translation Random Walk	$m^2/year$ $(m/s)^2/year$	3.65 3.65 3.65 0 0 0	0 0
apr_site	1 $\sigma$ A Priori Station Position/Velocity	$m$ $m/year$	10 1	10 1
apr_wob	1 $\sigma$ A Priori Earth Rotation Pole Location	mas mas/day	10 10 1 1	10 10 1 1
mar_wob	Earth Rotation Pole Random Walk	mas <sup>2</sup> /year (mas/day) <sup>2</sup> /year	3650 3650 0 0	3650 3650 365 365
apr_ut1	1 $\sigma$ A Priori Earth Rotation Speed	mas mas/day	10 1	10 1
mar_ut1	Earth Rotation Speed Random Walk	mas <sup>2</sup> /year (mas/day) <sup>2</sup> /year	365 0	365 365
apr_svs	1 $\sigma$ A Priori Satellite Position/Velocity	$m$ mm/second	100 100 100 10 10 10 0R†	100 100 100 10 10 10 0R†
apr_atm	1 $\sigma$ Zenith Delay	$m$	1	1
mar_atm	1 $\sigma$ Zenith Delay Random Walk	$m^2/hour$	3.65	3.65

As GLOBK sequentially runs one GAMIT solution to the next it assesses how well each successive datapoint fits within the overall model via a  $\chi^2$  (chi-square) “goodness of fit” statistical test, mathematically the sum of the squares of each observation’s residual normalised by its a priori uncertainty. Therefore adding a bad or otherwise anomalous piece of data to the process will result in a  $\chi^2$  value  $> 1$ , which is logged. The uncertainty of each incremental GAMIT solution can then be rescaled (i.e. weighted) to be higher or lower by its previous  $\chi^2$  in successive GLOBK runs in order to fit the data to its modelled uncertainty, steering its  $\chi^2$  towards 1.0 and closer to a scenario in which its modelled uncertainty reflects reality.

#### 4.4.4.1 Aggregating and Combining Daily Solutions

GNSS data for geodetic survey applications is typically archived and published in standard 24-hour intervals, making it the de facto unit of geodetic analysis. However this period can be excessively small for projects involving either a large volume of data, or spanning a large amount of time. Aggregating daily solutions into multi-day solutions is an effective way to reduce the numerical load while also reducing daily scatter at the expense of temporal resolution in the timeseries. As this project is primarily interested in the velocity estimates of decadal-scale timeseries, in addition to constraining very slow deformation, an interval of 10 days was chosen as an aggregation interval to speed up processing and achieve precise positions. It is assumed that the earth's motion is inconsequential over such a period with the exception of earthquakes, in which case 10-day data spanning large earthquakes were simply disregarded.

When combining solutions containing an asymmetric volume of data extra care must be taken so that the final combination is biased properly due to the  $\sigma \sim 1/\sqrt{N}$  relationship between uncertainty and the volume of data  $N$ . For example, assume that both stations AUCK and TIBB have equivalent "real" position uncertainties of 1 mm, and that the files used in a given 10-day combination contain seven 24-hour AUCK solutions but only two of TIBB. When combined, AUCK's modelled uncertainty will be lowered by  $\sim 1\text{ mm}/\sqrt{7}$  to 0.38 mm whereas TIBB's will be nearly twice as large but still unrealistically low,  $\sim 1\text{ mm}/\sqrt{2} = 0.71\text{ mm}$ . The solver will therefore unjustly over-weigh AUCK's position certainty relative to TIBB's as it attempts to stabilise the solution. To eliminate this effect white noise was assigned to each station proportional to the root of the number of its occurrences in each combination, e.g.  $A * \sqrt{N}\text{ mm}$  where  $A$  was the initially assumed uncertainty, e.g. 1 mm in this example. In practice, white noise amplitudes  $A_{Horizontal} = 1.1\text{ mm}$  and  $A_{Vertical} = 3.5\text{ mm}$  were assigned for all cGNSS sites, equivalent to those used by Beavan (2005) and Beavan et al. (2016).

#### 4.4.4.2 Mitigating Reference Station Dislocations

Fundamentally there is a "net" velocity incorporating the whole of the site's data from start to finish, and also an "interseismic" velocity which describes the constant tectonic crustal deformation which occurs between coseismic earthquake offsets. Assuming no offsets, the net velocity would theoretically describe tectonic motion, which is the aim of this project. However once a continuous station experiences any perceptible offset it will shift the velocity

away from its natural tectonic rate and thus must be corrected. For example, Figure 4.10 shows the timeseries data for the east component of NZ cGNSS station CHTI/Chatham Island which has been offset to the west by the 2016 Kaikōura earthquake. This has reduced the eastern component of the site's natural tectonic rate or "net" velocity (black arrow). Therefore implementing a site rename was required (e.g. to CHTI\_3PS) to calculate the interseismic velocity (red vectors) by calculating either rename separately with the implicit assumption that they should be equal within some degree of tolerance.

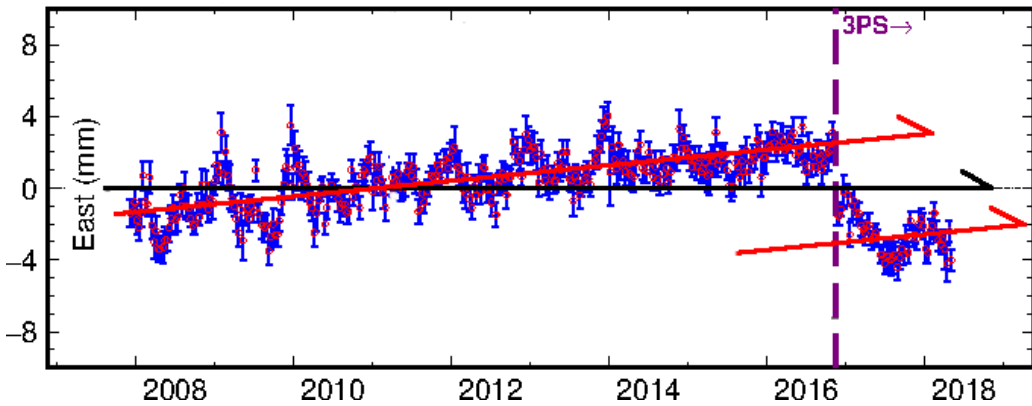


**Figure 4.10:** Residual timeseries for the east component of CHTI (Chatham Island) which provides a clear example. Following the 2016 Kaikōura earthquake, the site had to be renamed with each new component calculated separately to correctly interpret its interseismic tectonic velocity. The net velocity is drawn as a black arrow, the interseismic velocity as red.

This project dealt with station offsets by first examining the individual timeseries of each cGNSS site used and identifying potential offsets to be incorporated into GLOBK. Often this task has already been done by other agencies (e.g. SOPAC, MIT) who freely share their catalogue of known station dislocations, and SOPAC's data was applied to this work. However this project found that this information rarely included many New Zealand sites and generally cannot always be trusted to be up to date or consistent, confirming the necessity for manual review. GeoNet currently does not maintain a database for its NZ cGNSS stations but has plans to do so in the future [Elisabetta D'Anastasio, personal comm., 2018].

Once all offsets were identified and logged, the horizontal velocities of each cGNSS site's renamed velocities were numerically constrained in the software to be within  $0.1 \text{ mm/yr}$  tolerance of each other, and vertical within  $0.3 \text{ mm/yr}$ . After an initial GLOBK run the  $\chi^2$  fits to these equates were reported and all renames resulting in unusually high values (e.g.  $>5$ ) were reviewed, unequated, and in drastic circumstances removed from the solution outright. This was invariably the case for cGNSS sites near large earthquakes, including many of the NZ

continuous sites near Kaikōura which immediately began exhibiting prolonged and nonlinear postseismic behaviour.

#### 4.4.5 *Creating a Noise Model*

In GNSS geodesy the seemingly Gaussian distribution of system noise combined with an abundance of data can lead to deceptively optimistic velocity estimates [Zhang et al., 1997]. The remedy is to manually add noise to the model, but the magnitude and types of noise, as well as methods of applying it, have long been a subject of debate. Determining an appropriate noise model was especially crucial for this project because the low-displacement ( $\sim 1 \text{ mm/yr}$ ) environment of NWNZ is comparable to the magnitude of GNSS system noise, making an accurate estimate tantamount to the derivation of velocity estimates. Too much noise could render a velocity useless, whereas too little could wrongly over-weigh interpretations of crustal and tectonic activity. As this project surveyed a relatively large amount of campaign sites, it was decided best to err on the side of applying too much noise rather than too little to be sure that every velocity solution was truthful at the expense of widening the error ellipses throughout the velocity estimates.

##### 4.4.5.1 *White and Coloured Noise*

Noise in geodetic timeseries can be described by a power law relationship proportional to its frequency ( e.g.  $\sim 1/f^n$  ) where  $n$  is typically between -1 and 3 [Agnew, 1992]. A value of  $n=0$  implies frequency independence, or "white noise" and values of  $n=1$  or  $n=2$  are special cases commonly referred to as "flicker noise" and "random walk noise", respectively. Flicker noise ( $\sim 1/f$  ) can be thought of as an intermediary between white noise, whose effect is independent of time, and random walk noise whose affect increases quadratically proportional to the period of analysis.

The time independence of white noise implies a flat and linear power spectrum density plotted against frequency, and thus position estimates affected by white noise only should form a normal, Gaussian distribution over time. Further, the magnitude of this implied uncertainty should diminish as the amount of observations  $N$  increase, proportional to  $1/\sqrt{N}$  as per the standard deviation formula. Thus in theory after a single year a position estimate should fall to almost 5% of a single day's uncertainty, or about  $(1/\sqrt{365}) = 0.05 \text{ mm}$ . However even a casual

glance at a cGNSS station's timeseries (e.g. Figure 4.10) shows this is wildly optimistic. This discrepancy is due to the additional presence of frequency dependent "coloured" noise acting at periods of weeks to decades, typically caused by seasonal weather phenomena, ocean tidal loading, mark monument instability, an accumulation of tiny coseismic offsets, equipment degradation, or variability in the strain within the crust itself [Agnew, 1992; Langbein et al., 1993; Zhang et al., 1997; Mao et al., 1999; Beavan, 2005; Langbein 2012]. It is not always clear which type of coloured noise best describes each phenomena [Zhang et al., 1997; Mao et al., 1999; Williams, 2003; Langbein, 2004; Beavan, 2005; Langbein, 2008] but there is evidence that both white noise and flicker noise appear to be spatially correlated [Amiri-Simkooei, 2009] implying that time-dependent  $\sim 1/f$  flicker noise may be intrinsic to both the broad GNSS system and geographic location as a whole. It is uncertain if random walk noise ( $\sim 1/f^2$ ) is also spatially correlated, however ultra-high precision strainmeter studies within the crust [e.g. Agnew, 1992; Langbein et al., 1993] invariably contain a large random walk component in their power spectrum densities. Thus random walk may also be regionally correlated, insofar as sites within the same crustal strain regime with a large degree of noise  $\sim 1/f^2$  may share similar random walk characteristics.

The overall influence of coloured noise on velocity estimates is considerably larger than white noise [Zhang et al., 1997; Mao et al.; 1999], particularly at lower frequencies due to its inverse proportionality. That long-period, low-frequency noise dominates the velocity uncertainty makes sense on an intuitive level as it may introduce long, trending noise throughout the whole of the timeseries whereas short-period coloured noise on an annual scale will be neutralised after windowing a timeseries greater than a few years. The higher impact of coloured noise should therefore prioritise its importance in determining an overall noise model.

#### 4.4.5.2 Choosing a Time-Dependent Coloured Noise Model

There is little consensus as to what combination of time-dependent flicker, random walk, or otherwise power-law noise to employ with some favouring just flicker noise [Mao et al., 1997], power-law noise  $1 < n < 2$  [Williams et al., 2004], or combinations of flicker and random walk noise [Amiri-Simkooei et al., 2009; King and Williams, 2009; Dmitrieva et al., 2015]. Langbein (2008) suggests that the best model depends on the station and Dmitrieva et al. (2016) similarly recommend independent constraints to confirm the best combination. A flicker-only model tends to produce the smallest uncertainty while a random walk-only model the largest, with

general power-law or combinations of flicker and random walk falling somewhere in between [Langbein, 2012; Dmitrieva, 2015].

As white noise and random walk noise are effectively the end members of the  $0 < n < 2 \sim 1/f^n$  noise spectrum, they can be combined in such a way to replicate realistic velocity uncertainties without explicitly using flicker or general power-law noise [Herring et al., 2010]. This is fortunate for this project as the Kalman filter used in GLOBK is only capable of incorporating random walk noise alongside white noise. It is however noted though that at observation periods surpassing  $\sim 7\text{-}10$  years in length the power spectrum density of both a random walk only and composite flicker-and-random walk model tend to converge regardless [Langbein, 2012], which means that either should produce similar results in as the average age of NZ cGNSS stations in this project is over 13 years old.

The random walk estimates were found using the “Realistic Sigma” algorithm included in the GAMIT/GLOBK package [Herring, 2003; Williams et al., 2004; Reilinger, 2006; Herring et al. 2010]. This is a First-Order Gauss Markov maximum likelihood estimator which essentially works by averaging timeseries scatter over a series of windowed times to determine how these averages depart from a pure white noise regime, with the difference in uncertainty being the random walk component. The code has two settings, “FOGM” in which the uncertainties are exponentially weighted proportional to the length of each time frame, and “RW” in which they are not (e.g. evaluated over an “infinite” time, or the whole of the timeseries) [Reilinger et al., 2006]. In practice the FOGM approach produces smaller random walk noise estimates by down-weighting short term variance which may be exaggerated in the case of large offsets or brief and/or inexplicable noisy periods in the data. However as this project took painstaking means to document all perceptible antenna offsets for not only NZ cGNSS stations but all cGNSS stations used throughout the model, in addition to removing  $3\sigma$  timeseries outliers beforehand, and moreover considering long 20+ year length of the analysis, the conservative “RW” setting was selected for robustness. Furthermore, periodic seasonal effects were not removed from the timeseries beforehand as these were considered part of the overall coloured noise regime. The resulting North-East-Up random walk (Table 4.3) estimates were then individually applied in all subsequent GLOBK runs.

The Realistic Sigma “RW” estimates used in this study are predictably larger than those given by the timescale-weighted “FOGM” setting and generally agree with other researchers using the same method (e.g.  $\sim 0.5 \text{ mm/yr}^{1/2}$  [McCaffrey et al., 2013],  $0.25 - 0.65 \text{ mm/yr}^{1/2}$  [Shen et al., 2011]). The random walk uncertainties simply defined by  $A/T^{1/2}$  [Zhang et al., 1997;

Beavan et al. 2016] are much smaller but still offer a surprisingly good fit to many of the Realistic Sigma “FOGM” algorithm assuming  $A = 1 \text{ mm}/\text{yr}^{1/2}$  making it an excellent back of the envelope approximation for geologically quiet regions.

**Table 4.3:** Time-dependent uncertainty (units in  $\text{mm}/\text{yr}^{1/2}$ ) for North-East-Up components of cGNSS sites in the northern North Island, NZ. RW = Realistic Sigma “RW” setting (used in this study), FOGM = Realistic Sigma “FOGM” setting (time weighted), and  $\sigma = A/T^{1/2}$  is a quick approximation used by Zhang et al. (1997) and Beavan et al. (2016) assuming random walk amplitude  $A = 1 \text{ mm}/\text{yr}^{1/2}$ .

Site	RW (NEU)	FOGM (NEU)	$\sigma = A/T^{1/2}$ (NEU)	Age (yr)
AUCK	0.36 0.38 0.57	0.23 0.23 0.24	0.21	23.7
AUKT	0.37 0.37 0.60	0.23 0.24 0.34	0.34	9.3
BHST	2.72 1.65 1.07	0.67 0.44 0.46	0.32	9.9
CORM	0.35 0.35 0.45	0.23 0.24 0.25	0.26	16.0
HAMT	0.74 0.46 0.45	0.29 0.24 0.27	0.26	16.0
KTIA	0.32 0.33 0.51	0.23 0.23 0.30	0.31	11.6
MAHO	0.47 0.44 1.03	0.23 0.23 0.27	0.26	15.3
NPLY	0.55 1.65 0.45	0.25 0.27 0.25	0.26	16.2
RGWI	0.56 0.56 0.78	0.30 0.27 0.45	0.39	7.7
TAUP	2.03 3.29 2.44	0.33 0.68 0.30	0.25	16.7
TGHR	0.60 0.54 0.67	0.25 0.23 0.28	0.29	12.0
TRNG	0.96 1.77 0.69	0.24 0.48 0.25	0.26	16.3
VGMT	1.31 1.11 0.56	0.34 0.29 0.29	0.27	13.3
WANG	1.25 3.18 0.71	0.32 0.52 0.30	0.26	15.0
WARK	0.35 0.35 0.67	0.23 0.23 0.33	0.33	10.3
WHKT	0.96 0.62 1.38	0.24 0.24 0.33	0.33	10.2
WHNG	0.47 0.44 0.78	0.25 0.24 0.27	0.26	16.1

#### APPLYING TIME-DEPENDENT NOISE TO CAMPAIGN DATA

Determining random walk estimates for campaign stations cannot be done in the same fashion as cGNSS sites as the non-continuity of their data make numerical estimations of frequency-dependent noise impossible. A standard approach is to apply a median value of random walk uncertainties calculated for cGNSS stations [e.g. McCaffrey et al., 2013], or to apply some simplified (e.g.  $\sigma = 1 \text{ mm}/T_{\text{years}}^{1/2}$ ) age dependence [e.g. Beavan 2005; Shen et al., 2011; Beavan et al., 2016]. It was observed however that cGNSS stations with high random walk uncertainty (e.g. WANG, VGMT, BHST, TAUP, RGWI) are all located near regions thought to be influenced by a large degree of plate locking with the subducted Pacific slab [Wallace and Beavan, 2010; Wallace et al., 2012] or near active volcanism (TAUP, WHKT, RGWI), whereas

areas known to be relatively inactive or far from the plate boundary within the northern North Island (AUCK, AUKT, KTIA, WHNG, WARK) invariably show smaller values. Though this correlation is not perfect with sites like GISB, CKID, and MAST showing small random walk despite being in seismically active areas (e.g. Figure 2.11), the correlation seemed to be too strong to simply be proportional to site's construction, particularly because many of the sites near the plate boundary are younger and better engineered than the northern ones (Figure 4.1). Therefore a spatial correlation was assumed and campaign station random walk values were interpolated between the known values of cGNSS stations (Figure 4.11). While this may not be accurate for all regions, particularly where there are few cGNSS stations, it was deemed a better representation than applying the same values for wildly discordant tectonic regions such as Northland (KTIA) and southern Taranaki (WANG). In the worst case, campaign velocity uncertainties would be too large rather than too small.

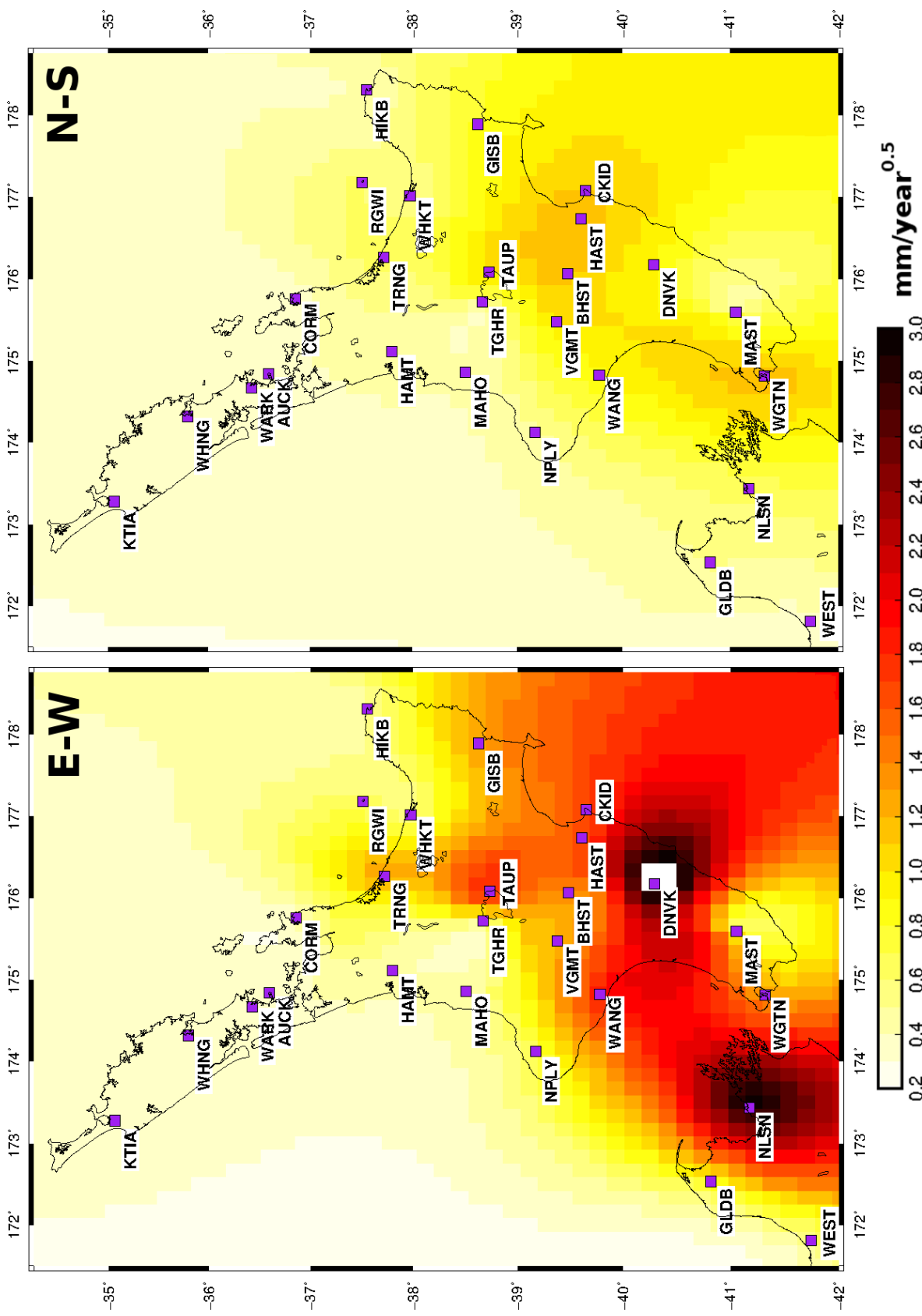
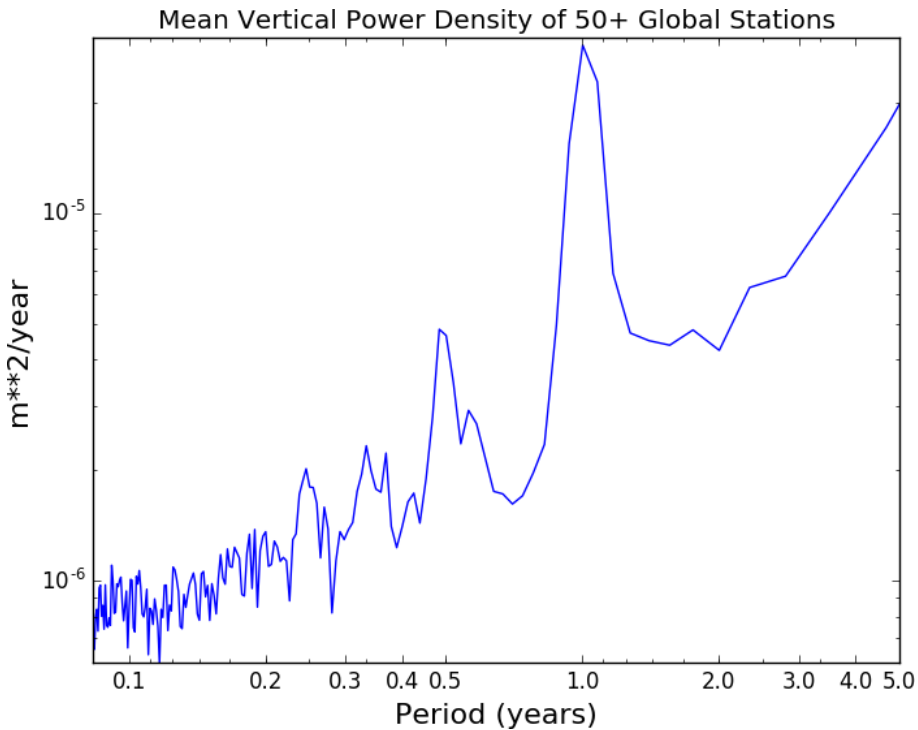


Figure 4.11: East and North Random Walk values derived from interpolating individual values at each cGNSS station.

As campaign data generally went as far back as 1995, it usually sampled many earthquakes which generated coseismic offsets that the cGNSS sites had themselves been renamed and corrected for. Therefore to produce realistic random walk components for campaign data, the cGNSS site random walk data used to create the surfaces in Figure 4.11 were only corrected for manual antenna offsets, with all coseismic and annual periodicity left intact between January 1 1995 and November 1 2016. This time range was set to intentionally exclude the November 13 2016 Kaikōura earthquake which generated historically large coseismic offsets throughout the North Island. Its inclusion would unfairly exaggerate random walk values for campaign sites in the NWNZ region surveyed between 1995-2016, therefore it was decided to side-step this issue by manually correcting the coseismic offset of campaign data surveyed in 2017 in a method discussed ahead in section 4.5.3.1.

#### 4.4.5.3 *Applying Time-Independent White Noise*

While the impact of white noise on velocity estimates is low relative to the addition of coloured noise, adding stochastic uncertainty helps to ensure that sites with a relative abundance of data are not over-weighted in the solver due to the  $\sim 1/\sqrt{N}$  relationship between uncertainty and the volume  $N$  of data. It also helps reduce scatter and produce a smoother timeseries at an expense of slightly larger error bars. White noise was applied in two different ways, initially it is added during the combination step (Section 4.4.4.1), then it is added to individual cGNSS stations during the GLOBK step.



**Figure 4.12:** Mean Power Spectrum Density ( $m^2/yr$ ) of the vertical component of 51 cGNSS stations interspersed globally. The annual seasonal cycle ( $T=1.0$  years) is clearly evident, in addition to the six (0.5), four (0.33), and three (0.25) month periods caused by the nutation around the earth's axis of rotation. This project assumed that nutation periods less than 80 (<0.22) days are primarily white noise.

Individual cGNSS station white noise was determined by applying an 80 day high pass filter to its timeseries. This interval was determined by assessing the smallest period time-dependent nutation signal present (Figure 4.12) which appears to be about 1/4th of a year or 90 days, then selecting a period slightly smaller to avoid including it. The resulting values were strongly dependent on station distribution with densely spaced networks (e.g. the NZ cGNSS network used in this project) showing much smaller time-independent white noise values due to the ease at which signal errors can be diminished via double-differencing.

In theory white noise is not needed for campaign data as it is not used to constrain or stabilise the model and is invariably sparse in volume relative to cGNSS stations, making average estimates difficult and unreliable. In practice however there can be a fair amount of field operator error (e.g. poor measurement, mobile tripod instability, etc) and accordingly a modest 0.5 mm and 1.0 mm of error was added to campaign data in the horizontal and vertical components respectively.

#### 4.4.6 Processing Flow

1. Daily GAMIT processing to derive unconstrained position estimates using ITRF14 a priori station positions.
2. Initial GLOBK run using daily position data and ITRF14 a priori positions and velocities to derive a custom position and velocity estimates for model.
3. Use custom position and velocity estimates to generate timeseries with GLRED.
4. Use timeseries to identify new offsets and remove outliers. Then, derive white and coloured noise values. Interpolate coloured noise for cGNSS sites to derive values for campaign sites.
5. Re-run GAMIT on days where necessary (e.g. poor solution or stations added or removed via QC) using newer custom position and velocity model. Return to step 4 until timeseries is without significant outliers or uncorrected offsets.
6. (Optional) Combine individual/daily GAMIT solutions into multi-day aggregate solutions.
  - a) Run GLOBK for combination timeframe without noise. Note resulting NEU noise amplitudes in output file.
  - b) Apply custom noise to each site scaled by square root of volume of station's data ( $\sqrt{N}$ ).
  - c) Return to step 2 using combined data.
7. Re-run GLOBK using updated offsets and noise model, noting the change in  $\chi^2$  of each piece of incoming combined or daily data.
8. Re-weight input data (file list, random walk values) re-scaled by the previous  $\chi^2$  values.
9. Re-run GLOBK until  $\chi^2$  for model and velocity constraints near 1.0.
10. Constrain the model to generalised reference frame using selected stabilisation sites, unconstrain poorly fitting renames.
11. Rotate this solution relative to some fixed position or tectonic plate via Euler pole.

#### 4.5 CRUSTAL RESPONSE TO EARTHQUAKES AND SLOW SLIP EVENTS

The interseismic deformation rate of the earth's crust due to tectonic motion is routinely affected by large earthquakes causing instantaneous coseismic offsets as well as a transient postseismic response which may continue for years [e.g. Tregoning et al., 2013]. Since the NZ cGNSS network came online in 1995, two major earthquakes have resulted in clear and systemic coseismic offsets at cGNSS stations in NWNZ: the M8.1 2004 Macquarie Island and M7.8 2016 Kaikōura earthquakes. A third event, the M7.8 2009 Fiordland earthquake did not result in significant coseismic offsets within NWNZ despite its epicentre being nearly 500 km closer than the Macquarie Island event [Hayes et al., 2017].

In addition to these two large earthquakes, there have been dozens of "slow slip events" recorded at the North Island's cGNSS stations [Wallace and Beavan, 2006; McCaffrey et al., 2008; Wallace and Beavan, 2010; Wallace et al., 2012; Wallace et al., 2014; Wallace et al., 2018], many of which have affected the greater Taranaki Peninsula region. These are events theoretically equal to M7+ earthquakes if they slipped instantaneously [Wallace et al., 2006] but due to their slow rate of motion over the course of months to years they typically go undetected by seismic instruments. Slow-slip events can initiate by themselves (e.g. the 2004-2005 Manawatu region [Wallace and Beavan, 2006] and 2013-2014 Kapiti Coast [Wallace and Beavan, 2010]) or may be triggered by a larger event nearby, as happened following the Kaikōura earthquake [Wallace et al., 2018]. Large earthquakes may also serve to terminate slow slip events by quickly releasing the remaining stress driving them [Wallace et al., 2014].

The response of the crust to both earthquakes and slow-slip events may contain a large amount of information. Spatial discrepancies in the magnitude and direction of coseismic offsets may be used to infer variability in the crust beneath the stations, or perhaps the presence of elastically or plastically deforming faults [Johnston et al., 1987; Marone et al., 1991]. Furthermore the subsequent postseismic nature of this deformation may provide insight as to the change in state of crustal stress. For example rigid or plastic deformation might mean that stress has been relieved, whereas elastic or plastic deformation with a matching change in velocity could mean that stress is accumulating. Either observable could benefit seismic risk studies.

Characterising the coseismic and postseismic behaviour of large earthquakes may also be required to reconcile campaign surveys. This was the case for this project's three year 2015-

2017 campaign as the November 2016 Kaikōura event produced permanent coseismic offsets greater than the region's annual strain rate. Therefore campaign data measured in 2017 had to be numerically "returned" to its theoretical pre-Kaikōura position in order to estimate each station's interseismic velocity (described ahead in section 4.5.3.1). The 2004 Macquarie Island event, which occurred in the middle of the broad 1995-2017 collection of North Island campaign data (Figure 4.8) similarly produced coseismic offsets larger than the annual velocity of much of the area. These offsets were also corrected for, but the extended age (11+ years) of the event given the application of time-dependent noise (Section 4.4.5.2) reduced its deleterious effect on velocity estimates on sites spanning the 22 year period between 1995-2017.

#### 4.5.1 Coseismic Estimation Method

A coseismic offset estimation can be produced by simply observing the difference between a residual timeseries datapoint the day before and after an earthquake. However, due to the nature of noise (Section 4.4.5.1) and scatter (e.g. Figure 4.6) in the GNSS system a single datapoint may not produce a reliable or statistically robust value. Uncertainty can be reduced with the addition of more data on either side of the coseismic offset, but this assumes a purely linear system with no seasonal or postseismic deformation, e.g. the only effect the earthquake had was the instantaneous coseismic offset. This is a fair approximation for distant cGNSS sites faintly affected but problematic for sites closer to the earthquake hypocentre which experience nonlinear postseismic motion. Furthermore in New Zealand earthquakes have been observed to trigger slow slip events [e.g. Wallace et al., 2018] which exacerbates a cGNSS site's postseismic motion. Accordingly some compromise must be made in determining the optimal amount of time to average timeseries data around an earthquake depending on one's objectives.

Due to the high precision required to properly resolve the low-rate campaign sites in the northern North Island, and because very few of the NWNZ cGNSS sites showed postseismic motion, an extended period of 10 days on either side of an earthquake was selected to determine a coseismic offset. This was done by generating a singular 10 day aggregate datapoint for the pre and post-position (e.g. Section 4.4.4.1) excluding the day of the earthquake. This method which was found to reduce uncertainty and improve consistency between stations relative to averaging individual daily solutions.

#### 4.5.2 23 December 2004 M8.1 Macquarie Island Earthquake

The Macquarie Island earthquake occurred 2004-12-23 14:59:04 UTC with an epicentre at  $161.345^{\circ}\text{E}$   $49.312^{\circ}\text{S}$  and depth of  $10.0\text{ km}$  [Hayes et al., 2017]. It originated via strike-slip faulting on oceanic lithosphere approximately  $150\text{ km}$  west of the Australia-Pacific plate boundary,  $500\text{ km}$  south of mainland New Zealand, and  $600\text{ km}$  north of the Macquarie Island despite its moniker [Hayes et al., 2017].

The earthquake generated sizeable coseismic displacements (Figure 4.13) at cGNSS stations as far north as Whangarei, NZ (WHNG,  $1800\text{ km}$ ) and Canberra, AUS (TID1/TID2/TIDB,  $1830\text{ km}$ ) but did not offset the Chatham Islands (CHAT,  $1800\text{ km}$ ) suggesting that the Pacific Plate was less affected. The January 2004-June 2006 Manawatu (~ WANG, VGMT, BHST) slow-slip event was already in progress [Wallace and Beavan, 2006] and experienced coseismic displacements atop motion already occurring. Coseismic offsets were uniformly E-NE in the North Island of NZ with magnitudes between  $\sim 2\text{-}5\text{ mm}$  with the notable exception of site CORM in the Coromandel Peninsula which is presumed to be an outlier, the reason for which is not clear. Because the event was so far away from NWNZ and thus unlikely to exhibit a strong spatial dependence, a generalised coseismic offset correction for the whole of the NWNZ campaign data was then calculated by averaging all solutions (ex. CORM) and found to be  $2.8\text{ mm}$  North and  $3.6\text{ mm}$  East.

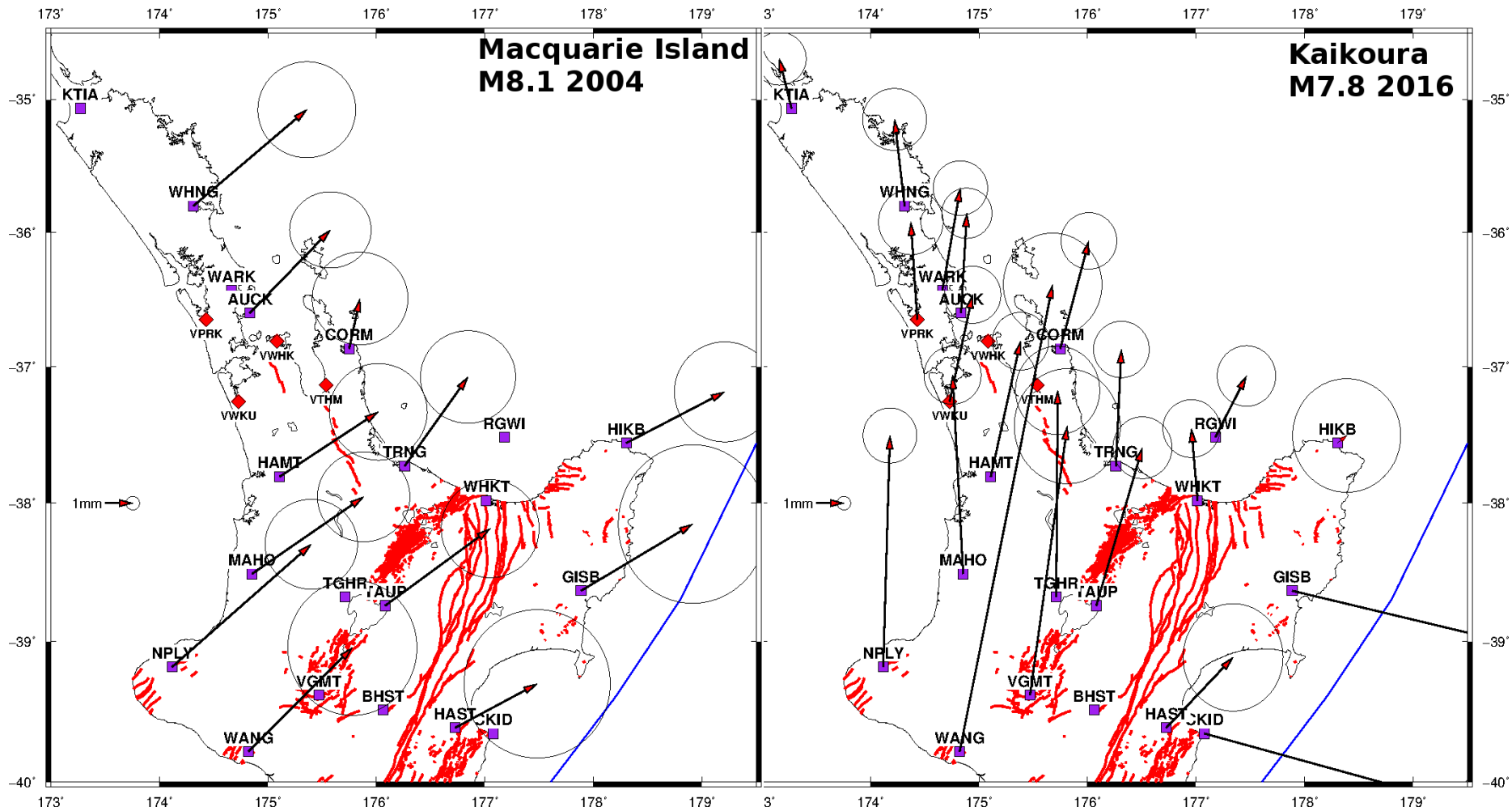


**Figure 4.13:** Coseismic offsets generated by the 2004 M8.1 Macquarie Island (top) and 2016 M7.8 Kaikōura earthquake. Red lines denote active faults [Langridge et al., 2016], purple squares are NZ cGNSS sites and red diamonds are cGNSS sites operated by the Allterra Co., with the approximate plate boundary drawn in blue [Bird, 2003].

### 4.5.3 13 November 2016 M7.8 Kaikōura Earthquake

The Kaikōura earthquake occurred at 2016-11-13 11:02:56 UTC with an epicentre at 173.054°E 42.737°S and depth of 15 km [Kaiser et al., 2016]. It originated and disseminated amidst a complex oblique thrust system on the Marlborough fault system, NE of the South Island [Kaiser et al., 2016; Cesca et al., 2017]. This event generated some of the largest offsets in New Zealand since the cGNSS network began in 1995, strongly affecting the whole country including Kaitaia (KTIA, 815 km north) (but not Norfolk Island/NORF, 1580 km north), in addition to the Chatham Islands (CHAT, 815 km east) and Macquarie Island (MAC1, 1700 km south). However unlike the 2004 Macquarie Island event this earthquake did not generate offsets at stations on continental Australia nor Lord Howe Island (LORD, 1775 km NE). Also unlike Macquarie Island, these offsets show a high degree of spatial variability in the North Island (Figure 4.13) which is probably due to the close proximity of the epicentre generating highly localised deformation as well as triggering separate strong slow-slip events in the south and east coast of the North Island [Wallace et al., 2018]. The sites strongly affected by slow slip events within 10 days of the earthquake are anomalous from the overall N-NE trend, including all sites on the east coast (HAST, CKID, GISB, HIKB) as well as WANG/Whanganui and possibly TGHR in the Manawatu region.

#### 4.5.3.1 Applying Kaikōura Offsets to 2017 Campaign Data

The 2016 Kaikōura earthquake coseismically significantly shifted all of this project's 2015–2017 campaign stations prior to their third and final year of surveying. They were displaced enough (>2 mm) such that they required a numerical "correction" in order produce a valid interseismic velocity estimate within their slow deforming (~1 mm/yr) environment. Nearby cGNSS sites were used to estimate the coseismic offsets throughout the region with the intent of interpolating values at campaign stations.

To create a continuous field of coseismic offset estimates, an elastic half-space model utilising some the cGNSS site vector data and uncertainties in Figure 4.13 was used via the "gpsgriddler" code in GMT [Haines et al., 2015; Sandwell and Wessel, 2016]. Anomalous sites (VTHM, VWHK) or sites showing postseismic behaviour (WANG, CKID, BHST, HAST, WHKT, HIKB,

TGHR, TAUP, RGWI) were removed, the crust was assumed to have a Poisson's ratio of 0.265 [Christensen, 1996], and a surface was fit via singular value decomposition with an overall RMS misfit of 2  $mm$ . The data was then gridded at 15 *arcminute* resolution producing the data in Figure 4.14. Estimates for coseismic offsets at campaign stations were then found by averaging the modelled data within a 0.5 degree radius in an attempt to further smooth the data. Any remaining uncertainty was ultimately mitigated by adding 0.5  $mm$  of white noise to the horizontal components for all 2017 campaign positions. For data incorporating historic RINEX data, particularly data anchored with 22 year old 1995 data, both the noise and coseismic offset ambiguity were not likely to be influential to the final velocity estimate.

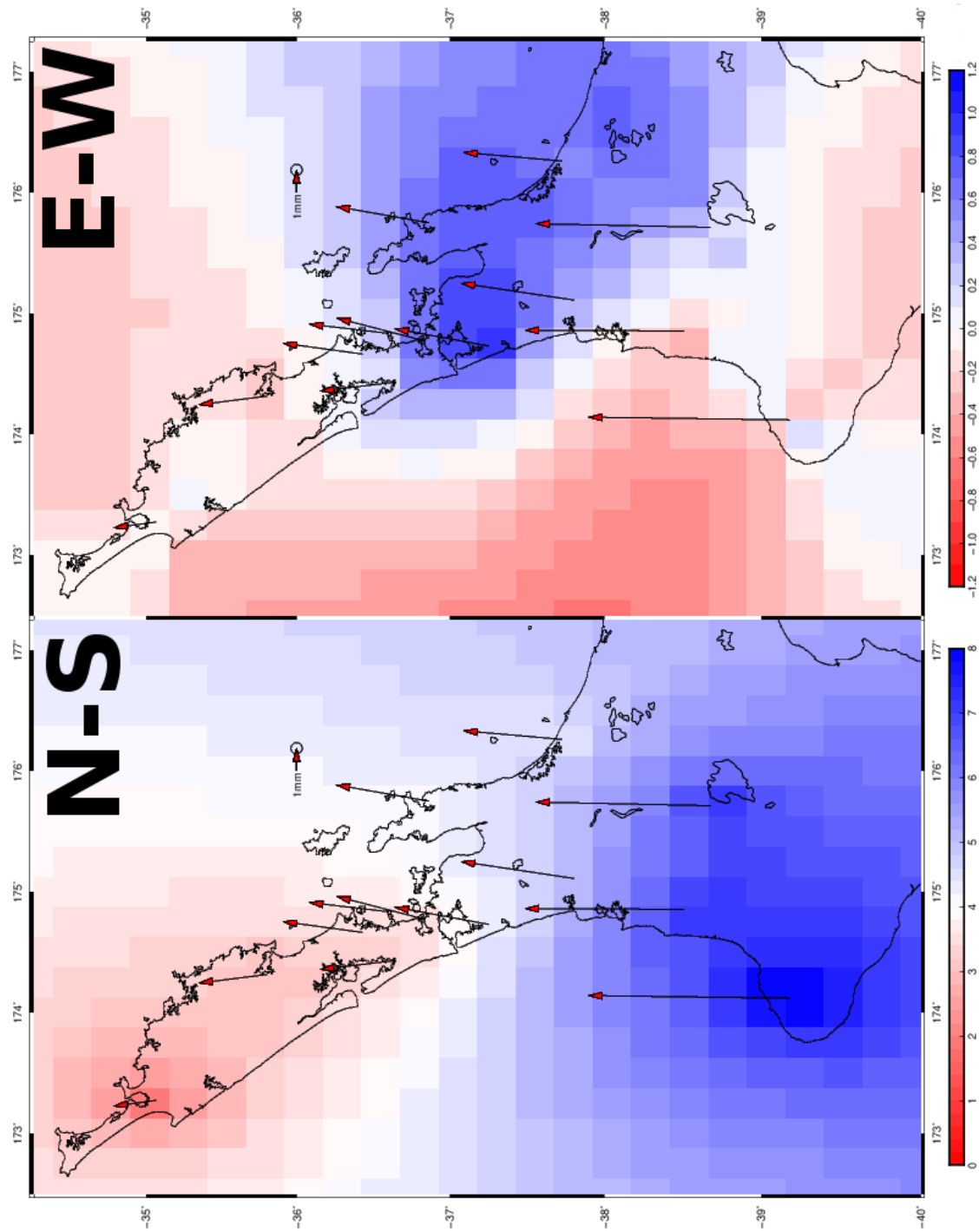


**Figure 4.14:** Coseismic offsets (mm) resulting from the 2016 Kaikōura earthquake, interpolated via the "gpsgridder" code [Haines et al., 2015; Sandwell and Wessel, 2016] with input coseismic vector data overlaid.

#### 4.6 A NEW AUSTRALIAN REFERENCE FRAME

For regional studies, velocities must ultimately be interpreted relative to a nearby fixed region in order to assess their geologic significance. This process can be as simple as defining a single cGNSS station to be fixed (zero velocity) and adjusting nearby velocities relative to it, but for tectonic-scale interpretations where flat earth approximations are invalid this is better accomplished by applying an angular velocity around a geocentric radial vector, or Euler pole. In New Zealand a logical reference frame is the Australian Plate as it is proximal, large, and features many stable cGNSS reference sites.

Euler poles representing most all of the Earth's tectonic plates have been previously derived and published (e.g. ITRF08 [Altamimi et al., 2012] and ITRF14 [Altamimi et al., 2017]), including one for the Australian Plate. These models become more robust over time with the ageing of the cGNSS sites defining them, as well as via the addition or removal of sites comprising them. The ITRF08 Australian Plate model included ~15 sites on continental Australia as well as two in New Caledonia (KOUC, NOUM) and two in New Zealand (AUCK, and TAKL, both near Auckland). Over time and with more data it was speculated by Tregoning et al. (2013) and Beavan et al. (2016) that the cGNSS sites in northern NZ appeared to be relatively fast with respect to this model. The subsequent ITRF14 model removed AUCK but kept TAKL, as well as keeping two New Caledonia sites (NMEA, NRMD), adding sites on Lord Howe Island (LORD) and Norfolk Island (NORF), and doubling the sites on continental Australia making it more robust overall.

Preliminary velocity estimates done in this project showed that the northern North Island was still moving  $\sim 1 \text{ mm/yr}$  fast relative to the ITRF14 Australian Plate. Furthermore, the velocities of New Caledonia and Norfolk Island were also observed to have a similar velocity character, though in the case of New Caledonia the vectors had large uncertainty. Thus the necessity of an alternative Australian Plate reference frame excluding these sites was supposed, as constraining the low rates in NWNZ required as precise and well-constrained a plate definition as possible. To test the sensitivity to the inclusion of cGNSS stations at various locations on the eastern Australian Plate, this project sought to compare four general Australian Plate models (Figure 4.15): One incorporating northern New Zealand (NZ), New Caledonia (NC), and Australia

(AUS) (similar to ITRF08/ITRF14, blue vectors and stars), one incorporating NC and AUS (similar to Beavan et al. 2016, green vectors and stars), one incorporating only AUS (e.g. this project, red vectors and no stars), and finally one incorporating only the eastern Australian Plate (New Caledonia, Norfolk Island, and North Island of NZ west of the Hauraki Rift; gold vectors and stars) to gauge the stability of these sites relative to each other. The data used at these sites typically spanned over 20 years (1995-2018) providing very robust velocity estimates and the resulting Euler pole data is collected in Table 4.4.

**Table 4.4:** Australian Reference Frame Definitions. Sites not on continental Australia are *italicised*.

	Euler Pole LAT LON $\Omega$ (°/Myr)	Cartesian $\Omega$ (°/Myr)	cGNSS Sites Used In Definition
Continental AUS + Lord Howe Island RED Vectors (This Study)	33.05 °N 38.37 °E 0.6280 $\Omega$	0.4129 $\Omega_X$ 0.3269 $\Omega_Y$ 0.3421 $\Omega_Z$	ADE1 ALIC CEDU DARW HOB2 KARR KAT1 KAT2 LORD NNOR STR1 STR2 SYDN TID1 TID2 TIDB TOW2 YAR1 YAR2 YAR3 YARR
+ New Caledonia GREEN Vectors (~Beavan et al., 2016)	32.93 °N 38.15 °E 0.6293 $\Omega$	0.4154 $\Omega_X$ 0.3263 $\Omega_Y$ 0.3421 $\Omega_Z$	+ KOUC NOUM NRMD
+ New Caledonia & Northern NZ BLUE Vectors (~ITRF08, Altamimi et al., 2012)	32.31 °N 38.08 °E 0.6451 $\Omega$	0.4291 $\Omega_X$ 0.3363 $\Omega_Y$ 0.3448 $\Omega_Z$	+ KOUC NOUM NRMD +NORF +KTIA WHNG AUCK
East Australian Periphery GOLD Vectors	32.90 °N 37.00 °E 0.6272 $\Omega$	0.4206 $\Omega_X$ 0.3169 $\Omega_Y$ 0.3407 $\Omega_Z$	KOUC NOUM NRMD NORF KTIA WHNG AUCK

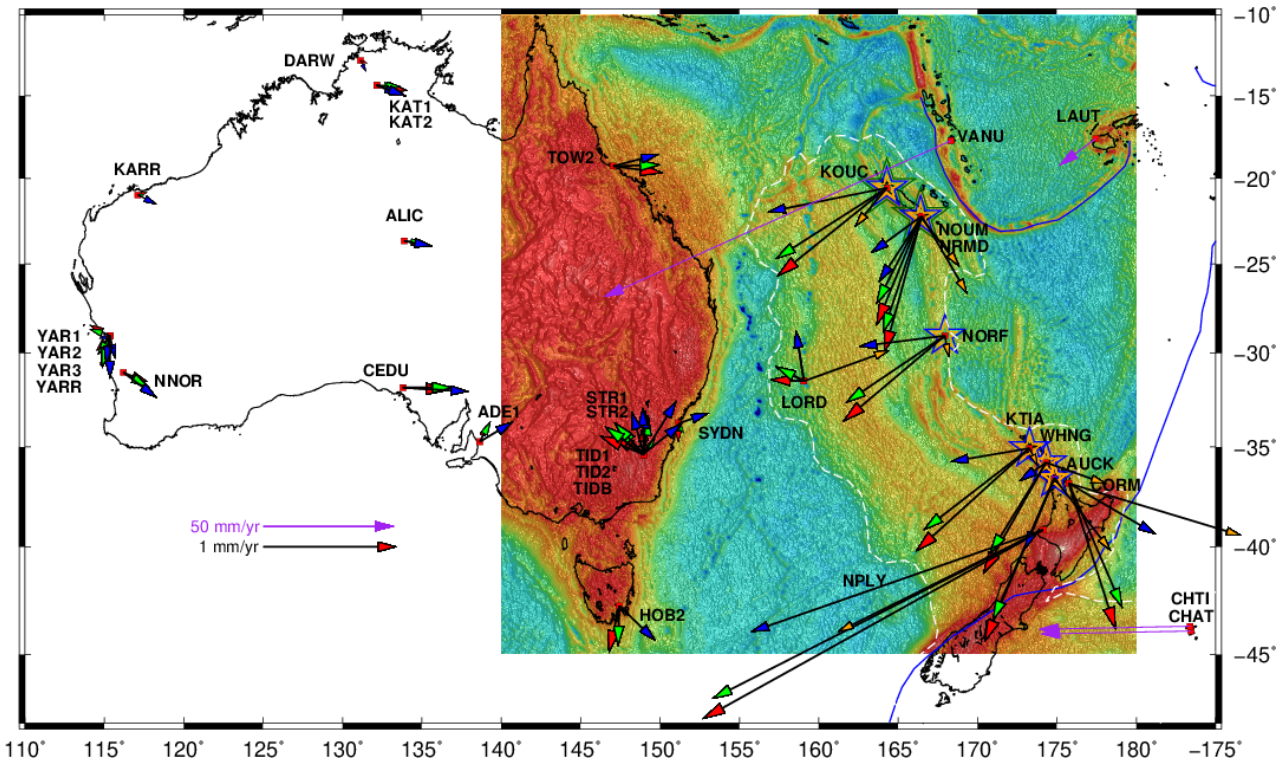


**Figure 4.15:** Velocity residuals relative to various Australian Plate reference frames (see Table 4.4) overlaid with a satellite Bouguer gravity anomaly. Error ellipses have been removed for clarity but were generally small (<0.1 mm/yr) with the exception of those on New Caledonia (0.2-0.6 mm/yr). Vectors with red arrowheads are relative to an Australian Plate model comprised of all cGNSS sites west of and including LORD, green arrowheads also include green-starred sites on New Caledonia (KOUC NOUM NRMD) similar to the model used by Beavan et al. (2016) and blue arrowheads further include blue-starred sites Norfolk Island site NORF and northern New Zealand sites (KTIA WHNG AUCK), similar to the ITRF08 and ITRF14 Australian Plate model [Altamimi et al., 2012; Altamimi et al. 2017] which includes New Caledonia, Norfolk Island, and New Zealand as far south as Auckland. Gold vectors on the eastern portion of the Australian plate are generated from a model derived by eastern periphery sites KOUC NOUM NRMD NORF KTIA WHNG and AUCK, all with gold stars. The continent of Zealandia [Mortimer et al., 2017] is outlined by a dashed white line and cGNSS sites on the Pacific Plate (VANU, LAUT, CHTI/CHAT, purple vectors) are drawn relative to our preferred Australian Plate model (red vectors) at 50x scale.

The AUS model (Figure 4.15, red vectors) used in this project has marginally smaller velocity residuals at all sites except HOB2, and those on the eastern plate east of Lord Howe Island/LORD. Therefore the AUS model which incorporates only continental Australia as well as Lord Howe Island appears to be the best-performing Australian Plate reference frame model. It is however noted that the resulting difference between the AUS and AUS+NC (green vectors) models is essentially negligible with velocity residuals typically within error, and therefore there is probably little harm in including New Caledonia in an Australian Plate definition. The AUS+NC+NZ model shown by the blue vectors gradually produces higher velocity residuals towards the east and quickly begins to disagree with both AUS and AUS+NC models east of

continental Australia. Furthermore the fact that these vectors on the eastern Australian Plate remain elevated relative to the AUS+NC+NZ model (blue vectors) should demonstrate that they are inappropriate additions when presuming a rigid Australian Plate reference frame.

The group of sites with similar SW velocity residuals at the eastern end of the Australian Plate at sites on Norfolk Island (NORF) and NC (NOUM, NRMD, KOUC) may further portend to the existence of some form of tectonic discontinuity separating the eastern Australian tectonic plate. Unfortunately their spatial distribution makes an Euler pole definition for these sites difficult to constrain. Nonetheless one was attempted and is listed in Table 4.4.

A statistical review of the anomalous eastern Australian Plate cGNSS sites is shown in Figure 4.16. These histograms show the data around the linear residual velocity fit are distributed normally and are tightly (0.01 - 0.12 mm) concentrated which indicates that these vectors are accurately drawn.

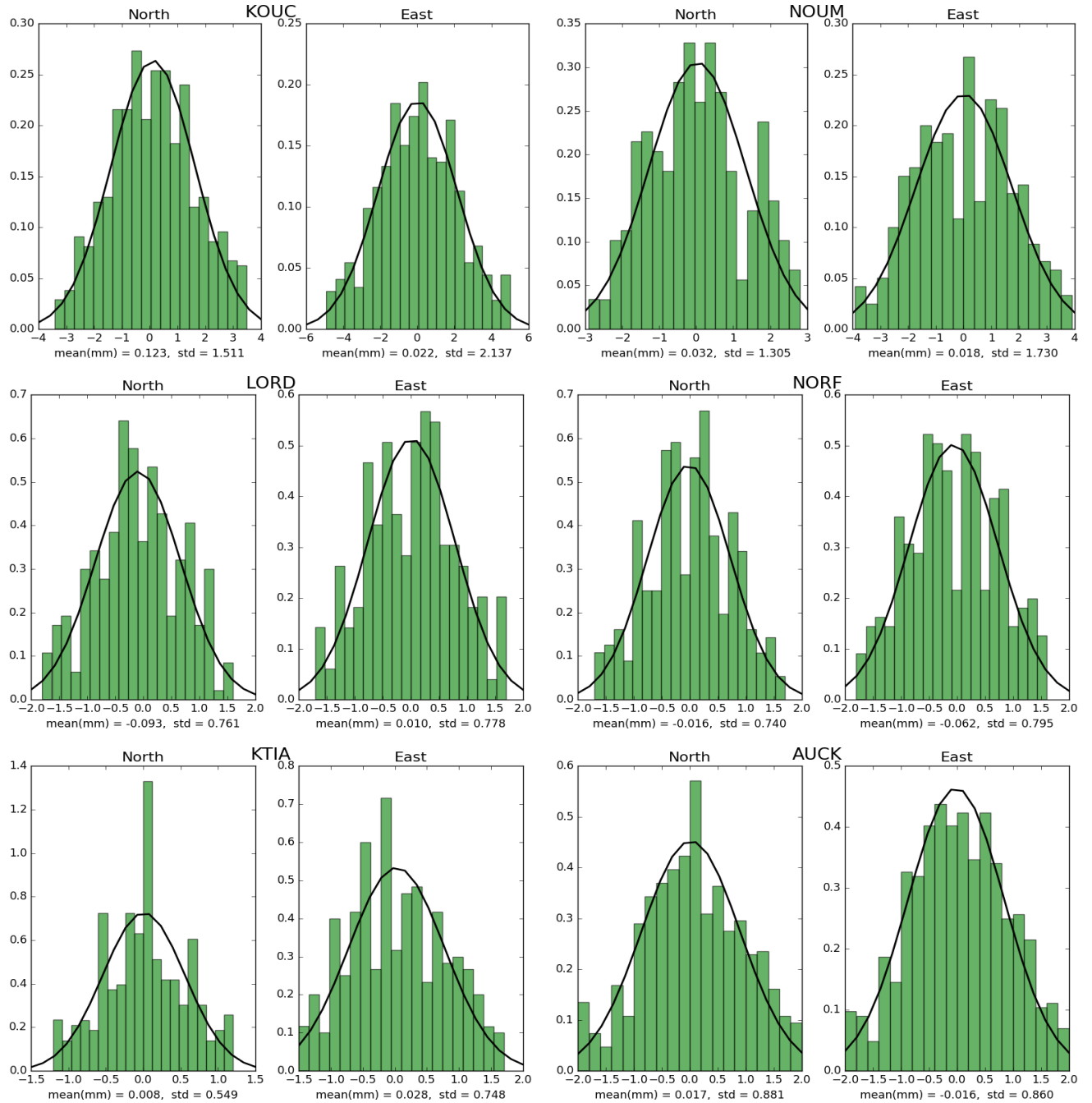


**Figure 4.16:** Distribution statistics for the key sites in Figure 4.15 relative to a residual linear velocity. Outliers greater than  $3\sigma$  have been removed and the equivalent Gaussian distribution for each dataset is plotted in black. The minimum timespan used to calculate the velocities is 9 years and sites NORF and LORD have experienced no antenna changes or coseismic offsets which may have required a discontinuity in their timeseries. All units are in mm except y-axis which is probability density.

#### 4.7 VELOCITY ESTIMATES

The final velocity model spanned from January 1 1995 to May 4 2018 and incorporated 1050 sites or renamed sites. The total change in  $\chi^2$  after applying 647 velocity equates was 0.98 and the total solution change in  $\chi^2$  was 0.99. In short, the model was solved as precisely as possible without being over-constrained despite its 22+ year duration and high degree of complexity. All velocities are shown with  $1\sigma$  error ellipses relative to the custom Australian reference frame described in Section 4.6 which notably does not include sites on New Zealand, or New Caledonia.

Much of the new campaign data collected 2015-2017 was unable to produce reliable velocity vectors, which in this project typically meant velocity errors less than  $0.4 \text{ mm/yr}$ . The reasons for this are three-fold. First, the precision of the 2016 Kaikōura coseismic offsets necessary to correct for the 2017 survey was inadequate to resolve velocities at the sub-millimetre scale. Second, is that this project likely overestimated the magnitude of time-dependent random walk noise implemented within the greater Auckland region in an effort to produce robust and conservative estimates which could then be used to infer active faulting with confidence. Third and finally, it is concluded that the combined degree of uncertainty in the GNSS system (e.g. random or time-dependent clock/satellite noise), local geology (e.g. local soil loading and weather effects), and station error (imprecise antenna mounting and monument instability) place a three year campaign survey on the cusp of resolvability for sub-millimetre analysis.

The resulting geodetic velocity estimates for this project are shown in Figure 4.17. Active faults [Langridge et al., 2016] and mapped faults not proven active [Edbrooke et al., 2005; Edbrooke and Brook, 2009; Kenny et al., 2012; Lee et al., 2008; Leonard et al., 2010] are shown in red and gold, in addition to a general trace of the offshore Taranaki Fault which is drawn in toothed gold [Stagpoole and Nicol, 2008; Uruski, 2014]. The general N-NW strike of the basement structure is outlined by the Junction Magnetic Anomaly [Coombs et al., 1976; Eccles et al., 2005].

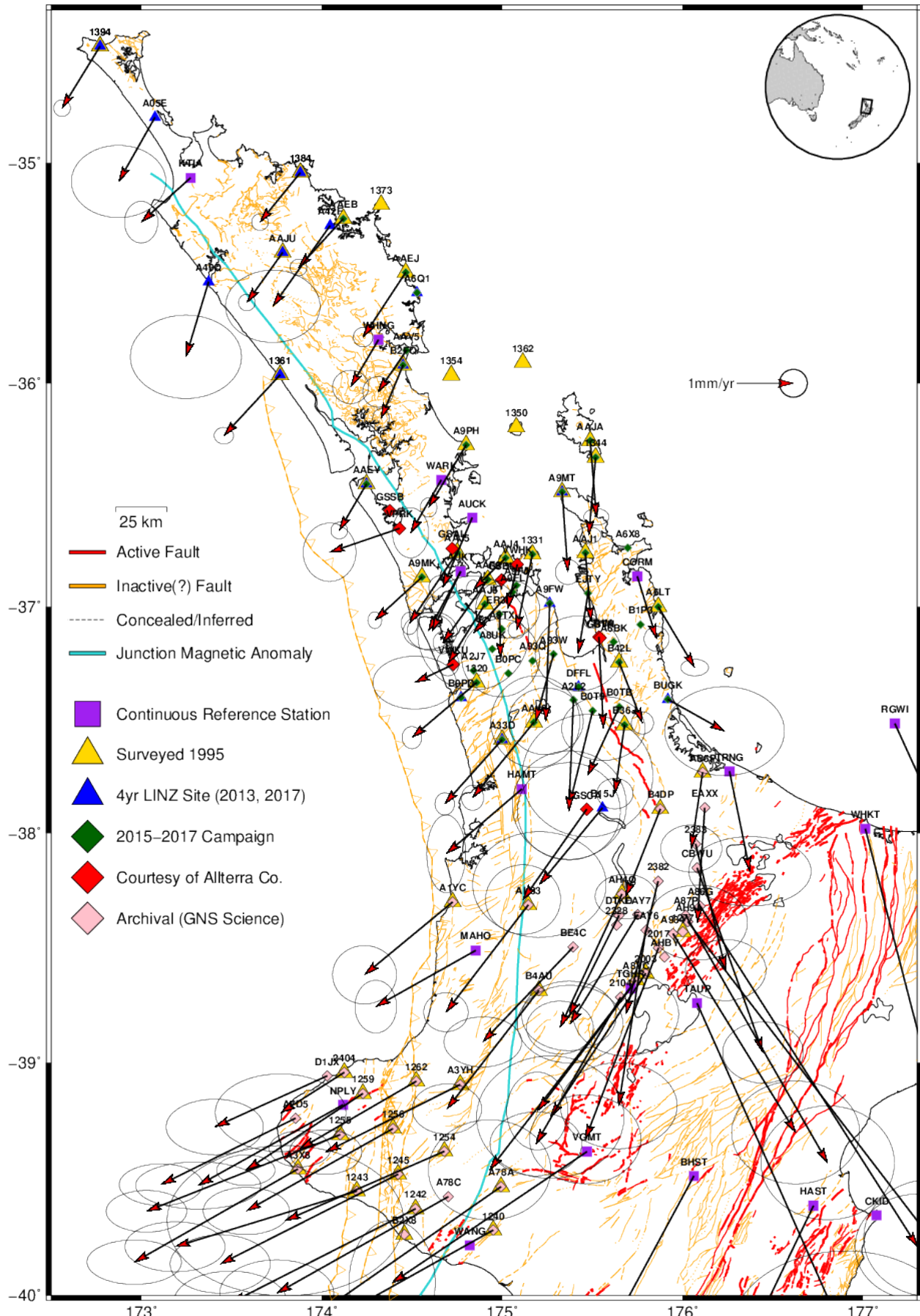


**Figure 4.17:** Geodetic velocity estimates throughout NWNZ 1995–2018. Icons are plotted for all sites in this project, but outlier velocity vectors are not.

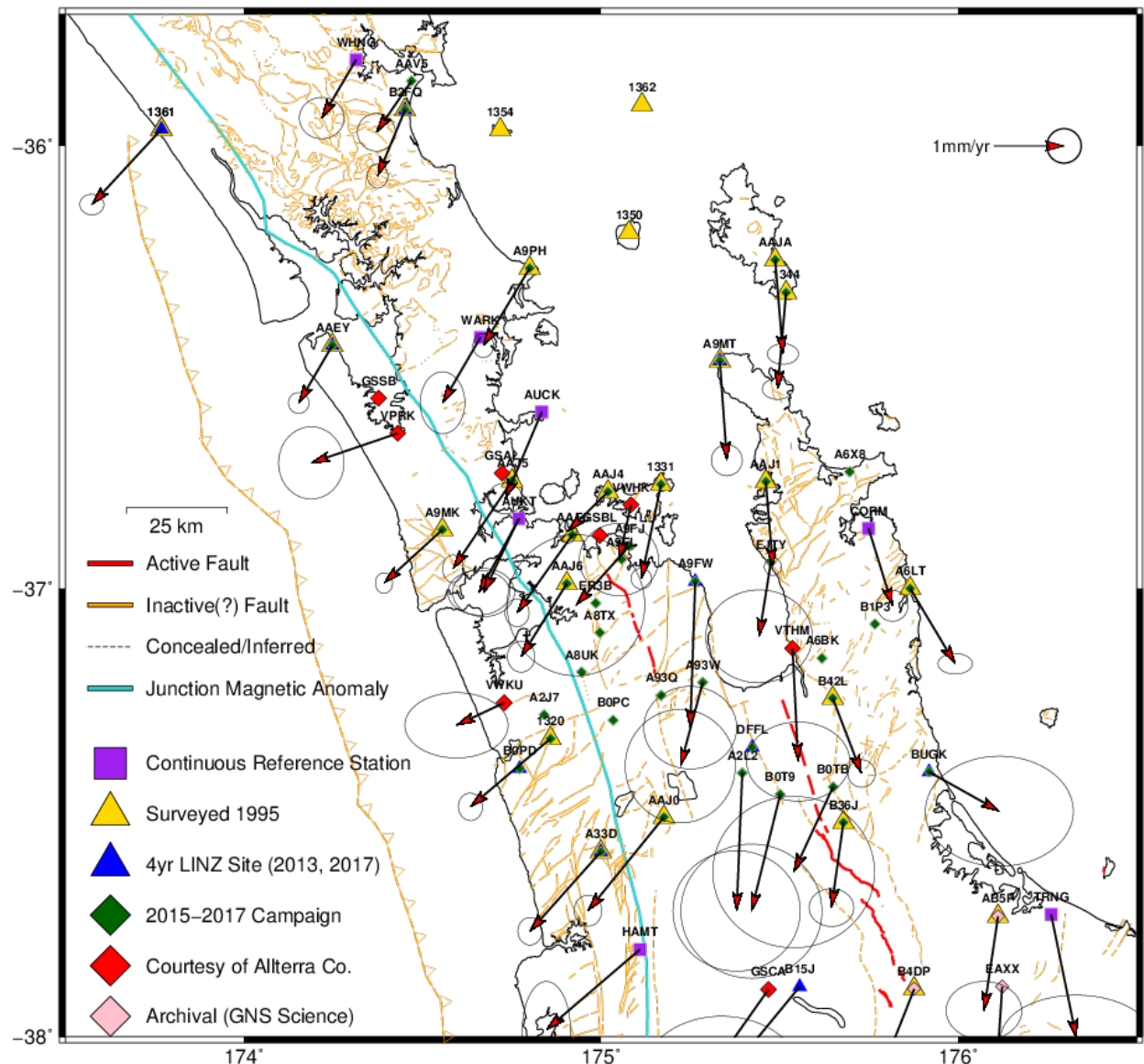


Figure 4.18: Auckland area GNSS velocity vectors.

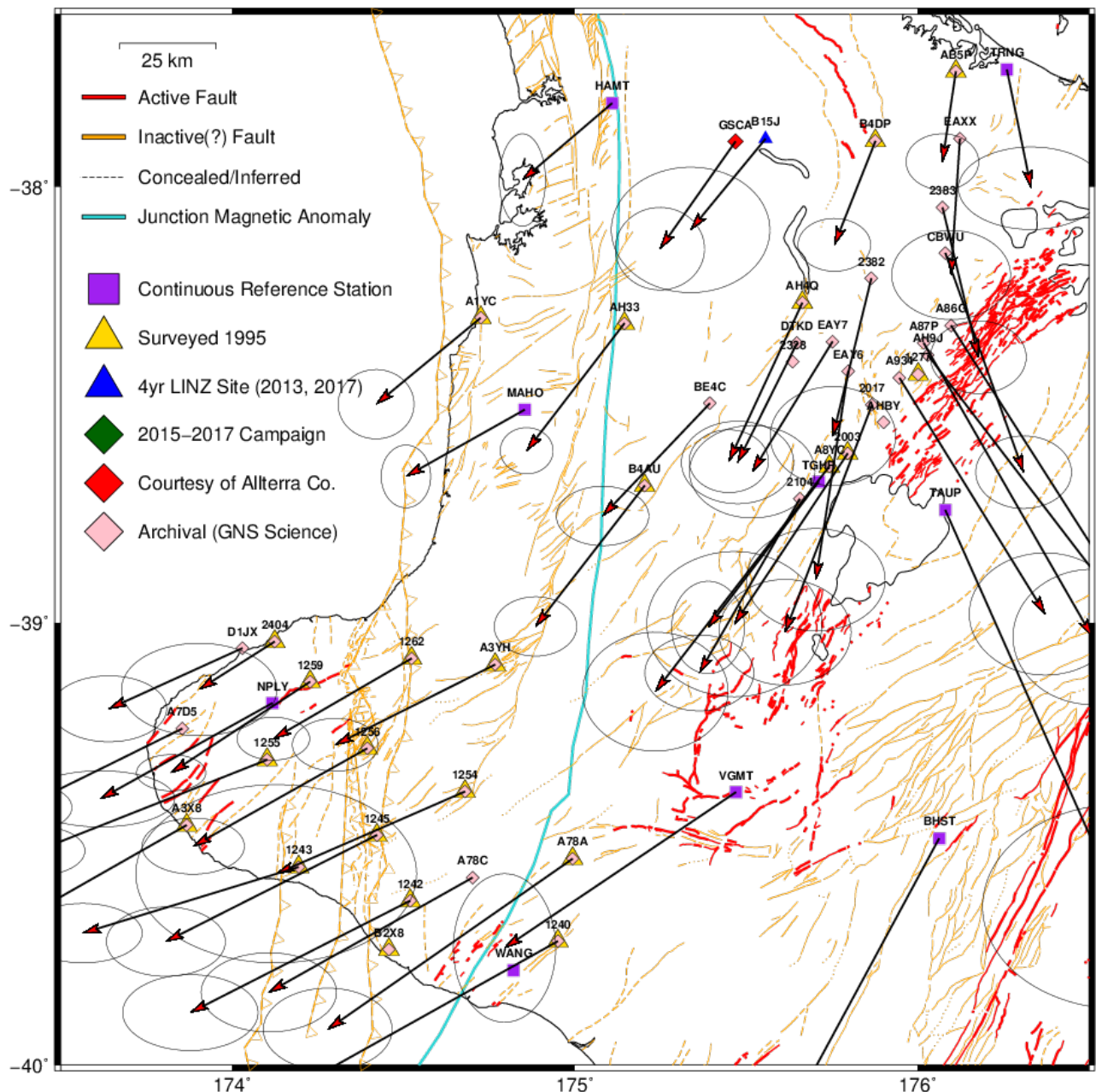
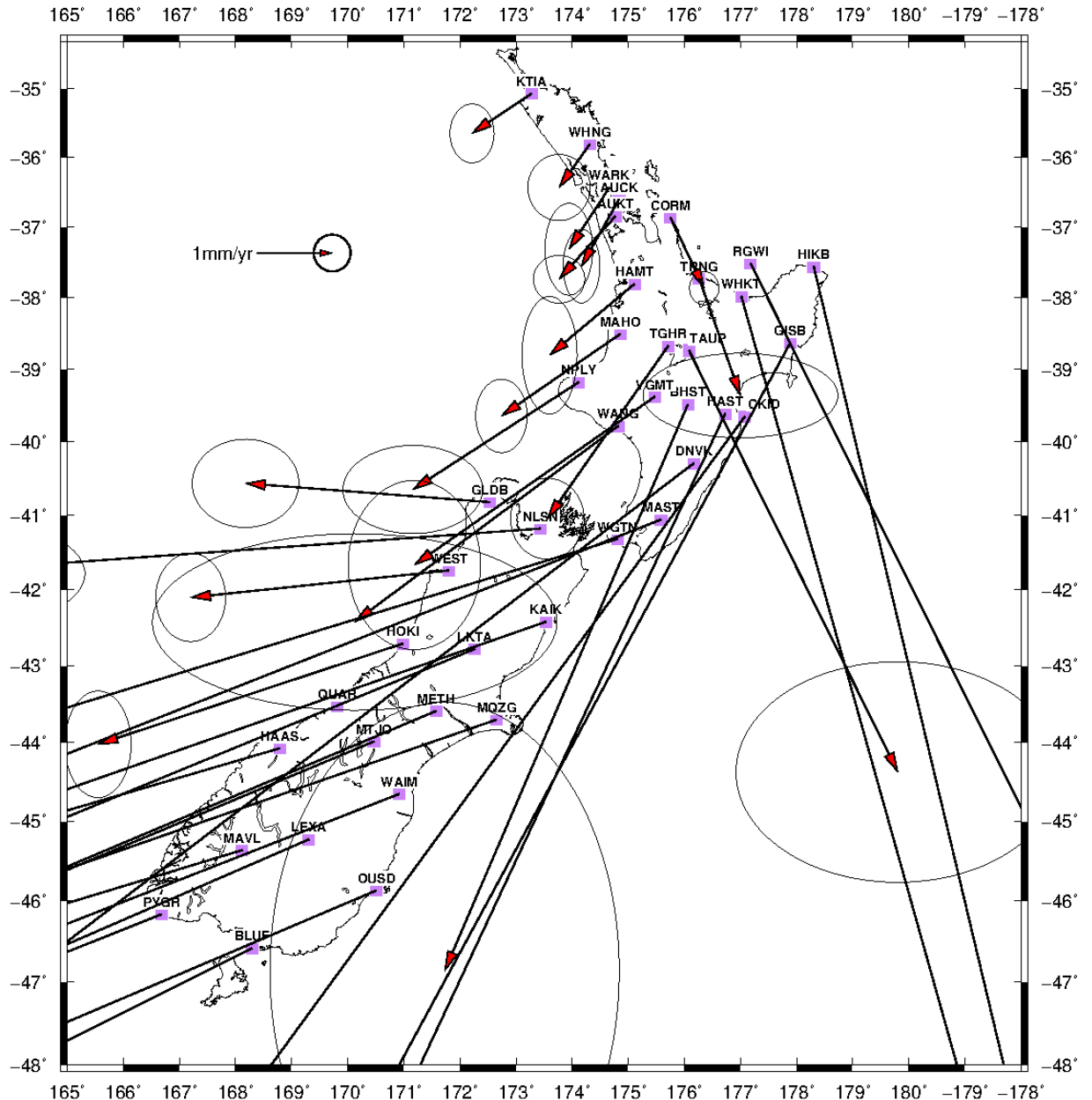


Figure 4.19: Western North Island GNSS velocity vectors.



**Figure 4.20:** Nationwide geodetic velocities of some older cGNSS sites.

#### 4.8 STRAIN RATE ESTIMATES

Whereas the velocity estimates in section 4.7 describe the absolute motion (e.g.  $m/s$ ) of a mark relative to a fixed Australian reference frame (section 4.6), it can also be useful to use velocities to interpret the local deformation of the crust relative to some initial state. This can be achieved by deriving a "strain rate" which is effectively the partial derivative of a velocity along its axis of

motion, in one dimension described mathematically as  $\dot{\varepsilon}_x = \delta u / \delta x$  where  $u$  is the  $x$ -component of a velocity. As strain is dimensionless, strain rates have units of  $1/s$ .

Strain rates in higher dimensions become more complex to interpret. In 2D, strain rates in both the longitudinal E-W  $x$  axis and latitudinal N-S  $y$  axis can be calculated relative to both longitudinal ( $x$ ) velocities  $u$  and latitudinal ( $y$ ) velocities  $v$ . Traditionally a dilational strain rate and rotational strain rate can be derived by:

$$\text{dilational strain rate } \dot{\sigma} = \frac{1}{2} \left( \frac{\partial u}{\partial x} + \frac{\partial v}{\partial y} \right)$$

$$\text{rotational strain rate } \dot{\omega} = \frac{1}{2} \left( \frac{\partial u}{\partial y} - \frac{\partial v}{\partial x} \right)$$

These values make intuitive sense with dilation occurring with velocities changing along their axis, and rotation perpendicular. To interpret strain rates which consist of a combination of either, this work follows Frank's method (1966) which derives two unique properties of shear strain rates,  $\dot{\gamma}_1 = \frac{\partial u}{\partial x} - \frac{\partial v}{\partial y}$  and  $\dot{\gamma}_2 = \frac{\partial u}{\partial y} + \frac{\partial v}{\partial x}$ , where the maximum shear strain rate can then be given by  $\dot{\Gamma} = \sqrt{\dot{\gamma}_1^2 + \dot{\gamma}_2^2}$ . This maximum shear strain can be used to highlight peak activity in the crust and has been proven effective in NZ, even for older point-to-point survey triangulations [e.g. Walcott, 1984].

Continuous surfaces for velocities the east component  $u$  and north component  $v$  (Figure 4.21) were derived via the GMT "gpsgridd" code [Haines et al., 2015; Sandwell and Wessel, 2016] from this project's velocity estimates with outlier vectors removed. A Poisson's ratio of 0.265 was assumed [Christensen, 1996] and the resulting mean ( $N=168$ ) misfit for both  $u$  and  $v$  velocity surfaces was  $0.9 \text{ mm}/\text{yr}$ , primarily due to the larger N-S velocities in the southern segment. The Poisson's ratio was also adjusted to be as high as 0.5 [e.g. Sandwell and Wessel, 2016] but this did not have a significant affect on the resulting velocity surface relative to the large degree of uncertainty already intrinsic to the input velocity data. Velocity data beyond the edge of these maps was incorporated to minimise edge effects and better depict the region's true velocity regime.

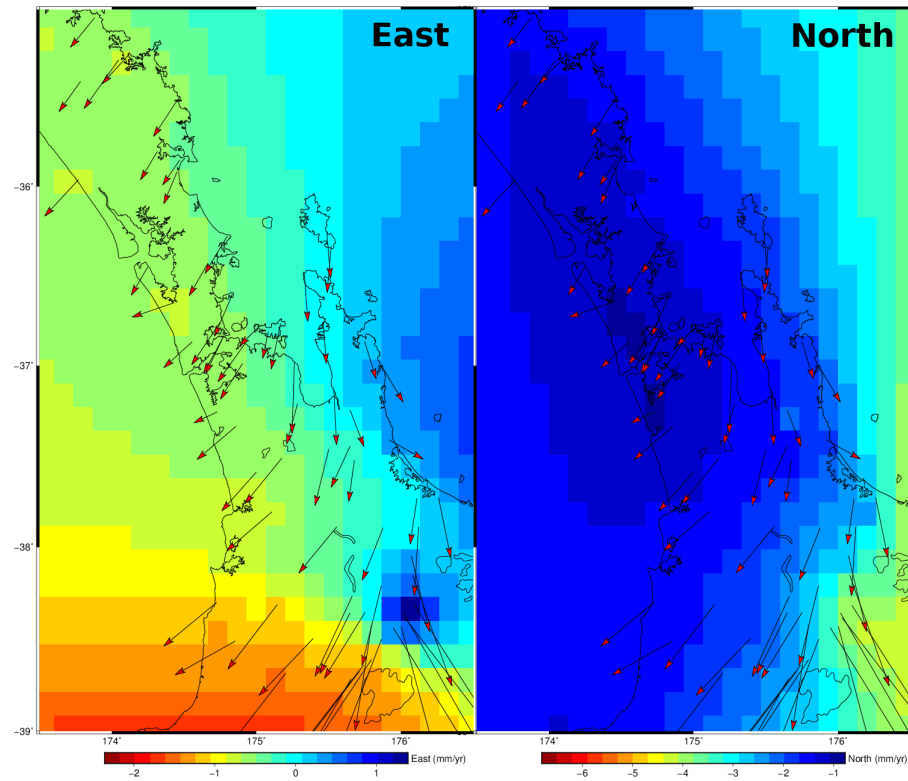


**Figure 4.21:** Interpolated east and north velocities ( $\text{mm/yr}$ ) for a subset of higher-quality GNSS velocity estimates.

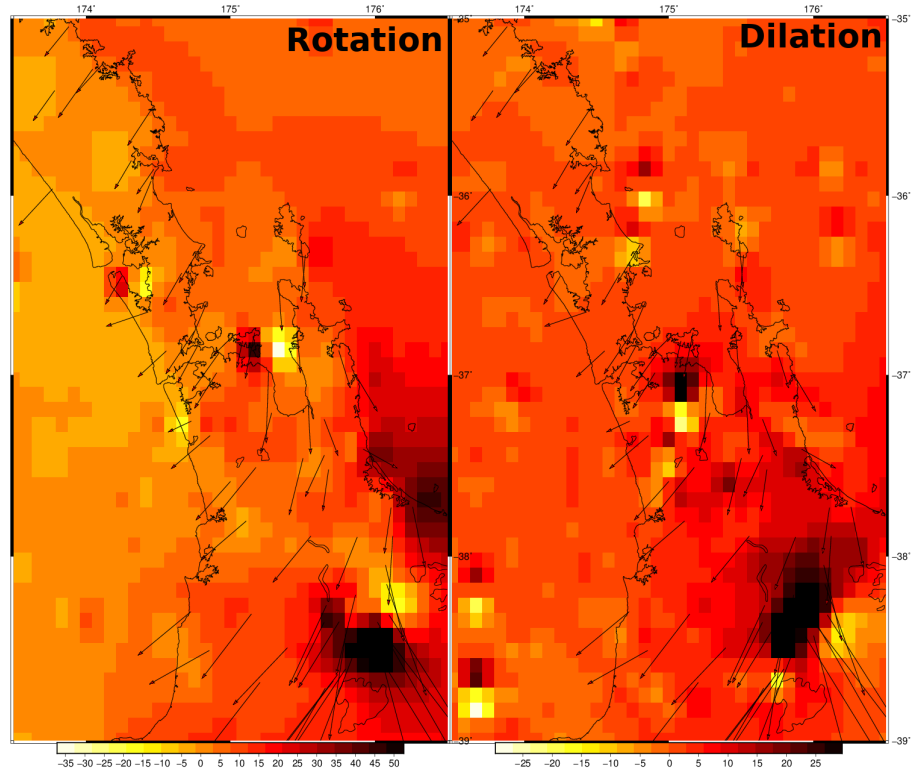


**Figure 4.22:** Rotational  $\dot{\omega}$  and dilational  $\dot{\sigma}$  strain rates ( $\text{nanostrain/yr}$ ) derived from the velocity field in Figure 4.21.

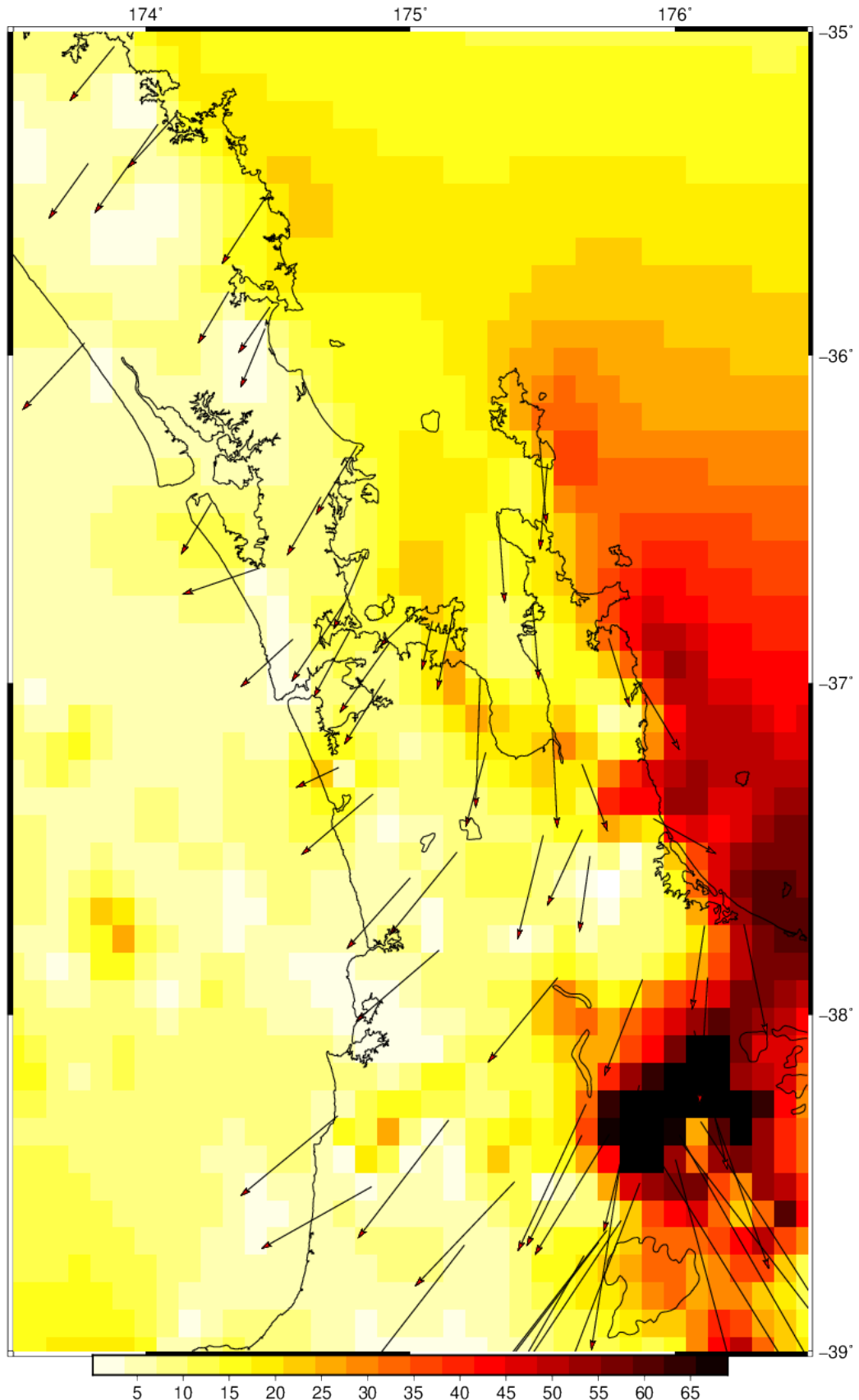


**Figure 4.23:** Maximum shear strain rate  $\dot{\Gamma}$  (nanostrain/yr) derived from the velocity field in Figure 4.21. While activity at the southern end of the Hauraki Rift and TVZ dominates, a large amount of stress between the Coromandel and the eastern North Island (east of the map) creates elevated strain rates throughout the Bay of Plenty and may continue to manifest itself north of 36°S.

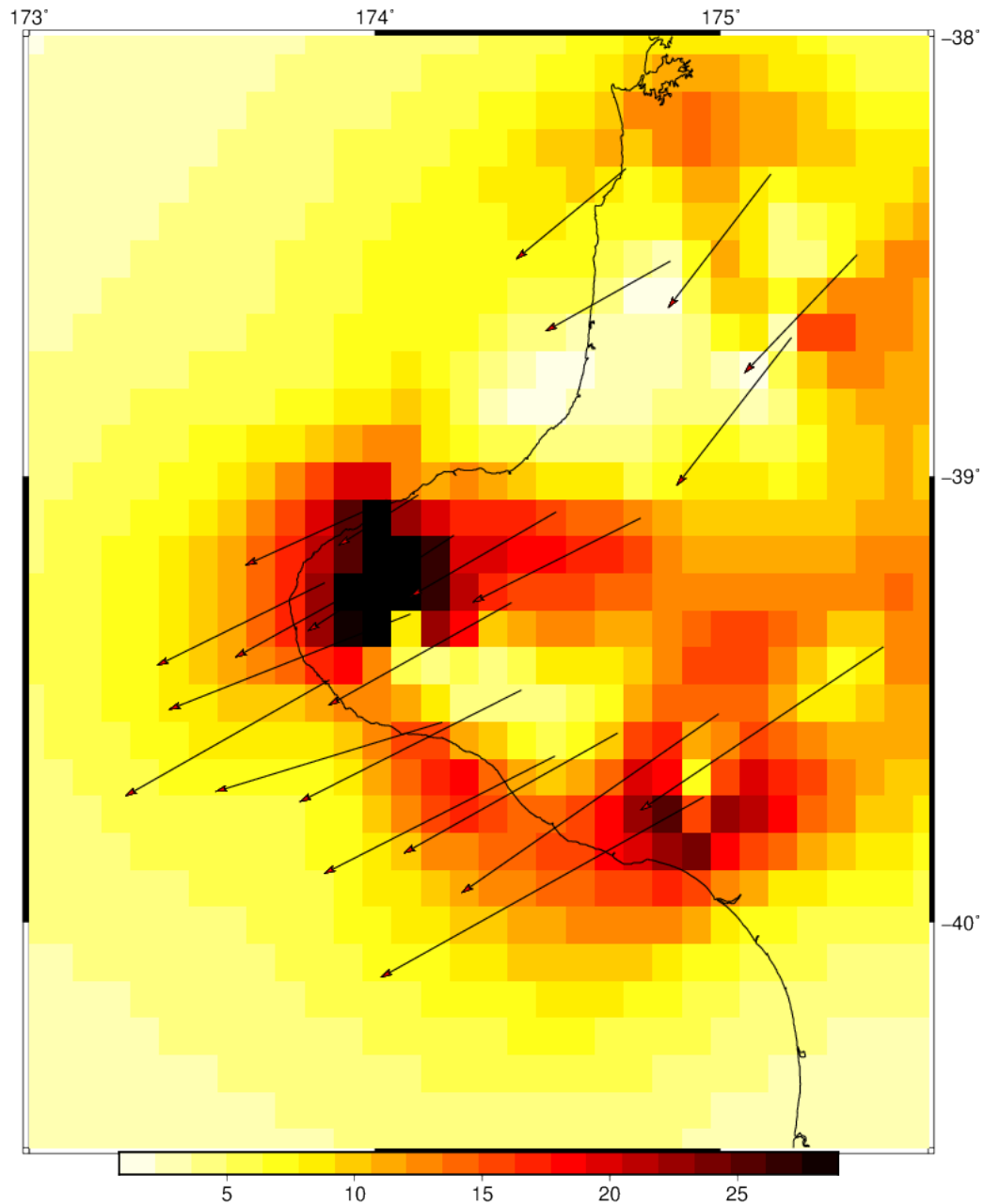


**Figure 4.24:** Maximum shear strain rate  $\dot{\Gamma}$  (nanostrain/yr) at the Taranaki Peninsula. The northern high-strain rate region corresponds to the active Cape Egmont Fault System.



## SEISMICITY OF NORTH-WESTERN NEW ZEALAND

---

Seismicity is a valuable tool to gain a 3D view of active motion within the earth, which in turn demarcates the location of faults, subducting slabs, or other features regularly and abruptly relieving stress. A reliable interpretation of activity is dependent on the accuracy of the located earthquake hypocentres as well as the volume of events found. Thus the goal of the seismic analysis in this work is not only to locate events with high precision, but to locate enough of them to support the interpretation of active structures. For much of north-western New Zealand (NWNZ) this is a difficult problem due to the lack of both seismic stations and the low rate of crustal deformation, likely analysis of event data spanning decades to derive a complete interpretation of activity.

### 5.1 NEW ZEALAND EARTHQUAKE MONITORING AND ARCHIVING: GEONET

New Zealand's nationwide seismic network is maintained by GeoNet ([geonet.org.nz](http://geonet.org.nz)), a government and NZ Earthquake Commission (EQC) funded entity who have a public good mandate for hazard monitoring and management. They are responsible both for the planning, installation, and maintenance of the stations as well as storing and sharing the raw data, interpreting it, ultimately publishing earthquake information in real time to both the scientific community as well as the general public.

GeoNet's goal for event location is an automatic framework to detect nationwide earthquakes  $M > 3$  with larger or interesting events typically being reviewed and supplemented by an analyst [Jerome Salichon, GeoNet, personal comm., 2017]. Accordingly the distribution of seismic stations and tolerance of software parameters is designed to meet this goal, with the microseismicity (e.g.  $M < 3$ ) throughout the northern North Island not explicitly targeted and thus potentially missing.

## 5.2 EARTHQUAKE LOCATION METHOD

There are many methods and tools to derive the location of an earthquake's hypocentre from data recorded amongst a network of seismic stations. This project chose to use the SeisComP3 software suite [Weber et al., 2007]. At its essence SeisComP3 is a front-end for the NonLinLoc code [Wittlinger, 1993; Lomax et al., 2000] which is a direct-search algorithm using predicted travel times through a known velocity model given "picked" seismic phase arrival time estimates. It takes a collection of phase arrival picks across several stations and inverts them to determine an event hypocentre, iteratively searching through an increasingly refined gridded 3D mesh describing a pre-defined velocity structure to find the most probable solution.

A relatively newer alternative to conventional "pick-based" methods such as NonLinLoc are "waveform-based" methods [e.g. Kao and Shan, 2004] in which seismic waveform data is stacked and/or cross-correlated to detect the probable occurrence of events by noting amplified coherence across various stations. These methods have the distinct advantage of not requiring phase arrival estimates, and have been shown to be as effective or better [Grigoli et al., 2018] at detecting microseismicity. However these methods can be highly dependent on both the quality of the velocity model used as well as the robustness of the seismic station network [e.g. Grigoli et al., 2016; Grigoli et al., 2018]. As both of these qualities are somewhat suspect in the northern North Island it was unclear if adopting these relatively complicated new methods would be beneficial. Furthermore by straying from a pick-based detection regime it would be difficult or impossible to review and relocate historic catalogue event data from GeoNet (who also use SeisComP3) which was a goal of this project. Also the fact that the state of the art NZ3DRX 3D New Zealand velocity model [Eberhart-Phillips et al., 2010] had already been configured and optimised for use with NonLinLoc would greatly reduce the potential workload in implementing the model independently. It was thus assumed that the most efficient and sensible way to resolve the seismic activity of northern North Island was to begin with GeoNet's SeisComP3/NonLinLoc default parameters and recalibrate them specifically towards finding small and shallow events within the northern North Island.

### 5.2.1 New Zealand Velocity Models

To locate an earthquake's epicentre a velocity structure for the propagation of energy must be calculated or assumed. In New Zealand a velocity structure describing the entire country initially began as a one dimensional P-wave and S-wave velocity model [Adams, 1963; Vere-Jones and Davies, 1966], taken from the Jeffreys-Bullen Tables (British Association for the Advancement of Science, 1958). This model was later refined to a discretised 1D model "NZ1DR" in which various regions (e.g. Taupō and Wellington) had customised velocity structures [Adams and Ware, 1997]. At depths below the crust (e.g. 30-50 km), NZ1DR was kept according to the Jeffreys-Bullen Tables and then later adapted to the IASP91 earth model [Kennett and Engdahl, 1991]. GeoNet used the NZ1DR model to locate earthquake hypocentres from 1986 to 2012 by applying the GROPE evaluation method, a weighted least squares inversion technique developed by the joint Caltech and USGS seismic processing system "CUSP" [Johnson and Stewart, 1986].

In 2010, a New Zealand-wide 3D velocity model NZ3DRX was published by Eberhart-Phillips et al. (2010). This model was derived by joining several regional 3D velocity models and iteratively correcting them by inverting 15 years of earthquake data. As the earth's crust is heterogeneous both vertically and laterally the motivation of creating a 3D model is immediately clear, and they showed that events relocated from 1D to their new 3D produced a clearer interpretation of active tectonic structure. Accordingly, GeoNet began implementing NZ3DRX in their published earthquake data beginning on Jan 1 2012 and continue as of this writing. This is also the model used in this work as it remains the latest New Zealand velocity model available.

### 5.2.2 Event Detection and Wave Picking

The detection effort begins in SeisComP3 by applying a bandpass filter (e.g. Butterworth) to the raw waveform data to increase the P-wave arrival signal relative to the background noise. GeoNet use a band of 2-15 Hz [e.g. Turino et al., 2009]. As seismic energy arrives at a station, it is automatically "detected" on this filtered waveform by using the traditional Short Term Average (STA) over Long Term Average (LTA) (e.g. STA/LTA) approach [Allen, 1982] which analyses a running calculation of the waveform amplitude over a "short term" time window

(s) relative to the average over a “long term”. When this ratio reaches a set “trigger on” value a detection is declared and the algorithm will not log another detection until this ratio falls below a specified lower “trigger off” value (e.g. Figure 5.1). The length of the STA and LTA values themselves are generally chosen according to the type of activity one is hoping to detect, with the STA length being sensitive to the arrival frequency of an earthquake and the LTA reflecting the length of the event as a whole in addition to the signal to noise ratio (SNR) expected across the study region. Low STA values will better capture high frequency and local, impulsive P-wave arrivals and high STA values are better suited to detect dispersed, emergent, and lower frequency teleseismic arrivals. Conversely, low LTA values are better at parsing large magnitude and long-lasting events whereas high LTA values are more suited towards short duration and small events [Trnkoczy, 1999; Trnkoczy and Bormann, 2002]. To reduce the volume of false detections, a “trigger on” threshold can also be determined in that best suits both the STA and LTA parameters speculated upon. GeoNet uses STA and LTA values of 0.5 and 20 s, with a trigger on and off value of 3.5 and 1.5 respectively [Jerome Salichon, GeoNet, personal comm., 2017]. These values are congruent with those typically used in local studies [Sleeman and van Eck, 1999; Trnkoczy and Bormann, 2002].

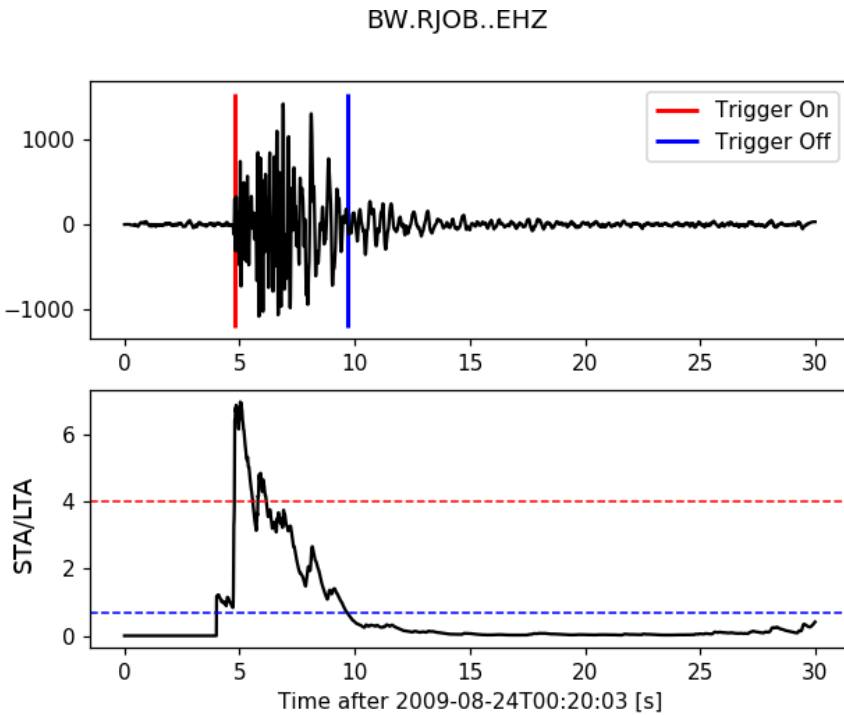


**Figure 5.1:** Example waveform (top) with a corresponding STA/LTA ratio (bottom). A detection is “triggered on” at the red line when the STA/LTA surpasses 4 and remains engaged until dropping below the “trigger off” value of 0.75. Figure is courtesy of the ObsPy documentation ([www.obspy.org](http://www.obspy.org)).

The window of data around a filtered detection is then optionally re-filtered and sent to a Akaike Information Criterion (AIC) picker [Akaike, 1974; Kitagawa and Akaike, 1978; Maeda, 1985; Zhang et al., 2003]. The AIC P-wave picker is well-established and can usually determine the true onset arrival time regardless of the quality of the STA/LTA detection provided that the window contains the true arrival time and an adequate amount of pre-arrival and post-arrival data [Sleeman and van Eck, 1999; Trnkoczy and Bormann, 2002; Zhang et al., 2003]. GeoNet's windowing and filtering values follow that of Turino et al. (2009) with an AIC picker "signal" window beginning 20 s before the STA/LTA detection and ending 8 s after it. A "noise" window beginning 40 s before the detection and ending 20 s before the detection is also calculated to determine an signal-to-noise ratio (SNR) for the event. This large, 20 s signal window relative to the STA/LTA detection ensures that a detection missing the P-wave but instead triggering on the later S-wave arrival will likely still encompass the P-wave arrival and thus theoretically still be able to detect it. This assumption a valid for shallow regional events originating within ~100 km which have an S-P wave moveout times under 20 s.

Once a collection of P-wave arrival picks have been found they are grouped based on temporal and spatial proximity between stations. If enough are found to be related they are sent to a preliminary 1-D locator LOCSAT [Bratt and Nagy, 1991] which uses the 1D IASP91 velocity model [Kennett and Engdahl, 1991] to quickly find a hypocentre. For GeoNet prior to 2012, this solution was final. Since 2012, this solution is refined further using the probabilistic grid-search NonLinLoc 3D locator [Wittlinger, 1993; Lomax et al., 2000] and the NZ3DRX velocity model [Eberhart-Phillips et al., 2010]) for both GeoNet and this project.

Figures 5.2 and 5.3 show earthquakes shallower than 50 km found by GeoNet between 2006-2011 using the 1D locator and between 2012-2017 using the 3D locator, respectively. As the size of the NZ seismic network doubled from roughly 80 stations to over 160 the amount of detected events correspondingly doubled from roughly 18,000 between 2006-2011 to 35,000 between 2012-2017, although the amount varied greatly year by year with an especially large amount occurring after the 2016 Kaikōura earthquake (Figure 5.4).

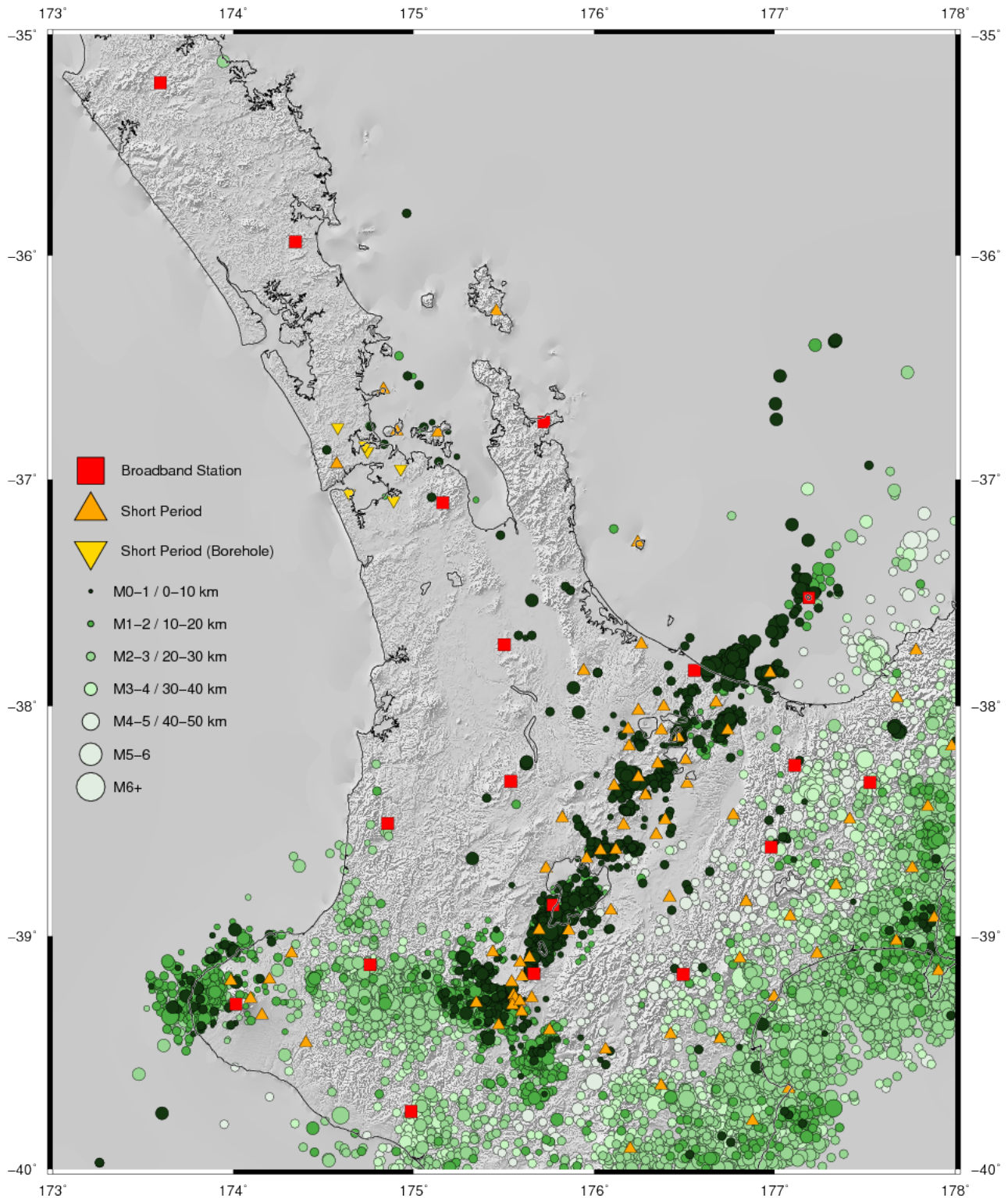


**Figure 5.2:** GeoNet Catalogue events Jan 1 2006 - Dec 31 2011 using the 1D NZ1DR velocity model [Adams and Ware, 1997] and the GROPE locator [Johnson and Stewart, 1986]. Stations plotted existed any time between 2006-2011. 18285 events shallower than 50 km were found within the displayed region.

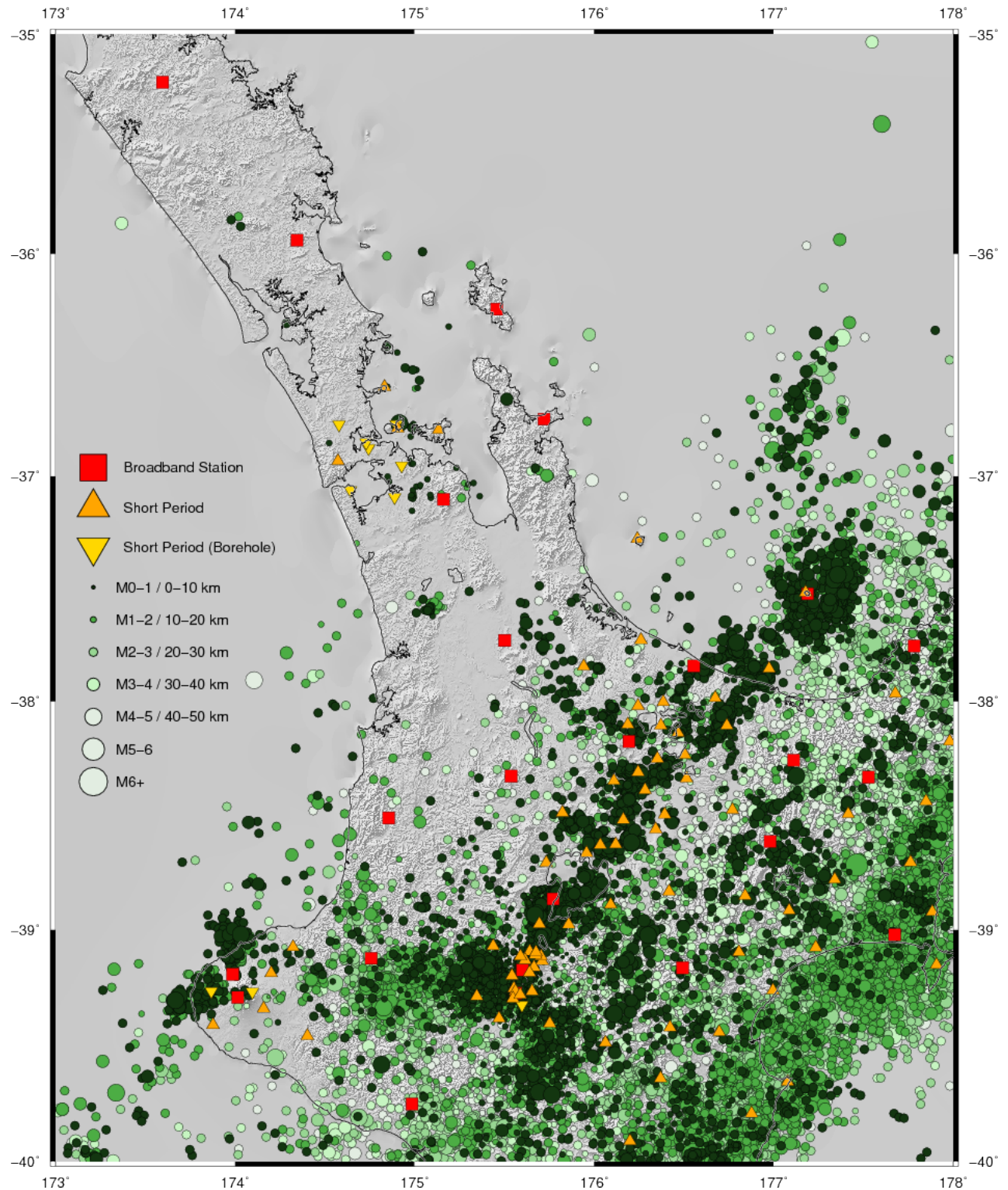


**Figure 5.3:** GeoNet Catalogue events Jan 1 2012 - Dec 31 2017 using the 3D NZ3DX velocity model [Eberhart-Phillips et al., 2010] and the NonLinLoc locator [Wittlinger, 1993; Lomax et al., 2000]. Stations plotted existed any time between 2012–2017. 35343 events shallower than 50 km were found within the displayed region. The increase in found events relative to 2006–2011 (Figure 5.2) is likely due to the increase in seismic stations.

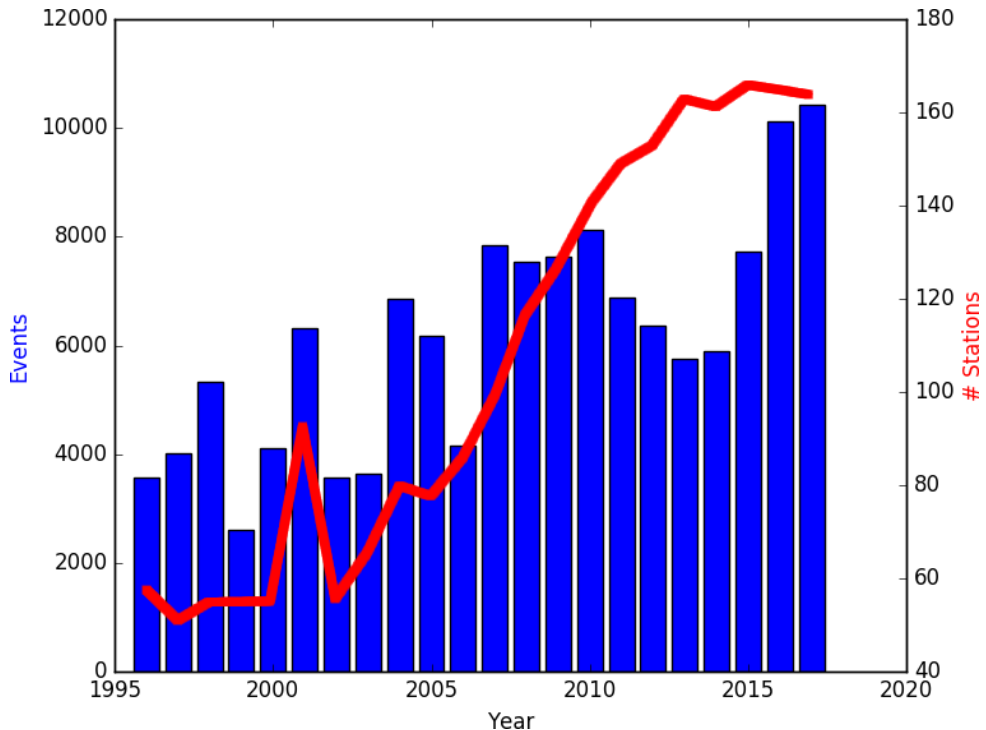


**Figure 5.4:** Events detected by GeoNet within the bounds of Figure 5.3 or 5.2 for each year 1996–2017. Though there is a general correlation, the amount of events (blue bars) varies with the amount of network stations (red line) dramatically from year to year. The 2016 Kaikōura earthquake in particular has generated thousands of excess aftershocks throughout New Zealand in 2016 and 2017.

To calculate earthquake magnitudes, GeoNet uses a combination of MLv, or the local magnitude ML [Gutenberg and Richter, 1956] measured on the vertical channel, and the Mw(mB) estimated moment magnitude using a Mw and mB regression by Bormann and Saul (2008). The MLv is computed for stations within 8 degrees and the Mw(mB) for stations within 5 degrees. These two readings are then combined into a summary magnitude M defined below as:

$$M = \frac{2 * MLv + (0.4 * N_{stations} * (Mw(mB) - 1) * Mw(mB))}{2 + (0.4 * N_{stations} * (Mw(mB) - 1))}$$

Where  $N_{stations}$  is the number of seismic stations used to compute the average.

### 5.3 REVIEW AND RELOCATION OF HISTORIC DATA

This project attempted to re-evaluate older earthquake data (where possible) by adding additional picks as well as relocating events previously located with lower precision 1D velocity models with the newer 3D NZ3DRX model [Eberhart-Phillips et al., 2010]. GeoNet archives publicly accessible seismic event, station, response and waveform data as far back as the 1960s

but only to varying degrees of completeness. For instance, 50 year old event information may be available, but many of the particulars involved in the location process are incomplete or incompatible with modern metadata specifications. As this work progressed it seemed that only data since 2012 appears to be more or less complete, with older events increasingly missing necessary sensor, picks, and waveform information for some sites in the accompanying event XML data files to utilise them in SeisComP3.

### 5.3.1 1D to 3D Relocation of Historical Events from the GeoNet Catalogue 2006-2011

Relocating events from 1D to 3D velocity models was a straightforward process requiring no additional information as the P-wave picks used at each station were simply re-applied to the 3D solver, with the results shown in Figure 5.5. It is unknown what solver parameters were used between 2006-2011 so GeoNet's 2012-2017 settings were applied.

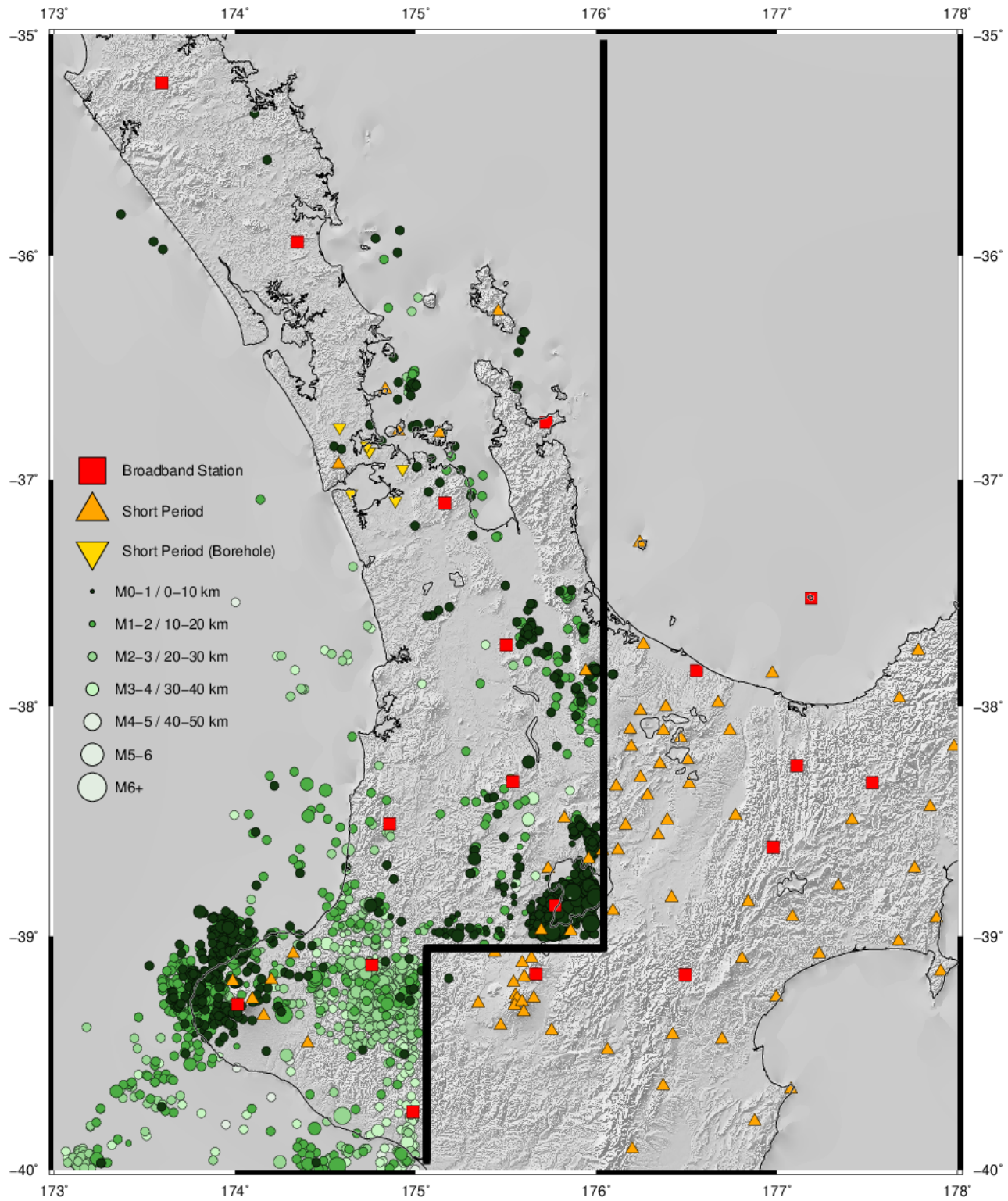


**Figure 5.5:** Selected GeoNet catalogue events between Jan 1 2006 and Jan 1 2012 shallower than 50 km relocated using the 3D NZ3DRX velocity model [Eberhart-Phillips et al., 2010] and the 3D NonLinLoc locator [Wittlinger, 1993; Lomax et al., 2000]. Events south and east of the TVZ which are out of interest for this project have been excluded for convenience due to their overwhelming volume and indistinguishably. All seismic stations existing between 2006-2012 or otherwise used in the relocation process are plotted.

Relative to GeoNet's original catalogue (Figure 5.2) the 3D relocated events 2006-2011 there are now many additional events within Hauraki Rift continuing as north as 36°S, presumably moved from nearby initial locations within the TVZ or from initial depths deeper than 50 km. Furthermore many additional events off the western coast are now visible along the general northern trend of the Taranaki Fault. There is also more variability in depth estimates, probably owing to the finer radial resolution of the NZ3DRX model. Overall the process of relocating from 1D to 3D is shown to be a good improvement, especially in light of the relative ease at which it is accomplished.

### 5.3.2 1D to 3D Relocation and Manual Review of Historical Events from the GeoNet Catalogue 2006-2017

Expanding on the previous section, GeoNet's catalogued 2012-2017 events were relocated from 3D to 3D in the same manner (e.g. from their 3D system configuration to this project's 3D configuration) to ensure model consistency with the 1D to 3D relocations. This comparison between GeoNet's original 2012-2017 data and the 3D-3D relocations done by this study were unsurprisingly negligible. After automatic relocation, the events from 2006-2017 north of 38°S were manually reviewed applying edits to pre-existing automatic P-wave picks as well as the addition of further P and S picks where possible, with the results shown in Figure 5.6.

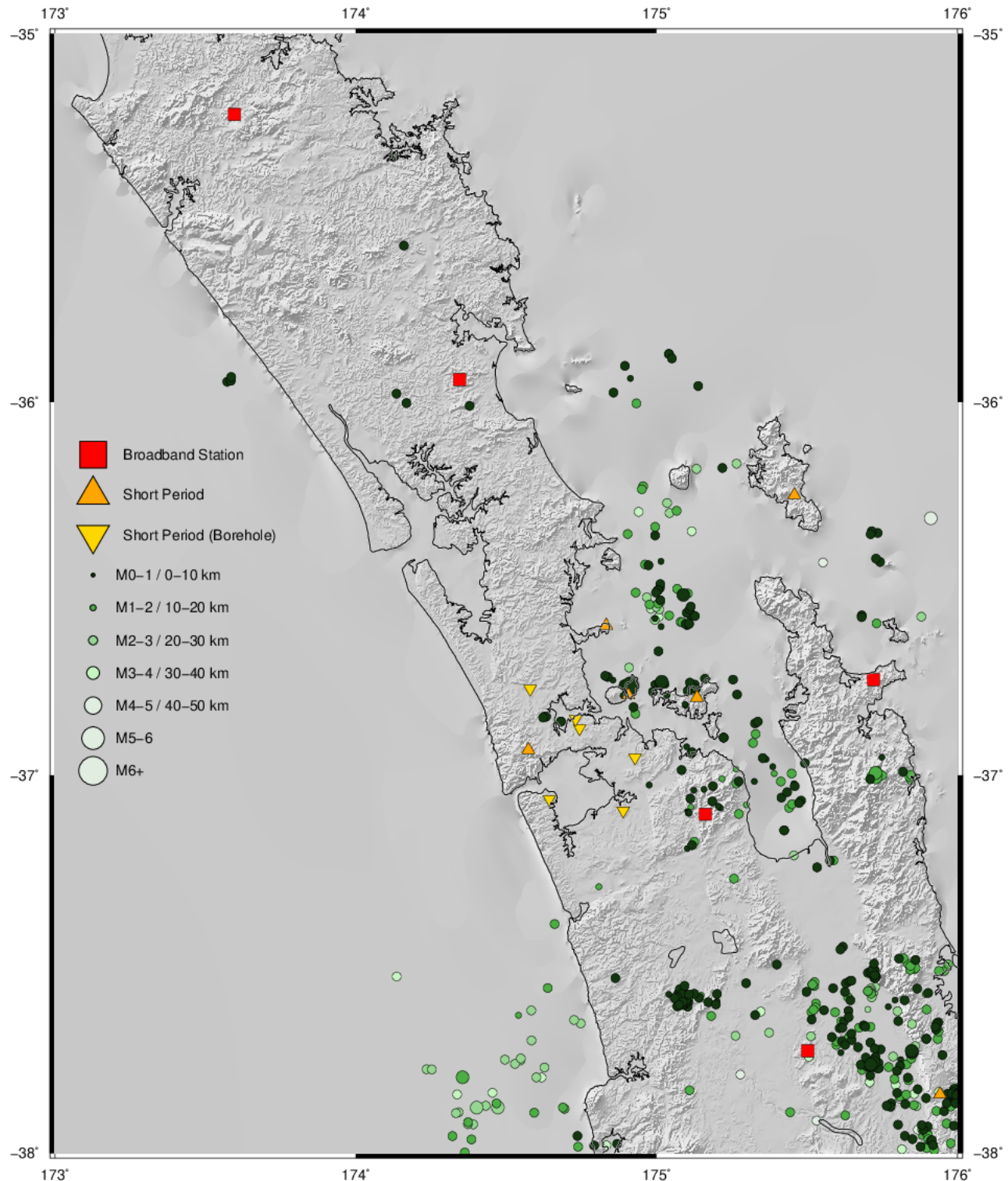


**Figure 5.6:** 2006-2017 catalogue GeoNet events which have been relocated from 1D to 3D (2006-2011) and 3D to 3D (2012-2017) which were also reviewed manually and supplemented with further phase picks where possible. The cluster of shallow events in the Waikato {175.2°E, 37.6°S} likely corresponds to blasting at a quarry here though they have not been labelled as such in the catalogue metadata.

The event data in Figure 5.6 span ~12 years and is likely to be a fair interpretation of the northern North Island seismicity achievable by GeoNet's network. However some conspicuously quiet regions remain, in particular within the Hauraki Rift between latitudes 37.25°S and 37.5°S in which there are few events reported relative to both the north and south of this region. Though it is possible there are in fact no earthquakes here, geodetic evidence for this region would suggest that activity here should be at least the same if not more vigorous than in the north (e.g. Figure 4.17) and maximum shear strain rate measurements (Figure 4.23) also support this. Thus it is likely that this lack of seismicity, and probably in other areas, reflects a lack of network coverage. As GeoNet's default of 10 minimum P-wave picks to initially define an event, several "shadow zones" exist in which there is insufficient station coverage to find small and nearby (<80 km) events (Figure 5.7). This could explain the dearth of reported events within the Hauraki Rift. It would further imply that the region SW of this along the western coast (between Hamilton and Mahoneui) may also have a high degree of unreported seismic activity, in addition to Northland (> 35°S), which is often assumed to be aseismic but only has a coverage of 1-2 broadband stations.

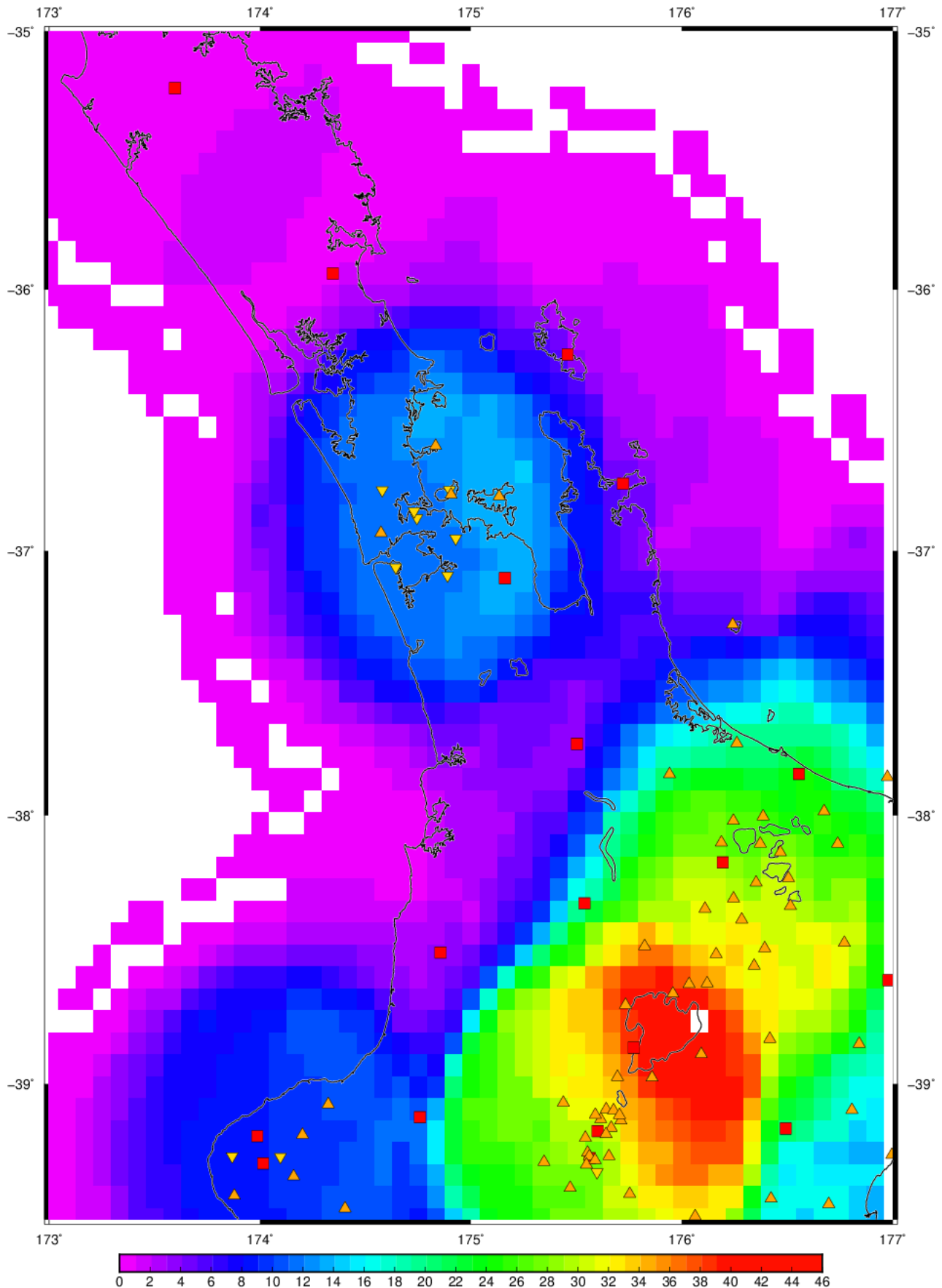


**Figure 5.7:** Number of stations within a distance of  $0.75^\circ$  ( $\sim 80$  km) distance. “Shadow zones” of poor station coverage (<10, dark blue and purple) may explain the lack of small events reported there.

## 5.4 LOCATING NEW EVENTS DURING 2017

To find many of the smaller ( $M < 3$ ) and shallow ( $< 50 \text{ km}$ ) events GeoNet's system isn't explicitly targeting, it is necessary to re-examine the seismic station data with specialised and/or lower-tolerance settings. Due to the large amount of data required this process can be computationally intensive, and as such only data collected during 2017 was used to test a new location scheme. Two additional stations were added which are not officially available in the GeoNet archives: short-period station HR1 (2 Hz, 3C) which was installed explicitly for this project in the Coromandel Peninsula {175.8°E, 37.1°S} and short-period borehole site RBAZ (2 Hz, 3C) on Rangitoto {174.9°E, 36.8°S}, with data courtesy of Jan Lindsey and Catherine Kenedi at the University of Auckland.

### 5.4.1 *Original GeoNet Data*

GeoNet's published findings during 2017 (Figure 5.8) are used as a baseline. As GeoNet's seismic network has densified considerably since 2006-2012 (e.g. Figure 5.2) a clear picture of the whole of North Island's tectonic activity is now largely achievable with only a single year's data. But this has not been the case in NWNZ where very few new stations have been added outside of the Auckland region, leaving the view of the activity there unchanged.

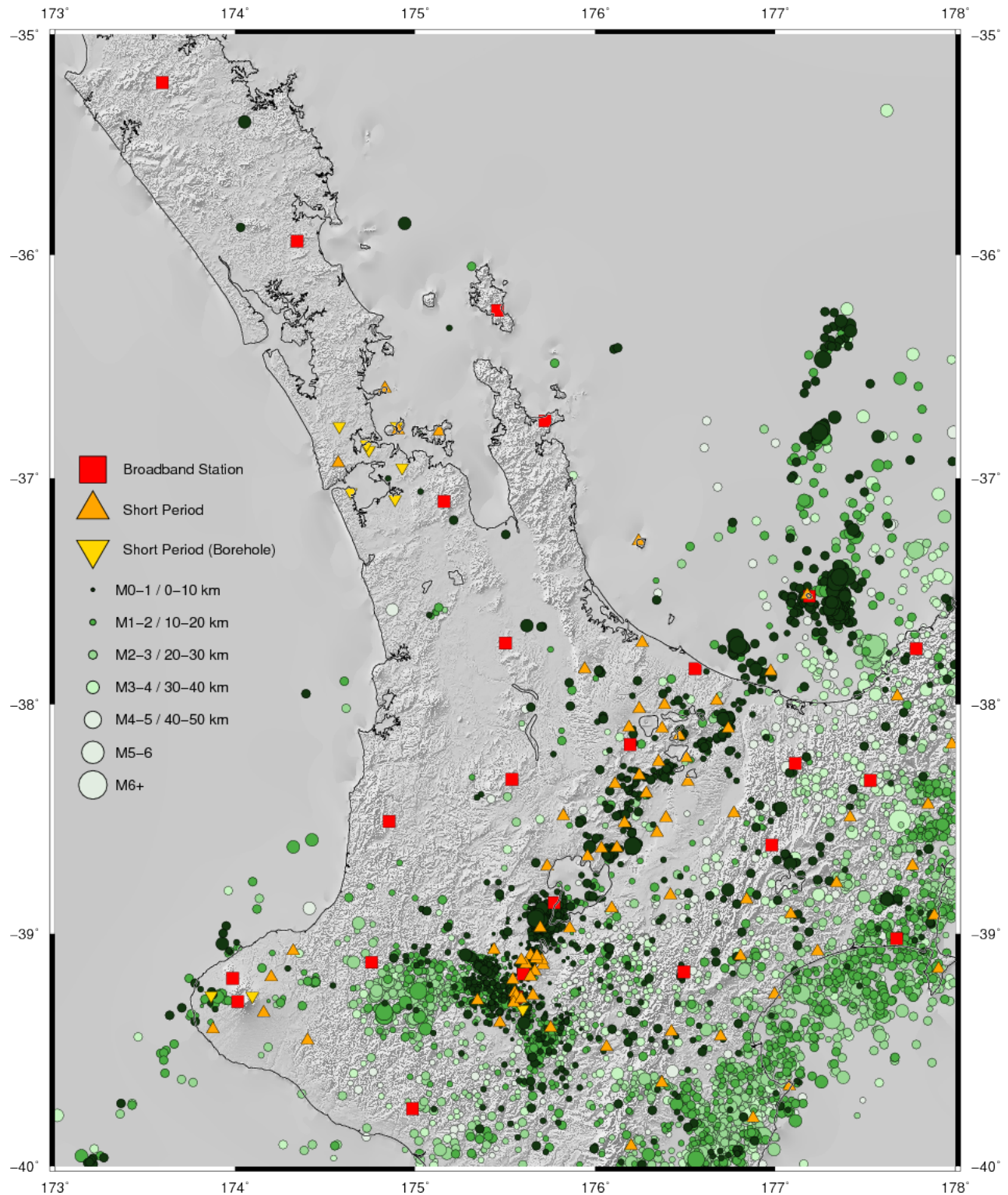


**Figure 5.8:** 2017 GeoNet catalogue events shallower than 50 km. Note that this includes many stations in the south-east of the North Island which were not necessarily included in the analysis targeting the north-west.

As this work is focused on small events in the NWNZ region, many seismic stations south and east of the TVZ have not been included in this analysis for the sake of computational expediency as these sites are likely to be too far away to detect faint activity over 200 km north. This has a detrimental effect on both the resolution and volume of events found within the greater TVZ, but as the activity here is otherwise already well documented and not of interest to this study it was deemed a fair concession. In order to test the detection capability of the remaining seismic stations and addition of sites HR1 and RBAZ, events were independently located using GeoNet's default location parameters (Section 5.2) with the results shown in Figure 5.9. As expected the TVZ and regions SE of it are poorly constrained but the greater Auckland and Hauraki Rift regions now feature more events which is presumably due to the contribution of the additional stations HR1 and RBAZ. It is thereafter assumed that the station selection used in this study (e.g. those in Figure 5.9), which neglects many located in the southern and east coast portions of the North Island, is appropriate to NWNZ.

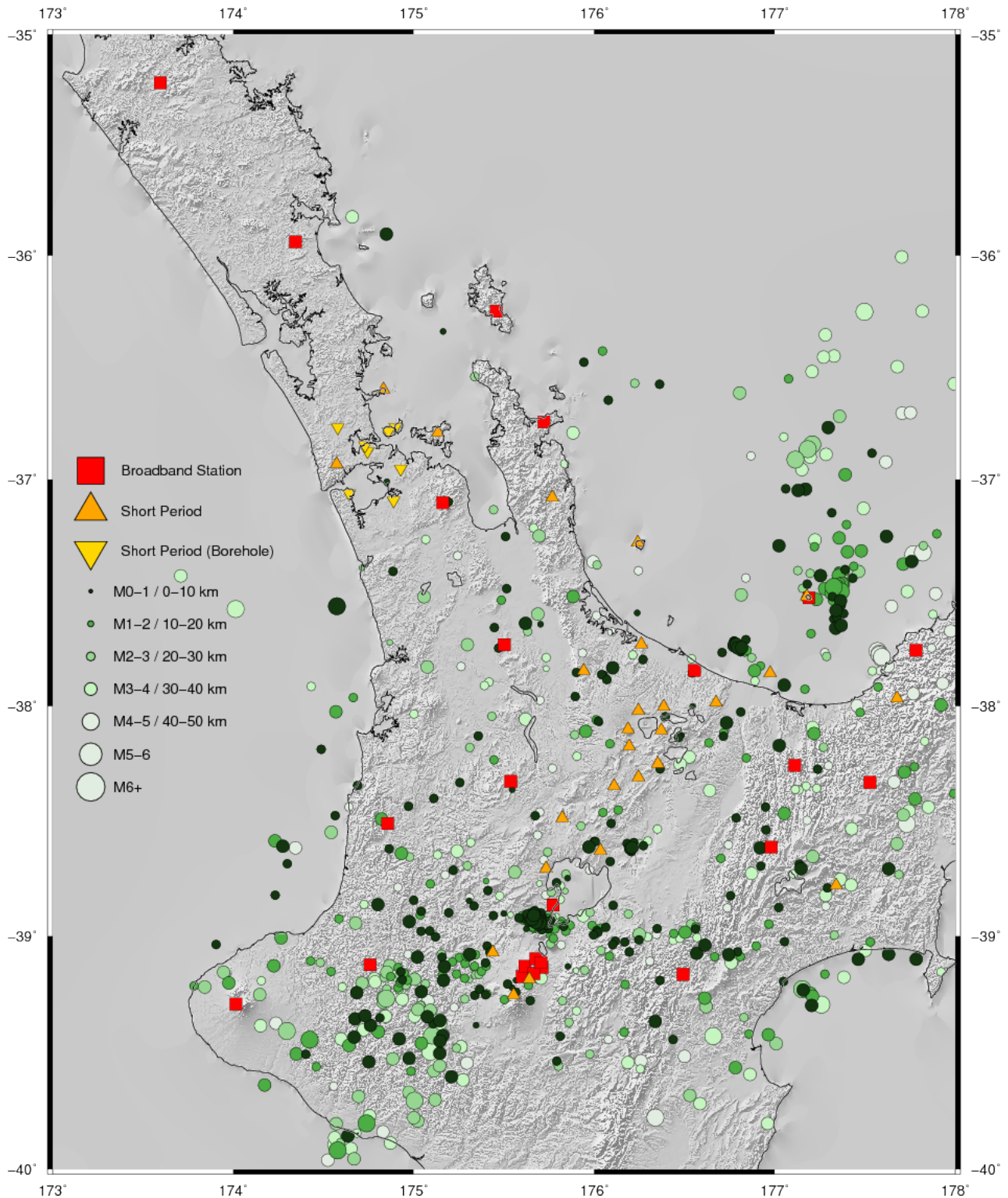


**Figure 5.9:** 2017 events shallower than 50 km found by this project using GeoNet's default parameters. Only the seismic stations shown here were used, which excluded many sites SE of the North Island but included additional sites RBAZ/Rangitoto and HR1/Coromandel Peninsula.

### 5.4.2 *Location of New Events 2017*

This project hypothesised that there are more earthquakes in the NWNZ region than are being detected by GeoNet, and that this is because their seismic network and automated monitoring detection parameters are not designed to do so. Therefore to resolve the missing events some combination of more sensors and an adjustment to the location algorithm would be needed.

The utility of adding the two sites RBAZ and HR1 to this project was uncertain at the onset of this project, so fieldwork was primarily dedicated to additional geodetic surveying (Chapter 4) at the expense of constructing additional seismic stations. Nevertheless the addition of only two sites has since proven to be exceptionally valuable. This fact was a finding in and of itself, the details of which described further ahead in section 5.4.2.6.

The determination of new detection parameter settings began by collecting and analysing over 2500 five-minute windows of waveform data at random stations containing the full extent of event waveform data. These events all occurred in 2017, were weak ( $M < 2.5$ ), shallow ( $< 50\text{ km}$ ) and originated north of  $37.5^\circ\text{S}$ . Though the source of this data was from events which had already been located by GeoNet, and not the missing and presumably smaller events this project was looking form their focal mechanisms, their hypocentres and wave travel paths should be similar and thus should also have similar frequency characteristics. Having a well-defined frequency spectrum for these events allows for the derivation of a narrow bandpass filter, which in turn amplifies STA/LTA signals used for detections and removes noise allowing for better P-wave arrival picking.

#### 5.4.2.1 *Expected Move-out and Travel Times for P and S-wave Arrivals*

When determining phase arrivals in a particular region it is good practice to begin with a general idea when to expect phase arrivals relative to each other. This provides a framework as to when to look for secondary arrivals when manually picking, as well as the degree to which the reflected arrivals may be clustered, and also helps define an appropriate windowing size to use for automatic pickers. In NWNZ it was presumed that events will mostly occur in the crust between 0-30 km with an average depth of 15 km. At this depth the 1D IASP91 velocity model [Kennett and Engdahl, 1991] gives an expected P-S move-out from 6 s at  $0.5^\circ$  distance to about 24 s at  $2.0^\circ$  (Figure 5.10). It is not expected for stations to detect small events past  $2^\circ$  ( $\sim 220\text{ km}$ ).

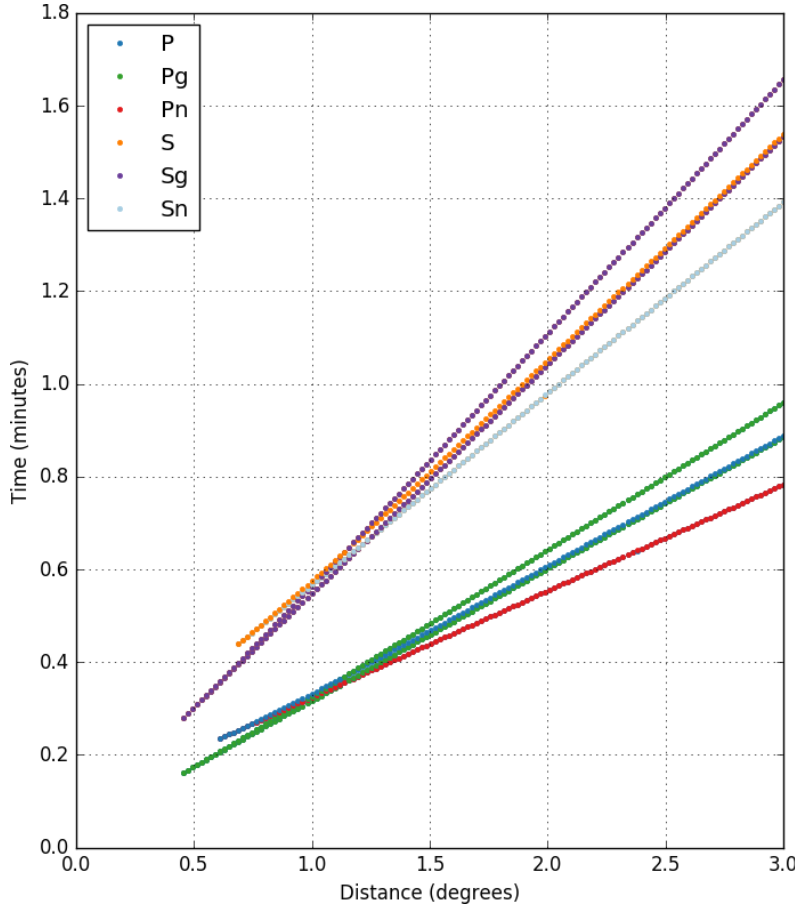


**Figure 5.10:** Move out times of various P- and S-wave phases at an event originating at 15 km depth through a layered medium described by the 1D IASP91 velocity model [Kennett and Engdahl, 1991].

#### 5.4.2.2 Power Spectrum Density of Local Events

Knowing the expected frequencies contained within event data allows for bandpass filtering to accentuate them. Unfortunately determining these frequencies is not trivial, and despite the ubiquity of generalised information on expected frequency ranges, the type of specific frequency information needed to detect very small events is highly dependent on the size and depth of the target earthquakes as well as geology of the region in which these waves traverse.

A novel approach was developed to determine the specific frequency ranges for earthquakes in this study area by averaging power spectrum densities (PSDs) of events, background noise, and individual P-wave arrivals themselves. This was done by calculating individual PSDs for windows of waveform data using Welch's method [Welch, 1967], and taking the mean of these values at each discrete frequency band with outliers greater than 3 standard deviations removed.

A "background" PSD was first calculated from 2500 five-minute windows taken at random times from a random selection of the ~60 stations used in this study, which was presumed to represent the typical baseline PSD signature. Then, another 2500 five-minute windows were taken from a random selection of these stations around 247 known events in the GeoNet catalogue which were shallow ( $< 50 \text{ km}$ ), weak ( $< 2.5\text{M}$ ), and located north of  $37.5^\circ\text{S}$ . This five-minute window was large enough to encompass the entire event, including the following S-wave and a great deal of the pre-arrival background noise. Finally, a PSD comprising an average of  $\sim 200$  2.5 s windows around hand-picked P-wave arrivals from a random selection of these same sites and events was also calculated to constrain the nature of the P-wave arrivals exclusively, with the results shown in Figure 5.11.

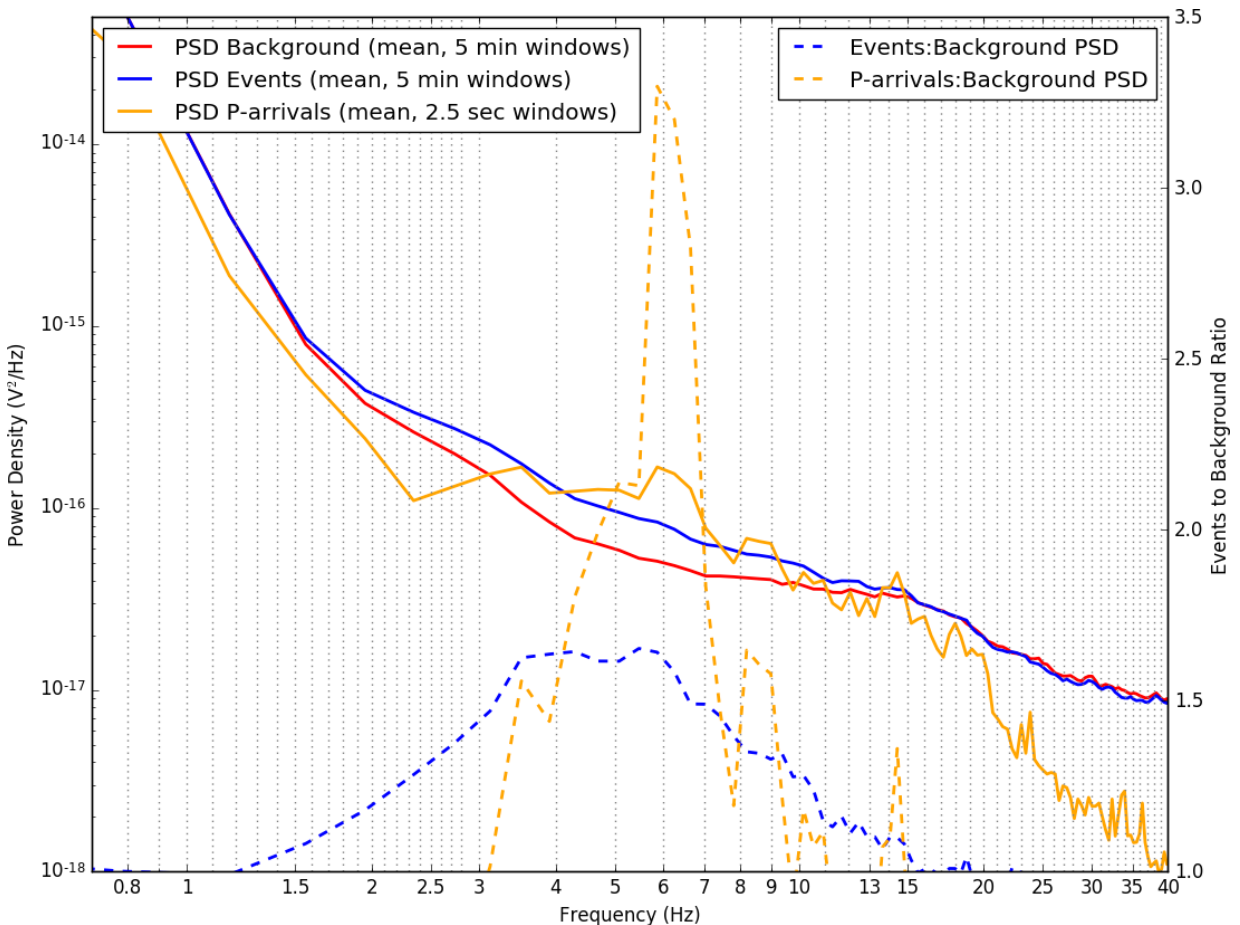


**Figure 5.11:** Power Spectrum Density of general "background noise" (solid red), broad events (solid blue), and targeted P-wave arrivals (solid gold) calculated by Welch's (1967) method and then averaged, with standard deviations greater than 3 removed. Ratios of event-to-background (dashed blue) and P-wave arrival-to-background (dashed gold) are also shown with scaling on the right. Event frequencies as a whole range from 1.2 - 16 Hz but P-wave arrivals have a narrower band, from 3-11 Hz or possibly as high as 15 Hz.

The Events-to-Background PSD ratio (blue dashed line, Figure 5.11) constitutes a new default event bandpass filter proposed between 1.2-16 Hz which encapsulates the entire spectrum of event frequencies, and is otherwise similar to GeoNet's 2-15 Hz default. However this may still be too wide for automatic P-wave picking as the frequency band of the pure P-wave arrivals relative to the background (dashed gold line) is much narrower, from 3-11 Hz, beyond which the spectrum becomes increasingly noisier until 15 Hz when it falls dramatically. Refining a bandpass filter from 1.2-16 Hz to 3-11 Hz band offers improvement by removing a great deal of lower and higher frequency signal which does not appear to contain much P-wave arrival information.

#### 5.4.2.3 *Exploration of STA/LTA Detection Parameters*

With new evidence for a narrower 3-11 Hz frequency band for expected P-wave arrivals (e.g. Figure 5.11), it is possible to increase the sensitivity of detection algorithms relative to GeoNet's default of 2-15 Hz. This band may speculatively be further narrowed to 4-8 Hz, which still manages to encapsulate over 90% of the average P-wave arrival energy. All three Butterworth bandpass filters were applied to a range of STA and LTA values to better understand how they affect the character of the resulting detections (Figure 5.12). The goal of this process is to calibrate STA and LTA values to engineer higher STA/LTA amplitudes to detect low-SNR events, reduce the number of false STA/LTA detections, and to reduce the time discrepancy between the P-wave arrival and STA/LTA detection trigger which assists the automatic P-wave picking by establishing a correct noise and signal window (ahead in Section 5.4.2.4).

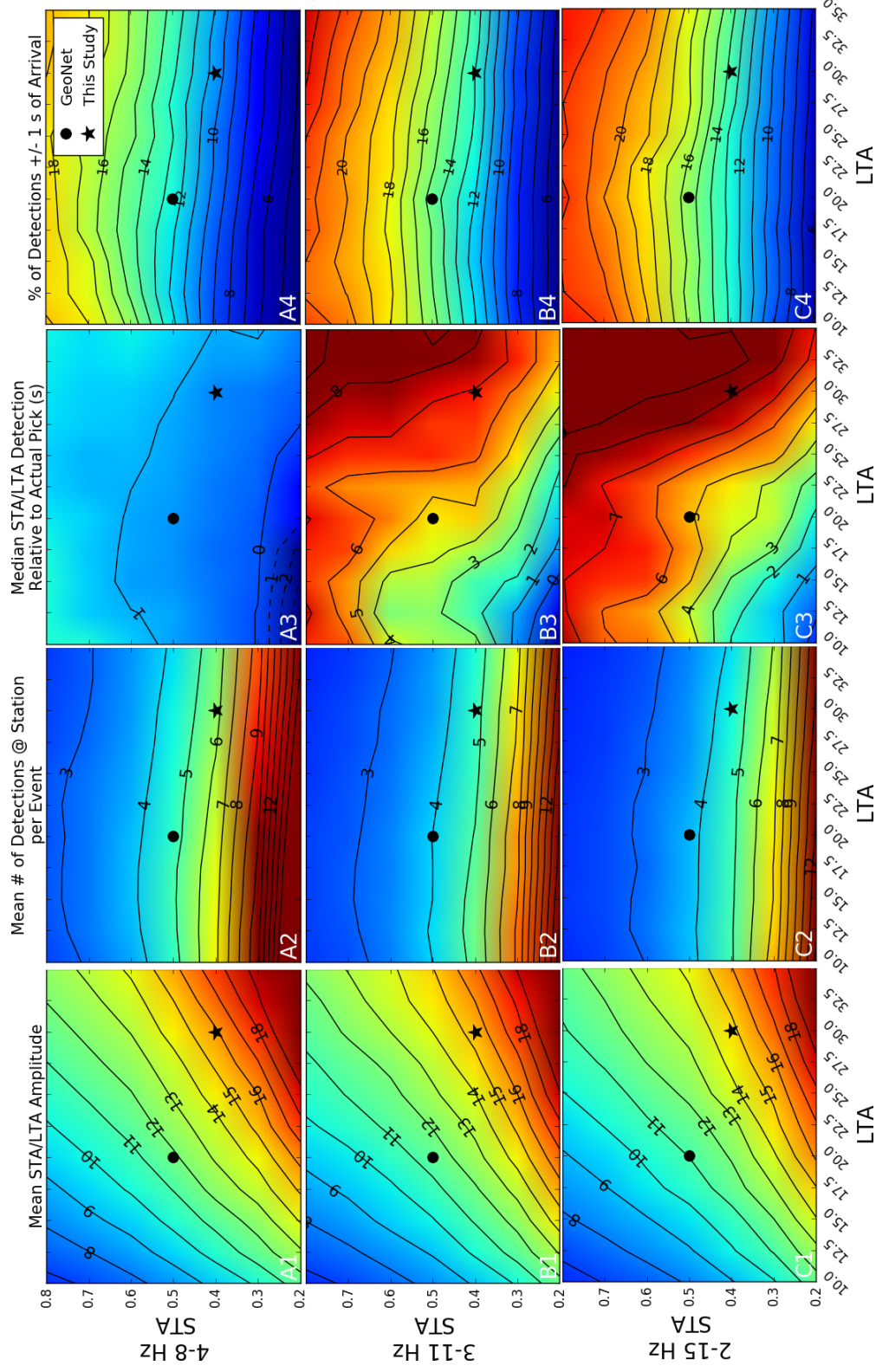


**Figure 5.12:** STA/LTA results over a spectrum of values for both the STA (0.2-0.8 s, left axis) and LTA (10-35 s, bottom axis) at waveform filters 2-15 Hz (used by GeoNet; bottom row C1-C4), 3-11 Hz (P-wave arrival band predicted by Figure 5.11; middle row B1-B4), and 4-8 Hz (a speculative narrower band, top row A1-A4). The figures are coloured blue to red from low to high and contours are drawn at intervals of 1 with their values labelled on the contours. The left-most column A1-C1 shows the resulting mean STA/LTA amplitude, A2-C2 show the mean volume of resulting detections, A3-C3 shows the mean time error between the detection and actual P-wave arrival, and A4-C4 show the percentage of “good” detections within 1 s of the P-wave arrival. GeoNet’s default STA/LTA detection parameters of 0.5/20 (s) are drawn with a circle and the values of 0.4/30 (s) are drawn with a star. The goal is to derive values for STA and LTA which maximise amplitude (A1-C3) while reducing the spurious detections (A2-C2, A3-C3) and generating detections nearer the P-wave arrival (A4-C4).

Universally, low STAs with high LTAs produce higher amplitude picks (Figure 5.12 A1-C1). Lower STAs generate more detections overall (A2-C2) which are correspondingly marginally poorer in quality (A4-C4). There is negligible overall difference between GeoNet's 2-15 Hz range (C1-C4) and the customised 3-11 Hz bandpass determined from Figure 5.11 (B1-B4), but the tighter 4-8 Hz filter (A1-A4) shows improvement in the lateness of the detection (A3), while maintaining roughly the same mean amplitude (A1), and without adding too many extra picks (A2), or sacrificing a disproportionate amount of quality picks (A4). Detections which are closer to the actual P-wave arrival are more likely to generate picks on the first P-wave arrival rather than mistakenly pick a subsequent arrival or even the S-wave [Trnkoczy, 1999]. It therefore appears that narrower detection bandpass of 4-8 Hz (A) offers tangible improvement over the PSD-derived 3-11 Hz or GeoNet's 2-15 Hz band.

It was desired to adjust the STA and LTA values such that the mean STA/LTA amplitude (Figure 5.12 A1-C1) was increased relative to the GeoNet default (STA=0.5 s, LTA=20 s, plotted in circles), which should then potentially increase the volume of smaller events detected. This meant a shift towards higher amplitudes in terms of raising the LTA and lowering the STA (A1). However, there is a trade-off as this shift also worsens the quality of the detection itself (Figure 5.12 A3, A4) and reducing the STA tends to increase the number of false detections (A2).

An appropriate STA was first decided by assuming a lower limit capable of sampling at least two periods of the most common P-wave arrival frequency (e.g. 6 Hz, Figure 5.11), which gives a conservative estimate of a STA period  $\sim 0.4$  s. This value is in the general range of 0.3-0.5 s for STA values targeting local events [Trnkoczy and Bormann, 2002] and does not seem to enter the realm of asymptotic or otherwise questionable detection increases at values less than 0.3 s (e.g. Figure 5.12 column A2-C2). At an STA of 0.4 s there is surprisingly little sensitivity towards the LTA in the resulting number of detections (A2, A3, A4) making a logical LTA selection difficult. It is known that larger LTA values increase SNR overall [Trnkoczy, 1999; Trnkoczy and Bormann, 2002], so a value at least equivalent to GeoNet's 20 s default was desired. A value of LTA=30 s was chosen as it produced an equivalent mean detection error as using GeoNet's settings (A3).

The effect on applying the aforementioned filters and STA/LTA parameters on an example arrival waveform with low signal to noise is shown in Figure 5.13. The P-wave arrival is around the 170 s mark with subsequent reverberations continuing until 200 s, with the possibility of a 2nd and/or 3rd smaller event arriving near 225 s. While all six combinations of filters

and STA/LTA parameter groups easily detect the initial P-wave arrival, the amplitude and distribution of these detections varies considerably.

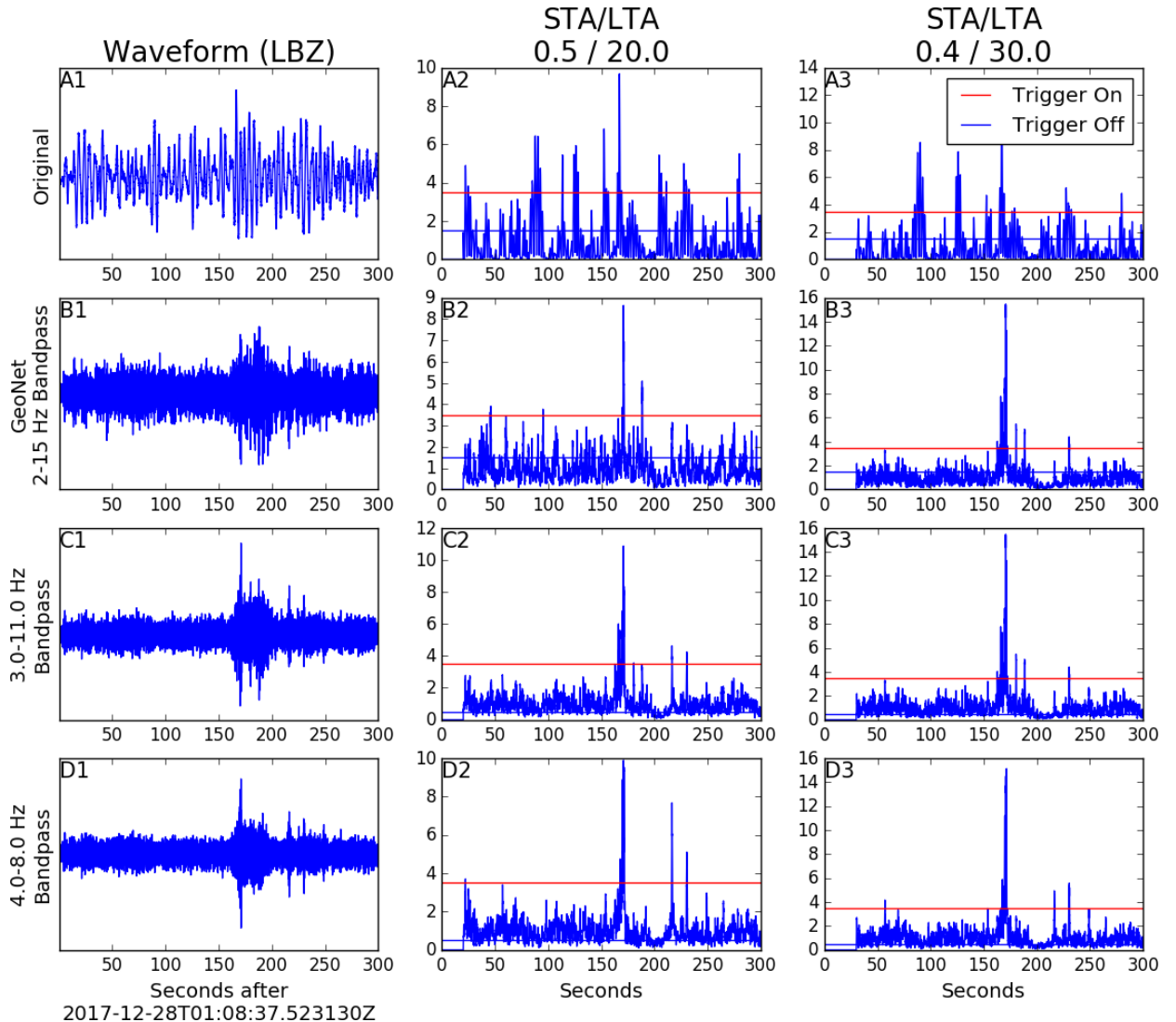


**Figure 5.13:** The resulting effect of STA/LTA calculations on an example  $M < 2$  event arrival at station LBZ with poor SNR on an unfiltered waveform (Figure 5.12, row A), bandpassed with GeoNet's default settings (row B), one using the 3-11 Hz P-wave arrival band determined by Figure 5.11 (row C), and using the speculative tighter 4-8 Hz band (row D). The "trigger on" value at which a detection is made is plotted in red, with the "trigger off" reset value plotted in blue. The STA/LTA detector will not re-trigger until the lower trigger off threshold is breached.

The original 0.5s/20s STA/LTA and 2-15 Hz plot (Figure 5.13, B2) using default GeoNet settings appears to trigger on the S-wave arrival in addition to the P, as well as a few noisier spots preceding it around 40 and 90 s. Tightening the bandpass to 3-11 Hz (C2) eliminates the early detections caused by high frequency noise while boosting the amplitude of the initial P-wave arrival and speculative aftershocks at 170 s and 200 s while simultaneously lowering

the amplitude of the S-wave arrival, which must have contained a lot of power in the 2-3 Hz range. Thinning the bandpass further to 4-8 Hz (D2) has a similar result, except that the S-wave arrival circa 180-200 s is now completely removed and the aftershocks are greatly amplified.

Moving to the speculative 0.4s/30s STA/LTA column (Figure 5.13 row 3), arrival amplitudes are greatly increased and background noise values remain well under the "trigger on" threshold of 3.5 (red lines) for each filter, and therefore, at least in this singular instance, it would appear a broad improvement over the default 0.5s/20s. Narrowing the filter progressively has the same effect as in column 2, in which P-wave arrivals are boosted while S-wave arrivals are muted.

The default "trigger off" lower threshold (Figure 5.13, blue lines) GeoNet uses is 1.5 (B2 and B3). This value does not hinder the detector's capability as it is often quickly breached after a detection. Still, there appears to be slight room for improvement, and this project thus assumed a value of 0.75 (C2, C3, D2, D3) in an attempt to reduce periods of rapid detections, altogether purely a concern of numerical efficiency.

#### 5.4.2.4 AIC P-Picking Parameters

The AIC picker effectively works by creating piecewise statistical model describing both a "noise" period and a "signal" period of an event waveform, then selecting a point along a windowed waveform in which the combination of both noise and signal models fit poorest. This point would then likely designate the event's arrival as it should be comprised of equal parts noise and signal [Akaike, 1974; Kitagawa and Akaike, 1978]. Therefore the most important parameters for the AIC picker are the window size around the STA/LTA detection, and to a lesser extent the bandpass filter used clean the waveform in advance.

The essential requirement of AIC picker's window size is that it must be large enough such that it contains the true P-wave arrival. If it is then assumed that many STA/LTA detections will trigger on the typically larger S-wave arrival in lieu of the P, a signal window at least as wide as the S-P moveout time (e.g. Figure 5.10) should be used. This appears to be the strategy of Turino et al. (2010) as well as GeoNet who use an AIC signal window beginning 20 s before the STA/LTA detection and ending 8 s after it, although the logic to their choice of these parameters is not explicitly defined. Regardless, a window of this size is capable of capturing P-wave arrivals of shallow events at distances less than  $\sim 1.5^\circ$  when only the S-wave arrival triggers. The downside to relying on S-detections is that it potentially places a larger portion of the signal (i.e. between the P and S arrivals) within one of the noisier parts of the

event waveform, reducing SNR and the ability of the AIC picker to determine an accurate arrival.

Noting that the average STA/LTA detection using this study's modified parameters (4-8 Hz bandpass, 0.4s/30s STA/LTA) was typically within a few seconds of the true P-wave arrival (Figure 5.12, A3), it was decided to assume that detections will occur at or around the P-wave arrival exclusively. This is more in line with the optimal parameters of Sleeman and van Eck (1999) who found that a pre-signal window beginning 8 s prior and ending 4 s after the detection produced the most accurate picks for local events. A window of this length is still long enough to capture P-wave arrivals on S-detections for events nearer than  $\sim 0.75^\circ$  and is still long enough to encompass clusters of reflective P-wave arrivals as far away as  $3^\circ$ , and as such should be wide enough to find the true arrival even when the STA/LTA triggers are exceptionally late due emergents waveforms associated with deep or distant events.

The AIC filter used in this project was 3-11 Hz, equivalent to the bandwidth of the P-wave arrivals shown in Figure 5.11. This is similar to the 2-10 Hz used by Sleeman and van Eck (1999) in their work in determining optimal AIC setting for local events. GeoNet uses the values of 2.5-15 Hz shared by Turino et al. (2010) in their local/regional detection in northern Italy. Other researchers [Douglas et al., 1997; Zhang, 2003] have opted for no filter at all, fearing that higher frequency information useful to the picking process may be lost. While it is true that at least some of the P-wave arrivals occur at frequencies higher than 11 Hz (Figure 5.11) a larger concern for this work was in elevating the SNR of extremely weak events to detectable levels. Therefore the strategy of eliminating the higher frequencies was chosen at the cost of increased pick latency due to the earlier arrival of higher frequencies.

Finally, the minimum SNR between the signal and noise window required for the AIC picker to predict an arrival was lowered from GeoNet's 3.0 to 1.5, with the explicit intention of increasing the volume of picks produced per detection. While this certainly lowers the overall quality of incoming picks, any outliers are subsequently down-weighted by the locator (e.g. NonLinLoc) or ignored outright, ultimately making their inclusion moot. Therefore it seems sound practice to include the picker's best estimate in any instance with even a marginally greater signal than noise despite the additional computational cost.

#### 5.4.2.5 Events Found in 2017 Using Custom Settings

All of the aforementioned parameter changes from GeoNet's defaults are collated in Table 5.1. These were used to trigger STA/LTA detections, then find P-wave picks used to locate in 1D

before finally being relocated in 3D for the whole of 2017. In all 15938 events were found using these new parameters relative to GeoNet's 9608 (Figure 5.14). However many of these newly found events are of poor quality with horizontal and depth uncertainties too large to infer the smaller structures within NWNZ that this project was searching for. Regardless it stands to reason that with a small amount of extra seismic stations (e.g. increasing the average phase count per event from 15 to 20) the number well-resolved events could potentially be boosted by hundreds per year.

**Table 5.1:** SeisComP3 parameter settings for this study and the GeoNet default.

	This Project	GeoNet
Max Pick Residual (s)	5.0	3.0
Max Location RMS (s)	2.0	2.0
Locator Default Depth (km)	10	10
STA/LTA Filter	4-8 Hz	2-15 Hz
STA (s)	0.4	0.5
LTA (s)	30	20
STA/LTA Trigger On	3.5	3.5
STA/LTA Trigger Off	0.75	1.5
AIC Filter	3-11 Hz	2.5-15 Hz
AIC Min SNR	1.5	3
AIC Noise Begin (s)	-12	-40
AIC Signal Begin (s)	-8	-20
AIC Signal End (s)	4	-8

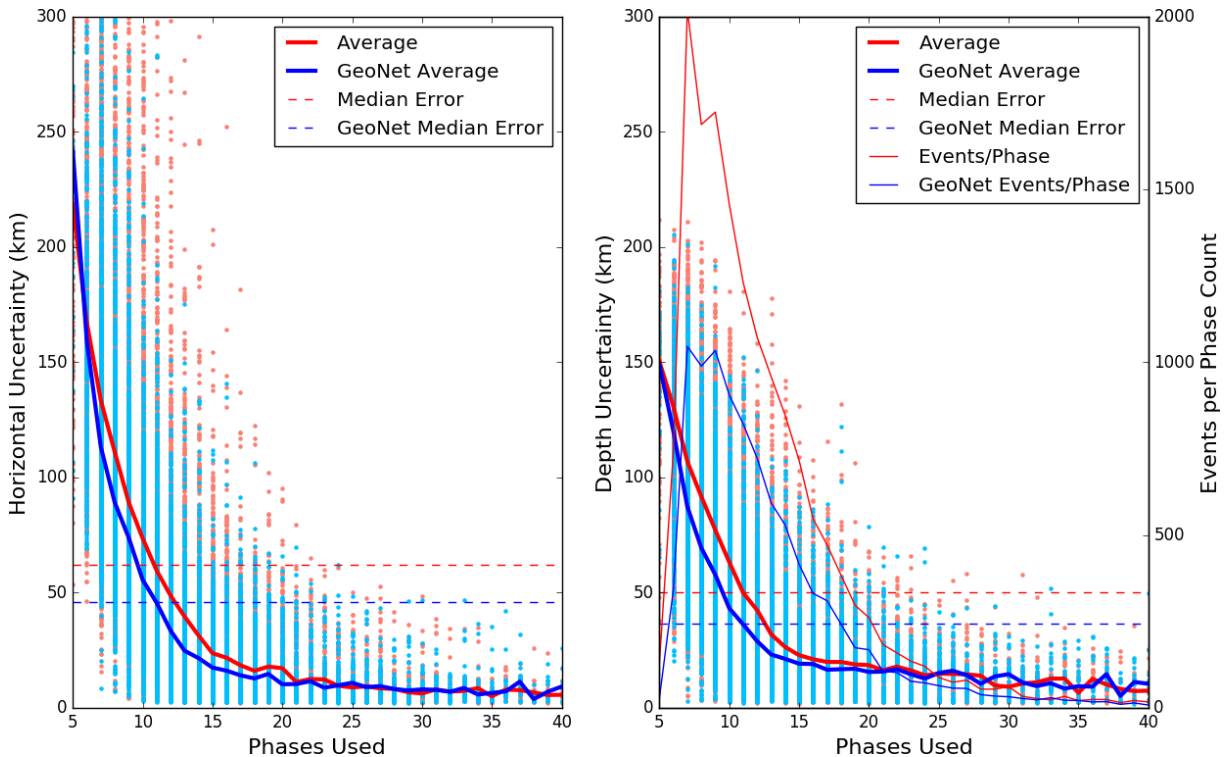


**Figure 5.14:** Horizontal (left) and depth (right) uncertainty vs. phase counts used to locate all events found in 2017 using the picking and location parameters for this study (red) and using GeoNet's (blue). The median value of each is drawn with a dashed line and the total number of events per phase count are shown in thin lines on the right plot. In total, 15938 events with a minimum of 7 phase picks using this study's customised parameters and 9608 were found using GeoNet's.

To compare this data in practical terms, only event data with horizontal and vertical position uncertainty  $<25\text{ km}$  was selected at depths  $<50\text{ km}$ , shown in Figure 5.15. The tighter parameters used by this project found 164 events within the plotted area vs. GeoNet's 120, a gain of 36% overall with over double the amount of small ( $M<2$ ) events discovered. This is particularly relevant near Auckland where five additional events were detected. The average horizontal uncertainties between these two datasets were both acceptable, 4.6 km for this study and 3.4 km for GeoNet's settings.

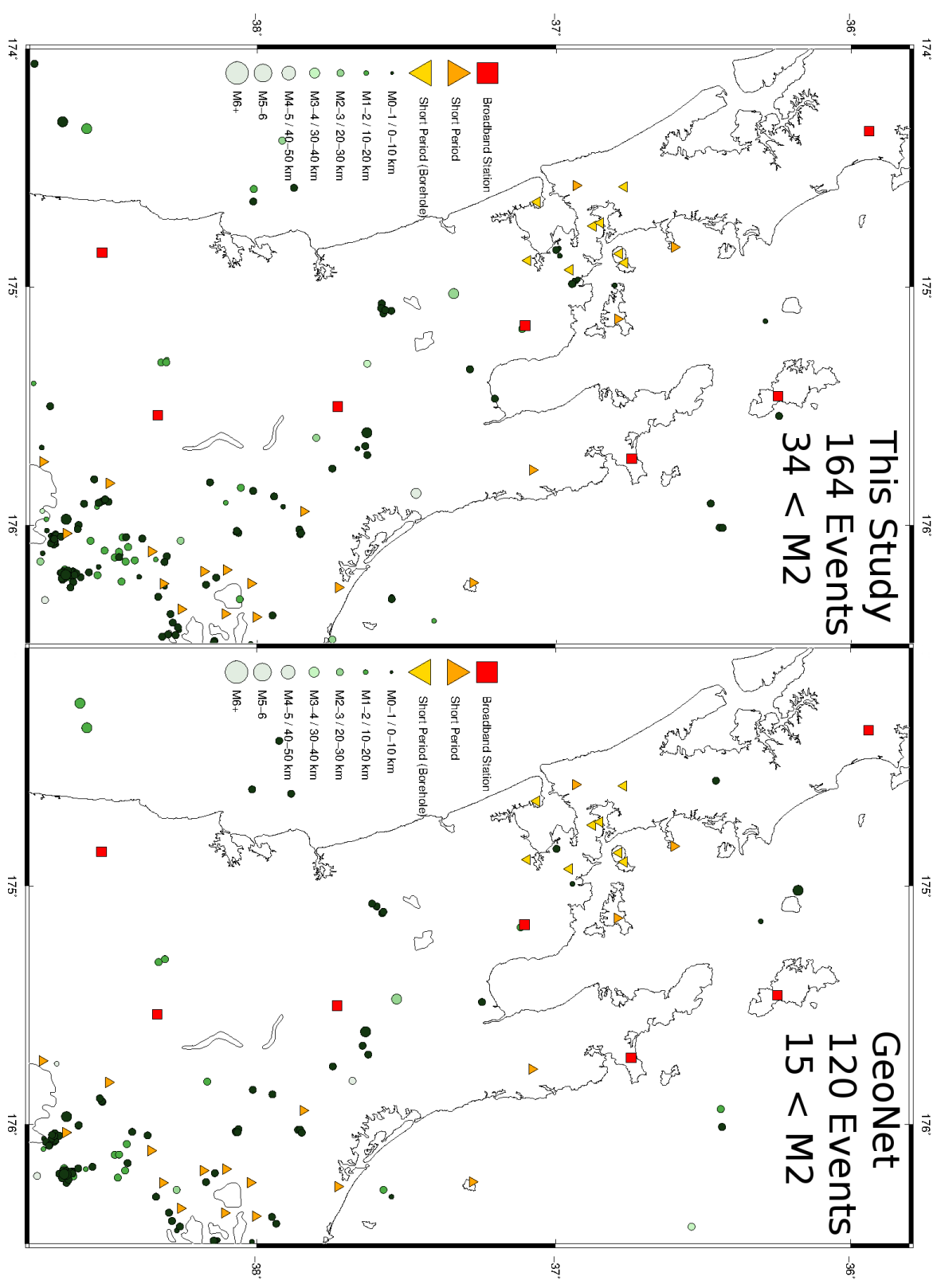


**Figure 5.15:** Events found in 2017 using this study's parameters and GeoNet's default parameters. "Well-resolved" (horizontal uncertainty  $< 25 \text{ km}$ ) shallow ( $< 50 \text{ km}$ ) events found in 2017 using the parameters in Table 5.1 and stations shown. This study found 164 events with 34 having a magnitude  $M < 2$ , whereas the GeoNet parameters found 120 with 15 below  $M_2$ .

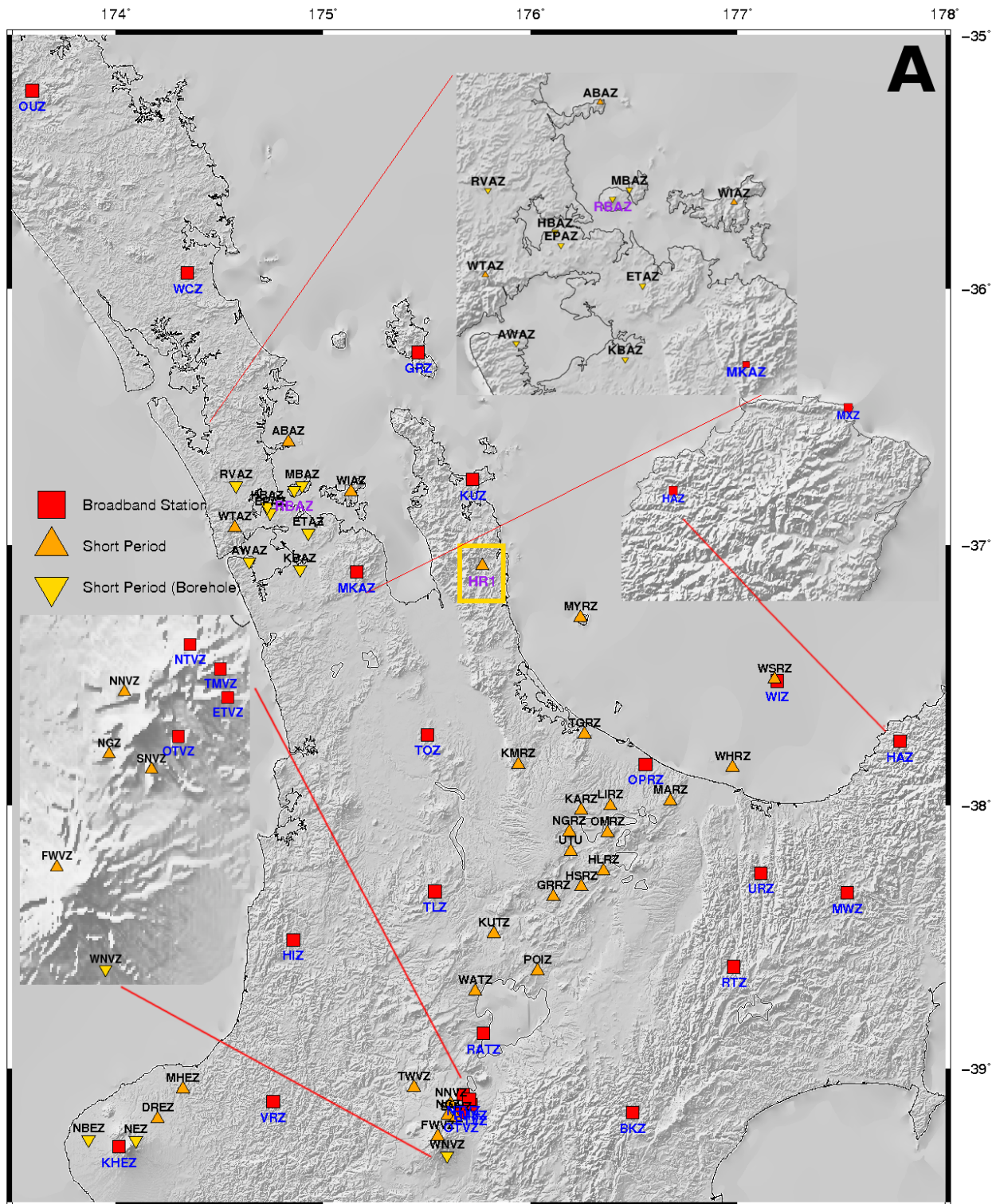
#### 5.4.2.6 Detection Statistics

The average event volume and reach of each station in the seismic network (arranged N-S) is shown in Figures 5.16 using this study's location parameters (B, Subfigure 5.16b) as well as GeoNet's (C, Subfigure 5.15c) for events north of 38°S and between longitude 174°E to 176°E. Southerly stations nearer to the active plate boundary generally detect more events (B1,C1) as well detect them from further away (B2,C2), though the higher-sensitivity broadband sensors (red) detect events consistently regardless of their latitude. Short period borehole sensors (green) under-perform broadband sensors (red) at detecting events at distance (B2,C2) but are comparable at detecting small events (B3,C3). This finding is interesting when factoring in the high cost of borehole drilling, though the human noise from Auckland in the north (left side) almost certainly plays a large role in degrading small event detection. Small events ( $M < 2.5$ ) are otherwise detected bi-modally and somewhat equally in both the north (e.g. the Auckland Volcanic Field) as well as the south (e.g. the Lake Taupō region).

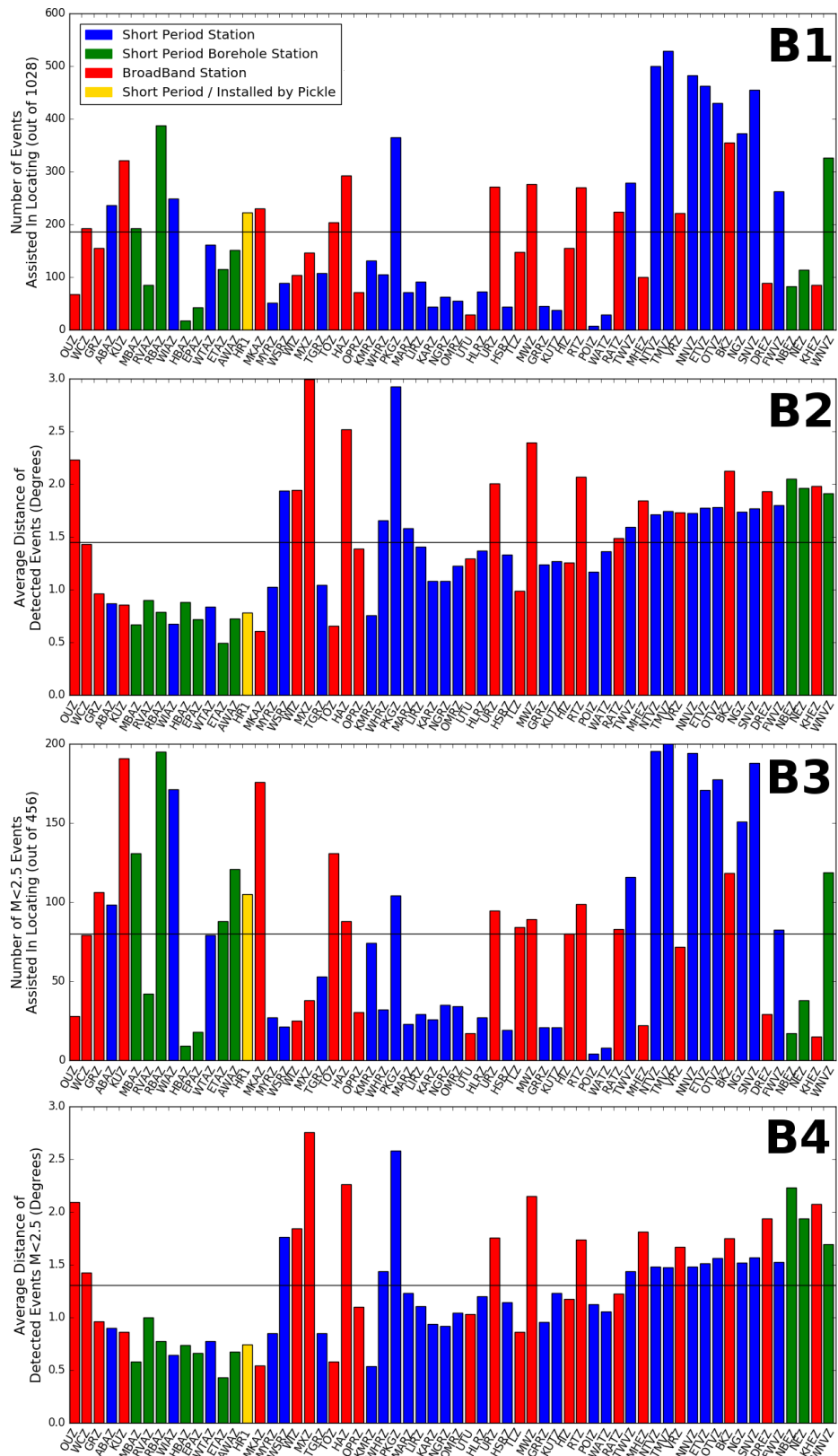
Directly contrasting the results of this project (Subfigure 5.16b-B) with those found using the GeoNet defaults (Subfigure 5.15c-C), the number of located events (B1,C1) falls 58% from 1028 to 424 but the average distance of detected events is effectively the same at  $\sim 1.5^\circ$ . This discrepancy is only partially accounted for by the decrease in 192  $M < 2.5$  events from 456 to 264 (B3-C3), both having an average detection distance of  $\sim 1.4$  degrees. It then appears that while the newer detection parameters (e.g. Table 5.1) do not largely increase the extent at which large events are detected, they do increase the extent at which smaller events are detected and thus the volume of events overall.

These statistics are also helpful in identifying the quality of individual stations by comparing their performance to stations with equivalent sensor types and latitudes. In particular, the performance of borehole sites HBAZ and EPAZ is poor. This is almost certainly due to their placement within Auckland City, which indicates that a borehole is insufficient to insulate human noise. This finding is further supported by the superior performance of nearby borehole sensor RBAZ on Rangitoto Island, an undeveloped nature reserve just  $\sim 10\text{ km}$  away. Short period sensor HR1 (Section 5.6) installed explicitly for this project has been a surprising success relative to both borehole and broadband sites despite the fact that it is a temporary site and therefore somewhat crudely constructed. Its high performance is thought to be predominately due to its isolated geographical location from human noise.

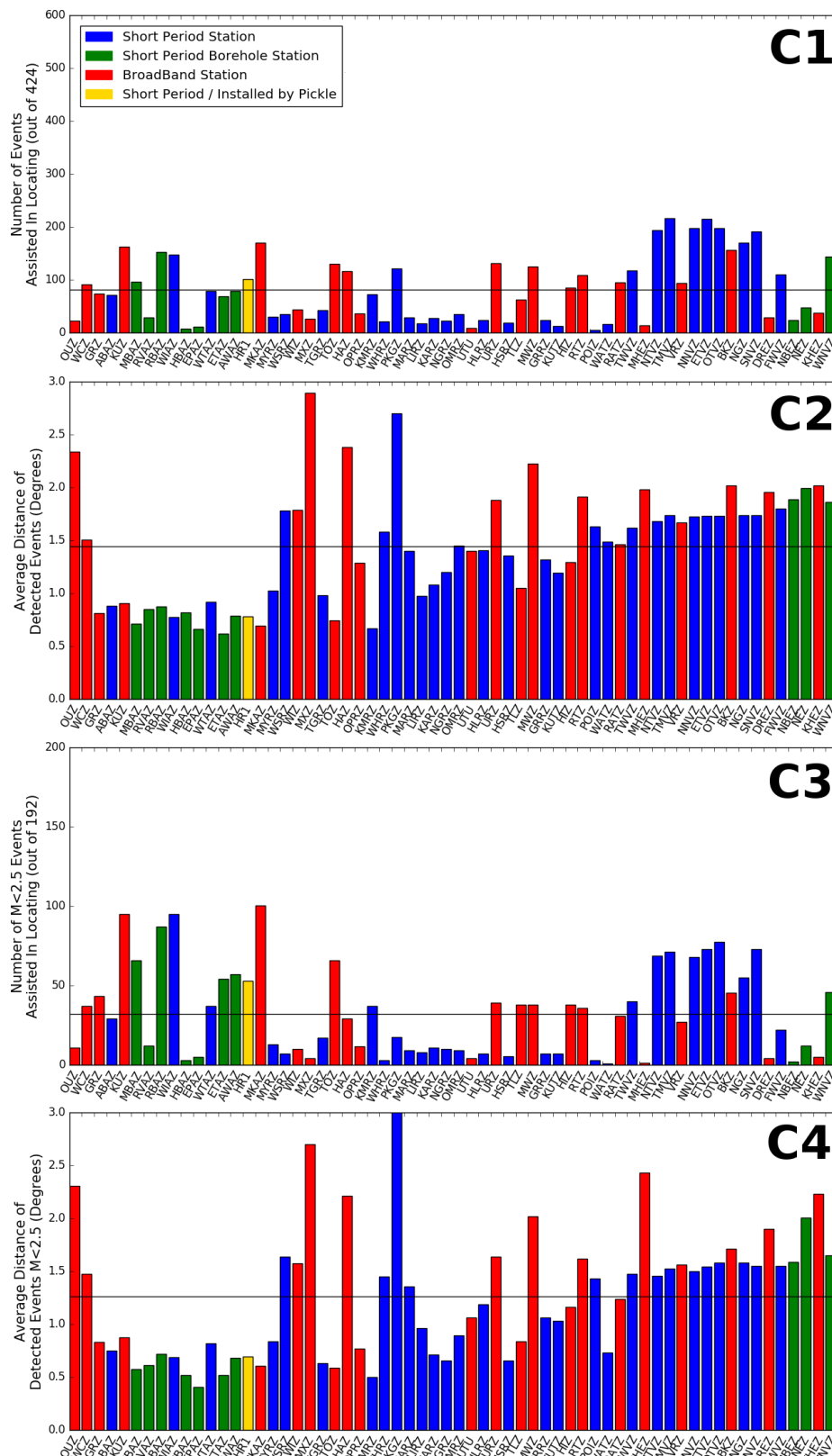
**Figure 5.16:** Station map (A) with this project (B) and GeoNet's (C) event detection statistics



(a) Map of stations used to locate events. The red lines assist in highlighting zoomed regions.



(b) Station statistics for all events in 2017 at all depths located within the general Hauraki Rift region bound by 174°E to 176°E and 38°S to 35.5°S using *this study's* customised event location parameters, arranged N-S from left to right. (B1) The number of events each station assisted in locating, (B2) the average distance to each of these events, (B3) the number of events each station assisted in locating with a magnitude  $M < 2.5$ , and (B4) the average distance of these  $M < 2.5$  events. The horizontal black line on each denotes the mean. These values have been normalised relative the each station's uptime during 2017.



(c) Station statistics for all events in 2017 at all depths located within the general Hauraki Rift region bound by 174°E to 176°E and 38°S to 35.5°S using *GeoNet's default* event location parameters, arranged N-S from left to right. (C1) The number of events each station assisted in locating, (C2) the average distance to each of these events, (C3) the number of events each station assisted in locating with a magnitude M <2.5, and (C4) the average distance of these M <2.5 events. The horizontal black line on each denotes the mean. These values have been normalised relative to each station's uptime during 2017.

## 5.5 MANUAL REVIEW OF 2017 EVENTS

All automatically located events (e.g. the data populating Figure 5.14) found within the Auckland and Hauraki Rift region with depths  $<50\ km$  were manually reviewed and supplemented, increasing the number of well-resolved (spatial uncertainty  $<25\ km$ ) events in 2017 circa the Hauraki Rift from 35 to 186 (Figure 5.17 with statistics given in Figure 5.18). This process often included the expulsion of false picks (particularly systemic high frequency impulse noise probably caused by construction machinery near Auckland City) as well as the manual addition of picks at nearby stations that were not automatically detected. S-wave arrivals were also added when their onset was clear though the small signal and close proximity between P and S-wave arrivals made this difficult.

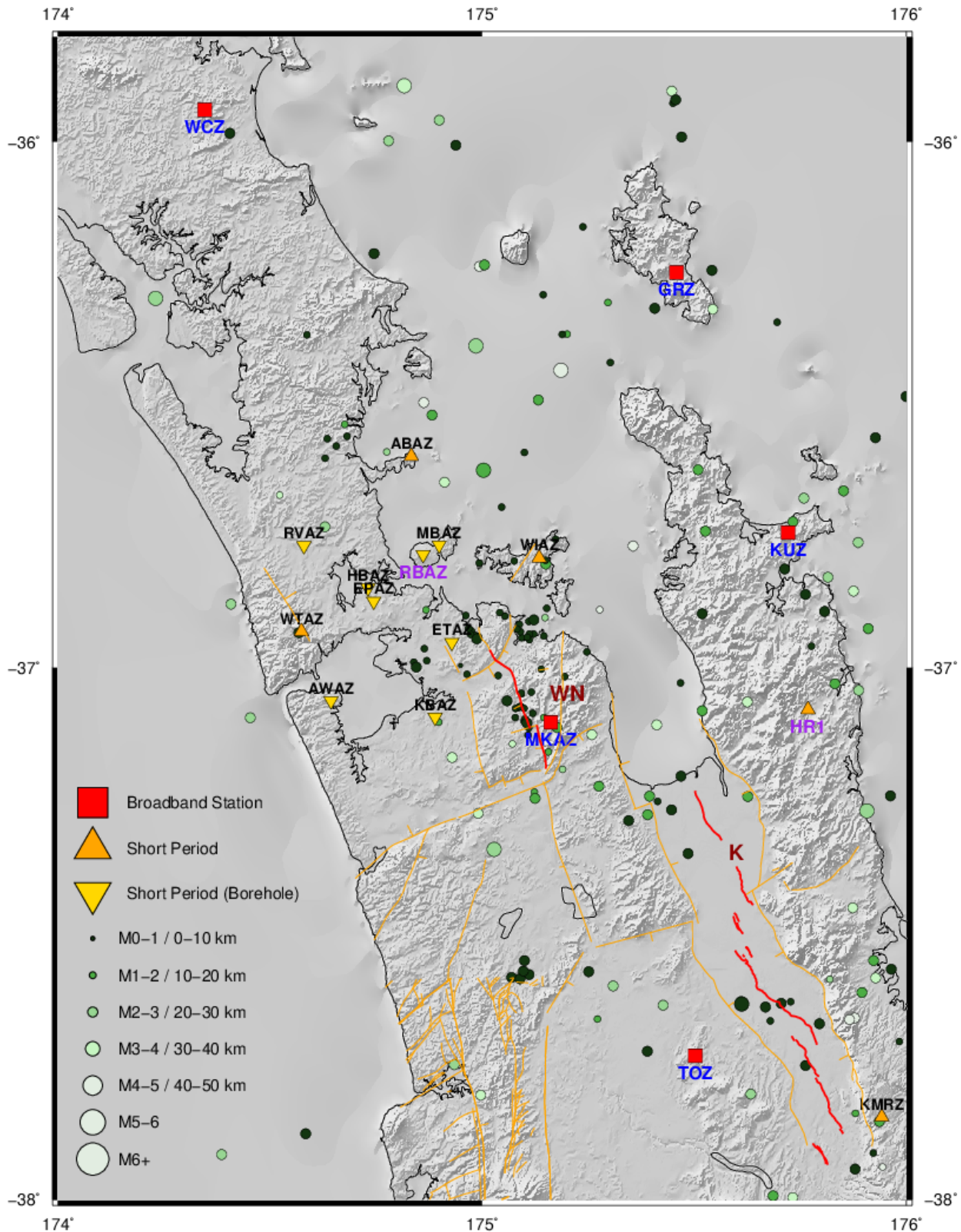


**Figure 5.17:** 186 Manually reviewed hypocentre locations of earthquakes in 2017 shallower than 50 km and horizontal and depth uncertainties <25 km (average 10.2 km). Spurious or inconsistent picks were removed and additional P- and S- wave phase picks were added where possible.

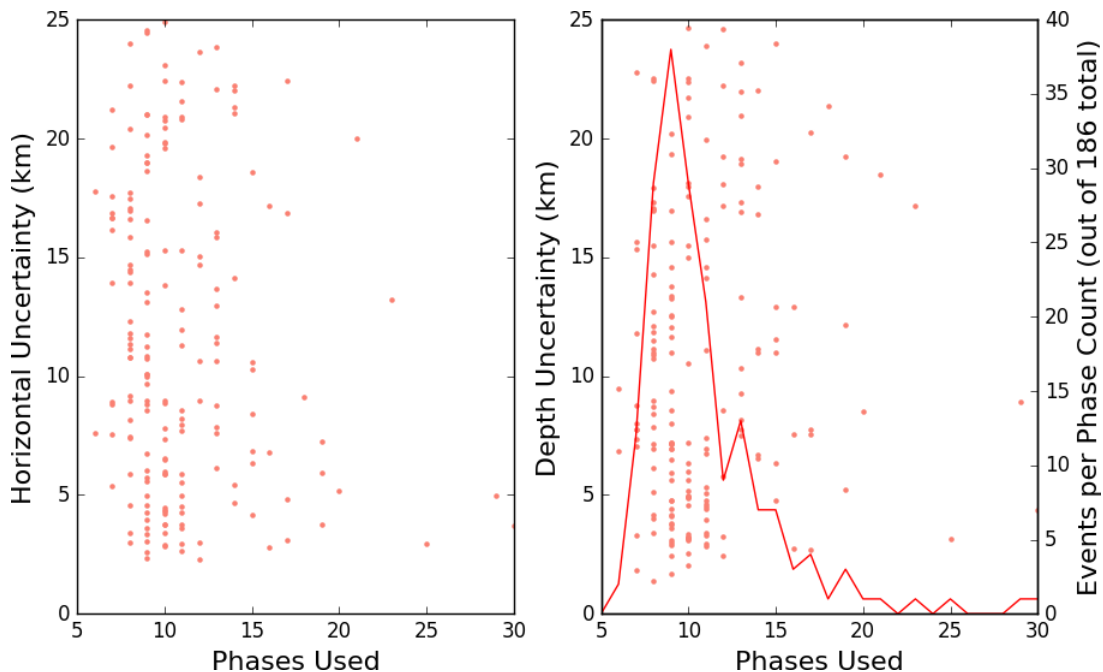


**Figure 5.18:** Horizontal (left) and depth (right) uncertainty vs. phase counts for the reviewed 2017 event data shown in Figure 5.17. Potential uncertainties rapidly decrease with the addition of additional phase picks.

The largest effect of manual reviewing is the removal of falsely located or grossly uncertain hypocentres, likely including the inadvertent expulsion of some real events. A typical "false location" was such that one or two disparate picks were biasing the solution strongly enough to erroneously shift its predicted epicentre as much as hundreds of kilometres. This was often the case when the location of stations contributing phase picks were tightly clustered instead of evenly distributed around an epicentre by distance and azimuth. The viability of hypocentre solutions in that scenario could be quickly tested by removing the outlier picks and recalculating the position using only the clustered picks, with a "fair" solution resulting in a similar location and a "false" hypocentre solution dramatically moving the hypocentre to another region altogether. If the solution was found to be "fair", the waveforms of nearby sites were searched for additional arrivals.

Near Auckland events noticeably clustered around the active Wairoa North Fault (Figure 5.17, "WN"), as well as some faults of uncertain activity (plotted in gold) to the west and north of it. This sharper resolution is not extended further east towards the active Kerepehi Fault ("K"), likely due to the relative lack of nearby sensors as well as the poor 0-5-0.7° "reach" (e.g. Figure 5.16b-B4) of the detection capability of sensors in the greater Auckland region. The amount of smaller events in the area is increased overall relative to the automatic discoveries in

Figure 5.15 due to the addition of hand-picked phase arrivals after manual review, however the number of these smaller events fall dramatically outside of the Auckland region as the average distance from the city's dense borehole array increases.

The volume and wide distribution of events within the Hauraki Gulf was surprising given the complete dearth of stations nearby, with some earthquakes extending north of 36°S. Though the uncertainty of these are much larger than those found nearer Auckland, they nevertheless portend to active strain occurring and support the idea that the Hauraki Rift may extend as north as the Whangarei Harbour (e.g. Figure 3.6 in Chapter 3). In fact, a M4.2 detected by GeoNet on Jan 3 2019 occurred at a depth of 12 km east of Whangarei as this work was being finalised, in addition to a M4.1 and M3.8 about a month later (Figure 5.19). These events were strong enough to generate dozens of citizen "felt reports" of moderate to light shaking throughout the gulf coast. Elsewhere, the volume of events parallel to the eastern shore of the Coromandel Peninsula is curious and may indicate that the presence of N-S faulting active faulting offshore in the Pacific Ocean.

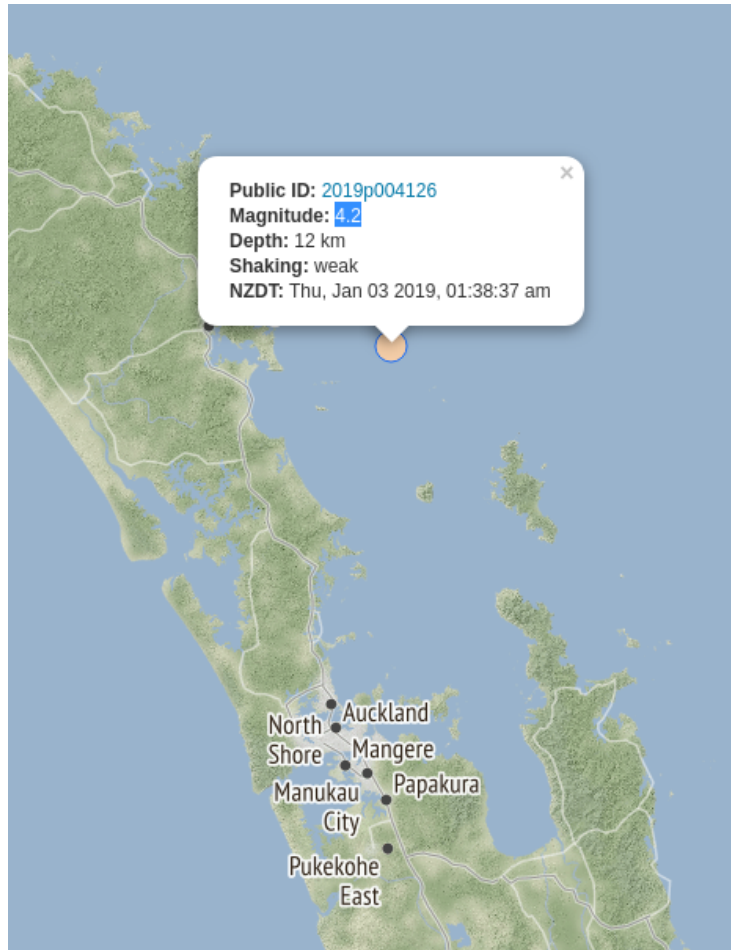


**Figure 5.19:** A M4.2 at 12 km depth detected east of Whangarei by GeoNet in early January 2019. Similar M3.8 and M4.1 earthquakes also occurred at this location in mid-February, 2019. These events seem to confirm the persistence of activity as north as 36°S and speculatively may have originated within the Hauraki Rift.

Finally the high impact that additional phase picks have on epicentre uncertainty (e.g. Figures 5.14 and 5.18) must be emphasised. In the northern North Island, the addition of just 3-5 phase picks to one of the hundreds of poorly defined solutions can have the effect of halving or even quartering its ambiguity. This has the potential to raise the yearly number of resolved events within the northern North Island by several hundred.

## 5.6 ADDITION AND UTILITY OF STATION HR1

Station HR1 (Figure 5.20) was installed in November 2016 to assist this project and to gauge the utility of temporary or otherwise non-professionally installed short period sensors in NWNZ. The site location was selected as it was near the Hauraki Rift and positioned on Coromandel

volcanic hard rock material which helps to diminish seismic wave attenuation, strengthening the signal-to-noise ratio of incoming events. It is located at a private residence which eases permitting burdens as well as provides good security and in this case, regular maintenance and upkeep of the area surrounding it. It has since proven extremely useful (plotted in gold, Figures 5.16b and 5.15c) and as such continues operating as of this writing.

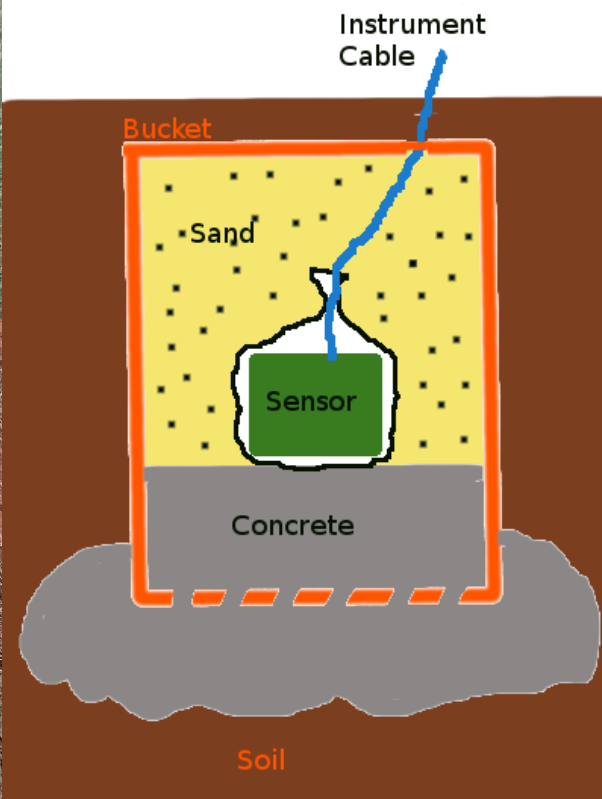


**Figure 5.20:** Seismic station HR1 installed by Pickle in November, 2016 at a private residence in Hikurangi, Coromandel, NZ. The site is on a rocky outcrop / hillside next to a garden approximately 100 m from a private residence.

The site was constructed by burying a small, sturdy, and cylindrical enclosure (here a traditional hardware store bucket) with a perforated base to facilitate pouring a significant concrete root within the soil. The sensor itself is then levelled on the dry concrete within a durable plastic bag, sealed, and carefully surrounded by dry sand to the top of the bucket,

which is then itself sealed and buried. Once the sand has settled (~days) the sensor becomes largely immune to additional shifting and the weight of the sand on the sensor minimises the loss of vibrational energy at the contact between the concrete and the feet of the sensor.

Of the ~16,000 total events throughout the North Island automatically found in 2017, HR1 contributed a phase pick to 16% of them, as well as 24% of events found within the greater Hauraki Rift region outlined by Figure 5.15. This was above average for the GeoNet network overall (Figure 5.15c) despite its northern location, short-period sensor, and presumed temporary installation period. HR1 also performed well at detecting quiet events (B-C), even surpassing several short period borehole sites in the Auckland region. Its success is probably attributed to its advantageous geographic location far from environment noise in addition to its favourable geologic position directly atop thick and dense Coromandel volcanic roots.



# 6

## DISCUSSION

---

### 6.1 INTERPRETATION OF NORTH-WESTERN NEW ZEALAND STRUCTURE

Gravity anomalies were predominantly used to interpret the general crustal structure of north-western New Zealand (NWNZ). Crustal structures (e.g faults, mountains) here are typically small enough such that they are likely to be supported by the rigidity of the  $\sim 25\text{-}30\text{ km}$  crust [Stern et al., 1987; Holt and Stern, 1991; Horspool et al., 2006; Behr et al., 2010] or  $20\text{-}30\text{ km}$  effective elastic thickness [Holt and Stern, 1991] rather than be isostatically compensated [e.g. Walcott, 1970]. This assumption is supported by the presence of large positive FAA anomalies throughout onshore NWNZ (e.g. Figure 3.2) and the approximation of Holt and Stern (1991) supposing that load widths less than four times the flexural parameter should be supported (e.g. Section 3.2.3.1, Figure 3.1). The assumption of flexural support was confirmed by numerically modelling the plate flexure in response to its topographic load throughout the northern half of the North Island (Figure 6.1) using the code "grdflexure" [e.g. Wessel, 2015] and satellite topography data [Smith and Sandwell, 1997; Becker et al., 2009] assuming a uniform  $T_e$  of  $25\text{ km}$  [Holt and Stern, 1991], uniform crustal thickness of  $27\text{ km}$  [Stern et al., 1987; Holt and Stern, 1991; Horspool et al., 2006; Behr et al., 2010], and  $2670, 3300$ , and  $1030\text{ kg/m}^3$  for the crust, mantle, and water respectively. Though the model is rudimentary, the low degree of broad plate flexure ( $< 5\text{ km}$ ) relative to the crust's thickness as well as its low spatial gradient show that nearly all of NWNZ crustal features are flexurally supported. Accordingly the Bouguer anomaly (BA) was believed to be of higher utility than the Free Air Anomaly (FAA) as it is primarily sensitive to subsurface density variations (e.g. crustal structure) which should not be strongly affected by the bowing of the crust.

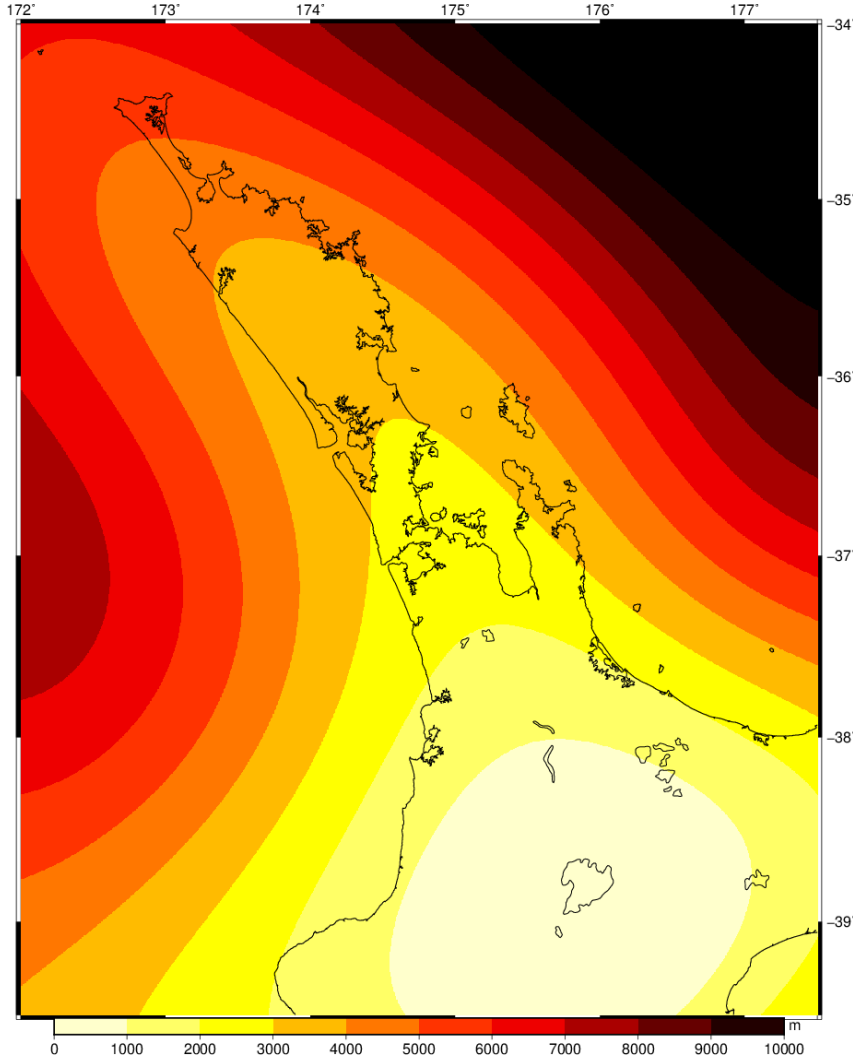


**Figure 6.1:** Numerical estimate of plate flexure ( $m$ ) in response to its topographic load, derived via GMT's "grdflexure" code [e.g. Wessel, 2015]. Assumptions included a  $T_e$  of 25 km [e.g. Holt and Stern, 1991], uniform crustal thickness of 27 km [Stern et al., 1987; Holt and Stern, 1991; Horspool et al., 2006; Behr et al., 2010], and 2670, 3300, and 1030  $\text{kg}/\text{m}^3$  for the crust, mantle, and ocean water respectively.

The satellite-derived BA (Figure 6.2) shows several on and off-shore lineaments of basement-parallel gravity lineaments throughout NWNZ which may correspond to significant structures. The negative BA associated with the Hauraki Rift (purple line) can be traced (Figure 6.2) parallel to the basement structure from near Lake Taupō {176°E, 39°S} northwards to Whangarei harbour {174.5°E, 36°S} at a length of  $\sim 330 \text{ km}$ . The explanation for rift axis' relative negative gravity anomaly is likely due to an excess of low density in-filled sediment and elevated temperatures below [Hochstein and Nixon, 1979; Hochstein et al., 1986; Hochstein and Ballance, 1993] and/or that it had a very low effective elastic thickness early in its development [e.g. Hackney et al., 2012]. The southern termination of the rift is difficult to discern but may speculatively continue

S-SW as it approaches the TVZ, as demarcated by the dotted purple line. North of 36°S, it is unclear if the Hauraki Rift terminates, continues east of the shoreline, or continues NW onshore. There is only faint evidence in the BA to support a continuation in either direction.

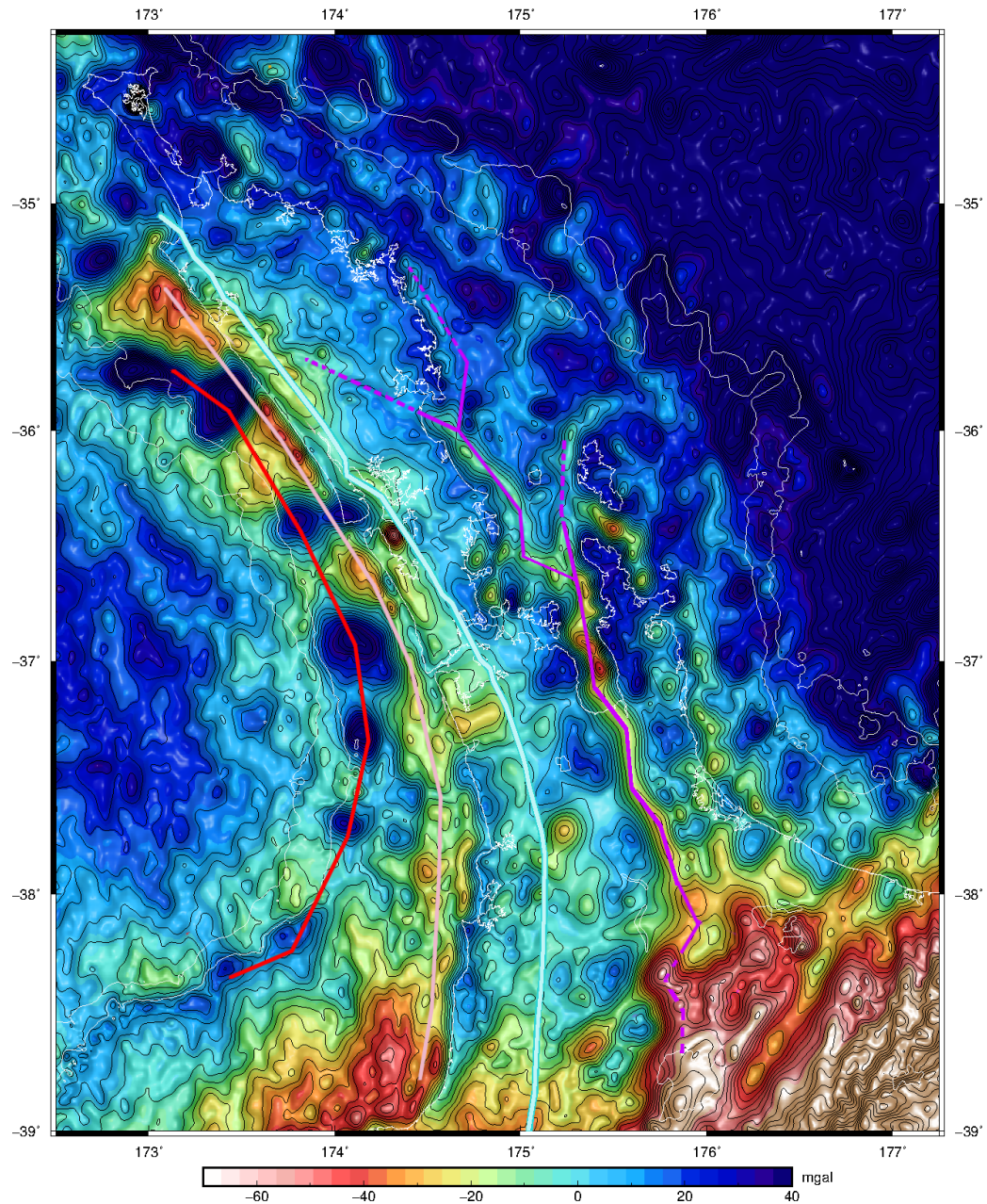


**Figure 6.2:** Structural interpretations (coloured lines) overlain on a satellite Bouguer anomaly, originally shown in Figure 3.6. Resolution is 1 arcminute and 5 mGal contours are plotted. The JMA is drawn in light blue and the Hauraki Rift in purple. The red and pink lines are speculative interpretations of a linear trend in volcanism and low-density crust, respectively. Bathymetry at 0 (shoreline), -500, and -1000 m are contoured in white.

On the western shore, a trend of strong BA lows (Figure 6.2, pink line) trace the west coast of NWNZ towards the Taranaki Peninsula. The cause of this feature is unclear but it appears to loosely coincide with the position of the Taranaki thrust fault. The bathymetry overlying this region immediately offshore is flat (Figure 2.2) and the existence of the Taranaki thrust fault parallel to this feature [Stagpoole and Nicol, 2008] should theoretically produce BA highs [e.g. Smithson et al., 1978]. The pink line's position west of the JMA (light blue line) [Eccles et al., 2005] implies that this region may overly the Murihiku Terrane [Mortimer et al., 2004; Mortimer et al., 2014] which is composed of relatively low density marine sediments [Ballance and Campbell, 1993; Black et al., 1993; Kamp and Liddell, 2000; Roser et al., 2002; Briggs et al., 2004]. Therefore the low BAs along the shore may simply be due to the presence of lower density material, however this inference is tenuous.

West and/or within the low BA lineament marked by the pink line (Figure 6.2) is a continuous chain of large buried volcanoes (red line) marked by sharp BA highs in blue. The volcanism here is aged ~23 Ma in the north and becomes progressively younger towards the south with an age of 15 Ma west of Auckland (37°S) [Herzer, 1995; Hayward et al., 2001; Booden et al., 2011; Figure 2.8]. South of Auckland the volcanoes continue becoming younger to ~2 Ma but also decrease in size and begin to curl SW away from the shore, distancing itself from the pink line of low BAs [Stagpoole and Funnel, 2001; Giba et al., 2010; Giba et al., 2013]. It is unclear if the volcanism demarcated by the red line is related to the low BAs marked by the pink line; north of ~37°S they generally overlap but begin to diverge south of this.

The red line of volcanism in Figure 6.2 also seems to correspond to a region of broad BA lows wider than those marked by the pink line. Seismic reflection data at ~38°S [e.g. Stagpoole and Nicol, 2008; Giba et al., 2010; Figure 6.3] shows both a basin and/or rift structure west of the Taranaki Fault thrust (highlighted in orange) with volcanism occurring within it. It is assumed that the volcanism demarcated by the red line overlies this basin, and that the BA lows surrounding it are the result of lower densities within this rifted structure. It is however unclear if this rifted structure has influenced or directed the location of this volcanism.

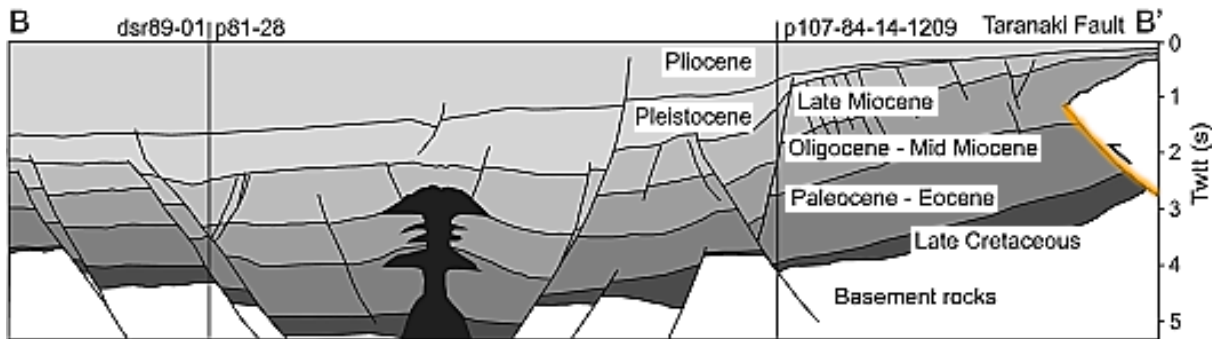


**Figure 6.3:** Interpreted seismic reflection data across the Taranaki Basin and thrust fault (highlighted in orange) at  $\sim 38^{\circ}\text{S}$ . Volcanism (black) is late Miocene. Figure is courtesy of Giba et al. (2010) with slight modifications.

#### 6.1.1 *Fault Location via Ground Station Gravity*

The ground station BA in Figure 6.4 offers a finer resolution which allows for the detection of smaller onshore faults beyond that achievable from the satellite-only data. Aside from the Hauraki Rift which was known to be a feature of gravity lows [Hochstein and Nixon, 1979] speculative faults were drawn along regions showing sharp and linear/continuous BA gradients which are implied to be the result of discontinuities between rocks of different densities. Of these, only one feature ("B") appears to be entirely new, with the remainder generally corresponding with previously known faults considered to be active ("K" and "T", black font) or faults of uncertain activity (yellow font).

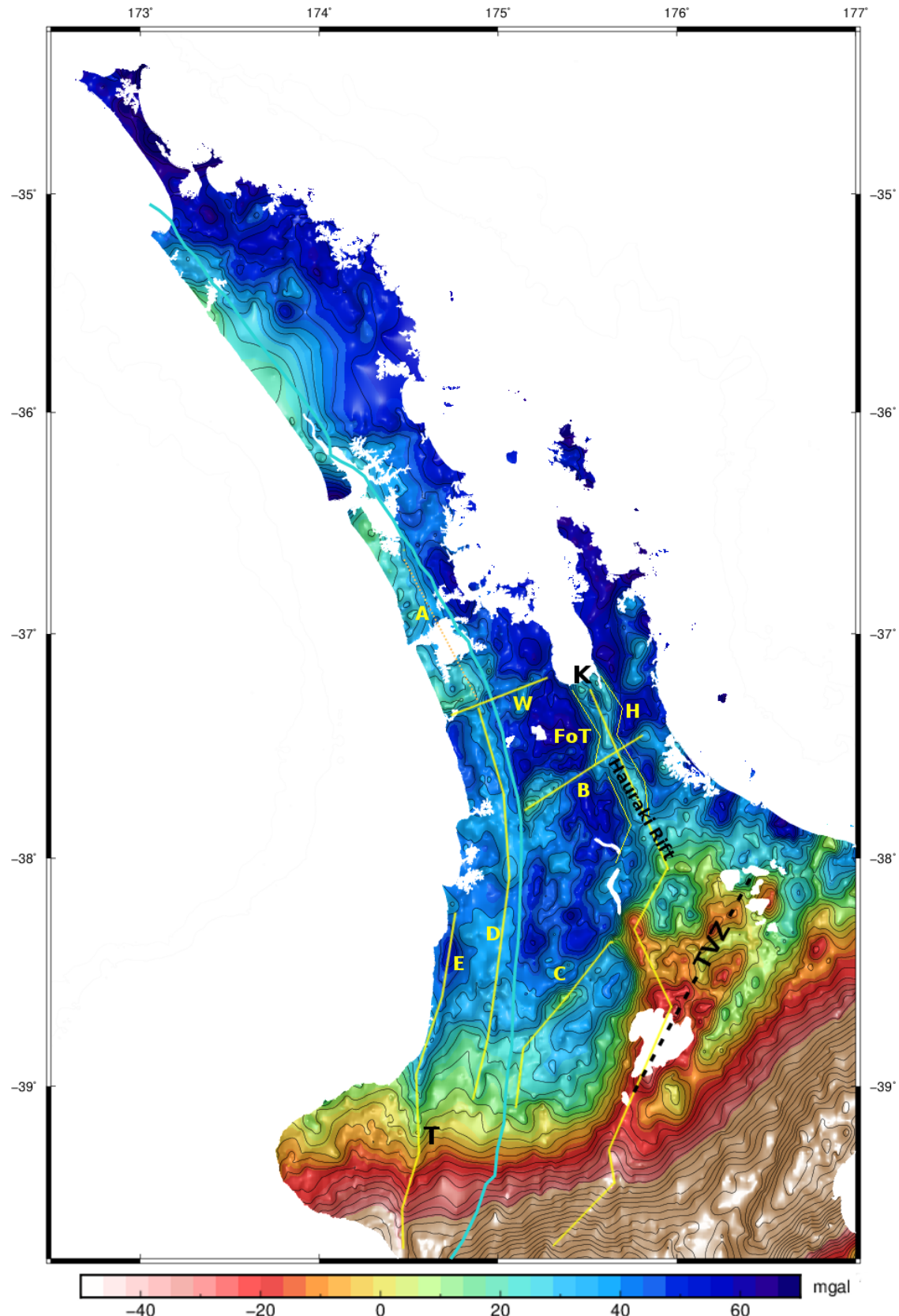


**Figure 6.4:** Bouguer gravity anomaly based on ground measurements [Robertson and Reilly, 1960], averaged and gridded at 1 *arcminute* resolution with 5 mGal contours. The JMA is plotted in light blue. Inferred faults from N-S are A = Awhitu Fault, W = Waikato Fault, K = Kerepehi Fault, H = Hauraki Fault, FoT= Firth of Thames Fault, B = Unknown/speculative, C = Ohurua-Whenuakura Fault system, D = Waipa Fault system, E = Manganui-Whareorino Fault system, and T = Taranaki Fault (continues northward offshore) [Edbrooke et al., 2005; Leonard et al., 2010; Kenny et al., 2012]. The Hauraki Rift is speculatively interpreted as continuing towards the TVZ south of 38°S.

The Waikato Fault ("W"), in combination with an unknown parallel BA feature presumed to be a fault ("B"), seems to divide the northern North Island between NE striking basement structure to the south and NW striking basement structure to the north. The fault dips normally 2.7 km to the north and is presumed to be of Cenozoic age [Hochstein and Nunns, 1976]. Its trend has been speculatively drawn here to continue east into the Hauraki Rift as part of a group of smaller, subparallel faults [e.g. the Pokeno Fault, Kenny et al., 2012]. The unproven, parallel fault "B" to the south is presumed to have been caused by the same stress field and thus may be of similar age, and is hypothetically drawn cross cutting the Hauraki Rift and into the Karangahake Gorge or Waihi Fault [Smith et al., 2006].

The Awhitu Fault ("A"), which is interpreted here as an aggregate of the Awhitu, North Scenic Drive, and Muriwai faults [e.g. Kenny et al., 2012] is speculatively drawn here as it partitions the strong low BAs east of the JMA (Figure 6.4). These low BAs could mark the presence of normal or reverse faulting, or possibly some other form of localised crustal compaction which could also explain the presence and character of the Awhitu Peninsula. The Awhitu Fault continues south into the Waikato Fault ("W") where it may terminate or possibly continue trending parallel to the basement as the greater Waipa Fault system ("D"). Both the Awhitu and Waipa fault systems are assumed to overly the Murihiku Terrane (e.g. Figure 2.5) and it is proposed that they may be part of a singular continuous feature.

Further east, the Taranaki Fault ("T") has a clear N-S gravity signature which severs the Taranaki Peninsula. This fault is known to continue south into the Alpine Fault and northwards offshore, remaining parallel to the basement structure [Stagpoole and Nicol, 2008; Giba et al., 2010]. The fault itself is hypothesised by this work to continue parallel to the shore throughout all of Northland, a notion supported by the satellite BA (Figure 6.2). The onshore BA (Figure 6.4) shows faint evidence that the Manganui-Whareorino ("E") faults may splinter off NE from the Taranaki Fault, remaining on shore.

The Hauraki Rift, with inactive Firth of Thames (Figure 6.4, "FoT") and Hauraki ("H") faults bounding the median and active Kerepehi Fault ("K"), generally trends SE until 38°S before becoming disorganised, seemingly veering SW towards Lake Taupō. The rift has been interpreted here as continuing further south towards the plate boundary but jointly, in combination with the TVZ axis. Alternatively the Hauraki Rift, or possibly just the Firth of Thames Fault, may link with the SW-NE trending Ohurua-Whenuakura Fault system ("C").

The overall faulting scheme of NWNZ is one with NW striking faults north of 37.5°S, gradually transitioning to NE striking south of 37.5°S in accordance with the overall orientation of the bending basement fabric delineated by the JMA. The transition zone between NW and NE striking basement fabric between 37°S and 38°S gives way to at least one and possibly two or more E-NE striking faults perpendicular to the basement geology which would have then presumably acted to accommodate the concentrated flexing of the crust here.

It is notable that the Wairoa North Fault between Auckland and the Hauraki Rift (e.g. Figure 2.9) which is arguably one of the most active faults in the northern North Island [Wise et al., 2011; Langridge et al., 2016] is not evident in the ground-based gravity data. Though tightly spaced 1D tracks of data perpendicular to its strike have been able to resolve it [Wise et al., 2011], this data is insufficient to produce a detailed 2D interpretation.

## 6.2 OVERVIEW OF NORTH-WESTERN NEW ZEALAND'S ACTIVITY

The sparsity of geodetic velocity vectors in NWNZ published prior to this study (Figure 6.5 [Beavan et al., 2016]), and hence the ambiguity of crustal velocities throughout NWNZ, has now been mostly filled (Figures 6.7, 6.6). NWNZ appears to be partitioned into three broad velocity regimes: Northland, and East/West Hauraki Rift. This is supported by the three distinct types of vectors produced in these areas by the custom "eastern Australian" plate definition comprising them all in Section 4.6 and Figure 4.15 (gold vectors). In Northland (north of Auckland ~37°S), velocities are consistently SW relative to continental Australia and tend to have a uniform magnitude throughout. West of the Hauraki Rift and south of Auckland sites also show a consistent SW direction but these now increase in magnitude towards the south as they approach the plate margin. Sites east of the Hauraki Rift (and south of Great Barrier Island ~36°S) all move S-SE with a consistent magnitude north of 37.5°S and an increasing magnitude south. These sites however show a large degree of variation in their direction, generally pointing mostly south in the north to SE or even SW in the south as they grow nearer to the TVZ.

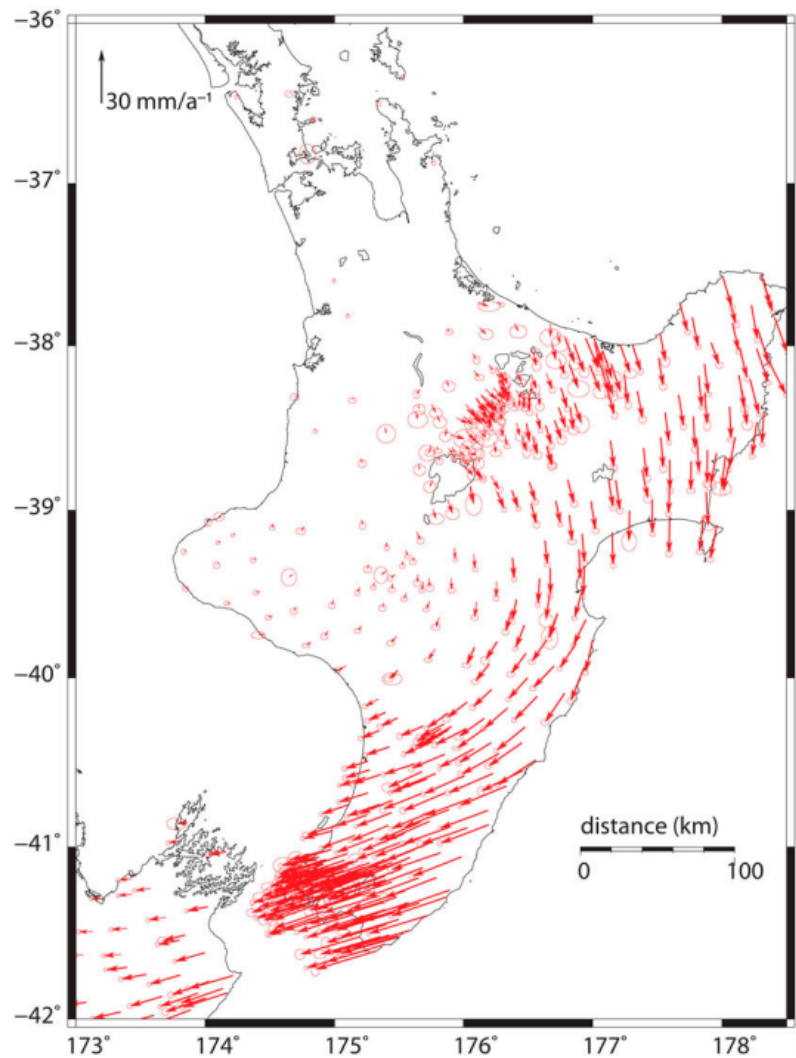


**Figure 6.5:** Geodetic velocities of the North Island 1995-2013 relative to an Australian Plate reference frame [Beavan et al., 2016].

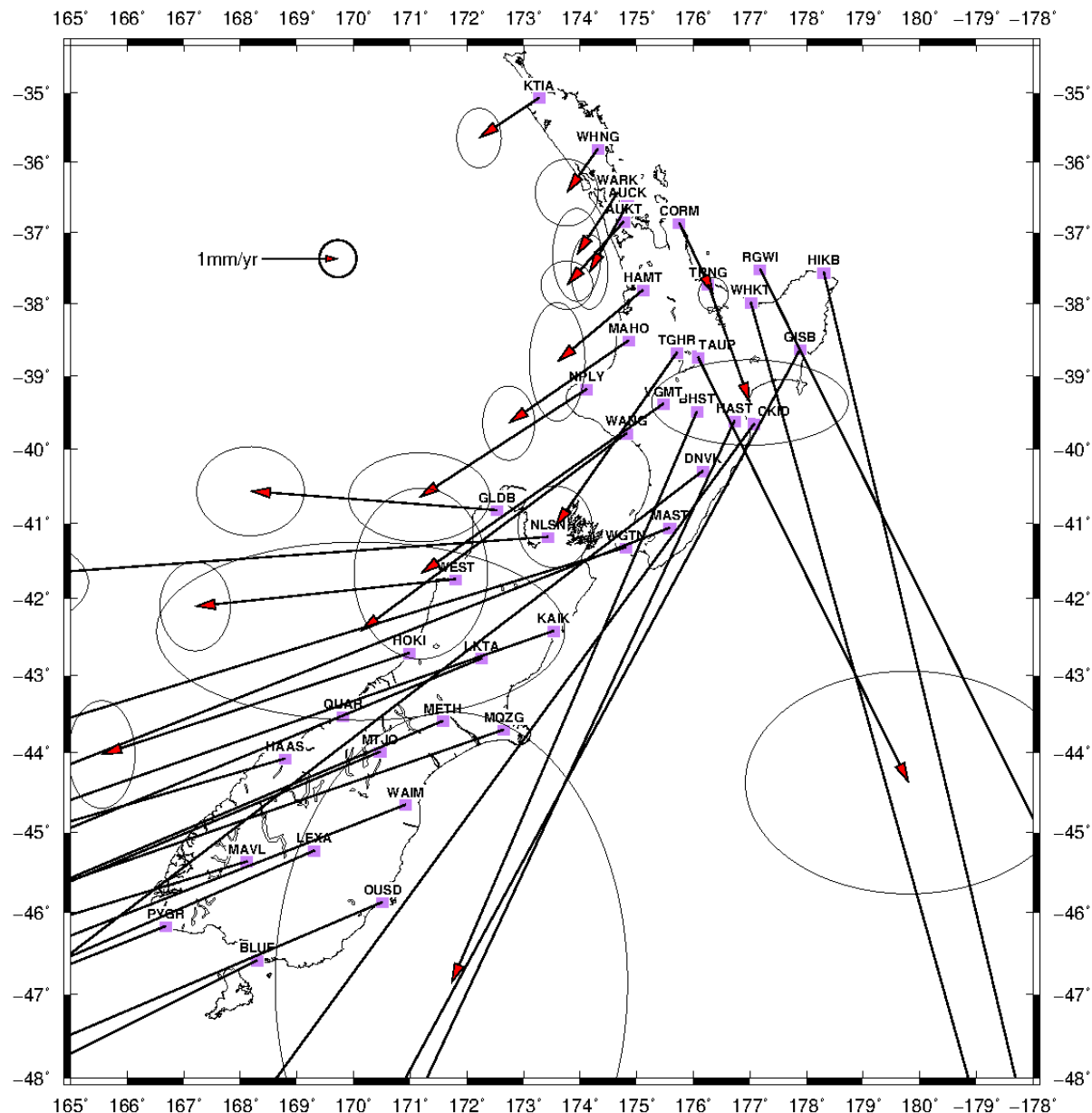


**Figure 6.6:** Nationwide geodetic velocities of various cGNSS sites with expanded velocity scale to resolve low-velocity sites.

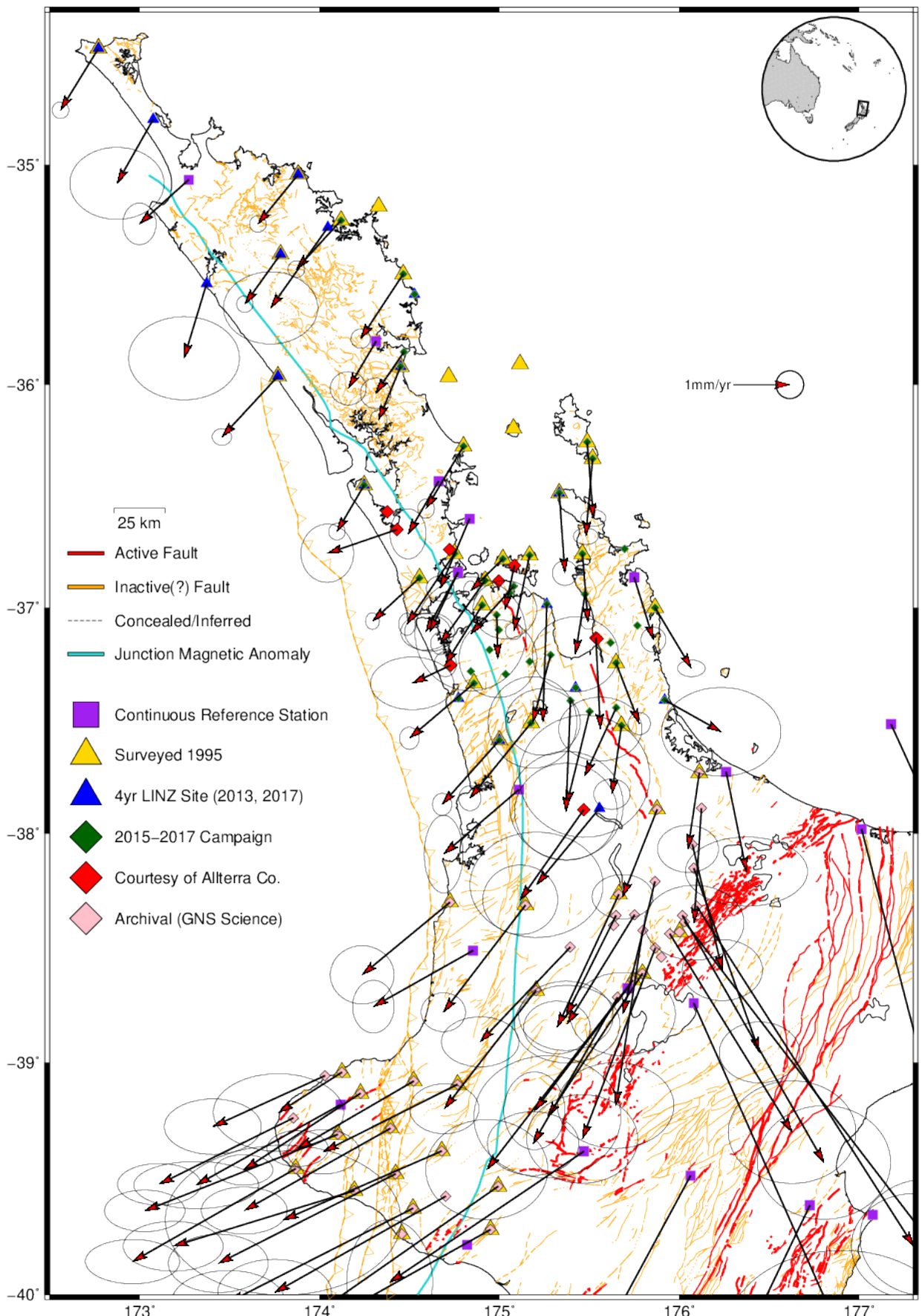


**Figure 6.7:** Geodetic velocities throughout north-west New Zealand. Some poorly fitting vectors have not been plotted, however their site markers remain.

The Hauraki Rift itself can be traced into Lake Taupō by following divergent site vectors (Figure 6.7), though the rift's geometry does not appear to be linear south of 37.5°S. This is not clearly evident in the gravity data (e.g. Figure 6.4). The nonlinearity of the rift's widening may imply that there is variation in the degree of strain accumulation along the rift zone, potentially jumping between the Kerepehi and Hauraki faults. The subtle widening observed between Tauranga/TRNG and the campaign sites west of it conspicuously coincides with a low BA signature (Figure 3.6) which may be evidence of additional widening here, though it is conceded that the velocity vector at TRNG has a high degree of uncertainty (e.g. Appendix A.2).

The larger-scale clockwise pattern of velocities observed throughout the southern North Island (Figure 6.5) does not appear to manifest itself at the Taranaki Peninsula {174°E, 39.4°S} nor anywhere NW of the TVZ, except for possibly at some sites east and south of the Hauraki Rift (e.g. Tauranga/TRNG). This observation in combination with the dramatic drop in vector magnitudes from 20-40  $mm/yr$  SE of the TVZ to 1-2  $mm/yr$  NW implies that the TVZ strongly insulates NWNZ from most of the stress generated at the plate boundary.

The non-zero magnitude of the Northland vectors relative to this project's Australian Plate reference model (e.g. Section 4.6) is interesting as several of these sites are over 700  $km$  from the active plate boundary. Globally, strain associated with an active plate boundary is atypical at these distances but are seen near Cascadia, Sumatra, and South America [e.g. Kreemer et al., 2014]. Beyond the mere presence of non-zero velocities in Northland, it is notable that the magnitude and direction of these surface velocities is consistent over the 300+  $km$  distance between Auckland and the northernmost North Island. If this motion were exclusively the product by plate margin stresses, it would be expected that velocity magnitudes should continue to diminish away from the plate boundary as stress is dissipated. However in NWNZ, strain only appears to diminish as far north as Auckland (37°S). In an attempt to remove the apparent "background" velocity throughout NWNZ, manifesting itself in the Northland sites, the velocity of cGNSS site KTIA in Northland was removed from all sites in Figure 6.7 producing Figure 6.8. This view highlights the extent of influence plate boundary stresses have on NWNZ, which clearly pulls the Coromandel Peninsula and Great Barrier Island east of the Hauraki Rift E-SE. West of the rift, the crust appears to be stable (within error) north of 37°S.

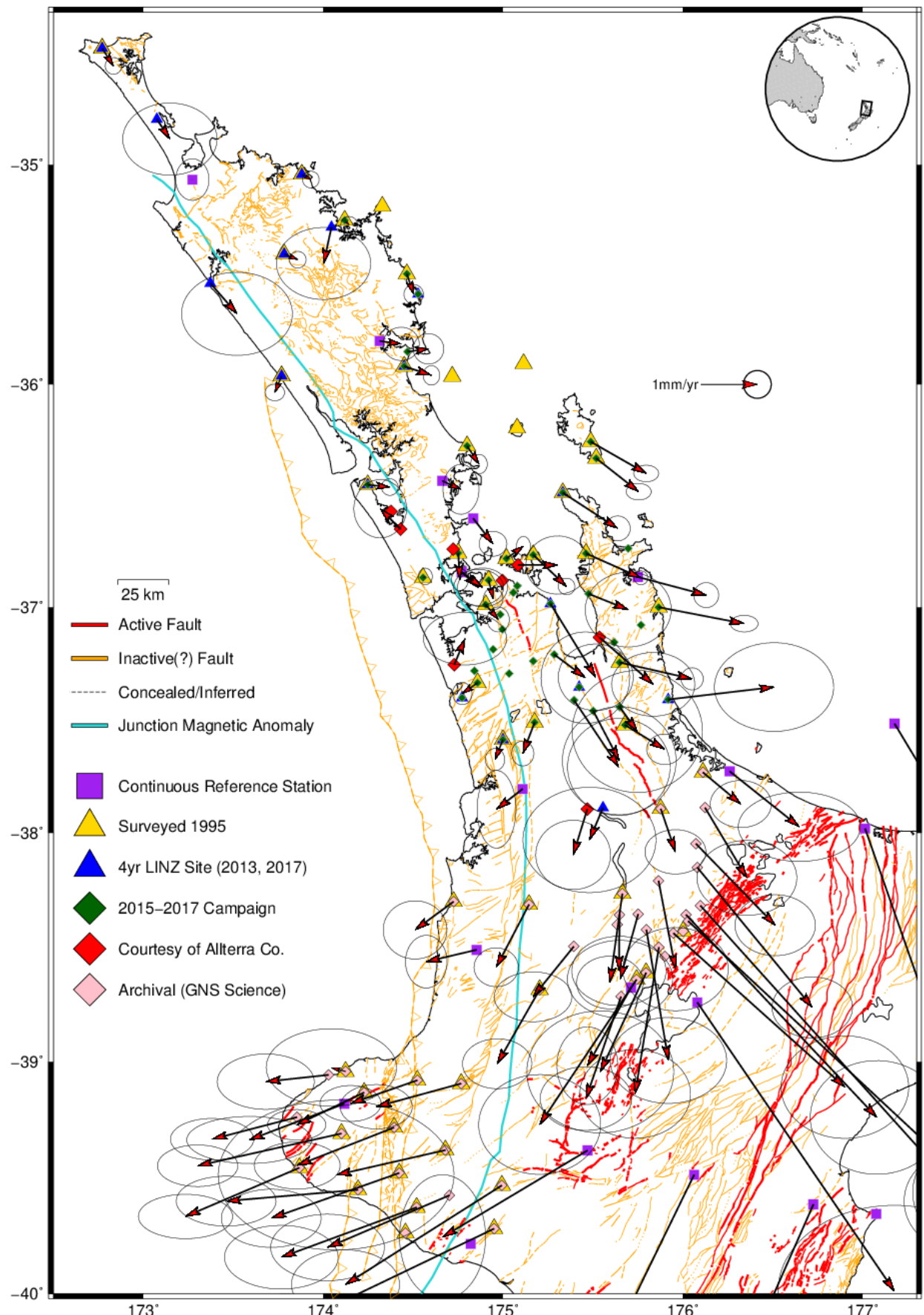


**Figure 6.8:** Velocity estimates relative to cGNSS site KTIA (northern-most Purple icon). In this view the clockwise rotation generated at the plate margin appears to affect the eastern half of the Hauraki Rift but the western half north of 37°S (including Northland) appears to be stable.

### 6.2.1 Is Plate Boundary Strain Driving the Hauraki Rift?

The horizontal velocity estimates with the “background” Northland velocities removed (e.g. Figure 6.8) strongly hint that the E-SE velocities east of the Hauraki Rift appear to be extensions of the clockwise velocity field throughout the eastern North Island [e.g. Figure 6.5; Wallace et al., 2004]. Thus it is presumed that the stress driving the Hauraki Rift wider W-E is generated from the oblique subduction of the Pacific Plate at the Hikurangi Margin. This stress appears to extend across the TVZ to distances 400-500 km from the subduction zone, potentially reaching Whangarei harbour (~36°S).

As an additional check, the second invariant strain rate tensor shown in Figure 6.9. The same methodology as in Section 4.8 was used except that the derivation of the second invariant of the strain rate tensor is computed via a slightly different [e.g. Frank, 1966] but fundamentally similar method for calculating a shear strain maximum. The data here only incorporates cGNSS sites within and/or SE of the TVZ which are presumed to directly represent stress from the plate boundary, which then is used to predict the extent to which strain may extend NW into the Hauraki Rift and Northland. This data shows that strain rates of 5-15 *nanostrain/yr* are possible throughout the greater Auckland and Hauraki Rift region, roughly 30% of those seen within the quickly deforming (~30 mm/yr) regions nearer the plate boundary. This would then imply that the thermally weakened TVZ significantly insulates much of NWNZ from plate boundary stresses.

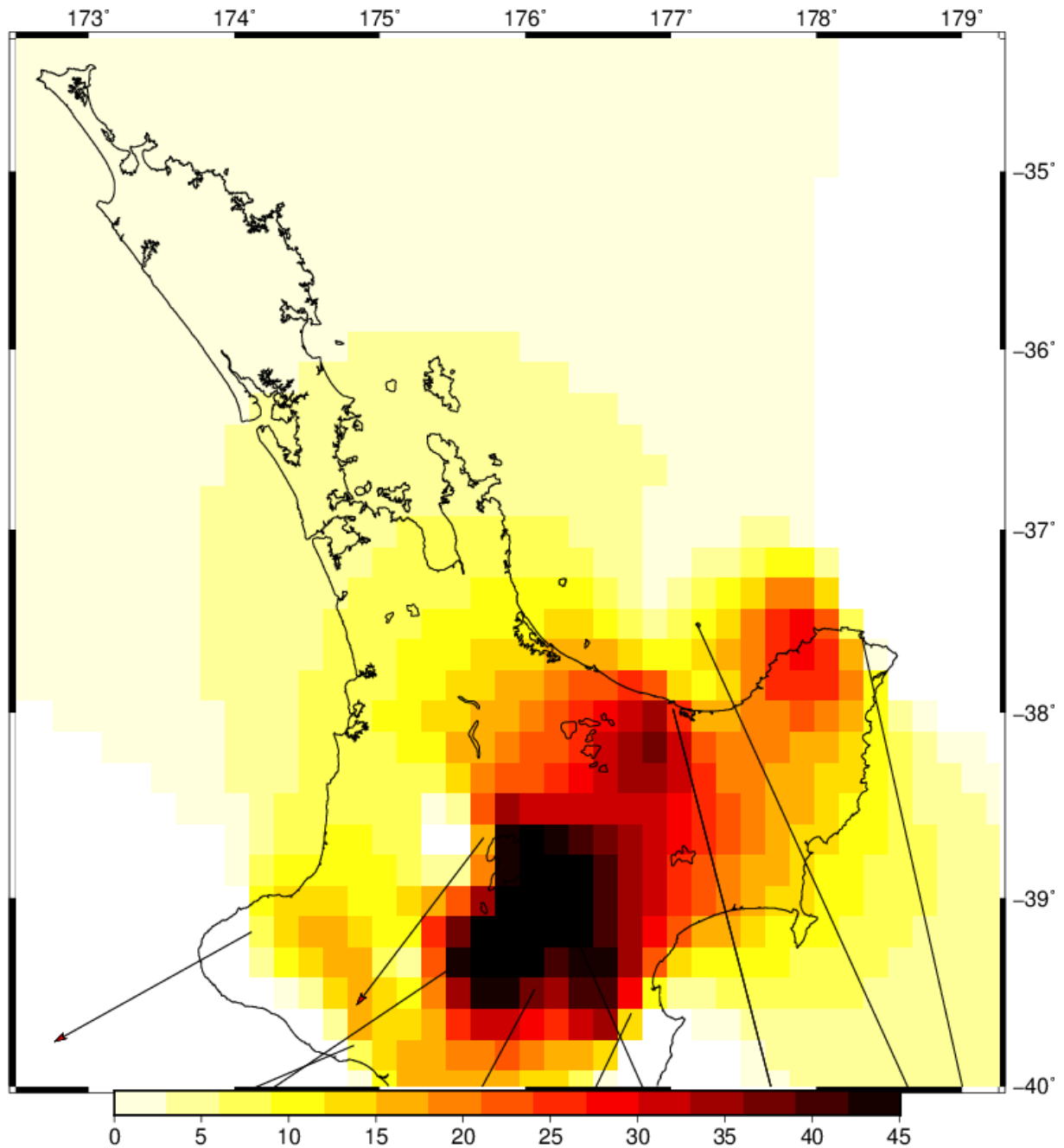


**Figure 6.9:** Second invariant of the strain rate tensor, NWNZ (nanostrain/yr) using only the velocity data plotted. Strain generated at the plate boundary appears to be capable of driving the Hauraki Rift's widening.

### 6.2.2 Vertical Deformation Estimates

The vertical resolution of GNSS systems is well-known to be poor relative to horizontal for a variety of reasons, but principally that satellites are unable to constrain the position of an

antenna from above *and* below it simultaneously in the same way that is possible E-W or N-S [Seeber, 2003]. However with a long enough timeseries (e.g. >4.5 years [Blewitt and Lavallée, 2002], or possibly as much as 6 years for New Zealand [Houlié and Stern, 2017]), reasonable estimates can still be made. Figure 6.10 shows the majority older (>10 years) cGNSS stations in the North Island. Vertical estimates were made by fitting a linear least-squares fit to weighted timeseries data (e.g. Appendix A.4) after all antenna and earthquake offsets were corrected.

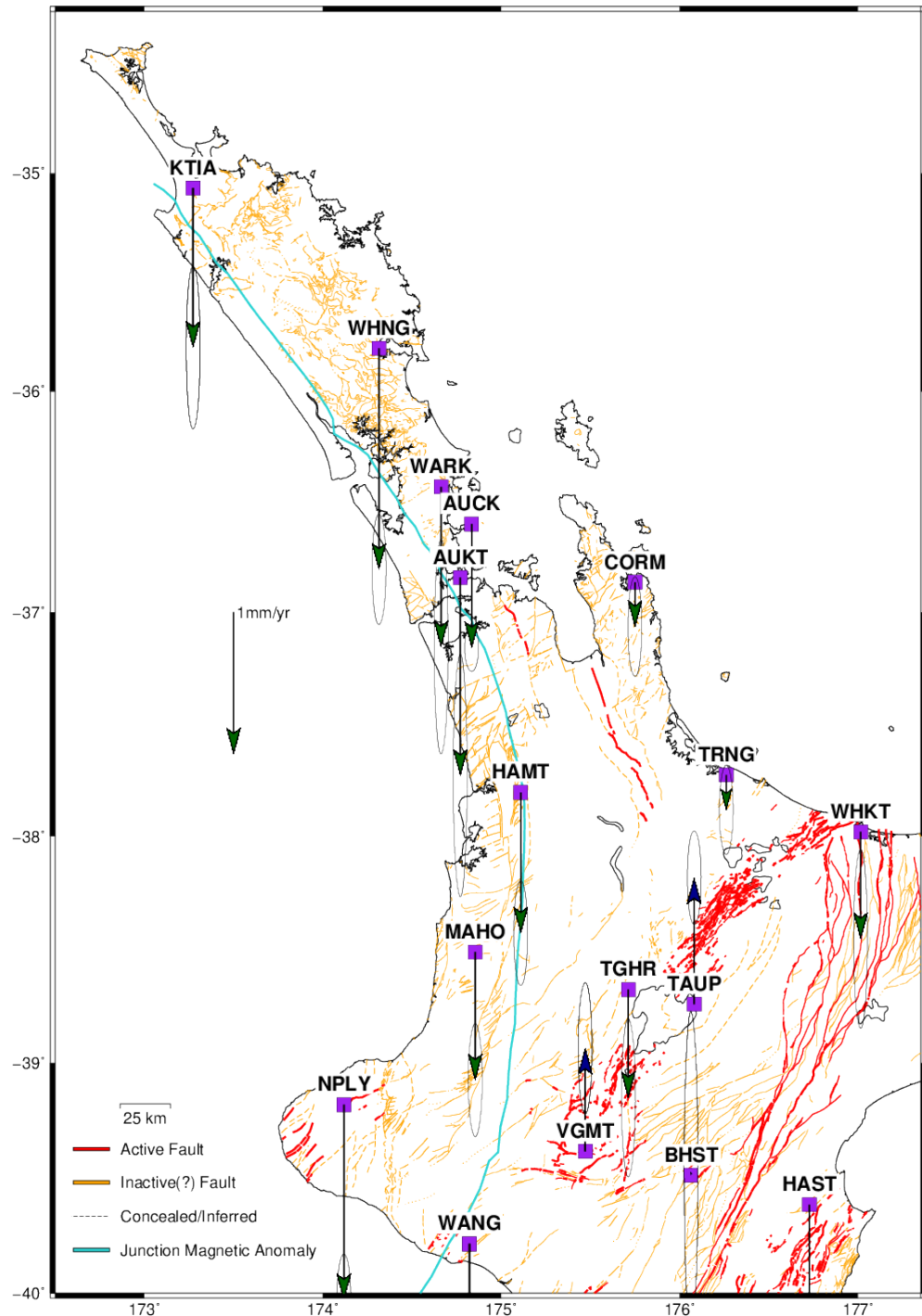


**Figure 6.10:** Vertical velocity estimates at cGNSS sites (>10 years) throughout north-western New Zealand.

The vertical component of most of the older (>10 years) cGNSS sites in the North Island are shown in Figure 6.10. By meticulously correcting for all offsets in the timeseries, as well as having an extended 10+ year history of available data, this project was able to constrain vertical velocities typically between 0.1-0.5 mm/yr (Table 6.1). Vertical velocities of each continuous

cGNSS Site	Vertical Velocity Without Random Walk (mm/yr) (negative = subsiding)	Vertical Random Walk $\sigma (\alpha * Age^{-0.5})$	Age (years)
KTIA	-1.12 +/- 0.23	0.15	11.6
WHNG	-1.56 +/- 0.16	0.19	16.1
WARK	-1.13 +/- 0.31	0.21	10.3
AUCK	-0.87 +/- 0.07	0.12	23.7
AUKT	-1.39 +/- 0.35	0.20	9.3
CORM	-0.31 +/- 0.14	0.11	16.0
HAMT	-0.99 +/- 0.15	0.11	16.0
TRNG	-0.25 +/- 0.13	0.17	16.3
MAHO	-0.90 +/- 0.16	0.26	15.3
TGHR	-0.76 +/- 0.23	0.19	12.0
NPLY	-1.38 +/- 0.13	0.11	16.2
WANG	-2.29 +/- 0.22	0.18	15.1

**Table 6.1:** Vertical subsidence estimates for most cGNSS sites in NWNZ. The average rate of high-quality Northland sites (KTIA, WARK, AUCK, HAMT) is -1.1 mm/yr (std = 0.17). Sites with 15+ years of continuous data tend to produce  $1\sigma$  errors < 0.3 mm/yr when also incorporating time-dependent Random Walk noise. The  $\alpha$  values used to calculate Random Walk uncertainty are given in the "RW" column of Table 4.3.

station are calculated by fitting a weighted least-squares linear trend to its offset-corrected timeseries data, and adding extra Random Walk ( $\sim f^{-2}$ ) uncertainty (Table 6.1). The average rate of subsidence in the northern North Island (KTIA, WARK, AUCK, HAMT) is 1.1 (std 0.17) mm/yr. Site WHNG (subsiding 1.56 +/- 0.35 mm/yr) is a probable outlier as its vertical position has been increasingly affected by a tree growing nearby which was removed in 2018 [Elisabetta D'Anastasio, personal comm., 2018]. The unfavourably located tidal station AUKT (1.39 +/- 0.55 mm/yr) is also likely to be an outlier. Subsidence rates are generally constant in NWNZ but increase to the south-west near the Taranaki Peninsula (south of MAHO). The north-west border of the TVZ (VGMT, TGHR, TRNG) has high variability with some sites showing no subsidence or even uplift between 0-1 mm/yr, also observed by Houlié and Stern (2017). Note that these sites are not within the TVZ, which is subsiding at the centimetre scale [e.g. Hamling et al. 2015; Holden et al., 2015]. The cause of this uplift between the subsiding northern North Island and the TVZ is unclear.

The 0.9-1.1 mm/yr subsidence in the greater Auckland area predicted here between 1995-2019 is marginally faster than ITRF14's 0.82 mm/yr estimate [Altamimi et al., 2016] but disagrees

with the  $0.42 \text{ mm/yr}$  average rate of *uplift* since 50 Ka estimated by dating nearby marine terraces [Claessens et al., 2009] and the  $0.3 \text{ mm/yr}$  of uplift estimated by terraces between Taranaki and Auckland [Chappell, 1975]. This could reflect a real geologically instantaneous change potentially caused by alterations in the region's local climate or hydrology [e.g. Davis et al., 2004]. Assuming coastal NWNZ is now actively subsiding, this will exacerbate the effect of the ongoing rise in global sea level recently estimated at rate of  $2\text{--}4 \text{ mm/yr}$  [Dangendorf et al., 2017] and tectonism should therefore be considered in planning for this hazard.

### 6.3 EVIDENCE FOR NEW ACTIVE FAULTS

This project attempted to find active faults in onshore NWNZ by first noting existing crustal discontinuities using the Bouguer anomaly of ground station gravity data (Section 6.1.1), then using geodetic (Section 6.2) and seismic (Chapter 5) data to confirm or deny that these gravity-deduced features were still active. It is acknowledged that in many cases this testing sometimes relies heavily upon very few geodetic vectors with subtle spatial variability. Further, the seismicity throughout the northern North Island outside of Auckland (e.g. Figure 5.6, and recent  $\sim\text{M4}$  events east of Whangarei in Figure 5.19) was often found to be too sparse to have much utility in fault-finding.

#### 6.3.1 Greater Auckland Region

The Auckland region is hypothesised to be divided into several discrete blocks with varying confidence (colour-coded, Figure 6.11) bounded by known or possible faults, with the clearest velocity discontinuities on either side of the Hauraki Rift as well as those near the west coast, west of the Awhitu Fault ("A") (dark blue). Within the rift, the western velocity of site B36J relative to sites east of it (red and yellow) may indicate that some degree of extension is occurring on the Hauraki Fault ("H"), the eastern boundary fault of the Hauraki Rift in addition to the sole "active" fault, the Kerepehi Fault, in the centre of the rift. East of the rift the discontinuity between the northern (yellow) and southern (red) vectors is tenuous and it is unclear which fault, if any, could be accommodating this. It is also likely that the increasing eastern component of the velocity vectors towards the south is due to an increased influence of

plate boundary stress (e.g. Figure 6.9) rather than a fault between the red and yellow vectors for which there is no significant gravity (Figure 6.11) nor seismic (Figure 5.17) evidence.

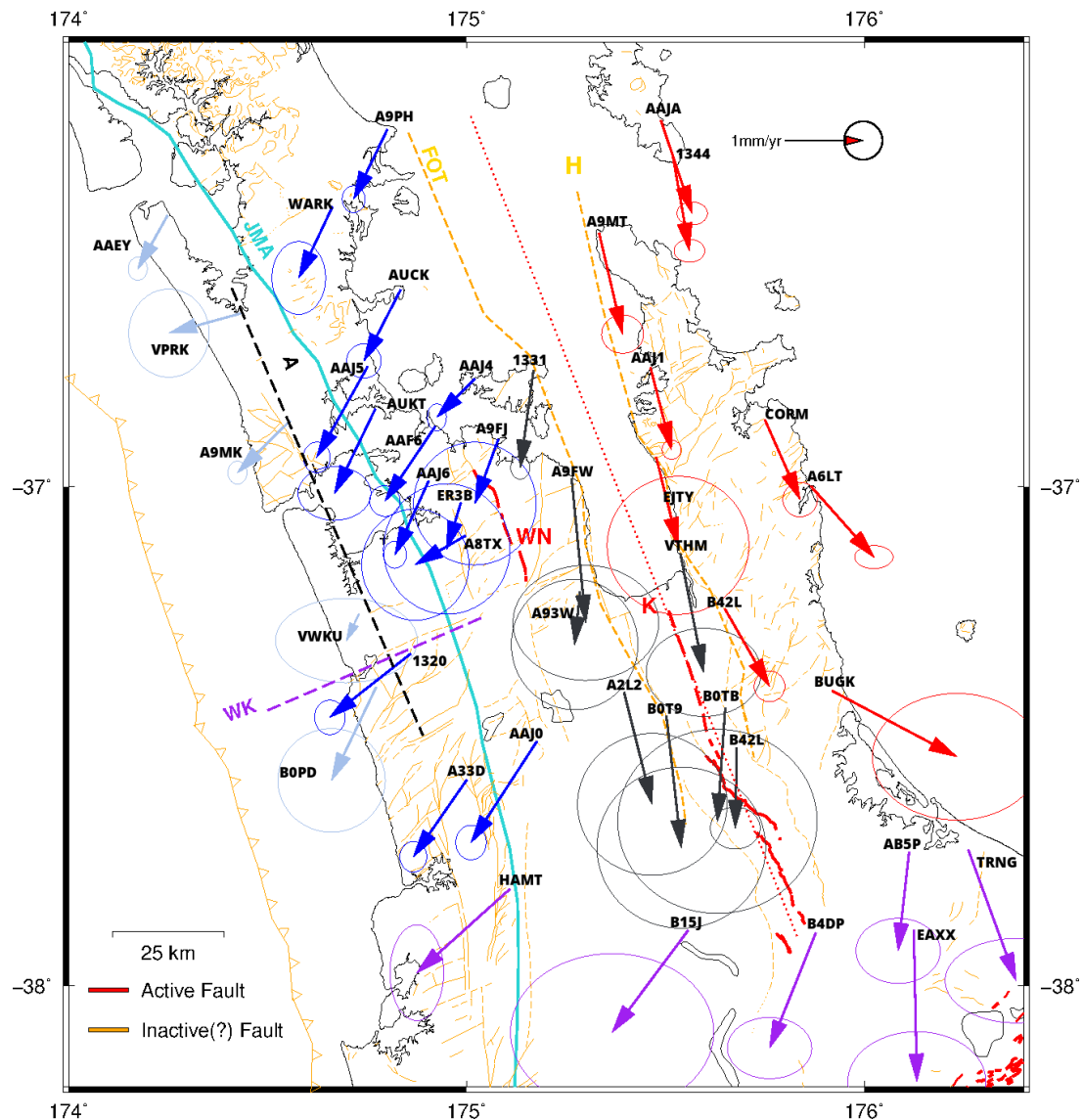


**Figure 6.11:** Geodetic vectors colour-coded by discrete regions. A = Awhitu Fault, WN = Wairoa North Fault, JMA = Junction Magnetic Anomaly (light blue), FOT = Firth of Thames Fault, H = Hauraki Fault, WK = Waikato Fault. An off-shore extension of the Taranaki Fault [e.g. Uruski, 2015] is drawn in toothed yellow. Faults are plotted in gold/white, known active faults in red [Langridge et al., 2016].

Geodetic velocity estimates indicate the Waikato Fault (Figure 6.11, "WK") may show right-lateral motion but its eastern extent is uncertain from the resolved GNSS data. Assuming the Wairoa North Fault ("WN") is the result of some form of west-transformed partitioning of strain on the Hauraki Rift, the Waikato Fault (or one its sub-parallel faults) may serve as an active transform between them. The field station BA (Figure 6.4) shows evidence for faulted structure from the western Tasman Sea coast along the Waikato Fault east to the Hauraki Rift

but there is no evidence for further continuation east into the Coromandel Peninsula which could separate the yellow and red vectors there.

Directly north of the Waikato Fault is the N-S trending "Awhitu" Fault ("A", Figure 6.11, technically an aggregate of the Awhitu, North Scenic Drive, and Muriwai faults of Kenny et al. (2012)). This fault separates the E-W shortened vectors near the coast (AAEY, VPRK, A9MK, VWKU) from those south of the Waikato Fault and those east towards Auckland. It is supposed that these shortened vectors are the result of the Awhitu Fault complex accommodating E-NE compression. The low BAs in this region may then be due in part to crustal thickening resulting from this compression, however the source of the stress generating this compression is unclear.

Sites east of the Wairoa North Fault ("WN") and west (or within) the Hauraki Rift zone (Figure 6.11, grey) generally feature low rift-perpendicular velocities with a strong southerly component relative to the sites near Auckland (light blue) to the west. While it is known that the Wairoa North Fault itself is active [Wise et al., 2003], the distribution of well-resolved GNSS stations in the area is too sparse to rule out that other faults may also be accommodating motion. In particular, the disparity between the vectors on either side of Waiheke Island (AAJ4 and 1331) may imply the existence of an additional sub-parallel fault north and to the east. Though GNSS data is lacking here the presence of the nearby seismic station array positioned around the Auckland Volcanic Field provided a means to detect microseismicity in the region (Figure 6.12). New events detected by this project found a high volume of shallow (<10 km) and small ( $M < 1$ ) events NW beyond the extent of the mapped Wairoa North Fault, as well as events veering NE bending through Clevedon { $175.1^{\circ}\text{E}$ ,  $36.9^{\circ}\text{S}$ } towards the centre of Waiheke Island, possibly along the Papakura Fault. This may confirm that the widening GNSS vectors on either side of Waiheke in fact represent active faulting.

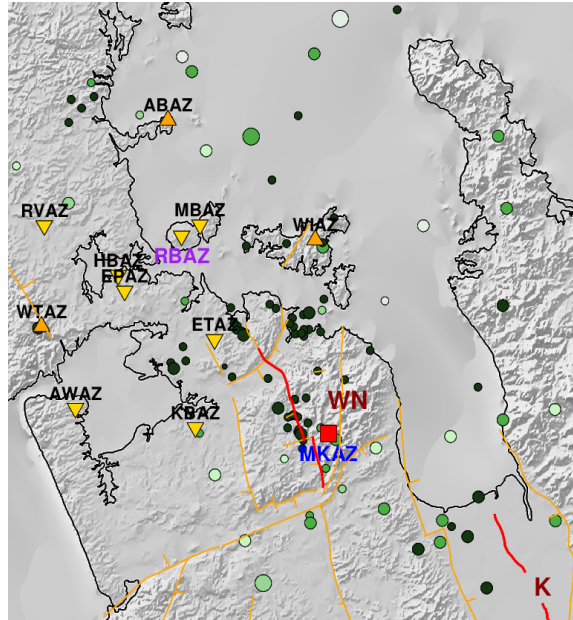


**Figure 6.12:** Seismicity around the Wairoa North Fault ("WN"), taken from Figure 5.17 in Chapter 5.

The overall structure of the Auckland and Hauraki Rift region appears to be partitioned N-S by at least three active N-S trending faults parallel to the structure of the basement: the rift axis itself (Kerepehi Fault, and possibly the Hauraki Fault), the Wairoa North Fault ~33 km east of the rift, and the Awhitu Fault another ~40 km east. The widening of the Hauraki Fault is presumed to be the result of plate boundary stress (Section 6.2.1) and the Wairoa North Fault is assumed to be as well. In contrast, apparent shortening on the Awhitu Fault may be driven by an unknown stress or presence of a compressional deformation zone offshore to the west as the region is better described by E-W shortening rather than extension. The source of this stress or deformation zone is hypothesised to be the same as that generating the elevated velocities throughout Northland (e.g. Figure 6.7) relative to this project's Australian reference frame. Activity on the Waikato Fault remains nebulous; while there is evidence that the geodetic vectors to the north and south of the fault are accommodating right-lateral strain (Figure 6.11) these vectors are poorly resolved. Furthermore this project did not note any unusual seismic activity in the vicinity of the Waikato Fault.

### 6.3.2 Greater Taranaki Region

The geodetic vectors in the Taranaki Region (Figure 6.13) are plotted relative to cGNSS stations Plymouth/NPLY (A) and Mahoneui/MAHO (B) to highlight the anomalies here. This region

is under a high degree of active and potentially non-rigid deformation (e.g. Figure 4.11) and frequently experiences large earthquakes and slow slip events [Wallace and Beavan, 2006; McCaffrey et al., 2008; Wallace and Beavan, 2010; Wallace et al., 2012; Wallace et al., 2014; Wallace et al., 2018] giving its interseismic velocity estimates a high degree of uncertainty. Regardless clear NE-striking right-lateral faulting is evident between site MAHO and campaign sites AH33/B34C/B4AU immediately east, confirmed by the presence of high strain measurements (Section 4.8). The fault(s) accommodating this is likely to be within the Waipa fault system, which is not currently classified as active.

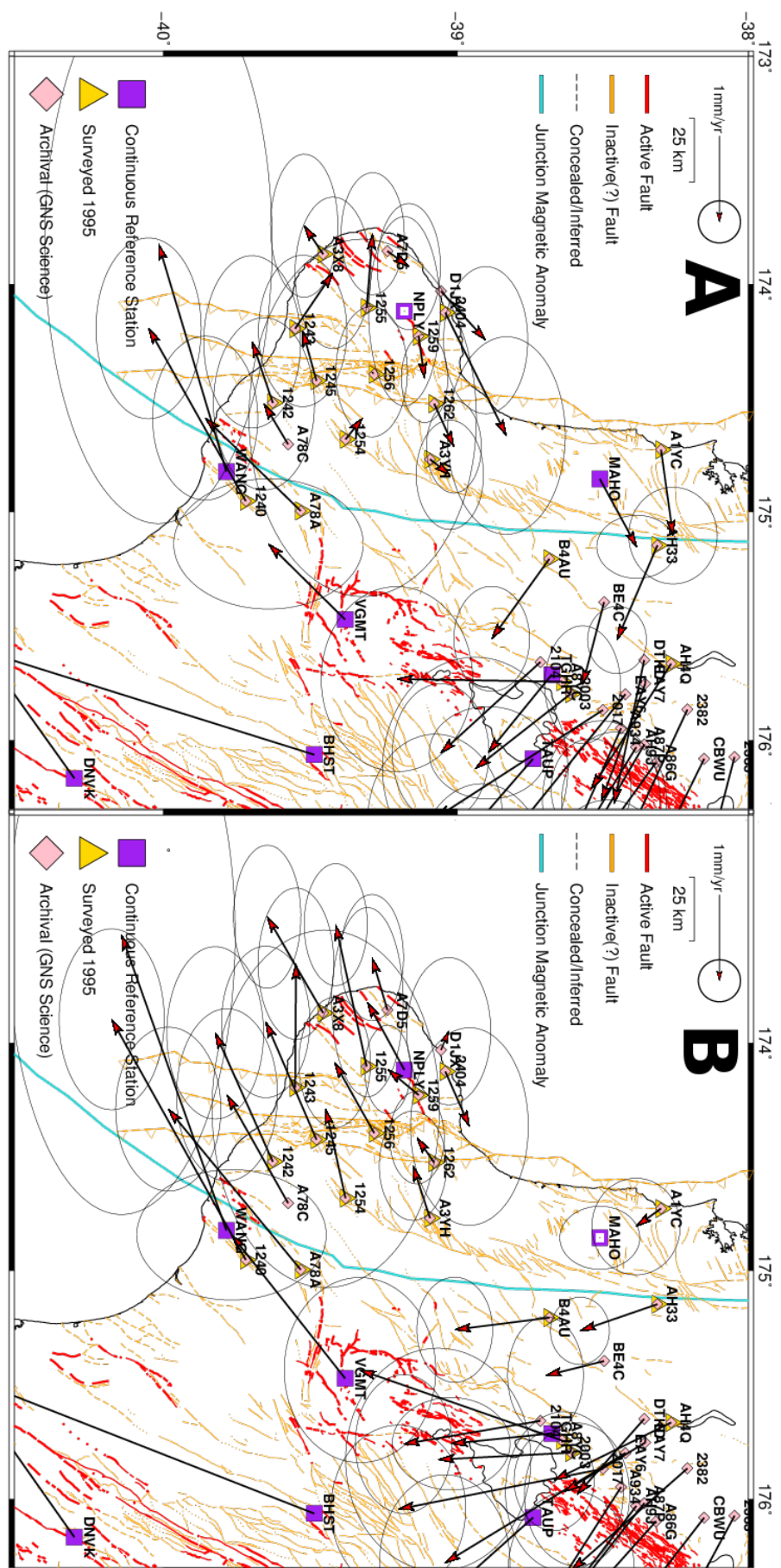


**Figure 6.13: Velocities relative to cGNSS stations NPLY/New Plymouth (A) and MAHO/Mahoneui (B). Both plots show compression occurring on the Taranaki Fault (toothed) as well as dextral motion on the northern Taranaki Peninsula (e.g. Cape Egmont Fault System) and Waipa Fault east of MAHO (e.g. Figure 6.4).**

Nearer the Taranaki Peninsula {174.1°E, 39.3°S} both NPLY and MAHO-relative interpretations show net E-W compression on either side of the Taranaki Fault (Figure 6.13, toothed) implying that it is still potentially active. As the northern extent of the Taranaki Fault continues off-shore [e.g. Stagpoole and Nicol, 2008] its activity cannot be inferred from geodesy. Its northern extent is also difficult to reconcile seismically due to the lack of seismometers in the region (e.g. Figure 5.7). Regardless this project's relocated earthquakes (Figure 5.6) show that there is still tectonic activity offshore in the vicinity of the Taranaki Fault at least as north as Hamilton (~37.5°S).

On the northern edge of the Taranaki Peninsula there appears to be relative eastern motion. This is probably accommodated by the active Cape Egmont Fault System [Nicol et al., 2005] (Figure 6.13, red lines on western end of peninsula) which therefore must trace further east than currently interpreted by the Active Faults Database [Langridge et al., 2016]. This NE motion of this fault system gives the impression of a net clockwise circular torsion though it is unclear how or why this may be.

#### 6.4 HAURAKI RIFT MODELLING

The new geodetic data collected throughout the Hauraki Rift allowed for analysis which could derive the rift's "true" far-field widening rate beyond the first order approximation given by station velocities on either side of the rift, in addition to an estimate of its mechanical thickness of the crust beneath it. A well-known method is via a "buried dislocation" or "screw dislocation" model [e.g. Savage and Burford, 1973; Árnadóttir et al., 2006; Le Beon et al., 2008; Heimisson et al., 2015; Drouin et al., 2017]. This is a simplified uniaxial rift model which solves for the rift's mechanical thickness and far-field velocity together as an inverse problem, given a distribution of surface velocities at various distances from an assumed linear rift axis. The problem may be presented as:

$$u(d) = \frac{U}{\pi} \arctan\left(\frac{d}{D}\right)$$

where  $u$  is the surface perpendicular rate of each station velocity relative to the rift axis,  $d$  is its perpendicular distance from the rift axis,  $U$  is the far-field rift widening rate, and  $D$  is the thickness of the mechanical layer accommodating the rifting. The mechanical thickness here is generally equivalent to an effective elastic thickness  $T_e$  assuming the crust is the thickest and/or strongest layer to this depth [e.g. Kusznir and Karner, 1985; Burov and Diament, 1995,

1996]. The inverse problem was solved by fitting an error function to the data (Figure 6.14-B) via a weighted least-squares misfit assuming boundary conditions  $0.1 < U < 2.5 \text{ mm/yr}$  and  $1 < D < 35 \text{ km}$ .

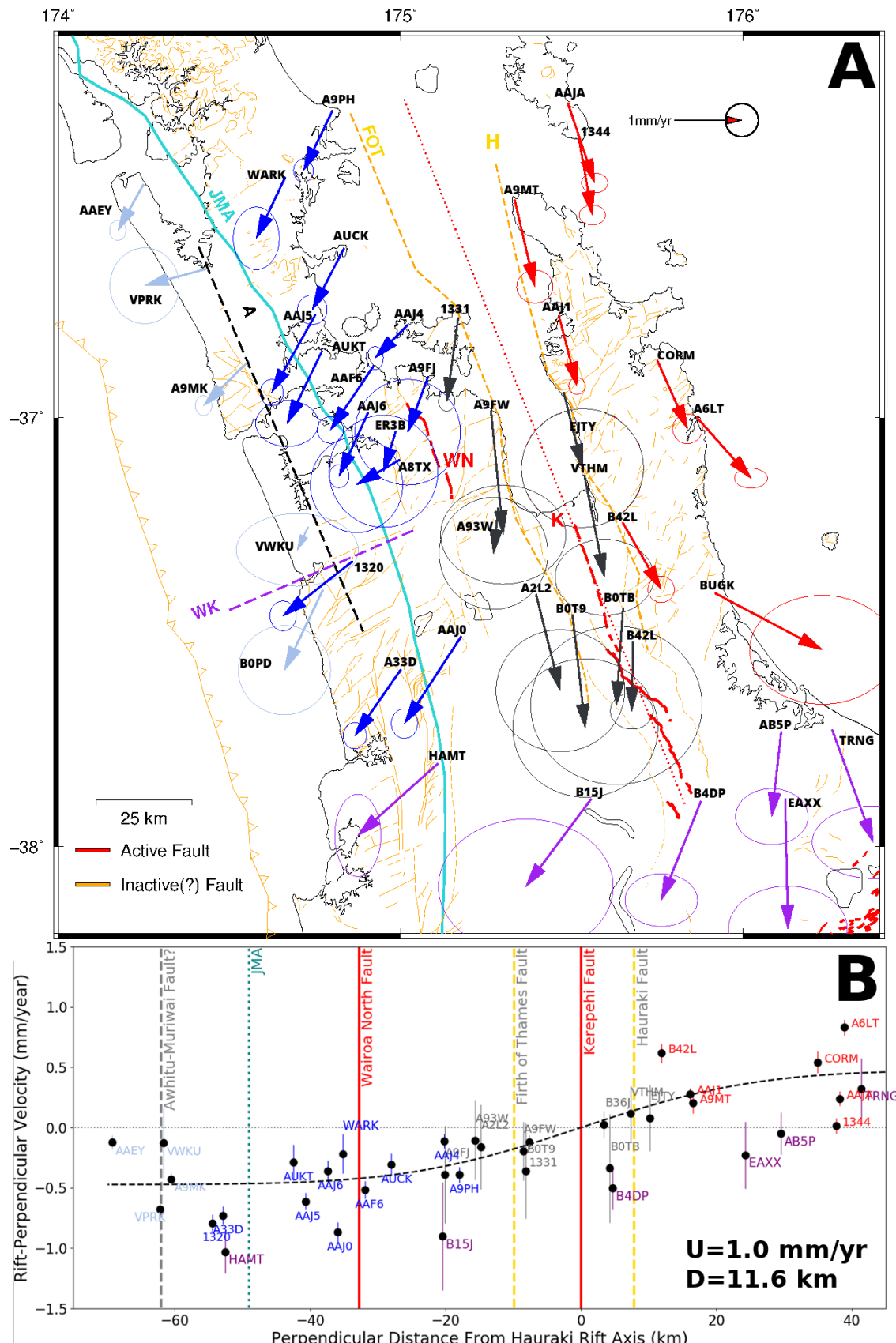


**Figure 6.14:** GNSS vector map (A) and coinciding 1D uniaxial screw dislocation model (B) colour-coded by region, with rift-perpendicular velocities normalised to be symmetric across the zero axis (dotted red line in A). The best fit using all of the 39 sites shown here produces a far-field velocity estimate  $U = 1.0 \text{ mm/yr}$  and a thickness of the rift's mechanical layer  $D = 11.6 \text{ km}$ . A = Awhitu Fault, WN = Wairoa North Fault, JMA = Junction Magnetic Anomaly, FOT = Firth of Thames Fault, H = Hauraki Fault, WK = Waikato Fault.

The local reference frame for the vectors shown in Figure 6.14-A had to be adjusted such that perpendicular velocities were generally negative west of the rift and positive east of the rift. This was done by simply adding a constant perpendicular velocity component to all sites until velocities on either side of the rift appeared to conform to the mathematical requirement for the rift model. The best fit is shown in Figure 6.14-B, and the inverse solution using that arrangement of data gave values  $U = 1.0 \text{ mm/yr}$  for the rate of rifting and  $D = 11.6 \text{ km}$  for the rift's mechanical thickness. However over the course of experimenting with the model it was found the inverse solution was highly sensitive to the magnitude of this perpendicular velocity adjustment in addition to which sites were used in the model, so a method was developed to run the model 100,000 times while allowing these parameters to adjust as much as 50%. In other words, in each inversion the perpendicular velocity adjustment was allowed to increase or decrease by as much as half as that shown in Figure 6.14-B, and up to half of the sites used were randomly removed. Accordingly in many instances these adjustments made the inversion impossible, but the result of N=78954 successful "Monte Carlo" iterations are shown in Figure 6.15.

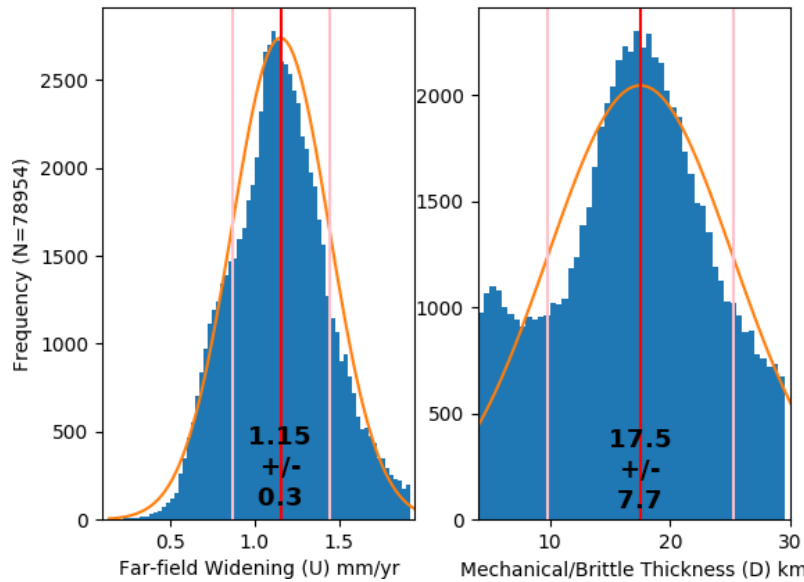


**Figure 6.15:** Histogram of 78,954 (out of 100,000) successful Monte Carlo "screw model" inversions using the GNSS vector data in Figure 6.14. A Gaussian fitting this data is drawn in orange, the mean is drawn in red and the  $+/- 1\sigma$  variance in pink. These robust solutions predict a far-field velocity estimate  $U = 1.15 +/ - 0.3 \text{ mm/yr}$  and a thickness of the rift's mechanical layer  $D = 17.5 +/ - 7.7 \text{ km}$ .

The histogram of randomised screw model inverse solutions shown in Figure 6.15 nullifies the effect of variable site selection as well as the local reference frame uncertainty, producing a new and robust estimate of  $U = 1.15 +/ - 0.3 \text{ mm/yr}$  for the rate of rifting and  $D = 17.5$

$\pm 7.7 \text{ km}$  for the rift's mechanical thickness (and approximate  $T_e$ ). These are this project's preferred estimates as they are insensitive to inaccuracies in initial model parameters and also provide a well-defined  $1\sigma$  uncertainty. The large variance in these estimates is likely due to instances where randomly selected sites are biased on either side of the rift, and instances where slower sites in the north or faster sites in the south are removed from the analysis. A solution utilising only the northern-most sites ( $> -36.6^\circ\text{S}$ ) predicts  $U = 0.6 \text{ mm/yr}$  and  $D = 7.3 \text{ km}$ ; only southern-most sites ( $< 37.7^\circ\text{S}$ ; purple) predicts  $U = 1.8 \text{ mm/yr}$  and  $D = 28.2 \text{ km}$ . These are effectively end-member solutions with the faster-moving southern sites increasingly affected by stress from the Hikurangi Margin. The range of mechanical thickness estimates here is consistent with the  $\sim 2\text{-}21 \text{ km}$  range of hypocentre depths observed within the rift by this study (e.g. Figure 5.17) and it appears as though the rift has been stretched  $\sim 10 \text{ km}$  thinner with respect to the average crustal thickness of this area (i.e. southern Northland) estimated to be  $\sim 25\text{-}30 \text{ km}$  [e.g. Stern et al., 1987; Holt and Stern, 1991; Horspool et al., 2006; Behr et al., 2010].

Assuming an average (and constant) rifting rate of  $1.15 \text{ mm/yr}$  and current width of  $25 \text{ km}$  [Hochstein et al., 1986] the Hauraki Rift would have had to began widening by 22 Ma. This is consistent with the VMFZ's initial activation at  $\sim 23 \text{ Ma}$  [Herzer et al., 2009], although the assumption of a constant rate of widening here over this period is dubious. It is likely that the Hauraki Rift was once widening at a much higher rate than it is now. It is supposed that the peak rate of its widening likely occurred following the termination of the VMFZ at  $\sim 15 \text{ Ma}$  [Herzer et al., 2009] and probably while the rift was in a high-strain back-arc environment coeval with Coromandel Volcanic Arc activity  $\sim 12\text{-}8 \text{ Ma}$  [e.g. Lamb, 2011; Booden et al., 2012; Seebeck et al., 2014].

#### 6.4.1 Relationship to the Auckland Volcanic Field

The geodetic data in the vicinity of the basaltic, monogenetic Auckland Volcanic Field does not show any obvious anomalous behaviour capable of generating or directing the location of volcanism, leaving the Hauraki Rift as the nearest apparent suspect. While the rift may have been capable of contributing to the eruption of the dacitic Little Barrier Island as recently as 1-3 Ma [Lindsay et al., 1999], it is unclear how fast the rift was widening at this time. At its current annual  $\sim$ millimetre rifting rate simple decompression models predict no degree of

generated melt regardless of ancillary parameters [e.g. Van Wijk et al., 2001; Schmeling et al., 2012]. However, slightly more exotic models have shown that young (<6 Ma) and similarly obliquely-rifting regions such as the Gulf of California may be assisted by the presence of convective heating [Wang et al., 2009] which could boost melt production. Additionally, slow (<6 mm/yr) continental rifts such as at Afar may generate sufficient decompression melting without plume influence if the matrix beneath them is sufficiently weakened or already contains a large amount of remnant melt [Rychert et al., 2012]. Regardless of melt production it remains unclear how it would migrate 40+ km westwards to erupt near Auckland.

## 6.5 WHY IS NORTHLAND NZ FAST RELATIVE TO AUSTRALIA?

The simplest and probable explanation for the majority of geodetic velocities observed throughout NWNZ is that they are the result of stress generated by the oblique subduction of the Pacific Plate at the Hikurangi Margin. This is corroborated by the presence of elevated shear strain rates derived from geodetic velocities throughout the North Island (e.g. Figure 4.23) off the eastern coast of the Coromandel Peninsula, which also continue as north as ~36°S, 350+ km from the plate margin. Stress generated at the plate margin is also likely responsible for the ongoing widening of the Hauraki Rift by pulling the east side of the rift SE in accord with the broader clockwise angular component originating from the North Island's East Cape region (e.g. Section 6.2.1, Figure 6.9, and Wallace et al., 2004). North of ~36°S (e.g. Northland) strain rates become indiscernible and velocities (Figure 6.7) become increasingly uniform in both direction (SW) and magnitude (~1 mm/yr). It is not clear why the geodetic velocities observed throughout Northland remain consistent and elevated rather than continue to diminish in magnitude further from the plate boundary, although it is possible that the region simply behaves as a perfectly rigid block in which stress propagates unimpeded.

In establishing an Australian reference frame for this project (Section 4.6) it was observed that Northland NZ is not the only region on the Australian Plate with an elevated ~1 mm/yr SW velocity character relative to continental Australia. Similar vectors also appear at sites on Norfolk Island/NORF and New Caledonia/KOUC+NOUM+NRMD (blue vectors, Figure 6.16) with no clear explanation. Furthermore no such motion was observed at equidistant Lord Howe Island/LORD which reduces the possibility that these velocities are the result of Australian-

Pacific plate boundary stresses, and instead suggests the presence of an independent tectonic-scale stress affecting the eastern Australian Plate as a whole.

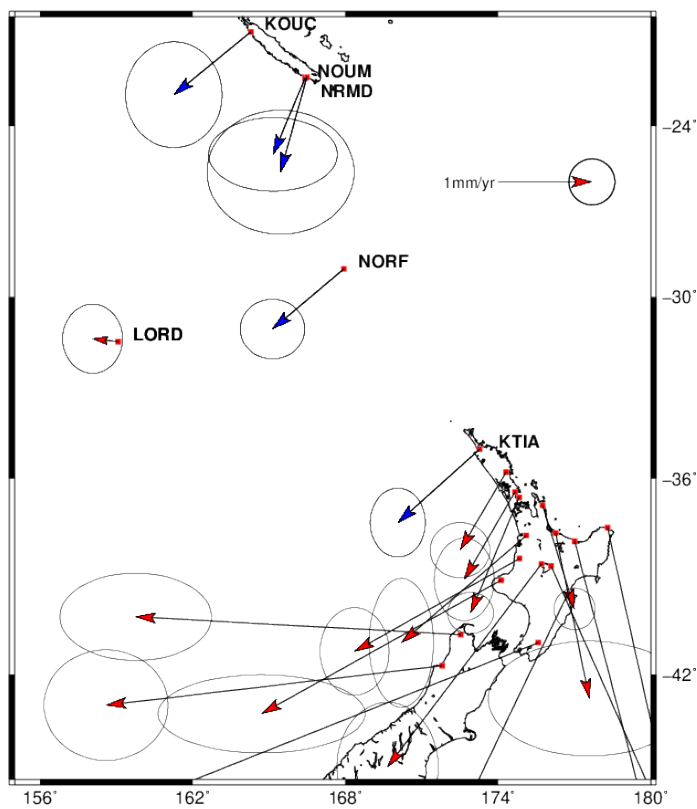


**Figure 6.16:** Geodetic velocity estimates for some cGNSS sites in NE Zealandia. Anomalously fast velocities are drawn with blue arrowheads.

The location of these anomalously fast geodetic velocities along the margin of NE Zealandia (Figure 6.16) may indicate that some crustal feature proximal to the continent's interface with the oceanic crust east of it is behaving non-rigidly, and/or is able to accommodate compression on the order of  $\sim 1 \text{ mm/yr}$ . This section explores ideas as to the source and orientation of this stress as well as the location of a possible deformation zone between Zealandia and a supposed hypothetical "East Australian" sub-plate. A coarse tectonic history of NE Zealandia is presented as well as a model from  $\sim 30 \text{ Ma}$  which could explain the origin of a boundary or lineament of potentially weakened crust allowing the apparent SW-NE compression of the blue geodetic vectors in Figure 6.16.

### 6.5.1 Anomalous Fast Velocities In the Eastern Australian Plate

A review of the Australian Plate reference model used in this project is shown in Figure 6.17, now superimposed with a satellite Bouguer anomaly (BA; Chapter 3) and a blue vector depicting the plate's  $\sim 65 \text{ mm/yr}$  motion relative to a fixed hotspot reference frame [O'Neill et al., 2005; Keep and Schellart, 2012]. Mantle drag beneath a plate is globally capable of dynamically raising topography as much as  $300 \text{ m}$  [Molnar et al., 2015] so it is not inconceivable that the Australian Plate, which is the fastest plate on earth [Keep and Schellart, 2012], could generate a meagre  $\sim 1 \text{ mm/yr}$  SW compression depending on the strength of whatever tectonic-scale discontinuity, weak zone, or otherwise non-rigid feature is accommodating it.

This hypothetical discontinuity must exist east of Lord Howe Island/LORD, west of both Norfolk Island/NORF and Northland/KTIA, and SW of New Caledonia. Notably this excludes the possibility of ongoing widening within the Tasman Basin west of Lord Howe Island, activity at Three Kings Ridge east of the Norfolk Ridge, and activity at the VMFZ NE of Northland. This narrows potentially accommodative crustal features to the NE periphery of Zealandia and further insinuates it may be continuous for over  $2000 \text{ km}$  between New Caledonia and New Zealand. This discontinuity may speculatively continue further north and east of New Caledonia along the D'Entrecasteaux Ridge and into the Vanuatu Trench [e.g. Dupont et al., 1975; Cluzel et al., 2012], as well as further south of Northland into the Alpine Fault, effectively completely separating and creating a mechanically distinct "East Australian" sub-plate.

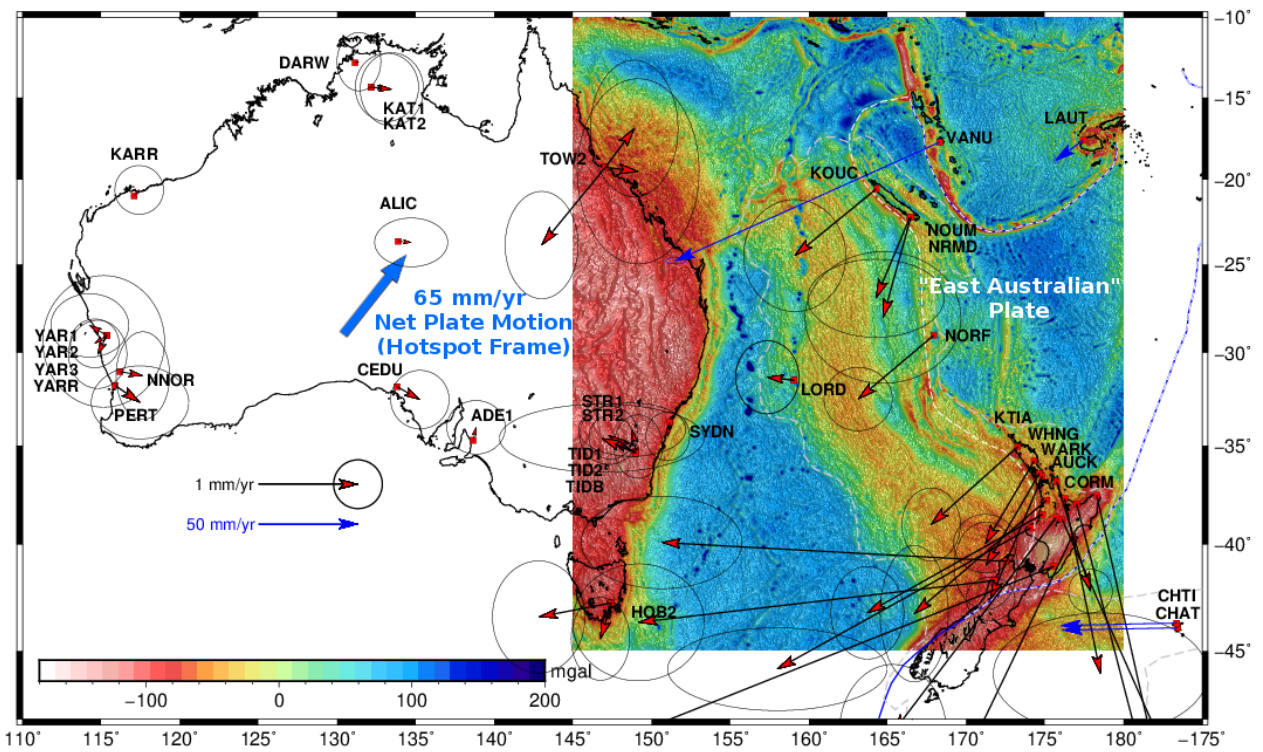


**Figure 6.17:** Geodetic velocity estimates throughout the Australian Plate, overlain with a satellite Bouguer gravity anomaly. All vectors are relative to a custom Australian reference frame defined by all of the sites shown west of and including LORD (Section 4.6). The approximate border of a supposed "East Australian" sub-plate is outlined by dashed white line, continental Zealandia by a faint grey dashed line. The Australian Plate is moving  $\sim 65 \text{ mm/yr}$  NE (blue arrow) relative to a hotspot reference frame [O'Neill et al., 2005; Keep and Schellart, 2012]. The magnitude of the velocity of sites on the Chatham Islands shown in the south-east with blue arrows is  $\sim 34.5 \text{ mm/yr}$ , VANU north-east of New Caledonia is  $\sim 87 \text{ mm/yr}$ . Plate boundary drawn in blue is Nuvel-1 [Bird, 2003].

While it is possible that the  $\sim 1 \text{ mm/yr}$  velocity anomaly between Lord Howe Island and the eastern margin of NE Zealandia is distributed evenly amongst the tectonic features and crust at the margin of NE Zealandia, it is nevertheless supposed that the two most likely discrete features possibly accommodating the bulk of the SW strain observed are the New Caledonia Basin and the Norfolk Ridge (continuous with the Southern Norfolk Ridge System) as they are nearest the periphery of Zealandia and thus are most likely to have been reactivated since separating from Gondwana in the Cretaceous. The Norfolk Ridge has bordered nearly all of the Eocene-Miocene tectonic reorganisation at NE Zealandia's margin (Section 2.2) and stratigraphic studies and drilling have interpreted Oligocene-Miocene activity in both the New Caledonia Basin [Klingelhoefer et al., 2007; Collot et al., 2008; Sutherland et al., 2010; Sutherland et al., 2018] and Southern Norfolk Ridge System [Herzer et al., 1997; Stagpoole et al., 2009; Bache et al., 2012; Bache et al., 2014]. Additionally, concurrent activity at the Taranaki

Fault offshore along the western coast of the North Island has been inferred within the same possible Murihiku Terrane basement structure as the Southern Norfolk Ridge System and New Caledonia Basin [King and Thrasher, 1996; Mortimer et al., 1997; Sutherland, 1999; Stagpoole and Nicol, 2008; Uruski, 2015]. West of the New Caledonia Basin and south of the Reinga Basin, the Fairway and Aotea Basins are assumed to have ceased most activity by the late Cretaceous [Lafoy et al., 2005; Rouillard et al., 2015] which potentially eliminates them, as well as regions further south or west, as candidates which may have been reactivated in recent geologic history.

### 6.5.2 *Tectonic Interpretation of NE Zealandia*

To investigate the possibility that either the Norfolk Ridge and/or New Caledonia Basin may be acting as some form of mechanical boundary separating an "East Australian" sub-plate this project utilised state of the art satellite-based gravity, topography, and magnetic datasets (Section 3.3) to interpret the structure at the margin of NE Zealandia. This data typically offered great improvement over data used in older tectonic interpretations of the region [e.g. Sutherland, 1999; Sdrolias et al., 2001; Sdrolias et al., 2004] and offers complete spatial coverage relative to newer shipboard datasets [e.g. Collot et al., 2009]. Uniform or near-uniform coverage allows for the derivation of a Bouguer Gravity Anomaly (BA, Section 3.2.2) which is better suited than the FAA (Figure 6.18) at interpreting crustal thickness and density variations. The satellite-based BA (Figure 6.19), and magnetic data (Figure 6.20, previously shown without annotation in Section 3.4) are now presented with labels and structural interpretations along 7-8 lineaments which will be referenced throughout this section. The BA and magnetic data exhibit the strongest evidence for structural continuity between New Zealand and New Caledonia whereas the FAA is often nebulous in areas. Accordingly the BA and magnetic data are primarily used to interpret the region's tectonic arrangement. An alternate 3D interpretation of the bathymetry of NE Zealandia (Figure 6.21) using the same data shown in Figure 2.2 is also presented for reference.

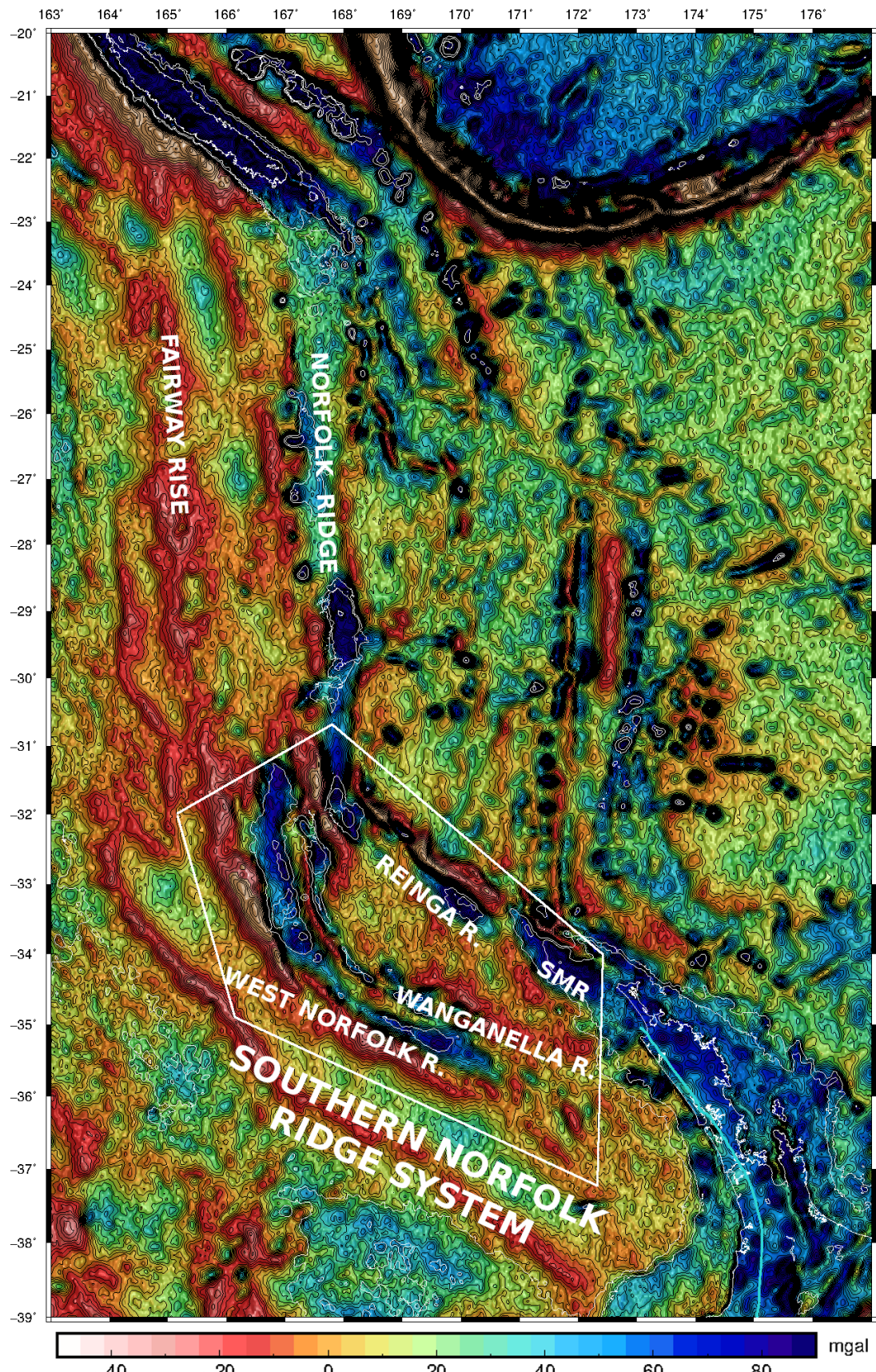


**Figure 6.18:** Satellite Free Air Anomaly [Sandwell and Smith, 2009; Sandwell et al., 2013; Sandwell et al., 2014; Garcia et al., 2014] of the SW Pacific. Resolution is 0.25 arcminute and 10 mGal contours are plotted. Bathymetry [Smith and Sandwell, 1997] contours at 0, -500, and -1000 m are overlain in white. The JMA is plotted in light blue. SMR = South Maria Ridge.

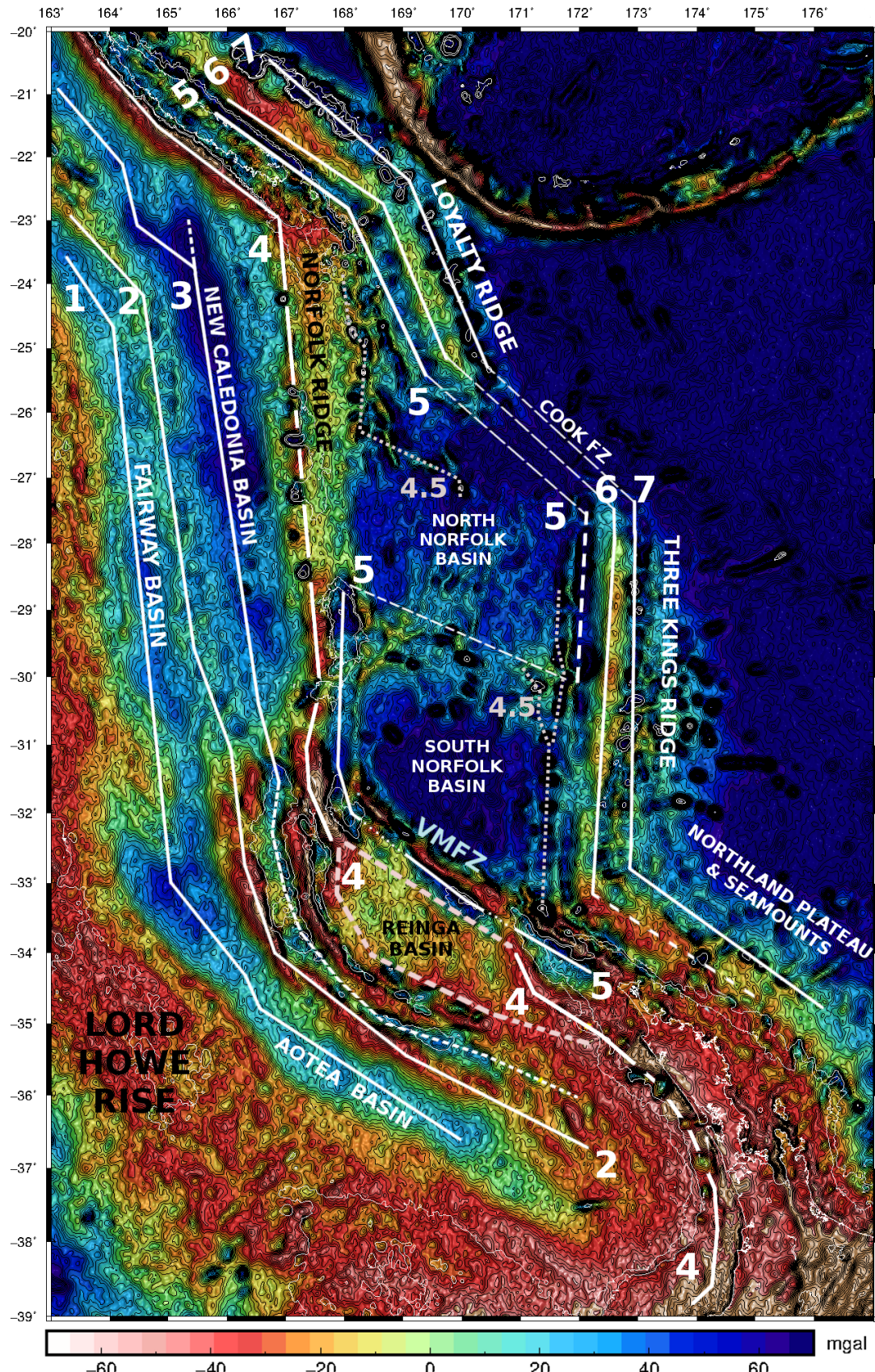


**Figure 6.19:** Satellite Bouguer Gravity Anomaly of the SW Pacific derived from satellite FAA (Figure 3.2) and satellite topography (Figure 2.2) data assuming ocean water and crustal densities of 1027 and 2670 kg/m<sup>3</sup>. Resolution is 0.25 arcminute and 10 mGal contours are plotted. Bathymetry [Smith and Sandwell, 1997] contours at 0, -500, and -1000 m are overlain in white. 7 lineaments (L1-L7) are interpreted and numbered W-E corresponding to unique tectonic structures with an eighth "4.5" lineament of volcanism assumed to be the result of the SE separation of the Loyalty-Three Kings arc.

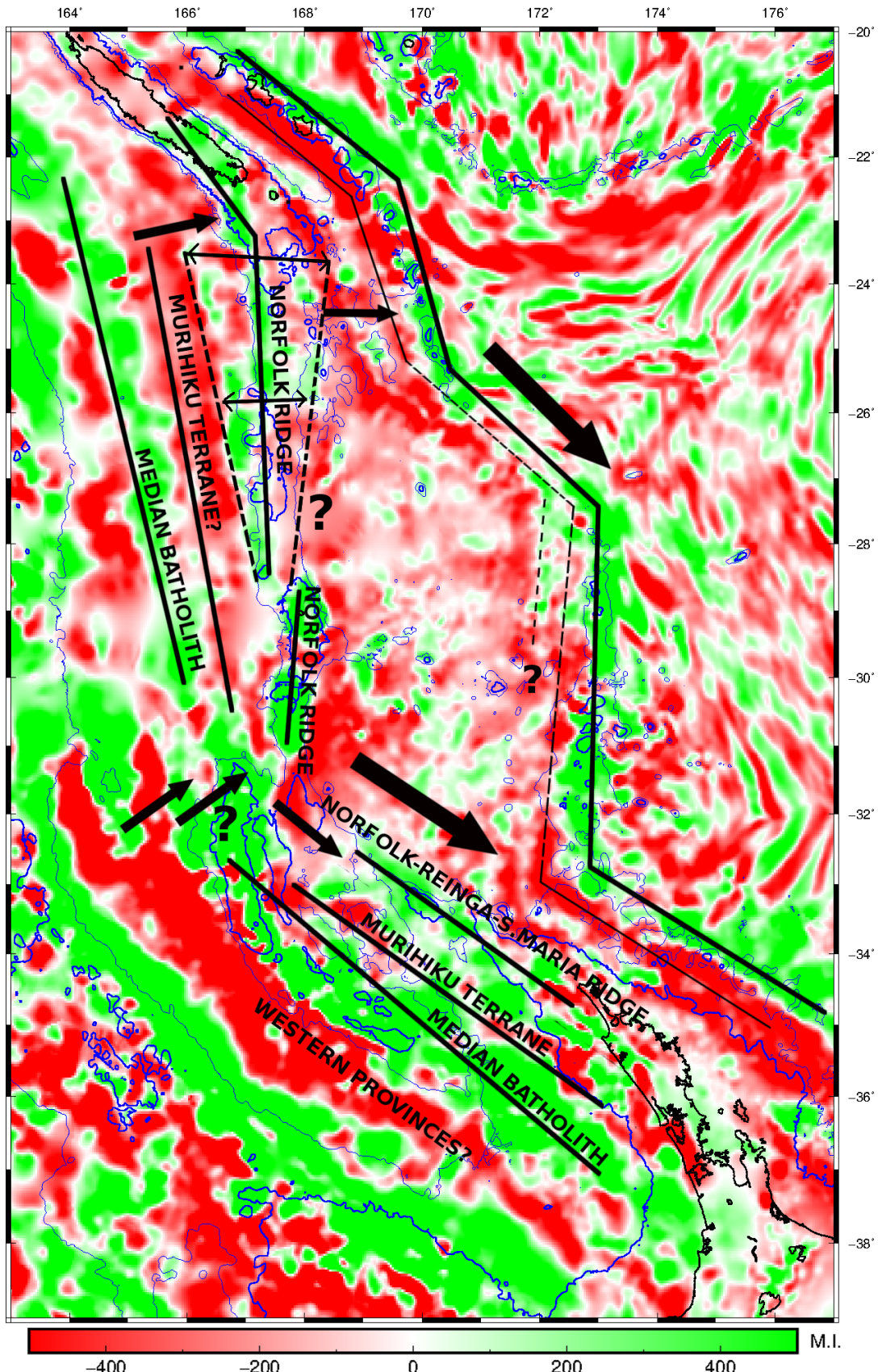


**Figure 6.20:** EMAG2 (v3) magnetic data compiled from satellite, ship, and airborne measurements upward continued 4 km above sea level in 2 arcminute resolution [Maus et al., 2009; Meyer et al., 2017]. Magnitudes have been capped at +/- 500 nT to improve clarity with positive anomalies are in green and negative in red. Bathymetry [Smith and Sandwell, 1997] contours at 0, -500, and -1000 m are overlain in blue/black.

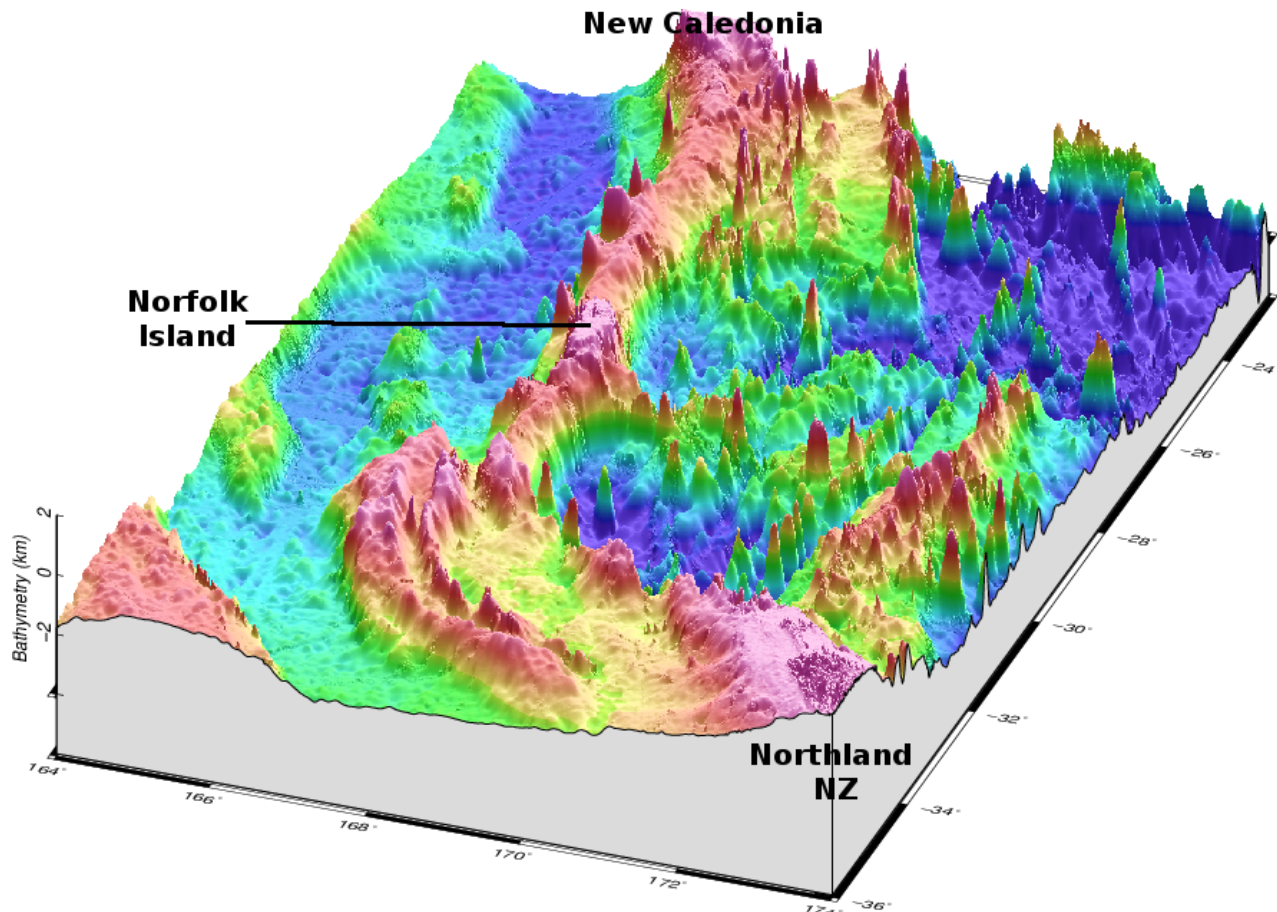


**Figure 6.21:** 3D bathymetry of NE Zealandia [Smith and Sandwell, 1997; Becker et al., 2009]. 2x vertical exaggeration. The equivalent data (with labels) is plotted in Figure 2.2.

#### 6.5.2.1 Fairway-Aotea Basin

Lineament 1 (L1, Figure 6.19) marked in the BA presumes that the Fairway and Aotea Basins are structurally linked and distinct from the New Caledonia Basin [e.g. Lafoy et al., 2005; Collot et al.; 2009]. The magnetic data (Figure 6.20) also shows that these structures share the same continuous negative anomaly. Immediately east (L2) this project interprets the shallow bathymetry of the Fairway Rise [e.g. Collot et al., 2008] as being continuous with the low BA, compressional crustal signature along the southern West Norfolk Ridge. This interpretation is also supported by the continuity of the magnetic data which may correlate to the Median Batholith and/or Brook Street Terrane [e.g. Sutherland, 1999; Mortimer et al., 2004; Spandler et al., 2005]. The continuity of L2 further implies that the West Norfolk Ridge is independent of the Norfolk Ridge [e.g. Eade, 1988], with its underlying structure remaining parallel throughout.

### 6.5.2.2 New Caledonia Basin

The negative magnetic anomaly associated with the New Caledonia Basin (L3, Figure 6.19) is hypothesised to continue within the Southern Norfolk Ridge System somewhere NE of the West Norfolk Ridge and partially within the Reinga Basin, generally coinciding with the location of the negative magnetic anomaly there inferred to be the Murihiku Terrane [Sutherland, 1999; Mortimer, 2004; Stagpoole et al., 2009]. However the Oligocene-Miocene compression observed within the Southern Norfolk Ridge System [Stagpoole et al., 2009; Bache et al., 2012] complicates this interpretation. East and north of L3 towards the Norfolk Ridge and easternmost margin of NE Zealandia, the structural continuity of the region becomes difficult to interpret.

The New Caledonia Basin (L3, Figure 6.19) becomes deeper towards the north (Figure 6.21) and also has progressively positive gravity anomalies (Figures 6.19, 6.18) interpreted as increasingly thinner crust. That the basin has positive gravity anomalies could be explained by a history in which the basin's Te was initially low (5-10 km) during its thinning phase which then strengthened over time to (20-40 km) [e.g. Hackney et al., 2012]. The structure of this region is commonly thought to have been the sole result of Gondwana-era Cretaceous rifting which has been unperturbed since [e.g. Eade, 1998; King and Thrasher, 1996; Lafay et al., 2005]. However newer research [e.g. Collot et al., 2008; Sutherland et al., 2010; Patriat et al., 2018] has speculated that the region may have undergone a second phase of alteration as recently as the Oligocene-Miocene. Collot et al. (2008) interpret the bathymetric subsidence (Figure 6.21) as being the result of overloading of mass from the early Oligocene New Caledonia obduction as well as simultaneous underthrusting from the tectonic compression. This interpretation appears reasonable however it does not explain the variability in the BA along L3 as material was obducted throughout New Caledonia [Cluzel et al., 2012] and thus should affect the Loyalty Basin more or less equally. Nor would it explain why the BA highs continue south along the New Caledonia Basin for nearly 600 km unless obduction also continued further south along the Norfolk Ridge, as speculated by Patriat et al. (2018). However this idea is speculative and would be invalidated if the Norfolk Ridge had subsequently lost mass on its eastern flank following the opening of the Norfolk Basin (e.g. Section 6.5.2.5). Sutherland et al. (2010) proposed that the lithosphere beneath the New Caledonia Basin was delaminated in the mid-late Eocene by the eastward shearing of a west-dipping slab and subduction zone. In this scenario the subsidence of the New Caledonia Basin is the result of subsequent isostatic re-equilibrium and the Norfolk Ridge was thickened/uplifted by thrust faulting as the slab

rolled backwards. This of course requires a west-dipping Loyalty Arc model but also does not adequately explain the N-S change in character of the BA along the New Caledonia Basin.

This project supposes that the subsidence of the New Caledonia Basin is due to E-W crustal thinning occurring coeval with the Miocene separation of the Loyalty-Three Kings Ridge eastward away from the Norfolk Ridge. This places the highest degree of New Caledonia Basin thinning in the north (e.g. highest BAs, Figure 6.19) adjacent to the highest degree of thinning/widening of the Norfolk Ridge and rifting [e.g. Patriat et al., 2018] between the still-locked Norfolk and Loyalty ridges. In addition to the BA, this is also evident in satellite magnetic data (Figure 6.20) but is clearer still in shipboard magnetic data (Figure 6.22) which appears to show that the Norfolk Ridge has been widened E-W and/or bifurcated down its axis. Further south in the centre segment (26-29°S) adjacent to the northern Norfolk Basin, the Three Kings Ridge's (3KR) dislocation from the Loyalty Ridge repartitioned a larger amount of E-W strain east within the basin, which is assumed to have alleviated the degree of crustal thinning within the Norfolk Ridge and New Caledonia Basin. Similarly at the southernmost segment (29-32°S), it is assumed that nearly all of the strain associated with the separation of the 3KR was concentrated east of the Norfolk Ridge and within the southern Norfolk Basin which would explain its higher BAs and thus probable thinner crust (elaborated in Section 6.5.2.6).

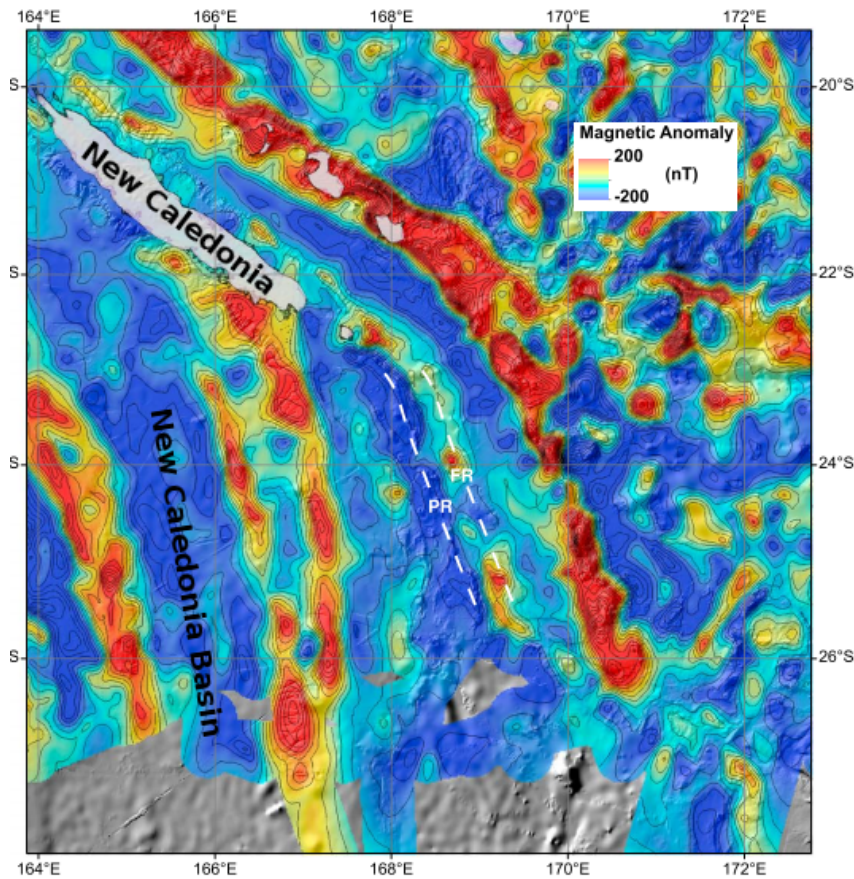


**Figure 6.22:** Shipboard magnetic data of New Caledonia, Loyalty Ridge, and northern Norfolk Ridge region. 50  $nT$  contours. Combined dataset across agencies previously published by Collot et al. (2009). Figure courtesy of Patriat et al. (2018).

### 6.5.2.3 Norfolk Ridge

The bathymetry of the Norfolk Ridge (Figure 6.21) shows a single continuous lineament that becomes deeper, wider, and less pronounced to the north, punctuated intermittently with volcanism on its western flank. However the gravity (Figures 6.18, 6.19) and magnetic (Figures 6.20, 6.22) data portray it as a surprisingly complex structure. This project observes two distinct features of the ridge, a western lineament of BA lows containing a long linear chain of volcanism (L4, Figure 6.19) and an eastern lineament of FAA and BA highs (L5). Furthermore the ridge appears to have two different regimes, a southern one in which it maintains a uniform width (south of  $\sim 29^\circ S$  and alongside L5) and a northern towards New Caledonia in which the BA becomes progressively wider and the magnetic data appears to bifurcate into two distinct positive anomalies (e.g. Figure 6.22). The Norfolk Ridge's crust at  $\sim 24^\circ S$  has been observed to be  $\sim 21\text{ km}$  thick from seismic studies [Klingelhoefer et al., 2007] which is thicker than typical ocean island volcanic arcs but thinner than continental crust.

Lineament 5 (L5, Figure 6.19) is interpreted as dense and/or uplifted material continuous from the Norfolk Island ~29°S SE towards Northland along both the Reinga and South Maria ridges [e.g. Eade, 1988]. However L5 has noticeably segmented bathymetry (Figure 6.21), gravity (Figures 6.18, 6.19) and magnetic (Figure 6.20) data within the Southern Norfolk Ridge System. This is hypothesised to be the result of NW-SE straining coeval with right-lateral motion at the VMFZ from ~23-15 Ma [Herzer et al., 2009]. North of Norfolk Island ~29°S the BA signature of L5 vanishes, and the positive magnetic signature associated with L5 (Figure 6.20) is either offset to the west or otherwise disappears between 29-26°S. North of ~26°S the positive magnetic anomaly associated with L5 and the eastern Norfolk Ridge returns, but further east and adjacent to the Loyalty Ridge. In between L5 and the Norfolk Ridge north of 26°S appears to be a high degree of rift-related tectonics [e.g. Patriat et al., 2018] and volcanism [Mortimer et al., 2018] associated with the separation of the Loyalty Ridge here. This chain of volcanism is interpreted to be continuous as lineament "4.5" (Figure 6.19).

Lineament 4 (L4, Figure 6.19) along the Norfolk Ridge is interpreted as a region of narrow rifted or fractured crust which has been in-filled with sediment, producing a well-defined trace of low BAs amidst the general low BAs of the Norfolk Ridge. Furthermore the crustal structure of L4 appears to be capable of focusing volcanic eruptions. The structure of the Norfolk Ridge has only peripherally been measured by seismic studies targeting the New Caledonia Basin to the east but generally support that L4 has a narrow basin or rift structure [Klingelhofer et al., 2007; Collot et al., 2008]. The volcanism within it has been inferred to be of Eocene-Miocene age and has been dredged, but age estimates have yet to be published [Mortimer et al., 2015; Mortimer et al., 2018]. It is supposed that the presence of this rifted, thinned, or otherwise low-density feature on the western Norfolk Ridge preceded the volcanism occurring within it, possibly serving to focus melt from depth, rather than the volcanism (e.g. a hotspot track) generating L4 in the opposite sense.

The degree of E-W crustal thinning along the Norfolk Ridge evident from the widening of its BA signature (Figure 6.19) appears to progressively increase north of Norfolk Island (and the disappearance of L5 ~29°S) towards New Caledonia. This is also reflected in the decreasing magnitude of the BA associated with L4 relative to the Norfolk Ridge. It thus appears that the crustal structure of L4 pre-dates the thinning of the Norfolk Ridge which this work speculates happened alongside the eastward separation of the Loyalty-Three Kings Ridge, constrained by volcanism to have had occurred ~25-23 Ma [e.g. Mortimer et al., 2007; Mortimer et al., 2018; Figure 2.8]. It is suggested that in the southern segment of the Norfolk Ridge (29-32°S) the

entirety of strain associated with the separation of the Three Kings Ridge occurred within the southern Norfolk Basin (east of L5). This would explain why there is little deformation evident in L4 and the Norfolk Ridge itself.

It was further observed that the trend of BA lows along the western coast of New Zealand had a similar width and character of volcanism within it as that noted on the western Norfolk Ridge. Furthermore magnetic data (Figure 6.20) showed that the basement fabric of these regions may be continuous. Thus the continuation of Lineament 4 (L4, Figure 6.19) SE of the Norfolk Ridge through the Reinga Basin and along the western shore of north-west New Zealand is proposed. Though there is no evidence of volcanism in the Reinga Basin in either the satellite BA or FAA (Figure 6.18) volcanism has been visualised and stratigraphically aged to the early Miocene by shipboard gravity and seismic studies in the region [Stagpoole et al., 2009; Figure 6.23]. This buried volcanism effectively connects the chain along the Norfolk Ridge to Northland. The volcanoes of L4 near New Zealand are arc-type and are progressively younger ~23.8 Ma N-S from the South Maria Ridge towards the Taranaki Peninsula ~38°S [Smith et al., 1993; Herzer, 1995; Hayward et al., 2001; Mortimer et al., 1998; Mortimer et al., 2007; Booden et al., 2011]. Assuming that this western belt of volcanism SW of Northland is of similar origin or character as the rest of L4, it is speculated that the volcanism along the western Norfolk Ridge should also have an age progression with arc-type rocks becoming older towards the north. Furthermore, if the volcanism along L4 is linked throughout, the structure of L4 may also be similar. In this case the low BAs along the western margin of the Norfolk Ridge may have a distinctive rifted crustal structure similar to the Taranaki Basin (e.g. Figure 6.3) rather than a compressive reverse faulted structure similar to the West Norfolk and Wanganella ridges [e.g. Stagpoole et al., 2009; Bache et al., 2012].

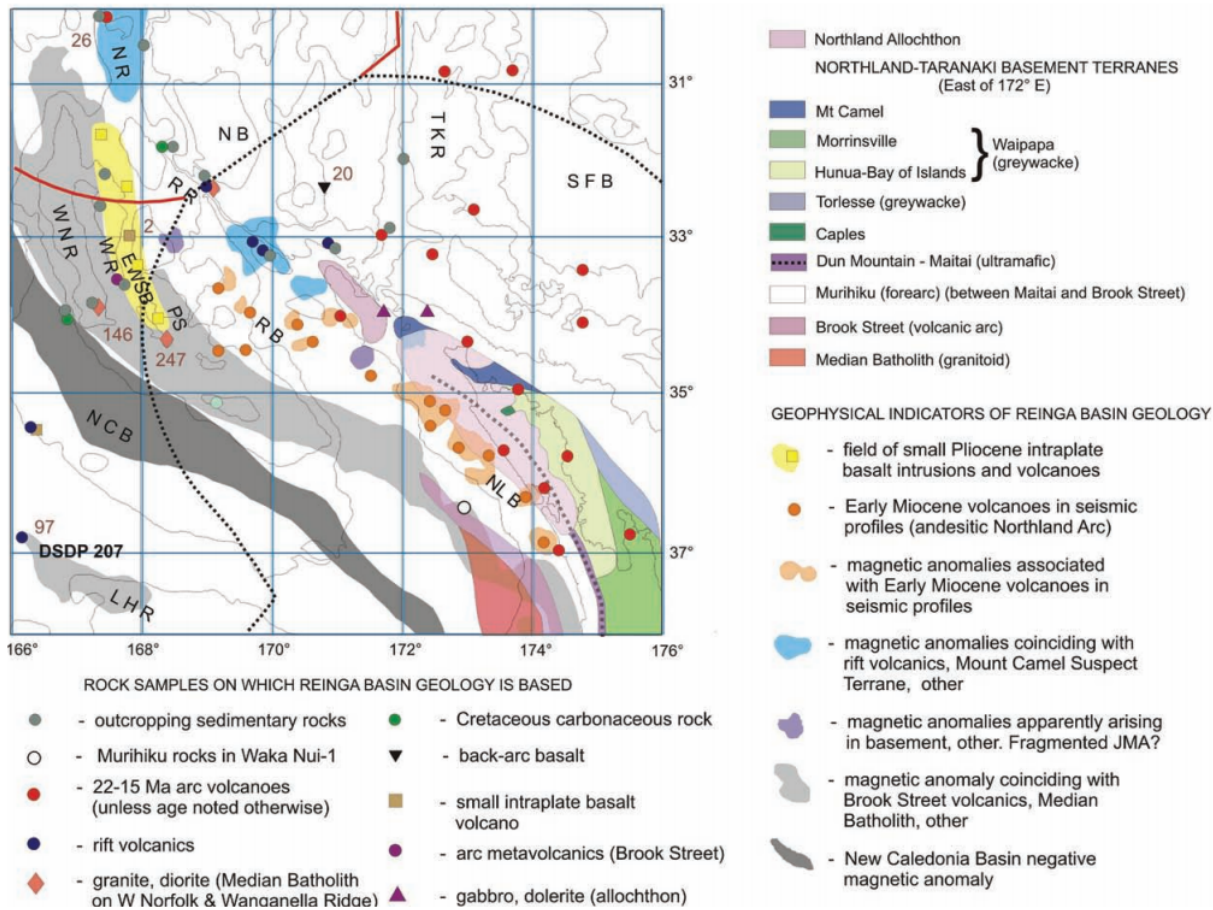


**Figure 6.23:** Basement structure and volcanism within the Southern Norfolk Ridge System from local gravity and seismic studies, courtesy of Stagpoole et al. (2009). This work notes early Miocene volcanism (orange) within the Reinga Basin.

Lineament 4 (L4, Figure 6.19) thus appears to be the best candidate for a tectonic feature along NE Zealandia capable of explaining the velocity anomalies observed on New Caledonia, Norfolk Island, and Northland NZ (Figure 6.17). There is evidence it is a zone of relative weakness capable of directing melt, and furthermore there is evidence that it could have been reactivated in the Miocene as the Norfolk Basin opened. Moreover, and unlike the New Caledonia Basin or any other tectonic feature of NE Zealandia, it can arguably be traced from New Caledonia or even the Vanuatu Trench along the D'Entrecasteaux Ridge [e.g. Dupont et al., 1975; Cluzel et al., 2012] in the north towards Northland and amidst the Taranaki Fault in the south. This means it could theoretically be able to separate the eastern Australian Plate into the proposed East Australian sub-plate whose relative motion would be responsible for the observed geodetic velocity anomalies observed at its margin (Section 6.5.1).

#### 6.5.2.4 Loyalty-Three Kings Arc Polarity

Prior to the opening of the Norfolk Basin, a Loyalty-Three Kings subduction arc of debatable polarity (Section 2.2.1) collided into the Norfolk Ridge (L4 and L5, Figure 6.19) from the east [Mortimer et al., 1998; King 2000; Crawford et al., 2003; Schellart et al., 2006; Mortimer et al., 2007; Whattam et al., 2008; Herzer et al., 2009]. The bathymetric highs here are interpreted as a volcanic arc corresponding to the easternmost lineament 7, which also has a strong FAA (Figure 6.18) signal due to the probable flexural support of this volcanism by the strength of the oceanic plate [e.g. Watts and Cochran, 1974]. Notably there is little to no gravitational signal east of either the Loyalty Ridge or 3KR. If the Loyalty-Three Kings arc was west-dipping there should theoretically be a fossil trench and/or fore-arc signal east of the arc, either of which should correspond to a low BA due to the subsequent in-fill of lower density sediment. This lack of a gravity low (or any gravity signal) casts a doubt on west-dipping subduction models. Conversely the presence of a clear BA low west of the ridge (L6) supports east-dipping models, and seismic profiles perpendicular to the 3KR further support the idea that these lows represent a fore-arc and/or possibly a former subduction trench [Kroenke and Eade, 1982; Kroenke and Dupont, 1982]. It is thereby assumed that an east dipping Loyalty Arc subduction model [e.g. Crawford et al., 2003; Schellart et al., 2006; Whattam et al., 2008; Herzer et al., 2009] is most probable, based on this evidence in conjunction with that described in Section 2.2.1.

#### 6.5.2.5 Collision and Locking of the Norfolk and Loyalty Ridges

Assuming an east-dipping Loyalty Arc model, the easternmost continental Norfolk Ridge as well as the NE boundary of continental Northland is presumed to have been partially subducted as the last of the hypothesised Loyalty Basin oceanic plate was subducted, leaving little or no evidence of a trench [e.g. Kroenke and Eade, 1982; Kroenke and Dupont, 1982; Schellart, 2007; Schellart et al., 2009]. This would generate widespread compressional faulting as well as high-pressure metamorphosed rocks at the subduction margin. The degree to which either the Norfolk Ridge and Northland were partially subducted to the east and north-east cannot be easily determined but may have been anywhere from 10-30 km based on various factors, including the thickness of the continental crust and age of the Loyalty Slab [Molnar and Gray, 1979]. It is speculated that the extent of continental subduction was sufficient to generate a mechanical bond comparable to the strength of the overall plate. The timing of this collision can be constrained by both the New Caledonia and Northland obduction events at

~38-34 [Spandler et al., 2005; Fitzherbert et al., 2004; Collot et al., 2008; Cluzel et al., 2012] and ~25-22 Ma respectively [Spörli, 1999; Rait, 2000; Spörli and Harrison, 2004], which implies that impact began in the north and continued south. It further implies that the impact and partial subduction occurred ~10 Ma prior to the ~25-23 Ma separation of the Loyalty-Three Kings arc in the north near New Caledonia [Mortimer et al., 2007] and roughly coeval in the south near Northland.

Patriat et al. (2018) show evidence that the southern extent of the westward New Caledonia obduction from the Loyalty-Three Kings arc was at least 25°S and speculate that it may have continued along the entire margin of NE Zealandia, including the westward obduction of the Northern Allochthon. Kroenke and Dupont (1982) argued the Norfolk Ridge obducted material eastwards onto the southern half of the 3KR in the opposite sense, depositing mass onto its fore-arc and into its subduction trench which negated their bathymetric (Figures 6.21; 6.24) and gravity lows (Figures 6.19; 6.18). This could explain the relative positive mass of the southern half of the 3KR observed in the bathymetry data, and may also explain the lack of a strong magnetic signal on the western margin of the southern 3KR (Figure 6.20). It is possible that both hypotheses are correct, with the arc collision depositing mass on both the eastern Norfolk Ridge as well as the western 3KR to varying degrees.

This project proposes that the strength of the mechanical bond generated by the partial subduction of the eastern margin of the continental Norfolk Ridge was sufficient to allow the Loyalty Ridge and 3KR to remove a large portion of the Norfolk Ridge (e.g. Lineament 5, Figure 6.19) in its northern (22-25°S) and centre (25-29°S) sections, respectively. However this process seemed to occur in distinct fashions, and in the southern Norfolk Ridge (25-32°S) the Norfolk Ridge does not appear to be dramatically altered.

#### 6.5.2.6 *Separation of the Norfolk and Loyalty-Three Kings Ridges*

The separation of the Loyalty-Three Kings Arc SE away from the Norfolk Ridge is hypothesised have occurred in three distinct fashions across the northern, centre, and southern segments. In the northern segment (north of 26°S) the still-connected Loyalty-Three Kings ridge pulled away eastwards taking the partially subducted eastern Norfolk Ridge away with it (e.g. Lineament 5, L5, Figure 6.19). Between L4 and L5 the continental crust was heavily rifted, resulting in ~23-25 Ma subalkaline/shoshonitic volcanism [e.g. Mortimer et al., 2018; Figure 2.8]. The Norfolk Ridge was also stretched and widened, evident by both the fanning and splitting of its positive magnetic anomalies (Figures 6.20, 6.22) as well as the weakening/widening of its BA (Figure

6.19). Further still, the New Caledonia Basin west of the Norfolk Ridge was also affected with this project interpreting its crust as having been thinned by its higher BAs in the north. This widespread E-W stretching is also assumed to have reactivated or otherwise weakened the thinner or rifted crust associated with Lineament 4 (Figure 6.19) despite reducing the strength of its anomaly overall.

In the centre segment of the Norfolk Ridge ( $25\text{--}29^{\circ}\text{S}$ ) the stress pulling the Loyalty Arc eastwards is hypothesised to have been increasingly focused east of the Norfolk Ridge, which was sufficient to separate the 3KR from the Loyalty Ridge along the Cook Fracture Zone at  $\sim 23$  Ma [Ballance, 1976; Kamp, 1986; Bernardel, 2002; Mortimer et al., 2007; Herzer et al., 2009]. This likely alleviated stress west of the northern Norfolk Basin and explains the reduced degree of crustal thinning in both the New Caledonia Basin and Norfolk Ridge relative to the northern segment, as inferred from the BA (Figure 6.19). Some of the material comprising Lineament 5 (L5, Figure 6.19) continues to be locked into the subduction trench of the 3KR as it is carried further east, and there is evidence that some of the positive magnetic material from the Norfolk Ridge has been scrapped onto the western fore-arc of the 3KR (Figure 6.20). However much of the missing L5 material appears to have been strewn onto the floor of northern Norfolk Basin (encircled in dotted lines, Figure 6.24) and then re-rifted apart as the basin continued to open.

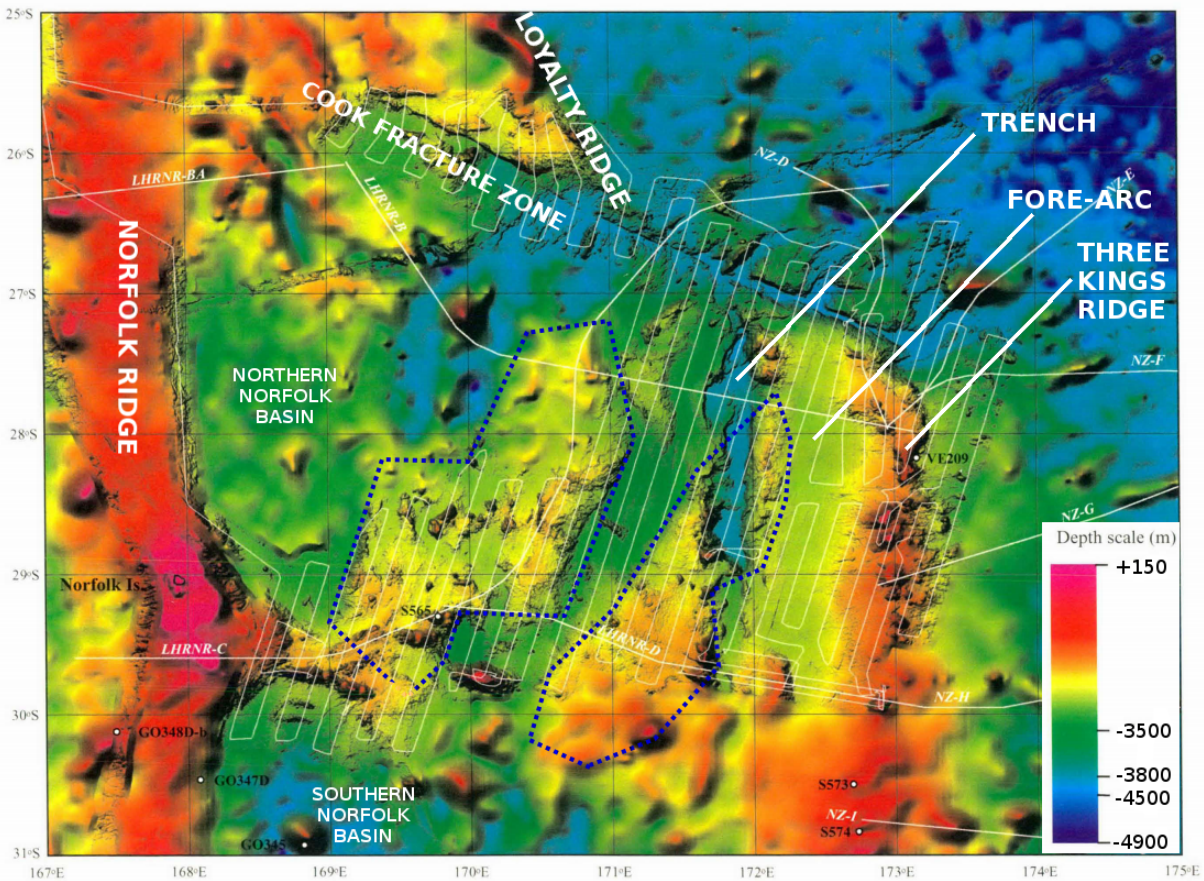


**Figure 6.24:** Multibeam bathymetry of the northern Norfolk Basin from the FAUST-2 project courtesy of Benkhelil et al. (2001). Additional labels have been added in white as well as the dotted boundaries of material hypothesised to be former pieces of the eastern Norfolk Ridge.

Finally in the southern region (e.g. south Norfolk Basin, south of and including Norfolk Island,  $\sim 29^\circ\text{S}$ ) the 3KR appears to have separated without dislocating the eastern Norfolk Ridge (e.g. L5, Figure 6.19) aside from a relatively small amount of material seemingly obducted from the Norfolk Ridge onto 3KR during the initial collision [e.g. Kroenke and Dupont, 1982]. An eastward obduction explains why the 3KR has more mass and muted gravity and magnetic signatures at these latitudes, as well as why the southern Norfolk Basin is flat and deep relative to the north (Figures 6.21; 6.24). Strain is hypothesised to have been almost entirely confined within the southern Norfolk Basin, which explains its apparent higher degree of thinning relative to the northern basin, as well as why the Norfolk Ridge and New Caledonia Basin show no degree crustal thinning in the BA data relative to points north. South-east of the Norfolk Ridge, the right-lateral VMFZ accommodating this motion at the southern margin of the south Norfolk Basin appears to have rifted L5 into several pieces, creating discrete the Reinga and South Maria ridges (Figure 6.18).

### 6.5.2.7 Slab Detachment and Volcanism

Following the Loyalty Arc collision into the Norfolk Ridge the last of the Loyalty Basin was consumed and the continental crust of NE Zealandia was partially subducted east beneath the Loyalty-Three Kings Ridge [e.g. Schellart et al., 2006, Schellart, 2007]. This partially subducted crust was mechanically and thermally weakened which accommodated the detachment of the Loyalty Basin [e.g. Davies and von Blanckenburg, 1995; Wortel and Spakman, 2000] and its subsequent sinking into the mantle as the "Loyalty Slab". The resulting volcanism from this process could generate classic arc-type lavas as well as those with a high component of continental crust (e.g. alkaline, potassic, or shoshonitic [Morrison, 1980]) via the melting of the partially subducted continental crust [von Blanckenburg and Davies, 1995]. Assuming a sinking rate of ~60 km/Ma for the recently detached Loyalty Slab [Schellart, 2007] melt could still theoretically be generated for 2-3 Ma following detachment assuming typical maximum depths of 120-180 km for dehydration melting [Kessel et al., 2005].

The timing and location of this slab detachment is poorly constrained. It must have occurred following the obduction events in New Caledonia ~38-34 Ma [Spandler et al., 2005; Fitzherbert et al., 2004; Collot et al., 2008; Cluzel et al., 2012] and Northland ~25-22 Ma [Spörli, 1999; Rait, 2000; Spörli and Harrison, 2004] but the position and timing of detachment between these events can only be inferred from a currently-sparse distribution of geochemical constraints supplied by volcanism throughout the Norfolk Ridge, Norfolk Basin, and Southern Norfolk Ridge System. It is proposed that the path of slab detachment volcanism can be traced N-S along either Lineament 4 (L4, Figure 6.19) and/or Lineament "4.5", either of which ultimately meeting with the ~23 Ma arc-type volcanism offshore of Northland [Herzer, 1995; Hayward et al., 2001; Booden et al., 2011] and continuing south along L4. It is noted however that unlike the volcanism along L4.5 which has a multitude of possible sources, the inferred Eocene-Miocene volcanoes along L4 at the Norfolk Ridge could only be caused by Loyalty Slab melting, hot spot volcanism, or west-directed Pacific Plate subduction, with the latter two believed to be less likely by this work. Thus a model with slab tear producing volcanism along L4, or both L4 and L4.5, is preferred over one in which melt only erupts at L4.5 until more geochemistry data is available [e.g. Mortimer et al., 2015].

### 6.5.3 A Unifying Norfolk Ridge and Northland Model 30-15 Ma

A model attempting to link the mechanism of arc collision, partial subduction, back-arc weakening, and subsequent volcanism at both the Norfolk Ridge ( $30^{\circ}\text{S}$ ) as well as Northland ( $36^{\circ}\text{S}$ ) is shown in Figure 6.25. This model expands on the premise of N-S migrating slab detachment producing arc-type or shoshonitic eruptions from New Caledonia to Northland [e.g. Schellart et al., 2006; Schellart, 2007; Figure 2.7] by including Zealandia's terranes as well as hypothesising the location of slab tear and the nature of melt focusing at Lineament 4 west of the Norfolk Ridge (Figure 6.19). It is constrained by the geologic structure of NE Zealandia [Mortimer, 2004; Mortimer et al., 2014], the dating of volcanism [Brothers, 1984; Herzer, 1995; Mortimer et al., 1998; Hayward et al., 2001; Mortimer et al., 2007; Stagpoole et al., 2009; Booden et al., 2011; Mortimer et al., 2018; Figure 2.8], as well as the timing of New Caledonia's obduction event [Spandler et al., 2005; Fitzherbert et al., 2004; Collot et al., 2008; Cluzel et al., 2012], timing of the obduction of the Northland Allochthon [Spörli, 1999; Rait, 2000; Spörli and Harrison, 2004], and timing of the opening of the Norfolk Basin [Bernardel, 2002; Mortimer et al., 2007; Herzer et al., 2009]. It is further constrained by the geodetic solutions presented in this work (e.g. Figure 6.17) which suppose the existence of an intraplate mechanical discontinuity west of the Norfolk Ridge and SW of onshore Northland, and possibly SW of New Caledonia. The model describes how the Norfolk Ridge and/or the Murihiku Terrane and/or specifically Lineament 4 (L4, Figure 6.19) may have been altered and reactivated by the early Miocene tectonic reconfiguration at the margin of NE Zealandia. However it could only explain the currently observed geodetic velocities defining the proposed "East Australian" sub-plate anomalies (e.g. Section 6.5.1) if one or more of these proposed features partitioning the Australian Plate were still zones of relative weakness some 15 Ma later.

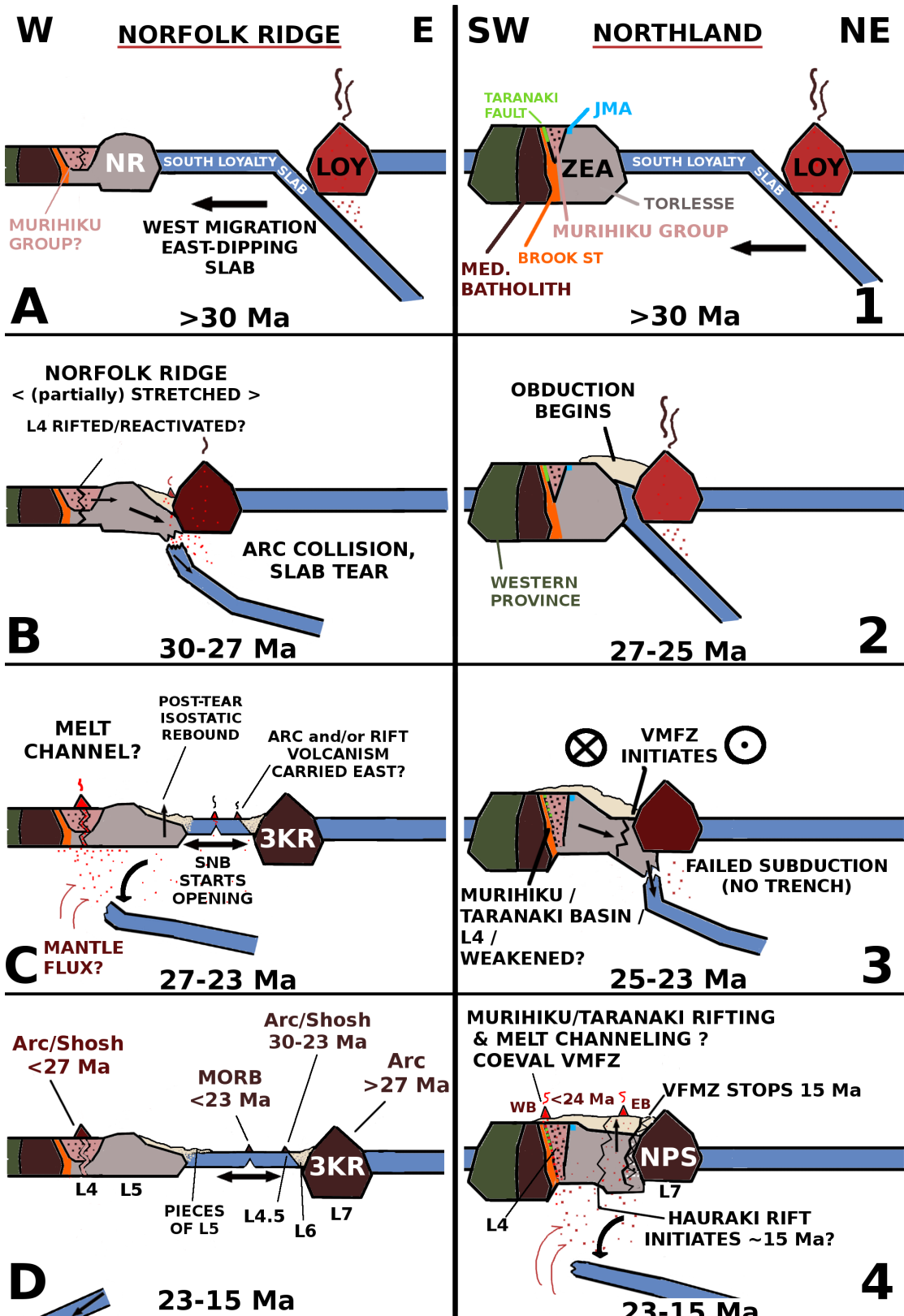


Figure 6.25: Model attempting to explain the concentrated volcanism and possible extension along Lineament 4 on the west flank of the Norfolk Ridge (Figure 6.19) resulting from hypothesised tearing of an east-dipping Loyalty Arc slab depicting both Norfolk Ridge (left, 30°S, A-D) and Northland NZ (right, 36°S, 1-4). An identical Zealandia basement structure at both the Norfolk Ridge and Northland is assumed and is coloured accordingly. NR = Norfolk Ridge, ZEA = Zealandia (~Northland), JMA = Junction Magnetic Anomaly, LOY = Loyalty Ridge, MORB = Mid-Ocean Ridge Basalt, SNB = South Norfolk Basin, 3KR = Three Kings Ridge, VMFZ = Veining Meinesz Fracture Zone, NPS = Northland Plateau Seamounts, WB/EB = Western/Eastern Belt of Miocene arc volcanism.

The model speculatively assumes that Lineament 4 (L4, Figure 6.19) is within the thinner and possibly weaker crust of the Murihiku Terrane [Ballance and Campbell, 1993; Black et al., 1993; Kamp and Liddell, 2000; Roser et al., 2002; Briggs et al., 2004; Mortimer, 2004] or at its eastern margin. It also assumes that the partial subduction of the Norfolk Ridge and Northland lithosphere created horizontal extension throughout the crust that reactivated or exacerbated the pre-existing thinner or rifted crustal feature interpreted as L4. The volcanoes along L4 and L4.5 are presumed to be the result of dehydration of the Loyalty Slab or melting of the partially subducted crust with L4 effectively channelling melt from below, possibly via faulted or porous weak zones, and L4.5 due to its position proximal to slab tear. Volcanism is assumed to have occurred anywhere from ~3-0 Ma following slab detachment based on the Loyalty Slab's calculated sinking rate of ~60 km/Ma [Schellart, 2007] and typical maximum depth of melt generation of 120-180 km [Kessel et al., 2005]. Finally it is speculated that the upward fluxing of the mantle around the slab's transition from vertical to down-dipping may elevate temperatures generating a greater amount of melt [e.g. Garfunkel et al., 1986], and that these melts may be relatively enriched owing to the addition of fresh mantle from depth.

The model does not attempt to explain the driving force behind the opening of the Norfolk Basin but it does suppose that the partially subducted continental crust at Northland may have been sufficiently weakened, allowing the VMFZ to form more easily. This provides another constraint on the timing of incipient activity on the VMFZ as occurring after the initial obduction of the Northland Allochthon ~25-22 Ma [Spörli, 1999; Rait, 2000; Spörli and Harrison, 2004] and also likely following slab detachment beneath Northland which generated volcanism 23 Ma and younger (e.g. Figure 2.8). Thus the ~23 Ma estimate for initial activity on the VMFZ [e.g. Bernardel, 2002; Mortimer et al., 2007; Herzer et al., 2009] may be on the younger side, with activity possibly beginning marginally earlier ~25-24 Ma. This could also mean that the separation of the Loyalty-Three Kings Ridge away from the Norfolk Ridge first began in the north at ~25 Ma but activity at the VMFZ did not begin in earnest until a few million years later.

The model also attempts to explain the variable geochemistry observed between two discrete west and east "belts" of Miocene arc-type volcanism (EB and WB in Figure 6.25) on either side of Northland. Booden et al. (2011) observed that the western rocks are more basaltic and primitive whereas eastern are more andesitic and feature a higher signature of assimilated crustal material. The western rocks could be explained assuming an influx of hotter, primitive mantle around the western edge of sinking slab. Furthermore its relatively basaltic composition could be explained

by a high degree of melt channelling which would limit interaction and partial remelting of the continental crust which is relatively thin beneath the Murihiku Terrane. Similarly, the eastern rocks are more andesitic which may simply be the result of higher exposure to a thicker continent which has since isostatically rebounded following slab detachment.

## 6.6 EVIDENCE FOR NONLINEAR CRUSTAL MOTION IN NWNZ

Many of the northern North Island velocity estimates (Figures 4.17, 6.11) show discrepancies between those sampling more recent periods (e.g. 2013-2017) vs. velocities spanning the entire range of 1995-2017. This is highlighted in Northland between cGNSS site KTIA (2008-2017, Figure 6.26), older campaign sites 1361 AAJU 1384 AAEB AAEJ (1995-2017, blue-yellow triangles, Figure 4.17), and newer campaign sites A49Q A42F A6Q1 (2013-2017, blue triangles, Figure 4.17) showing a significant degree of variation. This type of temporal discrepancy also occurs elsewhere in the North Island but in regions of much higher stress and high degree of melt in the crust [e.g. TVZ, Lamb et al., 2017]. As Northland appears to be mostly without measurable shear strain rates (e.g. Figure 4.23) variations in velocity estimates is not expected. Improperly correcting coseismic offsets in large earthquakes between 1995 and 2013 may also account for variations in velocity, but it is noted that despite correcting for the the <3 mm offsets generated by the 2004 Macquarie Island, neglecting to do so would not have a noticeable effect on velocity estimates due to both the extended 20+ year span of data as well as the 0.3 mm/yr<sup>1/2</sup> random walk noise applied throughout Northland (e.g. Figure A.4). Regardless, because campaign data can easily be corrupted by poor field surveying, only continuous sites were examined for nonlinear behaviour. Furthermore these continuous sites were not examined individually, but relative to other nearby continuous stations. This allowed for the cancellation of any local weather or GNSS system anomalies which would have affected either station equivalently. In this way the degree of perceived linearity in crustal behaviour can be isolated.

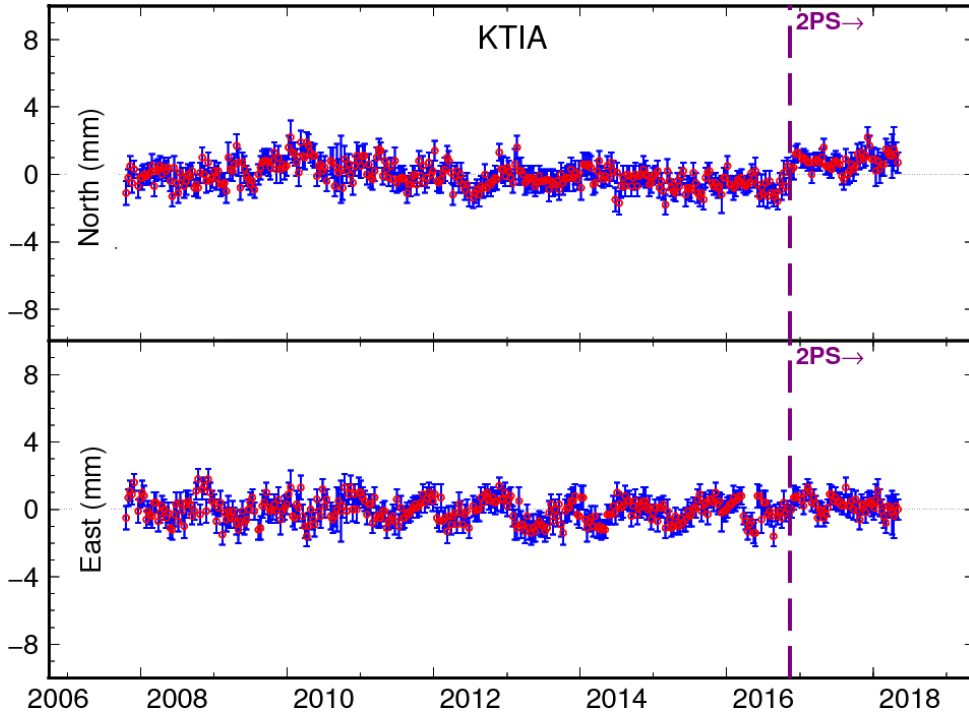


**Figure 6.26:** Timeseries for Northland cGNSS station KTIA. The 2PS rename marks the November 2016 Kaikōura earthquake which only slightly affected the station. This is one of the most consistent and stable sites in New Zealand.

Various pairs of cGNSS sites throughout NWNZ as well as between NZ and other sites throughout the Australian Plate were examined by comparing the horizontal geodetic (NEU) distances between each cGNSS station pair for each simultaneous 10-day aggregate position estimate in its timeseries, shown in Figure 6.27. All mechanical offsets (e.g. antenna changes) were manually corrected and heights of each stations were set as the average of both, eliminating the vertical component. A linear least-squares fit excluding data after the November 2016 Kaikōura earthquake (purple) is plotted as a black line and a yearly low-pass filter is plotted in red, which removes the influence of a majority of weather seasonality and the Earth's nutations (e.g. Figure 4.12). The magnitude of the error bars shown is the sum of the horizontal positional uncertainty of both sites.

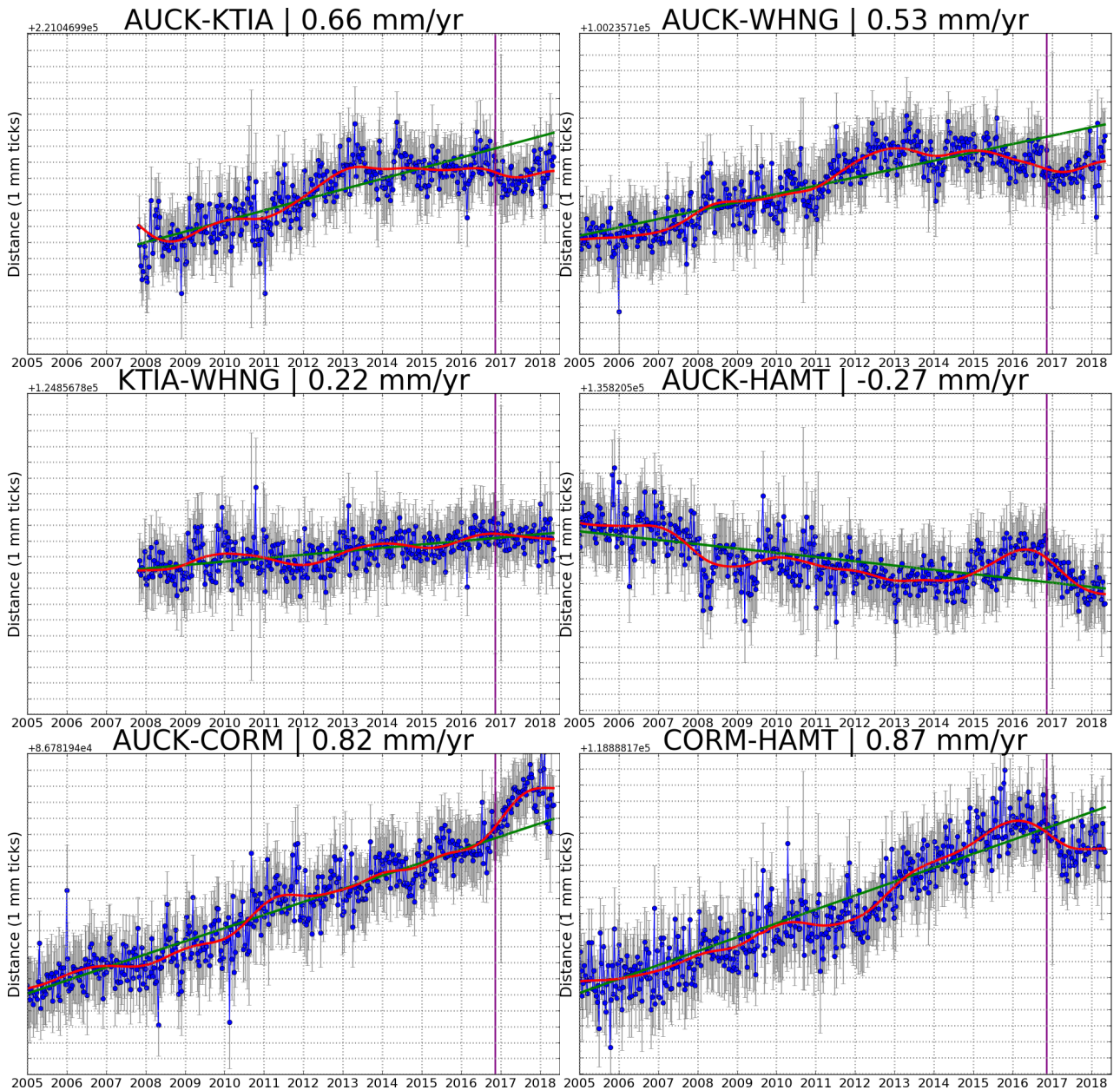


**Figure 6.27:** (part 1/2) Geodetic (NEU) distance between NZ cGNSS stations. Heights between stations were fixed, thus this data measures only horizontal change. A linear fit excluding data beyond the November 2016 Kaikōura earthquake (vertical purple line) is drawn in black and a 1 year low-pass filter in red. Error bars are the sum of the horizontal positional uncertainty of both stations. Positive slopes are separating, negative are compacting, and flat are fixed with the slope of this trend shown in each header. All plots are gridded at 1 mm and 1 year.

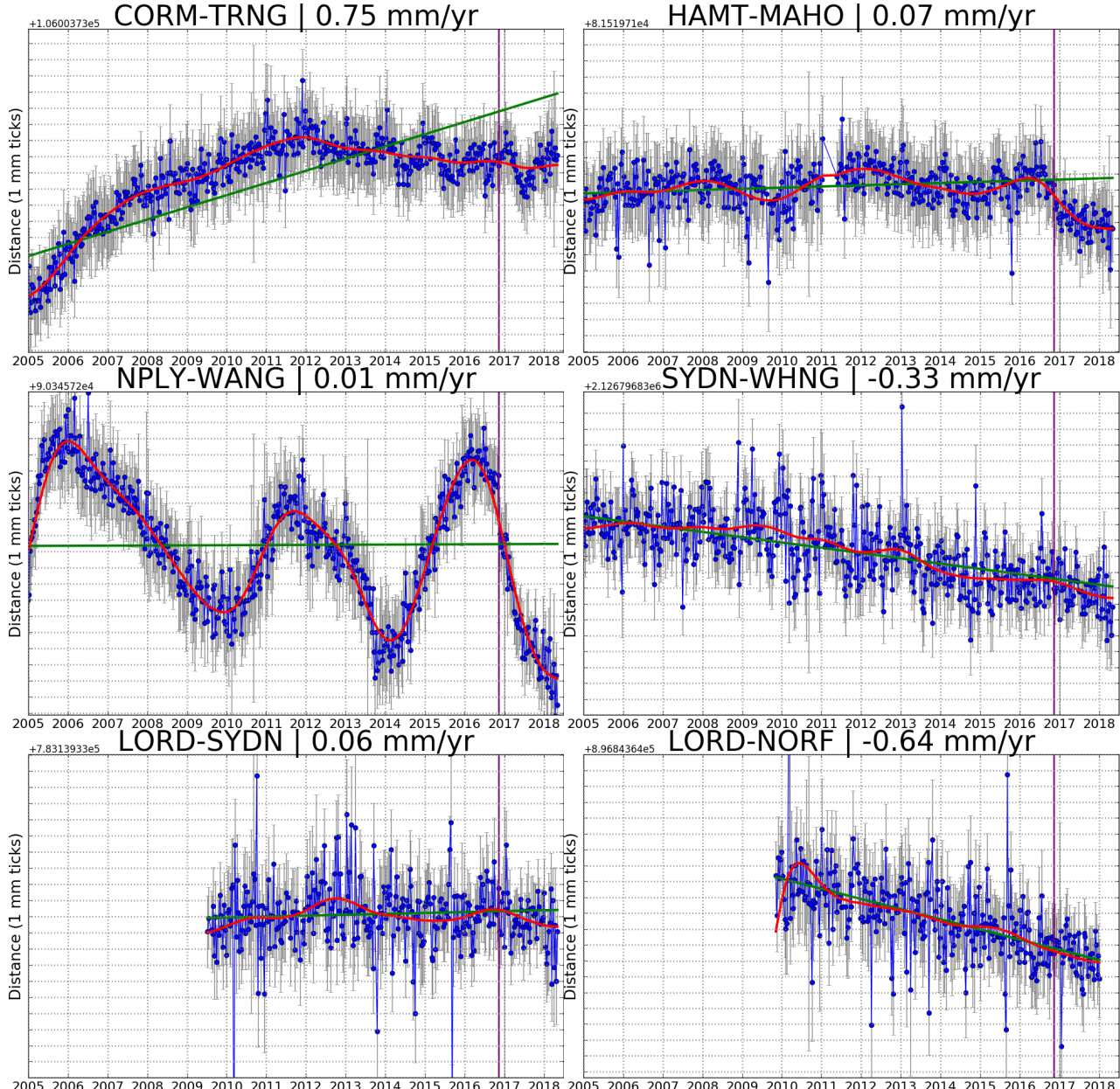


**Figure 6.27:** (part 2/2) Geodetic (NEU) distance between NZ cGNSS stations. Heights between stations were fixed, thus this data measures only horizontal change. A linear fit excluding data beyond the November 2016 Kaikōura earthquake (vertical purple line) is drawn in black and a 1 year low-pass filter in red. Error bars are the sum of the horizontal positional uncertainty of both stations. Positive slopes are separating, negative are compacting, and flat are fixed with the slope of this trend shown in each header. All plots are gridded at 1 mm and 1 year.

The paired data in Figure 6.27 showed a surprising degree of nonlinearity. In some cases the rate of widening or contraction seemed to fundamentally change at some point, particularly around 2011 or 2012 when pairs AUCK-KTIA, AUCK-WHNG, and CORM-TRNG all slowed their widening rates. Even for relatively linear behaving pairs (e.g. AUCK-CORM) some years could show year to year deviations of their annual average by as much as 1 mm off the linear

trend. This level of inconsistency could have a serious effect on short-duration campaign surveys.

The reason for this variance is not clear but it is likely to be a combination of several issues, including multi-year seasonality (e.g. El Niño), local monument instability or changes in a site's sky view (e.g. a tree growing nearby), changes in the selection of sites used in the numerical stability process, fundamental changes in the calculation of satellite orbits, or software/hardware bugs. The motion could also be the cumulative result of many small coseismic offsets from earthquakes or events that had not been accounted for or otherwise detected. It is also possible that these anomalies in fact do show that the crust in NWNZ may behave non-rigidly at multi-year periods at the  $\sim mm$  scale. This idea is controversial but is supported by the relative stability of non-NZ site pairs LORD-SYDN and LORD-NORF, which are truly beyond the reach of subduction stress emanating from the Hikurangi Margin. It is also supported by the strong oscillations of sites nearer the plate boundary (e.g. HAMT-MAHO) which have a faintly similar behaviour as those commonly affected by slow slip events (e.g. NPLY-WANG). It is speculated that stress generated by these slow slip events may extend through the crust as far north as HAMT/Hamilton and TRNG/Tauranga.

As the precision of geodetic data improves and amount of timeseries data increases it will be interesting to see what, if any, long period oscillations or other signs of nonlinear behaviour emerge throughout NWNZ. For now it is clear from this data that the degree of year to year variance in the estimated position of even stable cGNSS sites is such that campaign surveys should conservatively plan for errors or deviations on the order of  $\sim 1-2 mm$  beyond typical annual variations, intrinsic to the GNSS system and possibly the crust itself. It further highlights the advantage of continuous sites rather than campaign sites as a way to not only derive a linear velocity, but to observe the subtle ways the crust may be behaving over time.

## 6.7 REFLECTIONS AND FUTURE WORK

### 6.7.1 In New Zealand

#### 6.7.1.1 Geodesy

Many of the newer GNSS sites (>2013; green diamonds and blue triangles, Figure 4.17) surveyed in this project 2015-2017 were unable to be resolved with high confidence. It is assumed that the

2016 Kaikōura earthquake and poor resolution of its coseismic offsets throughout NWNZ (e.g. Section 4.5.3.1) were partly responsible, but it is also now apparent that a resolving a campaign site in only three surveys and three years is a challenging endeavour. This is particularly due to NWNZ's weak GNSS reference network, potential for  $\sim mm$  scale deviations from linearity (e.g. Figure 6.27), and principally its inherent low ( $\sim 1 \text{ mm/yr}$ ) rate of motion. However the data collected in this project will be able to easily resolve all of these sites with even a single year of future surveying. Furthermore this project showed that even an  $\sim$ hourly occupation of campaign sites with historic (>20 years) data can be sufficient to produce well-constrained velocities. In particular this would mean that the sites situated on islands within the Hauraki Gulf may be adequately survey-able with only a single day's travel, potentially halving the associated costs with reaching them. With additional and otherwise better-constrained data, the rift model presented in this work (e.g. Section 6.4) will also produce estimates with lower uncertainty. Further, a higher amount of well-constrained vectors may enable block modelling of the hypothesised discrete, fault-bound regions (e.g. Figure 6.11) which could produce fair estimates of fault slip rates [e.g. Wallace et al., 2004; McCaffrey et al., 2007].

Beyond additional (preferably routine) geodetic campaigns in NWNZ the addition of more cGNSS sites would be ideal as these would improve resolution of future campaigns as well as potentially identify any unusual crustal behaviour, possibly even providing an early warning to volcanic eruptions within the Auckland Volcanic Field. cGNSS sites within the gulf (e.g. Taranga and/or Mokohinau Islands), Hauraki Rift (e.g. Te Aroha), Hunua Ranges (e.g. Wairoa North Fault), or Tasman coast north-west of Auckland are recommended. It may also be beneficial to establish a working relationship between commercial survey companies (e.g. Allterra and Smartfix, both in Auckland) who both operate independent cGNSS reference networks throughout NWNZ. Though the quality of the construction and maintenance of these sites is not always suitable for tectonic surveys, they are often sufficient to produce well-constrained velocities (e.g. Figure 4.17, red diamonds). Furthermore their network distribution in NWNZ greatly exceeds the current network maintained by GeoNet/LINZ.

#### 6.7.1.2 *Seismic*

This project chose to predominately focus on geodetic surveying in lieu of seismic surveying as the potential benefit was larger, clearer, and more assured, despite its extended time commitment. Furthermore it was supposed that the high density of quality borehole sites already present throughout the Auckland Volcanic Field (e.g. Figure 5.17) would be sufficient

to resolve the microseismicity within the greater Hauraki Rift provided the derivation of customised event location parameters (e.g. Section 5.4.2). Thus only a single new sensor was installed in 2016 (Section 5.6) in addition to the the new site data borrowed from a the borehole site RBAZ on Rangitoto Island in order to test the utility of additional seismic stations outside of greater Auckland.

In analysing waveform data following this decision, it was soon realised that the sites surrounding Auckland were too affected by the city's high level of human noise to adequately resolve microseismicity within the Hauraki Rift, and that this project's new station, being favourably positioned far ( $>60\text{ km}$ ) from the city and atop bedrock, was exceptionally suited for it (e.g. Section 5.4.2.6). Thus it was determined that additional stations would indeed be highly beneficial despite a temporary construction, or use of a cheaper short-period sensor, so long as the sites are strategically located. Results from this project would estimate that the construction of just three to five more sensors could theoretically double the amount of detected events (e.g. Figures 5.17, 5.18) as well as halve the average positional uncertainty. Recommended placement for these would be on mountain ranges to the west and east of the rift at  $\sim 37^\circ\text{S}$ , in northern Coromandel, on the Tasman coast (e.g. Waitakeres or Woodhill Forest), and to the north in Whangarei Heads, especially in light of the recent  $\sim\text{M}4$  events immediately east of this region (e.g. Figure 5.19).

In light of this project's speculation that the margin of NE Zealandia may be accommodating some amount of tectonic stress between New Caledonia and Northland (Section 6.5.2), there may be a degree of associated seismicity occurring immediately offshore west of Northland. Thus a seismic deploy targeting this region near the shore here could be surprisingly fruitful. A review of the  $\sim 16$  months of data recorded by a five-station (TIKO, OUZ, WCZ, MATA, MKAZ) seismic deployment throughout Northland previously only used for anisotropy and ambient tomography studies [e.g Duclos, 2005; Behr et al., 2010] could serve as a pilot study.

Aside from new stations, a re-analysis of the station waveform data using newer waveform-based or waveform stacking [e.g. Kao and Shan, 2004] event locations is recommended as they are known to be effective at resolving microseismicity [e.g. Zhou et al., 2010; Castellanos and van der Baan, 2013; Grigoli et al., 2017; Grigoli et al., 2018] though it is unclear if the current seismic station infrastructure in the northern North Island is robust enough to take advantage of these new techniques. Furthermore it is noted that the New Zealand NZ3DRX velocity model [Eberhart-Phillips et al., 2010] is now almost a decade old and could likely be improved considerably with the vast amount of additional data that has been recorded.

### 6.7.1.3 *Gravity*

This project found that the ground-based gravity measurements collected within the New Zealand Primary Gravity Network [Robertson and Reilly, 1960] to be a valuable resource. Additional surface measurements would be advantageous but it was noticed that most of the regions with sparse coverage tended to be remote or difficult access and are therefore relatively unlikely to be surveyed. The recent advent of inexpensive and portable microchip-sized gravimeters viable for geophysical studies [e.g. Middlemiss et al., 2016] may one day allow for them to be mounted on drones which could blanket survey these areas easily, as well as offshore within the Hauraki Gulf.

It may also be a worthy endeavour to derive a Bouguer anomaly using point-to-point methods and a 3D crustal model [e.g. Fullea et al., 2008], particularly once a crustal model for the New Zealand is developed. Gridded Bouguer anomaly models will also enable the aerogravity survey data of McCubbine et al. (2017) to be re-used more effectively as it was often recorded at variable heights.

### 6.7.2 *In Zealandia*

The tectonic interpretations throughout Zealandia initially began simply as a means to better understand the structure of NWNZ, but quickly expanded in depth and scope after it was observed that cGNSS sites on the margin of NE Zealandia were noticeably distinct from those on continental Australia (Section 6.5.1). A model was proposed (Section 6.5.3) which postulated that there may be a tectonic-scale discontinuity connecting New Caledonia to Northland through the Norfolk Ridge and Southern Norfolk Ridge System (e.g. Lineament 4, Figure 6.19). Thus the recommendations or proposals for future research here are primarily specific to better understanding this feature. They are in addition to the never-ending need for more high-quality shipboard recordings of bathymetry, gravity, and magnetic data in addition to expanded seismic reflection, dredging, and drilling of the seafloor. It is acknowledged that this region is already under active study with highly anticipated analysis of dredged rocks and deep-drill data critical to this project's hypothesis forthcoming [e.g Mortimer et al., 2015; Sutherland et al., 2018].

### 6.7.2.1 *Geodesy*

The dearth of islands on the Australian Plate between Lord Howe Island, New Caledonia, Northland, and the Kermadec Islands far to the east is discouraging for the prospect of expanded GNSS geodetic work. Novel undersea GNSS methods have been developed by various workers but the extremely high precision required to measure the sub-mm yearly rate of motion make them impractical for this scenario. However undersea fibre-optic lines perpendicular to the Norfolk Ridge, perhaps based from Norfolk Island, would be able to detect infinitesimal strain [e.g. Kirkendall and Dandridge, 2004] and thus be able to confirm or deny that the Norfolk Ridge was accommodating any deformation. This may also be practical SW of Northland and New Caledonia.

### 6.7.2.2 *Seismic*

The hypothesised deformation at the periphery of NE Zealandia is at the same scale as that of the Hauraki Rift and thus should generate a similar amount of seismicity. As the geodetic evidence for this is strongest near the Norfolk Ridge and Northland (e.g. Section 6.5.1) these are the most sensible places for a seismic deployment. Ideally ocean bottom seismometers could be deployed, but practically it is sensible to first deploy in Northland, or revisit the data of past projects (previously mentioned in Section 6.7.1.2). There are also two currently active seismometers on Norfolk Island maintained by Geoscience Australia (NFK and NRFK) which may be able to at least detect the presence of proximal seismic activity despite not being able to determine its location.

Additional seismic reflection lines explicitly targeting the Norfolk Ridge from N-S would also be beneficial to constrain the evolution of its crustal structure. While some have already been done [e.g. Klingelhoefer et al., 2007; Collot et al., 2008] these targeted the basins to the west and only peripherally captured the Norfolk Ridge.



## CONCLUSIONS

---

The previously ambiguous character of tectonic motion throughout the Hauraki Rift and north-western New Zealand (NWNZ) has been greatly resolved by processing the three years of campaign geodetic data collected by this project 2015-2017 (Section 6.2) as well as 23 years of archived campaign and reference station data 1995-2018. It is shown that even northernmost New Zealand ~700 km from the Hikurangi plate margin appears to be moving anomalously (~1 mm/yr SW) relative to this project's Australian Plate reference frame (Section 4.6) and thus should not be considered a stable feature of the plate. What was known about the oblique and right-lateral nature of widening at the Hauraki Rift has been modelled and expanded on, with this work estimating the rift's far-field rate of widening to be about ~1.15 mm/yr and its mechanical thickness around ~17.5 km (Section 6.4). However these estimates include large uncertainties (0.3 mm/yr and 7.7 km respectively) which indicates that the rift's activity and structure likely has a strong latitude dependence. South of ~37°S the rift appears to be increasingly influenced by plate boundary stresses, with its widening becoming faster and its mechanical thickness summarily becoming thinner. This information is vital to any future tectonic modelling of NWNZ's crust as well as the mantle beneath it.

Analysis of timeseries data throughout the North Island show that the northern North Island is subsiding at an average rate of 1.1 mm/yr (Table 6.1) which may exacerbate the effect of rising sea levels on coastal communities. This project also shows that the application of ( $\sim 1/f^2$ ) "random walk" noise may be understated in the North Island when assuming an oversimplified  $\sim 1/\sqrt{T}$  correlation to only the age of the station (Table 4.3). This means that velocity models using these types of approximations could be significantly underestimating their uncertainties.

The new geodetic vectors throughout NWNZ may show current activity at several faults (Section 6.3). These include a fault system parallel to the Tasman coast west of Auckland, a possible northern extension of the Wairoa North Fault through Waiheke Island, strike-slip faulting parallel to the coast between Hamilton and Taranaki, probable northern continuations of the Cape Egmont and Taranaki Faults, and evidence that the Hauraki Rift's widening may also be accommodated by one or more of the parallel rift boundary faults binding the rift zone.

This project's analysis of seismic data collected in the greater Hauraki Rift was able to derive a power spectrum density representative of the region's microseismicity. This allowed for the

derivation of customised waveform frequency filters (e.g. 3-11 Hz) and automatic detection parameters which were used to uncover over twice the amount of small ( $M < 2$ ) earthquakes relative to the broad, nationwide default parameters employed by GeoNet. Additionally, a new station (Section 5.6) was installed east of the Hauraki Rift in the Coromandel Peninsula which has proven highly valuable in detecting new events. The subsequent statistical analysis done to determine its utility (Section 5.4.2.6) showed that the amount and ambiguity of detected events would improve dramatically with the addition of <5 additional sensors installed away from the noise of Auckland City. The presence of ongoing activity in Northland was hinted by the seismicity uncovered by this work (e.g. Figure 5.17) and dramatically emphasised by the recent M4 events in early 2019 near Whangarei (Figure 5.19).

The observation of similar elevated geodetic velocities relative to the Australian Plate on Norfolk Island and New Caledonia as those observed throughout Northland could imply that much of the eastern Australian Plate is affected by a secondary, E-NE-directed stress of uncertain origin beyond that generated at the Australian-Pacific plate boundary (Section 6.5.1). The existence of a 2000+ km continuous lineament of weakened crust capable of mechanically compressing the Australian Plate ~1 mm/yr is hypothesised, coinciding with a narrow Bouguer Gravity Anomaly low along the margin of NE Zealandia (e.g. Norfolk Ridge to Taranaki Basin, Lineament 4, Figure 6.19). It is further proposed that this feature has also focused Oligocene-Miocene aged volcanism along the western flank of the Norfolk Ridge, through the Reinga Basin, and along the western shore of Northland. A model from 30-15 Ma was constructed in an attempt to explain its origin and possible mid-Miocene reactivation (Section 6.5.3).

Finally this project's interpretation of NE Zealandia's tectonic history since the Oligocene implies that the western collision of the Loyalty-Three Kings arc into the Norfolk Ridge and subsequent SE opening of the Norfolk Basin along the VMFZ affected much of the periphery of NE Zealandia. Notably this includes the E-W crustal stretching of the Norfolk Ridge and Northland, which potentially reactivated structures within both (Section 6.5.2). Furthermore this work speculates that the separation of the Loyalty-Three Kings arc away from the Norfolk Ridge may have occurred in three distinct fashions, including one which separated and deposited a large portion of the eastern Norfolk Ridge material onto the floor of the northern Norfolk Basin (Section 6.5.2.5). This interpretation, in addition to the observation of a west dipping Three Kings Ridge via magnetic and Bouguer Gravity Anomalies, support an NE-dipping Loyalty Arc tectonic history model [e.g. Crawford et al., 2003; Schellart et al., 2006; Whattam et

al., 2008] in which the eastern portion of the Norfolk Ridge's continental crust was partially subducted and pulled away with the Three Kings Ridge as it migrated SE along the VMFZ.



# A

## APPENDIX

---

### A.1 SHORELINE DISCONTINUITY OF SATELLITE GRAVITY DATA?

While the satellite dataset purports to be seamless across land-sea boundaries [Sandwell and Smith, 2009; Sandwell et al., 2013; Sandwell et al., 2014; Garcia et al., 2014] it is good practice to confirm this by inspecting the satellite topographic data to see if these sharp FAA coastal gradients correspond to sharp changes in topography. It appears that they do. Nearly all of the coastline has a high topographic gradient, as evident by the high density of 25 m contours in Figure A.1. This would naturally correspond to a sharp FAA gradient. Furthermore, and more importantly, there is no sharp FAA gradient at the Firth of Thames shoreline {175.5°, -36.2°} which has a very low topographic gradient onshore and off. This eliminates the possibility that the gravity data is affected by any sort of numerical errors at shorelines and as such the satellite data presented throughout this work should be trusted.

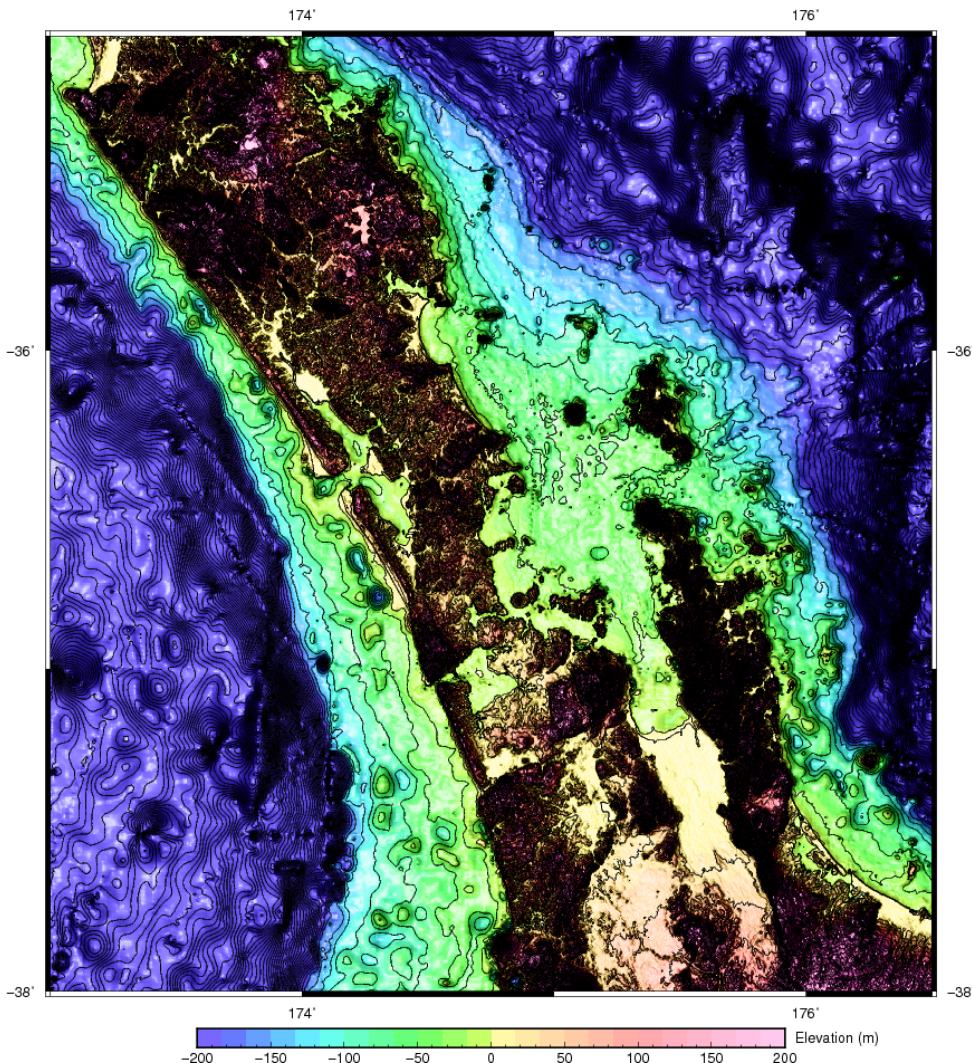


**Figure A.1:** Satellite topography [Smith and Sandwell, 1997] plotted at 0.25 *arcminute* resolution with 25 m contours. The excessive contouring is done to demonstrate how sharp the topography changes along much of the coastline in the Northern North Island.

## A.2 NZ CGNSS SITE TRNG / TAURANGA

Site TRNG (Figure A.2; Figure 4.17) was found to have an exceptional degree of unexplained nonlinear behaviour in its timeseries relative to all other cGNSS stations in NWNZ. The site is positioned at a high elevation away from potential influence from trees (e.g. Figure A.3) and it has been consistently mounted on a concrete pillar atop bedrock since its construction in 2003 [LINZ; [apps.linz.govt.nz](http://apps.linz.govt.nz)] so it is unlikely that its behaviour is due to the local site environment. It seems possible that the non-linearity is due to an antenna change at (6PS) but why this

would result in such a dramatic change in velocity is not clear. It is alternatively theorised that the greater rhyolitic caldera it resides in [e.g. Wilson et al., 1984] may be unstable.

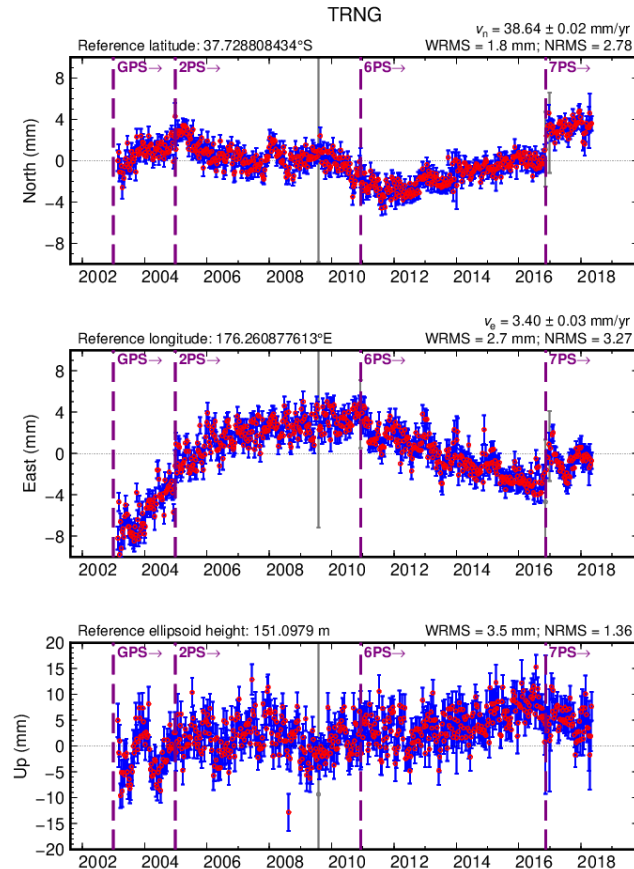


**Figure A.2:** Timeseries of NZ cGNSS site TRNG / Tauranga. Each datapoint is a 10-day aggregate. Purple lines mark seismic (2PS, 7PS) or antenna change (6PS) events which have been accounted for.



**Figure A.3:** Photo of NZ cGNSS site TRNG (LINZ, 2003).

### A.3 LINK BETWEEN TIME-DEPENDENT NOISE AND PLATE LOCKING?

While determining the degree of time-dependent ( $\sim 1/f^2$ ) random walk noise to apply to this study (Section 4.4.5.2) it was observed that many of the estimates at cGNSS sites seemed to be spatially correlated, particularly near the plate margin and within the TVZ. Further, these values visually seemed as if they could be correlated with the degree of plate locking predicted between the Australian and subducted Pacific plates estimated via modelling [e.g. Wallace and Beavan, 2010; Wallace et al., 2012]. A comparison of the predicted plate coupling and random walk magnitudes is shown in Figure A.4. Areas at the margin between a 0 and 1 coupling coefficient (dotted black lines) have a high degree of random walk noise in areas where this margin is nonlinear, particularly at the westward bend around Dannevirke/DNVK at the southernmost North Island. Conversely areas with a mostly linear coupled-uncoupled margin tend to correspond to discontinuous stick-slip behaviour at the surface and thus relatively low random walk magnitudes [e.g. McCaffrey et al., 2008]. In this sense the analysis of time-dependent noise in the timeseries of cGNSS stations may offer a simple first-order approach to finding probable locations where the plate interface geometry becomes nonlinear or otherwise complex. In the TVZ (e.g. TAUP and TRNG) high E-W random walk magnitudes are probably related to the thin and thermally weakened crust here [Sibson and Rowland, 2003; Hamling et al., 2015] or possibly due to the presence of a high degree of small and unaccounted coseismic offsets [Williams, 2003b] rather than plate interface effects. Notably Tauranga/TRNG (Appendix A.2) appears to have a less viscous crust than Whakatane/WHKT or White Island/RGWI.

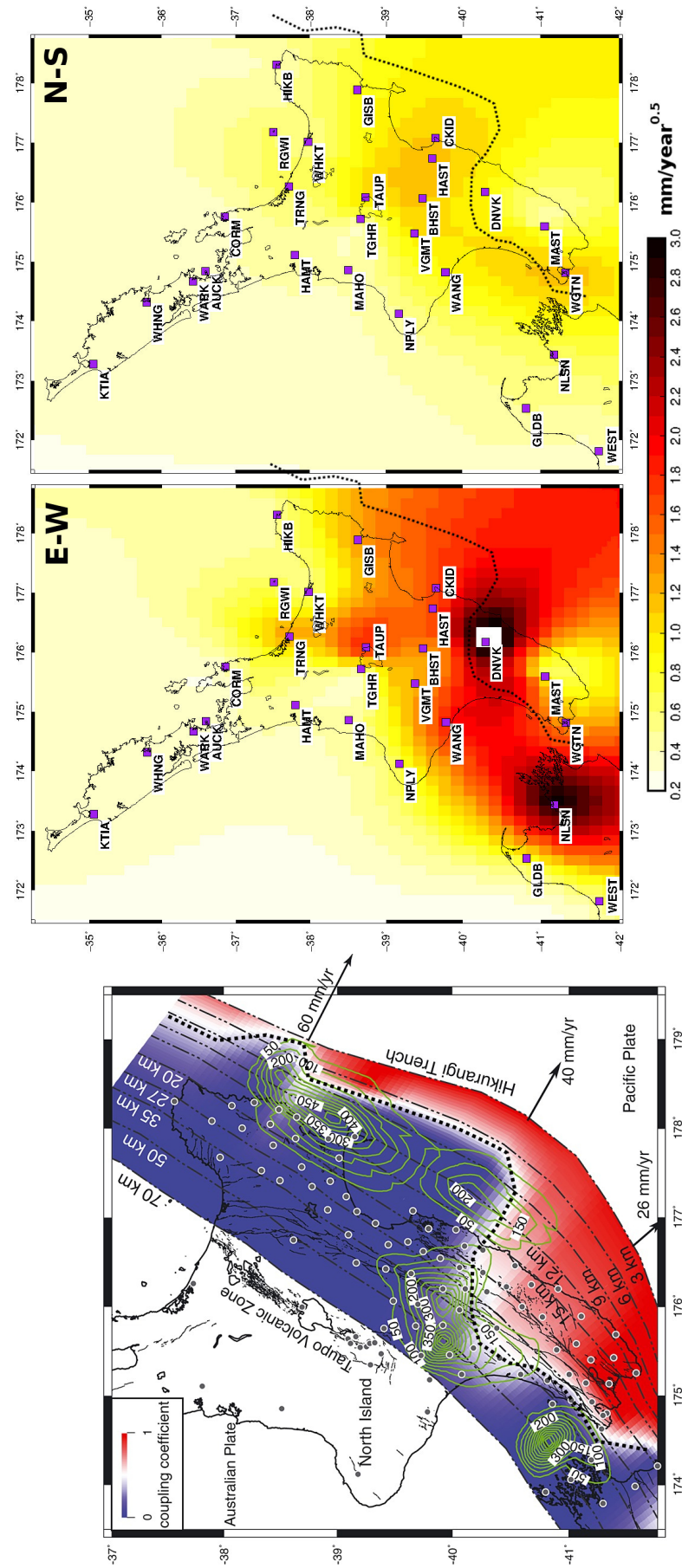


**Figure A.4:** LEFT: Degree of plate coupling inferred from modelling, courtesy of Wallace and Beavan (2010). Red areas correspond to a high degree of plate locking, blue where plates creep past each other. Green contours indicate the extent of slow slip events and black contours the depth of the subducted Pacific Plate. The inferred uncoupled and coupled plate boundary was added and drawn as black dotted line. RIGHT: E-W and N-S Random Walk values derived from interpolating individual values at each cGNSS station. The uncoupled-coupled plate boundary is drawn as a black dotted line.

#### A.4 TIMESERIES

For reference, the residual timeseries for all cGNSS stations in NWNZ are shown here (Figure 4.2), as well as relevant stations throughout the eastern Australian Plate. Linear velocities have been removed for all components. Each datapoint represents a 10-day aggregate with errors greater than  $3\sigma$  removed, antenna offsets have been manually corrected, coseismic offsets have *not* been corrected, and all sites are plotted at the same scale. Sites are approximately arranged N-S.

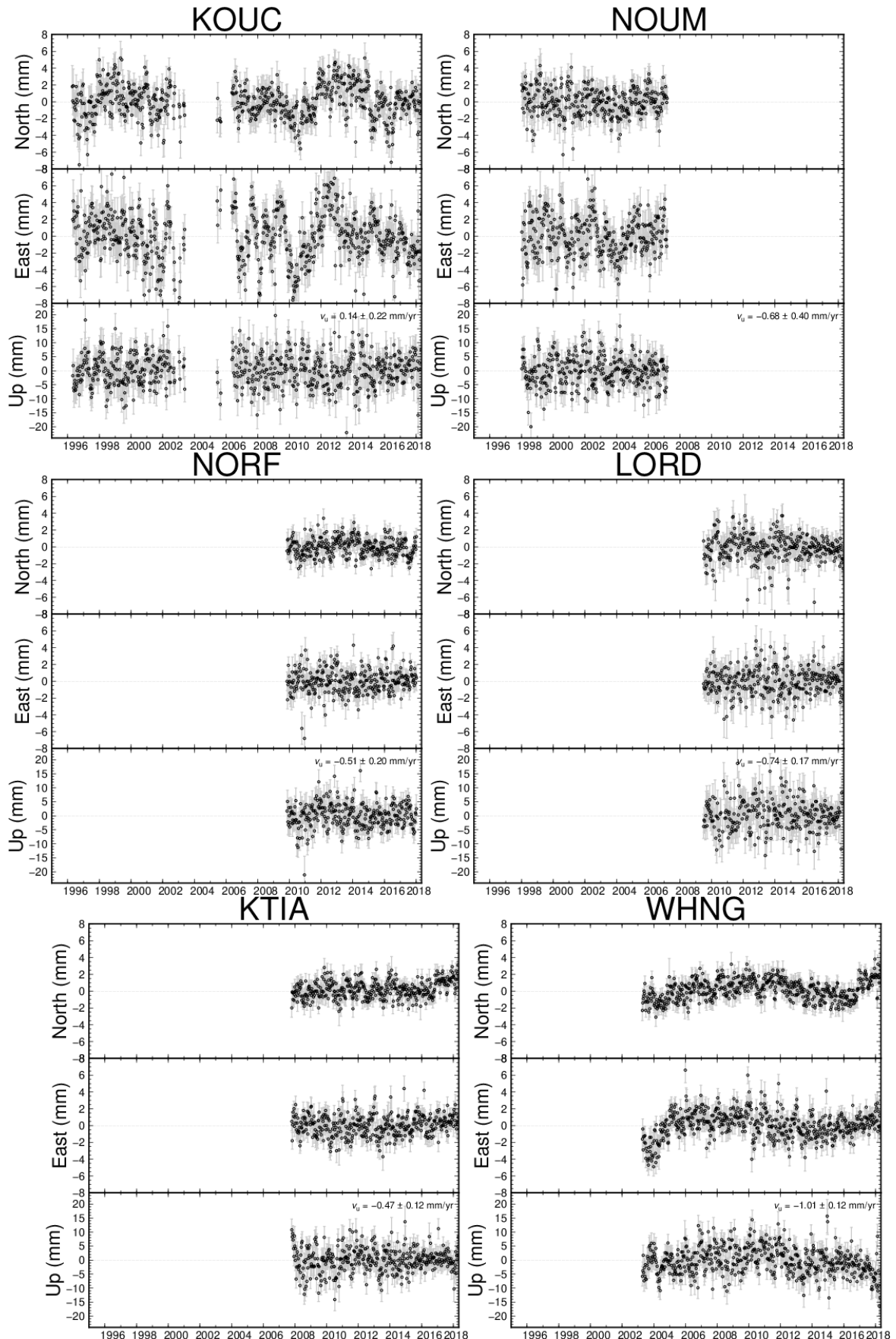


**Figure A.5:** Residual timeseries for some NZ cGNSS NZ sites (part 1/5)

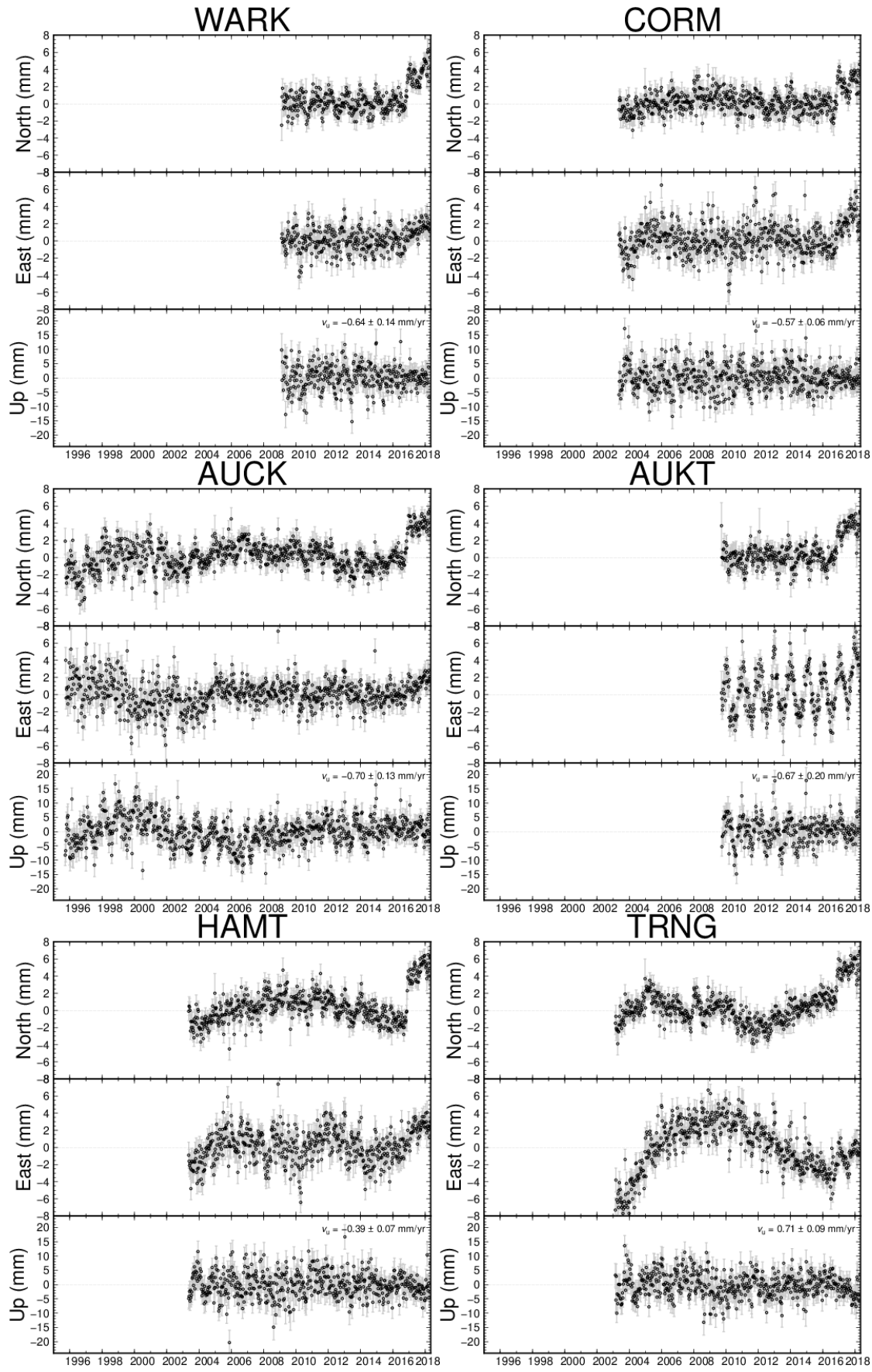


Figure A.5: (part 2/5)

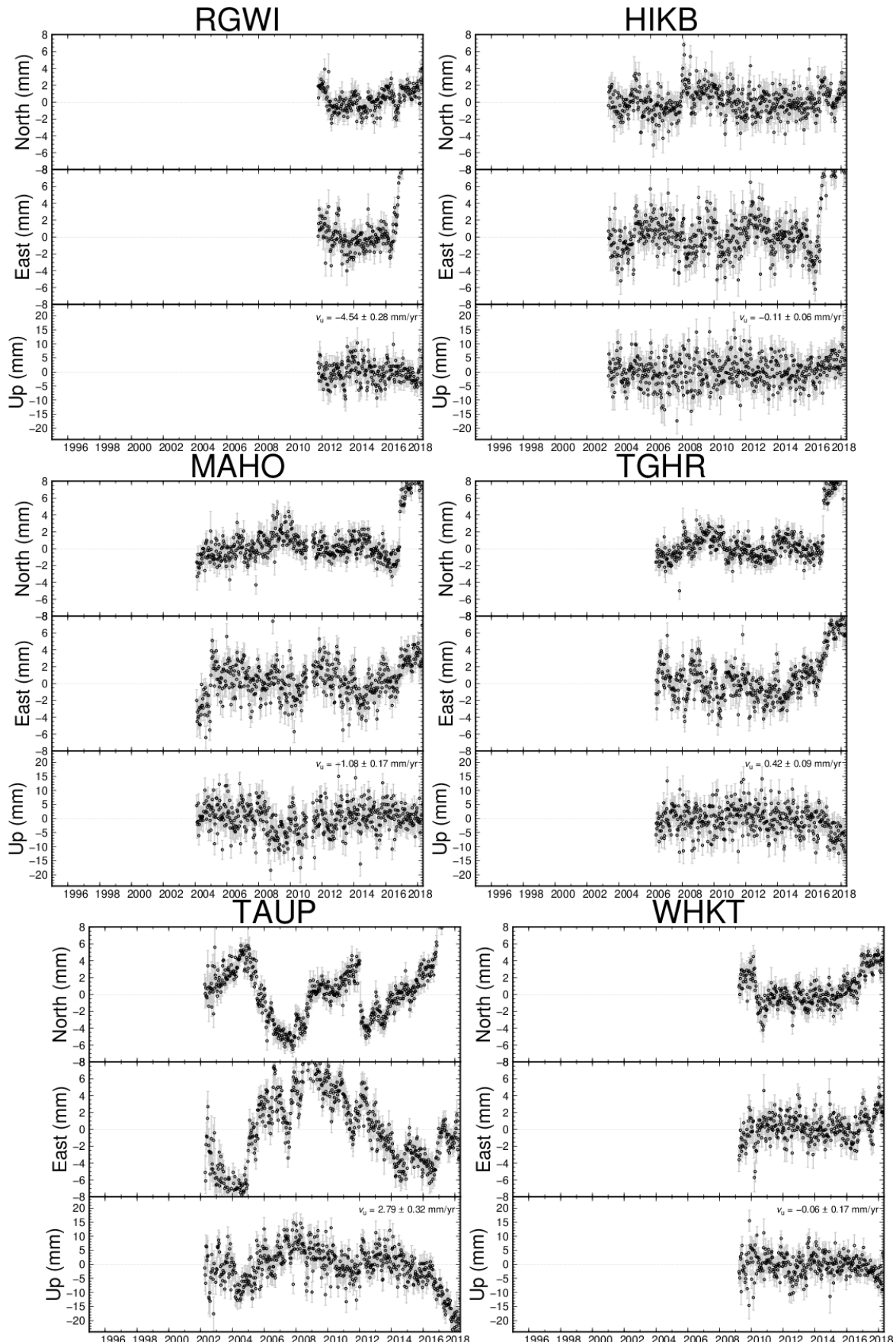


Figure A.5: (part 3/5)

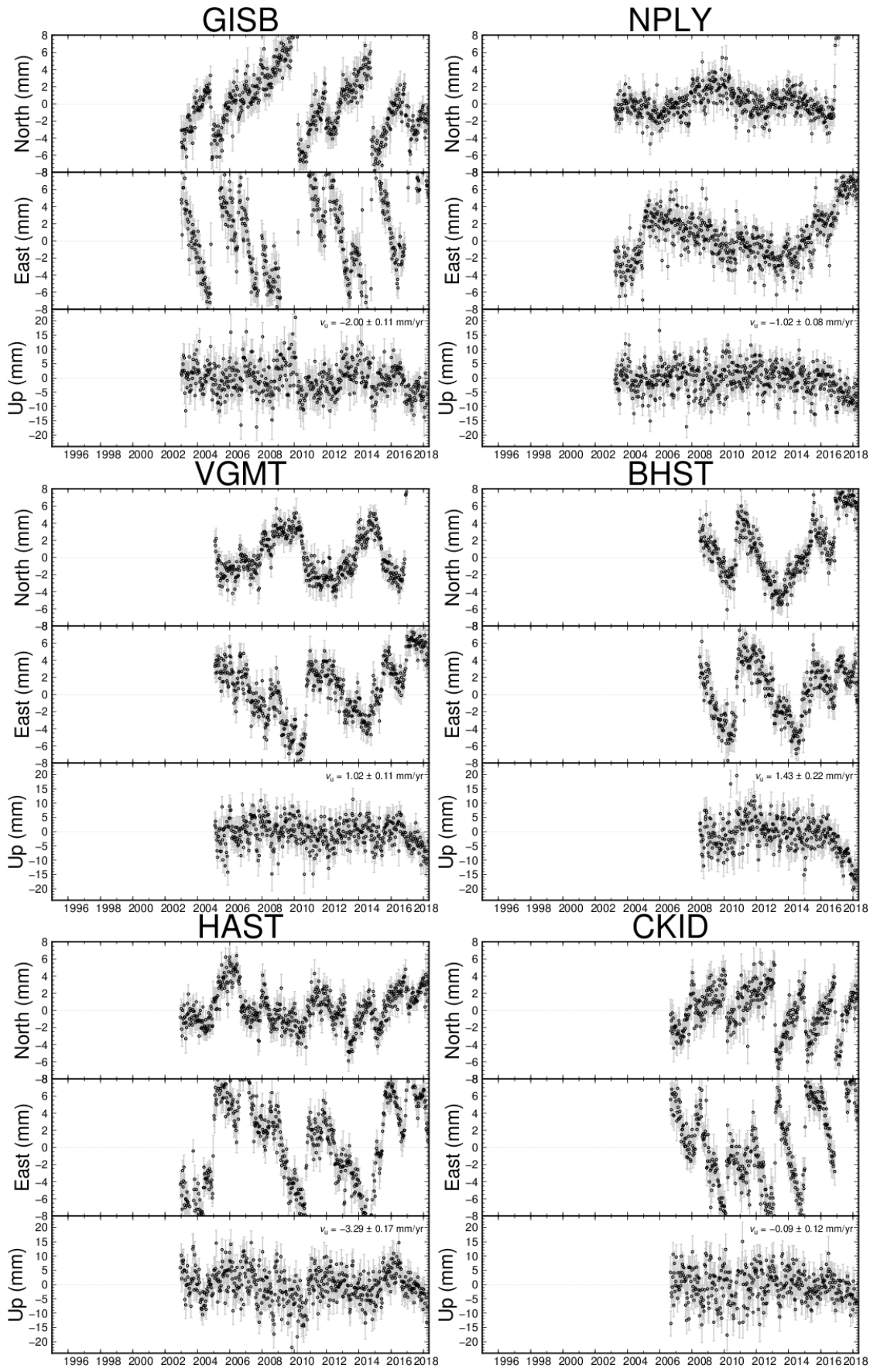
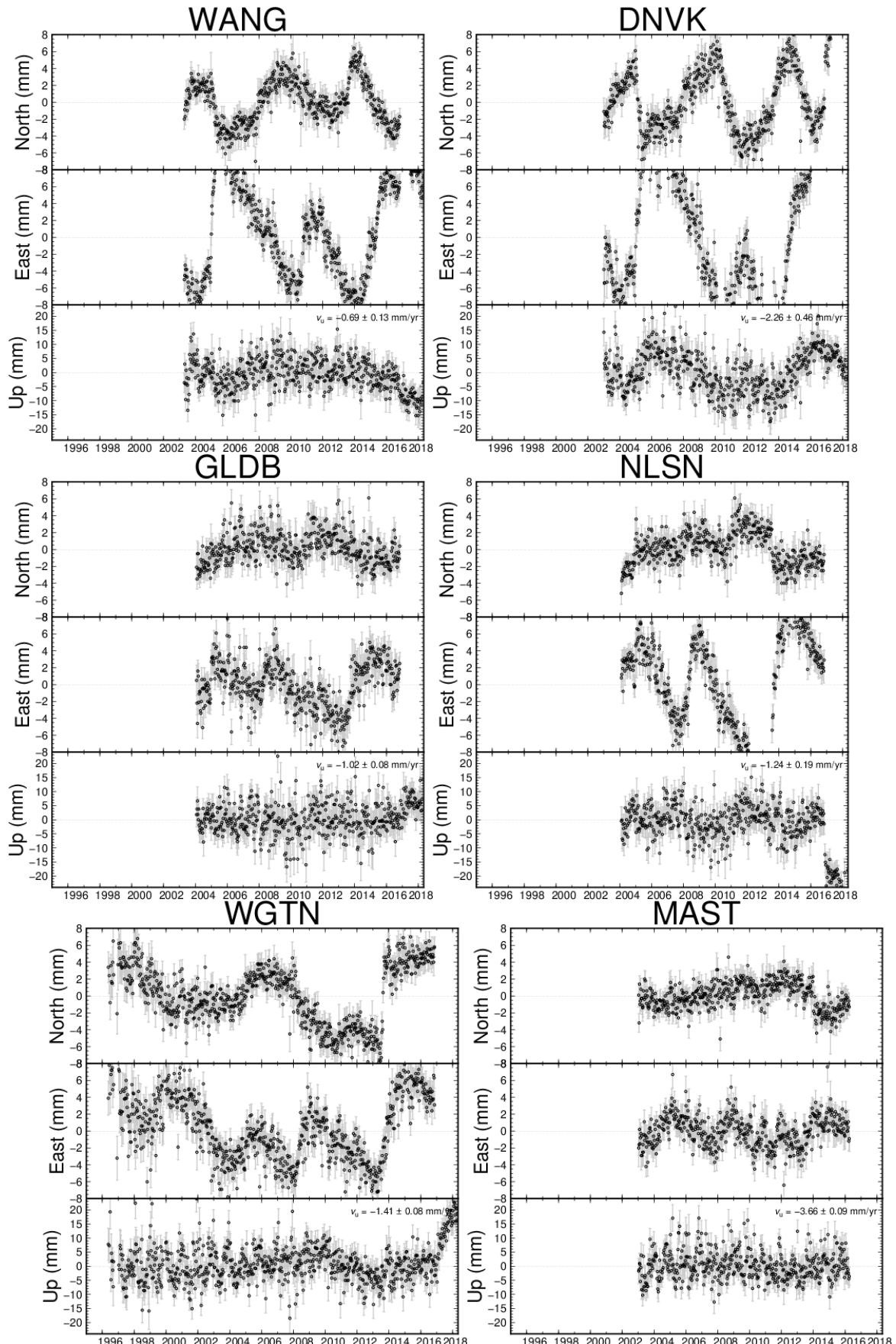


Figure A.5: (part 4/5)



**Figure A.5:** Residual timeseries for some NZ continuous sites arranged N-S. Each point is a 10-day aggregate. (part 5/5)

#### A.5 EQUIPMENT AND SURVEY TECHNIQUE

GNSS antenna/receiver units used in this project were predominantly Trimble 5700 receivers paired with Trimble Zephyr 1 antennas but occasionally newer NET R7 or NET R9 Trimble receivers paired with Zephyr 2 antennas were used. Antennas were aligned to true north and levelled using a rotating optical plumb, either on portable tripods or 2 metre fixed metal "Nelson" beacons mounted in cement, when available. When mounted via tripod, antenna heights were derived from an average of 3 different measurements using a pointed height stick from the top of the mark's pinhole to the bottom of the outer antenna edge, with this "slant height" being converted to a "bottom of antenna" height using antenna schematics and trigonometry. This is the same method used by GNS Science and LINZ. For both Trimble Zephyr 1 and 2 antennas which were used exclusively in this project the bottom of the outer antenna mark is 0.0444 metres above the bottom with a radius of 0.1698 metres.

## A.6 CAMPAIGN OCCUPATION DATA

CODE	NAME	CRDLAT	CRDLON	CRDHGT	BEACON	EQUIPMENT ID	RECEIVER	RECEIVER SN	ANTENNA	ANTENNA SN	DEPLOY	BOT OF ANT 0 (m)	AVG BON 0 (m)	HEIGHT 0 (m)	RETRIEVE
1320	PUKEOTAHINGA NO 2	-37.33684685	174.859025708	333.8074	4M	GNS-14	Trimble 5700	0440101786	Z1 TRM41249.00	12379137	02/04/15	0	1.3826666666666667	<b>1.3278</b>	09/04/15
1331	18 STONY BATTER	-36.76629582	175.168230141	255.2181	2M	LINZ-23	Trimble 5700	0440101187	Z1 TRM41249.00	12621960	21/05/15	1.374	0	<b>1.3740</b>	28/05/15
A2J7	A ELBOW HILL	-37.28350684	174.841236011	59.7885	NB	GNS-22	Trimble 5700	0220284004	Z1 TRM41249.00	12626084	20/03/15	0	1.3523333333333333	<b>1.2972</b>	26/03/15
A2L2	86 MAUNGAKAWA	-37.41398992	175.395750405	567.6264	2M	GNS-15	Trimble 5700	0440101196	Z1 TRM41249.00	12235000	19/05/15	1.538	0	<b>1.5380</b>	29/05/15
A33D	79 TE HERUNGA	-37.58938403	175.000023214	318.9118	4M	LINZ-23	Trimble 5700	0440101187	Z1 TRM41249.00	12621960	05/05/15	0	0.8936666666666667	<b>0.8330</b>	19/05/15
A6BK	4942	-37.15671541	175.618697428	210.3588	2M	LINZ-27	Trimble 5700	0440100689	Z1 TRM41249.00	12621942	26/03/15	0	1.01966666	<b>0.9610</b>	04/04/15
A6LT	PAKU NO 2	-37.00049813	175.866033313	212.1692	2M	LINZ-23	Trimble 5700	0440101187	Z1 TRM41249.00	12621960	04/04/15	1.299	0	<b>1.2990</b>	11/04/15
A6Q1	2032	-35.59088101	174.528214749	140.9484	2M	GNS-17	Trimble 5700	0220325940	Z1 TRM41249.00	12545600	06/04/15	1.368	0	<b>1.3680</b>	14/04/15
A6X8	II (Otama SD)	-36.73784721	175.6966685652	230.318	NB	GNS-21	Trimble 5700	0220287018	Z1 TRM41249.00	11889136	11/04/15	0	1.1106666666666667	<b>1.0532</b>	18/04/15
A8TX	4731	-37.09937776	174.997169256	283.4605	4M	GNS-17	Trimble 5700	0220325940	Z1 TRM41249.00	12545600	23/03/15	0	1.115	<b>1.0576</b>	02/04/15
A8UK	F NO 2	-37.1880821	174.945840624	180.4142	4M	GNS-14	Trimble 5700	0440101786	Z1 TRM41249.00	12379137	22/03/15	0	1.5753333333333333	<b>1.5218</b>	02/04/15
A93Q	F1 (Maramarua SD)	-37.24024835	175.168799129	79.6142	NB	LINZ-27	Trimble 5700	0440100689	Z1 TRM41249.00	12621942	13/04/15	0	1.0916666666666667	<b>1.0340</b>	19/04/15
A93W	26 PUKOKORO	-37.21116556	175.285233735	230.9067	2M	GNS-21	Trimble 5700	0220287018	Z1 TRM41249.00	11889136	19/04/15	1.338	0	<b>1.3380</b>	26/04/15
A9FJ	1345	-36.90521367	175.079674593	120.1785	4M	GNS-15	Trimble 5700	0440101196	Z1 TRM41249.00	12235000	23/03/15	0	1.1673333333333333	<b>1.1105</b>	03/04/15
A9FL	4341	-36.93493444	175.058072784	157.6295	4M	GNS-12	Trimble 5700	0440103874	Z1 TRM41249.00	12235078	03/04/15	0	1.272	<b>1.2162</b>	09/04/15
A9FW	21A	-36.9845656	175.264075437	161.45	2M	LINZ-27	Trimble 5700	0440100689	Z1 TRM41249.00	12621942	07/04/15	1.348	0	<b>1.3480</b>	13/04/15
A9MT	C3 (Colville SD)	-36.48800149	175.333054096	231.872	2M	GNS-12	Trimble 5700	0440103874	Z1 TRM41249.00	12235078	12/04/15	1.2065	0	<b>1.2065</b>	19/04/15
A9PH	VI CAPE RODNEY	-36.27762377	174.800602013	152.4096	2M	GNS-14	Trimble 5700	0440101786	Z1 TRM41249.00	12379137	14/04/15	0	1.3333333333333333	<b>1.2781</b>	21/04/15
AAEY	SOUTH HEAD	-36.45240172	174.248201507	115.7391	2M	GNS-15	Trimble 5700	0440101196	Z1 TRM41249.00	12235000	21/04/15	1.225	0	<b>1.2250</b>	28/04/15
AAJO	BM ? FROST ROAD	-37.51225353	175.176455721	59.355	NB	GNS-22	Trimble 5700	0220284004	Z1 TRM41249.00	12626084	26/04/15	0	0.808	<b>0.7456</b>	04/05/15
AAJ1	COROMANDEL	-36.76014038	175.461938955	89.3699	2M	LINZ-23	Trimble 5700	0440101187	Z1 TRM41249.00	12621960	11/04/15	1.276	0	<b>1.2760</b>	18/04/15
AAJ4	SM 6281 SO 60983	-36.78313953	175.019782508	81.255	NB	GNS-12	Trimble 5700	0440103874	Z1 TRM41249.00	12235078	21/05/15	0	1.0488333333333333	<b>0.9906</b>	28/05/15
AAJA	MEDLANDS	-36.25861336	175.48821018	76.498	NB	GNS-22	Trimble 5700	0220284004	Z1 TRM41249.00	12626084	16/04/15	0	1.5633333333333333	<b>1.5097</b>	24/04/15
BOPC	98 (Maramarua SD)	-37.29567112	175.034573029	125.3582	2M	GNS-15	Trimble 5700	0440101196	Z1 TRM41249.00	12235000	03/04/15	1.076	0	<b>1.0760</b>	09/04/15
BOPD	PUTATAKA	-37.40352913	174.772693429	386.1285	2M	GNS-21	Trimble 5700	0220287018	Z1 TRM41249.00	11889136	20/03/15	1.437	0	<b>1.4370</b>	02/04/15
BOT9	1992 MAUKORO	-37.46146316	175.502171216	123.7194	2M	GNS-21	Trimble 5700	0220287018	Z1 TRM41249.00	11889136	04/05/15	1.337	0	<b>1.3370</b>	11/05/15
BOTB	5371	-37.44488685	175.650001457	95.2533	2M	GNS-14	Trimble 5700	0440101786	Z1 TRM41249.00	12379137	04/05/15	1.3195	0	<b>1.3195</b>	11/05/15
B1P3	2094	-37.08009021	175.767799727	184.5362	2M	GNS-22	Trimble 5700	0220284004	Z1 TRM41249.00	12626084	20/05/15	1.356	0	<b>1.3560</b>	29/05/15
B2FQ	L (Ruakaka SD)	-35.91812759	174.451359824	71.7021	2M	GNS-22	Trimble 5700	0220284004	Z1 TRM41249.00	12626084	06/04/15	1.4505	0	<b>1.4505</b>	14/04/15
B42L	B 90	-37.24644446	175.649068091	41.34	NB	LINZ-23	Trimble 5700	0440101187	Z1 TRM41249.00	12621960	19/03/15	0	1.418	<b>1.3634</b>	26/03/15
BUGK	IT VII SO 59566	-37.41111702	175.918864643	146.4441	NB	LINZ-27	Trimble 5700	0440100689	Z1 TRM41249.00	12621942	19/03/15	0	1.4046666666666667	<b>1.3500</b>	26/03/15
DFFL	KAIHERE NO 2	-37.35622322	175.423864491	93.2107	4M	GNS-12	Trimble 5700	0440103874	Z1 TRM41249.00	12235078	19/03/15	0	1.4433333333333333	<b>1.3889</b>	26/03/15
EJTY	RM 2 SO 448200	-36.94054473	175.476238654	37.3708	NB	GNS-12	Trimble 5700	0440103874	Z1 TRM41249.00	12235078	11/05/15	0	1.158	<b>1.1011</b>	20/05/15
ER3B	ARDMORE STATION	-37.033148	174.985483	70.356	NB	GNS-15	Trimble 5700	0440101196	Z1 TRM41249.00	12235000	03/05/15	0	0.9423333333	<b>0.8825</b>	12/05/15
1367						GNS-17	Trimble 5700	0220325940	Z1 TRM41249.00	12545600	# #####	0	0.7743333333333333	<b>0.7111</b>	06/11/15

Figure A.6: 2015 Campaign occupation data

CODE	NAME	CRDLAT	CRDLON	CRDHGT	BEACON	EQUIPMENT ID	RECEIVER	RECEIVER SN	ANTENNA	ANTENNA SN	DEPLOY	BOT OF ANT 0 (m)	AVG BON 0 (m)	HEIGHT 0 (m)	RETRIEVE	I			
														#NUM!					
1320	PUKEOTAHINGA NO 2	-37.336846852	174.859025708	333.8074	4M	Trimble 5700	Z1 TRM41249.00												
1331	18 STONY BATTER	-36.766295816	175.168230141	255.2181	2M	GNS-19	Trimble 5700	0220320198	Z1 TRM41249.00	12469759	10/05/16	1.3735		1.3735	17/05/16				
A2J7	A ELBOW HILL	-37.2835068408	174.8412360108	59.7885	NB	GNS-15	Trimble 5700	0440101196	Z1 TRM41249.00	12235000	03/05/16		1.562	1.5083	12/05/16				
A2L2	86 MAUNGAKAWA	-37.413989917166	175.395750405224	567.6264	2M	GNS-17	Trimble 5700	0220325940	Z1 TRM41249.00	12545600	22/03/16		1.5365	1.5365	29/03/16				
A33D	79 TE HERUNGA	-37.589384029	175.000023214	318.9118	4M	Trimble 5700	Z1 TRM41249.00							#NUM!					
A6BK	4942	-37.156715414178	175.618697428173	210.3588	2M	GNS-19	Trimble 5700	0220320198	Z1 TRM41249.00	12469759	06/04/16		0.816	0.7537	12/04/16				
A6LT	PAKU NO 2	-37.000498128	175.866033313	212.1692	2M	GNS-17	Trimble 5700	0220325940	Z1 TRM41249.00	12545600	06/04/16		1.297	*** 0.0015 offset	1.2970	11/04/16			
A6Q1	2032	-35.590881012	174.528214749	140.9484	2M	GNS-19	Trimble 5700	0220320198	Z1 TRM41249.00	12469759	25/03/16		1.368	1.3680	01/04/16				
A6X8	II (Otama SD)	-36.737847214868	175.696685651652	230.318	NB	GNS-19	Trimble 5700	0220320198	Z1 TRM41249.00	12469759	13/04/16			1.007333333333	0.9485	20/04/16			
A8TX	4731	-37.099377758	174.997169256	283.4605	4M	GNS-14	Trimble 5700	0440101786	Z1 TRM41249.00	12379137	03/04/16			1.270333333333	1.2145	11/04/16			
A8UK	F NO 2	-37.188082099	174.945840624	180.4142	4M	GNS-15	Trimble 5700	0440101196	Z1 TRM41249.00	12235000	03/04/16			1.318666666667	1.2633	11/04/16			
A93Q	F1 (Maramarua SD)	-37.2402483494	175.1687991292	79.6142	NB	GNS-15	Trimble 5700	0440101196	Z1 TRM41249.00	12235000	21/04/16			1.1165	1.0591	02/05/16			
A93W	26 PUOKOROKO	-37.211165559109	175.285233734835	230.9067	2M	GNS-14	Trimble 5700	0440101786	Z1 TRM41249.00	12379137	12/04/16		1.337	1.3370	21/04/16				
A9FJ	1345	-36.905213666299	175.079674592716	120.1785	4M	GNS-16	Trimble 5700	0440101789	Z1 TRM41249.00	12214598	26/04/16			1.267	1.2112	03/05/16			
A9FL	4341	-36.934934435	175.058072784	157.6295	4M	GNS-14	Trimble 5700	0440101786	Z1 TRM41249.00	12379137	26/04/16			1.388666666667	1.3338	03/05/16			
A9FW	21A	-36.984565604	175.264075437	161.45	2M	GNS-16	Trimble 5700	0440101789	Z1 TRM41249.00	12214598	11/04/16		1.2645	1.2645	19/04/16				
A9MT	C3 (Colville SD)	-36.488001489	175.333054096	231.872	2M	GNS-17	Trimble 5700	0220325940	Z1 TRM41249.00	12545600	14/04/16		1.192	1.1920	21/04/16				
A9PH	VI CAPE RODNEY	-36.277623768	174.800602013	152.4096	2M	GNS-12	Trimble 5700	0440103874	Z1 TRM41249.00	12235078	01/04/16			1.242	1.1859	07/06/16			
AAEY	SOUTH HEAD	-36.452401723	174.248201507	115.7391	2M	GNS-20	Trimble 5700	0220320200	Z1 TRM41249.00	12612063	25/03/16		1.221	1.2210	01/04/16				
AAJ0	BM 7 FROST ROAD	-37.512253531	175.176455721	59.355	NB	GNS-17	Trimble 5700	0220325940	Z1 TRM41249.00	12545600	02/05/16			0.946666666667	0.8869	12/05/16			
AAJ1	COROMANDEL	-36.760140378	175.461938955	89.3699	2M	GNS-15	Trimble 5700	0440101196	Z1 TRM41249.00	12235000	13/04/16		1.277	1.2770	20/04/16				
AAJ4	SM 6281 SO 60983	-36.783139534	175.019782508	81.255	NB	GNS-16	Trimble 5700	0440101789	Z1 TRM41249.00	12214598	10/05/16			1.571	1.5174	17/05/16			
AAJA	MEDLANDS	-36.258613358	175.48821018	76.498	NB	GNS-17	Trimble 5700	0220325940	Z1 TRM41249.00	12545600	08/05/16			1.601333333333	1.5479	16/05/16			
BOPC	98 (Maramarua SD)	-37.295671120377	175.034573028989	125.3582	2M	GNS-13	Trimble 5700	0220320202	Z1 TRM41249.00	12589958	03/04/16		1.073	1.0730	11/04/16				
BOPD	PUTATAKA	-37.403529131117	174.772693429195	386.1285	2M	GNS-16	Trimble 5700	0440101789	Z1 TRM41249.00	12214598	03/04/16			1.439	1.4390	11/04/16			
BOT9	1992 MAUKORO	-37.4614631597	175.5021712164	123.7194	2M	GNS-12	Trimble 5700	0440103874	Z1 TRM41249.00	12235078	22/03/16		1.3345	1.3345	29/03/16				
BOT9	2nd occupation	-37.4614631597	175.5021712164	123.7194	2M	GNS-13	Trimble 5700	0220320202	Z1 TRM41249.00	12589958	02/05/16		1.338	1.3380	29/03/16				
BOTB	5371	-37.4448866854014	175.650001457471	95.2533	2M	GNS-17	Trimble 5700	0220325940	Z1 TRM41249.00	12545600	29/03/16			1.318	1.3180	06/04/16			
B1P3	2094	-37.080090212487	175.767799726593	184.5362	2M	GNS-20	Trimble 5700	0220320200	Z1 TRM41249.00	12612063	06/04/16		1.3575	1.3575	02/05/16				
B2FQ	L (Ruakaka SD)	-35.918127587	174.451359824	71.7021	2M	GNS-16	Trimble 5700	0440101789	Z1 TRM41249.00	12214598	25/03/16			1.451	1.4510	01/04/16			
B42L	B 90	-37.246444455	175.649068091	41.34	NB	GNS-14	Trimble 5700	0440101786	Z1 TRM41249.00	12379137	22/03/16			1.324	1.2687	29/03/16			
BUGK	IT VII SO 59566	-37.4111170225	175.9188864631	146.4441	NB	GNS-13	Trimble 5700	0220320202	Z1 TRM41249.00	12589958	22/03/16			1.018333333333	0.9597	29/03/16			
DFFL	KAIHERE NO 2	-37.356223216165	175.423864491471	93.2107	4M	GNS-15	Trimble 5700	0440101196	Z1 TRM41249.00	12235000	22/03/16			1.123	1.0657	29/03/16			
EJTY	RM 2 SO 448200	-36.940544732079	175.476238653523	37.3708	NB	GNS-13	Trimble 5700	0220320202	Z1 TRM41249.00	12589958	13/04/16			1.3685	1.3135	20/04/16			
ER3B	ARDMORE STATION	-37.033148	174.985483	70.356	NB	GNS-12	Trimble 5700	0440103874	Z1 TRM41249.00	12235078	19/04/16			0.905333333333	0.8449	12/05/16			
A9MK	SWANSON	-36.868191029	174.555969666	201.9737	2M	GNS-12	Trimble 5700	0440103874	Z1 TRM41249.00	12235078	07/04/16		1.189	1.1890	19/04/16				
														#NUM!					
AAF6	EASTERN BEACH	-36.879643218	174.920658852	67.7936	NB	GNS-17	Trimble 5700	0220325940	Z1 TRM41249.00	12545600	25/04/16			1.353	1.2979	25/04/16			
CAJP	IT XVI SO 45416	-36.774260316	175.123315016	103.1081	NB	GNS-20	Trimble 5700	0220320200	Z1 TRM41249.00	12612063	10/5/16				1.354666666667	1.2996	17/5/16		
B3G	STANLEY ROAD	-37.523993985	175.679090633	42.7066	NB	GNS-12	Trimble 5700	0440103874	Z1 TRM41249.00	12235078	26/8/16				1.650666666667	1.5975	28/8/16		
A6Q1	2032 #2	-35.590881012	174.528214749	140.9484	2M	GNS-14	Trimble 5700	0440101786	Z1 TRM41249.00	12379137	18/10/16		1.3715	1.3715	25/10/16				
AAEB	RUSSELL	-35.254907491	174.11985165	134.4013	NB	GNS-17	Trimble 5700	0220325940	Z1 TRM41249.00	12545600	18/10/16			1.084666666667	1.0269	25/10/16			
AAEJ	WHANANAKI	-35.498840043	174.465706841	82.5287	NB	GNS-17	Trimble 5700	0220325940	Z1 TRM41249.00	12545600	11/11/16			1.471	1.4168	15/11/16			
AAV5	DD 6	-35.85197	174.46975	44.246	NB	GNS-14	Trimble 5700	0440101786	Z1 TRM41249.00	12379137	11/11/16			1.409666666667	1.3550	15/11/16			

Figure A.7: 2016 Campaign occupation data

CODE	NAME	CRDLAT	CRDLON	CRDHGT	BEACON	EQUIPMENT ID	RECEIVER	RECEIVER SN	ANTENNA	ANTENNA SN	DEPLOY	OF ANT	BON 0	HEIGHT 0 (m)	RETRIEVE
1320	PUKEOTAHINGA NO 2	-37.336846852	174.859025708	333.8074	4M									#NUM!	
1331	18 STONY BATTER	-36.766295816	175.168230141	255.2181	2M	GNS-45	TRNTR9	5444R50057	Z2 TRM57971.00	1312118426	08/04/17	1.373		1.3730	12/04/17
A2J7	A ELBOW HILL	-37.2835068408	174.8412360108	59.7885	NB	GNS-13	Trimble 5700	0220320202	Z1 TRM41249.00	12589958	20/04/17	1.1987		1.1422	25/04/17
A2L2	86 MAUNGAKAWA	-37.413989917166	175.395750405224	567.6264	2M	GNS-37	TRNTR9	5133K77662	Z2 TRM57971.00	1441138156	25/02/17	1.54		1.5400	19/05/17
A33D	79 TE HERUNGA	-37.589384029	175.000023214	318.9118	4M	GNS-21	Trimble 5700	0220287018	Z1 TRM41249.00	11889136	07/06/17	0.7935		0.7307	17/06/17
A6BK	4942	-37.156715414178	175.618697428173	210.3588	2M									#NUM!	
A6LT	PAKU NO 2	-37.000498128	175.866033313	212.1692	2M	GNS-12	Trimble 5700	0440103874	Z1 TRM41249.00	12235078	14/05/17	1.299		1.2990	19/05/17
A6Q1	2032	-35.590881012	174.528214749	140.9484	2M									#NUM!	
A6X8	II (Otama SD)	-36.737847214868	175.696685651652	230.318	NB	GNS-17	Trimble 5700	0220325940	Z1 TRM41249.00	12545600	14/05/17	0.8577		0.7963	20/05/17
A8TX	4731	-37.099377758	174.997169256	283.4605	4M	GNS-14	Trimble 5700	0440101786	Z1 TRM41249.00	12379137	25/04/17	1.0427		0.9843	03/05/17
A8TX	#2	-37.099377758	174.997169256	283.4605	4M	GNS-14	Trimble 5700	0440101786	Z1 TRM41249.00	12379137	03/05/17	0.747		0.6830	10/05/17
A8TX	#3	-37.099377758	174.997169256	283.4605	4M	GNS-14	Trimble 5700	0440101786	Z1 TRM41249.00	12379137	03/05/17	1.0377		0.9793	14/12/17
A8UK	F NO 2	-37.188082209	174.945840624	180.4142	4M									#NUM!	
A93Q	F1 (Maramarua SD)	-37.2402483494	175.1687991292	79.6142	NB	GNS-35	TRNTR9	5130K77167	Z2 TRM57971.00	1441137889	15/03/17	1.235		1.1789	15/03/17
A93Q	F1 #2	-37.2402483494	175.1687991292	79.6142	NB	GNS-17	Trimble 5700	0220325940	Z1 TRM41249.00	12545600	27/04/17	0.847		0.7854	03/05/17
A93W	26 PUKOROKORO	-37.211165559109	175.285233734835	230.9067	2M	GNS-13	Trimble 5700	0220320202	Z1 TRM41249.00	12589958	18/11/17	1.338		1.3380	04/04/17
A93W	26 PUKOROKORO(bad)	-37.211165559109	175.285233734835	230.9067	2M	GNS-38	TRNTR9	5133K77679	Z2 TRM57971.00	5000116580	16/03/17	1.339		1.3390	04/04/17
A9FJ	1345	-36.905213669299	175.079674592716	120.1785	4M	GNS-12	Trimble 5700	0440103874	Z1 TRM41249.00	12235078	25/04/17	1.0403		0.9820	02/05/17
A9FL	4341	-36.9349344435	175.058072784	157.6295	4M	GNS-21	Trimble 5700	0220287018	Z1 TRM41249.00	11889136	25/04/17	1.0973		1.0397	02/05/17
A9FW	21A	-36.984565604	175.264075437	161.45	2M	GNS-45	TRNTR9	5444R50057	Z2 TRM57971.00	1312118426	15/03/17	1.265		1.2650	20/03/17
A9FW	21A #2	-36.984565604	175.264075437	161.45	2M	GNS-19	Trimble 5700	0220320198	Z1 TRM41249.00	12469759	26/04/17	1.264		1.2640	02/05/17
A9MT	C3 (Colville SD)	-36.488001489	175.333054096	231.872	2M	GNS-19	Trimble 5700	0220320198	Z1 TRM41249.00	12469759	13/05/17	1.197		1.1970	20/05/17
A9PH	VI CAPE RODNEY	-36.277623768	174.800602013	152.4096	2M									#NUM!	
AAEY	SOUTH HEAD	-36.452401723	174.248201507	115.7391	2M	GNS-19	Trimble 5700	0220320198	Z1 TRM41249.00	12469759	03/05/17	1.223		1.2230	10/05/17
AAJ0	BM ? FROST ROAD	-37.512253531	175.176455721	59.355	NB	GNS-45	TRNTR9	5444R50057	Z2 TRM57971.00	1312118426	31/03/17	0.8863		0.8255	04/04/17
AAJ0	#2	-37.512253531	175.176455721	59.355	NB	GNS-14	Trimble 5700	0440101786	Z1 TRM41249.00	12379137	07/06/17	0.8647		0.8034	04/04/17
AAJ1	COROMANDEL	-36.760140378	175.4619138955	89.3699	2M	GNS-13	Trimble 5700	0220320202	Z1 TRM41249.00	12589958	13/05/17	1.278		1.2780	
AAJ4	SM 6281 SO 60983	-36.783139534	175.019782508	81.255	NB	GNS-38	TRNTR9	5133K77679	Z2 TRM57971.00	5000116580	08/04/17	1.1983		1.1418	09/04/17
AAJA	MEDLANDS	-36.258613358	175.48821018	76.498	NB									#NUM!	
BOPC	98 (Maramarua SD)	-37.295671120377	175.034573028989	125.3582	2M	LINZ-26	Trimble 5700	220283944	Z1 TRM41249.00	12611631	26/04/17	1.0715		1.0715	03/05/17
BOPD	PUTATAKA	-37.403529131117	174.772693429195	386.1285	2M	LINZ-26	Trimble 5700	220283944	Z1 TRM41249.00	12611631	20/04/17	1.436		1.4360	25/04/17
BOT9	1992 MAUKORO	-37.4614631597	175.5021712164	123.7194	2M	GNS-35	TRNTR9	5130K77167	Z2 TRM57971.00	1441137889	04/03/17	1.336		1.3360	15/03/17
BOT9	2nd occupation	-37.4614631597	175.5021712164	123.7194	2M	GNS-19	Trimble 5700	0220320198	Z1 TRM41249.00	12469759	19/04/17	1.3375		1.3375	26/04/17
BOTB	5371	-37.444886854014	175.650001457471	95.2533	2M	GNS-38	TRNTR9	5133K77679	Z2 TRM57971.00	5000116580	04/03/17	1.318		1.3180	16/03/17
BOTB	#2	-37.444886854014	175.650001457471	95.2533	2M	LINZ-23	Trimble 5700	0440101187	Z1 TRM41249.00	12621960	19/04/17	1.3165		1.3165	27/04/17
B1P3	2094	-37.080090212487	175.76779726593	184.5362	2M	GNS-45	TRNTR9	5444R50057	Z2 TRM57971.00	1312118426	27/04/17	1.359		1.3590	01/06/17
B2FQ	L (Ruakaka SD)	-35.918127587	174.451359824	71.7021	2M									#NUM!	
B42L	B 90	-37.246444455	175.649068091	41.34	NB	GNS-35	TRNTR9	5130K77167	Z2 TRM57971.00	1441137889	31/03/17	1.1157		1.0583	04/04/17
BUGK	IT VII SO 59566	-37.411170225	175.918864631	146.4441	NB	GNS-35	TRNTR9	5130K77167	Z2 TRM57971.00	1441137889	25/02/17	1.3883		1.3335	04/03/17
DFFL	KAIHERE NO 2	-37.356223216165	175.423864491471	93.2107	4M	GNS-45	TRNTR9	5444R50057	Z2 TRM57971.00	1312118426	04/03/17	1.3837		1.3288	09/03/17
EJTY	RM 2 SO 448200	-36.940544732079	175.476238653523	37.3708	NB	GNS-14	Trimble 5700	0440101786	Z1 TRM41249.00	12379137	13/05/17	1.0787		1.0208	
ER3B	ARDMORE STATION	-37.033148	174.985483	70.356	NB	GNS-35	TRNTR9	5130K77167	Z2 TRM57971.00	1441137889	20/04/17	0.864		0.8028	10/05/17
ER3B	ARDMORE STATION #2	-37.033148	174.985483	70.356	NB	GNS-13	Trimble 5700	0220320202	Z1 TRM41249.00	12589958	08/12/17	0.7097		0.6447	14/12/17
A9MK	SWANSON	-36.868191029	174.555969666	201.9737	2M	GNS-12	Trimble 5700	0440103874	Z1 TRM41249.00	12235078	03/05/17	1.189		1.1890	10/05/17
														#NUM!	
AAF6	EASTERN BEACH	-36.879643218	174.920658852	67.7936	NB									#NUM!	
CAJP	IT XVI SO 45416	-36.774260316	175.123315016	103.1081	NB	GNS-35	TRNTR9	5130K77167	Z2 TRM57971.00	1441137889	8/4/17	1.032		0.9735	12/4/17
B36j	STANLEY ROAD	-37.523993985	175.679090633	42.7066	NB	GNS-38	TRNTR9	5133K77679	Z2 TRM57971.00	5000116580	25/02/17	1.6457		1.5925	4/3/17
B36j	#2	-37.523993985	175.679090633	42.7066	NB	GNS-17	Trimble 5700	0220325940	Z1 TRM41249.00	12545600	19/04/17	1.4063		1.3516	27/4/17

Figure A.8: 2017 Campaign occupation data (part 1/2)

CODE	NAME	CRDLAT	CRDLON	CRDHGT	BEACON	EQUIPMENT ID	RECEIVER	RECEIVER SN	ANTENNA	ANTENNA SN	DEPLOY	BOT OF ANT 0 (m)	AVG BON 0 (m)	HEIGHT 0 (m)
1344	V RUAHINE	-36.333055	175.518603	437.9609	4M	GNS-44	TRNTR9	5235K51840	Z2 TRM57971.00	5000113057	29/07/17		1.2329999999999999	<b>1.1769</b>
1361	734A MAHORA	-35.962064	173.769428	541.095	4M	GNS-34	TRNTR7	220412577	Z1 TRM41249.00	60220949	27/07/17		1.2939999999999998	<b>1.2384</b>
1384	8 WHAKARARA	-35.045447	173.881769	367.7132	2M	GNS-21	Trimble 5700	0220287018	Z1 TRM41249.00	11889136	26/07/17	<b>1.416</b>		<b>1.4160</b>
1394	TE PAKI	-34.841383	173.137635	350.9948	2M	GNS-12	Trimble 5700	0440103874	Z1 TRM41249.00	12482226	27/07/17	<b>1.327</b>		<b>1.3270</b>
A05E	1983 TE RAITE	-34.792468	173.075557	99.9578	2M	GNS-15	Trimble 5700	0440101196	Z1 TRM41249.00	12235000	27/07/17	<b>1.249</b>		<b>1.2490</b>
A33D	79 TE HERUNGA	-37.589384029	175.000023214	318.9118	4M	GNS-21	Trimble 5700	0220287018	Z1 TRM41249.00	11889136	07/06/17		<b>0.7935</b>	<b>0.7307</b>
A42F	1531	-35.286545	174.046745	131.7581	2M	LINZ-23	Trimble 5700	0440101187	Z1 TRM41249.00	12621960	26/07/17	<b>1.415</b>		<b>1.4150</b>
A49Q	PUKEKOHE NO 3	-35.540398	173.37579	195.3253	NB	LINZ-27	Trimble 5700	0440100689	Z1 TRM41249.00	12621942	27/07/17		0.8559999999999999	<b>0.7946</b>
A6Q1	2032	-35.590881012	174.528214749	140.9484	2M	GNS-32	TRNTR7	220389880	Z1 TRM41249.00	60162784	26/07/17	<b>1.371</b>		<b>1.3710</b>
A9FW	21A	-36.984565604	175.264075437	161.45	2M	LINZ-25	Trimble 5700	220267074	Z1 TRM41249.00	12652401	25/07/17	<b>1.264</b>		<b>1.2640</b>
A9MT	C3 (Colville SD)	-36.488001489	175.33054096	231.872	2M	GNS-19	Trimble 5700	0220320198	Z1 TRM41249.00	12469759	13/05/17	<b>1.197</b>		<b>1.1970</b>
AAEY	SOUTH HEAD	-36.452401723	174.248201507	115.7391	2M	GNS-19	Trimble 5700	0220320198	Z1 TRM41249.00	12469759	03/05/17	<b>1.223</b>		<b>1.2230</b>
AAJA	MEDLANDS	-36.258613358	175.48821018	76.498	NB	GNS-19	Trimble 5700	0220320198	Z1 TRM41249.00	12469759	29/07/17		1.3436666666666668	<b>1.2885</b>
AAJU	KAIKOHE	-35.509346	173.390356	310.1835	2M	GNS-29	TRNTR7	220389869	Z1 TRM41249.00	60154538	26/07/17		1.3586666666666667	<b>1.3036</b>
B2FQ	L (Ruakaka SD)	-35.918127587	174.451359824	71.7021	2M	GNS-33	TRNTR7	220389892	Z1 TRM41249.00	60162975	26/07/17	<b>1.452</b>		<b>1.4520</b>
BOPD	PUTATAKA	-37.403529131117	174.772693429195	386.1285	2M	GNS-43	TRNRR9	5235K51838	Z2 TRM57971.00	5000113049	25/07/17	<b>1.436</b>		<b>1.4360</b>
BUGK	IT VII SO 59566	-37.4111170225	175.9188864631	146.4441	NB	GNS-20	Trimble 5700	220320200	Z1 TRM41249.00	12612063	25/07/17		<b>1.382</b>	<b>1.3271</b>
DFL	KAHHERE NO 2	-37.356223216165	175.423864491471	93.2107	4M	GNS-28	TRNTR7	220389864	Z1 TRM41249.00	60154160	25/07/17		1.3223333333333334	<b>1.2670</b>
AAEJ	WHANANAKI	-35.498840043	174.465706841	82.5287	NB	GNS-16	Trimble 5700	0440101789	Z1 TRM41249.00	12214598	26/07/17		1.4013333333333333	<b>1.3466</b>
B15J	6642 SO 47957	-37.889373443056	175.556642521111	325.4297	4M	GNS-42	TRNTR9	5235K51834	Z2 TRM57971.00	5000113048	25/7/17		0.6623333333333333	<b>0.5958</b>
ECOT	RM 1 SO 400727	-34.434274	172.685288		NB	GNS-17	Trimble 5700	0220325940	Z1 TRM41249.00	12545600	27/7/17		1.5086666666666666	<b>1.4547</b>

Figure A.9: 2017 Campaign occupation data (part 2/2)

## A.7 GAMIT / GLOBK PARAMETERS

### A.7.1 *A Priori (APR) File*

1240\_GPS -4893923.41952 432390.29793 -4054594.81117 -0.02455 0.00461 0.02853 2008.905 0.0026 0.0042 0.0026  
 1242\_GPS -4896835.25180 469746.07564 -4046649.78439 -0.02596 0.00328 0.02912 2006.235 0.0030 0.0042 0.0027  
 1243\_GPS -4899226.81575 498115.52828 -4040004.87663 -0.02455 0.00296 0.03133 2008.019 0.0025 0.0035 0.0023  
 1245\_GPS -4906466.74845 479061.72273 -4033981.92181 -0.02397 0.00290 0.03099 2005.825 0.0027 0.0038 0.0024  
 1254\_GPS -4915754.98770 457726.42566 -4025743.63512 -0.02686 0.00265 0.02900 2001.456 0.0030 0.0048 0.0029  
 1255\_GPS -4916245.22332 507834.90330 -4019838.23225 -0.02252 0.00271 0.03269 2007.268 0.0021 0.0028 0.0018  
 1256\_GPS -4919960.13464 482863.76388 -4017106.45613 -0.02482 0.00226 0.03044 2007.423 0.0022 0.0031 0.0020  
 1259\_GPS -4929040.26103 498221.59999 -4004032.81877 -0.02429 0.00139 0.03119 2006.761 0.0018 0.0026 0.0016  
 1262\_GPS -4935359.43558 473109.79267 -3999564.89843 -0.02573 0.00146 0.02998 2007.317 0.0021 0.0026 0.0019  
 1277\_GPS -4991139.84333 348793.21910 -3943624.23447 -0.02023 -0.00218 0.03013 2010.634 0.0039 0.0031 0.0035  
 1320\_GPS -5057246.96124 454992.89479 -3847384.67174 -0.02438 -0.00127 0.03124 2013.530 0.0015 0.0008 0.0013  
 1331\_GPS -5097584.13538 430902.64495 -3796800.61018 -0.02258 -0.00286 0.03189 2017.528 0.0010 0.0005 0.0009  
 1333\_GPS -5095965.70620 492905.08852 -3791396.95432 -0.00978 -0.00697 -0.01155 1995.835 0.0011 0.0007 0.0009  
 1344\_GPS -5128814.55381 401970.86300 -3758285.80825 -0.02274 -0.00345 0.03145 2014.866 0.0016 0.0009 0.0015  
 1349\_GPS -5134213.97362 415140.62015 -3749374.65451 -0.03678 0.03478 0.13261 1995.849 0.0009 0.0006 0.0007  
 1361\_GPS -5138072.76230 560948.45700 -3724885.75305 -0.02311 -0.00293 0.03320 2012.790 0.0015 0.0008 0.0012  
 1367\_GPS -5167214.30600 496239.22148 -3693852.14477 -0.01683 -0.00561 0.03945 1996.858 0.0019 0.0008 0.0014  
 1384\_GPS -5198057.40005 557184.88364 -3642206.46456 -0.02235 -0.00418 0.03394 2015.362 0.0017 0.0009 0.0015  
 1394\_GPS -5222590.07252 662414.31782 -3589434.71390 -0.02099 -0.00502 0.03575 2013.967 0.0020 0.0009 0.0018  
 2003\_GPS -4977262.91292 365821.43897 -3959247.10920 -0.01975 0.00023 0.03184 2006.719 0.0034 0.0039 0.0032  
 2017\_GPS -4985487.28647 360226.20269 -3949665.53426 -0.02343 -0.00003 0.02785 2013.614 0.0027 0.0026 0.0025  
 2104\_GPS -4969203.30716 377408.20431 -3968276.84130 -0.02323 0.00048 0.02926 2013.190 0.0021 0.0022 0.0019  
 2328\_GPS -4990658.41630 380833.29070 -3940878.24472 -0.01966 -0.00067 0.02934 2006.935 0.0026 0.0032 0.0024  
 2382\_GPS -5005224.04648 361814.56610 -3924130.32970 -0.02351 -0.00100 0.02915 2013.354 0.0024 0.0025 0.0022  
 2383\_GPS -5017823.27317 344451.45705 -3909998.38702 -0.02358 -0.00222 0.02910 2012.813 0.0020 0.0024 0.0019  
 2404\_GPS -4934324.23161 507747.48382 -3996044.72582 -0.02362 0.00034 0.03286 1999.719 0.0028 0.0036 0.0024  
 A05E\_GPS -5205430.91793 632180.77808 -3619043.24712 -0.02474 -0.00421 0.03277 2015.753 0.0017 0.0008 0.0013  
 A1YC\_GPS -4990511.26884 460701.74489 -3931843.70870 -0.01829 -0.00066 0.03565 1996.974 0.0020 0.0015 0.0018  
 A2J7\_GPS -5060462.23756 456866.12347 -3842509.89307 -0.02386 -0.00155 0.03334 2016.433 0.0012 0.0006 0.0010  
 A2L2\_GPS -5056291.61013 407196.97367 -3854330.75304 -0.02870 -0.00182 0.02622 2016.863 0.0008 0.0006 0.0007  
 A33D\_GPS -5041355.52808 441059.35211 -3869623.77642 -0.02367 -0.00123 0.03144 2019.434 0.0009 0.0005 0.0008  
 A3X8\_GPS -4902910.10720 526750.87684 -4031839.84734 -0.02483 0.00266 0.03068 2007.762 0.0024 0.0032 0.0021  
 A3YH\_GPS -4936192.78284 452000.49871 -4000630.91755 -0.02588 0.00194 0.02957 2007.961 0.0022 0.0025 0.0020  
 A42F\_GPS -5184124.91949 540598.09734 -3663938.14159 -0.02339 -0.00345 0.03235 2015.886 0.0017 0.0008 0.0013  
 A49Q\_GPS -5161182.94419 599622.59867 -3687024.75481 -0.02319 -0.00389 0.03331 2015.428 0.0020 0.0009 0.0015  
 A6BK\_GPS -5074801.91929 388818.82567 -3831395.34239 -0.02311 -0.00290 0.03132 2015.911 0.0011 0.0006 0.0009  
 A6LT\_GPS -5086860.29363 367661.87532 -3817564.38623 -0.02356 -0.00346 0.03084 2018.457 0.0012 0.0008 0.0010  
 A6Q1\_GPS -5169002.71734 495149.35699 -3691453.77835 -0.02229 -0.00423 0.03206 2016.302 0.0010 0.0005 0.0008  
 A6X8\_GPS -5103205.44201 384008.74311 -3794256.11893 -0.02842 -0.00444 0.02684 2016.698 0.0009 0.0007 0.0007  
 A78A\_GPS -4907515.69497 429872.80846 -4038802.39375 -0.02529 0.00353 0.02799 2007.245 0.0027 0.0039 0.0026  
 A78C\_GPS -4902106.94390 454587.17677 -4042354.59638 -0.02567 0.00299 0.02906 2009.209 0.0025 0.0038 0.0024  
 A7D5\_GPS -4918184.94474 529512.92925 -4013143.49304 -0.02429 0.00187 0.03180 2007.250 0.0022 0.0029 0.0019  
 A86G\_GPS -4999273.87745 341004.96327 -3933647.56428 -0.01862 -0.00561 0.02842 2013.649 0.0025 0.0026 0.0024  
 A87P\_GPS -4995952.77669 347786.77689 -3937047.32402 -0.01976 -0.00415 0.02954 2013.009 0.0030 0.0029 0.0028  
 A8TX\_GPS -5074170.12202 444184.92444 -3826365.81712 -0.02517 -0.00149 0.03115 2016.718 0.0011 0.0005 0.0009  
 A8UK\_GPS -5067767.00278 448199.53019 -3834151.15850 -0.02366 -0.00364 0.02996 2015.800 0.0012 0.0005 0.0010  
 A8YC\_GPS -4974899.59613 370314.78421 -3961807.22530 -0.02266 0.00138 0.02857 2006.832 0.0034 0.0039 0.0032  
 A934\_GPS -4990041.74767 353530.49766 -3944102.93299 -0.02409 -0.00336 0.02731 2014.432 0.0025 0.0027 0.0024  
 A93Q\_GPS -5065903.64864 428174.03790 -3838700.88886 -0.02284 -0.00432 0.02776 2016.340 0.0011 0.0005 0.0009  
 A93W\_GPS -5068829.39127 418048.77748 -3836222.28723 -0.02283 -0.00234 0.03175 2016.866 0.0009 0.0005 0.0007  
 A9FJ\_GPS -5087595.71191 437978.86525 -3809058.63983 -0.02736 -0.00190 0.02901 2016.564 0.0010 0.0005 0.0008  
 A9FL\_GPS -5085486.08211 439728.86643 -3811718.09435 -0.02836 -0.00341 0.02822 2016.476 0.0010 0.0005 0.0008  
 A9FW\_GPS -5083736.83050 421168.40878 -3816121.62418 -0.02483 -0.00261 0.02919 2016.856 0.0008 0.0004 0.0007  
 A9MK\_GPS -5085900.16913 484702.63960 -3805821.44879 -0.02400 -0.00208 0.03211 2017.637 0.0013 0.0005 0.0011  
 A9MT\_GPS -5117148.21083 417734.17440 -3772001.46381 -0.02275 -0.00351 0.03155 2017.631 0.0008 0.0005 0.0007  
 A9PH\_GPS -5126772.52428 466518.48333 -3753159.64530 -0.02301 -0.00296 0.03225 2013.676 0.0015 0.0007 0.0012

AAEB\_GPS -5186829.13229 534190.32203 -3661073.54216 -0.02262 -0.00386 0.03351 2015.965 0.0016 0.0007 0.0014  
 AAEJ\_GPS -5174321.12436 501356.28406 -3683110.74602 -0.02250 -0.00366 0.03291 2011.004 0.0019 0.0010 0.0014  
 AAEY\_GPS -5110565.47208 514768.85377 -3768755.51787 -0.02340 -0.00291 0.03284 2018.095 0.0011 0.0005 0.0009  
 AAF6\_GPS -5088015.55158 452244.15516 -3806757.98326 -0.02689 -0.00183 0.02921 2007.944 0.0023 0.0014 0.0018  
 AAJ0\_GPS -5047683.67414 425954.72759 -3862678.60605 -0.02353 -0.00123 0.03111 2014.948 0.0012 0.0008 0.0011  
 AAJ1\_GPS -5100001.20096 404787.76427 -3796154.04159 -0.02312 -0.00319 0.03139 2019.434 0.0008 0.0005 0.0007  
 AAJ4\_GPS -5095196.91155 443999.26962 -3798193.68590 -0.02128 -0.00270 0.03397 2017.446 0.0011 0.0005 0.0010  
 AAJ5\_GPS -5094723.33630 468032.31381 -3796006.08595 -0.02296 -0.00232 0.03208 2010.741 0.0020 0.0010 0.0016  
 AAJ6\_GPS -5080663.12565 453029.75939 -3816540.19601 -0.02335 -0.00219 0.03192 2007.720 0.0025 0.0016 0.0020  
 AAJA\_GPS -5133185.05589 405053.15320 -3751413.76087 -0.02225 -0.00380 0.03186 2019.434 0.0013 0.0008 0.0010  
 AAJU\_GPS -5173953.91286 563569.52397 -3675072.57623 -0.02312 -0.00382 0.03348 2015.489 0.0017 0.0009 0.0015  
 AAV5\_GPS -5151581.53426 498785.98484 -3714916.91594 -0.02442 -0.00343 0.03207 2009.629 0.0017 0.0008 0.0013  
 AB5P\_GPS -5039004.03857 342461.37715 -3882110.26236 -0.02390 -0.00182 0.02994 2010.923 0.0021 0.0021 0.0019  
 AH33\_GPS -4992943.03441 424070.34883 -3932947.31328 -0.02246 -0.00015 0.03122 2006.946 0.0025 0.0017 0.0021  
 AH4Q\_GPS -5000041.16348 379099.76554 -3928996.18747 -0.02359 -0.00043 0.02924 2012.662 0.0024 0.0022 0.0022  
 AH9J\_GPS -4994047.29051 346584.62931 -3939424.61542 -0.01842 -0.00606 0.02914 2013.793 0.0029 0.0028 0.0027  
 AHBY\_GPS -4982861.53688 357047.49594 -3953117.47674 -0.02262 -0.00592 0.03096 2013.927 0.0030 0.0028 0.0028  
 B0PC\_GPS -5061212.15520 439721.42220 -3843623.69218 -0.02012 -0.00244 0.03481 2016.317 0.0010 0.0005 0.0009  
 B0PD\_GPS -5052123.56685 462207.05885 -3853298.23764 -0.02489 -0.00066 0.03005 2015.883 0.0011 0.0005 0.0009  
 B0T9\_GPS -503494.61628 397525.91463 -3858244.70388 -0.02175 -0.00211 0.03157 2016.420 0.0009 0.0007 0.0008  
 B0TB\_GPS -5055596.47827 384569.09033 -3856766.88438 -0.02053 -0.00193 0.03301 2016.617 0.0010 0.0008 0.0009  
 B15J\_GPS -5025088.04746 390484.78989 -3895960.02273 -0.02384 -0.00066 0.03044 2016.188 0.0018 0.0013 0.0016  
 B1P3\_GPS -508093.98550 375988.44963 -3824598.63602 -0.02884 -0.00201 0.02694 2016.601 0.0010 0.0006 0.0008  
 B2FQ\_GPS -5147160.92656 500025.61457 -3720879.91947 -0.02351 -0.00351 0.03248 2016.031 0.0012 0.0006 0.0009  
 B2X8\_GPS -4888308.84037 474293.03933 -4055865.77440 -0.02417 0.00438 0.03217 2000.760 0.0034 0.0055 0.0032  
 B34A\_GPS -5032838.63041 217975.34927 -3898923.02531 -0.00739 -0.00184 0.02094 2003.976 0.0031 0.0047 0.0026  
 B36J\_GPS -5050421.62998 381596.62584 -3863702.09020 -0.02376 -0.00210 0.03064 2012.747 0.0016 0.0011 0.0014  
 B42L\_GPS -5068869.33975 385661.78234 -3839225.15154 -0.02346 -0.00299 0.03111 2016.881 0.0012 0.0008 0.0011  
 B4AU\_GPS -4967909.70448 416777.60532 -3965401.20938 -0.02422 0.00059 0.02943 2008.617 0.0017 0.0017 0.0015  
 B4DP\_GPS -5026690.26144 362298.47222 -3896264.52253 -0.02451 -0.00120 0.02940 2012.669 0.0018 0.0021 0.0017  
 D1JX\_GPS -4932430.56219 515750.78550 -3997303.65994 -0.02517 0.00153 0.03108 2007.769 0.0020 0.0026 0.0017  
 DFFL\_GPS -5059995.57182 404996.39577 -3848948.26541 -0.02165 -0.00080 0.03188 2016.640 0.0011 0.0007 0.0009  
 EAXX\_GPS -5028805.14034 340734.85810 -3896012.72876 -0.02452 -0.00170 0.02860 2012.712 0.0020 0.0022 0.0018  
 EAY6\_GPS -4990030.31274 366635.54959 -3942696.34443 -0.02433 -0.00084 0.02763 2013.458 0.0023 0.0025 0.0022  
 EAY7\_GPS -4994431.07761 370953.07232 -3936742.60368 -0.02658 0.00004 0.02737 2015.728 0.0017 0.0021 0.0016  
 EC0T\_GPS -5223523.16935 670509.64502 -3586425.01583 -0.00898 -0.00622 -0.01053 2017.573 0.0022 0.0009 0.0016  
 EJTY\_GPS -5088091.04284 402564.62387 -3812143.45355 -0.02827 -0.00239 0.02771 2016.578 0.0008 0.0004 0.0007

### A.7.2 EQ Files

#### NZ.eq

```

rename RAUL RAUL_3PS 2008 01 01 00 00 2011 07 09 00 00 !eq
rename RAUL RAUL_4PS 2011 07 09 00 00 2014 07 09 00 00 !eq
rename RAUL RAUL_5PS 2014 07 09 00 00 2099 01 01 00 00 !eq
rename AUCK AUCK_GPS 1995 04 01 00 00 1997 12 16 12 00 !reset
rename AUCK AUCK_2PS 1997 12 16 12 00 2001 10 28 02 00 !ant?? conflicting reports. adding rename to deal with potential station.info error
rename AUCK AUCK_3PS 2001 10 28 02 00 2004 12 23 15 00 !ant
rename AUCK AUCK_4PS 2004 12 23 15 00 2005 11 03 04 00 !macquarie
rename AUCK AUCK_5PS 2005 11 03 04 00 2011 03 01 12 00 !ant
rename AUCK AUCK_6PS 2011 03 01 12 00 2016 11 13 11 00 !ant
rename AUCK AUCK_7PS 2016 11 13 11 00 2099 01 01 00 00 !Kaikoura
rename AUKT AUKT_GPS 2009 08 21 01 00 2012 01 27 01 00 !reset
rename AUKT AUKT_2PS 2012 01 27 01 00 2016 11 13 11 00 !ant? date is a guess
rename AUKT AUKT_3PS 2016 11 13 11 00 2099 01 01 00 00 !kaikoura EQ (only)
rename BHST BHST_GPS 2008 01 30 01 00 2010 09 03 16 36 !reset
rename BHST BHST_2PS 2010 09 03 16 36 2012 12 07 18 19 !darfield
rename BHST BHST_XPS 2010 09 03 16 36 2010 11 03 16 36 !darfield relax
rename BHST BHST_3PS 2012 12 07 18 19 2015 07 21 00 24 !TVZ
  
```

```

rename BHST BHST_4PS 2015 07 21 00 24 2016 11 13 11 00 !ant rec cutoff mangle
rename BHST BHST_5PS 2016 11 13 11 00 2099 01 01 00 00 !kaikoura
rename BHST BHST_XCL 2016 11 13 00 00 2016 11 20 00 00 !post kaikoura relax
rename CKID CKID_XCL 2006 05 01 00 00 2006 09 01 00 00 !toss first few months (middle of a SSE?)
rename CKID CKID_2PS 2007 12 20 08 00 2010 02 17 00 00 !east coast
rename CKID CKID_3PS 2010 02 17 00 00 2010 07 15 00 00 !mystery event (approx)
rename CKID CKID_4PS 2010 07 15 00 00 2011 08 11 00 00 !ant
rename CKID CKID_5PS 2011 08 11 00 00 2013 03 02 00 00 !mystery event (approx)
rename CKID CKID_6PS 2013 03 02 00 00 2014 11 16 22 30 !SSE
rename CKID CKID_XPS 2013 03 02 00 00 2013 04 15 00 00 !SSE void
rename CKID CKID_7PS 2014 11 16 22 30 2016 09 01 17 00 !6.7 NE of gisb
rename CKID CKID_8PS 2016 09 01 17 00 2016 11 13 11 00 !7.0 NE of gisb
rename CKID CKID_9PS 2016 11 13 11 00 2099 01 01 00 00 !kaikoura
rename CKID CKID_XCL 2016 11 13 00 00 2016 11 18 00 00 !post kaikoura relax
rename CHAT CHAT_GPS 1995 10 02 00 00 2001 11 28 03 00 !reset
rename CHAT CHAT_XPS 1995 10 02 00 00 1995 10 04 00 00 !first 2 days bad anntenna ?
rename CHAT CHAT_2PS 2001 11 28 03 00 2012 06 01 00 00 !ant
rename CHTI CHTI_GPS 1995 01 01 00 00 2011 04 05 12 00 !reset
rename CHTI CHTI_2PS 2011 04 05 12 00 2016 11 13 11 00 !ant receiver & cutoff
rename CHTI CHTI_3PS 2016 11 13 11 00 2099 01 01 00 00 !kaikoura
rename CORM CORM_2PS 2004 12 23 15 00 2011 02 11 17 00 !macquarie
rename CORM CORM_4PS 2011 02 11 17 00 2016 09 01 17 00 !ant 41249to57971
rename CORM CORM_5PS 2016 11 13 11 00 2099 01 01 00 00 !Kaikoura
rename DNVK DNVK_2PS 2004 12 23 15 00 2007 12 20 08 00 !macquarie
rename DNVK DNVK_XPS 2004 12 23 15 00 2005 02 15 00 00 ! mac sse
rename DNVK DNVK_3PS 2007 12 20 08 00 2009 07 15 09 00 !east coast
rename DNVK DNVK_4PS 2009 07 15 09 00 2010 12 08 12 00 !dusky
rename DNVK DNVK_5PS 2010 12 08 12 00 2014 01 20 03 00 !ant
rename DNVK DNVK_6PS 2014 01 20 03 00 2016 11 13 11 00 !masterton
rename DNVK DNVK_XPS 2014 01 20 03 00 2014 03 20 03 00 !masterton relax
rename DNVK DNVK_7PS 2016 11 13 11 00 2099 01 01 00 00 !kaikoura
rename DNVK DNVK_XCL 2016 11 13 00 00 2016 11 18 00 00 !kaikoura relax
rename DUND DUND_XCL 2009 07 15 09 00 2010 09 03 16 30 ! dusky, just toss it
rename DUND DUND_3PS 2010 09 03 16 30 2016 11 13 11 00 !darfield
rename DUND DUND_4PS 2016 11 13 11 00 2099 01 01 00 00 !kaikoura
rename GLDB GLDB_GPS 2003 01 01 00 00 2004 12 23 15 00
rename GLDB GLDB_2PS 2004 12 23 15 00 2009 07 15 09 00 !macquarie
rename GLDB GLDB_3PS 2009 07 15 09 00 2011 01 25 07 00 !dusky
rename GLDB GLDB_4PS 2011 01 25 07 00 2013 08 16 02 30 !ant
rename GLDB GLDB_XPS 2013 07 21 05 00 2013 08 16 02 30 !between quake mess
rename GLDB GLDB_5PS 2013 08 16 02 30 2016 11 13 11 00 !6.5 blenheim (2)
rename GLDB GLDB_6PS 2016 11 13 11 00 2099 01 01 00 00 !kaikoura
rename GLDB GLDB_XCL 2016 11 13 00 00 2016 11 14 00 00
rename GISB GISB_GPS 2002 12 23 14 49 2004 11 02 00 00
rename GISB GISB_2PS 2004 11 02 00 00 2006 07 04 12 00 !BEFORE macquarie (approx date)
rename GISB GISB_3PS 2006 07 04 12 00 2007 12 20 07 55 !kermadec no... it's a mystery SSE
rename GISB GISB_4PS 2007 12 20 07 55 2009 07 15 09 00 !east coast
rename GISB GISB_5PS 2009 07 15 09 00 2010 03 21 12 00 !dusky
rename GISB GISB_6PS 2010 03 21 12 00 2010 09 03 16 35 ! NO idea??
rename GISB GISB_7PS 2010 09 03 16 35 2011 01 25 12 00 !7.0 south island
rename GISB GISB_8PS 2011 01 19 03 34 2011 12 13 12 00 !ant
rename GISB GISB_9PS 2011 12 13 12 00 2013 06 28 00 00 ! unknown, between 345-350?
rename GISB GISB_HPS 2013 06 28 00 00 2014 10 06 00 00 !BEFORE blenheim? (approx date)
rename GISB GISB_IPS 2014 10 06 00 00 2016 06 15 00 00 !BEFORE 6.7 NE of gisb (approx date)
rename GISB GISB_JPS 2016 06 15 00 00 2016 11 13 11 00 !BEFORE 7.0 NE of gisb (VERY approx date)
rename GISB GISB_KPS 2016 11 13 11 00 2099 01 01 00 0 !kaikoura
rename HAAS HAAS_2PS 2004 12 23 15 00 2009 07 15 09 00 !macquarie
rename HAAS HAAS_3PS 2009 07 15 09 00 2011 02 08 21 00 ! 7.8 dusky sound
rename HAAS HAAS_4PS 2011 02 08 21 00 2016 04 19 02 06 !ant
rename HAAS HAAS_5PS 2016 04 19 02 06 2016 11 13 11 00 !ant
rename HAAS HAAS_6PS 2016 11 13 11 00 2099 01 01 00 0 !kaikoura
rename HAMT HAMT_GPS 2003 03 01 01 00 2004 12 23 15 00 !reset
rename HAMT HAMT_2PS 2004 12 23 15 00 2011 01 24 01 00 !macquarie

```

```

rename HAMT HAMT_3PS 2011 01 24 01 00 2016 11 13 11 00 !ant 41249to57971
rename HAMT HAMT_4PS 2016 11 13 11 00 2099 01 01 00 00 !kaikoura EQ
rename HAMT HAMT_XPS 2016 11 13 11 00 2016 12 01 00 00 !post kaikoura relax
rename HAST HAST_GPS 2003 01 01 00 0 2004 12 23 15 00
rename HAST HAST_2PS 2004 12 23 15 00 2006 07 04 12 00 !macquarie EQ
rename HAST HAST_3PS 2006 07 04 12 00 2007 12 20 08 00 !mystery event also affecting GISB? (approx)
rename HAST HAST_4PS 2007 12 20 08 00 2009 03 30 00 00 !east coast
rename HAST HAST_5PS 2009 03 30 00 00 2010 12 15 12 00 !BEFORE dusky (approx)
rename HAST HAST_6PS 2010 12 15 12 0 2013 03 01 00 0 !ant
rename HAST HAST_7PS 2013 03 01 00 0 2014 11 16 22 33 !unclear what EQ this is, date is approx
rename HAST HAST_8PS 2014 11 16 22 33 2016 09 01 17 00 !6.7 NE of gisb
rename HAST HAST_XPS 2014 11 16 22 33 2015 01 01 00 00 !post gisb cooldown
rename HAST HAST_9PS 2016 11 13 11 3 2099 01 01 00 00 !kaikoura EQ
rename HAST HAST_XPS 2004 12 23 00 00 2005 02 01 00 00 ! mac relax
rename HIKB HIKB_GPS 2003 03 01 00 00 2004 12 23 15 00 !reset
rename HIKB HIKB_2PS 2004 12 23 15 00 2006 05 15 11 00 !macquarie
rename HIKB HIKB_3PS 2006 05 15 11 00 2007 12 20 08 00 !kermadec
rename HIKB HIKB_4PS 2007 12 20 08 00 2011 01 13 12 00 !east coast
rename HIKB HIKB_5PS 2011 01 13 12 00 2016 09 01 17 00 !ant
rename HIKB HIKB_6PS 2016 09 01 17 00 2016 11 13 11 00 !7.0 NE of gisb
rename HIKB HIKB_7PS 2016 11 13 11 00 2099 01 01 00 00 !kaikoura
rename HIKB HIKB_XPS 2016 11 13 00 00 2017 01 01 00 00 !post kaikoura relax
rename HOKI HOKI_2PS 2000 01 20 00 00 2003 08 21 12 13 !ant
rename HOKI HOKI_XCL 2003 08 21 12 13 2003 09 05 22 57 ! too short to care
rename HOKI HOKI_4PS 2003 09 05 22 57 2004 12 23 15 00 !ant
rename HOKI HOKI_5PS 2004 12 23 15 00 2009 07 15 09 00 !macquarie
rename HOKI HOKI_6PS 2009 07 15 09 00 2010 09 03 16 36 !dusky sound EQ
rename HOKI HOKI_7PS 2010 09 03 16 36 2011 02 21 23 51 ! 7.0 darfield
rename HOKI HOKI_XPS 2011 02 08 20 13 2011 02 21 23 51 !ant
rename HOKI HOKI_8PS 2011 02 21 23 51 2016 11 13 11 00 !"south island" sort of south kaikoura eq
rename HOKI HOKI_9PS 2016 11 13 11 00 2099 01 01 00 00 !kaikoura
rename HOKI HOKI_XCL 2016 11 13 00 00 2016 11 14 00 00
rename KAIK KAIK_2PS 2004 12 23 15 00 2009 07 15 09 00 !macquarie
rename KAIK KAIK_4PS 2009 07 15 09 00 2010 09 03 16 36 !dusky sound EQ
rename KAIK KAIK_5PS 2010 09 03 16 36 2011 01 28 00 55 ! 7.0 darfield
rename KAIK KAIK_6PS 2011 01 28 00 55 2013 08 16 02 31 ! ant
rename KAIK KAIK_7PS 2013 08 16 02 31 2016 11 13 11 00 ! 6.5 blenheim cook strait #2
rename KAIK KAIK_8PS 2016 11 13 11 00 2099 01 01 00 00 !kaikoura
rename KAIK KAIK_XPS 2016 11 13 00 00 2017 06 01 00 00 !kaikoura relax
rename KAIK KAIK_XCL 2016 11 06 00 00 2016 11 18 00 00
rename KTIA KTIA_2PS 2016 11 13 11 00 2099 01 01 00 00 !kaikoura
rename LEXA LEXA_GPS 2004 01 01 00 00 2004 12 23 15 00
rename LEXA LEXA_XPS 2004 11 22 20 30 2004 12 23 15 00 ! 7.1 south of fjordland
rename LEXA LEXA_3PS 2004 12 23 15 00 2007 10 15 12 30 !macquarie
rename LEXA LEXA_4PS 2007 10 15 12 30 2009 07 15 09 00 ! 6.8 south island alpine f
rename LEXA LEXA_5PS 2009 07 15 09 00 2010 12 20 05 00 ! 7.8 dusky sound
rename LEXA LEXA_XPS 2009 07 15 09 00 2010 02 01 00 00 ! dusky cooloff
rename LEXA LEXA_6PS 2010 12 20 05 00 2012 01 19 12 00 !ant
rename LEXA LEXA_7PS 2012 01 19 12 00 2013 12 16 12 00 15.9 local EQ
rename LEXA LEXA_8PS 2013 12 16 12 00 2014 10 13 12 00 15.8 local EQ
rename LEXA LEXA_9PS 2014 10 13 12 00 2016 04 19 02 06 15.8 local EQ
rename LEXA LEXA_HPS 2016 04 19 02 06 2016 11 13 11 00 !ant
rename LEXA LEXA_IPS 2016 11 13 11 00 2099 01 01 00 00 !kaikoura
rename LEXA LEXA_XCL 2016 11 13 00 00 2016 11 14 00 00
rename LKTA LKTA_GPS 2004 01 01 00 00 2004 12 23 15 00
rename LKTA LKTA_2PS 2004 12 23 15 00 2009 07 15 09 00 !macquarie
rename LKTA LKTA_3PS 2009 07 15 09 00 2010 09 03 16 30 !dusky sound EQ
rename LKTA LKTA_4PS 2010 09 03 16 30 2011 02 08 01 00 ! 7.0 darfield
rename LKTA LKTA_5PS 2011 02 08 01 00 2016 11 13 11 00 !ant
rename LKTA LKTA_6PS 2016 11 13 11 00 2099 01 01 00 00 !kaikoura
rename LKTA LKTA_XCL 2016 11 12 00 00 2016 11 16 00 00
rename LYTT LYTT_2PS 2004 12 23 14 59 2009 07 15 09 22
rename LYTT LYTT_3PS 2009 07 15 09 22 2010 09 03 16 36

```

```

rename LYTT LYTT_4PS 2010 09 03 16 36 2011 02 21 23 52
rename LYTT LYTT_5PS 2011 02 21 23 52 2011 06 13 02 21
rename LYTT LYTT_6PS 2011 06 13 02 21 2011 12 23 02 18
rename LYTT LYTT_7PS 2011 12 23 02 18 2016 02 14 00 13
rename LYTT LYTT_8PS 2016 02 14 00 13 2016 11 13 11 02
rename LYTT LYTT_9PS 2016 11 13 11 02 2018 09 09 00 00
rename LYTT LYTT_JPS 2018 09 09 00 00 2100 01 01 00 00
rename MAHO MAHO_GPS 2004 01 01 00 00 2004 12 23 15 00
rename MAHO MAHO_2PS 2004 12 23 15 00 2008 07 15 00 00 !macquarie EQ
rename MAHO MAHO_4PS 2008 07 15 00 00 2011 05 17 07 30 !vertical drops for mystery reason
rename MAHO MAHO_XCL 2011 01 11 02 00 2011 05 17 07 30 !ant (this is a garbage period)
rename MAHO MAHO_5PS 2011 05 17 07 30 2016 11 13 11 00 !ant (again)
rename MAHO MAHO_6PS 2016 11 13 11 00 2099 01 01 00 00 !kaikoura EQ
rename MAHO MAHO_XPS 2016 11 13 00 00 2017 01 01 00 00 !post kaikoura relax
rename MAST MAST_GPS 2003 01 01 00 00 2004 12 23 15 00 !not sure if there's a 2ps
rename MAST MAST_XCL 2003 01 01 00 00 2003 01 11 00 00 !site settles
rename MAST MAST_2PS 2004 12 23 15 00 2010 11 05 01 00 !macquarie
rename MAST MAST_3PS 2010 11 05 01 00 2014 01 20 03 00 !ant
rename MAST MAST_4PS 2014 01 20 03 00 2014 11 16 22 30 ! 6.1 masterton
rename MAST MAST_5PS 2014 11 16 22 30 2016 11 13 11 00 ! 6.7 NE of gisb (ends before kaikoura)
rename MAVL MAVL_GPS 2004 01 01 00 00 2004 11 22 20 30
rename MAVL MAVL_2PS 2004 12 23 15 00 2007 10 15 12 30 !macquarie
rename MAVL MAVL_3PS 2007 10 15 12 30 2009 07 15 09 00 ! 6.8 south island alpine f
rename MAVL MAVL_4PS 2009 07 15 09 00 2010 12 20 21 30 ! 7.8 dusky sound
rename MAVL MAVL_XPS 2009 07 15 09 00 2010 01 01 00 00 !dusky cooloff
rename MAVL MAVL_XCL 2010 12 20 21 30 2011 07 21 12 00 !ant (bad job) NOW XCL
rename MAVL MAVL_6PS 2011 07 21 12 00 2012 01 19 12 00 !ant (corrected)
rename MAVL MAVL_7PS 2016 04 19 02 06 2016 11 13 11 00 !ant
rename MAVL MAVL_8PS 2016 11 13 11 00 2099 01 01 00 00 !kaikoura
rename METH METH_XCL 2010 09 01 00 00 2010 10 16 00 00 !some unknown eq but short enough to flush
rename METH METH_2PS 2016 11 13 11 00 2099 01 01 00 00 !Kaikoura (screwy rename i know)
rename MQZG MQZG_GPS 1999 09 27 00 00 2001 09 03 00 00
rename MQZG MQZG_XCL 1999 09 27 00 00 1999 10 10 00 00 !site settles
rename MQZG MQZG_2PS 2001 09 03 00 00 2004 12 23 15 00 !ant
rename MQZG MQZG_3PS 2004 12 23 15 00 2005 02 28 04 00 !macquarie
rename MQZG MQZG_4PS 2005 02 28 04 00 2009 07 15 09 00 !ant
rename MQZG MQZG_5PS 2009 07 15 09 00 2010 09 03 16 30 !dusky
rename MQZG MQZG_6PS 2010 09 03 16 30 2011 02 09 24 00 !darfield (the big one)
rename MQZG MQZG_7PS 2011 02 09 24 00 2011 06 13 12 00 !ant (manual return?)
rename MQZG MQZG_8PS 2011 06 13 12 00 2011 12 23 12 00 ! chch eq
rename MQZG MQZG_9PS 2011 12 23 12 00 2016 02 14 00 14 ! chch eq
rename MQZG MQZG_JPS 2016 02 14 00 14 2016 11 13 11 05 !chch valentines eq
rename MQZG MQZG_KPS 2016 11 13 11 05 2099 01 01 00 00 !Kaikoura
rename MQZG MQZG_XCL 2011 02 09 00 00 2011 02 23 00 00 !weird blips
rename MTJO MTJO_GPS 2000 11 01 00 00 2004 12 23 15 00
rename MTJO MTJO_2PS 2004 12 23 15 00 2009 07 15 09 00 !macquarie
rename MTJO MTJO_3PS 2009 07 15 09 00 2010 09 03 16 30 !dusky
rename MTJO MTJO_4PS 2010 09 03 16 30 2011 02 08 00 00 ! 7.0 darfield
rename MTJO MTJO_5PS 2011 02 08 00 00 2016 11 13 11 00 ! ant
rename MTJO MTJO_6PS 2016 11 13 11 00 2099 01 01 00 00 !Kaikoura
rename NLSN NLSN_GPS 2004 01 01 00 00 2004 12 23 15 00
rename NLSN NLSN_2PS 2004 12 23 15 00 2007 12 20 08 00 ! macquarie
rename NLSN NLSN_3PS 2007 12 20 08 00 2008 11 15 00 00 !east coast
rename NLSN NLSN_4PS 2008 11 15 00 00 2011 01 25 12 00 !BEFORE dusky.. not sure what this is but very interesting (approx)
rename NLSN NLSN_5PS 2011 01 25 12 00 2013 07 21 05 00 !ant
rename NLSN NLSN_6PS 2013 07 21 05 00 2016 11 13 11 00 !6.5 blenheim cook strait #2
rename NLSN NLSN_XPS 2013 07 21 05 00 2014 09 01 00 00 !cooldown (quite long)
rename NLSN NLSN_7PS 2016 11 13 11 00 2099 01 01 00 00 !obliterated post kaikoura
rename NLSN NLSN_XCL 2016 11 13 11 00 2016 11 14 00 00
rename NPLY NPLY_GPS 2003 01 01 00 00 2004 12 23 15 00
rename NPLY NPLY_2PS 2004 12 23 15 00 2010 11 24 02 00 ! macquarie
rename NPLY NPLY_3PS 2010 11 24 02 00 2013 07 21 05 00 !ant
rename NPLY NPLY_5PS 2013 07 21 05 00 2015 04 24 04 00 !

```

```

rename NPLY NPLY_6PS 2015 04 24 04 00 2016 11 13 11 00 ! 6.1 mini kaikoura
rename NPLY NPLY_7PS 2016 11 13 11 00 2099 01 01 00 00 !kaikoura
rename NPLY NPLY_XPS 2016 11 13 11 00 2017 01 01 00 00 !post kaikoura relax
rename NPLY NPLY_XCL 2016 11 13 00 00 2016 11 14 00 00
rename OUSD OUSD_2PS 1995 10 01 00 00 2003 08 21 12 00 !gap in data then offset. unclear what
rename OUSD OUSD_3PS 2003 08 21 12 00 2004 12 23 15 00 ! 7.2 a fjordland
rename OUSD OUSD_XPS 2004 11 22 20 00 2004 12 23 15 00 ! 7.1 south of fjordland
rename OUSD OUSD_4PS 2004 12 23 15 00 2006 06 21 12 00 ! 8.1 macquarie island
rename OUSD OUSD_5PS 2006 06 21 12 00 2007 09 30 05 00 !ant
rename OUSD OUSD_6PS 2007 09 30 05 00 2007 10 15 12 30 ! 7.4 Auckland Islands
rename OUSD OUSD_7PS 2007 10 15 12 30 2009 07 15 09 00 ! 6.8 south island alpine f
rename OUSD OUSD_8PS 2009 07 15 09 00 2010 09 03 16 30 ! 7.8 dusky sound
rename OUSD OUSD_XPS 2009 07 15 00 00 2009 12 15 09 00 ! post dusky cooloff
rename OUSD OUSD_9PS 2010 09 03 16 30 2011 07 25 12 00 ! 7.0 darfield
rename OUSD OUSD_HPS 2011 07 25 12 00 2016 11 13 11 00 !ant
rename OUSD OUSD_IPS 2016 11 13 11 00 2099 01 01 00 00 !kaikoura
rename PGNE PGNE_2PS 2016 11 13 11 00 2099 01 01 00 00 !kaikoura
rename PYGR PYGR_GPS 2007 01 01 00 00 2007 10 15 12 30
rename PYGR PYGR_2PS 2007 10 15 12 30 2009 07 15 09 00 ! 6.8 south island alpine f
rename PYGR PYGR_3PS 2009 07 15 09 00 2012 01 19 12 00 ! 7.8 dusky sound
rename PYGR PYGR_XPS 2009 07 15 09 00 2011 01 01 00 00 ! post dusky cooldown
rename PYGR PYGR_4PS 2012 04 03 12 00 2013 12 16 12 00 !ant rec cutoff
rename PYGR PYGR_5PS 2016 04 19 02 06 2016 11 13 11 00 !ant
rename PYGR PYGR_6PS 2016 11 13 11 00 2099 01 01 00 00 !kaikoura
rename QUAR QUAR_XCL 2000 02 04 00 00 2000 03 09 00 00
rename QUAR QUAR_3PS 2000 03 09 00 00 2004 12 23 15 00 !ant?
rename QUAR QUAR_4PS 2004 12 23 15 00 2009 07 15 09 00 !macquarie
rename QUAR QUAR_5PS 2009 07 15 09 00 2010 09 03 16 30 !dusky
rename QUAR QUAR_6PS 2010 09 03 16 30 2015 09 23 00 00 !darfield
rename QUAR QUAR_7PS 2015 09 23 00 00 2016 11 13 11 00 !ant
rename QUAR QUAR_8PS 2016 11 13 11 00 2017 07 29 00 00 !kaikoura
rename QUAR QUAR_9PS 2017 07 29 00 00 2100 01 01 00 00 !??? is this even real
rename QUAR QUAR_XCL 2017 09 01 00 00 2017 10 15 00 00 !mystery height problem
rename RGWI RGWI_3PS 2016 06 01 00 00 2016 11 13 00 00 !unclear what event this (date is approx) is but here is when east component takes off
rename RGWI RGWI_4PS 2016 11 13 11 00 2018 01 01 00 00 !kaikoura EQ
rename RGWI RGWI_5PS 2018 01 01 00 00 2099 01 01 00 00 !end of postseismic??
rename TAUP TAUP_GPS 2002 01 01 01 00 2004 12 23 15 00 !reset
rename TAUP TAUP_2PS 2004 12 23 15 00 2007 12 20 08 00 !macquarie EQ (& subsequent SSE/volcanic activity?)
rename TAUP TAUP_3PS 2007 12 20 08 00 2008 08 24 22 30 !M6.6 east coast
rename TAUP TAUP_4PS 2008 08 24 22 30 2010 12 01 22 00 !5.9 Hastings
rename TAUP TAUP_6PS 2010 12 01 22 00 2012 01 17 12 00 !ant 41249to57971
rename TAUP TAUP_7PS 2012 01 17 12 00 2014 11 16 22 30 !unknown??
rename TAUP TAUP_9PS 2014 11 16 22 30 2016 11 13 11 00 !6.7 NE of gisb
rename TAUP TAUP_HPS 2016 11 13 11 00 2099 01 01 00 00 !kaikoura EQ
rename TGHR TGHR_GPS 2006 05 08 00 00 2007 12 20 08 00
rename TGHR TGHR_2PS 2007 12 20 08 00 2010 09 03 16 30 !M6.6 east coast
rename TGHR TGHR_3PS 2010 09 03 16 30 2016 11 13 11 00 ! 7.0 darfield ???
rename TGHR TGHR_4PS 2016 11 13 11 00 2099 01 01 00 00 !kaikoura EQ
rename TRNG TRNG_GPS 2003 01 01 01 00 2004 12 23 15 00 !reset
rename TRNG TRNG_2PS 2004 12 23 15 00 2010 12 07 01 00 !macquarie EQ (about same time as ant change)
rename TRNG TRNG_6PS 2010 12 07 01 00 2016 11 13 11 00 !ant 41249to57971
rename TRNG TRNG_7PS 2016 11 13 11 00 2099 01 01 00 00 !Kaikoura
rename WAIM WAIM_GPS 2004 12 17 00 00 2004 12 23 15 00
rename WAIM WAIM_2PS 2004 12 23 15 00 2009 07 15 09 00 !macquarie
rename WAIM WAIM_3PS 2009 07 15 09 00 2010 09 03 16 30 !dusky
rename WAIM WAIM_4PS 2010 09 03 16 30 2010 11 22 06 00 ! 7.0 darfield
rename WAIM WAIM_5PS 2010 11 22 06 00 2016 11 13 11 00 ! ant
rename WAIM WAIM_6PS 2016 11 13 11 00 2099 01 01 00 00 !Kaikoura
rename WAIM WAIM_XCL 2016 11 13 00 00 2016 11 15 00 00
rename WANG WANG_GPS 2003 01 30 01 00 2004 12 23 15 00
rename WANG WANG_2PS 2004 12 23 15 00 2007 01 18 12 00 !macquarie
rename WANG WANG_XPS 2004 12 23 15 00 2005 06 01 00 00 !macquarie cool down
rename WANG WANG_3PS 2007 01 18 12 00 2007 12 20 08 00 !ant receiver

```

```

rename WANG WANG_4PS 2007 12 20 08 00 2010 11 04 12 00 !east coast
rename WANG WANG_6PS 2010 11 04 12 00 2013 07 21 05 00 !ant
rename WANG WANG_XPS 2010 09 03 16 30 2010 11 04 12 00 !between darfield and ant
rename WANG WANG_7PS 2013 07 21 05 00 2016 11 13 11 00 !blenheim
rename WANG WANG_8PS 2016 11 13 11 00 2099 01 01 00 00 !kaikoura
rename WANG WANG_XPS 2016 11 13 11 00 2017 01 01 00 00 !kaikoura relax
rename WARK WARK_2PS 2016 11 13 11 00 2099 01 01 00 00 !kaikoura EQ
rename WEST WEST_GPS 2005 01 01 00 00 2009 07 15 09 00
rename WEST WEST_XCL 2004 06 01 00 00 2005 01 01 00 00 !wipe the small amount before macquarie
rename WEST WEST_2PS 2009 07 15 09 00 2011 01 26 12 00 !dusky
rename WEST WEST_3PS 2011 01 26 12 00 2013 07 20 00 00 !ant
rename WEST WEST_4PS 2013 07 20 00 00 2016 11 13 11 00 !ant
rename WEST WEST_5PS 2016 11 13 11 00 2099 01 01 00 00 !obliterated post kaikoura
rename WEST WEST_XCL 2016 11 13 11 00 2016 11 20 00 00 !obliterated post kaikoura
rename WGTN WGTN_GPS 1996 01 01 00 00 2004 12 23 15 00
rename WGTN WGTN_2PS 2004 12 23 15 00 2005 03 21 02 00 !macquarie
rename WGTN WGTN_3PS 2005 03 21 02 00 2010 11 14 22 30 ! ant
rename WGTN WGTN_5PS 2010 11 14 22 30 2013 07 21 05 00 !ant (valid)
rename WGTN WGTN_6PS 2013 07 21 05 00 2015 04 24 04 00 !blenheim
rename WGTN WGTN_8PS 2015 04 24 04 00 2016 11 13 11 00 ! 6.1 mini kaikoura
rename WGTN WGTN_9PS 2016 11 13 11 00 2099 01 01 00 00 !kaikoura
rename WGTN WGTN_XCL 2016 11 13 00 00 2016 11 20 00 00
rename WGTT WGTT_2PS 2000 08 18 00 00 2004 12 23 15 00
rename WGTT WGTT_3PS 2004 12 23 15 00 2007 09 22 00 00 !macquarie
rename WGTT WGTT_4PS 2007 09 22 00 00 2009 01 29 00 00 !?a~nt
rename WGTT WGTT_5PS 2009 01 29 00 00 2013 07 21 05 00
rename WGTT WGTT_XCL 2013 07 21 05 00 2013 08 16 02 30
rename WGTT WGTT_7PS 2013 08 16 02 30 2099 01 01 00 00
rename WGTT WGTT_8PS 2016 11 13 11 00 2099 01 01 00 00 !kaikoura
rename WHKT WHKT_GPS 2009 01 01 00 00 2010 03 21 12 00
rename WHKT WHKT_3PS 2010 03 21 12 00 2011 01 27 12 00 !mystery event, also hit GISB(not HIKB?)
rename WHKT WHKT_4PS 2011 01 27 12 00 2016 11 13 11 00 ! ant receiver cutoff
rename WHKT WHKT_7PS 2016 11 13 11 00 2099 01 01 00 00 !kaikoura EQ
rename WHNG WHNG_GPS 2003 01 01 01 00 2004 12 23 15 00 !reset
rename WHNG WHNG_2PS 2004 12 23 15 00 2010 11 22 21 00 !dusky
rename WHNG WHNG_3PS 2010 11 22 21 00 2016 11 13 11 00 !ant 41249to57971
rename WHNG WHNG_4PS 2016 11 13 11 00 2099 01 01 00 00 !kaikoura EQ
rename VGMT VGMT_GPS 2005 01 30 01 00 2009 07 15 09 00
rename VGMT VGMT_2PS 2009 07 15 09 00 2010 09 03 16 30 ! dusky
rename VGMT VGMT_3PS 2010 09 03 16 30 2011 01 17 03 37 !darfield
rename VGMT VGMT_4PS 2011 01 17 03 37 2012 12 12 18 00 !ant
rename VGMT VGMT_5PS 2012 12 12 18 00 2013 07 21 05 00 !TVZ (something happens before this
rename VGMT VGMT_6PS 2013 07 21 05 00 2015 04 24 04 00 !blenheim
rename VGMT VGMT_7PS 2015 04 24 04 00 2016 11 13 11 00 ! 6.1 mini kaikoura 2016 09 01 17 00 !
rename VGMT VGMT_XPS 2015 04 24 04 00 2015 07 24 03 37 !coldown
rename VGMT VGMT_8PS 2016 11 13 11 00 2099 01 01 00 00 !kaikoura
rename VWHK VWHK_GPS 2010 01 01 00 00 2015 04 01 00 00 !reset
rename VWHK VWHK_2PS 2015 04 01 00 00 2099 01 01 00 00 !cancel whole thing
rename VPRK VPRK_GPS 2000 01 01 00 00 2016 11 13 11 00 ! reset
rename VPRK VPRK_3PS 2016 11 13 11 00 2099 01 01 00 00 !kaikoura EQ
rename VTHM VTHM_GPS 2000 01 01 00 00 2016 11 13 11 00 !reset
rename VTHM VTHM_XCL 2016 11 13 11 00 2099 01 01 00 00 !kaikoura EQ
rename VWKU VWKU_2PS 2015 05 01 00 00 2016 11 13 11 00 !suspect antenna was removed here, then put on wrong
rename VWKU VWKU_3PS 2016 11 13 11 00 2099 01 01 00 00 !kaikoura EQ

```

### banish.eq

\*\*2013

\*suspect A6Q1 is missing an offset? doesn't add up

?fine rename A6Q1 A6Q1\_XCL 2013 01 01 00 00 2013 12 31 00 00

\*two dfl occupations. first (077-081) was bunk, but they tried to fix it with a crazy offset. need to toss it

rename DFFL DFFL\_XCL 2013 01 18 00 00 2013 03 23 00 00

\*\*test.. AAEY..seems bad

?fine rename AAEY AAEY\_XCL 2013 01 01 00 00 2013 12 31 00 00 !ALL

\*B2FQ looks very off, toss  
? rename B2FQ B2FQ\_XCL 2013 01 01 00 00 2014 01 01 00 00  
rename A9MT A9MT\_XPS 2013 01 01 00 00 2014 01 01 00 00 !looks weird, can afford to toss  
\*\*2015  
rename A2J7 A2J7\_XCL 2015 03 26 00 00 2015 12 30 00 00 !085 on  
rename A33D A33D\_XCL 2015 05 14 00 00 2015 05 15 00 00 !134 on  
rename A6BK A6BK\_XCL 2015 01 01 00 00 2015 03 26 00 00 !seems overlapped with BUGK  
rename A6LT A6LT\_XCL 2015 04 06 00 00 2015 12 30 00 00 !96 on (mount came loose)  
rename A6LT A6LT\_XCL 2015 01 01 00 00 2015 12 30 00 00 !or just toss whole year  
rename A6Q1 A6Q1\_XCL 2015 04 10 00 00 2015 04 11 00 00 !100  
rename A6X8 A6X8\_XCL 2015 04 13 00 00 2015 04 14 00 00 !103 (probably ok but weird)  
rename A8TX A8TX\_XCL 2015 03 28 00 00 2015 03 30 00 00 !087-on (knocked)  
rename A87P A87P\_XCL 2015 02 02 00 00 2015 02 03 00 00 !033 (GNS survey)  
rename A93W A93W\_XCL 2015 04 26 00 00 2015 04 27 00 00 !116 on  
? rename A9FL A9FL\_XCL 2015 04 09 00 00 2015 04 10 00 00 !99 (missing data?)  
rename A9FW A9FW\_XCL 2015 04 11 00 00 2015 12 11 00 00 !think antenna comes loose  
\* A9MT had a height goof.. could just toss completely, see how that goes. or add massive error  
rename A9MT A9MT\_XPS 2015 01 15 00 00 2015 12 30 00 00 !probably bad occupation due to mount error  
rename AAEY AAEY\_XCL 2015 04 27 00 00 2015 12 30 00 00 !117 on  
? rename AAJ4 AAJ4\_XCL 2015 01 22 00 00 2015 12 30 00 00 !ban all 2015  
rename B0PD B0PD\_XCL 2015 03 28 00 00 2015 12 31 00 00 !087 on (ant came loose)  
rename B0TB B0TB\_XCL 2015 05 06 00 00 2015 12 31 00 00 !experiment losing 2nd half 126 on  
\* B1P3: (strange one.. the ant was wobbled out of alignment) think we toss 141-146  
rename B1P3 B1P3\_XCL 2015 05 21 00 00 2015 05 22 00 00 !141  
rename B1P3 B1P3\_XCL 2015 05 24 00 00 2015 05 27 00 00 !144-146  
rename B2FQ B2FQ\_XCL 2015 04 10 00 00 2015 04 11 00 00 !100  
rename EJTY EJTY\_XPS 2015 05 19 00 00 2015 05 20 00 00 !last day  
rename ER3B ER3B\_XCL 2015 05 07 00 00 2015 05 08 00 00 !127  
rename DFFL DFFL\_XCL 2015 01 01 00 00 2016 01 01 00 00 !whole year looks bad  
\*\*2016  
rename 1331 1331\_XCL 2016 05 17 00 00 2016 12 31 00 00 !138 on  
rename A2L2 A2L2\_XCL 2016 03 22 00 00 2016 03 24 00 00  
rename A6Q1 A6Q1\_XCL 2016 10 25 00 00 2016 10 26 00 00 !299, last day  
rename A8TX A8TX\_XCL 2016 04 11 00 00 2016 12 31 00 00 !102 last day  
rename A93W A93W\_XCL 2016 04 12 00 00 2016 04 13 00 00 !103  
rename A9PH A9PH\_XCL 2016 04 05 00 00 2016 12 31 00 00 !96 on (knocked over)  
rename AAEB AAEB\_XCL 2016 10 23 00 00 2016 12 30 00 00 !297 on  
rename AAEJ AAEJ\_XCL 2016 01 01 00 00 2016 12 30 00 00 !loose tripod leg, entire occupation was a failure  
rename AAJ4 AAJ4\_XCL 2016 05 17 00 00 2016 05 28 00 00 !138 on  
rename AAJ6 AAJ6\_XPS 2017 10 07 00 00 2017 10 08 00 00 !first day is a bit off  
rename B0PC B0PC\_XCL 2016 04 02 00 00 2016 04 03 00 00 !93  
z rename B0T9 B0T9\_XPS 2016 03 01 00 00 2016 03 27 00 00 !first occupation stinky  
rename B1P3 B1P3\_XCL 2016 04 11 00 00 2016 04 12 00 00 !102  
rename B1P3 B1P3\_XCL 2016 04 14 00 00 2016 04 15 00 00 !105  
rename B2FQ B2FQ\_XCL 2016 04 01 00 00 2016 12 31 00 00 !92 on  
rename B42L B42L\_XCL 2016 03 22 00 00 2016 03 24 00 00 !start to 084  
rename EJTY EJTY\_XPS 2016 04 17 00 00 2016 04 18 00 00 !last day  
\*2017  
? rename 1331 1331\_XPS 2017 01 01 00 00 2017 12 31 00 00 !not sure what's up  
rename A2J7 A2J7\_XCL 2017 04 25 00 00 2017 04 26 00 00 !115  
rename A6LT A6LT\_XCL 2017 05 17 00 00 2017 06 19 00 00 !137 on  
rename A6X8 A6X8\_XCL 2017 05 18 00 00 2017 06 20 00 00 !137-on (a mystery)  
\* suspect first A93W (075-094) occupation is distorting everything, shut it off?  
rename A8TX A8TX\_XCL 2017 04 29 00 00 2017 04 30 00 00 !119  
rename A8TX A8TX\_XCL 2017 12 11 00 00 2017 12 12 00 00 !345  
rename A8TX A8TX\_XCL 2017 12 13 00 00 2017 12 14 00 00 !last day  
rename A93W A93W\_XCL 2017 01 01 00 00 2017 08 01 00 00 !first occupation not level, complete trash  
rename A93W A93W\_XCL 2017 11 17 00 00 2017 11 18 00 00 !321, first day  
rename A93Q A93Q\_XCL 2017 01 01 00 00 2017 03 20 00 00 !first occupation.. don't think it was level  
rename A93Q A93Q\_XCL 2017 05 03 00 00 2017 06 20 00 00 !123 on  
rename A9MK A9MK\_XCL 2017 05 02 00 00 2017 05 03 00 00 !122  
rename AAJ0 AAJ0\_XCL 2017 01 01 00 00 2017 12 15 00 00 !don't really need it, can only hurt  
rename AAJ1 AAJ1\_XCL 2017 05 20 00 00 2017 05 21 00 00 !140

```

rename AAJ4 AAJ4_XCL 2017 04 09 00 00 2017 04 12 00 00 !stolen on 099
rename B36j B36j_XCL 2017 02 01 00 00 2017 03 01 00 00 ! the first occupation here is definitely bad
z rename B36j B36j_XCL 2017 01 01 00 00 2017 12 05 00 00 !possible kaikoura offset too crazy / test remove all 2017
rename B0TB B0TB_XPS 2017 01 01 00 00 2017 04 05 00 00 !bad first occupation?
?rename B0T9 B0T9_XCL 2017 03 10 00 00 2017 03 13 00 00 !69-71
z rename B0T9 B0T9_XCL 2017 01 01 00 00 2017 03 21 00 00 !first 2017 occupation suspect
rename B0PC B0PC_XCL 2017 05 03 00 00 2017 05 04 00 00 !end
rename B0PD B0PD_XCL 2017 04 25 00 00 2017 04 26 00 00
rename B0PD B0PD_XCL 2017 08 02 00 00 2017 08 03 00 00
rename B1P3 B1P3_XCL 2017 04 29 00 00 2017 05 01 00 00 !119-120
rename B1P3 B1P3_XCL 2017 05 03 00 00 2017 05 04 00 00 !
rename B1P3 B1P3_XCL 2017 05 10 00 00 2017 05 11 00 00
rename B1P3 B1P3_XCL 2017 05 16 00 00 2017 06 17 00 00 !136-on
rename B42L B42L_XCL 2017 04 03 00 00 2017 04 15 00 00 ! 093 (on)
rename BUGK BUGK_XCL 2017 02 26 00 00 2017 02 27 00 00 !
rename DFFL DFFL_XCL 2017 03 08 00 00 2017 03 09 00 00
rename EJTY EJTY_XCL 2017 05 20 00 00 2017 06 01 00 00 !140-on ?
rename ER3B ER3B_XCL 2017 11 01 00 00 2017 12 31 00 00 !2nd 2017 occ looks way off
****2017 part deux (LINZ survey)
? rename 1384 1384_XCL 2017 08 01 00 00 2017 08 15 00 00 !213 on
? rename 1394 1394_XPS 2017 07 27 00 00 2017 07 28 00 00 !208 not sure but theres a mystery here
rename A49Q A49Q_XCL 2017 07 26 00 00 2017 07 27 00 00 !207 only
rename B15j B15j_XCL 2017 07 24 00 00 2017 07 25 00 00 !205
rename B15j B15j_XCL 2017 08 03 00 00 2017 08 15 00 00 !215 on
rename B2FQ B2FQ_XCL 2017 07 25 00 00 2017 07 26 00 00 !206
newhmmmm rename B0PD B0PD_XCL 2017 07 01 00 00 2017 12 31 00 00 !their occupation seems off
rename DFFL DFFL_XCL 2017 07 24 00 00 2018 07 25 00 00 !205 (on? toss their occupation)
* did experiment with A8TX from 123 00 00.. looks like discontinuity needed
* A8TX day 123 is really bad for some reason, throws the rest off
* rename A8TX A8TX_XCL 2017 05 03 00 00 2117 05 04 00 00
rename A8TX A8TX_XCL 2017 05 03 00 00 2017 07 01 00 00
c*1995 first half of a lot of these is just garbage. toss if you can spare it. otherwise throw massive noise on them 5horiz 20 vert
n rename 1240 1240_XPS 1995 01 01 00 00 1995 06 01 00 00 !95 is just gone. wide variance between 00 & 03
n rename 1242 1242_XPS 1995 01 01 00 00 1995 06 01 00 00 !looks likely
n rename 1243 1243_XPS 1995 01 01 00 00 1995 12 01 00 00 ! can't even see it
n rename 1245 1245_XPS 1995 01 01 00 00 1995 06 01 00 00 !don't need and it seems bad
rename 2003 2003_XCL 1995 01 28 12 00 1995 01 29 12 00 ! 028 only
rename 2404 2404_XCL 1995 02 01 12 00 1995 10 02 12 00 !first bunch ok, second bunch bad?
rename A1YC A1YC_XCL 1995 04 03 12 00 1995 04 04 12 00 !094
rename AH33 AH33_XCL 1995 03 26 12 00 1995 03 27 12 00 !085
rename AH33 AH33_XCL 1995 04 04 12 00 1995 04 05 12 00 !094 bad
rename AH4Q AH4Q_XCL 1995 01 26 12 00 1995 06 27 12 00 !first half looks pretty bad
rename B4AU B4AU_XCL 1995 01 03 12 00 1996 04 04 12 00 !let's just toss all.. don't need 95 in the slightest
rename B2FQ B2FQ_XCL 1995 10 30 12 00 1995 10 31 12 00 !313
**etc
rename 1245 1245_XCL 2011 02 07 00 00 2011 02 08 00 00 !038
rename 2017 2017_XPS 2011 01 01 00 00 2012 01 01 00 00
rename 1361 1361_XPS 1997 01 01 00 00 1998 01 01 00 00 !don't need and obviously off
rename 1367 1367_XCL 1998 01 01 00 00 2016 11 01 00 00 !all gone. too risky
c rename 1394 1394_XCL 1998 01 01 00 00 1999 01 01 00 00 !1998 may be bad, not needed
rename 2328 2328_XPS 2011 01 01 00 00 2012 01 01 00 00 !2011 can go, don't really need & seems weird
rename A3YH A3YH_XCL 2003 01 01 00 00 2004 01 01 00 00 !EITHER 2003 or 2000 is 100% WRONG. seems like 03
rename A33D A33D_XPS 2002 12 19 00 00 2002 12 20 00 00 !353
rename A78A A78A_XCL 2011 02 10 00 00 2011 02 11 00 00 !041
rename A78C A78C_XCL 2000 03 27 00 00 2000 03 28 00 00 !yep
rename AB5P AB5P_XPS 2004 01 01 00 00 2006 01 01 00 00 !2005 completely wrong
rename AB5P AB5P_XCL 2011 02 17 00 00 2011 02 18 00 00 !048?
rename AB5P AB5P_XCL 2015 02 02 00 00 2015 02 03 00 00
rename A934 A934_XCL 2005 01 01 00 00 2006 01 01 00 00 ! inexplicable prob antenna error.. dont need
rename AH33 AH33_XPS 2011 02 15 00 00 2011 02 16 00 00 !046?
rename CBWU CBWU_XPS 2005 01 01 00 00 2006 01 01 00 00 !seems probably bad
rename EAY7 EAY7_XPS 2011 01 01 00 00 2012 01 01 00 00 !something wrong with this year and we don't need it
rename EAXX EAXX_XPS 2011 01 01 00 00 2012 01 01 00 00 !something wrong with this year and we don't need it

```

```
rename BE4C BE4C_XCL 2011 01 01 00 00 2012 01 01 00 00 !2011 only
rename A68G A68G_XCL 2011 01 01 00 00 2012 01 01 00 00 !2011 only
```

### A.7.3 Command Files

#### globk\_vel.cmd

```
* This group of commands must appear before any others:
srt_file glbsrt.bin !direct-access list of sorted input files don't need
com_file glbcom.bin !this is the important one
# Normally for combined files, make_svs is not needed. Only needed if
# orbits are to be estimated which they are not here.
make_svs expr.svs
GLR srt_file /dev/shm/ts.glbsrt.bin !direct-access list of sorted input files don't need
GLR com_file /dev/shm/ts.glbcom.bin !this is the important one
GLR make_svs /dev/shm/ts.expr.svs
srt_dir +1
* or run backwards.. unclear why you'd want to
no srt_dir -1
**** earthquake files ****
#listings
eq_file itrf14.less.eq #subset of itrf
VEL eq_file custom.eq #custom listings
VEL eq_file nz.eq #nz-centric
GLR eq_file custom_noXPS.eq #removed XPS listing (for glred)
GLR eq_file nz_noXPS.eq #ditto
! correct coseismic offsets
eq_file mac.eq
eq_file kaikoura.eq
! remove bad data
eq_file banish.eq
! manually fix commercial offsets (experimental)
eq_file alterra.eq
eq_file smartfix.eq
***** End commands that must appear first
* optionally decimate the run by #1 starting at #2
// DECIMATE 6 20
!scratch file. globk can get big but glred is small, put in /dev/shm imo
sol_file glbsol.bin
GLR sol_file /dev/shm/ts.glbsol.bin
#custom apr goes first to get the dates/renames right
apr_file globk_vel.apr
#itrf goes last to keep reference velocities consistent with model
apr_file itrf14.apr
* Set maximum chi2, prefilt coordinate difference (m), and rotation (mas) for an h-file to be used;
max_chii 30 10 100.
* apply pole tide corrections
app_ptid all
* Invoke glorg (can also invoke outside of globk)
org_cmd gsoln/glorg_vel.cmd
GLR org_cmd gsoln/glorg_glred.cmd
* Print file options CMDS=print used commands
crt_opt NOPR
prt_opt ERAS PSUM VSUM PBO
org_opt ERAS PSUM VSUM PBO RNRP GDLF
FIXA org_opt ERAS PSUM VSUM RNRP GDLF MIDP FIXA
GLR org_opt PBO MIDP
org_out globk_vel.org
GLR org_out globk_TS.org
```

```

* Translation a priori constraints
apr_tran 1 1 1 .1 .1
VEL mar_tran 3.65 3.65 3.65 0 0 0
GLR apr_tran 1 1 1 0 0 0
* site uncertainties (in m and m/yr) (too big and program becomes unstable) (now named apr_site?)
apr_neu all 10. 10. 10. 1 1 1
* glred technically velocity apr can be set to zero
GLR apr_neu all 10 10 10 0 0 0
* Rotation parameters to be estimated and a priori constraints
apr_wob 10 10 1 1
apr_utl 10 1
* For multiday combinations allow EOP's to change between days.
* The rate terms here depend on nature of gamit solutions:
* For RELAX solutions, EOP rates are estimated and when combined
* with daily MIT,GLX-files, the rates are allowed to change and
* will be jointly estimated between the MIT and local file. When
* baseline processing is used, the rates would only apply to MIT
* files.
COMB mar_wob 3650 3650 365 365
COMB mar_utl 365 365
VEL mar_wob 3650 3650 0 0
VEL mar_utl 365 0
* When combining multiple h-files from the same epoch,
* estimate atmospheric zenith delay at common sites
apr_atm common 1
COMB mar_atm common 3.65
VEL mar_atm common 3.65
# if using **mixed data**, try estimating rot independent of utl. good idea!
VEL apr_rot 10 10 10 0 0 0
### A PRIORI orbital parameters. not needed in BASELINE mode (as orbits are fixed)
*global / "kept free"
*****NEEDED if combining with SOPAC (RELAX mode)
*loose orbits don't seem to adversely affect things much with a strong network
apr_svs all 100 100 100 10 10 10 0 R
## set sites to use. this removes all sites, then adds sites individually
use_site clear
source usesite.list #list of sites to use
*or by file
source sig_cor.dat
##### introduce *time-dependent noise* e.g. random walk
# 4.e-6 = 2mm^2/yr, 2.5e-7 = 0.5, 10mm=.0001 units are mm^2/yr. mm=sqrt(X*1e6)
# mar_neu SITE x y z u v w (no time range)
*universally
*mar_neu all 5e-7 5e-7 5e-7 0.0 0.0 0.0
*or by file
VEL source mar_cor.dat
VEL source mar_campaign.dat
##### etc
* Turn off quake log estimates if in the eq_file
free_log -1
* Remove scratch files for repeatability runs (GOOD) (com = scratch file, so don't delete it)
del_sgra no
GLR del_sgra yes

```

### glorg\_vel.cmd

```

* Standard glorg coordinate solution processing
* FLAGS don't work here, like BBB or GLR or MOR etc.
#turn off rate_org for glred
pos_org xtran ytran ztran xrot yrot zrot
rate_org xtran ytran ztran xrot yrot zrot
stab_ite 3 0.5 3
! heavy downweight if ref frame robust (100 or so can be good for initial convergence)
cnd_hgtv 10 10 3 3

```

```

# if there is no apr file, and glorg calls one, org file craps out. just touch it, make an empty one is fine
# adding an apr optional, but can be used to re-constrain to different reference quickly
apr_file itrf14_comb.apr
stab_site clear
stab_site all
# remove bad reference sites (campaign, post-kaikoura, commercial, etc)
source ~/badstab.list
# also ban these NZ sites (nonlinear or wobbly) to be sure NI not affected by garbage
stab_site -aukt -takl -hamt -trng -whkt -rgwi -hikb
stab_site -maho -tghr -taup -gisb
stab_site -nply -wang -vgmt -bhst -hast -ckid
stab_site -dnvk -gldb -nsln -wgfn -mast
stab_site -hoki -west -kaik
stab_site -quar -meth -mqzg
stab_site -haas -mtjo -waim
stab_site -pygr -mavl -bluf -lexa -ousd
!suspect globals
stab_site -kouc -nrmd -noum -blyt -mac1_4ps
#add a few old renames because there weren't enough stations
stab_site hoki_2PS wgtn_GPS ousd_2PS quar_3PS quar_4ps
#campaign sites (list all)
#e.g. stab_site -1240
#define australian plate model 'main aus'
!normal
plate mainaus ADE1_GPS ALIC_5PS CEDU_3PS DARW_5PS HOB2_5PS KARR_GPS KAT1_GPS
plate mainaus KAT2_GPS LORD_GPS NNOR_GPS PERT_2PS STR1_3PS STR2_2PS SYDN_GPS TID1_3PS
plate mainaus TID2_2PS TIDB_4PS TOW2_4PS YAR1_2PS YAR2_3PS YAR3_GPS YARR_GPS
plate eastaus KOUC_6PS NRMD_8PS NOUM_3PS NORF_GPS AUCK_GPS KTIA_GPS WHNG_GPS HAMT_GPS
!with new cal (use ausnc flag in glorg)
ausnc plate mainaus KOUC_6PS NRMD_8PS NOUM_3PS
!with new cal and nni
ausncn plate mainaus KOUC_6PS NRMD_8PS NOUM_3PS
ausncn plate mainaus NORF_GPS AUCK_GPS KTIA_GPS WHNG_GPS
* set constraints for all site renames (m)
eq_4char ndot 0.0001
eq_4char edot 0.0001
eq_4char udot 0.0003
# unequate these mostly campaign sites (distance)
source ~/noequate.list
#extras (nearby sites or different names)
constrain .0001 chat ndot chti ndot
constrain .0001 chat edot chti edot
constrain .0001 aukt ndot takl ndot
constrain .0001 aukt edot takl edot
constrain .0001 kokb ndot kokv ndot
constrain .0001 kokb edot kokv edot
constrain .0001 BOGO ndot BOGI ndot
constrain .0001 BOGO edot BOGI edot
constrain .0001 IRKT ndot IRKM ndot IRKJ ndot
constrain .0001 IRKT edot IRKM edot IRKJ edot
constrain .0001 JOZE ndot JOZ2 ndot
constrain .0001 JOZE edot JOZ2 edot
constrain .0001 MALI ndot MAL2 ndot
constrain .0001 MALI edot MAL2 edot
constrain .0001 MAS1 ndot GMAS ndot
constrain .0001 MAS1 edot GMAS edot
constrain .0001 NYA1 ndot NYAL ndot
constrain .0001 NYA1 edot NYAL edot
# drop these
unequate kouc_5PS ndot kouc_5PS edot kouc_5PS udot
unequate wett ndot wett edot wett udot
#bad renames (toss these renames from the new _GPS combination)
#circa nz (mostly tossing post kaikoura)

```

```

unequate bhst_3ps xdot bhst_3ps ydot bhst_3ps zdot
unequate dund_gps xdot dund_gps ydot dund_gps zdot
unequate gldb_6ps xdot gldb_6ps ydot gldb_6ps zdot
unequate gisb_jps xdot gisb_jps ydot gisb_jps zdot
unequate hast_9ps xdot hast_9ps ydot hast_9ps zdot
unequate hikb_6ps xdot hikb_6ps ydot hikb_6ps zdot
unequate hoki_7ps xdot hoki_7ps ydot hoki_7ps zdot
unequate hoki_8ps xdot hoki_8ps ydot hoki_8ps zdot
unequate hoki_9ps xdot hoki_9ps ydot hoki_9ps zdot
unequate kaik_8ps xdot kaik_8ps ydot kaik_8ps zdot
unequate meth_2ps xdot meth_2ps ydot meth_2ps zdot
unequate nlsn_3ps xdot nlsn_3ps ydot nlsn_3ps zdot
unequate nlsn_7ps xdot nlsn_7ps ydot nlsn_7ps zdot
unequate nply_7ps xdot nply_7ps ydot nply_7ps zdot
unequate ousd_ips xdot ousd_ips ydot ousd_ips zdot
unequate vgnt_3ps xdot vgnt_3ps ydot vgnt_3ps zdot
unequate vgnt_8ps xdot vgnt_8ps ydot vgnt_8ps zdot
unequate waim_3ps xdot waim_3ps ydot waim_3ps zdot
unequate waim_6ps xdot waim_6ps ydot waim_6ps zdot
unequate wang_7ps xdot wang_7ps ydot wang_7ps zdot
unequate wang_8ps xdot wang_8ps ydot wang_8ps zdot
unequate west_5ps xdot west_5ps ydot west_5ps zdot
unequate wgtn_9ps xdot wgtn_9ps ydot wgtn_9ps zdot
#####stations whose velocities completely changed (probably a lot of kaikoura too but too early to say)
#queenstown land
unequate lexa_GPS xdot lexa_GPS ydot lexa_GPS zdot
unequate lexa_3PS xdot lexa_3PS ydot lexa_3PS zdot
unequate lexa_4ps xdot lexa_4ps ydot lexa_4ps zdot
!re-equate the names prior to dusky
constrain 0.0001 lexa_GPS xdot lexa_3PS xdot lexa_4ps xdot
constrain 0.0001 lexa_GPS ydot lexa_3PS ydot lexa_4ps ydot
constrain 0.0001 lexa_GPS zdot lexa_3PS zdot lexa_4ps zdot
#dunedin
unequate ousd_9ps xdot ousd_9ps ydot ousd_9ps zdot
unequate ousd_hps xdot ousd_hps ydot ousd_hps zdot
unequate ousd_ips xdot ousd_ips ydot ousd_ips zdot
!re-equate post-dusky
constrain 0.0001 ousd_9ps xdot ousd_hps xdot ousd_ips xdot
constrain 0.0001 ousd_9ps ydot ousd_hps ydot ousd_ips ydot
constrain 0.0001 ousd_9ps zdot ousd_hps zdot ousd_ips zdot
#psyguar trench / dusky (g up until dusky, then rest post)
unequate pygr_GPS xdot pygr_GPS ydot pygr_GPS zdot
unequate pygr_3PS xdot pygr_3PS ydot pygr_3PS zdot
#MAVL.. circa psyguar trench / dusky
unequate mavl_GPS xdot mavl_GPS ydot mavl_GPS zdot
unequate mavl_2PS xdot mavl_2PS ydot mavl_2PS zdot
unequate mavl_3PS xdot mavl_3PS ydot mavl_3PS zdot
unequate mavl_4ps xdot mavl_4ps ydot mavl_4ps zdot
#bluff
unequate bluf_GPS xdot bluf_GPS ydot bluf_GPS zdot
unequate bluf_2PS xdot bluf_2PS ydot bluf_2PS zdot
unequate bluf_3PS xdot bluf_3PS ydot bluf_3PS zdot
constrain 0.0001 bluf_GPS xdot bluf_2PS xdot bluf_3PS xdot
constrain 0.0001 bluf_GPS ydot bluf_2PS ydot bluf_3PS ydot
constrain 0.0001 bluf_GPS zdot bluf_2PS zdot bluf_3PS zdot
#macquarie island
unequate mac1_GPS xdot mac1_GPS ydot mac1_GPS zdot
unequate mac1_2PS xdot mac1_2PS ydot mac1_2PS zdot
unequate mac1_3PS xdot mac1_3PS ydot mac1_3PS zdot
unequate mac1_4ps xdot mac1_4ps ydot mac1_4ps zdot
!re-equate post-macquarie
constrain 0.0003 mac1_GPS xdot mac1_2PS xdot mac1_3PS xdot
constrain 0.0003 mac1_GPS ydot mac1_2PS ydot mac1_3PS ydot

```

```

constrain 0.0003 mac1_GPS zdot mac1_2PS zdot mac1_3PS zdot
#white island
unequate rgwi_3PS xdot rgwi_3PS ydot rgwi_3PS zdot
unequate rgwi_4ps xdot rgwi_4ps ydot rgwi_4ps zdot
#christchurch (MQZG 3 different velocities looks like)
#here just post kaikoura..leave on its own
#now unequate and requate between dusky and kaikoura
unequate mqzg_GPS xdot mqzg_GPS ydot mqzg_GPS zdot
unequate mqzg_3PS xdot mqzg_3PS ydot mqzg_3PS zdot
unequate mqzg_5PS xdot mqzg_5PS ydot mqzg_5PS zdot
unequate mqzg_6ps xdot mqzg_6ps ydot mqzg_6ps zdot
unequate mqzg_7ps xdot mqzg_7ps ydot mqzg_7ps zdot
unequate mqzg_8ps xdot mqzg_8ps ydot mqzg_8ps zdot
unequate mqzg_9ps xdot mqzg_9ps ydot mqzg_9ps zdot
unequate mqzg_hps xdot mqzg_hps ydot mqzg_hps zdot
#####
#global no-no's
unequate aqui_4ps xdot aqui_4ps ydot aqui_4ps zdot
unequate azry xdot azry ydot azry zdot
unequate bor1_3ps xdot bor1_3ps ydot bor1_3ps zdot
unequate cha1 xdot cha1 ydot cha1 zdot
unequate cit1_2ps xdot cit1_2ps ydot cit1_2ps zdot
unequate clgo_gps xdot clgo_gps ydot clgo_gps zdot
unequate cme1 xdot cme1 ydot cme1 zdot
unequate coco_2ps xdot coco_2ps ydot coco_2ps zdot
unequate coco_gps xdot coco_gps ydot coco_gps zdot
unequate dav1_gps xdot dav1_gps ydot dav1_gps zdot
unequate dav1_3ps xdot dav1_3ps ydot dav1_3ps zdot
unequate drao xdot drao ydot drao zdot
unequate eusk_gps xdot eusk_gps ydot eusk_gps zdot
unequate fair_4ps xdot fair_4ps ydot fair_4ps zdot
unequate farb xdot farb ydot farb zdot
unequate fort_gps xdot fort_gps ydot fort_gps zdot
unequate gol2_2ps xdot gol2_2ps ydot gol2_2ps zdot
unequate gold_4ps xdot gold_4ps ydot gold_4ps zdot
unequate guam xdot guam ydot guam zdot
unequate hob2_5ps xdot hob2_5ps ydot hob2_5ps zdot
unequate iisc_gps xdot iisc_gps ydot iisc_gps zdot
unequate invk_gps xdot invk_gps ydot invk_gps zdot
unequate joze_3ps xdot joze_3ps ydot joze_3ps zdot
unequate kely xdot kely ydot kely zdot
unequate kerg_4ps xdot kerg_4ps ydot kerg_4ps zdot
unequate kir0_2ps xdot kir0_2ps ydot kir0_2ps zdot
unequate kour_4ps xdot kour_4ps ydot kour_4ps zdot
unequate kosg xdot kosg ydot kosg zdot
unequate mcil xdot mcil ydot mcil zdot
unequate mcm4_gps xdot mcm4_gps ydot mcm4_gps zdot
unequate medi_gps xdot medi_gps ydot medi_gps zdot
unequate nyal_gps xdot nyal_gps ydot nyal_gps zdot
unequate newp_gps xdot newp_gps ydot newp_gps zdot
unequate pie1_3ps xdot pie1_3ps ydot pie1_3ps zdot
unequate pie1_4ps xdot pie1_4ps ydot pie1_4ps zdot
unequate pots_3ps xdot pots_3ps ydot pots_3ps zdot
unequate quin xdot quin ydot quin zdot
unequate sey1_gps xdot sey1_gps ydot sey1_gps zdot
unequate sua1 xdot sua1 ydot sua1 zdot
unequate teru_2ps xdot teru_2ps ydot teru_2ps zdot
unequate tow2 xdot tow2 ydot tow2 zdot
unequate usud xdot usud ydot usud zdot
unequate yibl xdot yibl ydot yibl zdot

```

## A.8 NONLINLOC PARAMETERS

### NLL.default.conf

```

CONTROL 1 52362
#geonet
TRANS SIMPLE -41.75 173.0 140.000000
#the real center of model? doesn't work any better
#TRANS SIMPLE -41.758 172.89 140.0
LOCSIG pickle at UoA
#sc3 sends this auto: LOCFILES /store/nz3drx/model NLLOC_OBS /home/seiscomp/nll/data/nz3dr/nz3r_X /home/seiscomp/nll/data/output/nlloc.EDT 1
LOCHYPOT SAVE_NLLOC_ALL NLL_FORMAT_VER_2
# (same as geonet)
LOCPHASEID P P p G Pn Pg
LOCPHASEID S S s G Sn Sg
#from .hdr download: 156 361 121 -375 -875 0 5 5 5 SLOW_LEN
#LOCGRID 156 361 121 -375 -875 0 5 5 5 SLOW_LEN SAVE
LOCGRID 156 361 121 -375 -875 0 5 5 5 MISFIT SAVE
#typical error in seconds for traveltimes, correlation length that controls covariance between stations
LOCGAU 0.25 0.0
#fraction of traveltimes to use as error, minimum traveltimes error in seconds, maximum traveltimes error in seconds
LOCGAU2 0.05 0.5 5.0
#LOCGAU2 0.03 0.3 3.0
#what geonet uses. i think only 5 are allowed
LOCQUAL2ERR 0.05 0.1 0.2 0.4 99999.9
#works good (same as GEONET)
LOCSEARCH OCT 20 30 10 0.01 20000 5000
#GEONET
LOCANGLES ANGLES_NO 5
#LOCANGLES ANGLES_YES 5
#LOCMETH method maxDistStaGrid minNumberPhases maxNumberPhases minNumberSphases VpVsRatio maxNum3DGridMemory minDistStaGrid iRejectDuplicatesArrivals
# following is for 50 max phases uses
#LOCMETH GAU_ANALYTIC 9999.0 4 -1 -1 -1.71 -1 -1
LOCMETH EDT_OT_WT_ML 9999.0 4 -1 -1 -1.71 -1 -1 1 -1
#geonet
#LOCMETH EDT_OT_WT 9999.0 4 -1 -1 -1.71 0 -1 1
# following is for 100 max phases uses
#LOCMETH EDT_OT_WT 9999.0 4 -1 -1 -1.71 0 -1 1
#
#positive elevation, pvel svel
LOCELEVCORR 1 5.8 3.36
# Calculates a weight for each station that is a function of the average distance between all stations used for location. This helps to correct for irregular station distribution,
# flag cutoffDist
LOCSTAWT 1 -1
# LOCPHSTAT RMS_Max NRdgs_Min Gap_Max P_ResidualMax S_ResidualMax Ell_Len3_Max Hypo_Depth_Min Hypo_Depth_Max Hypo_Dist_Max
# Specifies selection criteria for phase residuals to be included in calculation of average P and S station residuals. The average residuals are saved to a summary, phase statistics file (see Phase Statistics file formats).
#LOCPHSTAT 3. -1 -1

```

## A.9 SEISCOMP3 PARAMETERS

### scautoloc.cfg

```

# Defines the author name used to set creationInfo.author in data model objects.
author = scautoloc@UoA
# Defines the primary group of a module. This is the name of the group where a

```

```

# module sends its messages to if the target group is not explicitly given in
# the send call.
connection.primaryGroup = LOCATION
# Defines a list of message groups to subscribe to. The default is usually
# given by the application and does not need to be changed.
connection.subscriptions = PICK,AMPLITUDE
# Defines the output path for all native NonLinLoc input and output files.
NonLinLoc.outputPath = /dev/shm/sc3.nll
# The default NonLinLoc control file to use.
NonLinLoc.controlFile = /installed/NLL7/conf/NLL.default.conf
# The default pick error in seconds passed to NonLinLoc if a SC3 pick object
# does not provide pick time uncertainties.
NonLinLoc.defaultPickError = .1
# Defines a list of active profiles to be used by the plugin.
NonLinLoc.profiles = nz3drx
autoloc.maxAge = 3600
autoloc.cleanupInterval = 600
# For each location, scatoloc performs checks to test if the depth estimate is
# reliable. If the same location quality (e.g. pick RMS) can be achieved while
# fixing the depth to the default depth, the latter is used. This is most often
# the case for shallow events with essentially no depth resolution.
locator.defaultDepth = 10
# The locator might converge at a depth of 0 or even negative depths. This is
# usually not desired, as 0 km might be interpreted as indicative of e.g. a
# quarry blast or another explosive source. In the case of "too shallow"
# locations the minimum depth will be used.
# Note that the minimum depth can also be configured in scolv, possibly to a
# different value.
locator.minimumDepth = 1.0
# Max. permissible RMS for a location to be reported. GeoNet uses 2.0
autoloc.maxRMS = 2.0
# Max. individual residual (unweighted) for a pick to be used in locationMax.
# permissible RMS for a location to be reported. GeoNet = 3.0
autoloc.maxResidual = 3.0
# Stations outside the maximum distance range are ignored.
autoloc.maxStationDistance = 2.5
# Minimum number of phases. GeoNet = 10
autoloc.minPhaseCount = 7
# this number defines the threshold at which scatoloc will start discarding picks for a certain station
autoloc.dynamicPickThresholdInterval = 60
# If set to true, autoloc adopts a depth from a manual origin. If false,
# autoloc may set a default depth (autoloc.defaultDepth).
autoloc.adoptManualDepth = false
# Manual picks/origins can be fed back into autoloc for two purposes:
# * passive association to a solution from a "trusted" source so that we
# avoid fake or wrong locations due to events outside our area of interest
# * use the manual origins in further processing, especially the manual picks.
# Possibly also honor an operator specified fixed depth.
# Currently we only permit use of manual picks which are then used
# instead of the corresponding automatic picks (if existing)
autoloc.useManualPicks = true #false if we're testing the detections which are set to manual
# If this string is non-empty, an amplitude obtained from an amplitude object
# is used by ... . If this string is "mb", a period obtained from the amplitude
# object is also used; if it has some other value, then 1 [units?] is used. If
# this string is empty, then the amplitude is set to 0.5 * thresholdXXL, and 1
# [units?] is used for the period.
autoloc.amplTypeAbs = mb
# If this string is non-empty, it is used to obtain a pick SNR from an
# amplitude object. If it is empty, the pick SNR is 10.
autoloc.amplTypeSNR = snr
# Location of autoloc grid file.
autoloc.grid = /.seiscomp3/grid.conf
# Location of autoloc stations config file.

```

```

autoloc.stationConfig = ./seiscomp3/station.conf
# Location of autoloc stations config file.
autoloc.pickLog = autoloc-picklog.log
# If set to true, scautoloc will listen for manual origins. Manual picks and
# pick weights will be adopted from the manual origin and the processing
# continues with these. Origins produced this way by adding incoming automatic
# picks are nevertheless marked as automatic origins. But they may contain
# manual picks (even pP and S picks).
# Note that in order to listen to manual origins, make sure to add the LOCATION
# group to connection.subscriptions!
# This is an experimental feature relevant only for large regional and global
# networks, where interaction by the analyst is expected already before the
# event is over.
autoloc.useManualOrigins = false
# Sets the logging level between 1 and 4 where 1=ERROR, 2=WARNING, 3=INFO and
# 4=DEBUG.
logging.level = 2
#score.. unclear what this is, left at default
autoloc.minScore = 4
## This is only relevant in offline/testing mode
locator.stationLocations = ./seiscomp3/station-locations.conf

```

### scautopick.cfg

```

# Defines the author name used to set creationInfo.author in data model objects.
author = @appname@@@hostname@
# Defines the primary group of a module. This is the name of the group where a
# module sends its messages to if the target group is not explicitly given in
# the send call.
connection.primaryGroup = PICK
# Defines a list of message groups to subscribe to. The default is usually
# given by the application and does not need to be changed.
connection.subscriptions = CONFIG
# Defines the default filter used for picking. Station specific configurations
# will override this value.
#geonet
#filter = "RMHP(10)>>BW(4,2,15)>>STALTA(0.5,20)"
#me
filter = "RMHP(10)>>BW(4,4,8)>>STALTA(0.4,30)"
# Time correction applied for each pick made. Station specific values override
# this value.
timeCorrection = -0.1
# Defined the record ringbuffer size in seconds.
ringBufferSize = 1000
# The leadTime defines the time in seconds to start picking on waveforms before
# current time.
leadTime = 40
# The initTime defines a timespan in seconds for that the picker is blind after
# initialization. This time is needed to initialize the filter and depends on
# it.
initTime = 40
# Interpolate gaps linearly? This is valid for gaps shorter than
# thresholds.maxGapLength.
gapInterpolation = true
# Defines the amplitude types to be computed by the picker as well.
amplitudes = M,ML,v,mb,mB,MLr
# Configures the secondary picker to use.
spicker = ""
# If enabled the all streams are used for picking that are received by the
# picker. This option has only effect if a file is used as input which contains
# more data than the picker requests. If connected to a waveform server such as
# SeedLink the picker will only receive the data it subscribed to.
useAllStreams = false
# If enabled the all secondary pickers that were triggered by a previous pick

```

```

# will be terminated when a new detection or pick has been found. This aims to
# avoid the case where an S phase is wrongly picked as P but would also be
# picked as S by the secondary picker. But suppressing the S pick can lead to
# undesired results. It might be better in some situations to have two picks (P
# and S) instead only a wrong P.
killPendingSPickers = true

# If enabled and a :confval:'picker' is configured then detections are sent as
# well. To distinguish between detections and picks the evaluation mode of the
# pick is set to manual. This is meant to be a debug option which can be used
# to compare detections and picks by their evaluation mode.

sendDetections = false

# For which value on the filtered waveforms is a pick detected. Station
# specific values override this value.

thresholds.triggerOn = 3.5

# The value the filtered waveforms must reach to enable detection again.
# Between triggerOn and triggerOff the picker is blind and does not produce
# picks. Station specific values ovveride this value.

#geonet
#thresholds.triggerOff = 1.5

#me

thresholds.triggerOff = 0.75

# The maximum gap length in seconds to handle. Gaps larger than this will cause
# the picker to be reseted.

thresholds.maxGapLength = 0.5

# The time window used to compute a maximum (snr) amplitude on the filtered
# waveforms.

thresholds.amplMaxTimeWindow = 10 # after filtering between 4 and 20Hz we do not need a long time-window and this speed-up the release of the pick

# The dead time in seconds.

thresholds.deadTime = 1 # to prevent the blindness of the picker after releasing a pick.

#I think this ties into the picker minSNR??
thresholds.minAmplOffset = 1

# Group used to send amplitudes to.

connection.amplitudeGroup = AMPLITUDE

# Configures the picker to use. By default only a simple detections are emitted
# as picks. To enable real picking on a time window around the detection, an
# algorithm (plugin) can be defined with this parameter.

picker = "AIC"

#picker = ""

#spicker = "S-L2"

##### AIC params (NOT ARAIC.. maeda 95) #depends on good P-wave detections, but fine if they're a little late
# AIC filter parameters published in J Seismol (2010) 14:393411 (Turino et al., 2010 "reliability of the.." / AIC

#Picking for local monitoring purposes (Akaike information criteria)

#turino et al's values:

#picker.AIC.noiseBegin = -40
#picker.AIC.signalBegin = -20
#picker.AIC.signalEnd = 8
#picker.AIC.minSNR = 3
#picker.AIC.filter = "BW(4,2.5,15)"

#sleeman and van Eck (1999) (local):
#picker.AIC.noiseBegin = -8
#picker.AIC.signalBegin = -4
#picker.AIC.signalEnd = 0
#picker.AIC.minSNR = 3
#picker.AIC.filter = "BW(4,2.5,15)"

#over seems to work better with little bad effect according to 1999 paper
# Overrides the default filter which is "raw". The typical filter grammar can
# be used.

# picker.AIC.filter = "BW(4,5,22)"

#geonet
#picker.AIC.filter = "BW(4,2.5,15)"

# me
picker.AIC.filter = "BW(4,3,11)"

# Defines the mininum SNR. noise window to presignal window

```

```

# default/geonet picker.AIC.minSNR = 3.0
#geonet
#picker.AIC.minSNR = 3.0
#me
picker.AIC.minSNR = 1.5
# Overrides the relative data acquisition time (relative to the triggering
# pick). This adds a margin to the actual processing and is useful to
# initialize the filter (e.g. bandpass). The data is not used at all until
# signalBegin is reached. The data time window start is the minimum of
# noiseBegin and signalBegin.
#geonet?
#picker.AIC.noiseBegin = -40
#me
picker.AIC.noiseBegin = -12
# Overrides the default time (relative to the trigger time) of the begin of the
# signal window used to pick.
#geonet? picker.AIC.signalBegin = -20
#picker.AIC.signalBegin = -20
picker.AIC.signalBegin = -8
# Overrides the default time (relative to the trigger time) of the rnf of the
# signal window used to pick.
#geonet? picker.AIC.signalEnd = 8
#picker.AIC.signalEnd = 8
#me
picker.AIC.signalEnd = 4

```

### scevent.cfg

```

# Defines the primary group of a module. This is the name of the group where a
# module sends its messages to if the target group is not explicitly given in
# the send call.
connection.primaryGroup = EVENT
# Defines a list of message groups to subscribe to. The default is usually
# given by the application and does not need to be changed.
connection.subscriptions = LOCATION,MAGNITUDE,FOCMECH,EVENT
# Prefix for all Event IDs
eventIDPrefix = "UoAHR"
# Defines the pattern to generate an event ID.
# %p : prefix
# %Y : year
# %[w]c: alpha character
# %[w]C: upper case alpha character
# %[w]d: decimal
# %[w]x: hexadecimal
# %[w]X: upper case hexadecimal
# [w] is an optional width parameter.
eventIDPattern = "%p%Y%05c"
# Minimum number of station magnitudes referenced to a network magnitude to
# become a preferred magnitude.
eventAssociation.minimumMagnitudes = 2
# Minimum number of matching picks between two origins to be associated to the
# same event.
eventAssociation.minimumMatchingArrivals = 3
# Negative time window: compare only pickIDs to find matching arrivals. A non
# negative value (including 0) compares pick times regardless of the pickID.
# Pass: |pick1.time - pick2.time| <= threshold
eventAssociation.maximumMatchingArrivalTimeDiff = 30
# This parameter is only used in conjunction with
# eventAssociation.maximumMatchingArrivalTimeDiff. If a station has multiple
# associated arrivals for a particular event, this flag defines if the time
# distance of a new pick to all arrivals must be within
# eventAssociation.maximumMatchingArrivalTimeDiff or if one matching arrival is
# enough.
eventAssociation.compareAllArrivalTimes = true

```

```

# Allows to match picks that are associated with weight 0.
eventAssociation.allowLooseAssociatedArrivals = true

# Minimum number of Picks for an Origin that is automatic and cannot be
# associated with an Event to be allowed to form a new Event.
eventAssociation.minimumDefiningPhases = 7

# Time range before the origin time of an incoming origin to search for
# matching events.
eventAssociation.eventTimeBefore = 30

# Time range after the origin time of an incoming origin to search for matching
# events.
eventAssociation.eventTimeAfter = 60

# Associates an origin with an existing event if the origin time differs not
# more than 60 seconds unless the minimumMatchingArrivals criteria matches.
eventAssociation.maximumTimeSpan = 60

# Allowed location difference between an incoming origin compared with
# preferred origins to get associated.
eventAssociation.maximumDistance = 3

# Minimum number of station magnitudes required for Mw(mb) to be considered as
# preferred magnitude.
eventAssociation.minMwCount = 6

# Minimum number of station magnitudes which ensures that Mw(mb) will be
# preferred and not mb.
eventAssociation.mbOverMwCount = 30

# Average between mb and Mw(mb) which must be exceeded to become Mw(mb)
# preferred.
eventAssociation.mbOverMwValue = 6

# If true, one magnitude will be preferred even if magnitude criteria are not
# fulfilled.
eventAssociation.enableFallbackMagnitude = true

# Defines whether to associate or to ignore origins derived from CMT/MT
# inversions.
eventAssociation.ignoreFMDerivedOrigins = true

# If the preferred origin has evaluation status 'rejected' the event type will
# be set as 'not existing' unless the event type has been fixed by an operator
# or the preferred origin has been fixed.
eventAssociation.declareFakeEventForRejectedOrigin = true

# Magnitude type priority list for becoming a preferred magnitude for an event.
eventAssociation.magTypes = M,MLv

# The author priority list. When the eventtool comes to the point to select a
# preferred origin it orders all origins by its author priority and selects
# then the best one among the highest priority author. It also defines the
# author priority for custom priority checks (eventAssociation.priorities).
eventAssociation.authors = scolv@rpic927,screloc@UoA,scautoloc@UoA
eventAssociation.agencies = UoA

# The method priority list. When the eventtool comes to the point to select a
# preferred origin it orders all origins by its methodID priority and selects
# then the best one among the highest priority method. It also defines the
# method priority for custom priority checks (eventAssociation.priorities). A
# defined method string must match exactly the string in Origin.methodID.
eventAssociation.methods = NonLinLoc,LOCSAT

# The general priority list to decide if an origin becomes preferred. The
# priority decreases in the order of the parameters. This list is not used
# unless this parameter is activated.

# Empty priority list: sEvent replicates the default hard wired behaviour:
# AGENCY, STATUS, PHASES_AUTOMATIC, TIME_AUTOMATIC

# Each item in the list corresponds to a check that is performed. Each check
# computes a score of the incoming origin (s1) and the current preferred origin
# (s2). If the s1 is lower than s2, the incoming origin is rejected and does
# not become preferred. All subsequent checks are ignored. If s1 is equal to
# s2, the next check in the list is performed. If s1 is larger than s2, the
# origin becomes preferred and all subsequent checks are ignored.

# Available tokens:
# AGENCY: check based on agency priorities

```

```

# AUTHOR: check based on author priorities
# MODE: evaluation mode priority: 0 = unset, 1 = automatic, 2 = manual, manual
# over-rules automatic
# STATUS: priority combined from evaluation status and evaluation mode: -100 =
# status is rejected, -1 = status is reported, 0 = status is preliminary or
# status is unset and mode is automatic, 1 = status is confirmed or status is
# unset and mode is manual, 2 = status is reviewed, 3 = status is final,
# METHOD: check based on the method priorities
# PHASES: higher phase count = higher priority
# PHASES_AUTOMATIC: only checks phase priorities for incoming automatic origins
# RMS: lower rms = higher priority
# RMS_AUTOMATIC: only check RMS on incoming automatic origins
# TIME: more recent origins (creationTime) have higher priorities
# TIME_AUTOMATIC: only check creationTime priority on incoming automatic origins
eventAssociation.priorities = AGENCY,METHOD,RMS,PHASES,AUTHOR

```

### scmag.cfg

```

# Defines the author name used to set creationInfo.author in data model objects.
author = @appname@@@hostname@

# Defines the primary group of a module. This is the name of the group where a
# module sends its messages to if the target group is not explicitly given in
# the send call.
connection.primaryGroup = MAGNITUDE

# Defines a list of message groups to subscribe to. The default is usually
# given by the application and does not need to be changed.
connection.subscriptions = PICK,AMPLITUDE,LOCATION

# Definition of magnitude types to be calculated from amplitudes.
magnitudes = M,MLv,mb,mB,Mwp,mr

# Enables summary magnitude calculation.
summaryMagnitude.enabled = true

# Define the type/name of the summary magnitude.
summaryMagnitude.type = M

# This is the minimum station magnitude required for any magnitude to
# contribute to the summary magnitude at all. If this is set to 4 then no
# magnitude with less than 4 station magnitudes is taken into consideration
# even if this results in no summary magnitude at all. For this reason, the
# default here is 1 but in a purely automatic system it should be higher, at
# least 4 is recommended.
summaryMagnitude.minStationCount = 3

# Define the magnitude types to be excluded from the summary magnitude
# calculation.
#summaryMagnitude.blacklist = mB,Mwp

# Define the coefficients a. Unnamed values define the default value.
summaryMagnitude.coefficients.a = 0,Mw(mb):0.4,Mw(Mwp):0.4

# Define the coefficients b. Unnamed values define the default value.
summaryMagnitude.coefficients.b = 1,MLv:2,Mw(mb):-1,Mw(Mwp):-1

# Defines the average method to use when computing the network magnitude. To
# define the average method per magnitude type append the type, eg:
# "magnitudes.average = default, MLv:median"
# The default behaviour is to compute the mean if less than 4 contributed
# station magnitudes exist otherwise a trimmed mean of 25 percent is used.
# Options are "default", "mean" and "trimmedMean".
magnitudes.average = default

# The minimum weight of an arrival to be used for magnitude
# calculations.
minimumArrivalWeight = 0.2

# Interval between 2 sending processes. The interval has influence how often
# information is updated.
sendInterval = 1

```

### screloc.cfg

```

# Defines a list of modules loaded at startup.
plugins = ${plugins},locnll

```

```
#####
##### NonLinLoc configuration#####
#####

NLLROOT = /installed/NLL7/
# The default NonLinLoc control file to use
NonLinLoc.controlFile = ${NLLROOT}/NLL.default.conf
# The default pick error in seconds passed to NonLinLoc if a SC3 pick object
# does not provide pick time uncertainties
NonLinLoc.defaultPickError = 0.1
# Defines a list of active profiles to be used by the plugin.
NonLinLoc.profiles = nz3drx
# earthModelID that is stored in the created origin
NonLinLoc.profile.nz3drx.earthModelID = "NZ3D (eberhart2010)"
# Path to travel time tables (grids)
NonLinLoc.profile.nz3drx.tablePath = /store/nz3drx_DLd/model/nz3drx
# Control file of the current profile. If not set, the default control file
# will be used instead.
NonLinLoc.profile.nz3drx.controlFile = /installed/NLL7/conf/NLL.default.conf
# Defines the region values. If transform is GLOBAL 4 values (min_lat, min_lon,
# max_lat, max_lon) are expected. If transform is SIMPLE then 4 values are
# expected (xmin, ymin, xmax, ymax). *changing these seems to have very little effect
#here is GLOBAL but we're using SIMPLE?
NonLinLoc.profile.nz3drx.region = -56.6741,152.5158,-26.4296, 192.5234
#the conf file already sends this crap
#NonLinLoc.profile.nz3drx.transform = 'SIMPLE'
#NonLinLoc.profile.nz3drx.region = -1200,-1200,1200,1200
#NonLinLoc.profile.nz3drx.origin = '41.75,173.0'
#NonLinLoc.profile.nz3drx.rotation = '140.'
# Defines the locator to be used such as NonLinLoc.
reloc.locator = NonLinLoc
# The locator profile to use.
reloc.profile = nz3drx
# Whether to use the weight of the picks associated with the input origin as
# defined in the input origin as input for the locator or not. If false then
# all picks associated with the input origin will be forwarded to the locator
# with full weight.
reloc.useWeight = true
```

## BIBLIOGRAPHY

---

- Abe, Katsuyuki (1995). 'Estimate of tsunami run-up heights from earthquake magnitudes'. In: *Tsunami: Progress in prediction, disaster prevention and warning*. Springer, pp. 21–35.
- Adams, RD (1963). 'Source characteristics of some deep New Zealand earthquakes'. In: *New Zealand Journal of Geology and Geophysics* 6.2, pp. 209–220.
- Adams, Robin Dartrey and DE Ware (1977). 'Subcrustal earthquakes beneath New Zealand; locations determined with a laterally inhomogeneous velocity model'. In: *New Zealand Journal of Geology and Geophysics* 20.1, pp. 59–83.
- Agnew, Duncan Carr (1992). 'The time-domain behavior of power-law noises'. In: *Geophysical Research Letters* 19.4, pp. 333–336.
- Akaike, Hirotugu (1974). 'A new look at the statistical model identification'. In: *Selected Papers of Hirotugu Akaike*. Springer, pp. 215–222.
- Alchalbi, Abdulmutaleb et al. (2010). 'Crustal deformation in northwestern Arabia from GPS measurements in Syria: Slow slip rate along the northern Dead Sea Fault'. In: *Geophysical Journal International* 180.1, pp. 125–135.
- Allen, Rex (1982). 'Automatic phase pickers: their present use and future prospects'. In: *Bulletin of the Seismological Society of America* 72.6B, S225–S242.
- Altamimi, Zuheir, Laurent Métivier, Paul Rebischung, Hélène Rouby and Xavier Collilieux (2017). 'ITRF2014 plate motion model'. In: *Geophysical Journal International* 209.3, pp. 1906–1912.
- Altamimi, Zuheir, Paul Rebischung, Laurent Métivier and Xavier Collilieux (2016). 'ITRF2014: A new release of the International Terrestrial Reference Frame modeling nonlinear station motions'. In: *Journal of Geophysical Research: Solid Earth* 121.8, pp. 6109–6131.
- Amaru, ML (2007). 'Global travel time tomography with 3-D reference models'. PhD thesis. Utrecht University.
- Amiri-Simkoeei, AR, CCJM Tiberius and sand PJG Teunissen (2007). 'Assessment of noise in GPS coordinate time series: methodology and results'. In: *Journal of Geophysical Research: Solid Earth* 112.B7.
- Anderson, Helen and Terry Webb (1994). 'New Zealand seismicity: patterns revealed by the upgraded National Seismograph Network'. In: *New Zealand Journal of Geology and Geophysics* 37.4, pp. 477–493.
- Argus, Donald F and Richard G Gordon (1991). 'No-net-rotation model of current plate velocities incorporating plate motion model NUVEL-1'. In: *Geophysical Research Letters* 18.11, pp. 2039–2042.
- Argus, Donald F, Richard G Gordon and Charles DeMets (2011). 'Geologically current motion of 56 plates relative to the no-net-rotation reference frame'. In: *Geochemistry, Geophysics, Geosystems* 12.11.

- Árnadóttir, Thóra, Weiping Jiang, Kurt L Feigl, Halldór Geirsson and Erik Sturkell (2006). 'Kinematic models of plate boundary deformation in southwest Iceland derived from GPS observations'. In: *Journal of Geophysical Research: Solid Earth* 111.B7.
- Bache, François, Nick Mortimer et al. (2014). 'Seismic stratigraphic record of transition from Mesozoic subduction to continental breakup in the Zealandia sector of eastern Gondwana'. In: *Gondwana Research* 26.3-4, pp. 1060–1078.
- Bache, François, Rupert Sutherland et al. (2012). 'Stratigraphy of the southern Norfolk Ridge and the Reinga Basin: A record of initiation of Tonga–Kermadec–Northland subduction in the southwest Pacific'. In: *Earth and Planetary Science Letters* 321, pp. 41–53.
- Baer, M and U Kradolfer (1987). 'An automatic phase picker for local and teleseismic events'. In: *Bulletin of the Seismological Society of America* 77.4, pp. 1437–1445.
- Ballance, PF (1976). 'Evolution of the Upper Cenozoic magmatic arc and plate boundary in northern New Zealand'. In: *Earth and Planetary Science Letters* 28.3, pp. 356–370.
- Ballance, PF and JD Campbell (1993). 'The Murihiku Arc-Related Basin of New Zealand (Triassic–Jurassic). South Pacific Sedimentary Basins. Sedimentary Basins of the World 2, PF Balance'. In: *South Pacific sedimentary basins. Sedimentary basins of the world 2*, pp. 21–33.
- Bamler, Richard and Philipp Hartl (1998). 'Synthetic aperture radar interferometry'. In: *Inverse Problems* 14.4, R1.
- Bar-Sever, Yoaz E (1996). 'A new model for GPS yaw attitude'. In: *Journal of Geodesy* 70.11, pp. 714–723.
- Barnes, Philip M and Bernard Mercier de Lépinay (1997). 'Rates and mechanics of rapid frontal accretion along the very obliquely convergent southern Hikurangi margin, New Zealand'. In: *Journal of Geophysical Research: Solid Earth* 102.B11, pp. 24931–24952.
- Barraclough, DR, BM Hodder and Stuart RC Malin (1982). 'The IGS proposal for the new international geomagnetic Reference Field'. In: *Journal of Geomagnetism and Geoelectricity* 34.6, pp. 351–356.
- Bartlow, Noel M, Laura M Wallace, R John Beavan, Stephen Bannister and P Segall (2014). 'Time-dependent modeling of slow slip events and associated seismicity and tremor at the Hikurangi subduction zone, New Zealand'. In: *Journal of Geophysical Research: Solid Earth* 119.1, pp. 734–753.
- Barylka, Radosław, Jacek Paziewski, Paweł Wielgosz, Katarzyna Stepińska and Marta Krukowska (2014). 'Accuracy assessment of the ground deformation monitoring with the use of GPS local network: open pit mine Koźmin case study'. In: *Acta Geodynamica et Geomaterialia* 11.4, p. 176.
- Beanland, Sarah and Kelvin Raymond Berryman (1986). *The Kerepehi Fault, Hauraki Depression*. Earth Deformation Section, New Zealand Geological Survey.
- Beavan, John (2005). 'Noise properties of continuous GPS data from concrete pillar geodetic monuments in New Zealand and comparison with data from US deep drilled braced monuments'. In: *Journal of Geophysical Research: Solid Earth* 110.B8.

- Beavan, John and John Haines (2001). 'Contemporary horizontal velocity and strain rate fields of the Pacific-Australian plate boundary zone through New Zealand'. In: *Journal of Geophysical Research: Solid Earth* 106.B1, pp. 741–770.
- Beavan, John, Laura M Wallace et al. (2016). 'New Zealand GPS velocity field: 1995–2013'. In: *New Zealand Journal of Geology and Geophysics* 59.1, pp. 5–14.
- Becker, J.J. et al. (2009). 'Global bathymetry and elevation data at 30 arc seconds resolution: SRTM30 PLUS'. In: *Marine Geodesy* 32.4, pp. 355–371.
- Behr, Y, J Townend, S Bannister and MK Savage (2010). 'Shear velocity structure of the Northland Peninsula, New Zealand, inferred from ambient noise correlations'. In: *Journal of Geophysical Research: Solid Earth* 115.B5.
- Benkhelil, J., G. Bernardel, C. Buchanan, E. D'Acremont and C. Gorini (2001). 'Collaborative Australia/-France Multibeam Seafloor Mapping Survey - Norfolk Ridge to Three Kings Ridge Region : FAUST-2, Preliminary Results'. In: *Geoscience Australia.dataset*.
- Bennett, Richard A et al. (2012). 'Syn-convergent extension observed using the RETREAT GPS network, northern Apennines, Italy'. In: *Journal of Geophysical Research: Solid Earth* 117.B4.
- Beon, Maryline Le et al. (2008). 'Slip rate and locking depth from GPS profiles across the southern Dead Sea Transform'. In: *Journal of Geophysical Research: Solid Earth* 113.B11.
- Berggren, William A, Dennis V Kent, John J Flynn and John A Van Couvering (1985). 'Cenozoic geochronology'. In: *Geological Society of America Bulletin* 96.11, pp. 1407–1418.
- Bernardel, G (2002). 'Geological and morphological framework of the Norfolk Ridge to Three Kings Ridge region'. In: *Geoscience Australia Record*.
- Bird, Peter (2003). 'An updated digital model of plate boundaries'. In: *Geochemistry, Geophysics, Geosystems* 4.3.
- Black, PM, ASB Clark and AA Hawke (1993). 'Diagenesis and very low-grade metamorphism of volcaniclastic sandstones from contrasting geodynamic environments, North Island, New Zealand: the Murihiku and Waipapa terranes'. In: *Journal of Metamorphic Geology* 11.3, pp. 429–435.
- Blanckenburg, Friedhelm von and J Huw Davies (1995). 'Slab breakoff: a model for syncollisional magmatism and tectonics in the Alps'. In: *Tectonics* 14.1, pp. 120–131.
- Blanquat, Michel De Saint, Basil Tikoff, Christian Teyssier and Jean Louis Vigneresse (1998). 'Transpressional kinematics and magmatic arcs'. In: *Geological Society, London, Special Publications* 135.1, pp. 327–340.
- Blewitt, Geoffrey and David Lavallée (2002). 'Effect of annual signals on geodetic velocity'. In: *Journal of Geophysical Research: Solid Earth* 107.B7, ETG–9.
- Blewitt, Geoffrey, David Lavallée, Peter Clarke and Konstantin Nurutdinov (2001). 'A new global mode of Earth deformation: Seasonal cycle detected'. In: *Science* 294.5550, pp. 2342–2345.

- Bock, Y, J Behr, P Fang, J Dean and R Leigh (1997). 'Scripps Orbit and Permanent Array Center (SOPAC) and Southern Californian Permanent GPS Geodetic Array (PGGA)'. In: *The Global Positioning System for the Geosciences*, pp. 55–61.
- Booden, Mathijs A, Ian EM Smith, Philippa M Black and Jeffrey L Mauk (2011). 'Geochemistry of the Early Miocene volcanic succession of Northland, New Zealand, and implications for the evolution of subduction in the Southwest Pacific'. In: *Journal of Volcanology and Geothermal Research* 199.1-2, pp. 25–37.
- Booden, Mathijs A, Ian EM Smith, Jeffrey L Mauk and Philippa M Black (2012). 'Geochemical and isotopic development of the Coromandel Volcanic Zone, northern New Zealand, since 18 Ma'. In: *Journal of Volcanology and Geothermal Research* 219, pp. 15–32.
- Bormann, Peter and Joachim Saul (2008). 'The new IASPEI standard broadband magnitude m B'. In: *Seismological Research Letters* 79.5, pp. 698–705.
- Bossier, John D (1983). 'The impact of VLBI and GPS on geodesy'. In: *Eos, Transactions American Geophysical Union* 64.39, pp. 569–570.
- Bratt, SR and W. Nagy (1991). 'The LocSAT Program'. In: *Science Applications International Corporation, San Diego*.
- Briggs, RM, T Okada, T Itaya, H Shibuya and IEM Smith (1994). 'K-Ar ages, paleomagnetism, and geochemistry of the South Auckland volcanic field, North Island, New Zealand'. In: *New Zealand Journal of Geology and Geophysics* 37.2, pp. 143–153.
- Briggs, Roger M, Matthew P Middleton and Campbell S Nelson (2004). 'Provenance history of a Late Triassic-Jurassic Gondwana margin forearc basin, Murihiku Terrane, North Island, New Zealand: Petrographic and geochemical constraints'. In: *New Zealand Journal of Geology and Geophysics* 47.4, pp. 589–602.
- Brothers, RN (1984). 'Subduction regression and oceanward migration of volcanism, North Island, New Zealand'. In: *Nature* 309.5970, p. 698.
- Brown, Robert Grover, Patrick YC Hwang et al. (1992). *Introduction to random signals and applied Kalman filtering*. Vol. 3. Wiley New York.
- Bryan, CJ, S Sherburn, HM Bibby, SC Bannister and AW Hurst (1999). 'Shallow seismicity of the central Taupo Volcanic Zone, New Zealand: its distribution and nature'. In: *New Zealand Journal of Geology and Geophysics* 42.4, pp. 533–542.
- Bull, William B (1996). 'Prehistorical earthquakes on the Alpine fault, New Zealand'. In: *Journal of Geophysical Research: Solid Earth* 101.B3, pp. 6037–6050.
- Burov, E and M Diament (1996). 'Isostasy, equivalent elastic thickness, and inelastic rheology of continents and oceans'. In: *Geology* 24.5, pp. 419–422.
- Burov, Evgene B and Michel Diament (1995). 'The effective elastic thickness ( $T_e$ ) of continental lithosphere: what does it really mean?' In: *Journal of Geophysical Research: Solid Earth* 100.B3, pp. 3905–3927.

- Cande, Steven C and Dennis V Kent (1995). 'Revised calibration of the geomagnetic polarity timescale for the Late Cretaceous and Cenozoic'. In: *Journal of Geophysical Research: Solid Earth* 100.B4, pp. 6093–6095.
- Cande, Steven C and Joann M Stock (2004). 'Cenozoic reconstructions of the Australia-New Zealand-South Pacific sector of Antarctica'. In: *American Geophysical Union*.
- Castellanos, Fernando and Mirko van der Baan (2013). 'Microseismic event locations using the double-difference algorithm'. In: *CSEG Recorder* 38.3, pp. 26–37.
- Cesca, S et al. (2017). 'Complex rupture process of the Mw 7.8, 2016, Kaikoura earthquake, New Zealand, and its aftershock sequence'. In: *Earth and Planetary Science Letters* 478, pp. 110–120.
- Chappell, J (1975). 'Upper Quaternary warping and uplift rates in the Bay of Plenty and west coast, North Island, New Zealand'. In: *New Zealand Journal of Geology and Geophysics* 18.1, pp. 129–154.
- Chemenda, A., S. Lallemand and A. Bokun (2000). 'Strain partitioning and interplate friction in oblique subduction zones: Constraints provided by experimental modeling'. In: *Journal of Geophysical Research: Solid Earth* 105.B3, pp. 5567–5581.
- Chemenda, Alexander I, Maurice Mattauer, Jacques Malavieille and Alexander N Bokun (1995). 'A mechanism for syn-collisional rock exhumation and associated normal faulting: Results from physical modelling'. In: *Earth and Planetary Science Letters* 132.1, pp. 225–232.
- Chick, LM, WP De Lange and TR Healy (2001). 'Potential tsunami hazard associated with the Kerepehi Fault, Firth of Thames, New Zealand'. In: *Natural Hazards* 24.3, pp. 309–318.
- Christensen, Nikolas I (1996). 'Poisson's ratio and crustal seismology'. In: *Journal of Geophysical Research: Solid Earth* 101.B2, pp. 3139–3156.
- Claessens, L, A Veldkamp, EM Ten Broeke and H Vloemans (2009). 'A Quaternary uplift record for the Auckland region, North Island, New Zealand, based on marine and fluvial terraces'. In: *Global and Planetary Change* 68.4, pp. 383–394.
- Cluzel, Dominique, Pierre Maurizot, Julien Collot and Brice Sevin (2012). 'An outline of the geology of New Caledonia; from Permian-Mesozoic Southeast Gondwanaland active margin to Cenozoic obduction and supergene evolution'. In: *Episodes-News magazine of the International Union of Geological Sciences* 35.1, p. 72.
- Collot, Julien, Louis Geli et al. (2008). 'Tectonic history of northern New Caledonia Basin from deep offshore seismic reflection: Relation to late Eocene obduction in New Caledonia, southwest Pacific'. In: *Tectonics* 27.6.
- Collot, Julien, R. Herzer, Y. Lafay and Louis Geli (2009). 'Mesozoic history of the Fairway-Aotea Basin: Implications for the early stages of Gondwana fragmentation'. In: *Geochemistry, Geophysics, Geosystems* 10.12.
- Conrad, C. P. and C. Lithgow-Bertelloni (2002). 'How mantle slabs drive plate tectonics'. In: *Science* 298.5591, pp. 207–209.

- Cook, Craig, Roger M Briggs, Ian EM Smith and Roland Maas (2004). 'Petrology and geochemistry of intraplate basalts in the South Auckland volcanic field, New Zealand: evidence for two coeval magma suites from distinct sources'. In: *Journal of Petrology* 46.3, pp. 473–503.
- Coombs, DS et al. (1976). 'The Dun Mountain ophiolite belt, New Zealand, its tectonic setting, constitution, and origin, with special reference to the southern portion'. In: *American Journal of Science* 276.5, pp. 561–603.
- Cooper, AF, BA Barreiro, DL Kimbrough and JM Mattinson (1987). 'Lamprophyre dike intrusion and the age of the Alpine fault, New Zealand'. In: *Geology* 15.10, pp. 941–944.
- Cooper, Mark, Ronald Carter and Richard Fenwick (2011). 'Canterbury earthquakes royal commission interim report'. In: *Canterbury Earthquakes Royal Commission, Wellington, NZ*.
- Cordell, Lindrith and Roland G. Henderson (1968). 'Iterative three-dimensional solution of gravity anomaly data using a digital computer'. In: *Geophysics* 33.4, pp. 596–601.
- Crawford, AJ, S. Meffre and PA Symonds (2003). '120 to 0 Ma tectonic evolution of the southwest Pacific and analogous geological evolution of the 600 to 220 Ma Tasman Fold Belt System'. In: *Special Papers-Geological Society of America*, pp. 383–404.
- Dangendorf, Sönke et al. (2017). 'Reassessment of 20th century global mean sea level rise'. In: *Proceedings of the National Academy of Sciences*. pmid:28533403, p. 201616007.
- Davey, FJ, SA Henrys and E. Lodolo (1995). 'Asymmetric rifting in a continental back-arc environment, North Island, New Zealand'. In: *Journal of Volcanology and Geothermal Research* 68.1, pp. 209–238.
- Davidge, Shaun Christopher (1982). 'A geophysical study of the south Hauraki lowlands'. PhD thesis. University of Auckland.
- Davies, J. Huw and Friedhelm von Blanckenburg (1995). 'Slab breakoff: a model of lithosphere detachment and its test in the magmatism and deformation of collisional orogens'. In: *Earth and Planetary Science Letters* 129.1-4, pp. 85–102.
- Davis, JL, P Elósegui, JX Mitrovica and ME Tamisiea (2004). 'Climate-driven deformation of the solid Earth from GRACE and GPS'. In: *Geophysical Research Letters* 31.24.
- Davy, Bryan, Kaj Hoernle and Reinhard Werner (2008). 'Hikurangi Plateau: Crustal structure, rifted formation, and Gondwana subduction history'. In: *Geochemistry, Geophysics, Geosystems* 9.7.
- Davy, BW and TG Caldwell (1998). 'Gravity, magnetic and seismic surveys of the caldera complex, Lake Taupo, North Island, New Zealand'. In: *Journal of Volcanology and Geothermal Research* 81.1-2, pp. 69–89.
- Decker, B LOUIS (1986). *World geodetic system 1984*. Tech. rep. Defense Mapping Agency Aerospace Center St Louis Afs Mo.
- Dimitrova, LL, LM Wallace, AJ Haines and CA Williams (2016). 'High-resolution view of active tectonic deformation along the Hikurangi subduction margin and the Taupo Volcanic Zone, New Zealand'. In: *New Zealand Journal of Geology and Geophysics* 59.1, pp. 43–57.

- Dissen, Russ J. Van and Kelvin R. Berryman (1996). 'Surface rupture earthquakes over the last 1000 years in the Wellington region, New Zealand, and implications for ground shaking hazard'. In: *Journal of Geophysical Research: Solid Earth* 101.B3, pp. 5999–6019.
- Dixon, Timothy H, Manuher Naraghi, MK McNutt and SM Smith (1983). 'Bathymetric prediction from Seasat altimeter data'. In: *Journal of Geophysical Research: Oceans* 88.C3, pp. 1563–1571.
- Dmitrieva, Ksenia, Paul Segall and Charles DeMets (2015). 'Network-based estimation of time-dependent noise in GPS position time series'. In: *Journal of Geodesy* 89.6, pp. 591–606.
- Douglas, A., D. Bowers and JB Young (1997). 'On the onset of P seismograms'. In: *Geophysical Journal International* 129.3, pp. 681–690.
- Dow, John M., Ruth E. Neilan and Chris Rizos (2009). 'The international GNSS service in a changing landscape of global navigation satellite systems'. In: *Journal of Geodesy* 83.3-4, pp. 191–198.
- Drouin, Vincent, Kosuke Heki, Freysteinn Sigmundsson, Sigrún Hreinsdóttir and Benedikt G Ófeigsson (2016). 'Constraints on seasonal load variations and regional rigidity from continuous GPS measurements in Iceland, 1997–2014'. In: *Geophysical Journal International* 205.3, pp. 1843–1858.
- Drouin, Vincent, Freysteinn Sigmundsson et al. (2017). 'Deformation in the Northern Volcanic Zone of Iceland 2008–2014: An interplay of tectonic, magmatic, and glacial isostatic deformation'. In: *Journal of Geophysical Research: Solid Earth* 122.4, pp. 3158–3178.
- Duclos, Mathieu (2005). 'Insights on Plate Boundary Deformation from Seismic Anisotropy in the New Zealand Upper Mantle: A Thesis Presented to the Victoria University of Wellington in Fulfilment of the Requirements for the Degree of Doctor of Philosophy in Geophysics'. PhD thesis. Victoria University of Wellington.
- Dupont, J., J. Launay, C. Ravenne and C.E. De Broin (1975). 'Donnes nouvelles sur la ride de Norfolk (Sud-Ouest Pacifique)'. In: *C. R. Acad. Sci., Ser. D* 281.10. cited By 8, pp. 605–608.
- Eade, James V. (1988). 'The Norfolk Ridge System and Its Margins'. In: *The Ocean Basins and Margins: Volume 7B: The Pacific Ocean*. Ed. by Alan E. M. Nairn, Francis G. Stehli and Seiya Uyeda. Boston, MA: Springer US, pp. 303–324. ISBN: 978-1-4615-8041-6.
- Eberhart-Phillips, Donna, Martin Reyners, Stephen Bannister, Mark Chadwick and Susan Ellis (2010). 'Establishing a versatile 3-D seismic velocity model for New Zealand'. In: *Seismological Research Letters* 81.6, pp. 992–1000.
- Ebinger, CJ and NJ Hayward (1996). 'Soft plates and hot spots: Views from Afar'. In: *Journal of Geophysical Research: Solid Earth* 101.B10, pp. 21859–21876.
- Eccles, JD, J. Cassidy, CA Locke and KB Spörli (2005). 'Aeromagnetic imaging of the Dun Mountain Ophiolite Belt in northern New Zealand: insight into the fine structure of a major SW Pacific terrane suture'. In: *Journal of the Geological Society* 162.4, pp. 723–735.
- Eck, Torild van and Abraham Hofstetter (1990). 'Geologic and Tectonic Processes of the Dead Sea Rift Zone Fault geometry and spatial clustering of microearthquakes along the Dead Sea-Jordan rift fault zone'. In: *Tectonophysics* 180.1. ID: 271882271882, pp. 15–27.

- Edbrooke, SW and FJ Brook (2009). 'Geology of the Whangarei area'. In: *Lower Hutt: Institute of Geological & Nuclear Sciences* 1.250.
- Edbrooke, SW, C. Mazengarb and W. Stephenson (2003). 'Geology and geological hazards of the Auckland urban area, New Zealand'. In: *Quaternary International* 103, pp. 3–21.
- Elósegui, PI et al. (1995). 'Geodesy using the Global Positioning System: The effects of signal scattering on estimates of site position'. In: *Journal of Geophysical Research: Solid Earth* 100.B6, pp. 9921–9934.
- Ergintav, Semih et al. (2009). 'Seven years of postseismic deformation following the 1999, M= 7.4 and M= 7.2, Izmit-Düzce, Turkey earthquake sequence'. In: *Journal of Geophysical Research: Solid Earth* 114.B7.
- Estey, Louis H. and Charles M. Meertens (1999). 'TEQC: the multi-purpose toolkit for GPS/GLONASS data'. In: *GPS Solutions* 3.1, pp. 42–49.
- Ferguson, S.R., M.P. Hochstein and A.C. Kibblewhite (1980). 'Seismic Refraction Studies in the Northern Hauraki Gulf, New-Zealand'. In: *New Zealand Journal of Geology and Geophysics* 23.1. PT: J; UT: WOS:A1980KP76700002, pp. 17–25.
- Fitch, Thomas J. (1972). 'Plate convergence, transcurrent faults, and internal deformation adjacent to southeast Asia and the western Pacific'. In: *Journal of Geophysical Research* 77.23, pp. 4432–4460.
- Fitzherbert, JA, GL Clarke, B. Marmo and R. Powell (2004). 'The origin and P-T evolution of peridotites and serpentinites of NE New Caledonia: prograde interaction between continental margin and the mantle wedge'. In: *Journal of Metamorphic Geology* 22.4, pp. 327–344.
- Forsyth, Donald W. (1985). 'Subsurface loading and estimates of the flexural rigidity of continental lithosphere'. In: *Journal of Geophysical Research: Solid Earth (1978-2012)* 90.B14, pp. 12623–12632.
- Fournier, Marc and Carole Petit (2007). 'Oblique rifting at oceanic ridges: Relationship between spreading and stretching directions from earthquake focal mechanisms'. In: *Journal of Structural Geology* 29.2, pp. 201–208.
- Fowler, CM (n.d.). *R. 1990. The solid earth: An introduction to global geophysics.*
- Frank, FC (1966). 'Deduction of earth strains from survey data'. In: *Bulletin of the Seismological Society of America* 56.1, pp. 35–42.
- Fullea, J., M. Fernàndez and H. Zeyen (2008). *FA2BOUG-A FORTRAN 90 code to compute Bouguer gravity anomalies from gridded free-air anomalies- Application to the Atlantic-Mediterranean transition zone.*
- Furlong, Kevin P. and Peter JJ Kamp (2009). 'The lithospheric geodynamics of plate boundary transpression in New Zealand: Initiating and emplacing subduction along the Hikurangi margin, and the tectonic evolution of the Alpine Fault system'. In: *Tectonophysics* 474.3, pp. 449–462.
- Gaina, Carmen et al. (1998). 'The tectonic history of the Tasman Sea: a puzzle with 13 pieces'. In: *Journal of Geophysical Research: Solid Earth* 103.B6, pp. 12413–12433.
- Garcia, Emmanuel S., David T. Sandwell and Walter HF Smith (2014). 'Retracking CryoSat-2, Envisat and Jason-1 radar altimetry waveforms for improved gravity field recovery'. In: *Geophysical Journal International*, ggt469.

- Garfunkel, Z, CA Anderson and G Schubert (1986). 'Mantle circulation and the lateral migration of subducted slabs'. In: *Journal of Geophysical Research: Solid Earth* 91.B7, pp. 7205–7223.
- Garfunkel, Zvi (1981). 'Internal structure of the Dead Sea leaky transform (rift) in relation to plate kinematics'. In: *Tectonophysics* 80.1-4, pp. 81–108.
- Gelb, Arthur (1974). *Applied optimal estimation*. MIT press.
- Giba, M., A. Nicol and JJ Walsh (2010). 'Evolution of faulting and volcanism in a back-arc basin and its implications for subduction processes'. In: *Tectonics* 29.4.
- Giba, M., JJ Walsh and A. Nicol (2012). 'Segmentation and growth of an obliquely reactivated normal fault'. In: *Journal of Structural Geology* 39, pp. 253–267.
- Giba, M., JJ Walsh, A. Nicol, V. Mouslopoulou and H. Seebek (2013). 'Investigation of the spatio-temporal relationship between normal faulting and arc volcanism on million-year time scales'. In: *Journal of the Geological Society* 170.6, pp. 951–962.
- Gibbs, AD (1984). 'Structural evolution of extensional basin margins'. In: *Journal of the Geological Society* 141.4, pp. 609–620.
- Gladkikh, Vladislav and Robert Tenzer (2012). 'A mathematical model of the global ocean saltwater density distribution'. In: *Pure and Applied Geophysics* 169.1-2, pp. 249–257.
- Gouédard, Pierre, Cécile Cornou and Philippe Roux (2008). 'Phase-velocity dispersion curves and small-scale geophysics using noise correlation slantstack technique'. In: *Geophysical Journal International* 172.3, pp. 971–981.
- Govers, R. and MJR Wortel (2005). 'Lithosphere tearing at STEP faults: response to edges of subduction zones'. In: *Earth and Planetary Science Letters* 236.1, pp. 505–523.
- Green, Trevor H. (1973). 'Petrology and geochemistry of basalts from Norfolk Island'. In: *Journal of the Geological Society of Australia* 20.3, pp. 259–272.
- Grigoli, Francesco, Maren Boese et al. (2017). 'Picking vs Waveform based detection and location methods for induced seismicity monitoring'. In: *EGU General Assembly Conference Abstracts*. Vol. 19, p. 10562.
- Grigoli, Francesco, Simone Cesca et al. (2016). 'Automated microseismic event location using master-event waveform stacking'. In: *Scientific Reports* 6, p. 25744.
- Grigoli, Francesco, Luca Scarabello et al. (2018). 'Pick-and waveform-based techniques for real-time detection of induced seismicity'. In: *Geophysical Journal International* 213.2, pp. 868–884.
- Griscom, Andrew and Robert C Jachens (1989). 'Tectonic history of the north portion of the San Andreas fault system, California, inferred from gravity and magnetic anomalies'. In: *Journal of Geophysical Research: Solid Earth* 94.B3, pp. 3089–3099.
- Gutenberg, Beno and Carl F. Richter (1956). 'Earthquake magnitude, intensity, energy, and acceleration: (Second paper)'. In: *Bulletin of the seismological society of America* 46.2, pp. 105–145.
- Hackney, Ron, Rupert Sutherland and Julien Collot (2012). 'Rifting and subduction initiation history of the New Caledonia Trough, southwest Pacific, constrained by process-oriented gravity models'. In: *Geophysical Journal International* 189.3, pp. 1293–1305.

- Haines, A. John, Lada L. Dimitrova, Laura M. Wallace and Charles A. Williams (2015). *Enhanced surface imaging of crustal deformation: obtaining tectonic force fields using GPS data*. Springer.
- Hamling, IJ, S. Hreinsdottir and N. Fournier (2015). 'The ups and downs of the TVZ: Geodetic observations of deformation around the Taupo Volcanic Zone, New Zealand'. In: *Journal of Geophysical Research: Solid Earth* 120.6, pp. 4667–4679.
- Hamling, IJ and LM Wallace (2015). 'Silent triggering: Aseismic crustal faulting induced by a subduction slow slip event'. In: *Earth and Planetary Science Letters* 421, pp. 13–19.
- Hammer, Sigmund (1939). 'Terrain corrections for gravimeter stations'. In: *Geophysics* 4.3, pp. 184–194.
- Hayes, Gavin P., David J. Wald and Rebecca L. Johnson (2012). 'Slab1.0: A three-dimensional model of global subduction zone geometries'. In: *Journal of Geophysical Research: Solid Earth* (1978–2012) 117.B1.
- Hayes, GP et al. (2017). 'Tectonic summaries of magnitude 7 and greater earthquakes from 2000 to 2015 (No. 2016-1192)'. In: *US Geological Survey*.
- Hayward, Bruce W et al. (2001). 'K-Ar ages of early Miocene arc-type volcanoes in northern New Zealand'. In: *New Zealand Journal of Geology and Geophysics* 44.2, pp. 285–311.
- Heimisson, Elías Rafn, Andrew Hooper and Freysteinn Sigmundsson (2015). 'Forecasting the path of a laterally propagating dike'. In: *Journal of Geophysical Research: Solid Earth* 120.12, pp. 8774–8792.
- Henrys, S. et al. (2013). 'SAHKE geophysical transect reveals crustal and subduction zone structure at the southern Hikurangi margin, New Zealand'. In: *Geochemistry, Geophysics, Geosystems* 14.7, pp. 2063–2083.
- Herring, TA, RW King and SC McClusky (2010). 'Introduction to Gamit/Globk'. In: *Massachusetts Institute of Technology, Cambridge, Massachusetts*.
- Herring, Thomas (2003). 'MATLAB Tools for viewing GPS velocities and time series'. In: *GPS Solutions* 7.3, pp. 194–199.
- Herring, Thomas A et al. (2016). 'Plate Boundary Observatory and related networks: GPS data analysis methods and geodetic products'. In: *Reviews of Geophysics* 54.4, pp. 759–808.
- Herzer, RH, DHN Barker, WR Roest and N. Mortimer (2011). 'Oligocene-Miocene spreading history of the northern South Fiji Basin and implications for the evolution of the New Zealand plate boundary'. In: *Geochemistry, Geophysics, Geosystems* 12.2.
- Herzer, RH, BW Davy et al. (2009). 'Seismic stratigraphy and structure of the Northland Plateau and the development of the Vening Meinesz transform margin, SW Pacific Ocean'. In: *Marine Geophysical Researches* 30.1, pp. 21–60.
- Herzer, Richard H. (1995). 'Seismic stratigraphy of a buried volcanic arc, Northland, New Zealand and implications for Neogene subduction'. In: *Marine and Petroleum Geology* 12.5, pp. 511–531.
- Herzer, Richard H., GCH Chaproniere et al. (1997). 'Seismic stratigraphy and structural history of the Reinga Basin and its margins, southern Norfolk Ridge system'. In: *New Zealand Journal of Geology and Geophysics* 40.4, pp. 425–451.

- Herzer, Richard H. and Jean Mascle (1996). 'Anatomy of a continent-backarc transform-the Vening Meinesz Fracture Zone northwest of New Zealand'. In: *Marine Geophysical Researches* 18.2-4, pp. 401–427.
- Heuret, Arnauld and Serge Lallemand (2005). 'Plate motions, slab dynamics and back-arc deformation'. In: *Physics of the Earth and Planetary Interiors* 149.1, pp. 31–51.
- Hochstein, M. P. (1995). 'Crustal heat transfer in the Taupo Volcanic Zone (New Zealand): comparison with other volcanic arcs and explanatory heat source models'. In: *Journal of Volcanology and Geothermal Research* 68.1-3, pp. 117–151.
- Hochstein, M.P. and P.F. Ballance (1993). 'Hauraki Rift: a young, active, intra-continental rift in a back-arc setting'. In: *South Pacific Sedimentary Basins, Sedimentary Basins of the World* 2, pp. 295–305.
- Hochstein, M.P. and I.M. Nixon (1979). 'Geophysical study of the Hauraki Depression, North Island, New Zealand'. In: *New Zealand Journal of Geology and Geophysics* 22.1, pp. 1–19.
- Hochstein, M.P. and A.G. Nunns (1976). 'Gravity measurements across the Waikato Fault, North Island, New Zealand'. In: *New Zealand Journal of Geology and Geophysics* 19.3, pp. 347–358.
- Hochstein, M.P., K. Tearney et al. (1986). 'Structure of the Hauraki Rift (New Zealand)'. In: *Royal Society of New Zealand Bulletin* 24, pp. 333–348.
- Hodder, APW (1984). 'Late Cenozoic rift development and intra-plate volcanism in northern New Zealand inferred from geochemical discrimination diagrams'. In: *Tectonophysics* 101.3, pp. 293–318.
- Holden, L. et al. (2015). 'Contemporary ground deformation in the Taupo Rift and Okataina Volcanic Centre from 1998 to 2011, measured using GPS'. In: *Geophysical Journal International* 202.3, pp. 2082–2105.
- Holdsworth, RE, CA Butler and AM Roberts (1997). 'The recognition of reactivation during continental deformation'. In: *Journal of the Geological Society* 154.1, pp. 73–78.
- Holt, WE and TA Stern (1991). 'Sediment loading on the western platform of the New Zealand continent: Implications for the strength of a continental margin'. In: *Earth and planetary science letters* 107.3-4, pp. 523–538.
- Horspool, NA, MK Savage and S. Bannister (2006). 'Implications for intraplate volcanism and back-arc deformation in northwestern New Zealand, from joint inversion of receiver functions and surface waves'. In: *Geophysical Journal International* 166.3, pp. 1466–1483.
- Houlié, Nicolas and Tim A Stern (2017). 'Vertical tectonics at an active continental margin'. In: *Earth and Planetary Science Letters* 457, pp. 292–301.
- Hreinsdóttir, Sigrún and Richard A. Bennett (2009). 'Active aseismic creep on the Alto Tiberina low-angle normal fault, Italy'. In: *Geology* 37.8, pp. 683–686.
- Hunt, Trevor (1978). 'Stokes magnetic anomaly system'. In: *New Zealand Journal of Geology and Geophysics* 21.5, pp. 595–606.

- Hurst, AW, HM Bibby and RR Robinson (2002). 'Earthquake focal mechanisms in the central Taupo Volcanic Zone and their relation to faulting and deformation'. In: *New Zealand Journal of Geology and Geophysics* 45.4, pp. 527–536.
- Hurst, Tony, Wiebke Heise, Sigrun Hreinsdóttir and Ian Hamling (2016). 'Geophysics of the Taupo Volcanic Zone: A review of recent developments'. In: *Geothermics* 59, pp. 188–204.
- Ishizuka, Osamu et al. (2011). 'The timescales of subduction initiation and subsequent evolution of an oceanic island arc'. In: *Earth and Planetary Science Letters* 306.3, pp. 229–240.
- Islam, Md Tariqul and Erik Sturkell (2015). 'Temperature-dependent Newtonian rheology in advection-convection geodynamical model for plate spreading in Eastern Volcanic Zone, Iceland'. In: *Journal of Geoscience and Environment Protection* 3.05, p. 14.
- Jackson, JA (1980). 'Reactivation of basement faults and crustal shortening in orogenic belts'. In: *Nature* 283.5745, pp. 343–346.
- Jin, Shuanggen, Tonie Van Dam and Shimon Wdowinski (2013). 'Observing and understanding the Earth system variations from space geodesy'. In: *Journal of Geodynamics* 72, pp. 1–10.
- Johnson, P. and SW Stewart (1986). 'Caltech-USGS seismic processing system (CUSP): User documentation'. In: *US Geol.Surv., Open-File Rept.*
- Johnston, MJS, AT Linde, MT Gladwin and RD Borcherdt (1987). 'Fault failure with moderate earthquakes'. In: *Tectonophysics* 144.1-3, pp. 189–206.
- Kaiser, A. et al. (2012). 'The Mw 6.2 Christchurch earthquake of February 2011: preliminary report'. In: *New Zealand Journal of Geology and Geophysics* 55.1, pp. 67–90.
- Kaiser, Anna et al. (2017). 'The 2016 Kaikōura, New Zealand, earthquake: preliminary seismological report'. In: *Seismological Research Letters* 88.3, pp. 727–739.
- Kamp, Peter JJ and Ivan J Liddell (2000). 'Thermochronology of northern Murihiku Terrane, New Zealand, derived from apatite FT analysis'. In: *Journal of the Geological Society* 157.2, pp. 345–354.
- Kao, Honn and Shao-Ju Shan (2004). 'The source-scanning algorithm: Mapping the distribution of seismic sources in time and space'. In: *Geophysical Journal International* 157.2, pp. 589–594.
- Keep, Myra and Wouter P. Schellart (2012). 'Introduction to the thematic issue on the evolution and dynamics of the Indo-Australian plate'. In: *Australian Journal of Earth Sciences* 59.6, pp. 807–808.
- Keller, Tobias, Dave A. May and Boris JP Kaus (2013). 'Numerical modelling of magma dynamics coupled to tectonic deformation of lithosphere and crust'. In: *Geophysical Journal International* 195.3, pp. 1406–1442.
- Kenny, J. A., J. M. Lindsay and T. M. Howe (2012). 'Post-Miocene faults in Auckland: insights from borehole and topographic analysis'. In: *New Zealand Journal of Geology and Geophysics* 55.4, pp. 323–343.
- Kessel, Ronit, Max W Schmidt, Peter Ulmer and Thomas Pettke (2005). 'Trace element signature of subduction-zone fluids, melts and supercritical liquids at 120–180 km depth'. In: *Nature* 437.7059, p. 724.

- Kimbrough, David L., James M. Mattinson, Douglas S. Coombs, Charles A. Landis and Mike R. Johnston (1992). 'Uranium-lead ages from the Dun Mountain ophiolite belt and Brook Street terrane, South Island, New Zealand'. In: *Geological Society of America Bulletin* 104.4, pp. 429–443.
- King, Matt A. and Simon DP Williams (2009). 'Apparent stability of GPS monumentation from short-baseline time series'. In: *Journal of Geophysical Research: Solid Earth* 114.B10.
- King, Peter R. (2000). 'Tectonic reconstructions of New Zealand: 40 Ma to the present'. In: *New Zealand Journal of Geology and Geophysics* 43.4, pp. 611–638.
- King, Peter R. and Glenn P. Thrasher (1996). *Cretaceous Cenozoic geology and petroleum systems of the Taranaki Basin, New Zealand*. Vol. 2. Institute of Geological & Nuclear Sciences.
- King, RW and Y. Bock (2004). 'Documentation for the MIT GPS analysis software: GAMIT'. In: *Mass. Inst. of Technol., Cambridge*.
- Kirkby, Alison Louise (2008). In: *A Geophysical Investigation of the Structure and Evolution of the Southern Kaimai Range and Hauraki Rift*.
- Kirkendall, Clay K and Anthony Dandridge (2004). 'Overview of high performance fibre-optic sensing'. In: *Journal of Physics D: Applied Physics* 37.18, R197.
- Kitagawa, Genshiro and Hirotugu Akaike (1978). 'A procedure for the modeling of non-stationary time series'. In: *Annals of the Institute of Statistical Mathematics* 30.1, pp. 351–363.
- Klingelhoefer, Frauke et al. (2007). 'Crustal structure of the basin and ridge system west of New Caledonia (southwest Pacific) from wide-angle and reflection seismic data'. In: *Journal of Geophysical Research: Solid Earth* 112.B11.
- Kreemer, Corné, Geoffrey Blewitt and Elliot C. Klein (2014). 'A geodetic plate motion and global strain rate model'. In: *Geochemistry, Geophysics, Geosystems* 15.10, pp. 3849–3889.
- Kreemer, Corné, William E. Holt, Saskia Goes and Rob Govers (2000). 'Active deformation in eastern Indonesia and the Philippines from GPS and seismicity data'. In: *Journal of Geophysical Research: Solid Earth* 105.B1, pp. 663–680.
- Kroenke, LW and Jacques Dupont (1982). 'Subduction-obduction: a possible north-south transition along the west flank of the Three Kings Ridge'. In: *Geo-Marine Letters* 2.1-2, pp. 11–16.
- Kroenke, LW and JV Eade (1982). 'Three Kings Ridge: a west-facing arc'. In: *Geo-Marine Letters* 2.1-2, pp. 5–10.
- Küperkoch, Ludger, Thomas Meier and Tobias Diehl (n.d.). 'Automated event and phase identification'. In: () .
- Kusznir, Nick and Garry Karner (1985). 'Dependence of the flexural rigidity of the continental lithosphere on rheology and temperature'. In: *Nature* 316.6024, p. 138.
- Lafoy, Y, I Brodien, R Vially and NF Exon (2005). 'Structure of the basin and ridge system west of New Caledonia (Southwest Pacific): a synthesis'. In: *Marine Geophysical Researches* 26.1, pp. 37–50.

- Lagemaat, Suzanna HA van de, Douwe JJ van Hinsbergen, Lydian M Boschman, Peter JJ Kamp and Wim Spakman (2018). 'Southwest Pacific Absolute Plate Kinematic Reconstruction Reveals Major Cenozoic Tonga-Kermadec Slab Dragging'. In: *Tectonics* 37.8, pp. 2647–2674.
- Laird, MG and JD Bradshaw (2004). 'The break-up of a long-term relationship: the Cretaceous separation of New Zealand from Gondwana'. In: *Gondwana Research* 7.1, pp. 273–286.
- Lallemand, Serge, Arnauld Heuret and David Boutelier (2005). 'On the relationships between slab dip, back-arc stress, upper plate absolute motion, and crustal nature in subduction zones'. In: *Geochemistry, Geophysics, Geosystems* 6.9.
- Lamarche, Geoffroy, Jonathan M. Bull, Phil M. Barnes, Susanna K. Taylor and Huw Horgan (2000). 'Constraining fault growth rates and fault evolution in New Zealand'. In: *EOS, Transactions American Geophysical Union* 81.42, pp. 481–486.
- Lamb, Simon (2011). 'Cenozoic tectonic evolution of the New Zealand plate-boundary zone: A paleomagnetic perspective'. In: *Tectonophysics* 509.3-4, pp. 135–164.
- Lamb, Simon, James DP Moore, Euan Smith and Tim Stern (2017). 'Episodic kinematics in continental rifts modulated by changes in mantle melt fraction'. In: *Nature* 547.7661, p. 84.
- Lamb, Simon and Euan Smith (2013). 'The nature of the plate interface and driving force of interseismic deformation in the New Zealand plate-boundary zone, revealed by the continuous GPS velocity field'. In: *Journal of Geophysical Research: Solid Earth* 118.6, pp. 3160–3189.
- Langbein, John (2012). 'Estimating rate uncertainty with maximum likelihood: differences between power-law and flicker-random-walk models'. In: *Journal of Geodesy* 86.9, pp. 775–783.
- Langbein, John, Eddie Quilty and Katherine Breckenridge (1993). 'Sensitivity of crustal deformation instruments to changes in secular rate'. In: *Geophysical Research Letters* 20.2, pp. 85–88.
- Lange, P. J. De and D. J. Lowe (1990). 'History of vertical displacement of Kerepehi Fault at Kopouatai bog, Hauraki Lowlands, New Zealand, since c. 10 700 years ago'. In: *New Zealand Journal of Geology and Geophysics* 33.2, pp. 277–283.
- Langridge, RM et al. (2016). 'The New Zealand active faults database'. In: *New Zealand Journal of Geology and Geophysics* 59.1, pp. 86–96.
- Lee, JM, KJ Bland, DB Townsend and PJJ Kamp (2011). 'Geology of the Hawke's Bay area, Institute of Geological and Nuclear Sciences 1: 250,000 geological map 8.1 sheet 93 p'. In: *GNS Science, Lower Hutt*. OpenURL.
- Lensen, G. J. (1981). 'Tectonic strain and drift'. In: *Tectonophysics* 71.1-4, pp. 173–188.
- (1981). 'Tectonic strain and drift'. In: *Tectonophysics* 71.1-4, pp. 173–188.
- Leonard, GS, JG Begg, CJN Wilson and GS Leonard (2010). *Geology of the Rotorua area*. GNS Science.
- Leonard, M. (2000). 'Comparison of manual and automatic onset time picking'. In: *Bulletin of the Seismological Society of America* 90.6, pp. 1384–1390.

- Levitt, Daniel A. and David T. Sandwell (1995). 'Lithospheric bending at subduction zones based on depth soundings and satellite gravity'. In: *Journal of Geophysical Research: Solid Earth* 100.B1, pp. 379–400.
- Lin, Fan-Chi, Michael H. Ritzwoller, John Townend, Stephen Bannister and Martha K. Savage (2007). 'Ambient noise Rayleigh wave tomography of New Zealand'. In: *Geophysical Journal International* 170.2, pp. 649–666.
- Lindsay, Jan M., Tim J. Worthington, Ian EM Smith and Philippa M. Black (1999). 'Geology, petrology, and petrogenesis of Little Barrier Island, Hauraki Gulf, New Zealand'. In: *New Zealand Journal of Geology and Geophysics* 42.2, pp. 155–168.
- Litchfield, Nj et al. (2014). 'A model of active faulting in New Zealand'. In: *New Zealand Journal of Geology and Geophysics* 57.1, pp. 32–56.
- Liu, Xinping, Karen C. McNally and Zheng-Kang Shen (1995). 'Evidence for a role of the downgoing slab in earthquake slip partitioning at oblique subduction zones'. In: *Journal of Geophysical Research: Solid Earth* 100.B8, pp. 15351–15372.
- Lohman, Rowena B. and Mark Simons (2005). 'Some thoughts on the use of InSAR data to constrain models of surface deformation: Noise structure and data downsampling'. In: *Geochemistry, Geophysics, Geosystems* 6.1.
- Lomax, Anthony, Jean Virieux, Philippe Volant and Catherine Berge-Thierry (2000). 'Probabilistic earthquake location in 3D and layered models'. In: *Advances in seismic event location*. Springer, pp. 101–134.
- Luis, JF and MC Neves (2006). 'The isostatic compensation of the Azores Plateau: A 3D admittance and coherence analysis'. In: *Journal of Volcanology and Geothermal Research* 156.1-2, pp. 10–22.
- Lyakhovsky, Vladimir, Yehuda Ben-Zion and Amotz Agnon (2001). 'Earthquake cycle, fault zones, and seismicity patterns in a rheologically layered lithosphere'. In: *Journal of Geophysical Research: Solid Earth* (1978–2012) 106.B3, pp. 4103–4120.
- Lyard, Florent, Fabien Lefevre, Thierry Letellier and Olivier Francis (2006). 'Modelling the global ocean tides: modern insights from FES2004'. In: *Ocean dynamics* 56.5-6, pp. 394–415.
- Maccaferri, Francesco, Eleonora Rivalta, Derek Keir and Valerio Acocella (2014). 'Off-rift volcanism in rift zones determined by crustal unloading'. In: *Nature Geoscience* 7.4, p. 297.
- Maeda, N. (1985). 'A method for reading and checking phase times in auto-processing system of seismic wave data'. In: *Zisin* 38.3. Cited By :110, pp. 365–379.
- Mao, Ailin, Christopher GA Harrison and Timothy H. Dixon (1999). 'Noise in GPS coordinate time series'. In: *Journal of Geophysical Research: Solid Earth* 104.B2, pp. 2797–2816.
- Marone, Chris J., CH Scholtz and Roger Bilham (1991). 'On the mechanics of earthquake afterslip'. In: *Journal of Geophysical Research: Solid Earth* 96.B5, pp. 8441–8452.
- Matthews, Kara J., Maria Seton and R. Dietmar Müller (2012). 'A global-scale plate reorganization event at 105–100 Ma'. In: *Earth and Planetary Science Letters* 355, pp. 283–298.

- Matthews, Kara J., Simon E. Williams et al. (2015). 'Geologic and kinematic constraints on Late Cretaceous to mid Eocene plate boundaries in the southwest Pacific'. In: *Earth-Science Reviews* 140, pp. 72–107.
- Maurer, Vincent et al. (2015). 'Seismic monitoring of the Rittershoffen EGS project (Alsace, France)'. In: *Proceedings World Geothermal Congress*, pp. 19–25.
- Maus, S. et al. (2009). 'EMAG2: A 2-arc min resolution Earth Magnetic Anomaly Grid compiled from satellite, airborne, and marine magnetic measurements'. In: *Geochemistry, Geophysics, Geosystems* 10.8.
- Mazzotti, Stéphane et al. (2003). 'Current tectonics of northern Cascadia from a decade of GPS measurements'. In: *Journal of Geophysical Research: Solid Earth* 108.B12.
- McCaffrey, Robert, Robert W. King, Suzette J. Payne and Matthew Lancaster (2013). 'Active tectonics of northwestern US inferred from GPS-derived surface velocities'. In: *Journal of Geophysical Research: Solid Earth* 118.2, pp. 709–723.
- McCaffrey, Robert, Anthony I. Qamar et al. (2007). 'Fault locking, block rotation and crustal deformation in the Pacific Northwest'. In: *Geophysical Journal International* 169.3, pp. 1315–1340.
- McCaffrey, Robert, Laura M. Wallace and John Beavan (2008). 'Slow slip and frictional transition at low temperature at the Hikurangi subduction zone'. In: *Nature Geoscience* 1.5, pp. 316–320.
- McCubbin, JC et al. (2017). 'Gravity anomaly grids for the New Zealand region'. In: *New Zealand Journal of Geology and Geophysics* 60.4, pp. 381–391.
- McDougall, Ian and Gerrit J van der Lingen (1974). 'Age of the rhyolites of the Lord Howe Rise and the evolution of the southwest Pacific Ocean'. In: *Earth and Planetary Science Letters* 21.2, pp. 117–126.
- McKenzie, Dan and Derek Fairhead (1997). 'Estimates of the effective elastic thickness of the continental lithosphere from Bouguer and free air gravity anomalies'. In: *Journal of Geophysical Research: Solid Earth* 102.B12, pp. 27523–27552.
- McNutt, Marcia (1980). 'Implications of regional gravity for state of stress in the Earth's crust and upper mantle'. In: *Journal of Geophysical Research: Solid Earth* 85.B11, pp. 6377–6396.
- Metzger, Sabrina et al. (2012). 'Present kinematics of the Tjörnes Fracture Zone, North Iceland, from campaign and continuous GPS measurements'. In: *Geophysical Journal International* 192.2, pp. 441–455.
- Meyer, B, R Saltus and A Chulliat (2017). 'EMAG2: Earth magnetic anomaly grid (2-arc-minute resolution) version 3'. In: *National Centers for Environmental Information, NOAA*. 10, V5H70CVX.
- Middlemiss, RP et al. (2016). 'Measurement of the Earth tides with a MEMS gravimeter'. In: *Nature* 531.7596, p. 614.
- Molnar, Peter, Tanya Atwater, Jacqueline Mammerickx and Stuart M Smith (1975). 'Magnetic anomalies, bathymetry and the tectonic evolution of the South Pacific since the Late Cretaceous'. In: *Geophysical Journal of the Royal Astronomical Society* 40.3, pp. 383–420.
- Molnar, Peter, Philip C England and Craig H Jones (2015). 'Mantle dynamics, isostasy, and the support of high terrain'. In: *Journal of Geophysical Research: Solid Earth* 120.3, pp. 1932–1957.
- Molnar, Peter and Dale Gray (1979). 'Subduction of continental lithosphere: Some constraints and uncertainties'. In: *Geology* 7.1, pp. 58–62.

- Molnar, Peter and Paul Tapponnier (1975). 'Cenozoic tectonics of Asia: effects of a continental collision'. In: *science* 189.4201, pp. 419–426.
- Morrison, Gregg W (1980). 'Characteristics and tectonic setting of the shoshonite rock association'. In: *Lithos* 13.1, pp. 97–108.
- Mortimer, N (2014). 'The oroclinal bend in the South Island, New Zealand'. In: *Journal of Structural Geology* 64, pp. 32–38.
- (2004). 'New Zealand's geological foundations'. In: *Gondwana Research* 7.1, pp. 261–272.
- Mortimer, N., PB Gans et al. (2010). 'Location and migration of Miocene-Quaternary volcanic arcs in the SW Pacific region'. In: *Journal of Volcanology and Geothermal Research* 190.1-2, pp. 1–10.
- Mortimer, N., R. H. Herzer, P. B. Gans, C. Laporte-Magoni et al. (2007). 'Oligocene-Miocene tectonic evolution of the South Fiji Basin and Northland Plateau, SW Pacific Ocean: Evidence from petrology and dating of dredged rocks'. In: *Marine Geology* 237.1-2, pp. 1–24.
- Mortimer, N., R. H. Herzer, P. B. Gans, D. L. Parkinson and D. Seward (1998). 'Basement geology from Three Kings Ridge to West Norfolk Ridge, southwest Pacific Ocean: evidence from petrology, geochemistry and isotopic dating of dredge samples'. In: *Marine Geology* 148.3-4, pp. 135–162.
- Mortimer, N., K. Hoernle et al. (2006). 'New constraints on the age and evolution of the Wishbone Ridge, southwest Pacific Cretaceous microplates, and Zealandia-West Antarctica breakup'. In: *Geology* 34.3, pp. 185–188.
- Mortimer, N., JI Raine and RA Cook (2009). 'Correlation of basement rocks from Waka Nui-1 and Awhitu-1, and the Jurassic regional geology of Zealandia'. In: *New Zealand Journal of Geology and Geophysics* 52.1, pp. 1–10.
- Mortimer, N., MS Rattenbury et al. (2014). 'High-level stratigraphic scheme for New Zealand rocks'. In: *New Zealand Journal of Geology and Geophysics* 57.4, pp. 402–419.
- Mortimer, N., AJ Tulloch and TR Ireland (1997). 'Basement geology of Taranaki and Wanganui Basins, New Zealand'. In: *New Zealand Journal of Geology and Geophysics* 40.2, pp. 223–236.
- Mortimer, N., AJ Tulloch, RN Spark et al. (1999). 'Overview of the Median Batholith, New Zealand: a new interpretation of the geology of the Median Tectonic Zone and adjacent rocks'. In: *Journal of African Earth Sciences* 29.1, pp. 257–268.
- Mortimer, N, FJ Davey, A Melhuish, J Yu and NJ Godfrey (2002). 'Geological interpretation of a deep seismic reflection profile across the Eastern Province and Median Batholith, New Zealand: crustal architecture of an extended Phanerozoic convergent orogen'. In: *New Zealand Journal of Geology and Geophysics* 45.3, pp. 349–363.
- Mortimer, N, M Patriat et al. (2015). 'The VESPA research cruise (volcanic evolution of South Pacific Arcs): A voyage of discovery to the Norfolk, Loyalty And Three Kings ridges, northeast Zealandia'. In: *Geoscience Society of New Zealand Miscellaneous Publication A* 143, pp. 98–99.
- Mortimer, Nick, Hamish J. Campbell et al. (2017). 'Zealandia: Earth's hidden continent'. In: *GSA Today* 27.3, pp. 27–35.

- Mortimer, Nick, Phillip B. Gans et al. (2014). 'Eocene and Oligocene basins and ridges of the Coral Sea-New Caledonia region: Tectonic link between Melanesia, Fiji, and Zealandia'. In: *Tectonics* 33.7, pp. 1386–1407.
- Mouslopoulou, V., A. Nicol, TA Little and JJ Walsh (2007a). 'Displacement transfer between intersecting regional strike-slip and extensional fault systems'. In: *Journal of Structural Geology* 29.1, pp. 100–116.
- (2007b). 'Terminations of large strike-slip faults: an alternative model from New Zealand'. In: *Geological Society, London, Special Publications* 290.1, pp. 387–415.
- Müller, R. Dietmar, Maria Sdrolias, Carmen Gaina and Walter R. Roest (2008). 'Age, spreading rates, and spreading asymmetry of the world's ocean crust'. In: *Geochemistry, Geophysics, Geosystems* 9.4.
- Naliboff, John B., Susanne JH Buiter, Gwenn Péron-Pinvidic, Per Terje Osmundsen and Joya Tetreault (2017). 'Complex fault interaction controls continental rifting'. In: *Nature Communications* 8.1, p. 1179.
- Nelson, Campbell S., Sandra L. Keane and Philip S. Head (1988). 'Non-tropical carbonate deposits on the modern New Zealand shelf'. In: *Sedimentary Geology* 60.1-4, pp. 71–94.
- Nicholson, K. N., P. M. Black, P. W. O. Hoskin and I. E. M. Smith (2004). 'Silicic volcanism and back-arc extension related to migration of the Late Cainozoic Australian-Pacific plate boundary'. In: *Journal of Volcanology and Geothermal Research* 131.3-4, pp. 295–306.
- Nicol, Andrew, Colin Mazengarb et al. (2007). 'Tectonic evolution of the active Hikurangi subduction margin, New Zealand, since the Oligocene'. In: *Tectonics* 26.4.
- Nicol, Andrew, John Walsh, Kelvin Berryman and Scott Nodder (2005). 'Growth of a normal fault by the accumulation of slip over millions of years'. In: *Journal of Structural Geology* 27.2, pp. 327–342.
- O'Neill, Craig, Dietmar Müller and Bernhard Steinberger (2005). 'On the uncertainties in hot spot reconstructions and the significance of moving hot spot reference frames'. In: *Geochemistry, Geophysics, Geosystems* 6.4.
- Okal, Emile A. (1988). 'Seismic parameters controlling far-field tsunami amplitudes: a review'. In: *Natural Hazards* 1.1, pp. 67–96.
- Okubo, Shuhei (1992). 'Gravity and potential changes due to shear and tensile faults in a half-space'. In: *Journal of Geophysical Research: Solid Earth* 97.B5, pp. 7137–7144.
- Parker, RL (1973). 'The rapid calculation of potential anomalies'. In: *Geophysical Journal of the Royal Astronomical Society* 31.4, pp. 447–455.
- Parsons, Barry and John G. Sclater (1977). 'An analysis of the variation of ocean floor bathymetry and heat flow with age'. In: *Journal of Geophysical Research* 82.5, pp. 803–827.
- Paterson, Norman R and Colin V Reeves (1985). 'Applications of gravity and magnetic surveys: The state-of-the-art in 1985'. In: *Geophysics* 50.12, pp. 2558–2594.
- Patriat, Martin et al. (2018). 'New Caledonia obducted peridotite nappe: Offshore extent and implications for obduction and postobduction processes'. In: *Tectonics* 37.4, pp. 1077–1096.
- Pavlis, Nikolaos K., Simon A. Holmes, Steve C. Kenyon and John K. Factor (2008). 'An earth gravitational model to degree 2160: EGM2008'. In: *EGU General Assembly* 10, pp. 13–18.

- Persaud, M. et al. (2016). 'The Kerepehi Fault, Hauraki Rift, North Island, New Zealand: active fault characterisation and hazard'. In: *New Zealand Journal of Geology and Geophysics* 59.1, pp. 117–135.
- Pillans, Brad (1986). 'A late quaternary uplift map for North Island, New Zealand'. In: *Royal Society of New Zealand Bulletin* 24, pp. 409–417.
- Pinet, N. and PR Cobbold (1992). 'Experimental insights into the partitioning of motion within zones of oblique subduction'. In: *Tectonophysics* 206.3, pp. 371–388.
- Rait, GJ (2000). 'Thrust transport directions in the Northland allochthon, New Zealand'. In: *New Zealand Journal of Geology and Geophysics* 43.2, pp. 271–288.
- Ramillien, Guillaume and Ian C. Wright (2002). 'Seamount gravity anomaly modelling with variably thick sediment cover'. In: *Marine Geophysical Research* 23.1, pp. 13–23.
- Ranalli, Giorgio and Donald C Murphy (1987). 'Rheological stratification of the lithosphere'. In: *Tectonophysics* 132.4, pp. 281–295.
- Rangin, C. et al. (1999). 'Plate convergence measured by GPS across the Sundaland/Philippine Sea plate deformed boundary: the Philippines and eastern Indonesia'. In: *Geophysical Journal International* 139.2, pp. 296–316.
- Rawlinson, Zara (2011). 'Microseismicity associated with actively exploited geothermal systems: earthquake detection and probabilistic location at Rotokawa and statistical seismic network design at Kawerau'. In:
- Rawson, Stephen John (1983). In: *A marine geophysical survey of the Hauraki Gulf*.
- Reford, MS (1980). 'Magnetic method'. In: *Geophysics* 45.11, pp. 1640–1658.
- Reilinger, Robert et al. (2006). 'GPS constraints on continental deformation in the Africa-Arabia-Eurasia continental collision zone and implications for the dynamics of plate interactions'. In: *Journal of Geophysical Research: Solid Earth* 111.B5.
- Reyes, A. G. (2015). 'Low-temperature geothermal reserves in New Zealand'. In: *Geothermics* 56, pp. 138–161.
- Reyners, Martin (2013). 'The central role of the Hikurangi Plateau in the Cenozoic tectonics of New Zealand and the Southwest Pacific'. In: *Earth and Planetary Science Letters* 361, pp. 460–468.
- (2018). 'Impacts of Hikurangi Plateau subduction on the origin and evolution of the Alpine Fault'. In: *New Zealand Journal of Geology and Geophysics*, pp. 1–12.
- Reyners, Martin, Donna Eberhart-Phillips, Graham Stuart and Yuichi Nishimura (2006). 'Imaging subduction from the trench to 300 km depth beneath the central North Island, New Zealand, with V<sub>p</sub> and V<sub>p</sub>/V<sub>s</sub>'. In: *Geophysical Journal International* 165.2, pp. 565–583.
- Robertson, David John (1983). In: *Paleomagnetism and geochronology of volcanics in the northern North Island, New Zealand*.
- Robertson, EI and WI Reilly (1960). 'The New Zealand primary gravity network'. In: *New Zealand Journal of Geology and Geophysics* 3.1, pp. 41–68.

- Rosen, Paul A. et al. (2000). 'Synthetic aperture radar interferometry'. In: *Proceedings of the IEEE* 88.3, pp. 333–382.
- Roser, BP, DS Coombs, RJ Korsch and JD Campbell (2002). 'Whole-rock geochemical variations and evolution of the arc-derived Murihiku Terrane, New Zealand'. In: *Geological Magazine* 139.6, pp. 665–685.
- Rößler, Dirk et al. (2016). 'Cluster-search based monitoring of local earthquakes in SeisComP3'. In: *AGU Fall Meeting Abstracts*.
- Rouillard, Pierrick et al. (2015). 'Seismic stratigraphy and paleogeographic evolution of Fairway Basin, Northern Zealandia, Southwest Pacific: from Cretaceous Gondwana breakup to Cenozoic Tonga–Kermadec subduction'. In: *Basin Research* 29, pp. 189–212.
- Rowland, JV and RH Sibson (2001). 'Extensional fault kinematics within the Taupo Volcanic Zone, New Zealand: soft-linked segmentation of a continental rift system'. In: *New Zealand Journal of Geology and Geophysics* 44.2, pp. 271–283.
- Rundle, John B (1978). 'Viscoelastic crustal deformation by finite quasi-static sources'. In: *Journal of Geophysical Research: Solid Earth* 83.B12, pp. 5937–5945.
- Rychert, Catherine A. et al. (2012). 'Volcanism in the Afar Rift sustained by decompression melting with minimal plume influence'. In: *Nature Geoscience* 5.6, p. 406.
- Sandwell, David T., R. Dietmar Müller, Walter H. F. Smith, Emmanuel Garcia and Richard Francis (2014). 'New global marine gravity model from CryoSat-2 and Jason-1 reveals buried tectonic structure'. In: *Science* 346.6205, pp. 65–67.
- Sandwell, David T. and Walter HF Smith (2009). 'Global marine gravity from retracked Geosat and ERS-1 altimetry: Ridge segmentation versus spreading rate'. In: *Journal of Geophysical Research: Solid Earth* 114.B1.
- Sandwell, David T. and Paul Wessel (2016). 'Interpolation of 2-D vector data using constraints from elasticity'. In: *Geophysical Research Letters* 43.20.
- Savage, JC and RO Burford (1973). 'Geodetic determination of relative plate motion in central California'. In: *Journal of Geophysical Research* 78.5, pp. 832–845.
- Schellart, W. P., G. S. Lister and V. G. Toy (2006). 'A Late Cretaceous and Cenozoic reconstruction of the Southwest Pacific region: Tectonics controlled by subduction and slab rollback processes'. In: *Earth-Science Reviews* 76.3-4, pp. 191–233.
- Schellart, Wouter P. (2007). 'North-eastward subduction followed by slab detachment to explain ophiolite obduction and Early Miocene volcanism in Northland, New Zealand'. In: *Terra Nova* 19.3, pp. 211–218.
- Schellart, WP (2004). 'Quantifying the net slab pull force as a driving mechanism for plate tectonics'. In: *Geophysical Research Letters* 31.7.
- Schellart, WP, BLN Kennett, W. Spakman and M. Amaru (2009). 'Plate reconstructions and tomography reveal a fossil lower mantle slab below the Tasman Sea'. In: *Earth and Planetary Science Letters* 278.3-4, pp. 143–151.

- Schellart, WP and W. Spakman (2012). 'Mantle constraints on the plate tectonic evolution of the Tonga-Kermadec-Hikurangi subduction zone and the South Fiji Basin region'. In: *Australian Journal of Earth Sciences* 59.6, pp. 933–952.
- Schmeling, Harro and Herbert Wallner (2012). 'Magmatic lithospheric heating and weakening during continental rifting: A simple scaling law, a 2-D thermomechanical rifting model and the East African Rift System'. In: *Geochemistry, Geophysics, Geosystems* 13.8.
- Schmidt, Max W. and Stefano Poli (1998). 'Experimentally based water budgets for dehydrating slabs and consequences for arc magma generation'. In: *Earth and Planetary Science Letters* 163.1-4, pp. 361–379.
- Slater, John G, Lawrence A Lawver and Barry Parsons (1975). 'Comparison of long-wavelength residual elevation and free air gravity anomalies in the North Atlantic and possible implications for the thickness of the lithospheric plate'. In: *Journal of Geophysical Research* 80.8, pp. 1031–1052.
- Scotese, Christopher R, Lisa M Gahagan and Roger L Larson (1988). 'Plate tectonic reconstructions of the Cretaceous and Cenozoic ocean basins'. In: *Tectonophysics* 155.1-4, pp. 27–48.
- Sdrolias, M, RD Müller and C Gaina (2001). 'Plate tectonic evolution of eastern Australian marginal ocean basins'. In:
- Sdrolias, Maria, R. Dietmar Müller, Alain Mauffret and George Bernardel (2004). 'Enigmatic formation of the Norfolk Basin, SW Pacific: A plume influence on back-arc extension'. In: *Geochemistry, Geophysics, Geosystems* 5.6, n/a–n/a.
- Seebeck, Hannu, Andrew Nicol, Marc Giba, Jarg Pettinga and John Walsh (2014). 'Geometry of the subducting Pacific plate since 20 Ma, Hikurangi margin, New Zealand'. In: *Journal of the Geological Society* 171.1, pp. 131–143.
- Seebeck, Hannu, Andrew Nicol, Pilar Villamor, John Ristau and Jarg Pettinga (2014). 'Structure and kinematics of the Taupo Rift, New Zealand'. In: *Tectonics* 33.6, pp. 1178–1199.
- Seeber, Günter (2003). *Satellite geodesy: foundations, methods, and applications*. Walter de Gruyter.
- Segev, Amit, Michael Rybakov and Nick Mortimer (2012). 'A crustal model for Zealandia and Fiji'. In: *Geophysical Journal International* 189.3, pp. 1277–1292.
- Sherburn, Steven, Stephen Bannister and Hugh Bibby (2003). 'Seismic velocity structure of the central Taupo Volcanic Zone, New Zealand, from local earthquake tomography'. In: *Journal of Volcanology and Geothermal Research* 122.1, pp. 69–88.
- Sherburn, Steven and Robert S. White (2005). 'Crustal seismicity in Taranaki, New Zealand using accurate hypocentres from a dense network'. In: *Geophysical journal international* 162.2, pp. 494–506.
- Sibson, Richard H. and Julie V. Rowland (2003a). 'Stress, fluid pressure and structural permeability in seismogenic crust, North Island, New Zealand'. In: *Geophysical Journal International* 154.2, pp. 584–594.
- (2003b). 'Stress, fluid pressure and structural permeability in seismogenic crust, North Island, New Zealand'. In: *Geophysical Journal International* 154.2, pp. 584–594.

- Sleeman, Reinoud and Torild Van Eck (1999). 'Robust automatic P-phase picking: an on-line implementation in the analysis of broadband seismogram recordings'. In: *Physics of the Earth and Planetary Interiors* 113.1-4, pp. 265–275.
- Smith, Ian EM, T Okada, T Itaya and Philippa M Black (1993). 'Age relationships and tectonic implications of late Cenozoic basaltic volcanism in Northland, New Zealand'. In: *New Zealand Journal of Geology and Geophysics* 36.3, pp. 385–393.
- Smith, N, J Cassidy, CA Locke, JL Mauk and AB Christie (2006). 'The role of regional-scale faults in controlling a trapdoor caldera, Coromandel Peninsula, New Zealand'. In: *Journal of Volcanology and Geothermal Research* 149.3-4, pp. 312–328.
- Smith, Walter HF and David T. Sandwell (1997). 'Global sea floor topography from satellite altimetry and ship depth soundings'. In: *Science* 277.5334, pp. 1956–1962.
- Smith, Warwick D. (1979). 'Documentation for earthquake location programs LOCAL and MICRO and supporting software'. In: *Geophysics Division. Department of Scientific and Industrial Research, Wellington* 80, pp. 1–35.
- Smith, WHF and P. Wessel (1990). 'Gridding with continuous curvature splines in tension'. In: *Geophysics* 55.3, pp. 293–305.
- Smithson, Scott B, Jon Brewer, S Kaufman, Jack Oliver and Charles Hurich (1978). 'Nature of the Wind River thrust, Wyoming, from COCORP deep-reflection data and from gravity data'. In: *Geology* 6.11, pp. 648–652.
- Spandler, Carl, Kurt Worden, Richard Arculus and Steve Eggins (2005). 'Igneous rocks of the Brook Street Terrane, New Zealand: implications for Permian tectonics of eastern Gondwana and magma genesis in modern intra-oceanic volcanic arcs'. In: *New Zealand Journal of Geology and Geophysics* 48.1, pp. 167–183.
- Spörli, KB (1989). 'Tectonic framework of Northland, New Zealand'. In: *Royal Society of New Zealand Bulletin* 26, pp. 3–14.
- Spörli, KB and Rebecca E. Harrison (2004). 'Northland Allochthon infolded into basement, Whangarei area, northern New Zealand'. In: *New Zealand Journal of Geology and Geophysics* 47.3, pp. 391–398.
- Stagpoole, M et al. (2011). 'Northland airborne magnetic and radiometric survey: a geological interpretation'. In: *GNS Science Report* 54, p. 113.
- Stagpoole, V. and A. Nicol (2008). 'Regional structure and kinematic history of a large subduction back thrust: Taranaki Fault, New Zealand'. In: *Journal of Geophysical Research: Solid Earth (1978-2012)* 113.B1.
- Stagpoole, Vaughan and Rob Funnell (2001). 'Arc magmatism and hydrocarbon generation in the northern Taranaki Basin, New Zealand'. In: *Petroleum Geoscience* 7.3, pp. 255–267.
- Stagpoole, V et al. (Jan. 2009). 'Petroleum prospectivity of Reinga Basin, New Zealand. (Seisware 2D seismic interpretation and incorporation of 1D basin modelling, swath bathymetry, NPA satellite seep analysis, tide history, fishing boat logs)'. In: *GNS Science Consultancy Report*.

- Steblov, GM, NF Vasilenko, AS Prytkov, DI Frolov and TA Grekova (2010). 'Dynamics of the Kuril-Kamchatka subduction zone from GPS data'. In: *Izvestiya, Physics of the Solid Earth* 46.5, pp. 440–445.
- Stern, T. A., G. M. Quinlan and W. E. Holt (1992). 'Basin formation behind an active subduction zone: three-dimensional flexural modelling of Wanganui Basin, New Zealand'. In: *Basin Research* 4.3-4, pp. 197–214.
- (1992). 'Basin formation behind an active subduction zone: three-dimensional flexural modelling of Wanganui Basin, New Zealand'. In: *Basin research* 4.3-4, pp. 197–214.
- Stern, Tim, EGC Smith, FJ Davey and KJ Muirhead (1987). 'Crustal and upper mantle structure of the northwestern North Island, New Zealand, from seismic refraction data'. In: *Geophysical Journal International* 91.3, pp. 913–936.
- Strong, DT, RE Turnbull, S. Haubrock and N. Mortimer (2016). 'Petlab: New Zealand's national rock catalogue and geoanalytical database'. In: *New Zealand Journal of Geology and Geophysics* 59.3, pp. 475–481.
- Sutherland, Rupert (1995). 'The Australia-Pacific boundary and Cenozoic plate motions in the SW Pacific: Some constraints from Geosat data'. In: *Tectonics* 14.4, pp. 819–831.
- (1999a). 'Basement geology and tectonic development of the greater New Zealand region: an interpretation from regional magnetic data'. In: *Tectonophysics* 308.3, pp. 341–362.
  - (1999b). 'Cenozoic bending of New Zealand basement terranes and Alpine Fault displacement: a brief review'. In: *New Zealand Journal of Geology and Geophysics* 42.2, pp. 295–301.
- Sutherland, Rupert, L Alegret et al. (2018). *Tasman frontier subduction initiation and paleogene climate*. Tech. rep.
- Sutherland, Rupert, Julien Collot et al. (2010). 'Lithosphere delamination with foundering of lower crust and mantle caused permanent subsidence of New Caledonia Trough and transient uplift of Lord Howe Rise during Eocene and Oligocene initiation of Tonga-Kermadec subduction, western Pacific'. In: *Tectonics* 29.2.
- Sutherland, Rupert, P. Viskovic et al. (2012). *Compilation of seismic reflection data from the Tasman Frontier region, southwest Pacific*. GNS Science.
- Syracuse, Ellen M. and Geoffrey A. Abers (2006). 'Global compilation of variations in slab depth beneath arc volcanoes and implications'. In: *Geochemistry, Geophysics, Geosystems* 7.5.
- Tearney, Kevin William (1980). In: *A marine geophysical study of the Hauraki Depression, North Island, New Zealand*.
- Tenzer, R. and V. Gladkikh (2014). 'Assessment of density variations of marine sediments with ocean and sediment depths'. eng. In: *The Scientific World Journal* 2014, pp. 823–296.
- Tenzer, Robert, Wenjin Chen and Shuanggen Jin (2015). 'Effect of upper mantle density structure on Moho geometry'. In: *Pure and Applied Geophysics* 172.6, pp. 1563–1583.

- Topper, Jeffrey and Takuji Kawahara (1978). 'Approximate equations for long nonlinear waves on a viscous fluid'. In: *Journal of the Physical society of Japan* 44.2, pp. 663–666.
- Tregoning, Paul et al. (2013). 'A decade of horizontal deformation from great earthquakes'. In: *Journal of Geophysical Research: Solid Earth* 118.5, pp. 2371–2381.
- Trenkamp, Robert, James N. Kellogg, Jeffrey T. Freymueller and Hector P. Mora (2002). 'Wide plate margin deformation, southern Central America and northwestern South America, CASA GPS observations'. In: *Journal of South American Earth Sciences* 15.2, pp. 157–171.
- Trnkoczy, Amadej (1999). 'Topic Understanding and parameter setting of STA/LTA trigger algorithm'. In: *New manual of seismological observatory practice* 2.
- Turcotte, DL and G Schubert (2002). *Geodynamics*, 456 pp.
- Turino, Chiara, Paola Morasca, Gabriele Ferretti, Davide Scafidi and Daniele Spallarossa (2010). 'Reliability of the automatic procedures for locating earthquakes in southwestern Alps and northern Apennines (Italy)'. In: *Journal of Seismology* 14.2, pp. 393–411.
- Twiss, Robert J. and Eldridge M. Moores (1992). *Structural geology*. Macmillan.
- Uruski, Chris (2015). 'The contribution of offshore seismic data to understanding the evolution of the New Zealand continent'. In: *Geological Society, London, Special Publications* 413.1, pp. 35–51.
- Vere-Jones, D. and RB Davies (1966). 'A statistical survey of earthquakes in the main seismic region of New Zealand: Part 2-Time series analyses'. In: *New Zealand Journal of Geology and Geophysics* 9.3, pp. 251–284.
- Walcott, RI (1970). 'Flexural rigidity, thickness, and viscosity of the lithosphere'. In: *Journal of Geophysical Research* 75.20, pp. 3941–3954.
- (1984). 'The kinematics of the plate boundary zone through New Zealand: a comparison of short-and long-term deformations'. In: *Geophysical Journal International* 79.2, pp. 613–633.
  - (1987). 'Geodetic strain and the deformational history of the North Island of New Zealand during the late Cainozoic'. In: *Philosophical Transactions of the Royal Society of London A: Mathematical, Physical and Engineering Sciences* 321.1557, pp. 163–181.
  - (1989). 'Paleomagnetically observed rotations along the Hikurangi margin of New Zealand'. In: *Paleomagnetic rotations and continental deformation*. Springer, pp. 459–471.
- Waldhauser, Felix and David P Schaff (2008). 'Large-scale relocation of two decades of northern California seismicity using cross-correlation and double-difference methods'. In: *Journal of Geophysical Research: Solid Earth* 113.B8.
- Wallace, Laura M. and John Beavan (2006). 'A large slow slip event on the central Hikurangi subduction interface beneath the Manawatu region, North Island, New Zealand'. In: *Geophysical Research Letters* 33.11.
- (2010). 'Diverse slow slip behavior at the Hikurangi subduction margin, New Zealand'. In: *Journal of Geophysical Research: Solid Earth* 115.B12.

- Wallace, Laura M., John Beavan, Stephen Bannister and Charles Williams (2012). 'Simultaneous long-term and short-term slow slip events at the Hikurangi subduction margin, New Zealand: Implications for processes that control slow slip event occurrence, duration, and migration'. In: *Journal of Geophysical Research: Solid Earth* 117.B11.
- Wallace, Laura M., John Beavan, Robert McCaffrey and Desmond Darby (2004). 'Subduction zone coupling and tectonic block rotations in the North Island, New Zealand'. In: *Journal of Geophysical Research: Solid Earth* (1978-2012) 109.B12.
- Wallace, Laura M., Sigrun Hreinsdóttir et al. (2018). 'Triggered slow slip and afterslip on the southern Hikurangi subduction zone following the Kaikōura earthquake'. In: *Geophysical Research Letters*.
- Wallace, Laura M., Martin Reyners et al. (2009). 'Characterizing the seismogenic zone of a major plate boundary subduction thrust: Hikurangi Margin, New Zealand'. In: *Geochemistry, Geophysics, Geosystems* 10.10.
- Wang, Yun, Donald W. Forsyth and Brian Savage (2009). 'Convective upwelling in the mantle beneath the Gulf of California'. In: *Nature* 462.7272, p. 499.
- Watts, AB (1982). 'Gravity anomalies over oceanic rifts'. In: *Continental and Oceanic Rifts*, pp. 99–105.
- Watts, AB and James R Cochran (1974). 'Gravity anomalies and flexure of the lithosphere along the Hawaiian-Emperor seamount chain'. In: *Geophysical Journal International* 38.1, pp. 119–141.
- Weber, B. et al. (2007). 'SeisComP3 Automatic and interactive real time data processing'. In: *Geophysical Research Abstracts*. Vol. 9. Chap. 09,219.
- Welch, Peter (1967). 'The use of fast Fourier transform for the estimation of power spectra: a method based on time averaging over short, modified periodograms'. In: *IEEE Transactions on Audio and Electroacoustics* 15.2, pp. 70–73.
- Wessel, Paul (2015). 'Regional–residual separation of bathymetry and revised estimates of Hawaii plume flux'. In: *Geophysical Journal International* 204.2, pp. 932–947.
- Whattam, Scott A., John Malpas, Jason R. Ali and Ian EM Smith (2008). 'New SW Pacific tectonic model: Cyclical intraoceanic magmatic arc construction and near-coeval emplacement along the Australia-Pacific margin in the Cenozoic'. In: *Geochemistry, Geophysics, Geosystems* 9.3.
- Wijk, JW Van, RS Huismans, M. Ter Voorde and SAPL Cloetingh (2001). 'Melt generation at volcanic continental margins: no need for a mantle plume?' In: *Geophysical Research Letters* 28.20, pp. 3995–3998.
- Williams, AL et al. (2006). 'Active Faulting in the Auckland Region'. In: *Earthquakes and Urban Development: New Zealand Geotechnical Society 2006 Symposium, Nelson, February 2006*. Institution of Professional Engineers New Zealand, p. 23.
- Williams, Simon DP (2003a). 'Offsets in global positioning system time series'. In: *Journal of Geophysical Research: Solid Earth* 108.B6.
- (2003b). 'The effect of coloured noise on the uncertainties of rates estimated from geodetic time series'. In: *Journal of Geodesy* 76.9-10, pp. 483–494.
  - (2008). 'CATS: GPS coordinate time series analysis software'. In: *GPS Solutions* 12.2, pp. 147–153.

- Williams, Simon DP, Yehuda Bock et al. (2004). 'Error analysis of continuous GPS position time series'. In: *Journal of Geophysical Research: Solid Earth* 109.B3.
- Williams, Simon DP and NT Penna (2011). 'Non-tidal ocean loading effects on geodetic GPS heights'. In: *Geophysical Research Letters* 38.9.
- Williams, Simon DP and Pascal Willis (2006). 'Error analysis of weekly station coordinates in the DORIS network'. In: *Journal of Geodesy* 80.8-11, pp. 525–539.
- Wilson, CJN, BF Houghton et al. (1995). 'Volcanic and structural evolution of Taupo Volcanic Zone, New Zealand: a review'. In: *Journal of Volcanology and Geothermal Research* 68.1-3, pp. 1–28.
- Wilson, CJN, AM Rogan et al. (1984). 'Caldera volcanoes of the Taupo volcanic zone, New Zealand'. In: *Journal of Geophysical Research: Solid Earth* 89.B10, pp. 8463–8484.
- Wise, Darryn J., John Cassidy and Corinne A. Locke (2003). 'Geophysical imaging of the quaternary Wairoa North Fault, New Zealand: a case study'. In: *Journal of Applied Geophysics* 53.1, pp. 1–16.
- Wittlinger, G, G Herquel and T Nakache (1993). 'Earthquake location in strongly heterogeneous media'. In: *Geophysical Journal International* 115.3, pp. 759–777.
- Wood, RA and VM Stagpoole (2007). 'Validation of tectonic reconstructions by crustal volume balance: New Zealand through the Cenozoic'. In: *Geological Society of America Bulletin* 119.7-8, pp. 933–943.
- Wortel, MJR and Wim Spakman (2000). 'Subduction and slab detachment in the Mediterranean-Carpathian region'. In: *Science* 290.5498, pp. 1910–1917.
- Zhang, Jie et al. (1997). 'Southern California Permanent GPS Geodetic Array: Error analysis of daily position estimates and site velocities'. In: *Journal of Geophysical Research: Solid Earth* 102.B8, pp. 18035–18055.
- Zhou, Rongmao, Lianjie Huang and James Rutledge (2010). 'Microseismic event location for monitoring CO<sub>2</sub> injection using double-difference tomography'. In: *The Leading Edge* 29.2, pp. 208–214.
- Zhu, SY and E Groten (1989). 'Various aspects of numerical determination of nutation constants. I-Improvement of rigid-earth nutation'. In: *The Astronomical Journal* 98, pp. 1104–1111.
- Zumberge, JF, MB Heflin, DC Jefferson, MM Watkins and Frank H. Webb (1997). 'Precise point positioning for the efficient and robust analysis of GPS data from large networks'. In: *Journal of Geophysical Research: Solid Earth* 102.B3, pp. 5005–5017.